

ISSN 0911-5730

UVSOR-51

August 2024

UVSOR ACTIVITY REPORT 2023

UVSOR Synchrotron Facility
Institute for Molecular Science
National Institutes of Natural Sciences



Preface



This Activity Report covers scientific and technological activities carried out using the UVSOR-III Synchrotron in FY2023 (April 2023 - March 2024). We present scientific examples of how the users study at the UVSOR Synchrotron Facility.

The present UVSOR-III Synchrotron is one of the most advanced low-energy SR facilities of the 3rd generation SR in the world and is now one of the critical resources to accelerate the investigation of molecular science. The UVSOR-III Synchrotron has a small electron storage ring but has powerful 6-undulator beamlines (3 VUV and 3 in-vacuum soft X-ray undulators) with 7-dipole beamlines. The BL2B of ARPES beamline has been closed for user operation, the function for the ARPES for organic materials has been moved to BL4B. We continue improving and upgrading our micro- and nano-scale photoabsorption and photoemission approaches and in situ/operando measurements in the IR, VUV, and soft X-ray regions, based on our strategic international collaboration program in molecular

science. We will also carry out a feasibility study to develop the instrumentation to be adopted for a complicated and inhomogeneous sample system. Since winter 2023, the beam current cannot cover the 300-mA operation due to lower efficiency of the electron beam injection. We are struggling to solve this problem, but it remains to be unsolved at the moment, and to the operation below 200 mA will have to be maintained till the end of FY2024. We are grateful to all the people who use our facility and support our efforts.

UVSOR operates for 40 weeks/year (ca. 2,200 h user time for 36 weeks), accepts ~230 proposals, about ~500 individual researchers counting total ~5,000 people*day/year. Most users stay for one or two weeks for experimenting. To continue high-level achievements in science and technology at the UVSOR-III Synchrotron, our in-house staff is constantly committed to maintaining and improving high-performance accelerators and beamlines.

On the experimental side, technological development never stops, hence we will make a progress on the operando and/or imaging-related techniques to inspire advanced molecular science. We have started to construct the new end-station at the undulator-based soft X-ray beamline BL6U since 2020. The cutting-edge instrumentation of the photoelectron momentum microscope (PMM) with a double-hemispherical analyzer with 2D spin detector. The present status of the instrumental development is summarized in this article. In the beamline BL1U, we have conducted in developing the novel light sources, including novel experiments using twin-Undulator configuration to demonstrate atto-second interference experiments. The advanced SR-related instrument will offer opportunities in characterizing the electronic structure of surface atomic sites, thin films, molecular adsorbates, bulk crystals, and so on.

We have discussed to construct the post-UVSOR-III as a long-term plan for sustainable development since 2019 (find the special website*). In FY2023, we hold several workshops for discussing the perspectives, including UVSOR's 40th anniversary commemorative event** and the annual UVSOR users' meeting with the 6th Next-Facility-Construction Review Meeting entitled "Development of Photoscience in Biosystems" to achieve our goal of merging different fields of life science and photoscience. We look forward to receiving your feedback and suggestions on the continuing evolution of the UVSOR Synchrotron Facility. We hope many users will perform excellent work by fully utilizing the UVSOR-III Synchrotron as a unique international hub for the SR research in advanced molecular science.

*"Next-Generation Facility Home Page"



***"Meeting Report: UVSOR Synchrotron Facility 40th Anniversary"



April 2024

Satoshi Kera

Director of the UVSOR Synchrotron Facility

UVSOR 40th Commemorative Lecture and Ceremony were held on December 1st, 2023

UVSOR 40th Commemorative Lecture and Ceremony were held on December 1st, 2023. The event was followed by the UVSOR Symposium 2023 held on December 2-3. In the Commemorative Lecture, opening addresses by distinguished guests and six lectures were given. With the event, "The 40th Book" and "UVSOR-IV Conceptual Design Report (Ver. 1.1)" were published.



"The 40th Book"



"Conceptual Design Report"

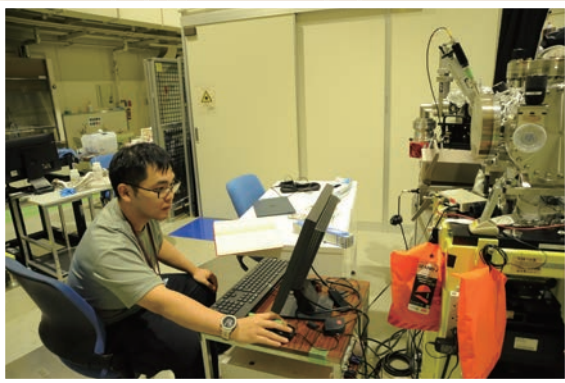
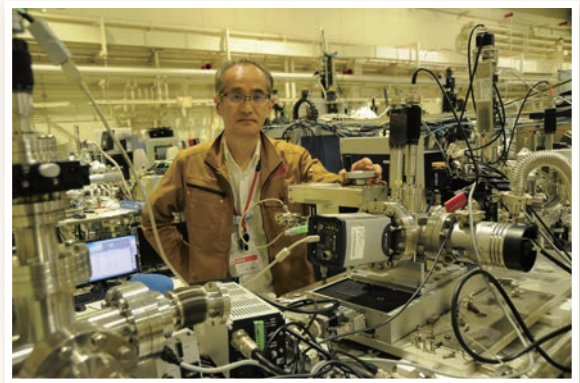
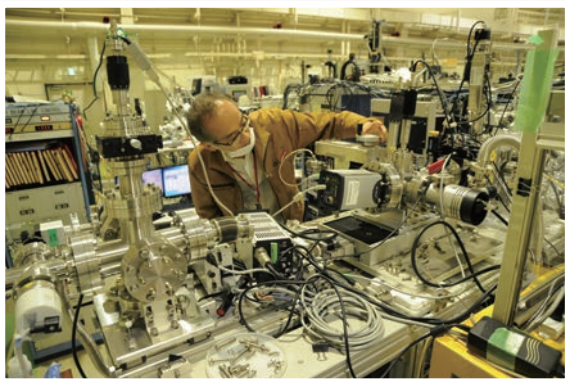
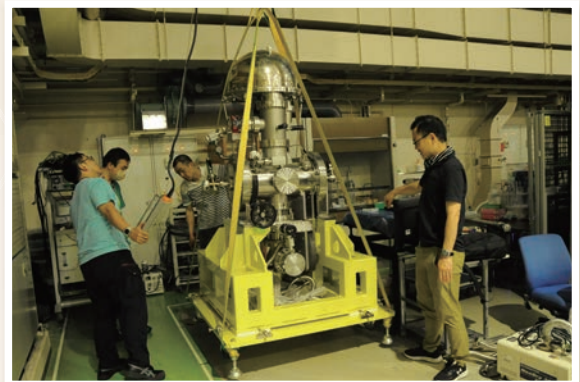
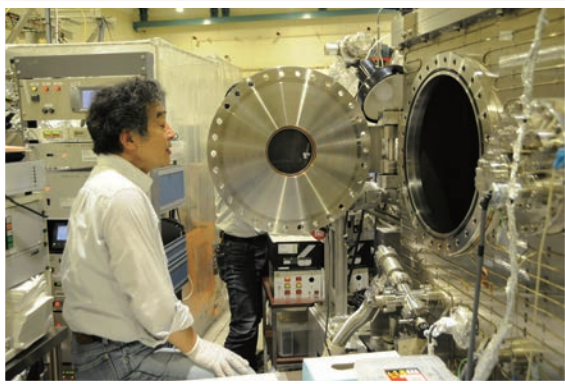
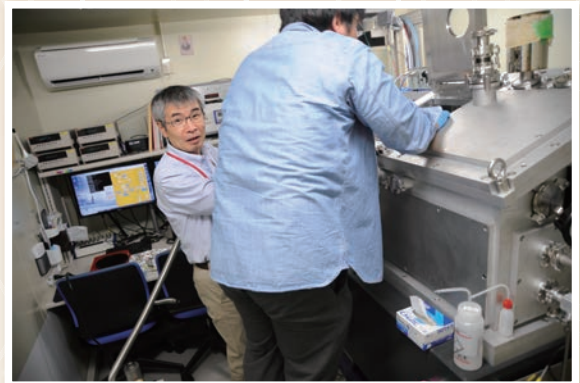
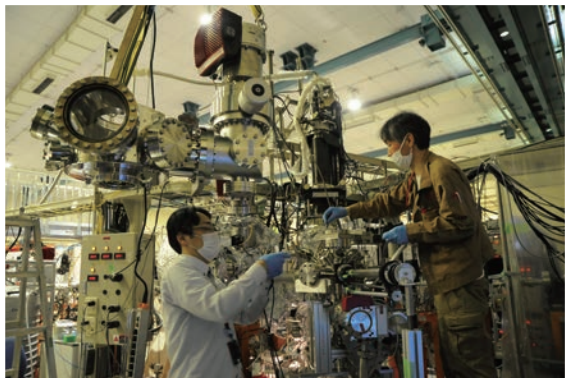


The Encouragement Award of the Japanese Positron Science Society Given to Associate Professor Yoshikata Taira in the UVSOR Synchrotron Facility

Associate Professor Yoshikata Taira received the Encouragement Award of the Japanese Positron Science Society for his work on “Development of positron annihilation spectroscopy using ultrashort pulsed gamma-rays at UVSOR”. The Encouragement Award of the Japanese Positron Science Society is intended to encourage researchers who are expected to play an important role in the field of positron science in the future.



Staff



UVSOR ACTIVITY REPORT 2023

Preface

S. Kera

News

I Organization and Staff List

1

II Current Status of Light Sources and Beamlines

9

Light Source in 2023 (Y. Taira)

11

Beamlines in 2023 (F. Matsui)

14



The Dual-Beamline Photoelectron Momentum Microscope
at UVSOR [6U, 7U]

F. Matsui, K. Hagiwara, Y. Sato, E. Nakamura, T. Yano,
Y. Okano, S. Makita, R. Sagehashi, S. Kera,
Shin-ichiro Tanaka and S. Suga

31

III Research Activities

III-1 Accelerators and Instruments

39



Spin-Polarized Band Mapping in Au(111) Surface States [5U]
J. Okabayashi and K. Tanaka

41

Improvement of Accuracy of Non-Destructive Nuclide Assay by
Transmission NRF Method [1U]

T. Shizuma, M. Omer, R. Hajima, M. Koizumi, H. Zen, H. Ohgaki and
Y. Taira

42

Gamma-ray Polarization Measurement with GAGG Pixel Detectors
[1U]

K. Shimazoe, R. Sato, M. Uenomachi and Y. Taira

43

Generation of F-LCS Gamma-rays for Isotope Selective Imaging Study
in UVOSR BL1U [1U]


H. Ohgaki, S. Tanizaki, H. Zen, T. Kii, T. Hayakawa and T. Shizuma

44

Experimental Study on Radiation from Single Electron [1U]

Y. Asai, H. Miyauchi, M. Shimada and M. Katoh

45

Frequency-Domain Determination of Time Delay between Two Light Wave Packets Generated by a Tandem Undulator [1U] Y. Hikosaka, T. Kaneyasu, S. Wada, H. Kohguchi, H. Ota, E. Nakamura, H. Iwayama, M. Fujimoto, M. Hosaka and M. Katoh	46
Diffraction of Optical Vortex from Undulator [1U] Y. Nishihara, M. Shimada, H. Miyauchi, K. Matsuo and M. Katoh	47
Evaluation of CMOS Detector Abord the Sounding Rocket Experiment FOXSI-4 for a Solar Flare Observation in X-rays [2A] N. Narukage, R. Shimizu, Y. Sato and S. Kashima	48
Development of Operando Measurement of Battery Materials by Soft X-ray Absorption Spectroscopy using Sample Transfer Vessel [2A] E. Kobayashi and A. Inoishi	49
Reflectivity Measurement on SiC/Mo/Si Multilayer Coated Mirrors for Future Planetary Exploration [5B] M. Kuwabara, Y. Suzuki, A. Yamazaki and I. Yoshikawa	50
Radiometric Calibration of a High-Resolution EUV Spectrometer [5B] T. Kawate, H. A. Sakaue and C. Suzuki	51
Calibration of Position-Sensitive Microchannel Plate Detectors [5B] S. Matoba, S. Kanda, H. Ohshita, K. Hirata, H. Iwayama and T. Kaneyasu	52
Development of a Program to Analysis Multi-Dimensional Data of the Photoelectron Momentum Microscopy [6U] S. Tanaka	53
Numerical Correction of α^2 Aberration on PMM Imaging at BL6U [6U] R. Sagehashi, K. Hagiwara, S. Kera and F. Matsui	54
Development of Dual-Beamline Photoelectron Momentum Microscope [6U, 7U] K. Hagiwara, E. Nakamura, S. Makita, S. Suga, S. Tanaka, S. Kera and F. Matsui	55
Development of a Uniaxial Pressure Cell for Infrared and ARPES Measurements [6B] H. Watanabe, H. Ishida and S. Kimura	56
Performance Evaluation of Nuclear Emulsion Sensitized by Hydrogen Gas [Others] H. Rokujo, Y. Isayama and T. Nakano	57
III-2 Material Sciences	59
 Anisotropy in the Far-Infrared Absorption Davydov Doublet of the Single-Crystal Pentacene [6B] Y. Nakayama, K. Yamauchi, Y. Baba and J. Miyamoto	61

Change in Positron Lifetime of Deformed Pure Iron before and after Unloading Tensile Stress [1U] M. Fujinami, R. Awaji, H. Abe, A. Yabuuchi, T. Hirade, N. Oshima and Y. Taira	62
Changes of the Gamma-ray Induced Positron Annihilation Lifetimes for CeO ₂ by Desorption and Re-adsorption of Surface Adsorption Species [1U] S. Dohshi, K. Maeda, Y. Taira and T. Hirade	63
GiPALS Study of Ca ₂ MgSi ₂ O ₇ :Eu,Dy Long-Persistent Phosphorescence Phosphors [1U] M. Kitaura, H. Masai, S. Watanabe and Y. Taira	64
Gamma-ray Induced Positron Annihilation Lifetime Spectroscopy of As-Doped CdTe [1U] T. Sumi, M. Kitaura, A. Nagaoka, Y. Taira, H. Masai and K. Kimura	65
Study on Evaluation of Material Defects by Positron Annihilation Method Using Ultrashort Pulsed Gamma Rays [1U] Y. Takashima, N. Kishimoto and Y. Taira	66
Change in Positron Lifetime of Tungsten Caused by Electrolytic Hydrogen Charging [1U] A. Yabuuchi, T. Hirade, R. Awaji, M. Fujinami, N. Oshima, K. Saito, K. Takai and Y. Taira	67
Attempts for Intermolecular Phonon Measurement of High Mobility Organic Semiconductors by Terahertz Absorption Spectroscopy [1B] K. Yamauchi, Y. Baba and Y. Nakayama	68
Local Structure of Catalytically Active Mo-Carbide Species on H-MFI Zeolites for Methane Aromatization at High Pressure [2A] K. Kuramochi, A. Kosuge, Y. Sonobe, Y. Uchimura and H. Aritani	69
X-ray Absorpton Near Edge Structure Analysis of Deintercalation of Ni-Al Layered Double Hydroxide Dense Bodies [2A] H. Murata, K. Yone and A. Nakahira	70
Local Structure Investigations of Zincate Spinel [2A] S. Yoshioka, E. Kobayashi and K. Okudaira	71
Direct Observation of 4-Layer Structure in the Chiral SmC Variant Phase Delicate Balance of Ferroelectricity and Antiferroelectricity by Resonant Soft X-ray Scattering (RSoXS) at UVSOR [3U] Y. Takanishi, F. Araoka and H. Iwayama	72
Evaluation of Measurements of Fluorescence Lifetimes in Multi Bunch Mode [3B, 7B] Y. Tajima, Y. Hayashi, K. Shintate, R. Abe, T. Naito, S. Sakano and H. Y. Yoshida	73
Effect of Ce Co-Doping to Cr:GGG as a Scintillator for Dose-Rate Monitoring System [3B] D. Matsukura, S. Kurosawa, C. Fujiwara and A. Yamaji	74

Optical Properties of Li-Containing $\text{Cs}_3\text{Cu}_2\text{I}_5$ for Neutron Monitor [3B] Y. Urano, S. Kurosawa and A. Yamaji	75
Luminescence Characteristics of Synthetic Diamonds [3B] A. Umemoto	76
Photoluminescence Properties of CsI Crystals Obtained Via the Melt Aging Procedure Using I_2 Gas [3B] S. Omiya, S. Kodama, N. Shimoyama, T. Saito, I. Yanase and H. Takeda	77
Bandgap Determination of CaCO_3 by Excitation Spectrum in the VUV Range [3B] H. Miyata and J. Ueda	78
Luminescence Properties of CsAg_2I_3 and Cs_2AgI_3 Crystals [3B] T. Kawai and S. Ibuki	79
Luminescence Properties of Co-Doped NaCl:I^- , Ce^{3+} Crystals [3B] R. Oda and T. Kawai	80
Electronic Structure Identification of the Free-Standing Hexagonal Boron Nitride Membranes [4U] C. O. M. Mariano, J. S. D. Rodriguez, T. Araki and C.-H. Chuang	81
Transition Metal Dopants on Graphitic Carbon Nitride ($\text{g-C}_3\text{N}_4$) for Electrocatalytic Carbon Dioxide Reduction Reaction [4U] W.-T. Chen, H. W. Shiu, Y.-L. Lai, T. Araki and Y.-J. Hsu	82
Nm-scale NEXAFS Spectra of Styrene-Butadiene Rubber (SBR) Compounds Mixed with Silica Fillers [4U] T. Ejima and Y. Tamura	83
Investigation of Micro Voids in Rubber by STXM with a Tensile-Stress Sample Cell [4U] T. Ohigashi, F. Kaneko, H. Yuzawa, T. Yano, T. Araki and H. Kishimoto	84
Electronic Structure Analysis of Electrolyte for Redox Flow Battery [4U] E. Hosono, D. Asakura, H. Yuzawa, T. Ohigashi and A. Ohira	85
A Scanning Transmission X-ray Microscopy Study of $\text{LiFe}_{0.6}\text{Mn}_{0.4}\text{PO}_4$ Nanowires to Observe Partial Degradation by Natural Oxidation [4U] D. Asakura, E. Hosono, H. Yuzawa, T. Ohigashi, W. Zhang, M. Kobayashi, H. Kiuchi and Y. Harada	86
Hierarchically Structured $\text{ZnCo}_2\text{O}_4@\text{CoS}/\text{NF}$ Binder-Free Electrode for Multifunctional Applications [4U] P. Mannu, T. T. T. Nga, Y.-C. Huang, C.-L. Dong, W. F. Pong, W.-C. Chou, T. Araki and T. Ohigashi	87
Unveiling the Interfacial Electronic Structure of $\text{MnO}_2/\text{CuO}_x$ Heterostructure by Spectro-Microscopy [4U] K. T. Arul, C.-L. Pan, H.-W. Chang, C.-L. Dong, W.-F. Pong, T. Araki and T. Ohigashi	88

Photoresponse of C ₆₀ on a Two-Dimensional van der Waals Material [4B] Y. Nakayama, T. Yamada and M.-K. Lin	89
C K-edge XAS Measurement of Carbon-Containing Porous Silica [4B] S. Dohshi	90
Mg L _{2,3} -Edge and Al L _{2,3} -Edge XAS of MgAl ₂ O ₄ Induced on Swift Heavy Ion Irradiations [4B] S. Yoshioka, E. Kobayashi and K. Okudaira	91
Observation of Electronic Structure of THPB/Cu(111) [4B] H. Yamazaki, R. Moue, S. Kera, K. Fukutani, S. Makita and K. Kanai	92
Photoelectron Measurements for Rubrene Derivatives on Rubrene Single Crystals [4B] T. Yamada, N. Ohtsuka, N. Momiyama and Y. Nakayama	93
Local Environment of Dopants in (Co, Nb) and (Mn, Nb) Co-Doped TiO ₂ [4B] H. Murata, Y. Nagatomo and A. Nakahira	94
Soft X-ray Absorption Study of Semiconductor Photocatalysts under UV Light Irradiation [4B] T. Yoshida, N. Ichikuni, H. Onishi and Y. H. Chew	95
Observation of Electronic Reconstruction in Kagome Superconductors [5U] T. Kato, K. Nakayama, Y. Li, Z. Wang, S. Souma, K. Tanaka, T. Takahashi, Y. Yao and T. Sato	96
ARPES Study of Monolayer Germanene Grown on Ag [5U] T. Terasawa, S. Suzuki, D. Katsube, S. Tanaka and K. Tanaka	97
Pure Electron-Doping Effect in the T'-type Cuprate High-Temperature Superconductors Studied by Angle-Resolved Photoemission Spectroscopy [5U] M. Miyamoto, M. Horio, K. Moriya, A. Takahashi, K. Tanaka, Y. Koike, T. Adachi and I. Matsuda	98
Surface Electronic State of Single Crystal Mg Surface Treated by Ar Sputtering and Annealing [5U] T. Akatsuka, H. Miyazaki, T. Tokunaga and K. Hagihara	99
Measurement and Development of the Analytical Method to Determine the 3D Fermi Surface of TiSe ₂ [5U] S. Tanaka	100
High-Resolution ARPES Study of the Electronic Structure in a Kagome Superconductor [5U] T. Kato, T. Osumi, A. Honma, K. Nakayama, S. Souma, T. Takahashi and T. Sato	101
Enantiomeric Differentiations in Chiral Ferroelectric Oxides by Angle- Resolved Photoemission Circular Dichroism [5U] K. Fukutani, F. Nishino, S. Makita, K. Tanaka and S. Kera	102

Origin of High Thermopower in Heavy Fermion Yb-Based Compounds [5U, 7U] D. Goto, K. Kuga, M. Matsunami and T. Takeuchi	103
Angle-Resolved Photoemission Study of Layered MAX Phase Compound Zr_2SnC [5U] M. Mita, K. Tanaka, M. Nakatake, T. Ouisse and T. Ito	104
ARPES Study of the CDW and Anisotropic Band Splitting in 4H-NbSe ₂ and NbSeS [5U] Y. Kumar, S. Ideta and K. Shimada	105
Upgrading of the Photoelectron Momentum Microscope at BL6U of UVSOR to Integrate Data to be Reliably Analyzable by Theories [6U] S. Suga, K. Hagiwara and F. Matsui	106
Electronic States of a Weyl Semimetal Candidate Revealed by Momentum Microscope [6U] Y. Morita, K. Nakayama, K. Hagiwara, F. Matsui, T. Takahashi, K. Kudo and T. Sato	107
Electronic Structure of a Nodal Line Semimetal IrO ₂ Proved via Optical Spectroscopy [6B] D. Hirai, K. Maruyama, Y. Kusanose and K. Takenaka	108
ARPES Study of Pure Electronic Nematicity in Epitaxial FeSe Thin Films Grown on LaAlO ₃ [7U] K. Nakayama, T. Kobayashi, F. Nabeshima, S. Souma, T. Takahashi, A. Maeda and T. Sato	109
Photoemission Measurements on Crystalline Thin-Films of a Tetrabenzoporphyrin with Alkylsilyl Side Groups [7U] Y. Nakayama, T. Tasaki, K. Teranishi, H. Hattori, K. Matsuo and H. Yamada	110
Unexpected Two-Fold Symmetry of the Electronic Structure in Heavily Overdoped Bi2201 Observed by Angle-Resolved Photoemission Spectroscopy [5U, 7U] Y. Miyai, S. Ideta, T. Kurosawa, M. Oda, M. Arita, K. Tanaka and K. Shimada	111
Estimation of the Hole Concentration in the Normal State of Overdoped Bi2212 by Angle-Resolved Photoemission Spectroscopy [5U, 7U] Y. Tsubota, Y. Miyai, S. Kumar, K. Tanaka, S. Ishida, H. Eisaki, S. Nakagawa, T. Kashiwagi, M. Arita, K. Shimada and S. Ideta	112
Electronic Structure of Garnet-Type Solid Electrolytes $\text{Li}_{6.5}\text{La}_3\text{Zr}_{1.5}\text{Ta}_{0.5}\text{O}_{12}$ Bulk Single Crystal [7U] K. Masuda, S. Koyama, S. Takakura, M. Nakatake, K. Tanaka, K. Kataoka, J. Akimoto, Y. Iriyama and T. Ito	113
ARPES Study of the Coexistence of Superconductivity and Pure Electronic Nematicity in FeSe Thin Films on LaAlO ₃ [7U] K. Nakayama, T. Kobayashi, F. Nabeshima, S. Souma, T. Takahashi, A. Maeda and T. Sato	114

High-Resolution ARPES Study of Monolayer Germanene Grown on Ag [7U] T. Terasawa, S. Suzuki, D. Katsube, S. Tanaka and K. Tanaka	115
Measurement of Valence Band Dispersion in 2- <i>n</i> -Octyl-[1] benzothieno[3,2- <i>b</i>]naphtho[2,3- <i>b</i>]thiophene (2-C8-BTNT) Crystals [7U] T. Tasaki, S. Inoue, K. Kikuchi, H. Hattori, T. Hasegawa and Y. Nakayama	116
Orbital-Resolved Observations of Molecular Electronic Structures and Many-Body Interactions in Rubrene Single Crystal [7U] K. Fukutani, F. Nishino, P. I. Jaseela, N. Kasuya, J. Takeya, S. Makita, K. Tanaka and S. Kera	117
Excitation Spectra and Decay Curves of Plastic Scintillators with VUV Excitation [7B] M. Koshimizu	118
Vacuum Ultraviolet Characterization of Li-Glass as a Potential Neutron Scintillator [7B] T. Shimizu, K. Shinohara, K. Yamanoi and N. Sarukura	119
III-3 Chemistry	121
Search for Chiral Systems Exhibiting Novel Type of Photoelectron Circular Dichroism [1U] H. Kohguchi, Y. Hikosaka, T. Kaneyasu, S. Wada, H. Ota, M. Katoh and Y-I. Suzuki	123
Time-Domain Double Slit Interference of Electrons Produced by Light Wave Packets from a Tandem Undulator [1U] T. Kaneyasu, Y. Hikosaka, S. Wada, M. Fujimoto, H. Ota, H. Iwayama and M. Katoh	124
Measurement of Arbitrary Polarization by Zeeman Quantum Beat of Helium Atom [1U] T. Kaneyasu, Y. Hikosaka, S. Wada, H. Kohguchi, M. Fujimoto, H. Ota, H. Iwayama M. Hosaka and M. Katoh	125
Observation of the Electronic Structure of Aggregating Polymers in Shear Thickening Solutions [3U] K. Akada, S. Sato, M. Kobayashi and J. Fujita	126
Near-Edge X-ray Absorption Spectroscopy in a Ferroelectric Nematic Liquid Crystal [3U] F. Araoka, H. Nishikawa, Y. Takanishi and H. Iwayama	127
Oxygen K-Edge X-ray Absorption Spectroscopy for Identifying Active Surface Oxygen Species on Metal Oxide Catalysts [3U] H. Tedzuka, N. Matsumoto, H. Saito, M. Nagasaka T. Sugimoto and Y. Sekine	128

The Electronic States of 1-Methylimidazole in the Acetic Acid/1-Methylimidazole Mixture [3U] Y. Horikawa, M. Okazaki and M. Nagasaka	129
Soft X-ray Absorption of Semiconductor Photocatalyst Particles Suspended in Water [3U] H. Onishi, Y. H. Chew, N. Ichikuni and T. Yoshida	130
Probing the H-Bonding Network in the Vicinity of Aqueous Ammonia and Ammonium Ion by X-ray Absorption Spectroscopy [3U] D. Céolin, T. Saisopa, Y. Rattanachai, W. Sailuam, H. Yuzawa and N. Kosugi	131
Elucidation of Oxygen Evolution Reaction Mechanism on γ -MnO ₂ Electrocatalyst during Electrolysis of Acidic Aqueous Solution by <i>Operando</i> Soft X-ray XAFS [3U] A. Li, K. Adachi, D. Hashizume and R. Nakamura	132
Isolated Water Molecules in Aqueous Acetonitrile Solutions Probed by Oxygen K-Edge X-ray Absorption Spectroscopy [3U] M. Nagasaka	133
Observation of Electrochemically Generated Reactive Intermediate for Methane Oxidation by <i>Operando</i> Electrochemical Soft X-ray Absorption Spectroscopy [3U] Y. Yamada and M. Nagasaka	134
Photoelectron–Photoion Coincidence (PEPICO) for Hydrofluoroethanes [3B] T. T. Nguyen, K. Ishikawa, T. Hayashi, S. N. Hsiao and H. Iwayama	135
Fragmentation of OCS ³⁺ States Studied by Multi-Electron–Ion Coincidence Spectroscopy [4B] Y. Hikosaka	136
Dissociation of Doubly Charged Ion States in Xenon Difluoride Molecules [4B] Y. Hikosaka	137
High-Resolution Photoelectron Spectroscopy of Substituted Oxiranes [7B] H. Kohguchi, Y. Hikosaka, T. Kaneyasu, S. Wada and Y.-I. Suzuki	138
Photoionization Experiments in UVSOR-III for Study of Divertor Plasmas in a Nuclear Fusion Reactor and of Interstellar Plasmas in a Context of Astrobiology [7B] M. Kobayashi, S. Yoshimura, J. Takahashi, H. Iwayama, N. Kondo, M. Katoh, K. Kobayashi and H. Nakamura	139
III-4 Surface, Interface and Thin Films	141
 Momentum-Dependent Two-Dimensional Heavy-Fermion Formation in a Monoatomic-Layer Kondo Lattice YbCu ₂ [5U, 7U] T. Nakamura, H. Sugihara, Y. Chen, K. Tanaka and S. Kimura	143

Surface Treatment Dependence of Mo L-Edge NEXAFS Spectrum of Molybdenum Oxide [2A] E. Kobayashi, S. Yoshioka and K. K. Okudaira	144
Characterization of Electronic Structure in (Ba, Sn)S Thin Film Using XANES [2A] T. Nagai, H. Murata, H. Tampo and F. Kawamura	145
X-ray Absorption Spectroscopy Study of Dodenanethiol on Gold Surfaces [3U] F. Sato, I. Imahori, I. Tsukamoto, S. Ohno, Y. Sugimoto and M. Nagasaka	146
Ionic Layers at the Electrode Interface of Ionic Liquids Studied Using Interface-Selective Soft X-ray Absorption Spectroscopy [3U] T. Furuya, Y. Sugimoto, M. Nagasaka and N. Nishi	147
Probing Interfacial Water on SiO ₂ in Colloidal Dispersion [3U] Y. Hao, S. Wang, M. Nagasaka, Z. Abbas and X. Kong	148
Evaluation of Crystallinity of Substrate Interface Region of Deep Ultraviolet Emitting Zinc Aluminate Thin Film [3B] H. Kominami, A. Adachi, R. Ishihara, K. Yabe, J. Kamikawa, T. Sadamori, D. Takeya, M. Mimura, M. Yasuda, A. Yokoya, N. Yoshimura and S. Kurosawa	149
Interfacial Lattice Strain Induced Spin Reorientation Transition in Pd/Ni Thin Film Heterostructures [4B] T. Miyamachi, K. Tsutsui, H. Ono, O. Ishiyama, T. Yokoyama and M. Mizuguchi	150
Stabilizing In-Plane Magnetization of Pd/Ni Thin Film Heterostructures by Interfacial Lattice Strain [4B] T. Miyamachi, K. Tsutsui, H. Ono, O. Ishiyama, T. Yokoyama and M. Mizuguchi	151
XMCD Measurements on van der Waals Magnets [4B] R. Ichikawa, T. Miyamachi, H. Ishii, W. Wulfhekel, A.-A. Haghighirad, O. Ishiyama, H. Iwayama, E. Nakamura, T. Yokoyama and T. K. Yamada	152
Charge Transfer in Solution-Mixed and Sequential Doping P3HT:F4-TCNQ Films by NEXAFS Spectroscopy [4B] Y. Hoshi and K. K. Okudaira	153
Angle-Resolved Photoemission Circular Dichroism for Chiral Molecule Overlayer on Monolayer WS ₂ [4B] F. Nishino, K. Fukutani, P. I. Jaseela, J. Brandhoff, F. Otto, M. Grünewald, M. Schaal, J. Picker, Z. Zhang, A. Turchanin, S. Makita, H. Iwayama, T. Hirose, T. Fritz and S. Kera	154
Photoemission Spectroscopy Measurement on Germanium Incorporated Carbon-Based Nanoribbon Structures [4B] K. Sun, K. Fukutani, S. Kera and S. Kawai	155

Geometry-Induced Photoelectron Spectroscopy from Si{111} Facet Surfaces on Three-Dimensionally Fabricated Facet-Lined Structures [5U] K. Hattori, Ni'matil Mabarroh, Juharni, Y. Kimoto, Y. Kitagawa, K. Tsubosaki, R. M. Tumbelaka, S. Tanaka, A. N. Hattori, S. Suga and K. Tanaka	156
Van Hove Singularity Induced by an Interfacial Metallic Layer in Ca-Intercalated Bilayer Graphene on SiC [5U] S. Ichinokura, K. Tokuda, M. Toyoda, K. Tanaka, S. Saito and T. Hirahara	157
Characterization of Amorphous and Polycrystalline Selenium Thin Films by Vacuum Ultraviolet Absorption Spectroscopy [5B] K. Hayashi	158
Electronic Study of Large-Area Hydrogen Boride Sheets by X-ray Absorption Spectroscopy [5B] K. Yamaguchi, M. Niibe, T. Sumi, E. Nakamura, K. Tanaka and I. Matsuda	159
Deposition of High-Quality Ir(111) Thin Films by Molecular Beam Epitaxy [6U] E. Hashimoto, Y. Onuma, H. Kurosaka, Y. Nishio, F. Matsui and S. Koh	160
Linear Polarization Turntable Measurement of the Band Structure of Au(111) [6U, 7U] K. Hagiwara, S. Suga, S. Tanaka and F. Matsui	161
ARPES Study of Anomalous Secondary Photoemission from SrTiO ₃ (100) [7U] C.Y. Hong, P.X. Ran, X.P. Xie and R.-H. He	162
Metal-Insulator Transition in Si(111)√3×√3-Sn [7U] H. Nishimichi, K. Ishihara, S. Ichinokura, K. Tanaka and T. Hirahara	163
Anisotropic Surface Atomic Structure and Electronic State in a YbSb/GaSb(001) Thin Film [7U] Y. Chen, T. Nakamura, S. Sugihara, K. Nishihara, K. Tanaka and S. Kimura	164
Photoelectron Spectra of Thermoelectric Oxide Ba _{1/3} CoO ₂ [7U] S. Tanaka, K. Kang and H. Ohta	165
Electronic States at Ionic Liquid/Electrode Interfaces by Multi-Angle Incident-Angle ATR-UV-Vis Spectroscopy [7B] I. Tanabe, T. Kakinoki and K. Fukui	166
III-5 Life, Earth and Planetary Sciences	169
 Spring in the Arctic Ocean during ARTofMELT Expedition: A STXM/NEXAFS Analysis of Aerosol Particle Composition and Mixing State [4U] N. Fauré, T. Araki., E. S. Thomson and X. Kong	171

Optical Activity Emergence of Organic Molecules Induced by Circularly Polarized Lyman- α Light Irradiation and Magnetic Field Application [1U] M. Kobayashi, J. Takahashi, H. Ota, K. Matsuo, G. Fujimori, Y. Taira, M. Katoh, K. Kobayashi, Y. Kebukawa and H. Nakamura	172
Toward Observation of the Interaction between Ultraviolet Optical Vortex and Biomaterials [1U] K. Matsuo, R. Imaura, S. Hashimoto, Y. Nishihara and M. Katoh	173
X-ray Absorption Spectra of Lipid Bilayer Membranes in Aqueous Solutions and Its Dependence on Cation Concentration [3U] R. Tero, Y. Kinjo and M. Nagasaka	174
Laser Excited Photochemical Reaction of Dissolved Oxygen on Lipid Bilayer Measured by Oxygen K-Edge XAS [3U] F. Kumaki, M. Nagasaka, Y. Kinjo, R. Tero, Y. Okano and J. Adachi	175
Soft X-ray Absorption Spectroscopic Study of Myoglobin Heme in Solution [3U] Y. Sugimoto and M. Nagasaka	176
The Effect of Freeze-Defrosting Cycles on the Spherule Size, Morphology, and Chemical Compositions of HCN Polymer [4U] H. Yabuta, N. Nishii and T. Araki	177
Aerosol Particle Mixing States in Delhi: A STXM/NEXAFS Investigation into Nighttime Growth Mechanisms [4U] M. Wickramanayake, E. Tsiligiannis, T. Araki., E. S. Thomson and X. Kong	178
STXM Characterization of Salla Disease Patient Fibroblasts [4U] T. Mansikkala, I. Miinalainen, S. M. Kangas, R. Hinttala, J. Uusimaa, M. Huttula and M. Patanen	179
Evaluation of Radiation-Induced NEXAFS Profile-Changes for Biomolecules in Imaging Biological Specimens [4U] A. Ito, K. Shinohara, A. Matsuura, S. Toné, K. Tohya, Y. Asada, H. Yuzawa, T. Araki and T. Ohigashi	180
Chemical Structures of Macromolecular Organic Matter in Ryugu Grain. [4U] T. Matsumoto, T. Noguchi, T. Araki, T. Ohigashi, Y. Igami and A. Miyake	181
Development of Contact X-ray Microscope for Biological Sample [4B] H. Iwayama and R. Sasaba	182
Development of the Super Continuum Laser-Based Infrared Spectro-Microtomography for the Three-Dimensional Imaging of Extraterrestrial Organic Matter [6B] H. Yabuta, Y. Ikemoto, F. Teshima, and K. Tanaka	183
Structural Analysis of Amyloid Oligomers by Using Synchrotron Radiation Infrared Microspectroscopy [6B] T. Kawasaki, F. Teshima and K. Tanaka	184

IV List of Publications

187

V Workshops

195

UVSOR 40th Commemorative Lecture and Ceremony

197

UVSOR Symposium 2023

198

Poster Session

200

IMS workshop
“Seeds and Needs for Tomorrow’s Synchrotron Radiation
Photoelectron Spectroscopy Research”

202

Poster Session

204

UVSOR/SPRING-8 Infrared Beamline Joint Users Meeting

206

60 years of Synchrotron Radiation in Japan (JPSR60)

208

Facility Posters

210

Poster Program

210

NINS Frontier Photonic Science Project Workshop
Exploring innovative metrologies based on quantum/coherence
nature of synchrotron radiation

212

Facts and Figures

215

I

Organization and Staff List

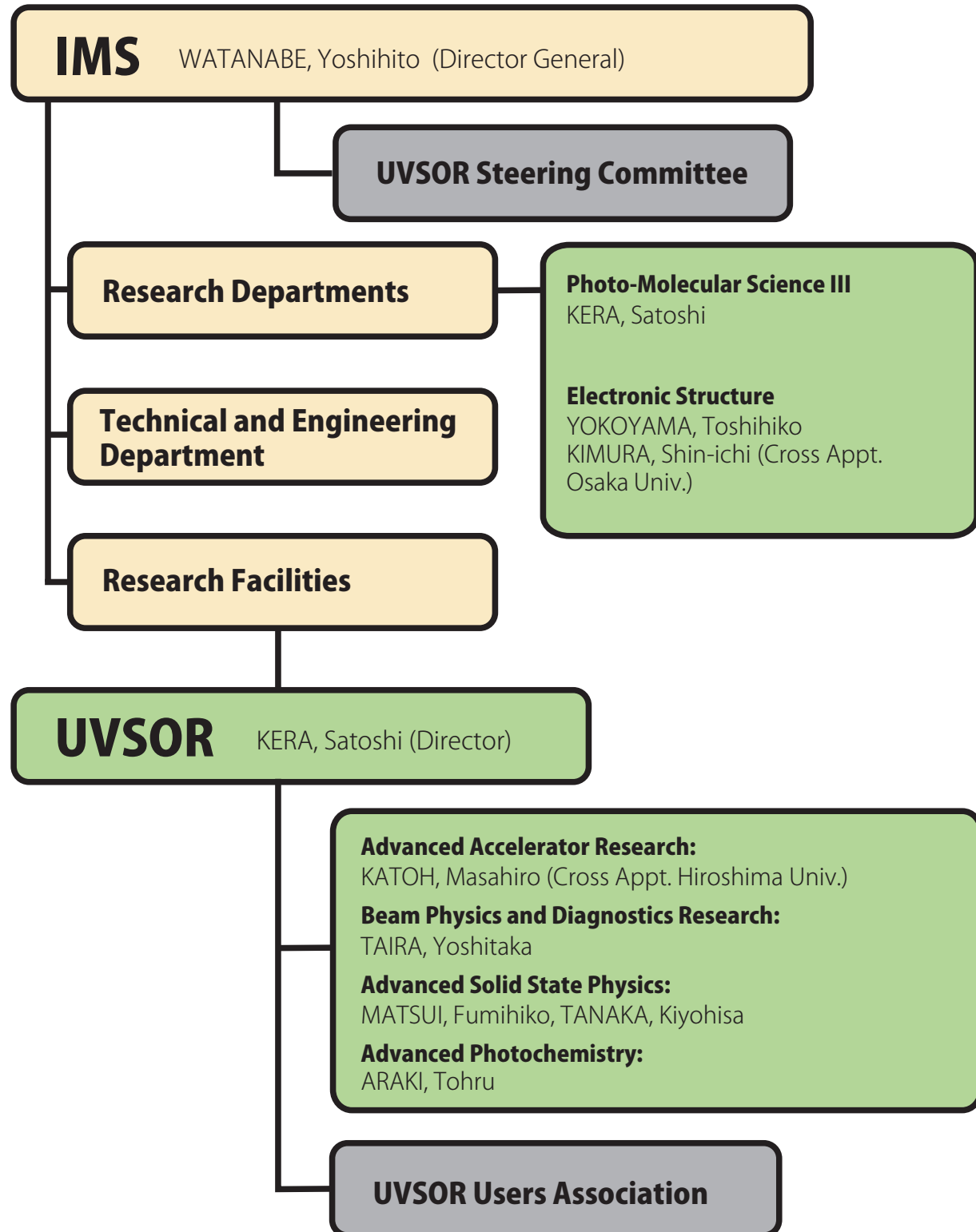




UVSOR Synchrotron Facility Organization

Mar. 2024

I



Staff List

Mar. 2024

UVSOR Staff

Director

KERA, Satoshi Professor kera@ims.ac.jp

Division of Advanced Accelerator Research

KATOH, Masahiro Project Professor mkatoh@ims.ac.jp
(Cross Appt. Hiroshima Univ.)

SALEHI, Elham Project Research Staff elham@ims.ac.jp (until Mar. 2024)

Division of Beam Physics and Diagnostics Research

TAIRA, Yoshitaka Associate Professor yostaira@ims.ac.jp

MATSUDA, Hiroyuki Project Research Staff hmatsuda@ims.ac.jp

Division of Advanced Solid State Physics

MATSUI, Fumihiko Professor matui@ims.ac.jp

TANAKA, Kiyohisa Associate Professor k-tanaka@ims.ac.jp

HAGIWARA, Kenta Project Research Staff k-hagiwara@ims.ac.jp

Division of Advanced Photochemistry

ARAKI, Tohru Senior Researcher araki@ims.ac.jp

IWAYAMA, Hiroshi Assistant Professor iwayama@ims.ac.jp

Research Cooperative Staff

KANEYASU, Tatsuo Associate Professor (Concurrent Appt. SAGA-LS)

KATAYANAGI, Hideki Research Associate kata@ims.ac.jp (since Jul. 2023)

SUGIMOTO, Yasunobu Specially Appointed Senior Specialist

Technical Staff

HAYASHI, Kenji Engineer (Unit Leader)

NAKAMURA, Eiken Chief Engineer

MAKITA, Seiji Engineer

OKANO, Yasuaki Engineer

SAKAI, Masahiro Chief Technician

YANO, Takayuki Chief Technician

TESHIMA, Fumitsuna Chief Technician

KONDO, Naonori Chief Technician

YUZAWA, Hayato Chief Technician

OTA, Hiroshi Technician

SHIMIZU, Kohei Technician

YAMAZAKI, Jun-ichiro	Technical Fellow
MIZUKAWA, Tetsunori	Technical Fellow
MINAKUCHI, Aki	Technical Fellow

Secretary

ISHIHARA, Mayumi	
KAMO, Kyoko	
YOKOTA, Mitsuyo	(since Jul. 2023)

Departments in IMS (*Group Leader)

Division of Photo-Molecular Science III

KERA, Satoshi*	Professor	
NAGASAKA, Masanori	Assistant Professor	
FUKUTANI, Keisuke	Assistant Professor	
SAGEHASHI, Ryunosuke	Research Assistant Professor	(since Oct. 2023)

Division of Electronic Structure

YOKOYAMA, Toshihiko*	Professor
KIMURA, Shin-ichi	Professor (Cross Appt. Osaka Univ.)
KURAHASHI, Naoya	Assistant Professor
MAEJIMA, Naoyuki	Research Assistant Professor

Graduate Students

KOYAMA, Shotaro	Nagoya University	(until Sep. 2023)
MITA, Manaya	Nagoya University	(until Sep. 2023)
OZAWA, Shunnosuke	Nagoya University	(until Sep. 2023)
SHIOHARA, Keisuke	Nagoya University	(until Sep. 2023)
KAWANO, Kento	Nagoya University	(since Nov. 2023)
MASUDA, Keisuke	Nagoya University	(since Nov. 2023)
WAKITA, Yukiya	Nagoya University	(since Nov. 2023)

UVSOR Steering Committee (*Chair)

KERA, Satoshi*	UVSOR, IMS	Chair
MATSUI, Fumihiko	UVSOR, IMS	
KATOH, Masahiro	UVSOR, IMS	
TANAKA, Kiyohisa	UVSOR, IMS	
TAIRA, Yoshitaka	UVSOR, IMS	
ARAKI, Tohru	UVSOR, IMS	
MASE, Kazuhiko	UVSOR, IMS (KEK)	

KANEMITSU, Yoshihiko	Kyoto University
KIMURA, Shin-ichi	Osaka University
HARADA, Yoshihisa	University of Tokyo
FUKUSHIMA, Takanori	Tokyo Institute of Technology
NAKAMURA, Tetsuya	Tohoku University
YABASHI, Makina	RIKEN
ITO, Takahiro	Nagoya University
WATANABE, Yoshihito	IMS, Director General
YOKOYAMA, Toshihiko	IMS
IINO, Ryota	IMS
SEGAWA, Yasutomo	IMS
KURAMOCHI, Hikaru	IMS
SHIGEMASA, Eiji	IMS
HAYASHI, Kenji	IMS
NAKAMURA, Toshikazu	IMS

UVSOR Users Association (*Chair)

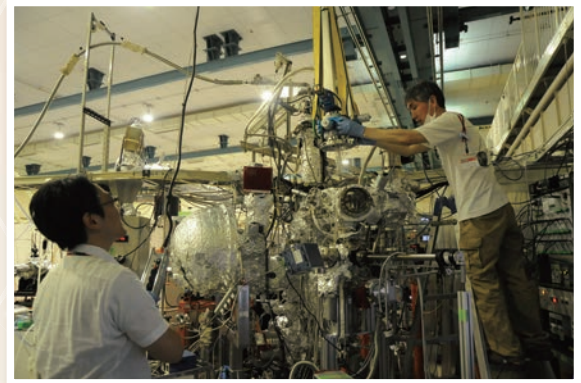
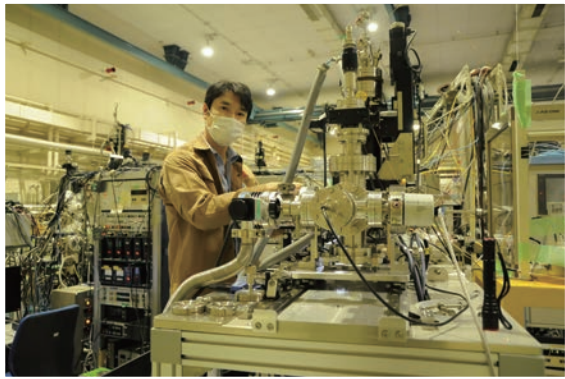
KITAURA, Mamoru*	Yamagata University	(until Mar. 2023)
HIKOSAKA, Yasumasa	Toyama University	(until Mar. 2023)
ITO, Takahiro	Nagoya University	
MIYAMACHI, Toshio	Nagoya University	
HIRAHARA, Toru	Tokyo Institute of Technology	

Visiting Scientists

MANSIKKALA, Tuomas	University of Oulu	May 2023, Jun. 2023
PATANEN, Minna	University of Oulu	May 2023, Jun. 2023
HONG, Caiyun	Westlake University	Jul. 2023
JIANG, Congying	Westlake University	Jul. 2023
HE, Ruihua	Westlake University	Jul. 2023
CHEN, Wan-Ting	National Synchrotron Radiation Research Center	Jul. 2023
LAI, Yu-Ling	National Synchrotron Radiation Research Center	Jul. 2023
SHIU, Hung Wei	National Synchrotron Radiation Research Center	Jul. 2023
HSU, Yao-Jane	National Synchrotron Radiation Research Center	Jul. 2023
Jan Sebastian Dominic Rodriguez		
	Department of Physics, Tamkang University	Aug. 2023
Carl Osby M. Mariano	Department of Physics, Tamkang University	Aug. 2023
CHUANG, Cheng-Hao	Department of Physics, Tamkang University	Aug. 2023
LU, Hsin-Chan	Department of Physics, Tamkang University	Aug. 2023
HAO, Yuxin	Northwest University	Aug. 2023, Sep. 2023
KONG, Xiangrui	University of Gothenburg Sweden	Aug. 2023, Sep. 2023
THANIT, SAISOPA	Rajamangala University of Technology Isan	Aug. 2023
ATTANACHAI, Yuttakarn	Rajamangala University of Technology Isan	Aug. 2023

SAILUAM, Wutthigrai	Rajamangala University of Technology Isan (Khon Kaen Campus)	Aug. 2023
CÉOLIN, Denis	Synchrotron SOLEIL	Aug. 2023
ZHU, Yupeng	Southern University of Science and Technology	Oct. 2023
ZENG, Meng	Southern University of Science and Technology	Oct. 2023
PONG, Way-Faung	Tamkang University	Dec. 2023
DONG, Chung-Li	Tamkang University	Dec. 2023
Ta Thi Thuy Nga	National Yang Ming Chiao Tung University	Dec. 2023
Kumaravelu Thanigai Arul	Tamkang University	Dec. 2023
YANG, Cheng-Chieh	National Taiwan University of Science and Technology	Dec. 2023
WANG, Pin-Cyuan	National Taiwan University of Science and Technology	Dec. 2023
HONG, Caiyun	Westlake University	Jan. 2024
JIANG, Congying	Westlake University	Jan. 2024
XIE, Xiaopeng	Westlake University	Jan. 2024
KONG, Xiangrui	University of Gothenburg Sweden	Feb. 2023, Mar. 2023
THOMSON, Erik	University of Gothenburg Sweden	Feb. 2023, Mar. 2023

Staff





Current Status of Light Sources and Beamlines



Light Source in 2023

Yoshitaka Taira

UVSOR Synchrotron Facility, Institute for Molecular Science, Okazaki 444-8585, Japan

In FY2023, UVSOR-III was operated for users as scheduled for 36 weeks from end of May 2023 to March 2024. Monthly statistics of operation time and integrated beam current are shown in Fig. 1. From the beginning of April to early May, during which periodic inspections were conducted. The two weeks following the shutdown were allocated to the adjustment of the accelerator and beamlines.

The weekly operation schedule is as follows. Mondays are assigned to machine studies from 9:00 AM to 9:00 PM. User operation is assigned Tuesday through Friday, with Tuesday and Wednesday operating from 9:00 AM to 9:00 PM, and Thursday from 9:00 AM to 9:00 PM on Friday for 36 continuous hours. Thus, the user's beam time per week is 60 hours.

Instantaneous voltage drops due to lightning strikes occurred frequently during the July-August period. This caused beam dumps, leading to loss of operation time. Several insulation breakdowns of the high-voltage charging cable of the pulse power supply for the synchrotron first kicker have occurred, but have been restored by replacing the cable. A malfunction of the S-band pulse amplifier for the linear accelerator occurred, but has been addressed by adjusting the amplifier gain. We are considering updating the S-band pulse amplifier due to concerns that the problem may recur.

Injection efficiency of the electron beam into the storage ring started to decrease around January 2023. The injection efficiency is calculated as the ratio of the increase in the stored current value, δI , to the current value passing through the transport line between the booster synchrotron and the storage ring. Under normal conditions, the injection efficiency was 60~70% and δI was 0.4~0.6 mA/shot, but after January 2023, the efficiency dropped to 20~30% and δI 0.1~0.3 mA/shot. The limited number of electrons that can be injected into the storage ring per week makes it difficult to continue 300 mA operation. Therefore, user operation has been conducted with the stored current value reduced to 200 mA since May 2023. Various investigations are continuing to determine the cause, but so far no clear cause has been identified. However, it has been confirmed that the quality of the electron beam extracted by the booster synchrotron has deteriorated. The vacuum ducts in the bending magnet section of the booster synchrotron have experienced multiple vacuum leaks, and there is concern that opening the ducts to the atmosphere may induce serious vacuum leaks, so it is currently impossible to visually check inside the ducts. All vacuum ducts in the bending magnet section are scheduled to be replaced with new

ones in the spring of 2025. At that time, we will check the inside of the vacuum ducts of the booster synchrotron to see if there are any foreign objects that are scattering the beam.

We started a design study for the future plan of UVSOR-IV. As a first step, we have analyzed the present magnetic lattice, seeking a possibility to reduce the emittance more [1]. Although, we did not find a solution to drastically reduce emittance, we have found a few interesting solutions that achieved lower emittance than the current situation. As the second step, we have started designing a totally new storage ring, which is close to the diffraction limit in the VUV range [2].

The light source development and utilization beamline BL1U, constructed under the support of Quantum Beam Technology Program by MEXT/JST, continue to develop new light source technologies and their applications such as free electron laser, coherent harmonic generation, coherent synchrotron radiation, coherent control [3], laser Compton scattered gamma rays [4, 5], and optical vortices [6].

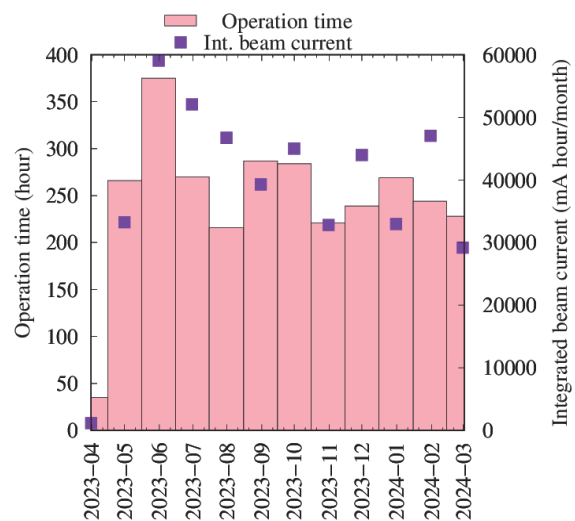


Fig. 1. Monthly statistics in FY2023.

- [1] E. Salehi and M. Katoh, Proceedings of IPAC2021 (2021) 3970.
- [2] E Salehi *et al.*, J. Phys.: Conf. Ser. **2420** (2023) 012062.
- [3] Y. Hikoska *et al.*, Sci. Rep. **13** (2023) 10292.
- [4] Y. Taira *et al.*, Phys. Rev. A **107** (2023) 063503.
- [5] H. Ohgaki *et al.*, Phys. Rev. Acc. Beams **26** (2023) 093402.
- [6] S. Wada *et al.*, Sci. Rep. **13** (2023) 22962.

UVSOR Accelerator Complex

Injection Linear Accelerator

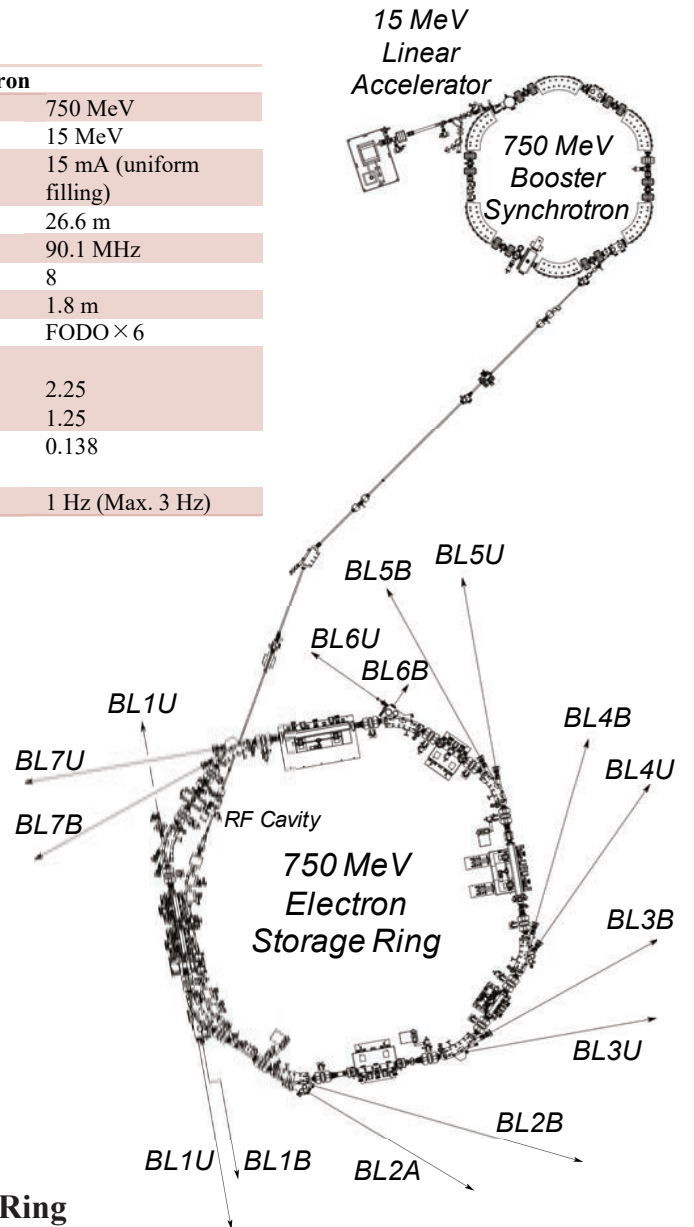
Energy	15 MeV
Length	2.5 m
RF Frequency	2856 MHz
Accelerating RF Field	$2\pi/3$ Traveling Wave
Klystron Power	1.8 MW
Energy Spread	~ 1.6 MeV
Repetition Rate	1 Hz (Max. 3 Hz)

UVSOR-III Storage Ring

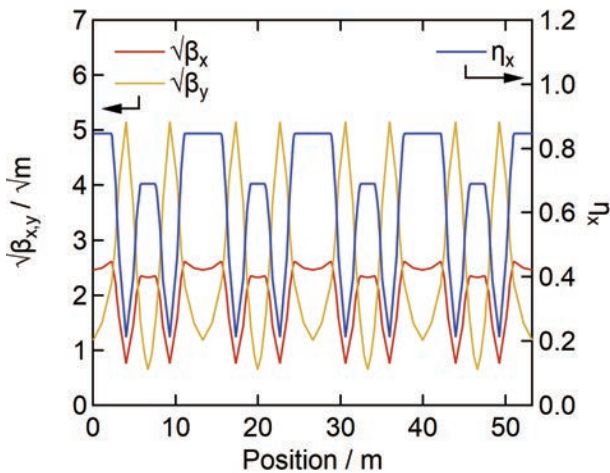
Energy	750 MeV
Injection Energy	750 MeV
Normal Operation	300 mA (multi bunch)
Current (Top-up)	40 mA (single bunch)
Natural Emittance	17.5 nm rad
Circumference	53.2 m
RF Frequency	90.1 MHz
RF Voltage	120 kV
Harmonic Number	16
Bending Radius	2.2 m
Lattice	Extended DB $\times 4$
Straight Section	$(4 \text{ m} \times 4) + (1.5 \text{ m} \times 4)$
Betatron Tune	
Horizontal	3.75
Vertical	3.20
Momentum Compaction	0.030
Natural Chromaticity	
Horizontal	-8.1
Vertical	-7.3
Energy Spread	5.26×10^{-4}
Coupling Ratio	1%
Natural Bunch Length	128 ps

Booster Synchrotron

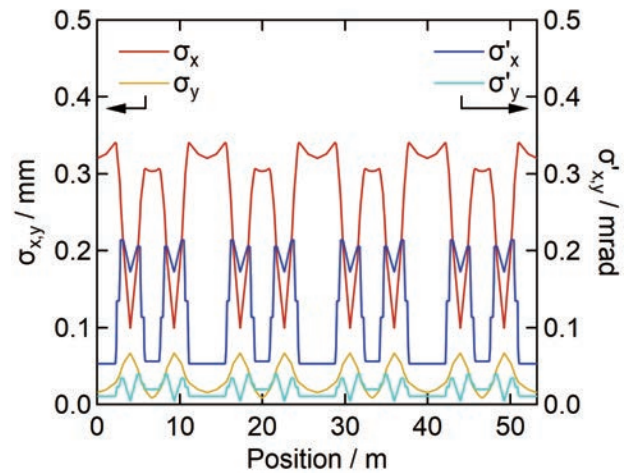
Energy	750 MeV
Injection Energy	15 MeV
Beam Current	15 mA (uniform filling)
Circumference	26.6 m
RF Frequency	90.1 MHz
Harmonic Number	8
Bending Radius	1.8 m
Lattice	FODO $\times 6$
Betatron Tune	
Horizontal	2.25
Vertical	1.25
Momentum	0.138
Compaction	
Repetition Rate	1 Hz (Max. 3 Hz)



Electron Beam Optics of UVSOR-III Storage Ring

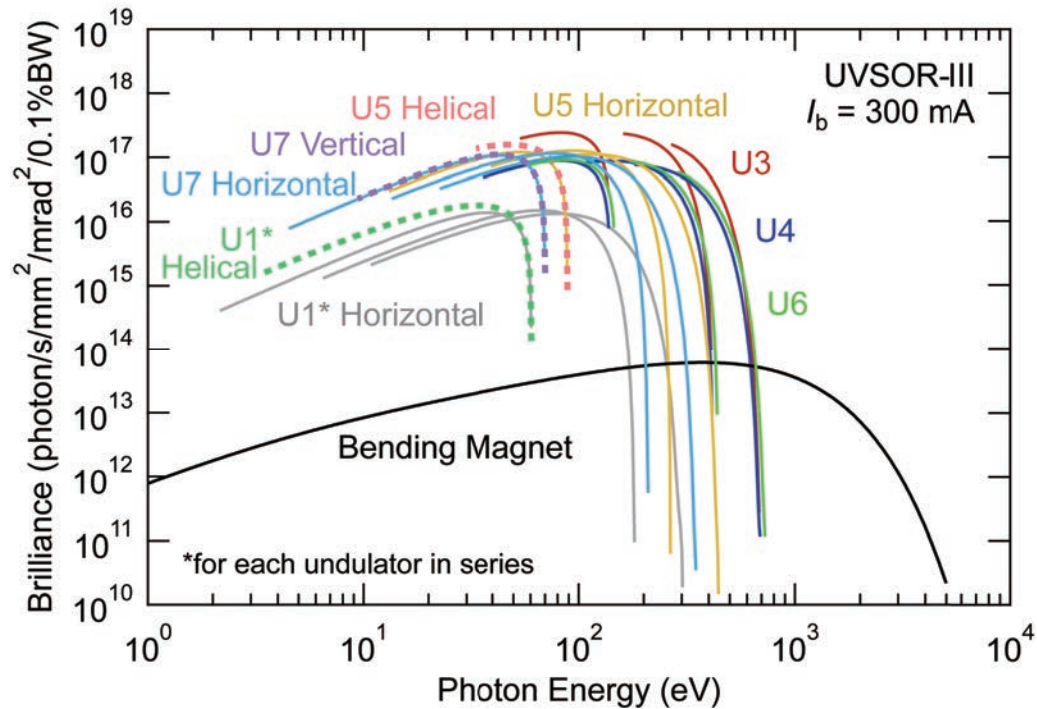


Horizontal / vertical betatron functions and dispersion functions



Horizontal / vertical electron beam size and beam divergences

Insertion Devices



Brilliance of radiation from the insertion devices (U1, U3, U4, U5, U6 and U7) and a bending magnet of UVSOR-III

U1 Apple-II Undulator / Optical Klystron

Number of Periods	10 + 10
Period Length	88 mm
Pole Length	0.968 m + 0.968 m
Pole Gap	24–200 mm
Deflection Parameter	7.36 (Max. Horizontal) 4.93 (Max. Vertical) 4.06 (Max. Helical)

U3 In-Vacuum Undulator

Number of Periods	50
Period Length	38 mm
Pole Length	1.9 m
Pole Gap	16.5–40 mm
Deflection Parameter	1.8–0.24

U4 In-Vacuum Undulator

Number of Periods	26
Period Length	38 mm
Pole Length	0.99 m
Pole Gap	13–40 mm
Deflection Parameter	2.4–0.19

Bending Magnets

Type	Combined × 8
Magnetic Length	1.728 m
Bending Radius	2.2 m
Bending Angle	45 deg.
Pole Gap	55.2 mm
Pole Width	140 mm
Critical Energy	425 eV

U5 Apple-II Variable Polarization Undulator

Number of Periods	38
Period Length	60 mm
Pole Length	2.28 m
Pole Gap	24–190 mm
Deflection Parameter	3.4 (Max. Horizontal) 2.1 (Max. Vertical) 1.8 (Max. Helical)

U6 In-Vacuum Undulator

Number of Periods	26
Period Length	36 mm
Pole Length	0.94 m
Pole Gap	13–40 mm
Deflection Parameter	1.78–0.19

U7 Apple-II Variable Polarization Undulator

Number of Periods	40
Period Length	76 mm
Pole Length	3.04 m
Pole Gap	24–200 mm
Deflection Parameter	5.4 (Max. Horizontal) 3.6 (Max. Vertical) 3.0 (Max. Helical)

(Last updated, August, 2024)

Beamlines in 2023

Fumihiko Matsui

UVSOR Synchrotron Facility, Institute for Molecular Science, Okazaki 444-8585, Japan

UVSOR is one of the highest-brilliance light sources in the extreme-ultraviolet region among the synchrotron radiation facilities with electron energies of less than 1 GeV. The low natural emittance of the UVSOR-III storage ring, 17.5 nm-rad, was accomplished after the successful completion of the storage ring upgrade project (the UVSOR-III project) in 2012. Eight bending magnets and six insertion devices are available as synchrotron light sources at UVSOR. There are a total of thirteen operational beamlines. Eleven of them are the so-called “Public beamlines”, which are open to scientists from universities and research institutes belonging to the government, public organizations, private enterprises and also those from foreign countries. The beamline BL6U is the “In-house beamlines”, and are dedicated to the use of research groups within Institute for Molecular Science (IMS). The beamline BL1U is a partially “Public” and partially “In-house” beamline. There is one tender X-ray (TX) station equipped with a double-crystal monochromator, six extreme ultraviolet (EUV) and soft X-ray (SX) stations with grazing incidence monochromators, three vacuum ultraviolet (VUV) stations with normal incidence monochromators, two infrared (IR) stations equipped with Fourier Transform interferometers, and one direct radiation station located after two tandem undulators, as shown in the appended table (next page) for all available beamlines at UVSOR in 2023. The details of the updates for undulator beamlines are the followings.

- In **BL1U**, the development of a new light source and the utilization of gamma-rays are being carried out. This beamline is equipped with a tandem undulators with a buncher section, which can be used for free electron laser in the range from visible to deep UV, VUV coherent harmonic generation, and generation of spatiotemporal structured light such as an optical vortex beam, a vector beam and double-pulsed wave packets. It is also equipped with a femto-second laser system synchronized with the accelerator, which is used for the generation of Compton scattered gamma-rays. Users are provided with gamma-ray induced positron annihilation spectroscopy that can analyze nanometer-order defects in bulk materials. To increase the counting rate of annihilation gamma rays, an array detector with eight BaF₂ scintillators was developed. The measurement can be completed in a few hours for metal samples.
- In **BL3U**, the ultrathin-liquid cell for low-energy XAS has been developed. The studies of local structures of several aqueous solutions and various chemical processes in solution such as catalytic and electrochemical reactions, and laminar flows in microfluidics by using operando XAS in C, N, and O K-edges were demonstrated. Moreover, an argon gas window that is effective from 60 to 240 eV with the removal of high-order X-rays, which will develop chemical research since it includes K-edges of Li and B and L-edges of Si, P, S, and Cl was established.
- Resonant soft X-ray scattering (RSoXS) for soft materials is also applicable. RSoXS is similar to small angle X-ray scattering (SAXS) and can provide information on the mesoscopic structure (1-100 nm) of sample. This method has selectivity of elements, functional groups and molecular orientation. Since soft X-ray region include K-edge energies of light element (C, N, O), RSoXS is a powerful tool to investigate soft matters.
- **BL4U**, which is equipped with a scanning transmission soft X-ray microscope (STXM), is actively used not only by academic users but also by many industrial users. The STXM can be applied to wide range of sciences, such as polymer science, material science, cell biology, environmental science, and so on. In FY2020, it became possible to image the lithium K-edge with a spatial resolution of 72 nm. Final adjustments for the airtight sample transport system and the sample transport container were carried out for the organic substance analysis of the Hayabusa2 returned samples for the summer of FY2021.
- In **BL5U**, high energy resolution angle-resolved photoemission spectroscopy (ARPES) is available. Users can now use so-called “deflector mapping” for all kinetic energies and lens modes by using the latest version of ARPES analyzer. Users can also obtain spatial-dependence of the electronic structure of solid surfaces using micro-focused beam (50 μm). An alkali-metal deposition system has been installed. Potassium for example can be deposited while the sample is still mounted on the manipulator at low temperatures. As part of the development of spin-resolved ARPES, two-dimensional images of the spin-resolved spectrum of the Rashba splitting of Au(111) surface has been successfully obtained.
- At **BL6U**, one of the In-house beamlines, photoelectron momentum microscope (PMM), which is a new-concept multi-modal electronic structure analysis system with high resolution in real space and momentum space, has been installed and is in operation. A key feature of the PMM is that it can very effectively reduce radiation-induced damage by directly projecting a single

photoelectron constant energy contour in reciprocal space with a radius of a few \AA^{-1} or real space with a radius of a few hundred μm onto a 2D detector. Experiments such as valence band photoelectron spectroscopy on the micrometer scale and resonance photoelectron diffraction by soft X-ray excitation are performed. In FY2023, PMM's capabilities were further expanded by introducing an additional 2D spin filter. Two-dimensional images of the spin-resolved spectrum of the Rashba splitting of Au(111) surface has been also successfully obtained too following BL5U. In addition to grazing-incidence soft X-ray excitation, normal-incidence vacuum ultraviolet (VUV) beam with variable polarizations (horizontal/vertical) became also available at the same focal position of the PMM via a newly added branch from the next BL7U. This highly symmetrical measurement geometry completely eliminates the p-polarized linear dichroism effect in the circular dichroism measurements of valence band, making transition matrix element analysis

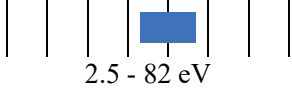
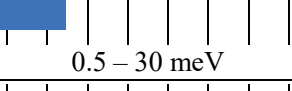
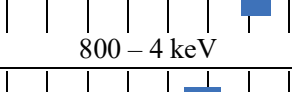
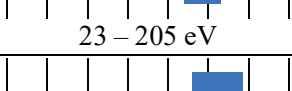
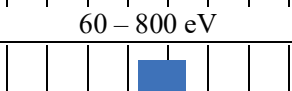
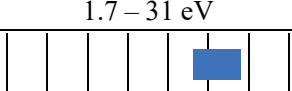
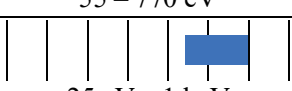

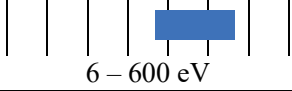
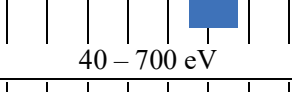
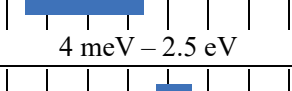
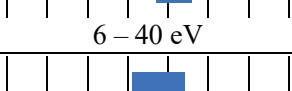
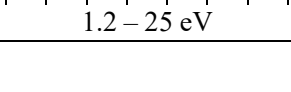

much simpler and reliable.

- At **BL7U**, high-energy resolution ARPES is available with extremely low energy of photons (6 eV~) using the low-temperature 6-axis manipulator with a sample temperature 4.5-350 K. In FY2021, the deflector-type detector for the hemispherical analyzer was installed to realize an effective 2D measurement with the automated manipulator control. Users can perform the measurement of the bulk sensitive electronic structure of solids and the high-throughput measurement for molecular materials using high-photoionization cross-section using low-excitation photon energy.

Those wishing to use the open and in-house beamlines are recommended to contact the appropriate beamline contact persons (see next page). Applications can be submitted at NOUS (<https://nous.nins.jp/user/signin>). All users are required to refer to the beamline manuals and the UVSOR guidebook, on the occasion of conducting the actual experimental procedures. For updated information on UVSOR, please see <http://www.uvsor.ims.ac.jp>.

Beamlines at UVSOR

II

Beamline	Monochromator / Spectrometer	Energy Range	Targets	Techniques	Contact
BL1U	Light Source Development Gamma-ray FEL	 2.5 – 82 eV		Irradiation (UV and Gamma-rays)	Y. Taira yostaira@ims.ac.jp
BL1B	Martin-Puplett FT-FIR	 0.5 – 30 meV	Solid	Reflection Absorption	K. Tanaka k-tanaka@ims.ac.jp
BL2A	Double crystal	 800 – 4 keV	Solid	Reflection Absorption	F. Matsui matui@ims.ac.jp
BL2B	18-m spherical grating (Dragon)	 23 – 205 eV	Solid	Photoemission	S. Kera kera@ims.ac.jp
BL3U	Varied-line-spacing plane grating (Monk-Gillieson)	 60 – 800 eV	Gas Liquid Solid	Absorption Photoemission Photon-emission	H. Iwayama iwayama@ims.ac.jp
BL3B	2.5-m off-plane Eagle	 1.7 – 31 eV	Solid	Reflection Absorption Photon-emission	F. Matsui matui@ims.ac.jp
BL4U	Varied-line-spacing plane grating (Monk-Gillieson)	 55 – 770 eV	Gas Liquid Solid	Absorption (Microscopy)	T. Araki araki@ims.ac.jp
BL4B	Varied-line-spacing plane grating (Monk-Gillieson)	 25 eV – 1 keV	Gas Solid	Photoionization Photodissociation Photoemission	H. Iwayama iwayama@ims.ac.jp
BL5U	Varied-line-spacing plane grating (Monk-Gillieson)	 20 – 220 eV	Solid	Photoemission	K. Tanaka k-tanaka@ims.ac.jp
BL5B	Plane grating	 6 – 600 eV	Solid	Calibration Absorption	K. Tanaka k-tanaka@ims.ac.jp
BL6U*	Variable-included-angle varied-line-spacing plane grating	 40 – 700 eV	Solid	Photoelectron Momentum Microscopy	F. Matsui matui@ims.ac.jp
BL6B	Michelson FT-IR	 4 meV – 2.5 eV	Solid	Reflection Absorption IR microscope	K. Tanaka k-tanaka@ims.ac.jp
BL7U	10-m normal incidence (modified Wadsworth)	 6 – 40 eV	Solid	Photoemission	K. Tanaka k-tanaka@ims.ac.jp
BL7B	3-m normal incidence	 1.2 – 25 eV	Solid	Reflection Absorption Photon-emission	F. Matsui matui@ims.ac.jp

Yellow columns represent undulator beamlines.

***In-house beamline**

BL1U

Light Source Development Station

▼ Description

BL1U is dedicated for developments and applications of novel light sources. This beamline is equipped with a dedicated tandem undulator for variable polarization with a buncher section, which can be used for free electron laser in the range from visible to deep UV, VUV coherent harmonic generation (CHG), and generation of spatiotemporal structured light such as an optical vortex beam, a vector beam and double-pulse wave packets. It is also equipped with a femto-second laser system synchronized with the accelerator, which is used for the generation of CHG, laser Compton scattered gamma-rays, and coherent THz radiation. Nowadays, material analysis by positron annihilation spectroscopy using laser Compton scattered gamma rays is actively used.

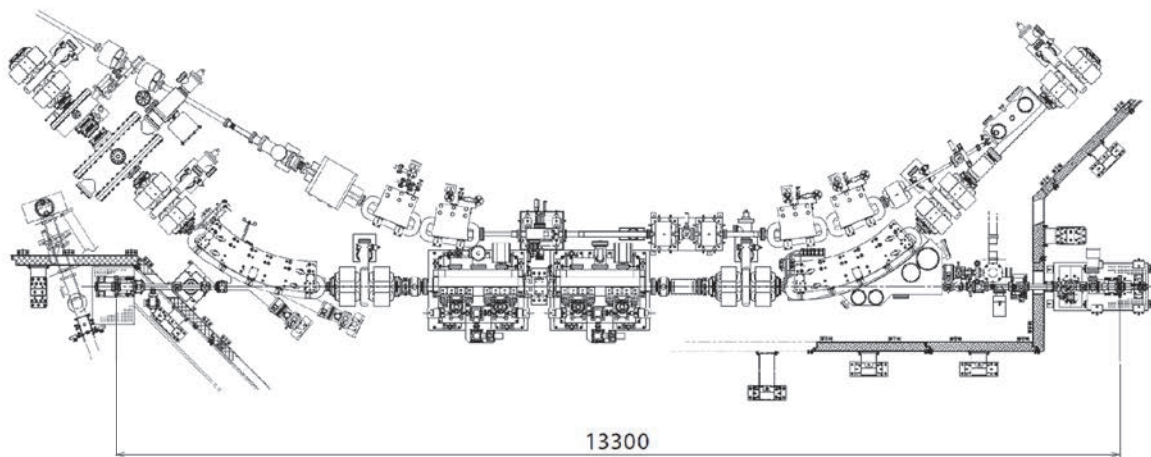


Fig. 1. Configuration of the free electron laser

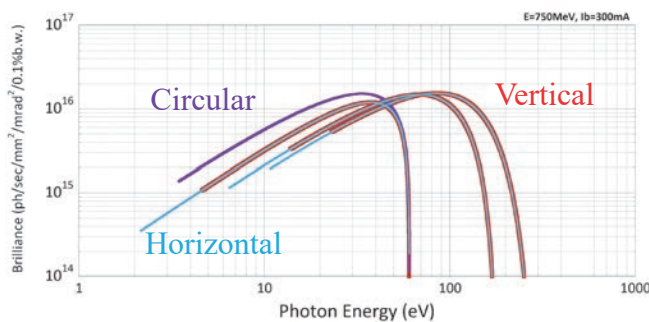


Fig. 2. Brilliance of BL1U Apple-II Undulator.



Fig. 3. Accelerator Synchronized Laser System.

▼ Technical Data of FEL

Wave Length	199-800 nm
Spectral Band Width	$\sim 10^{-4}$
Polarization	Circular/Linear
Pulse Rate	11.26 MHz
Max. Ave. Power	~ 1 W

▼ Technical Data of Ti:Sa Laser

Wave Length	800 nm
Pulse Length	130 fsec
Oscillator	90.1 MHz
Pulse Energy	2.5 mJ 10 mJ 50 mJ
Repetition Rate	1 kHz 1 kHz 10 Hz

BL1B

Terahertz Spectroscopy Using Coherent Synchrotron Radiation

▼ Description

Coherent synchrotron radiation (CSR) is a powerful light source in the terahertz (THz) region. This beamline has been constructed for basic studies on the properties of THz-CSR. However, it can be also used for measurements of reflectivity and transmission spectra of solids using conventional synchrotron radiation.

The emitted THz light is collected by a three-dimensional magic mirror (3D-MM, M0) of the same type as those already successfully installed at BL43IR in SPring-8 and BL6B in UVSOR-II. The 3D-MM was installed in bending-magnet chamber #1 and is controlled by a 5-axis pulse motor stage (x, z translation; $\theta_x, \theta_y, \theta_z$ rotation). The acceptance angle was set at 17.5-34 degrees (total 288 mrad) in the horizontal direction. The vertical angle was set at ± 40 mrad to collect the widely expanded THz-CSR.

The beamline is equipped with a Martin-Puplett type interferometer (JASCO FARIS-1) to cover the THz spectral region from 4 to 240 cm^{-1} ($h\nu = 500 \mu\text{eV}$ -30 meV). There is a reflection/absorption spectroscopy (RAS) end-station for large samples (\sim several mm). At the RAS end-station, a liquid-helium-flow type cryostat with a minimum temperature of 4 K is installed.

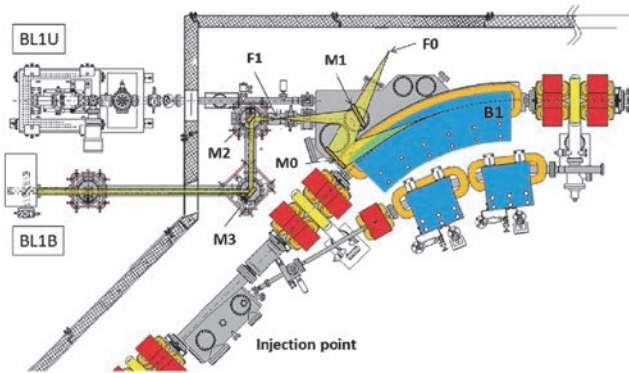


Fig. 1. Schematic top view of the beam extraction part of the THz-CSR beamline, BL1B. The three-dimensional magic mirror (3D-MM, M0) and a plane mirror (M1) are located in the bending-magnet chamber. A parabolic mirror (M2) is installed to form a parallel beam. The straight section (BL1U) is used for coherent harmonic generation (CHG) in the VUV region.

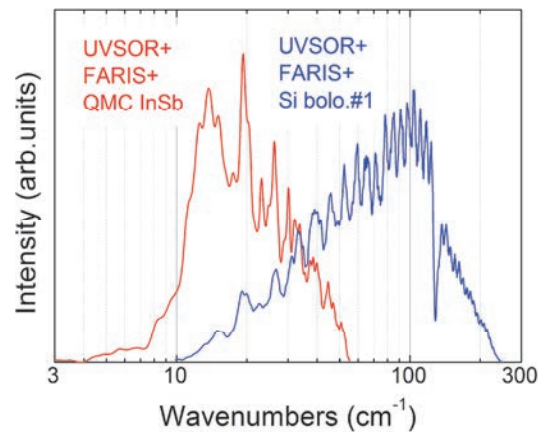


Fig. 2. Obtained intensity spectra with the combination of a light source (UVSOR), interferometer (FARIS-1), and detectors (Si bolometer and InSb hot-electron bolometer).

▼ Technical Data

Interferometer	Martin-Puplett (JASCO FARIS-1)
Wavenumber range (Energy range)	4-240 cm^{-1} (500 μeV -30 meV)
Resolution in cm^{-1}	0.25 cm^{-1}
Experiments	Reflection/transmission spectroscopy
Miscellaneous	Users can use their experimental system in this beamline.

BL2A

Soft X-Ray Beamline for Photoabsorption Spectroscopy

▼ Description

BL2A is a soft X-ray beamline for photoabsorption spectroscopy. The beamline is equipped with a pre-focusing mirror and a double-crystal monochromator [1]. The monochromator serves soft X-rays in the energy region from 585 to 4000 eV using several types of single crystals, such as beryl, KTP (KTiOPO₄), and InSb. The throughput spectra measured using a Si photodiode (AXUV-100, IRD Inc.) are shown in Fig. 1. The typical energy resolution ($E/\Delta E$) of the monochromator is approximately 1500 for beryl and InSb.

There is a small vacuum chamber equipped with an electron multiplier (EM) detector. Photoabsorption spectra for powdery samples are usually measured in total electron yield mode, with the use of the EM detector. In addition, a hemispherical electron analyzer for photoelectron spectroscopy is equipped.

Recently, a new omnidirectional photoelectron acceptance lens (OPAL) has been developed aiming to realize 2π -steradian photoelectron spectroscopy and photoelectron holography [2]. By combining OPAL and the existing hemispherical electron analyzer, a photoelectron spectrometer with high energy resolution can be realized, and a full range ($\pm 90^\circ$) 1D angular distribution can be measured at once. This upgrade is currently in the commissioning phase.

[1] Hiraya *et al.*, Rev. Sci. Instrum. **63** (1992) 1264.

[2] H. Matsuda and F. Matsui, Jpn. J. Appl. Phys. **59** (2020) 046503.

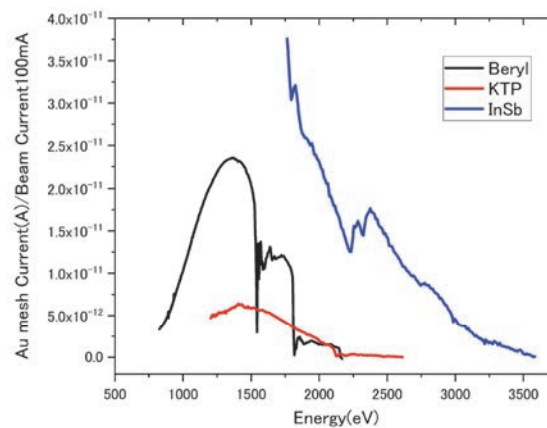


Fig. 1. Throughput spectra of the double-crystal monochromator at BL2A.

▼ Technical Data

Monochromator	Double crystal monochromator
Monochromator crystals: (2d value, energy range)	beryl (15.965 Å, 826–2271 eV), KTP (10.95 Å, 1205–3310 eV), InSb (7.481 Å, 1764–4000 eV), Ge (6.532 Å, 2094–4000 eV)
Resolution	$E/\Delta E = 1500$ for beryl and InSb
Experiments	Photoabsorption spectroscopy (total electron yield using EM and partial fluorescence yield using SDD)

BL2B

Photoelectron spectroscopy of molecular solids

▼ Description

This beamline previously dedicated for experiments in the field of gas phase photoionization and reaction dynamics. Then, the beamline has been reconstructed for photoelectron spectroscopy of molecular solids with a new end station, and experiments can be performed from May 2014. The monochromator is a spherical grating Dragon type with 18-m focal length. High throughput (1×10^{10} photons s^{-1}) and high resolution ($E/\Delta E = 2000 - 8000$) are achieved simultaneously under the condition of the ring current of 100 mA [1]. The optical system consists of two pre-focusing mirrors, an entrance slit, three spherical gratings (G1 - G3), two folding mirrors, a movable exit slit, and a refocusing mirror [2]. The monochromator is designed to cover the energy range of 23–205 eV with the three gratings: G1 (2400 lines mm^{-1} , $R = 18$ m) at 80–205 eV; G2 (1200 lines mm^{-1} , $R = 18$ m) at 40–100 eV; G3 (2400 lines mm^{-1} , $R = 9.25$ m) at 23–50 eV. The percentage of the second-order light contamination at $h\nu = 45.6$ eV is 23 % for G2 or 7 % for G3.

A UHV chamber is placed downstream of the refocusing mirror chamber and equipped silicon photodiode, sapphire plate Au mesh and filters for absolute photon flux measurement, monitor the photon-beam position, relative photon flux measurements and attenuate higher order light, respectively.

The new end station consists of a main chamber with a hemispherical analyzer (SCIENTA R3000) and a liquid-He-cooled cryostat (temperature range of 15–400 K) with 5-axis stage, a sample preparation chamber with a fast-entry load-lock chamber and a cleaning chamber with LEED, ion gun for sputtering and IR heating unit.

[1] M. Ono, H. Yoshida, H. Hattori and K. Mitsuke, Nucl. Instrum. Meth. Phys. Res. A **467-468** (2001) 577.

[2] H. Yoshida and K. Mitsuke, J. Synchrotron Radiation **5** (1998) 774.

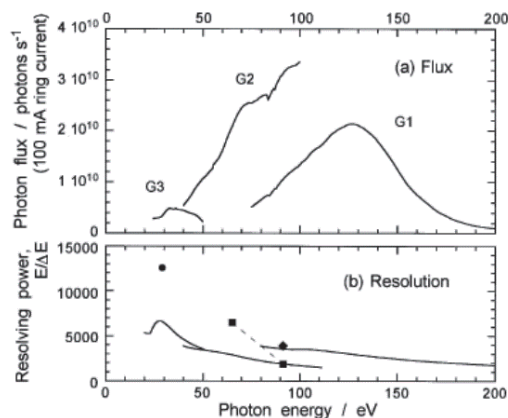


Fig. 1. Throughput from Dragon monochromator.

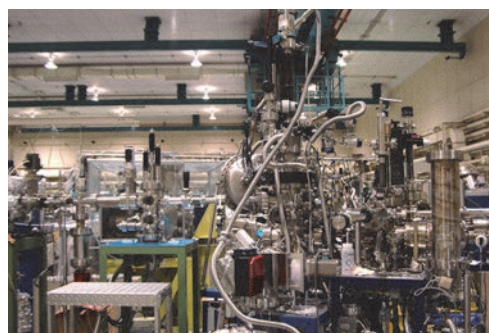


Fig. 2. End station of BL2B for photoelectron spectroscopy of molecular solids.

▼ Technical Data

Monochromator	18 m spherical grating Dragon-type
Wavelength Range	23-205 eV
Resolution	2000–8000 depending on the gratings
Experiments	Angle-resolved ultraviolet photoelectron spectroscopy

BL3U

Varied-Line-Spacing Plane Grating Monochromator for Molecular Soft X-Ray Spectroscopy

▼ Description

The beamline BL3U is equipped with an in-vacuum undulator composed of 50 periods of 3.8 cm period length. The emitted photons are monochromatized by the varied-line-spacing plane grating monochromator (VLS-PGM) designed for various spectroscopic investigations in the soft X-ray range. Three holographically ruled laminar profile plane gratings are designed to cover the photon energy range from 40 to 800 eV. The beamline has liquid cells for soft X-ray absorption spectroscopy (XAS) in transmission mode as shown in Fig. 1. The liquid cell is in the atmospheric helium condition, which is separated by a 100 nm thick Si_3N_4 membrane with the window size of $0.2 \times 0.2 \text{ mm}^2$ from the beamline in an ultrahigh vacuum condition. The thin liquid layer is assembled by using two 100 nm thick Si_3N_4 membranes. The thickness of the liquid layer is controllable from 20 to 2000 nm by adjusting the helium pressures around the liquid cell in order to transmit soft X-rays. Liquid samples are exchangeable *in situ* by using a tubing pump. The liquid cell has two types of windows: one is the liquid part to obtain the soft X-ray transmission of liquid (I), and the other is the blank part to obtain the transmission without liquid (I_0). We can obtain the reliable XAS spectra based on the Lambert-Beer law $\ln(I_0/I)$. Since the liquid cell is in the atmospheric condition, we can measure XAS of liquid samples in the real environment. *Operando* XAS observation of several chemical reactions such as catalytic, electrochemical reactions are also possible by using our liquid cells developed for these purposes.

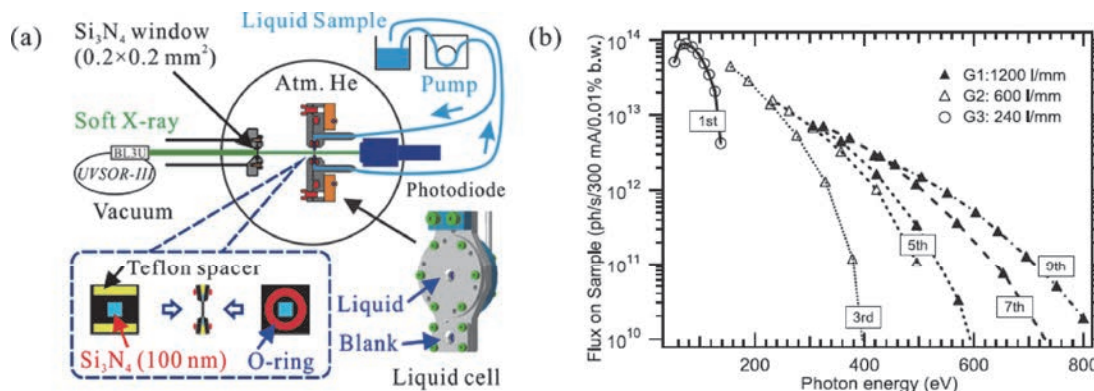


Fig. 1. (a) Schematics of a liquid cell for XAS in transmission mode settled in BL3U. The blowup shows a thin liquid layer assembled by two Si_3N_4 membranes with the thickness of 100 nm. (b) Flux at the sample position with the resolving power of $\lambda/\Delta\lambda=10^4$.

▼ Technical Data

Monochromator	Varied-line-spacing plane grating monochromator
Energy Range	40-800 eV
Resolution	$E / \Delta E > 10\,000$
Experiments	Soft X-ray absorption spectroscopy of liquid in transmission mode

BL3B (HOTRLU)

VIS-VUV Photoluminescence and Reflection/Absorption Spectroscopy

▼ Description

BL3B has been constructed to study photoluminescence (PL) in the visible (VIS) to vacuum ultraviolet (VUV) region. This beamline consists of a 2.5 m off-plane Eagle type normal-incidence monochromator, which covers the VUV, UV, and VIS regions, i.e., the energy (wavelength) region of 1.7-31 eV (40-730 nm), with three spherical gratings having constant grooving densities of 1200, 600, and 300 l/mm optimized at the photon energies of ~ 20 , ~ 16 , and ~ 6 eV, respectively. The schematic side view and top view layouts are shown in Figs. 1(a) and 1(b), respectively. The FWHM of the beam spot at the sample position is 0.25 mm (V) \times 0.75 mm (H). Low energy pass filters (LiF, quartz, WG32, OG53) can be inserted automatically to maintain the optical purity in the G3 (300 l/mm) grating region (1.7 \sim 11.8 eV). Figure 2 shows the throughput spectra (photon numbers at a beam current of 300 mA) for each grating with entrance and exit slit openings of 0.1 mm (resolving power $E / \Delta E$ of ~ 2000 (G3, ~ 6.8 eV)). Since both slits can be opened up to 0.5 mm, a monochromatized photon flux of 10^{10} photons/s or higher is available for PL measurements in the whole energy region.

The end station is equipped with a liquid-helium-flow type cryostat for sample cooling and two detectors; one of which is a photomultiplier with sodium salicylate and the other a Si photodiode for reflection/absorption measurement. For the PL measurements in the wide energy region from VIS to VUV, two PL monochromators, comprising not only a conventional VIS monochromator but also a VUV monochromator with a CCD detector, are installed at the end station.

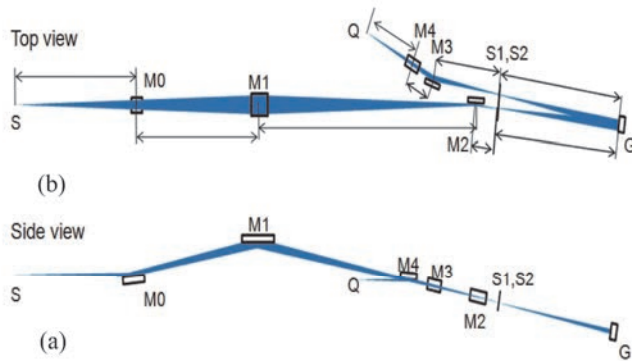


Fig. 1. Schematic layout of the BL3B (a) side view and (b) top view.

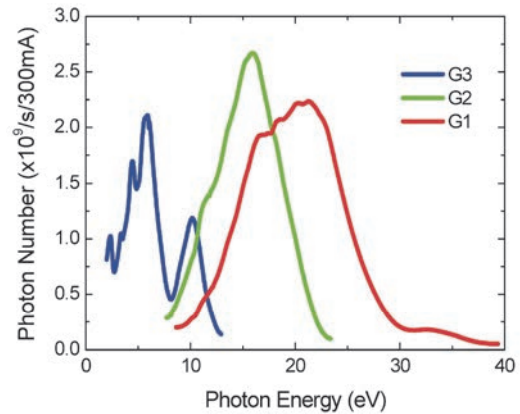


Fig. 2. Throughput spectra for each grating (G1:1200 l/mm, G2:600 l/mm and G3:300 l/mm) with $S1 = S2 = 0.1$ mm.

▼ Technical Data

Monochromator	2.5 m normal-incidence monochromator
Energy range	1.7-31 eV (40~730 nm)
Resolution ($\Delta h\nu / h\nu$)	≥ 12000 (at ~ 6.9 eV, 0.02 mm slits, G1 (1200 l/mm))
Experiments	Photoluminescence, reflection, and absorption spectroscopy, mainly for solids

BL4U

Scanning Transmission X-ray Microscopy in the Soft X-ray Region

▼ Description

In the soft x-ray region, there are several absorption edges of light elements and transition metals. The near edge X-ray absorption fine structure (NEXAFS) brings detailed information about the chemical state of target elements. A scanning transmission X-ray microscope (STXM) in the soft X-ray region is a kind of extended technique of the NEXAFS with high spatial resolution. The STXM has a capability of several additional options, for example, in-situ observations, 3-dimensional observation by computed tomography and ptychography, by utilizing the characteristics of the X-rays. The STXM can be applied to several sciences, such as polymer science, material science, cell biology, environmental science, and so on.

This beamline equips an in-vacuum undulator, a varied-line-spacing plane grating monochromator and a fixed exit slit. The soft X-ray energy range from 50 to 770 eV with the resolving power ($E/\Delta E$) of 6,000 is available. The aperture size of the fixed exit slit determines not only the resolving power but also the size of a microprobe. A Fresnel zone plate is used as a focusing optical device through an order select aperture and its focal spot size of ~30 nm is available at minimum. An image is acquired by detecting intensities of the transmitted X-rays by a photomultiplier tube with scintillator with scanning a sample 2-dimensionally. By changing the energy of the incident beam, each 2-dimensional NEXAFS image is stacked. A main chamber of STXM is separated from the beamline optics by a silicon nitride membrane of 50-nm thickness; therefore, sample holders can be handled in vacuum or in helium.

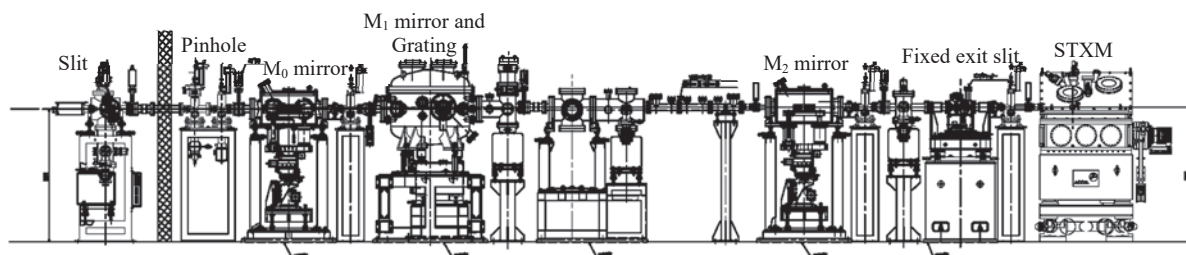


Fig. 1. Schematic image of BL4U

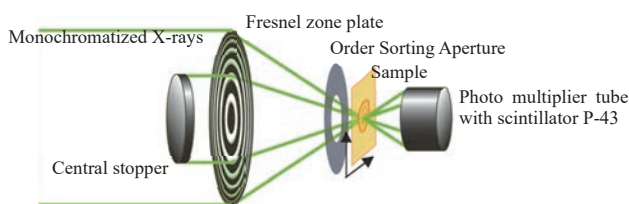


Fig. 2. Schematic image of STXM.

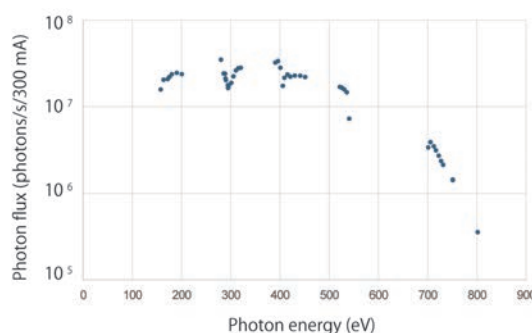


Fig. 3. Photon flux at the sample.

▼ Technical Data

Energy range (E)	50 -770 eV
Resolving power ($E/\Delta E$)	~6,000
Photon flux on a sample (photons/s)	~2×10 ⁷ @400 eV
Focusing optical element	Fresnel zone plate
Spatial resolution	~30 nm
Experiments	2-dimensional absorption spectroscopy
Measurement environment	standard sample folder in vacuum or in helium, specially designed sample cell in ambient condition

BL4B

Varied-Line-Spacing Plane Grating Monochromator for Molecular Soft X-Ray Spectroscopy

▼ Description

The beamline BL4B equipped with a varied-line-spacing plane grating monochromator (VLS-PGM) was constructed for various spectroscopic investigations in a gas phase and/or on solids in the soft X-ray range. Three holographically ruled laminar profile plane gratings with SiO₂ substrates are designed to cover the photon energy range from 25 to 800 eV. The gratings with groove densities of 100, 267, and 800 l/mm cover the spectral ranges of 25–100, 60–300, and 200–1000 eV, respectively, and are interchangeable without breaking the vacuum. Figure 1 shows the absolute photon flux for each grating measured using a Si photodiode (IRD Inc.), with the entrance- and exit-slit openings set at 50 and 50 μm , respectively. The maximum resolving power ($E/\Delta E$) achieved for each grating exceeds 5000.

There is no fixed endstation on this beamline. A small vacuum chamber equipped with an electron multiplier (EM) detector is available. Soft X-ray absorption spectra of solid samples are usually measured by means of the total electron yield method using EM, and the partial fluorescence yield method using a silicon drift detector (SDD).

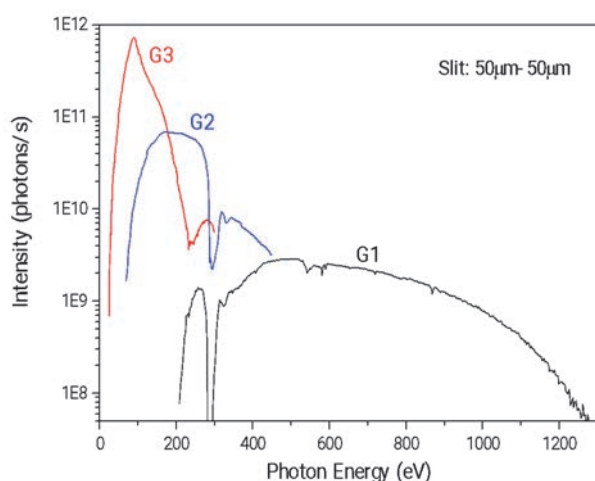


Fig. 1. Throughput from the VLS-PGM monochromator on BL4B.



Fig. 2. Photo of BL4B.

▼ Technical Data

Monochromator	Varied-line-spacing Plane Grating Monochromator
Energy range	25-1000 eV
Resolution	$E / \Delta E > 5000$ (at maximum)
Experiments	Soft X-ray spectroscopy (mainly, photoabsorption spectroscopy for solid targets by means of total electron yield method using EM and partial fluorescence yield method using SDD)

BL5U

Photoemission Spectroscopy of Solids and Surfaces

▼ Description

Since the monochromator of BL5U was an old-style spherical grating type SGMTRAIN constructed in 1990s and the throughput intensity and energy resolution were poor, the whole beamline has been replaced to state-of-the-art monochromator and end station. The new beamline has been opened to users from FY2016 as high-energy resolution ARPES beamline. Samples can be cooled down to 3.8 K with newly developed 5-axis manipulator to perform high energy resolution measurements. Users can also obtain spatial-dependence of the electronic structure of solids using micro-focused beam ($\sim 50 \mu\text{m}$). The new electron lens system makes it possible to obtain ARPES spectra without moving samples. This beamline will also have new capability to perform high-efficient spin-resolved ARPES in the future.

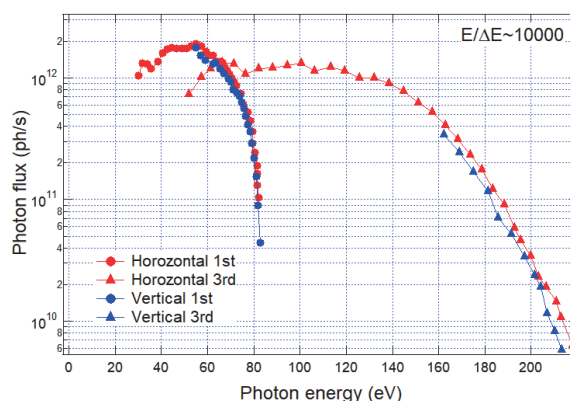
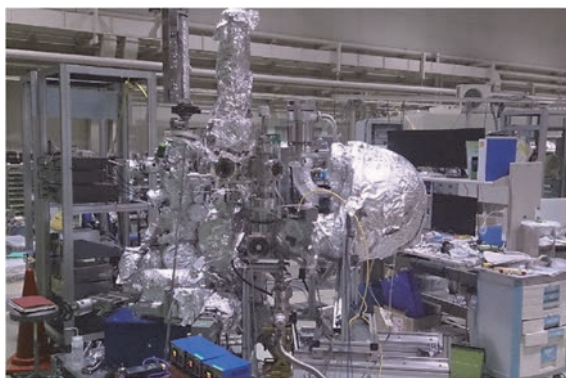


Fig. 1. Picture and photon flux of BL5U.

▼ Technical Data (Expected Performance)

Light source	APPLE-II type undulator ($\lambda_u = 60 \text{ mm}$, $N = 38$) vertical/horizontal, right/left circular (depending on $h\nu$)
Monochromator	Monk-Gillieson VLS-PGM
Energy Range	20-200 eV
Resolution	$h\nu / \Delta E > 10,000$ for $< 10 \mu\text{m}$ slits
Experiment	ARPES, Space-resolved ARPES, Spin-resolved ARPES
Flux	$< 10^{12}$ photons/s for $< 10 \mu\text{m}$ slits (at the sample position)
Beam spot size	23 (H) x 40 (V) μm
Main Instruments	Hemispherical photoelectron analyzer with deflector scan (MBS A-1 Lens#4), Liq-He flow cryostat with 5-axis manipulator (3.8 K-350 K)

BL5B

Calibration Apparatus for Optical Elements and Detectors

▼ Description

BL5B has been constructed to perform calibration measurements for optical elements and detectors. This beamline is composed of a plane grating monochromator (PGM) and three endstations in tandem. The most upstream station is used for the calibration measurements of optical elements, the middle one for optical measurements for solids, and the last for photo-stimulated desorption experiments. The experimental chamber at the most downstream station is sometimes changed to a chamber for photoemission spectroscopy. The calibration chamber shown in Fig. 2 is equipped with a goniometer for the characterization of optical elements, which has six degrees of freedom, X-Y translation of a sample, and interchanging of samples and filters. These are driven by pulse motors in vacuum. Because the polarization of synchrotron radiation is essential for such measurements, the rotation axis can be made in either the horizontal or vertical direction (s- or p-polarization).

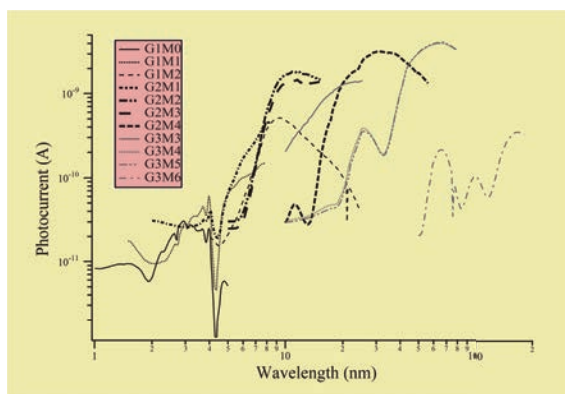


Fig. 1. Throughput spectra for possible combinations of gratings and mirrors at BL5B measured by a gold mesh.

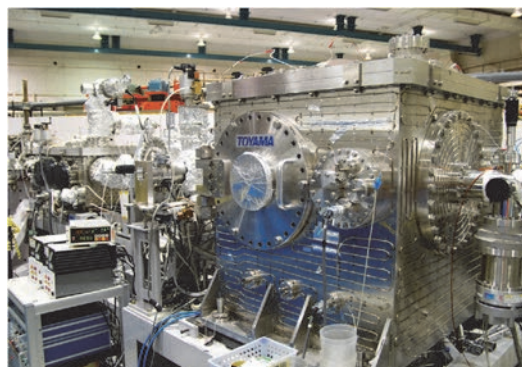


Fig. 2. A side view of the experimental chamber for calibration measurements.

▼ Technical Data

Monochromator	Plane Grating Monochromator
Energy range	6-600 eV (2-200 nm)
Resolution	$E / \Delta E \sim 500$
Experiments	Calibration of optical elements, reflection and absorption spectroscopy mainly for solids

BL6U

Variable-Included-Angle / Variable-Line-Spacing Plane Grating Monochromator for Soft X-Ray photoelectron Spectroscopy

▼ Description

The beamline BL6U equipped with a variable-included-angle Monk-Gillieson mounting monochromator with a varied-line-spacing plane grating was constructed for various spectroscopic investigations requiring high-brilliance soft X-rays on solid surfaces. Through a combination of undulator radiation and sophisticated monochromator design (entrance slit-less configuration and variable-included-angle mechanism), using a single grating, the monochromator can cover the photon energy ranging from 40 to 500 eV, with resolving power of greater than 10000 and photon flux of more than 10^{10} photons/s. Figure 1 shows an example of the monochromator throughput spectra measured using a Si photodiode, with the exit-slit opening set at 30 μm , which corresponds to the theoretical resolving power of 10000 at 80 eV.

A new Momentum Microscope experimental station for photoelectron spectroscopy resolved in 3D momentum space with a microscopic field of view has been built at BL6U (SPECS KREIOS 150 MM). A momentum resolution of 0.01 \AA^{-1} in k_x/k_y as well as k_z is achieved. A spatial resolution of 50 nm, an energy resolution of 20 meV at 9 K, and a field of view of 2 μm for ARPES are successfully demonstrated. This experimental station specializes in characterizing the electronic structure of surface atomic sites, thin films, molecular adsorbates, and bulk crystals. This method opens the door to direct observation of the Fermi surface of μm -sized crystals, which was difficult with conventional ARPES-type hemispherical analyzers.

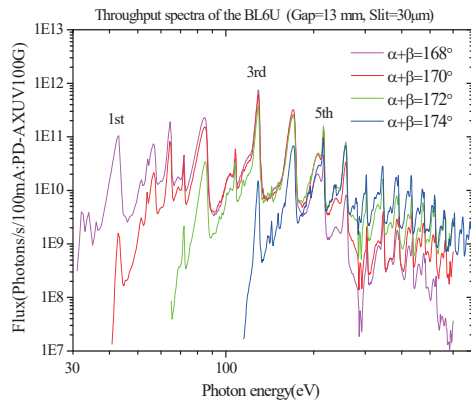


Fig. 1. Throughput spectra of the BL6U monochromator at various included angles.

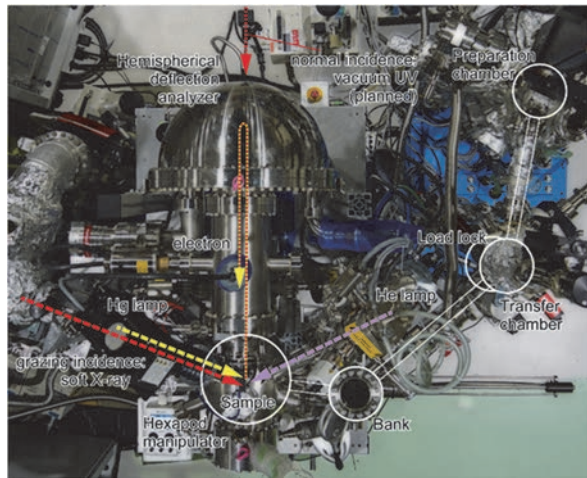


Fig. 2. Photograph of BL6U end station.

▼ Technical Data

Monochromator	Variable-included-angle Varied-line-spacing Plane Grating Monochromator
Energy range	40-500 eV(practical)
Resolution	$E / \Delta E > 10000$ (at maximum)
Experiments	High-resolution soft X-ray spectroscopy (photoelectron spectroscopy for solid surfaces)

BL6B

Infrared and Terahertz Spectroscopy of Solids

▼ Description

Synchrotron radiation (SR) has good performance (high brilliance and high flux) not only in the VUV and soft X-ray (SX) regions but also in the infrared (IR) and THz regions. BL6B covers the IR and THz regions. The previous beamline, BL6A1, which was constructed in 1985, was the pioneer in IRSR research. The beamline was deactivated at the end of FY2003 and a new IR/THz beamline, BL6B (IR), was constructed in FY2004. The front-end part including bending duct #6 was replaced with a new part having a higher acceptance angle ($215\text{ (H)} \times 80\text{ (V) mrad}^2$) using a magic mirror, as shown in Fig. 1.

There are two Michelson type interferometers in this endstation; with first one (Bruker Vertex70v), which covers a wide spectral region from $30\text{ to }20,000\text{ cm}^{-1}$ ($h\nu = 4\text{ meV}-2.5\text{ eV}$), reflection/absorption spectroscopy measurements of large samples (up to several mm) and IR/THz microscopy measurements of tiny samples (up to several tens of μm) can be performed. For reflection/absorption spectroscopy measurements, a liquid-helium- flow type cryostat with a minimum temperature of 4 K is installed. The other interferometer (Jasco FT/IR-6100), which covers $350\text{ to }15,000\text{ cm}^{-1}$ ($h\nu = 45\text{ meV}-1.8\text{ eV}$), has been available for IR microscopy imaging measurements from FY2014. One can also perform ATR measurements using diamond ATR prism.

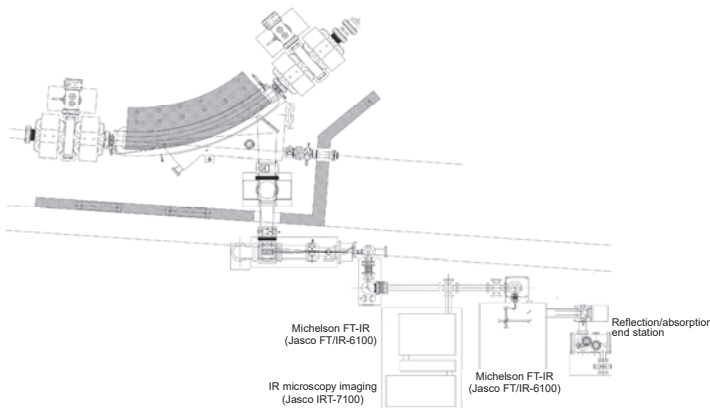


Fig. 1. Schematic top view of BL6B.

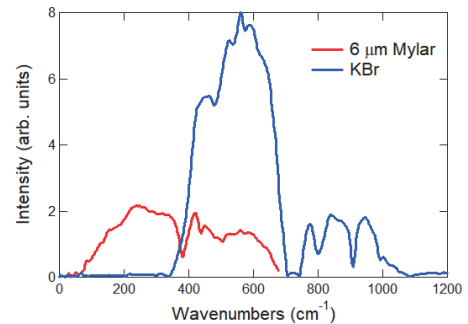


Fig. 2. Obtained intensity spectra with the combination of a light source (UVSOR), detector (Si bolometer), and interferometer (Bruker Vertex70v) with different beamsplitters ($6\text{ }\mu\text{m}$ Mylar and KBr). (Only low energy side is shown).

▼ Technical Data

Interferometer	Michelson (Bruker Vertex70v)	Michelson (Jasco FT/IR-6100)
Wavenumber Range (Energy range)	$30\text{-}20,000\text{ cm}^{-1}$ ($4\text{ meV}-2.5\text{ eV}$)	$350\text{-}15,000\text{ cm}^{-1}$ ($45\text{ meV}-1.8\text{ eV}$)
Resolution in cm^{-1}	0.1 cm^{-1}	0.5 cm^{-1}
Experiments	Reflectivity and transmission spectroscopy THz Microspectroscopy	IR microscopy imaging (JASCO IRT-7000) ATR spectroscopy

BL7U (SAMRAI)

Angle-Resolved Photoemission of Solids in the VUV Region

▼ Description

Beamline 7U, named the Symmetry- And Momentum-Resolved electronic structure Analysis Instrument (SAMRAI) for functional materials, was constructed to provide a photon flux with high energy resolution and high flux mainly for high-resolution angle-resolved photoemission spectroscopy, so-called “ARPES”, of solids [1]. An APPLE-II-type variable-polarization undulator is installed as the light source. The undulator can produce intense VUV light with horizontal/vertical linear and right/left circular polarization. The undulator light is monochromatized by a modified Wadsworth type monochromator with three gratings (10 m radius; 1200, 2400, and 3600 lines/mm optimized at $h\nu = 10, 20$, and 33 eV). The energy resolution of the light ($h\nu/\Delta h\nu$) is more than 10^4 with a photon flux of 10^{11} - 10^{12} ph/s or higher on samples in the entire energy region. The beamline has a photoemission end-station equipped with a 200 mm-radius hemispherical photoelectron analyzer (MB Scientific AB, A-1 analyzer) with a wide-angle electron lens and a liquid-helium-cooled cryostat with 6-axis pulse motor control. The main function of the beamline is to determine the electronic structure of solids and its temperature dependence in order to reveal the origin of their physical properties.

[1] S. Kimura, T. Ito, M. Sakai, E. Nakamura, N. Kondo, K. Hayashi, T. Horigome, M. Hosaka, M. Katoh, T. Goto, T. Ejima and K. Soda, Rev. Sci. Instrum. **81** (2010) 053104.

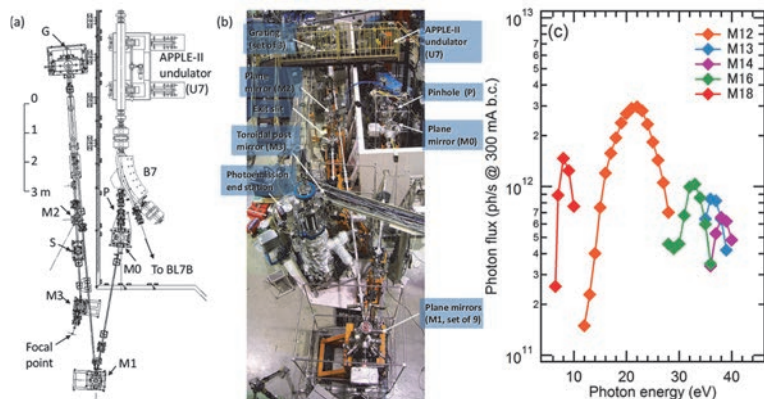


Fig. 1. SAMRAI beamline [(a), (b)] consisting of an APPLE-II type undulator (U7), a modified Wadsworth type monochromator (M0-S), and a high-resolution photoemission analyzer at the focal point. The monochromator has five major optical components: two plane mirrors (M0 and M1) with water cooling, one set of three spherical gratings (G), an exit slit (S), and one toroidal refocusing mirror (M3). (c) Example of flux intensity *versus* photon energy [1].

▼ Technical Data

Light source	APPLE-II type undulator ($\lambda_u = 76$ mm, $N = 36$) vertical/horizontal, right/left circular (depending on $h\nu$)
Monochromator	10 m normal-incidence monochromator (modified Wadsworth type)
Photon energy range	6 – 40 eV ($\lambda = 30 - 200$ nm)
Resolution ($h\nu/\Delta h\nu$)	$E / \Delta E > 10000$ -50000
Photon flux on sample	$\geq 10^{11}$ - 10^{12} ph/s (depending on $h\nu$)
Beam size on sample	200 (H) \times 50 (V) μm^2
Experiments	Angle-resolved photoemission of solids (MV Scientific A-1 analyzer, acceptance angle: ± 18 deg)

BL7B

3 m Normal-Incidence Monochromator for Solid-State Spectroscopy

▼ Description

BL7B has been constructed to provide sufficiently high resolution for conventional solid-state spectroscopy, sufficient intensity for luminescence measurements, wide wavelength coverage for Kramers–Kronig analyses, and minimum deformation to the polarization characteristic of incident synchrotron radiation. This beamline consists of a 3-m normal incidence monochromator, which covers the vacuum ultraviolet, ultraviolet, visible, and infrared, i.e., the wavelength region of 50–1000 nm, with three gratings (1200, 600, and 300 1/mm). Two interchangeable refocusing mirrors provide two different focusing positions. For the mirror with the longer focal length, an LiF or a MgF₂ window valve can be installed between the end valve of the beamline and the focusing position. Figure 1 shows the absolute photon intensity for each grating with the entrance and exit slit openings of 0.5 mm. A silicon photodiode (AXUV-100, IRD Inc.) was utilized to measure the photon intensity and the absolute photon flux was estimated, taking the quantum efficiency of the photodiode into account.

The cooling system for the pre-focusing mirror has been removed, resulting in longer beam settling times. Currently, BL7B is opened during single bunch mode, but limited use is possible during multi bunch mode.

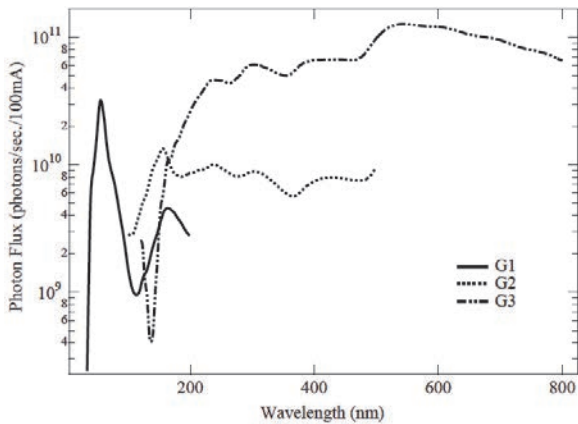


Fig. 1. Throughput spectra of BL7B measured using a silicon photodiode.

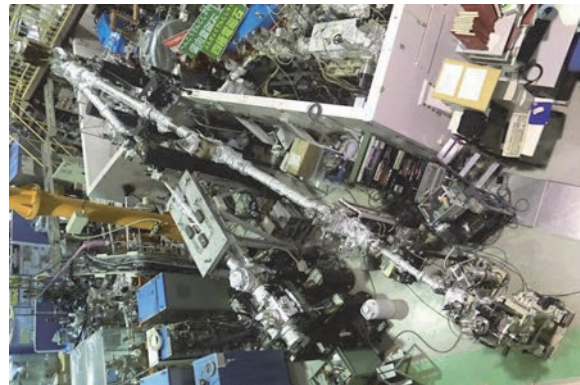


Fig. 2. Photo of BL7B.

▼ Technical Data

Monochromator	3 m Normal-Incidence Monochromator
Wavelength Range	50-1000 nm (1.2-25 eV)
Resolution	$E / \Delta E = 4000-8000$ for 0.01 mm slits
Experiments	Absorption, reflection, and fluorescence spectroscopy, mainly for solids



BL6U, 7U

The Dual-Beamline Photoelectron Momentum Microscope at UVSOR

F. Matsui^{1,2}, K. Hagiwara¹, Y. Sato¹, E. Nakamura¹, T. Yano¹, Y. Okano¹, S. Makita¹,
R. Sagehashi¹, S. Kera^{1,2}, Shin-ichiro Tanaka³ and S. Suga³

¹UVSOR Synchrotron Facility, Institute for Molecular Science, Okazaki, Aichi, Japan

²The Graduate University for Advanced Studies (SOKENDAI), Okazaki, Aichi, Japan

³SANKEN, Osaka University, Ibaraki, Osaka, Japan

1. Introduction

Elucidating the behavior of electrons in materials is of great importance for the development of materials science and device engineering. Photoelectron spectroscopy (PES) provides deep insight into the nature of the atomic and electronic structure of solids. The demand for the development of PES technique has increased further in recent years. In particular, selective observation of electronic structures from micro-sized structures is desired by various scientific communities. Currently, research efforts on the μm and sub- μm scale are underway around the world.

Photoelectron momentum microscopes (PMMs) are novel imaging photoelectron spectroscopy systems that combines a photoemission electron microscope (PEEM)-type objective lens with an energy filtering analyzer [1-3]. PMMs are revolutionizing the study of detailed electronic structures of materials and devices at the nm to tens of nm scale. We have constructed a PMM station [4,5] at BL6U [6]. This makes it possible to analyze the behavior of electrons on a μm scale. Furthermore, this advanced analytical and experimental station has been upgraded to enable the use of two undulator beamlines as excitation sources [7]. By branching off the existing vacuum ultraviolet (VUV) beamline BL7U, PMM can now simultaneously use tunable polarized VUV light in addition to the soft X-ray beam from beamline BL6U.

This world's first “*dual beamline photoelectron momentum microscope*” performs element-selective measurements using grazing incidence soft X-rays and

highly symmetric measurements using normal incidence VUV light at the same position on the sample and under the same conditions. Leveraging the flexibility of these light sources opens up new ways to analyze electron behavior in a multimodal manner. In particular, we emphasize that PES in normal incidence configuration is only available at this instrument at UVSOR worldwide. Such a highly symmetric configuration at normal incidence facilitates an accurate analysis of the valence orbitals, especially by photon polarization dependent transition matrix element analysis.

2. Details of dual beamline PMM station

2.1 BL6U

Figure 1 shows the photograph of beamline BL6U, and BL7U together with newly constructed BL7U branch [7]. The schematic layout is shown in Fig. 2. In-vacuum undulator U6 installed as the light source for BL6U provides horizontal linearly-polarized soft X-ray ($h\nu = 40\text{--}700\text{ eV}$) [8]. Figure 3(a) is a schematic of the beam and sample geometry. Typical width of the horizontal exit slit (H-slit) is set to $2\text{--}100\text{ }\mu\text{m}$ in the vertical direction. The slit size of $25\text{ }\mu\text{m}$ corresponds to the resolving power $E/\Delta E$ of 10,000. A refocusing mirror of 1:1 convergence focuses the monochromatized soft X-ray onto the sample position. The incident X-ray beam is shaped by a vertical slit (V-slit) installed at the entrance of the analysis chamber so that the soft X-ray beam is maintained at the focal point of the analyzer. The final footprint of the irradiation spot

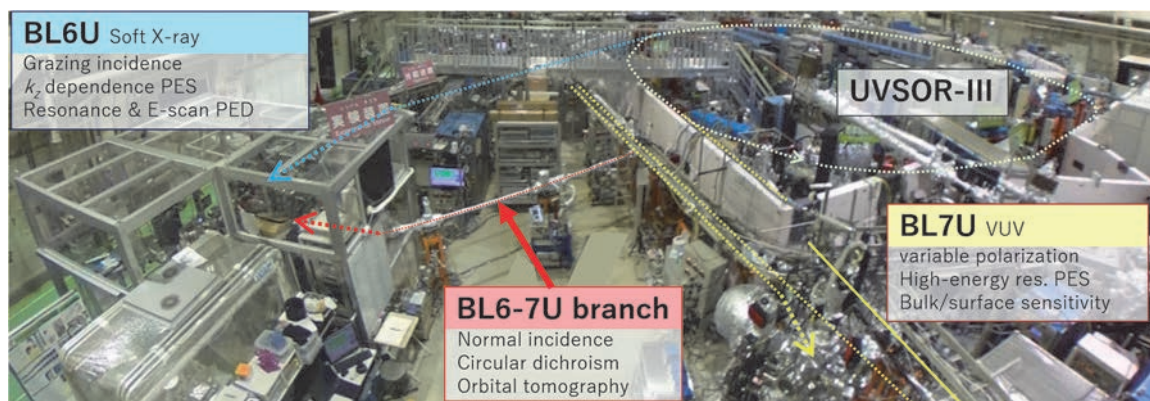


Fig. 1. Photograph of beamlines BL6U, BL7U and the newly constructed BL7U branch at the UVSOR Synchrotron Facility. The soft-X-ray (BL6U) and VUV (BL7U) beam-focusing optics and the PMM station are housed in a thermostatic hutch (300 K) so that the frame temperature fluctuation and beam fluctuation are suppressed within 0.1 K and $1\text{ }\mu\text{m}$, respectively, for hours.

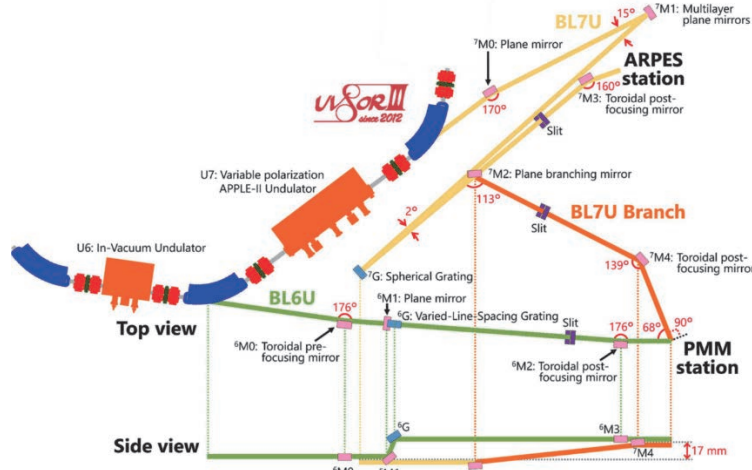


Fig. 2. Schematic layout of beamlines BL6U, BL7U and the newly constructed BL7U branch. Top and side views are shown. After the reflection on the ⁶M1 mirror and the ⁶G grating at BL6U, the beam path heightens by 17 mm. At BL7U, after reflection on the ⁷M2 mirror, the beam is reflected upward and becomes 17 mm higher at the ⁷M4 mirror than the undulator center. The beam focal point at the sample is accordingly higher than the height of the undulator center. From Ref. [6].

on the sample is 100–300 μm horizontally and 2–100 μm vertically. Typical maximum photon flux density is on the order of 10^5 – 10^7 photons/s/ μm^2 . By varying the undulator gap from its optimal position, the photon flux density can be continuously reduced to achieve optimal measurement conditions for fragile molecular adsorbates and compound samples.

The sample surface lies in the xy plane. The upper direction of the vertical axis was defined as the $+x$ direction. The photon beam from BL6U is incident at an angle of 68° from the sample surface normal (z) axis. The PMM consists of a PEEM optics as an input lens [2] and a hemispherical deflection analyzer (HDA) [9]. The PEEM axis is set along the sample normal direction z . The yz plane, which contains the incident photon axis, its p-polarized electric field vector, and the PEEM optics axis, forms the mirror plane of the experimental geometry.

2.2 BL7U

Variable-polarization APPLE-II-type undulator U7 of BL7U can produce horizontal/vertical linearly and right/left circularly polarized VUV photons. The undulator light is guided to the ⁷G spherical grating by the ⁷M0 and ⁷M1 plane mirrors and is monochromatized by the ⁷G grating. High-energy-resolution ARPES experimental station (SAMRAI beamline) [10] is available at the end of BL7U.

The BL7U branch is designed to deliver a sufficiently high photon flux in both horizontal and vertical polarization to the same spot on the sample illuminated by the BL6U SX beam. By inserting /retracting the ⁷M2 mirror installed after the ⁷G grating, we can switch experiments of PMM at the end of BL7U branch [7] or ARPES at the end of BL7U [10]. The reflectance for the horizontally polarized light is lower than that for vertically polarized light and even becomes zero in the case of the Brewster angle. In order to avoid this configuration and also to hold a workspace for BL7U users, the beamline arrangement with a reflection angle of 113° at the ⁷M2 mirror and 139° at the ⁷M4 mirror was adopted. After reflection on the ⁷M4 mirror, the

beam goes horizontally and the beam focal point of BL7U branch matches that of BL6U. The photon beam from BL7U comes in along the surface normal axis (s-polarized). The light linearly polarized in either xz or yz planes, *i.e.*, horizontally polarized light (H-pol.) and vertically polarized light (V-pol.), respectively, is available at the PMM experimental station. We are currently commissioning the undulator U7 for

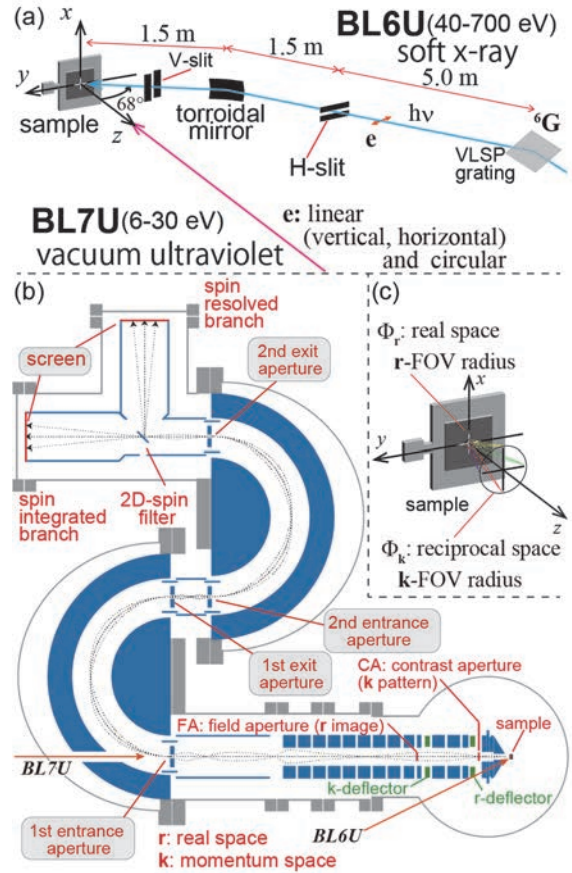


Fig. 3. (a) Incidence of photon and sample orientation. (b) Schematic drawing of photoelectron momentum microscope. (c) Fields of view (FOV) in real and reciprocal spaces.

generating circularly polarized VUV light.

Note that the use of the SAMRAI beamline and the branch PMM beamline is exclusive and cannot be used simultaneously. Fortunately, the position repeatability of $^7\text{M}2$ makes it possible to switch between them in a short time. Currently, part of the beamtime at BL7U (about two weeks per semester) is allocated to developmental use at the branch.

2.3 PMM sample stage and chamber

The sample manipulator is equipped with a six-axis sample motion system (HESTIA) and a liquid-helium-flow cryostat. Samples can be cooled down below 10 K and heated up to 400 K. During the cooling process, the sample position shifted within 10 μm . The soft-X-ray (BL6U) and VUV (BL7U) beam-focusing optics and the PMM station (SPECS KREIOS 150MM DI spin) is housed in a thermostatic hutch (300 K). Within the hutch, the frame temperature fluctuation and beam fluctuation are suppressed within 0.1 K and 1 μm , respectively, for hours in our system.

Bellows with a diameter of 35 mm are used to connect the PMM analytical chamber to each of the two beamlines and to the preparation chamber complex. The vacuum force pulls the vacuum chamber horizontally from three directions, so if left alone, it will constantly be pulled toward BL7U. To prevent this, we used a 10-kg weight as a counterbalance to ensure that the chamber remained stable and in the same position.

2.4 PEEM column and HDA

The diffraction pattern is projected onto the back focal plane at the contrast aperture (CA) position (Fig.3(b)). The sample image is magnified 10 times in the first image plane at the FA position by the objective lens at an extraction voltage of 15 keV. By decreasing (increasing) the extraction voltage, the projection range in momentum space at the CA position is decreased (increased), while the size of real-space field of view (FOV) at the FA position is increased (decreased). The second half of the PEEM lens switches between microscopy (R mode) and momentum (K mode) observations (Fig.4). Further-more, the magnification of the sample image or reciprocal space pattern can be varied by setting multilens parameters. A real space image (x, y) or reciprocal space pattern (k_x, k_y) at the PEEM lens exit is transferred through the transfer lens and then projected onto the HDA entrance.

Apertures of different sizes can be selected for the HDA entrance and exit, as well as CA and FA, allowing control over the cropping extent of the 2D data projected onto them. When the CA and FA are fully open for electrons with sufficiently large kinetic energies and the extraction voltage is fixed, then the performance of the PMM is determined by the HDA apertures. The maximum \mathbf{r} -FOV in the R mode (Φ_r^R) and the maximum \mathbf{k} -FOV in the K mode (Φ_k^K), are determined by the magnification factor and the extraction voltage (Fig.3(c)). The \mathbf{k} -FOV in the R mode (Φ_k^R) and the

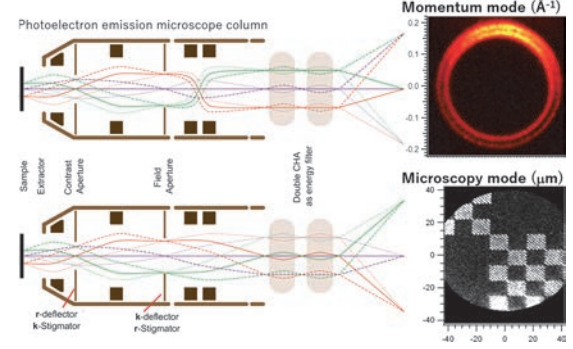


Fig. 4. Trajectory of electron in the PEEM column operated in momentum and microscopy modes. Field and contrast apertures are used to select the region of interests in real and reciprocal spaces in momentum and microscopy modes, respectively. The Rashba surface state of Au(111) surface and a checkerboard pattern are shown as examples for R and K mode observations.

\mathbf{r} -FOV in the K mode (Φ_r^K) are proportional to the diameter of the HDA entrance aperture. See Ref. [11] for details. By choosing the appropriate aperture size for the CA and FA, we can control the \mathbf{k} -FOV and \mathbf{r} -FOV, respectively, and realize momentum-selective photoelectron microscopy and domain-selective momentum-resolved PES, respectively [4,12]. Note that when the photoelectron momentum, $\mathbf{k}_{\parallel, \max} = 0.5123\sqrt{E_{\text{kin}}}k$, is smaller than Φ_k , photoelectrons emitted to all hemispheres are projected onto the screen.

PMMs utilize the imaging function of the HDA. Only electrons in the energy window centering on a specific energy that corresponds to the path energy (E_{pass}) reach the HDA exit. At this exit aperture position, the real space image or reciprocal space pattern at the HDA entrance position is reconstructed. Recently, we upgraded the PMM with a single HDA [4,11] to the PMM with twin HDAs [7]. For the normal incidence experiment, the entrance slit of the first HDA is set to be open so that the beam can go through the optical lens of the PMM and arrive at the sample position. The exit slit of the first HDA is set to smaller one instead [13].

2.5 Detector

A Fourier transform lens converts this two-dimensional (2D) electron distribution from the real space to the reciprocal space, or vice versa, and projects it onto a fluorescent screen. This screen image is digitized by a CMOS camera. The volume data of band dispersion $I(E, k_x, k_y)$ or micro-spectroscopy $I(E, x, y)$ were constructed by measuring a series of 2D constant energy contours (CECs) of band (k_x versus k_y) [12] and PEEM images (x versus y) [5], respectively, as a function of the binding energy, E_{binding} .

An In(001) single crystal on a retractable manipulator is installed as a 2D spin filter. By retracting and inserting the spin filter, spin-integrated and spin-resolved photoelectron 2D intensity distribution data are acquired by one of two identical 2D detectors,

respectively (Fig. 3(b)).

3. Examples of comprehensive valence band characterization

3.1 Advantage of 2D-CEC measurement

In the past, to measure a wide range of angular distributions using analyzers with small acceptance angles, the sample orientation was rotated in 2D (θ , ϕ) and the data was spliced together. This measurement style remains the standard and effective method for spin-polarized angle-resolved PES. The equivalent set of data may be now acquired by using a conventional HDA with the latest deflection-type lenses; measuring 2D $I(E_{\text{binding}}, k_y)$ data as a function of k_x [8,14]. Furthermore, the use of the PMM is much more efficient than the use of such a method for measuring $I(k_x, k_y)$. The PMM that can simultaneously measure 2D CEC data eliminates the need to reorient the sample step-by-step, increasing the detection efficiency and reliability. Since the 2D Fermi surface can be simultaneously observed in real time [15] by our system, the use of the PMM is much better for confirming the location dependence of heterogeneous samples and polycrystalline samples, aligning the crystal orientation, and performing microscopic Fermi surface measurements within a good quality location [16]. Rotating the azimuthal angle of the sample can change the orientation of the electric field vector of incident photon (e) for evaluating the matrix element effect for atomic orbital analysis of valence band and molecular orbitals [17]. Short measurement times help to reduce possible damage of fragile molecular adsorbates and compound samples. Furthermore, 2D spin-polarized PMM measurements are a cutting-edge application of the CEC projection-type energy analyzer.

3.2 Normal and grazing incidence photoemission

Figure 5 shows the 2D momentum (k_x, k_y) distribution of photoelectron intensity of Au(111) at the Fermi level with an energy window of ± 50 meV [7]. The measurements were performed with V-pol. light at $h\nu = 20$ eV (a, c) and H-pol. light at $h\nu = 20$ eV from the BL7U branch (b). Note that, in Figs. 5(a-c), we captured all photoelectrons emitted up to the emission angle of $\theta = \pm 90^\circ$ (or within the emission cone of 2π steradian) by the PMM, covering the maximum wide k_{\parallel} space. Furthermore, Figs. 5(d) and (e) show the 2D patterns measured using p-polarized light at $h\nu = 100$ eV and 80 eV, respectively, from BL6U. Shockley surface states centered at the Γ point as small circular contours is clearly observed with p-polarized excitation (Figs. 5(d-e)). These features exhibit very weak intensity for normal incidence light (Figs. 5(a-c)). This surface state mainly comprises $6s$ and $6p_z$ orbitals. In the normal-incidence geometry, the transition-matrix element from the initial s and p_z orbitals becomes 0 at the photoemission direction orthogonal to the excited electric field vector. The relationship between the orbital angular momentum and the effects of the transition matrix elements can be directly investigated

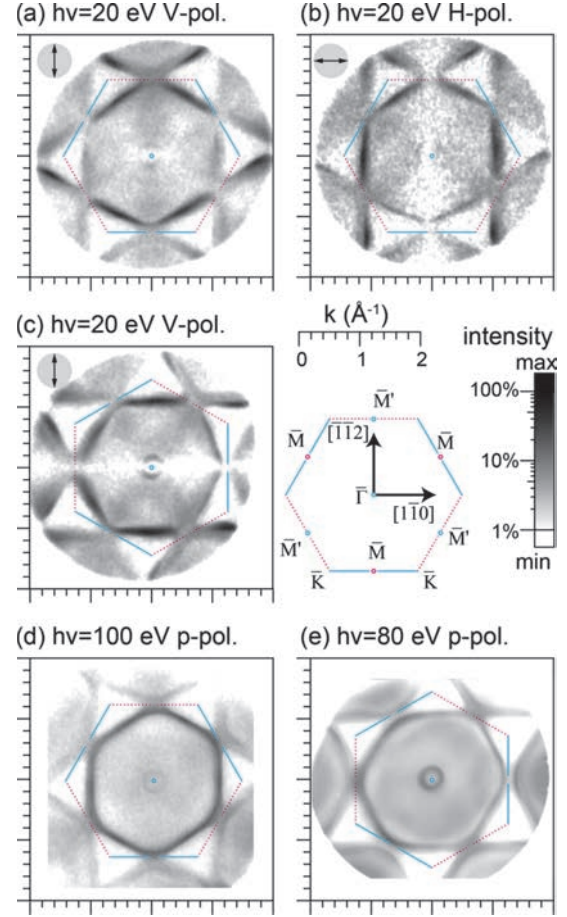


Fig. 5. 2D momentum (k_x, k_y) distribution of the photoelectron intensity of the Au(111) surface at the Fermi level plotted on a logarithmic contrast scale. Measurements were performed with V-pol. at $h\nu = 20$ eV (a, c), H-pol. at $h\nu = 20$ eV from the BL7U branch (b) and p-pol. at $h\nu = 100$ eV from BL6U (d). (e) High-resolution measurement taken using p-pol. at $h\nu = 80$ eV from BL6U. In (c) and (e), the sample is in-plane rotated by -30° . The upper left insets describe the experimental geometry of the electric field vector of the incident light. From Ref. [7].

using this normal incidence geometry.

3.3 3D band dispersion and 3D Fermi surface

3D band dispersion data $I(E_{\text{binding}}, k_x, k_y)$ can be obtained by scanning the kinetic energy (E_{kin}) with a fixed excitation photon energy or by scanning the excitation photon energy with a fixed E_{kin} . The Fermi surface and valence band dispersion in a 3D momentum space are obtained by measuring the CECs at the Fermi level and at certain binding energies while sweeping the photon energy and kinetic energy of the photoelectron (constant initial state mode) [18].

3.4 Soft X-ray resonance PES

Resonant photoelectron spectroscopy (RPES) is a widely used technique for highlighting specific elemental components of the valence band by adjusting the photon energy to a core-level excitation threshold.

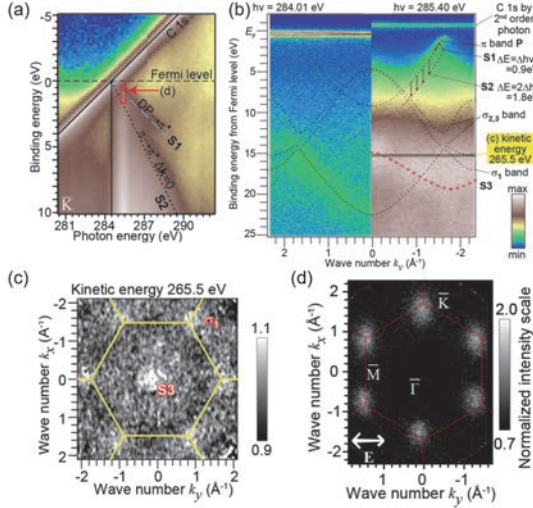


Fig. 6. (a) Momentum-resolved intensity maps at \bar{K} as functions of the binding energy and excitation photon energy near C K-shell absorption threshold. A logarithmic color scale was used for the contrast gradation. (b) Valence photoelectron and Auger electron spectra along the $\bar{K}\Gamma$ direction excited at the photon energy of 284.01 eV and 285.40 eV. Black (red) dotted lines indicate the valence band (Auger electron) dispersions. (c) Momentum-resolved Auger electron intensity distribution (c) at the photon and photoelectron kinetic energy of 285.40 eV and 266.5 eV, respectively, and (d) at the binding energy and photon energy ranges of 0.4–1.6 eV and 285.3–285.5 eV, respectively. A linear color scale was used for the normalized intensity contrast gradation. Six bright spots at \bar{K} points correspond to S1 shakeup process. After Ref. [19].

In RPES, the valence band dispersion around the excitation threshold of the core level is measured. We measured the momentum-resolved RPES of graphite

crystals and found unique dispersion structures embedded in Auger electrons (Fig. 6). This phenomenon was clarified based on the conservation and transfer of momentum [19,20]. This element-selective valence excitation technique provides a versatile means for creating and characterizing a valence exciton band selectively and is effective for investigation of various materials.

3.5 Dark Field imaging

The dark-field imaging technique has been developed for various electron and X-ray diffraction methods to select diffraction spots in the momentum space and visualize the spatial distribution of specific domains. We have applied this dark-field imaging technique to PMMs and established a momentum-selective photoelectron microscopy method, which is a quite useful for microscopic electronic structure investigations [12]. The π -dispersion of the valence band of graphite is the strongest at the M saddle point in the Brillouin zone (BZ). Selectively measuring the photoelectron intensity in the M direction of each region resulted in the successful projection of photoelectron microscopic images with each region highlighted with a resolution of approximately 100 nm. This momentum-selective photoelectron microscopy technique was also applied to visualize of the single-atomic-height step edges on the graphite surface [18]. An image of graphite step edge along zig-zag atomic bonding direction (Fig. 7) was obtained by selecting one of the three-fold symmetric L-point photoelectron intensities characteristic of different terrace atomic arrangements.

4. Outlook

The most distinctive advantage of PMM is its snapshot-style of measuring photoelectron CEC in real

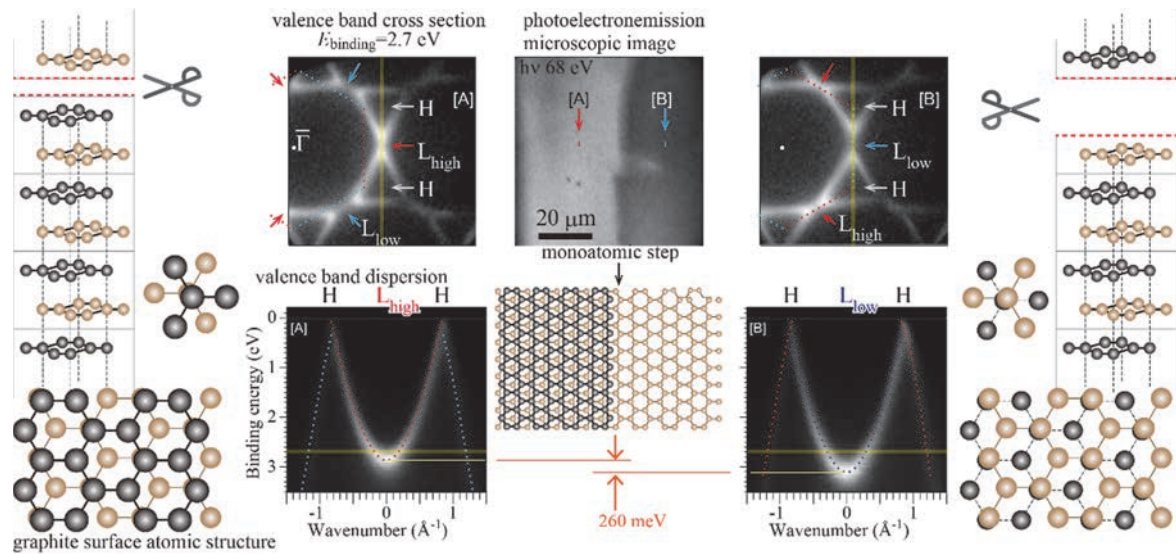


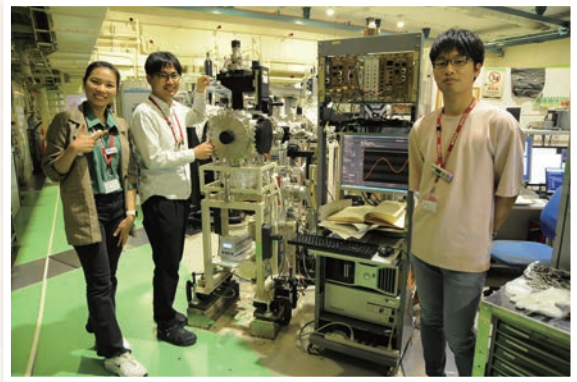
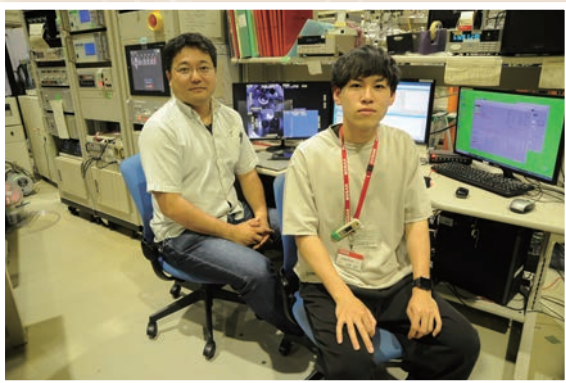
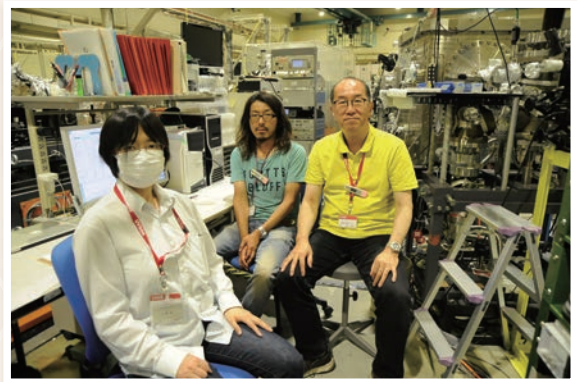
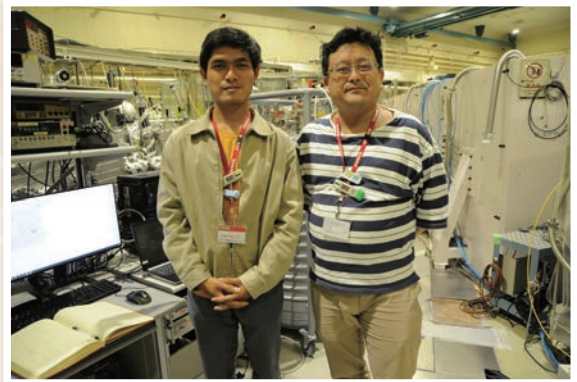
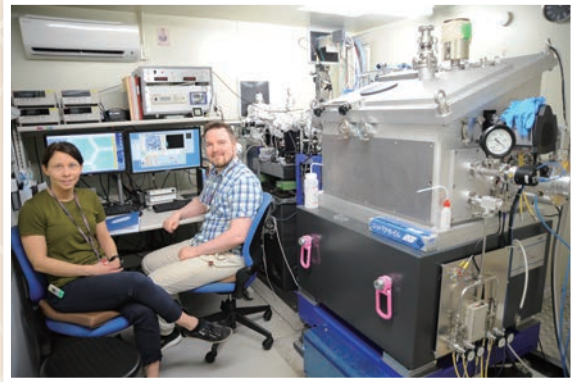
Fig. 7. Graphite surface microscopic image and valence band structure together with atomic structure models. The valence band cross-sections and dispersions of two different graphite terrace regions are shown. A step edge is visualized in μm -scale area image by selecting one of the three-fold symmetric L-point photoelectron intensities characteristic of different terrace atomic arrangements. After Ref. [18].

and reciprocal spaces. Recently we succeeded in the development of on-the-fly scans for temperature-dependent Fermi surface and valence band measurements during phase transitions, taking advantage of the rapid acquisition (seconds to minutes) of CECs. Polarization-dependent transition matrix elemental analysis is underway to study the molecular orbitals of fragile organic adsorbates on surfaces [20,21]. Finally, our main goal is to employ all these techniques with spin polarization sensitivity. We have just started obtaining spin-polarized valence band dispersion data for typical materials having spin polarized surface states. The combination of PMM with synchrotron SX and VUV undulators paves the way for comprehensive characterization of atomic orbitals and spins in the Fermi surface and valence band on the μm scale.

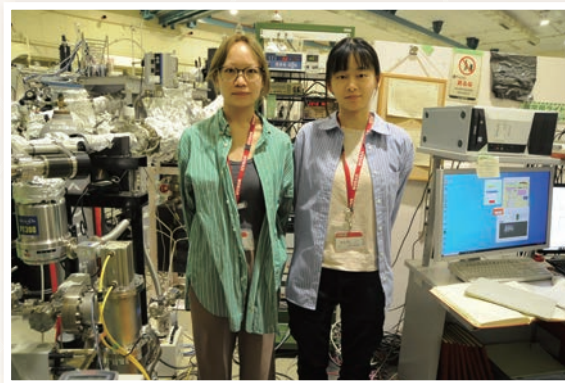
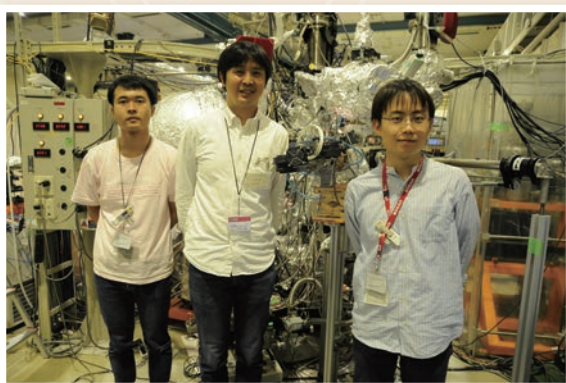
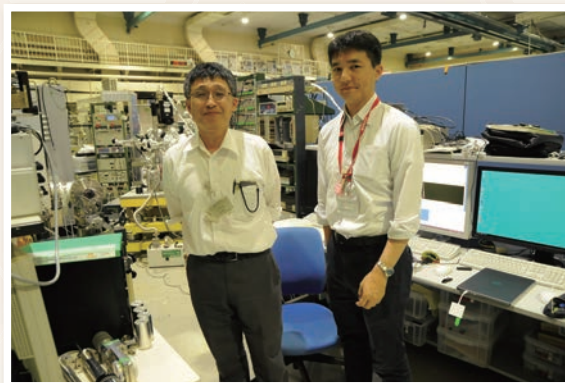
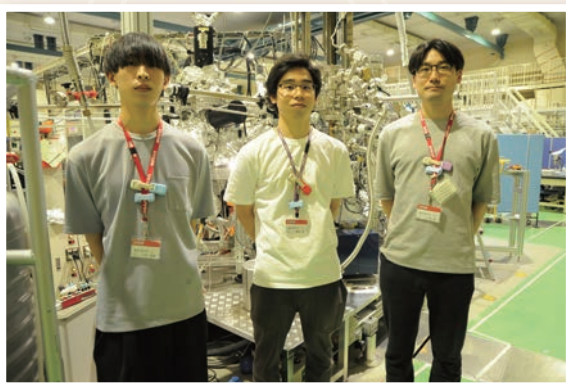
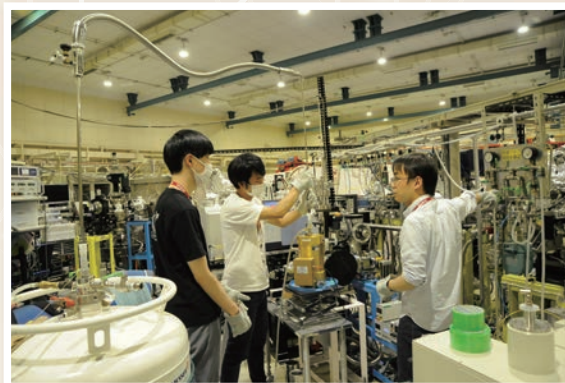
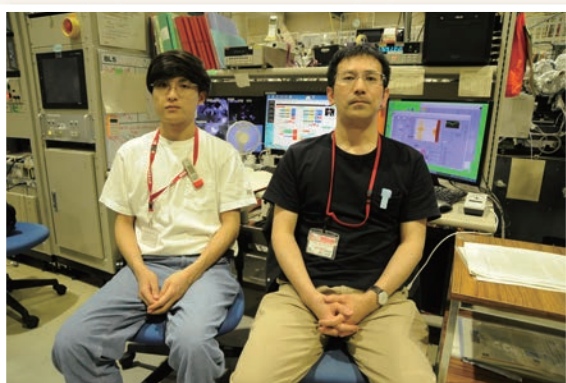
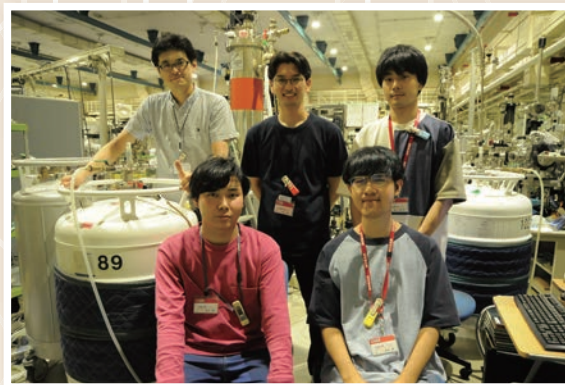
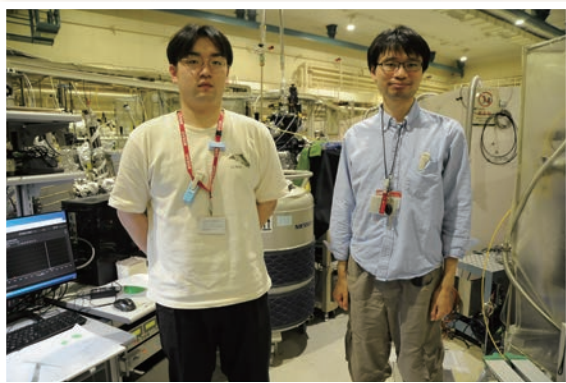
References

- [1] B. Kromker, *et al.*, *Rev. Sci. Instrum.* **79**, 053702 (2008).
- [2] C. Tusche, *et al.*, *Ultramicroscopy* **159**, 520 (2015).
- [3] G. Schönhense, *et al.*, *Rev. Sci. Instrum.* **91**, 123110 (2020).
- [4] F. Matsui, *et al.*, *Jpn. J. Appl. Phys.* **59**, 067001 (2020).
- [5] S. Makita, *et al.*, *e-J. Surf. Sci. Nanotechnol.* **19**, 42 (2021).
- [6] H. Ota, *et al.*, *J. Phys.: Conf. Ser.*, **2380**, 012003 (2022).
- [7] K. Hagiwara, *et al.*, *J. Synchrotron Radiat.* **31**(3) 540-546 (2024).
- [8] H. Yamane, *et al.*, *Rev. Sci. Instrum.* **90**, 093102 (2019).
- [9] C. Tusche, *et al.*, *Ultramicroscopy* **206**, 112815 (2019).
- [10] S.-I. Kimura, *et al.*, *Rev. Sci. Instrum.* **81**, 053104 (2010).
- [11] F. Matsui, *et al.*, *Rev. Sci. Instrum.* **94**, 083701 (2023).
- [12] F. Matsui, *et al.*, *J. Phys. Soc. Jpn.* **91**, 094703 (2022).
- [13] C. Tusche, and J. Kirschner, (2006). German Patent DE102014019408.
- [14] Y. Ishida and S. Shin, *Rev. Sci. Instrum.* **89**, 043903 (2018).
- [15] T. Kato, *et al.*, *Phys. Rev. Lett.* **129**, 206402 (2022).
- [16] E. Hashimoto, *et al.*, *Jpn. J. Appl. Phys.* **61**, SD1015 (2022).
- [17] O. Endo, *et al.*, *J. Phys. Chem. C* **126**, 15971 (2022).
- [18] F. Matsui and S. Suga, *Phys. Rev. B* **105**, 235126 (2022).
- [19] F. Matsui, *et al.*, *J. Phys. Soc. Jpn.* **90**, 124710 (2021).
- [20] Y. Hasegawa, *et al.*, *e-J. Surf. Sci. Nanotechnol.* **20**, 174 (2022).
- [21] O Endo *et al.*, *e-J. Surf. Sci. Nanotechnol.* **21**, 236 (2023).

UVSOR User 1

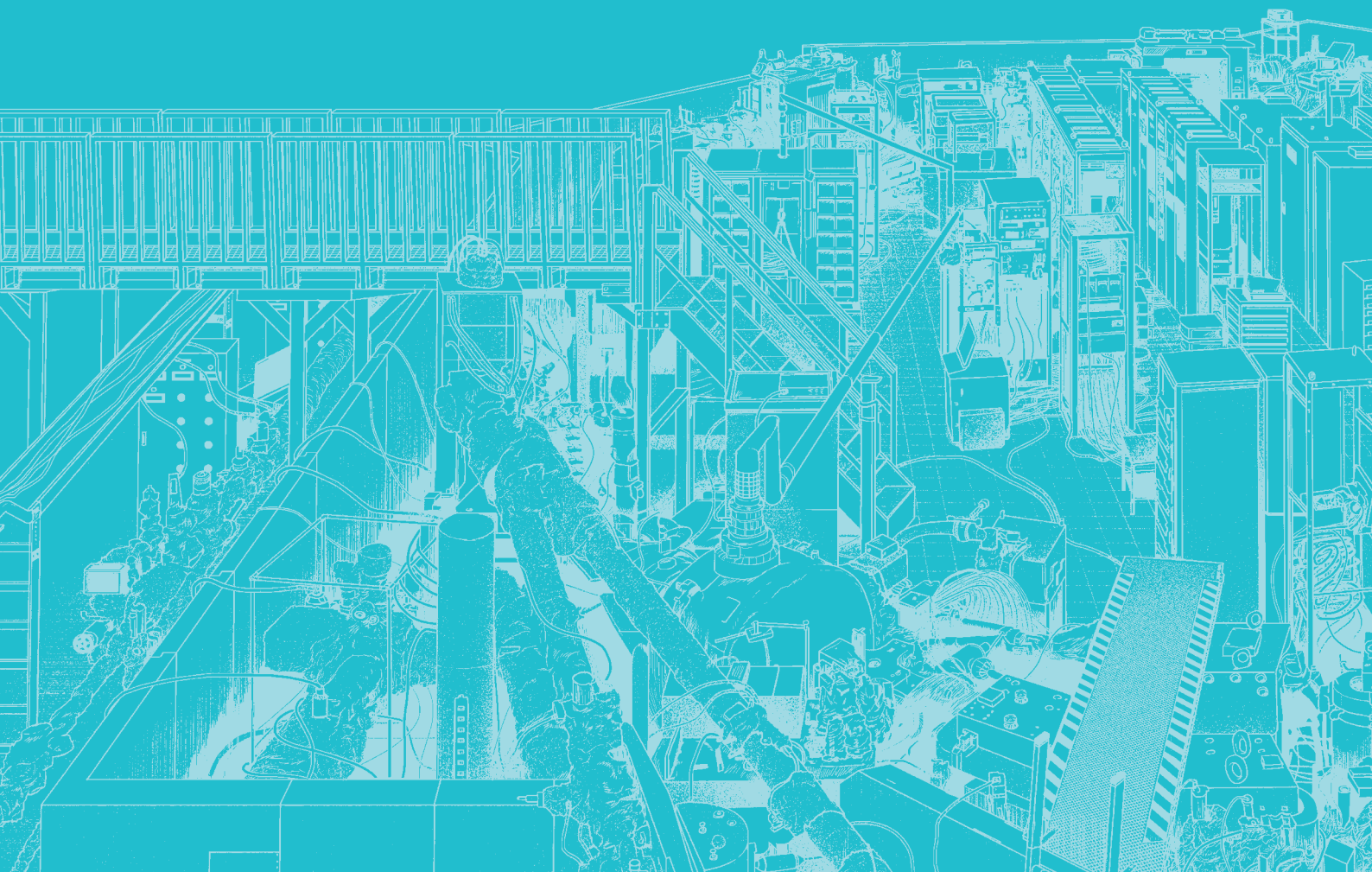


UVSOR User 2



III-1

Accelerators and
Instruments





Spin-Polarized Band Mapping in Au(111) Surface States

J. Okabayashi¹ and K. Tanaka²

¹Research Center for Spectrochemistry, The University of Tokyo, Bunkyo-ku, Tokyo 113-0033, Japan

²UVSOR Synchrotron Facility, Institute for Molecular Science, Okazaki 444-8585

Spintronics is a rapidly emerging field of science and technology that will most likely have a significant impact on the future of all aspects of electronics. Understanding magnetism of surfaces, interfaces, and nanostructures is greatly important for realizing the spintronics which aims to control and use the function of spin as well as the charge of electrons. Spin- and angle-resolved photoemission spectroscopy (spin-resolved ARPES) is one of the most powerful experimental techniques to investigate the magnetic properties of such materials, where one can know the “complete” information of the electronic states of materials, that is, energy, momentum, and spin direction. Recent development of high energy and angle-resolved photoelectron analyzer as well as the contemporary light sources makes it possible for the photoemission spectroscopy to investigate not only band structures but also many body interactions of electrons in solids. However, appending the spin resolution to photoemission spectroscopy is quite difficult because of an extremely low efficiency (10^{-4}) of Mott-type spin detections.

Recently, very low-energy electron diffraction (VLEED-type) spin detector with 100 times higher efficiency than that of conventional Mott-type has been developed and spin-resolved ARPES has been started to be realized [1-3]. So far, most of the spin-resolved ARPES systems are using the single-channel detector and efficiency is still a problem. We have developed high-efficient spin-resolved ARPES system with multi-channel detection (we call “image-spin” detection) to achieve the 100 times better efficiency and the 10 times

better momentum resolution than the current spin-resolved ARPES system, which can be a breakthrough in this research field.

Figure 1 shows the ARPES and spin-resolved ARPES images in Au(111) surface states. Rashba-type spin-split surface states are clearly detected with the Fermi surface mapping. We succeeded in obtaining a spin-resolved signal on the Au(111) surface as shown in Fig. 1(c). According to rough estimates, the efficiency of spin-resolved ARPES was 100 times higher than that of the single-channel detection systems currently used in the world. However, the spin-resolved ARPES bands were broad compared to the normal ARPES ones shown in Fig. 1(b), meaning that the momentum resolution was not so good. To overcome these problems, we have introduced a new “spin manipulator” that can change the spin direction of the passing electrons in any direction. The installation of the spin manipulator and optimization of the spin target deposition conditions have greatly improved the spin-resolved images, and we were able to obtain spin-resolved images with momentum resolution comparable to that of normal ARPES, as shown in Fig. 1(d). We are currently optimizing the lens parameters of the spin manipulator to obtain spin information in the remaining two axial directions.

[1] C. Bigi *et al.*, J. Synchrotron Rad. **24** (2017) 750.

[2] T. Okuda, J. Phys.: Condens. Matter **29** (2017) 483001.

[3] F. Ji *et al.*, Phys. Rev. Lett. **116** (2016) 177601.

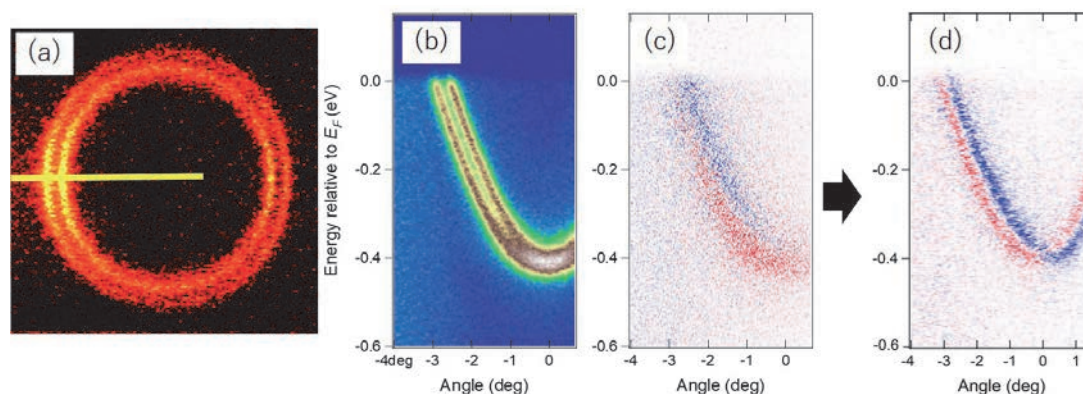


Fig. 1. a) Fermi surface of Rashba spin splitting in Au(111) surface states and (b) image plot of normal ARPES along the yellow bar in (a). Spin-resolved ARPES data showing the spin polarization (blue–red scale) with the previous experimental setup (c) and the current setup (d).

Improvement of Accuracy of Non-Destructive Nuclide Assay by Transmission NRF Method

T. Shizuma^{1,2}, M. Omer², R. Hajima¹, M. Koizumi², H. Zen³, H. Ohgaki³ and Y. Taira⁴

¹National Institutes for Quantum Science and Technology, Kizugawa 619-0215, Japan

²Japan Atomic Energy Agency, Tokai 319-1195, Japan

³Institute of Advanced energy, Kyoto University, Uji 611-0011, Japan

⁴UVSOR Synchrotron Facility, Institute for Molecular Science, Okazaki 444-8585, Japan

Nuclear resonance fluorescence (NRF) is a process in which atomic nuclei absorb and emit γ rays. Because the emitted γ rays have energies specific to each nuclide, it is possible to identify the nuclide by measuring the energy of emitted NRF γ rays. Furthermore, because a γ -ray beam at MeV energy range that has high penetrating power is used in NRF experiments, non-destructive measurement is possible even when the sample is placed in a heavy shield. In transmission NRF, a γ -ray beam that passes through an absorption target is irradiated to another target (called witness plate, WP) which consists of the same nuclide as the absorption target, and NRF γ rays emitted from the WP target are measured. Transmission NRF is favorable over scattering NRF measurements because the effect of background radiation can be reduced [1].

The absorption amount of γ rays in transmission NRF depends on the temperature of absorption and WP targets due to the Doppler broadening of resonant width. Therefore, the temperature of the absorption or WP targets may affect the time and sensitivity of the measurement. To study the temperature dependence of the self-absorption, we irradiated ^{206}Pb samples at room or LN_2 temperatures with a laser Compton scattering (LCS) γ -ray beam. LCS γ rays with maximum energy of 5.54 MeV were produced from the collision of 746-MeV electrons with laser photons with a wavelength of 1.895 μm . A lead collimator with 20-cm thickness and 3-mm aperture size was used to confine the LCS γ -rays to the energy width to approximately 8% (FWHM). Two high-purity Ge detectors, located horizontally at a scattering angle 90° with respect to the incident γ -ray direction, were used to detect NRF γ -rays, as shown in Fig. 1.

Figure 2 shows typical spectra measured with (black) and without (red) the absorption target at room temperature. NRF peaks of ^{206}Pb [2] are observed at 4971, 5037, 5127, 5377, 5459, 5470, and 5524 keV. The spectrum with the absorption target is corrected for atomic absorption, therefore showing only nuclear resonant absorption (so called self-absorption) effect. The upper spectrum (blue) represents the difference of the counts obtained with and without the absorption target which visualizes the self-absorption yields by negative counts. The largest self-absorption occurs in the resonance at 5037 keV which has the integrated cross section of 1150 eV b. From the present measurements, self-absorption amounts consistent with

theory are obtained.

This work is in part a contribution of JAEA to IAEA coordinated research program, J02015.

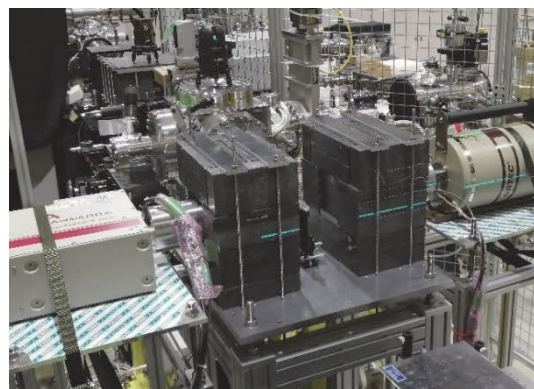


Fig. 1. Photo of the experimental setup used for the transmission NRF measurements.

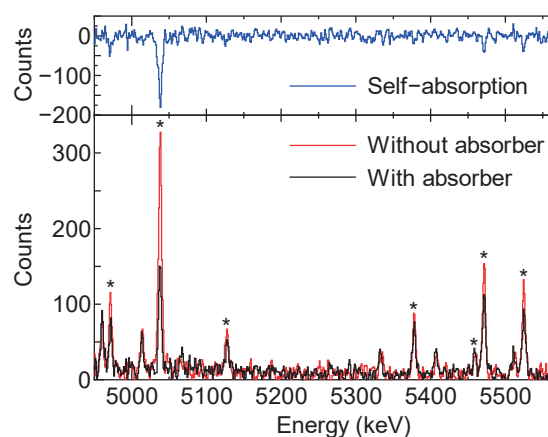


Fig. 2. Typical γ -ray spectra obtained in transmission NRF experiments. In the lower panel, the red (black) spectrum corresponds to the measurement without (with) the absorption target at room temperature. Asterisks indicate NRF peaks of ^{206}Pb . The upper spectrum (blue) represents the difference of the spectra measured with and without absorption target, indicating the amount of self-absorption.

[1] C.T. Angell *et al.*, Nucl. Instrum. Methods Phys. Res., Sect. B **347** (2006) 11.

[2] T. Shizuma *et al.*, Phys. Rev. C: Nucl. Phys. **98** (2018) 064317.

BLIU

Gamma-ray Polarization Measurement with GAGG Pixel Detectors

K. Shimazoe¹, R. Sato¹, M. Uenomachi² and Y. Taira³

¹Graduate School of Engineering, The University of Tokyo, Tokyo 113-8656, Japan

²Space Unit, Kyoto University, Kyoto 606-8502, Japan

³UVSOR Synchrotron Facility, Institute for Molecular Science, Okazaki 444-8585, Japan

Polarization measurement of gamma-rays emitted from nuclei can give a useful information in nuclear physics and medical application. For example, recently the use of quantum entanglement in polarization of two gamma-rays emitted from positron-electron annihilation is proposed and it can contribute the image quality improvement in PET (Positron Emission Tomography) [1]. Generally, the measurement of polarization in gamma-rays can be conducted through the detection of Compton scattering angle influenced by polarization angle. Our group have been developing a Compton-PET imaging system[2] for visualizing multi-nuclides simultaneously in the nuclear medical imaging framework.

In this study, we have designed a multi-channel gamma-ray pixel detector system with modules composed of 8×8 GAGG scintillators coupled to 8×8 SiPM array. 8 modules with 512 pixels are used to detect the scattered gamma-ray for recording the scattering angle of linearly polarized, circularly polarized and non-polarized gamma-rays. All the pixels' signals are readout with individually coupled dynamic time-over-threshold circuit [3] to record its energy, time and position for reconstructing the scattering angle. Figure 1 shows the experimental setup with 8 modules. All the pixel timing is recorded with a synchronized digital time-to-digital converter system with FPGA based DAQ [4].

6.6 MeV polarized gamma-rays generated in UVSOR

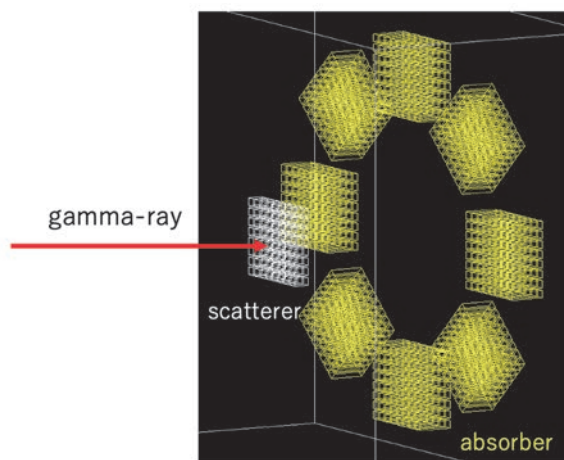


Fig. 1. Polarization detection setup with 512 channel GAGG-SiPM pixel detectors.

are irradiated to scatterer and Compton scattered events are extracted from the recorded list-mode data. Fig. 2 shows the coincidence time histogram between scatterer and absorber.

Using the coincidence events, the angle of Compton scattering was calculated and plotted calibrated by the non-polarized gamma-rays. Figure 3 shows the case of 135-degree polarization.

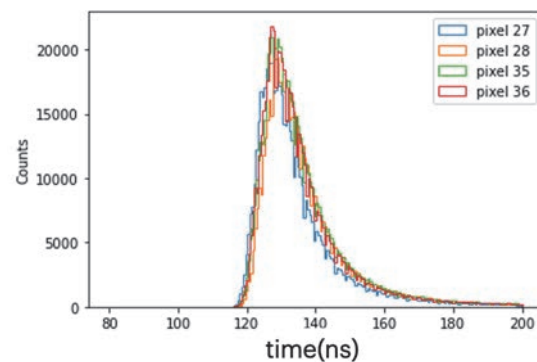


Fig. 2. Coincidence time histogram between scatterer and absorber for measuring Compton scattering events.

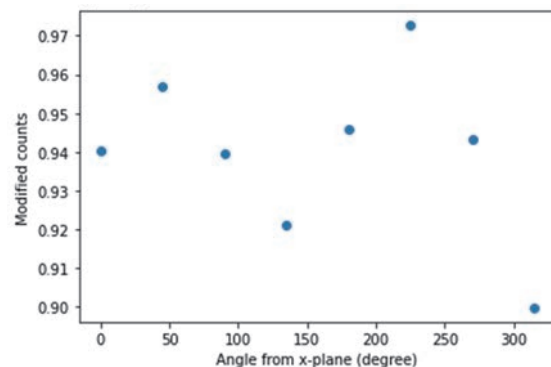


Fig. 3. Measured counts in 135-degree polarization. Sine curve is successfully observed.

[1] Kim, Donghwan *et al.*, J. Instrum. **18.07** (2023) P07007.

[2] Uenomachi, Mizuki *et al.*, Sci. Rep. **11.1** (2021) 17993.

[3] Shimazoe, Kenji, *et al.* IEEE Trans. Nucl. Sci. **59.6** (2021) 3213.

[4] Sato, S., Uenomachi, M. and Shimazoe, K. IEEE Trans. Nucl. Sci. **68** (2021) 1801.

Generation of F-LCS Gamma-rays for Isotope Selective Imaging Study in UVOSR BL1U

H. Ohgaki¹, S. Tanizaki¹, H. Zen¹, T. Kii¹, T. Hayakawa^{2,3} and T. Shizuma²

¹Institute of Advanced Energy, Kyoto University, Kyoto 611-0011, Japan

²Kansai Photon Science Institute, National Institutes for Quantum Science and Technology, Kizugawa, Kyoto 619-0215, Japan

³Institute of Laser Engineering, Osaka University, Suita 565-0871, Japan

Flat Laser Compton Scattering Gamma-ray beam (F-LCS), which has a flat distribution in the energy spectrum and the spatial distribution with a few mm diameter beam size, has been developed to study an isotope selective CT Imaging application in the beamline BL1U in UVSOR. By using a circular motion of the electron beam which is excited by a helical undulator installed in a storage ring, and collision with an intense laser beam, an F-LCS beam can be generated.

A POP experiment was carried out at the BL1U in UVSOR in 2022 machine time and we obtained larger K-value of undulator, the broader energy bandwidth of the LCS was observed as predicted by EGS5 simulation [1,2].

In 2023, we tried to obtain a multi-isotopes imaging by using F-LCS beam generated in BL1U to excite NRF levels of ²⁰⁶Pb, ²⁰⁷Pb, ²⁰⁸Pb as the target isotopes. Three enriched isotope targets of 8 mm ϕ rods were prepared for the imaging sample, and three enriched isotope witness targets were placed behind the imaging sample, as shown in Fig.1. Two large high-purity Ge detectors recorded NRF gamma rays from the witness targets. A normal LCS beam (undulator K-value=0) and F-LCS (K=0.2) were generated by using a Tm-fiber laser system (TLR-50-AC-Y14, IPG Laser GmbH) with an output power of around 30 W colliding with the electron beam of 746 MeV whose beam current was 200 mA. Due to the available gamma ray yields and the machine time, the scanning step of 7 mm was chosen to measure the F-LCS irradiation and 14 mm to the LCS irradiation. Figure 2 shows the NRF spectra with LCS (black line) and F-LCS (red line). Using F-LCS, the 5037 keV peak from ²⁰⁶Pb was clearly observed because of broader energy spectrum of the F-LCS beam.

Figures 3 show the results of NRF imaging of ²⁰⁸Pb (a) and ²⁰⁷Pb (b) with the LCS beam (black lines) and F-LCS beam (red lines). As the results, we obtained multi-isotopes NRF imaging with LCS and F-LCS beams. However, we could not obtain the NRF imaging of ²⁰⁶Pb even with the F-LCS beam.

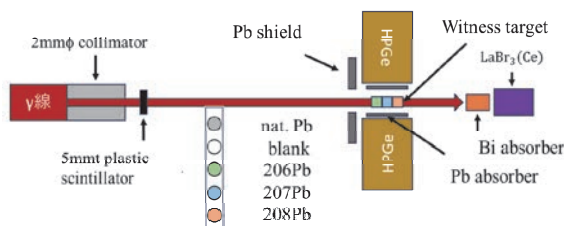


Fig. 1. Schematic drawing of the experimental set-up.

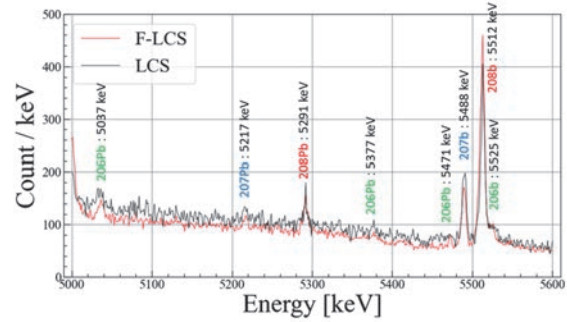


Fig. 2. LCS gamma-ray energy distribution in the vertical axis with the undulator K-value of K=0.2.

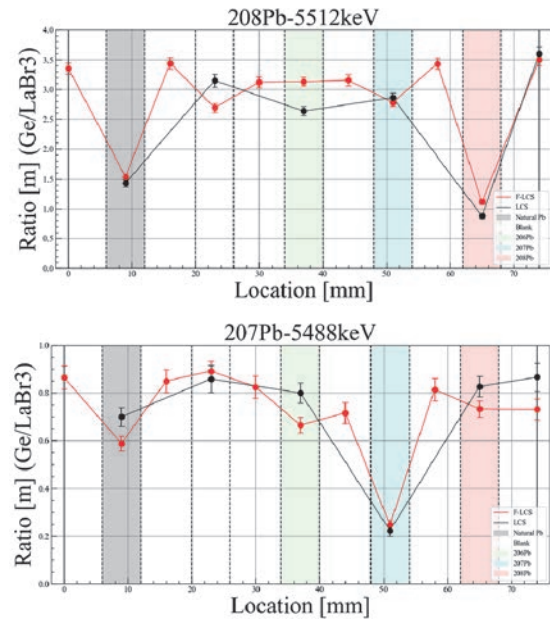


Fig. 3. Upper (a) Measured 1D NRF imaging of ²⁰⁸Pb and lower (b) ²⁰⁷Pb. Black lines shows the result with the LCS beam and Red lines shows the result with the F-LCS beam.

[1] H. Ohgaki *et al.*, UVSOR Activity Report **50** (2023) 40.

[2] H. Ohgaki *et al.*, Phys. Rev. Accel. Beams **26** (2023) 093402.

BL1U

Experimental Study on Radiation from Single Electron

Y. Asai¹, H. Miyauchi^{2,3}, M. Shimada^{2,3} and M. Katoh^{2,4}

¹Graduate School of Advanced Science and Engineering, Hiroshima University,
Higashi-Hiroshima 739-8526, Japan

²Hiroshima Synchrotron Radiation Center, Hiroshima University, Higashi-Hiroshima 739-0046

³High Energy Accelerator Research Organization (KEK), Tsukuba 305-0801, Japan

⁴UVSOR Synchrotron Facility, Institute for Molecular Science, Okazaki 444-8585, Japan

We have demonstrated experimentally at UVSOR BL1U that undulator radiation has characteristic spatiotemporal structures. For example, helical undulator radiation possesses spiral phase structures [1] and tandem undulator (two undulators in series) double-pulse waveforms [2]. Undulator radiation from synchrotron light sources is considered as an incoherent mixture of wave packets emitted from each individual electron, in contrast to the coherent radiation emitted from free electron lasers. There arises a question whether radiation from a single electron has those spatiotemporal structures that we have shown for the radiation from an ensemble of huge number of electrons, typically 10^{11-12} [1, 2].

To realize an experimental study on the radiation from a single electron, the simplest approach is accumulating only one electron in synchrotron. Such single electron storage has been realized in a few synchrotrons, aiming to studies on electron dynamics [3, 4, 5], radiation [6, 7] and primary standard [8]. We have started single electron storage experiments at UVSOR since 2021 with the aim of conducting fundamental research on electromagnetic radiation from a single electron. The method is basically same as the previous studies. We inject one pulse of electron beam from the booster synchrotron to the storage ring. The accumulated beam current is typically much smaller than 1mA. Then, we insert the beam scraper to reduce the electron beam intensity, as observing the undulator radiation intensity tuned at the wavelength of 355 nm at the beamline BL1U by using a photomultiplier tube. We succeeded in observing a step-function-like intensity change under a small number of electron storage conditions with a good SN ratio and in confirming the single electron storage [9, 10]. In 2022, we continue improving the method of observing the accumulation state of single electron and, then, attempted to observe undulator radiation from single electron [11, 12].

We tried to observe radiation emitted from a tandem undulator, which consists of two undulators arranged in series. It is known that the synchrotron radiation from the tandem undulator shows a finely modulated spectrum with the envelope of that from one undulator [13]. This modulation is the result of the spectral interference between the radiation from two undulators.

The number of photons emitted during single passage of an electron in the undulator is much less than unity, which is in the same order of the fine structure constant.

Therefore, under the single electron storage, the probability that the electron emits more than two photons is negligible. The aim of this experiment is to show that, even in the condition that the single electron radiate only one photon in the tandem undulator, the spectrum shows the modulation or not. This is similar to Young's interference experiment in the photon counting regime but in the time domain.

We constructed a simple measurement system consisting of a grating and a cooled CCD camera. Because the photon beam intensity was very low, we had to make the exposure time as long as 1 hour. To get a clear data, the background subtraction should be made very carefully. After trial and error, we found that the background taken for same exposure time should be used. This gave very clear data which shows that the spectrum of the tandem undulator radiation emitted by single electron shows clear modulation as that emitted from ensemble of electrons. The result has been reported elsewhere [14, 15, 16], and will be published in the nearest future.

- [1] M. Katoh *et al.*, Sci. Rep. **7** (2017) 6130.
- [2] T. Fuji *et al.*, Optica **10** (2023) 302.
- [3] I.V. Pinayev *et al.*, Nucl. Instrum. Methods Phys. Res., Sect. A **375** (1996) 71.
- [4] A. N. Aleshaev *et al.*, Nucl. Instrum. Methods Phys. Res., Sect. A **359** (1995) 80.
- [5] A. Romanov *et al.*, JINST **16** (2021) P12009.
- [6] I.V. Pinayev *et al.*, Nucl. Instrum. Methods Phys. Res., Sect. A **341** (1994) 17.
- [7] I. Lobach *et al.*, JINST **17** (2022) P02014.
- [8] R. Klein *et al.*, Phys. Rev. Accel. Beams **11** (2008) 110701.
- [9] R. Shinomiya *et al.*, UVSOR Activity Report **49** (2022) 40.
- [10] R. Shinomiya *et al.*, presented at JSR2022, 9PS01S (Jan., 2022).
- [11] Y. Asai *et al.*, presented at JSR2023, 1F03S (Jan., 2023).
- [12] Y. Asai *et al.*, UVSOR Activity Report **49** (2023) 42.
- [13] M. Billardon *et al.*, J. Phys. Collques **44** (1983) 29.
- [14] Y. Asai *et al.*, presented at PASJ2023, WEP26 (Aug. 2023).
- [15] Y. Asai *et al.*, presented at 2023 Annual meeting of JPS, 19aRD11, 3 (Sep., 2023).
- [16] Y. Asai *et al.*, presented at 2023 HiSOR Symp., P02S (Mar., 2023).

Frequency-Domain Determination of Time Delay between Two Light Wave Packets Generated by a Tandem Undulator

Y. Hikosaka¹, T. Kaneyasu^{2,3}, S. Wada⁴, H. Kohguchi⁴, H. Ota³, E. Nakamura³, H. Iwayama^{3,5}, M. Fujimoto⁶, M. Hosaka⁷ and M. Katoh^{3,5,8}

¹*Institute of Liberal Arts and Sciences, University of Toyama, Toyama 930-0194, Japan*

²*SAGA Light Source, Tosu 841-0005, Japan*

³*Institute for Molecular Science, Okazaki 444-8585, Japan*

⁴*Graduate School of Advanced Science and Engineering, Hiroshima University, Higashi-Hiroshima 739-8526, Japan*

⁵*Sokendai (The Graduate University for Advanced Studies), Okazaki 444-8585, Japan*

⁶*Synchrotron Radiation Research Center, Nagoya University, Nagoya 464-8603, Japan*

⁷*National Synchrotron Radiation Laboratory, University of Science and Technology of China, Hefei 230029, China*

⁸*Hiroshima Synchrotron Radiation Center, Hiroshima University, Higashi-Hiroshima 739-0046, Japan*

Our recent works [1-5] have demonstrated that time-domain interferometry of atoms, which was thought to be possible only with lasers with excellent temporal coherence, can be realized with synchrotron radiation generated by a tandem undulator. The tandem undulator radiation consists of pairs of light wave packets [6], and the longitudinal coherence within each light wave packet pair is used to realize time-domain interferometry.

The time delay between each light wave packet pair is the key parameter of time-domain interferometry and can be adjusted using phase shifter magnets that form a chicane of the electron trajectory between the two undulators. In time-domain interferometry experiments, the temporal precision of the time delay should be better than or at least comparable to the optical periods of light. Thus, its required accuracy in the temporal precision is as short as attoseconds in the XUV regime. While an autocorrelation measurement is a simple way to optically observe the time delay with attosecond precision [6], it is difficult to construct an autocorrelation interferometer in the XUV regime.

In this study [7], we show that frequency-domain spectroscopy enables us to determine the time delay between a light wave packet pair with an accuracy on the order of attoseconds. Figure 1 presents the frequency-domain tandem undulator spectra observed at three different current conditions of the phase shifter magnets. Both undulators were set to generate radiation with central photon energies of approximately 24 eV. These spectra exhibit fringe structures whose envelopes delineate the radiation spectra of the individual undulators. One finds that the number of fringes increases as increasing the phase shifter current (i.e., as increasing the time delay between the light wave packets).

The fringe structures result from the optical interference between two light wave packets, exhibiting a spacing of h/τ [7]. Here, h is Planck's constant, and τ is the delay time between a light wave packet pair. To accurately determine the time delays from the fringe structures, we use a fitting function considering the radiation spectra of the individual undulators [7]. The

value determined by fitting to each frequency-domain spectrum is given in the corresponding panel of Fig. 1. The error in the frequency-domain determination can be estimated to be about 1.5% [7]. This study proves that the time delay between XUV light wave packet pairs can be determined by frequency-domain spectroscopy with an accuracy on the order of attoseconds.

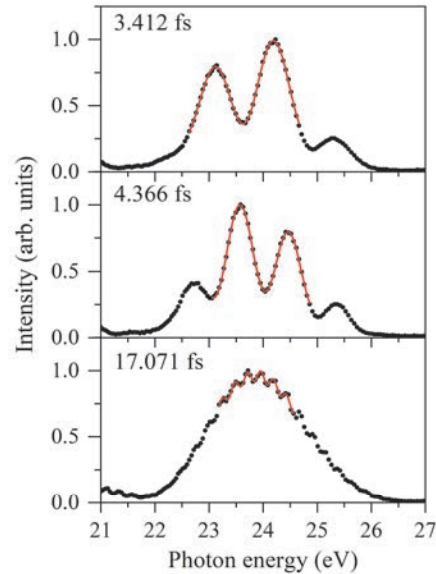


Fig. 1. Frequency-domain tandem undulator spectra (dots) measured at three different phase shifter conditions, and fitting results (red solid line).

[1] Y. Hikosaka *et al.*, Nat. Commun. **10** (2019) 4988; **12** (2021) 3782.

[2] T. Kaneyasu *et al.*, Phys. Rev. Lett. **123** (2019) 233401.

[3] T. Kaneyasu *et al.*, New J. Phys. **22** (2020) 083062.

[4] T. Kaneyasu *et al.*, Phys. Rev. Lett. **126** (2021) 113202.

[5] T. Kaneyasu *et al.*, Sci. Rep. **13** (2023) 6142.

[6] T. Kaneyasu *et al.*, Sci. Rep. **12** (2022) 9682.

[7] Y. Hikosaka *et al.*, Sci. Rep. **13** (2023) 10292.

BL1U

Diffraction of Optical Vortex from Undulator

Y. Nishihara¹, M. Shimada^{2,3}, H. Miyauchi^{3,2}, K. Matsuo^{1,3} and M. Katoh^{3,1,4}

¹*School of Science, Hiroshima University, Higashi-Hiroshima 739-8526, Japan*

²*High Energy Accelerator Research Organization (KEK), Tsukuba 305-0801, Japan*

³*Hiroshima Synchrotron Radiation Center, Hiroshima University, Higashi-Hiroshima 739-0046*

⁴*UVSOR Synchrotron Facility, Institute for Molecular Science, Okazaki 444-8585, Japan*

Optical vortex is a light beam possessing helical wavefront and carrying orbital angular momentum [1]. It has been attracting researchers in various field and its applications has been being explored [2]. To make experimental studies, various methods have been developed to convert normal light beam to optical vortex beam by using specially designed optical devices or elements [2]. On the other hand, it was theoretically shown that radiation from an electron in circular motion with a relativistic speed has vortex property [3]. Electron motion in a helical undulator radiation may be regarded as combination of mildly relativistic circular motion and ultra-relativistic drift motion along the rotation axis, which is identical with the undulator axis in this case. Therefore, helical undulator radiation has vortex property such that the fundamental component is circularly polarized plane wave and the higher harmonics are circularly polarized but optical vortex with helical wavefront [4].

Undulator vortex radiation can cover much wider wavelength range than vortex light beam based on conventional light sources. In particular, it can cover the vacuum ultraviolet and X-ray wavelength ranges, where the light and matters show strong interactions. Undulator vortex radiation may play important roles in the material science or the life science.

When we apply the undulator vortex radiation to some experiments, it is desirable to have a method for observing the helicity and the topological charge of the vortex beam at various position along the beam-line. It is well known that optical vortex shows interesting diffraction patterns for various apertures [5, 6, 7]. We may obtain information on the vortex property from the diffraction patterns. Among these, diffraction from triangular aperture seemed most feasible for this purpose, because it gives the information on the vortex property as a visible form which is easily identified by eye [3].

To make a systematic study on the triangular diffraction, we have prepared triangular aperture of several size. The experiment was carried out at BL1U of UVSOR-III storage ring. This beam-line equipped with APPLE-II type undulator. By setting it in the helical mode with the fundamental wavelength at 710 nm, the second harmonic radiation at 355 nm was

extracted to the air. By using conventional CCD camera with a bandpass filter centered at 355 nm with a moderate bandwidth, we made observation on the diffraction pattern.

Some of the results are shown in Figure 1. We succeeded in observing the characteristic pattern which shows the helicity and the topological charge of the vortex undulator radiation. We also observed the diffraction pattern for the fundamental undulator radiation tuned at 355 nm, which is not vortex but normal plane wave. The result was also shown in Figure 1, which is as expected for normal plane wave.

From the experiment, we found that the size of the triangular aperture should be fitted to the size of the vortex beam. We also found the tolerance of the alignment of the center of the vortex and the aperture. The details of these results were presented elsewhere [8].

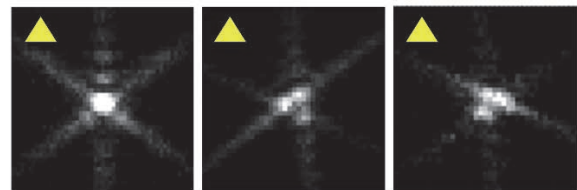


Fig. 1. Diffraction by triangular aperture of helical undulator radiation observed at UVSOR BL1U, for 1st harmonic (left) and 2nd harmonic radiation (center and right, the helicity is reversed). The wavelength is centered at 355 nm.

- [1] L. Allen *et al.*, Phys. Rev. A: At. Mol. Opt. Phys. **45** (1992) 8185.
- [2] Y. Shen *et al.*, Light Sci. Appl. **8** (2019) 90.
- [3] M. Katoh *et al.*, Phys. Rev. Lett. **118** (2017) 094801.
- [4] M. Katoh *et al.*, Sci. Rep. **7** (2017) 6130.
- [5] J.M. Hickmann *et al.*, Phys. Rev. Lett. **105** (2010) 053904.
- [6] G. G. C. Berkhout *et al.*, Phys. Rev. Lett. **101** (2008) 100801.
- [7] H. I. Sztul *et al.*, Opt. Lett. **31** (2006) 999.
- [8] Y. Nishihara, Bachelor thesis (Hiroshima University), (2024).

Evaluation of CMOS Detector Abord the Sounding Rocket Experiment FOXSI-4 for a Solar Flare Observation in X-rays

N. Narukage^{1,2}, R. Shimizu^{2,3}, Y. Sato^{2,1} and S. Kashima³

¹National Astronomical Observatory of Japan (NAOJ), Mitaka, 181-8588, Tokyo, Japan

²The Graduate University for Advanced Studies, SOKENDAI, Hayama, 240-0193, Kanagawa, Japan

³Institute of Space and Astronautical Science (ISAS), Japan Aerospace Exploration Agency (JAXA), Sagami-hara, 252-5210, Kanagawa, Japan

The solar corona is full of dynamic phenomena such as solar flares. The understandings of these phenomena have been progressing step-by-step with the evolution of the observation technology in EUV and X-rays from the space. But there are fundamental questions remain unanswered or haven't even addressed so far. Our scientific objective is to understand underlying physics of the dynamic phenomena in the solar corona, covering some of the long-standing questions in solar physics such as particle acceleration in flares and coronal heating. To achieve this objective, we identify the imaging spectroscopy (the observations with spatial, temporal and energy resolutions) in the soft X-ray range (from ~ 0.5 keV to ~ 10 keV) is a powerful approach for the detection and analysis of energetic events [1]. This energy range contains many lines emitted from below 1 MK to beyond 10 MK plasmas plus continuum component that reflects the electron temperature.

The soft X-ray imaging spectroscopy is realized with the following method. We take images with a short enough exposure to detect only single X-ray photon in an isolated pixel area with a fine pixel Silicon detector. So, we can measure the energy of the X-ray photons one by one with spatial and temporal resolutions. When we use a high-speed soft X-ray camera that can perform the continuous exposure with a rate of more than several hundred times per second, we can count the photon energy with a rate of several 10 photons / pixel / second. This high-speed exposure is enough to track the time evolution of spectra generated by dynamic phenomena in the solar corona, whose lifetimes are about from several ten seconds to several minutes. For the first imaging spectroscopic observation of the solar corona in soft X-ray range, we launched a NASA's sounding rocket (FOXSI-3) on September 7th, 2018 and successfully obtained the unprecedented data [2] using a high-speed X-ray camera [3] with a back-illuminated CMOS detector [4].

Based on the success of FOXSI-3, we will launch the sounding rocket experiment FOXSI-4 in April 2024, which will conduct the world's first X-ray focusing imaging spectroscopic observation of a solar flare. This FOXSI-4 uses a fully depleted CMOS detector with a silicon thickness of 25 microns, which provides high sensitivity to high-energy X-rays.

In FY2023, we evaluated this CMOS detector by

emitting the monochromatic X-rays with a resolution of 25 eV from 0.8 keV to 4.5 keV at UVSOR BL2A and 4.5 keV to 10 keV at SPring-8 BL20B2.

Figure 1 is the evaluated response matrix, which represents what kind of signal the detector outputs when monochromatic X-rays are incident on it. The color shows the fractional distribution of the output signal values (horizontal axis) when X-rays with the energy indicated on the vertical axis are incident. The features shown by (1), (2) and (3) are the main peak, silicon escape and silicon emission, respectively. The main peak is proportional to the energy of the incident X-rays, and its full width at half maximum is small and its intensity is higher than the other peaks. These facts mean that this detector has excellent performance in X-ray energy measurement.

Although a response matrix is indispensable for analyzing observation data, this is the first time that such a detailed matrix has been obtained by actual measurements. This matrix is extremely useful for the analysis of solar flare data obtained by FOXSI-4.

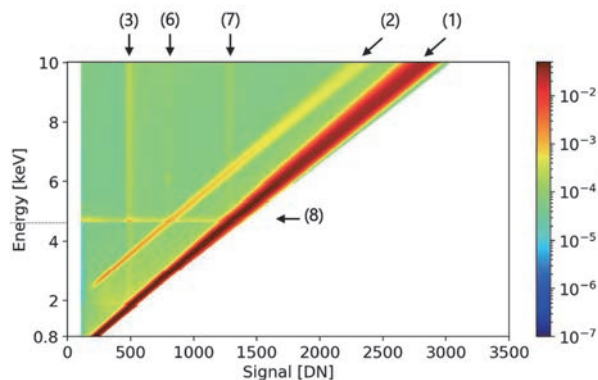


Fig. 1. Evaluated response matrix of the CMOS detector aboard the sounding rocket experiment FOXSI-4.

[1] N. Narukage *et al.*, arXiv:1706.04536 (2017).

[2] N. Narukage and S. Ishikawa, UVSOR Activity Report **46** (2019) 36.

[3] S. Ishikawa *et al.*, Nucl. Instrum. Methods Phys. Res., Sect. A **912** (2018) 191-194.

[4] N. Narukage *et al.*, Nucl. Instrum. Methods Phys. Res., Sect. A **950** (2020) 162974.

[5] N. Narukage, UVSOR Activity Report **49** (2022) 42.

BL2A

Development of Operando Measurement of Battery Materials by Soft X-ray Absorption Spectroscopy using Sample Transfer Vessel

E. Kobayashi¹ and A. Inoishi²

¹Kyushu Synchrotron Light Research Center, 8-7 Yayoigaoka, Tosu, Saga 841-0005, Japan

²Institute for Materials Chemistry and Engineering, Kyushu University
6-1 Kasuga-koen, Kasuga-Shi, Fukuoka 816-8580, Japan

In recent years, secondary batteries have been used in a wide range of fields such as mobile phones, and electric vehicles, and further improvements in performance are desired. Most battery materials are sensitive against atmospheric components such as oxygen, carbon monoxide, and moisture, so they must be handled without exposure to the atmosphere. So far, we have developed a sample transfer vessel that can transport the sample to the analyzer without exposing it to the atmosphere [1, 2]. In addition, when performing analysis using soft X-ray absorption spectroscopy, light elements contained in battery materials have a wide range of absorption edge energy, from lithium to chlorine, so there are cases where measurement cannot be performed using a single beamline or cannot be handled within the facility. Therefore, we have developed a device based on the sample transfer vessel [1, 2] that can measure soft X-ray absorption spectra across beam lines or facilities without exposure to the atmosphere. Furthermore, in order to more accurately evaluate the reactions occurring in batteries, it is important to measure the conditions in which the reactions are actually occurring. Therefore, we are developing a device that can measure soft X-ray absorption spectra across a beamline or facility without exposure to the atmosphere, with the addition of a function that can apply voltage to the sample.

Figure 1 is a photograph of the developed transfer vessel installed on the beamline. The device was attached to the conflat flange (CF) 70 port at the end of the beam line. The silicon drift detector (SDD), which detects soft X-rays emitted from the sample, was installed at 90 degrees to the direction of light incidence. Figure 2 is a photograph of the sample holder. The front and back surfaces of the sample are insulated, and a potential can be applied to each of these surfaces. Using this vessel, we observed the soft X-ray absorption spectra of all-solid-state batteries during charging and discharging. As a result, it was confirmed that the chemical state of the battery changes due to charging and discharging.

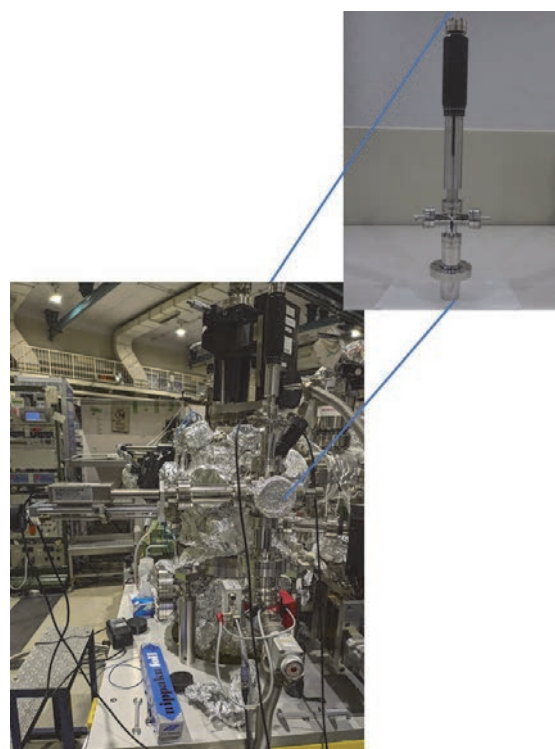


Fig. 1. Photograph of the developed transfer vessel.



Fig. 2. Photograph of the sample holder.

[1] E. Kobayashi *et al.*, Japanese Patent No. 5234994.

[2] E. Kobayashi *et al.*, J. Surf. Anal. **19** (2012) 2.

Reflectivity Measurement on SiC/Mo/Si Multilayer Coated Mirrors for Future Planetary Exploration

M. Kuwabara¹, Y. Suzuki², A. Yamazaki³ and I. Yoshikawa⁴

¹Department of Physics, College of Science, Rikkyo University, Tokyo 171-8501, Japan

²Institute of Space and Astronautical Science, Japan Aerospace Exploration Agency, Kanagawa 252-5210, Japan

³Department of Earth and Planetary Science, Graduate School of Science,
The University of Tokyo, Tokyo 113-0033, Japan

⁴Department of Complexity Science and Engineering, Graduate School of Frontier Science,
The University of Tokyo, Chiba 277-8561, Japan

Optical observations of planetary atmospheres have been conducted across various wavelength ranges. Particularly, ultraviolet (UV) light is notably useful in planetary science for acquiring spatial structure and temporal evolution of planetary upper atmospheres. However, detection of UV light through ground-based observations is hindered by absorption caused by the Earth's atmosphere.

Periodic multilayer coating technique has been developed for normal incidence optics in the soft X-ray and extreme ultraviolet (EUV) spectral regions. By applying multiple materials with different complex refractive indices in layers on the surface of a mirror, the reflectivity can be dramatically improved through the interference of reflected light at each interface.

In the field of planetary science, this technique for EUV radiation has been utilized in many missions. High reflectivity multilayer coatings for He II radiation (30.4 nm) have been developed for several applications, among which Mo/Si multilayer coated mirrors have been widely used for He II observations due to their high stability [1]. However, their reflectivity reaches at best approximately 18%. In recent years, with the increasing opportunities for missions by ultra-small spacecraft, there has been a demand for the development of multilayer coatings with higher reflectivity. To achieve higher reflectivity, Mg/SiC multilayer coated mirrors have also been developed. While Mg/SiC mirrors achieve reflectivity exceeding 30% at 30.4 nm [2], instability due to the deliquescence of Mg hampers their practical application.

In this study, we developed multilayer mirrors with a new SiC/Mo/Si coating expected to achieve higher reflectivity than conventional ones. We evaluated their reflectivity for s-polarized and p-polarized light, respectively.

Figure 1 shows the experimental configuration for reflectivity measurement for p-polarized light. Measurements have been performed on two mirrors (#1 and #2) with identical design parameters but different production lots. Five stacked microchannel plates (MCPs) and a resistive anode encoder (RAE) are assembled and used as a photon detector. A goniometer is moved to measure reflectivity for an incident angle of 20 degrees. For reflectivity measurements for s-polarized light, the phase of the goniometer relative

to the diffracted light is changed by 90 degrees.

The initial results of the reflectivity measurements of the SiC/Mo/Si multilayer coated mirrors are shown in Figure 2. The newly developed SiC/Mo/Si mirrors have been found to have reflectivity potentially comparable to or exceeding that of the conventional Mo/Si mirrors. However, there are some uncertainties in these preliminary findings, highlighting the need for further detailed analysis in future studies.

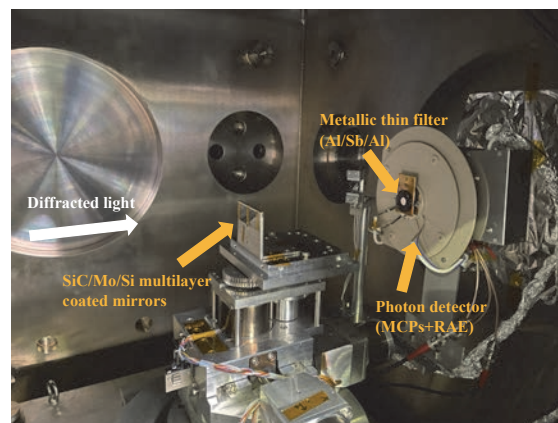


Fig. 1. Configuration of the experiment for reflectivity measurement for p-polarized light.

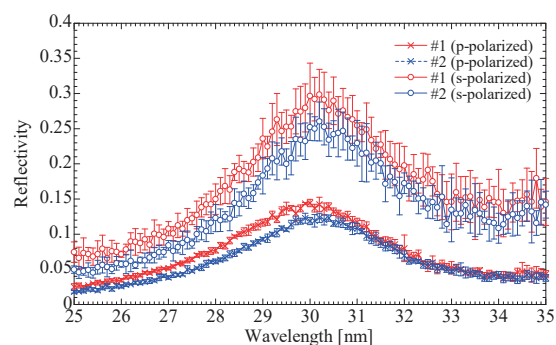


Fig. 2. Reflectivity of the SiC/Mo/Si multilayer coated mirrors.

[1] I. Yoshikawa *et al.*, *Earth Planets Space* **60** (2008) 407.

[2] M. Kuwabara, Doctoral thesis (The University of Tokyo, 2018).

BL5B

Radiometric Calibration of a High-Resolution EUV Spectrometer

T. Kawate^{1,2}, H. A. Sakaue¹ and C. Suzuki^{1,2}

¹National Institute for Fusion Science, Toki 509-5292, Japan

²The Graduate University for Advanced Studies (SOKENDAI), Toki 509-5292, Japan

Understanding the structures of Unresolved Transition Array (UTA) observed in emission spectra from many-electron atoms is essential for many application fields, for example, developing the future light sources of semiconductor lithography and impurity transport in magnetically confined fusion plasmas. To model and validate the fine structures of the UTA spectra especially from tin at around 13.5 nm, gadolinium and terbium at around 6.8 nm, and tungsten at around 5.0 nm, we develop a high-resolution and high-throughput extreme ultraviolet spectrometer. Since UTA spectra span wide wavelength ranges, the radiometric calibration as a function of wavelength is crucial for the newly developed spectrometer.

In the UVSOR experiments, we measured the quantum efficiency of the CCD camera and the diffraction efficiency of the gratings for the high-resolution spectrometer using the calibration beamline [1] installed on BL5B. The CCD camera, PIXOS-XO:400B (Teledyne Princeton Instruments), was mounted on the backside of the chamber (Fig. 1(a)) with an XY-axis translation stage. We scanned the wavelengths using the monochromator in the beamline as well as the positions of the beam onto the detector using the translation stage. By inserting the calibrated photodiode AXUV100 in the middle of the beamline, we obtained the quantum efficiency of the CCD as a function of wavelength and position on the detector. The obtained quantum efficiency shows good agreement with the one provided by the manufacturer.

The gratings were a custom-made laminar type with spherical varied-line spacing manufactured by Shimadzu Corporation. The central groove density and the ruled area were 2300-line/mm and 90 x 30-mm², respectively. We designed the gratings to measure ~13 nm for first-order diffraction and 4-8 nm for second-order diffraction. It was mounted on the sample holder in the calibration chamber (Fig. 1(b)). To compare the diffraction efficiency under different polarization conditions, we performed experiments by changing the axis of coaxial rotation of the goniometer to vertical and horizontal directions. The measured diffraction efficiency is shown in Fig. 2. Although the difference between the polarization directions of the beam is not significant, the averaged efficiencies over the vertical and horizontal configurations agree with the calculation by PCGrate-SX software version 6.6 (I.I.G. Inc.).

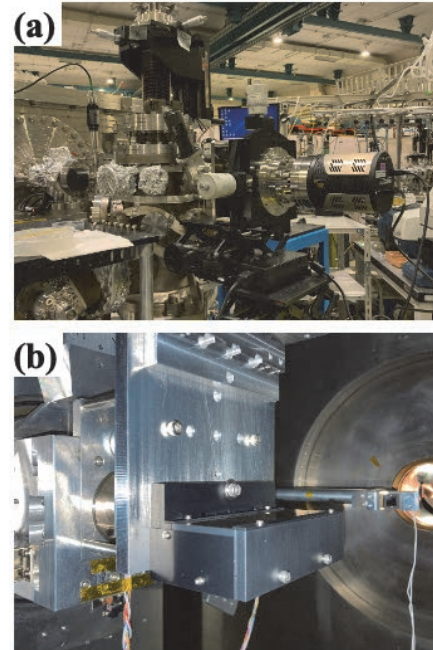


Fig. 1. Photos of the (a) CCD and (b) grating mounted on/in the calibration chamber.

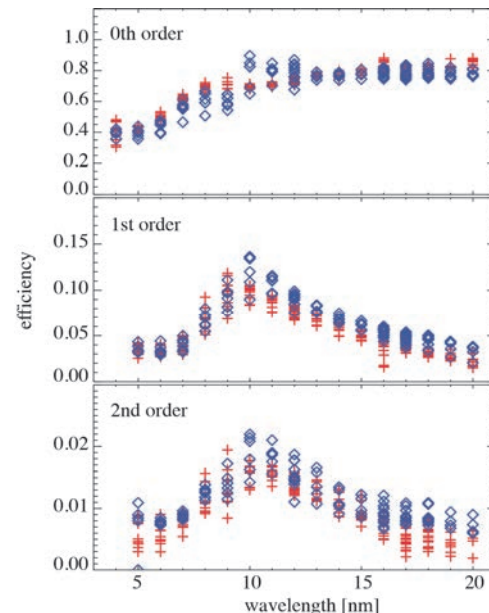


Fig. 2. Measured diffraction efficiencies of the grating with the axis of coaxial rotation of horizontal (blue diamond) and vertical (red cross) directions. The vertical scattering of the data points represents the efficiency at different positions on the grating.

[1] M. Sakurai *et al.*, Rev. Sci. Instrum. **60** (1989) 2089.

Calibration of Position-Sensitive Microchannel Plate Detectors

S. Matoba¹, S. Kanda¹, H. Ohshita¹, K. Hirata², H. Iwayama^{3,4} and T. Kaneyasu⁵

¹*Institute of Materials Structure Science, KEK, Tsukuba 305-0801, Japan*

²*National Institute of Advanced Industrial Science and Technology, Tsukuba, 305-8569, Japan*

³*UVSOR Synchrotron Facility, Institute for Molecular Science, Okazaki 444-8585, Japan*

⁴*School of Physical Sciences, The Graduate University for Advanced Studies (SOKENDAI), Okazaki 444-8585, Japan*

⁵*SAGA Light Source, Tosu 841-0005, Japan*

We are developing a compact imaging system that can be inserted into the beamline to monitor neutron and muon beams. In this system, a carbon resistive anode is placed at the rear of the microchannel plate (MCP), and the position of the incident particle can be detected. The resistive anode encoder has a square shape, and charge is extracted from the four corners. The coordinates of the center of charge on the resistor anodes are derived from

$$\begin{aligned} x/L &= (Q_2+Q_3)/(Q_1+Q_2+Q_3+Q_4), \\ y/L &= (Q_3+Q_4)/(Q_1+Q_2+Q_3+Q_4), \end{aligned} \quad (1)$$

where $Q_i (i = 1, 2, 3, 4)$ represents the amount of charge collected by each electrode on the resistive anode and L represents the distance between adjacent vertices, as shown in Fig. 1. Charges extracted from the four corners are measured by a 4-channel digitizer with 500MHz. The measurement was performed under the condition that the yield was limited to a few hundred counts per second and that no simultaneous injection into the MCP occurred. The signal from ch1 was used as the trigger, and the position was calculated according to Equation 1 by capturing the electric charge from each channel within 20 nanoseconds before and after the trigger.

We calibrated the position of the particle detection position of the system using 122 nm light at BL5b. The synchrotron radiation was incident on the microchannel plate through the attenuation filter and a 3 mm circular slit. Figure 2 shows the distribution of light detection positions in the horizontal (x) and vertical (y) directions. Figure 3 shows the position distribution of the noise signal when the shutter is closed. The reconstructed noise positions are not uniform but have a certain distribution. However, since the position distribution is not peaky, the effect on the analysis of the illuminated data is small. By using the RAE charge output as a self-trigger, the beam spot could be determined with high S/N.

From the above, it was confirmed that the constructed detector system is working properly. In the future, we plan to measure the optical detection efficiency using this system.

I would like to thank Mr. E. Nakamura for his great support of this experiment.

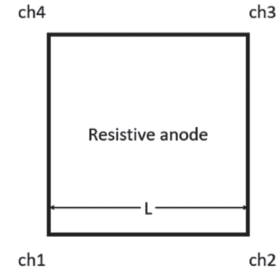


Fig. 1. Schematic of resistive anode.

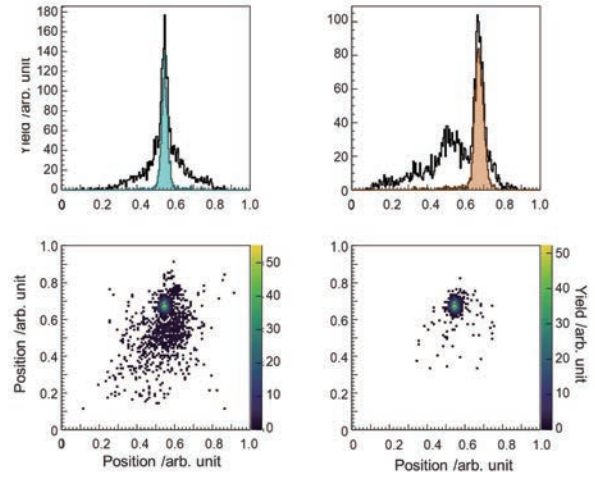


Fig. 2. Signal position distribution. X and Y distributions are shown above, respectively. Colored signals are those synchronized with the light trigger. The lower panel is a two-dimensional map. The right panel shows the signal synchronized with the light trigger.

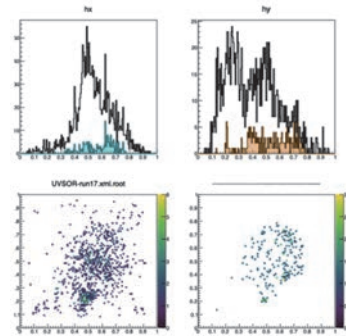


Fig. 3. Signal position distribution with shutters closed.

BL6U

Development of a Program to Analysis Multi-Dimensional Data of the Photoelectron Momentum Microscopy

S. Tanaka

SANKEN, Osaka University, Ibaraki 464-0056, Japan

The photoelectron momentum microscopy (PMM) is a revolutionary experimental method in which both the angle-resolved photoelectron spectroscopy (ARPES) and the photoemission electron microscopy (PEEM) techniques are combined in highly sophisticated way[1]. The PMM operated with the synchrotron radiation beamline provides huge amount of data in multi-dimensions, i.e., momentum, binding energy, position in the real space, polarization, photon energy, etc[2]. However, the distributed program from the manufacture has limited functions and not very convenient to use. Therefore, the development of a new program which enable us to conveniently analyze the multi-dimensional data of the PMM is highly desired.

The program now under developing holds following benefits:

- 1) The program is written in the Python language, which is a standard language in many fields including the data science, and runs under multiple OSs (Windows 10/11, Mac OS, and Linux).
- 2) The whole program consists of self-standing functional programs, *i.e.*, a data-reading, a 2D-data analysis, a 3D-data analysis (Fig.1), a 3D-volumetric presentation, a multiple-peak-fitting, a Fermi-Dirac fitting, a curvature method including the second-derivative to clarify the structure in the 2D intensity map, *etc.* Adding to these procedures commonly used in the angle-resolved photoelectron spectroscopy, analytic tools specified for the PMM with the synchrotron radiation are provided (Fig.2).
- 3) The program can be used as a data-format converter. Raw data can be obtained directly from an “sle” file which is produced by the experimental program. Then, these are calculated for the analysis (integration, calibration, conversion, smooth, *etc.*). These can be saved not only in “npz” (the binary format of python) file but also in “csv” (“comma-separated value” in ascii format), “h5” (the HDF format), “ibw” (igor binary wave), “itx” (igor text) formats. Then, users can complete the figures by using their own programs.

An example of working windows of the program (running on the Mac OS) are shown in Figs. 1 and 2. The next function will be a reading and analyzing the result of the spin-resolved measurements.

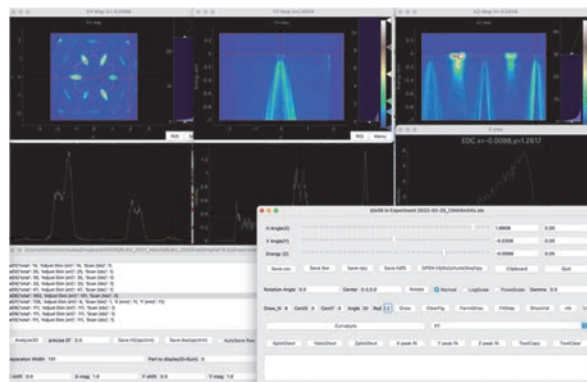


Fig. 1. Windows of the 3D-analysis mode. 2D intensity maps along k_x, k_y , k_x -BE (Biding Energy) and k_y -BE are shown together with intensity plots as functions of k_x , k_y and BE. The points of plotting can be easily chosen using slide bars.

The sample is TiSe_2 at 30K.

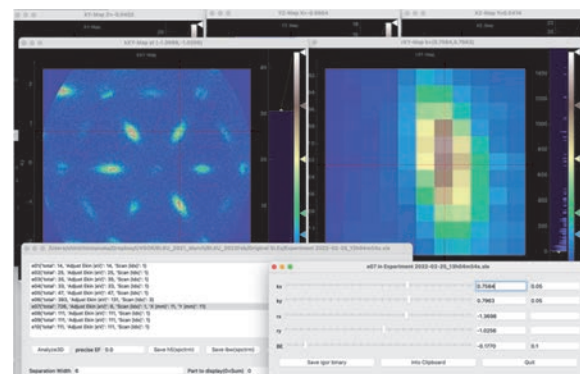


Fig. 2. Windows of the ARPES/microscopy analyzing program. Left window shows the photoelectron intensity map in the momentum space, and the right one shows that in the real space. The data acquisition point is shown by the crossing point of the red line in both spaces. In this case, the sample is TiSe₂ as well as in Fig.1, and the real space distribution is mainly affected by the angular distribution of the photoelectron because the sample surface is not perfectly flat.

- [1] F. Matsui *et al.*, Rev. Sci. Instrum. **94** (2023) 083701.
[2] K. Hagiwara *et al.*, J. Synchrotron Radiat. **31** (2024) 540.

Numerical Correction of α^2 Aberration on PMM Imaging at BL6U

R. Sagehashi¹, K. Hagiwara², S. Kera^{1,2} and F. Matsui²

¹Department of Photo-Molecular Science, Institute for Molecular Science, Okazaki 444-8585, Japan

²UVSOR Synchrotron Facility, Institute for Molecular Science, Okazaki 444-8585, Japan

Hemispherical deflection analyzers (HDAs) are often used for angle-resolved photoelectron spectroscopy measurements to achieve high energy resolution by acquiring photoelectrons as a two-dimensional (2D) function of kinetic energy versus angle. Furthermore, HDA allows energy-selected imaging the 2D angular distribution of electrons entering the HDA entrance aperture. However, the pass energy of electrons varies with the entrance angle along the energy dispersion axis (α). The effective pass energy is expressed by the following formula:

$$E_{\text{pass}}(\alpha)/E_{\text{pass}}(0^\circ) = (1 - \sin^2\alpha)^{-1} \approx (1 + \alpha^2). \quad (1)$$

This phenomenon is called α^2 aberration [1]. Due to this aberration, imaging results such as band structure and photoelectron angular distribution are accompanied by energy shift. When HDA is used for imaging angle-resolved spectra, the α^2 aberration reduces the energy resolution. On the other hand, when using HDA to image a 2D angular distribution, α^2 aberration occurs at different detector positions. The photoelectron momentum microscope (PMM) installed at BL6U uses this type of detection [2]. In this case, since the influence of α^2 aberration can be removed as described later, the energy resolution is not affected.

Figure 1 shows the experimental data of the band structure of Au(111) surface obtained by PMM at BL6U in 2024.02. It showed clear energy shift of Fermi level along k_a axis (the energy axis in HDA) due to α^2 aberration. This energy shift can be fitted by second polynomial function. In order to detect Fermi level (E_F) at every spectrum, they were fitted by Fermi-Dirac function:

$$f(E) = (1 + \exp((E - E_F)/k_B T))^{-1}. \quad (2)$$

By using these results, E_F at each angle α can be evaluated. As a result, the energy difference between maximum and minimum was around 25 meV. Next, $E_F(k_a)$ was fitted by second polynomial function. In this case, the following function was obtained as fitting function:

$$E_F(k_a) = -7.34k_a^2 - 5.78k_a + 1.60. \quad (3)$$

Finally, every spectrum was readjusted considering with this equation. Figure 2 indicates original data of photoelectron momentum pattern at Fermi level (a) and corrected pattern (b). Comparing them, the pattern after correction was clearly seen at $k_a < -1.8 \text{ \AA}^{-1}$ and $+1.8 \text{ \AA}^{-1} < k_a$ more than the original data.

We also performed same analysis on the data about Au(111) taken in 2022.01. As a result, the coefficient of k_a^2 in the fitting function became -1.69, which is less than a quarter of the data in 2024.02. The pass energy

were 20 eV and 50 eV in 2022 and 2024, respectively. According to Eq. (1), the α^2 aberration get bigger when pass energy becomes bigger. In 2022, the single HDA was used at BL6U, while double HDA system is installed now. Since it is equivalent to doubling the radius of HDA, the α^2 aberration also becomes bigger. On the other hand, there was little difference of energy resolution after aberration correction between 2022 and 2024, both values were around 15 meV. Nevertheless, the transmission of HDA is related to the squared pass energy. As a result, the double HDA allows PMM measurements approximately 4 times more efficiently than the single HDA in this case.

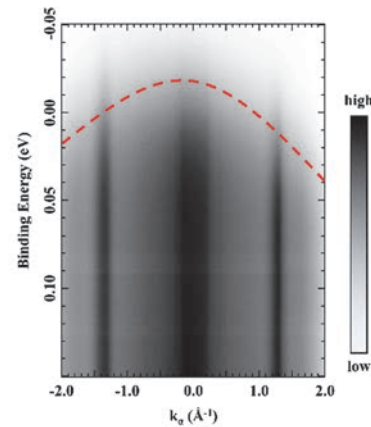


Fig. 1. The band structure of Au(111) surface around valence band obtained by PMM measurement at BL6U. (Red dashed line indicates α^2 aberration.)

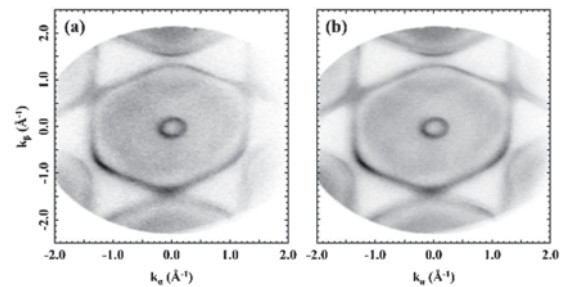


Fig. 2. Photoelectron momentum pattern of Au(111) surface (Fig. 1) at Fermi level. (a) Before correction. (b) After correction.

[1] C. Tusche, A. Krasnyuk and J. Kirschner, *Ultramicroscopy* **159** (2015) 520.

[2] F. Matsui *et al.*, *Jpn. J. Appl. Phys.* **59** (2020) 067001.

BL6U, BL7U

Development of Dual-Beamline Photoelectron Momentum Microscope

K. Hagiwara¹, E. Nakamura¹, S. Makita¹, S. Suga², S. Tanaka², S. Kera^{1,3} and F. Matsui^{1,3}

¹UVSOR Synchrotron Facility, Institute for Molecular Science, Okazaki 444-8585, Japan

²SANKEN, Osaka University, Mihogaoka 8-1, Ibaraki 567-0047, Japan

³School of Physical Sciences, The Graduate University for Advanced Studies (SOKENDAI), Okazaki 444-8585, Japan

We have developed a unique dual-beamline photoelectron spectroscopy experimental station combined with a state-of-the-art photoelectron momentum microscopy (PMM) analyzer [1]. PMM combines a photoemission electron microscope (PEEM)-type objective lens and an energy-filtering hemispherical deflection analyzer. PMM allows photoelectron imaging in real and momentum spaces, facilitating electronic structure analyses in local μm -scale domains. PMM has been installed at the soft X-ray beamline BL6U of UVSOR synchrotron facility [2, 3]. In 2023, by branching the vacuum ultraviolet (VUV) beamline BL7U [4], a VUV beam was successfully guided to the same sample position as the soft X-ray beam from BL6U [1] as shown in Fig. 1. This upgrade allowed us to use wide-energy photons $h\nu = 6 - 30$ and $40 - 800$ eV in the PMM experimental station. The VUV beam with variable polarization in the normal-incidence geometry now became available. The detailed experimental geometry of PMM is illustrated in Fig. 2. We note here that momentum-resolved photoelectron spectroscopy in such normal-incidence geometry is currently only available with this UVSOR PMM. Such highly symmetric photoemission geometry with normal incidence offers direct access to atomic orbital information via photon polarization-dependent transition-matrix-element analysis.

We measured the photoelectron momentum distribution of the Au(111) surface using horizontally and vertically polarized light from BL7U in addition to p-polarized light from BL6U as shown in the two insets of Fig. 2. Colored intensities show contribution of corresponding photon polarizations.

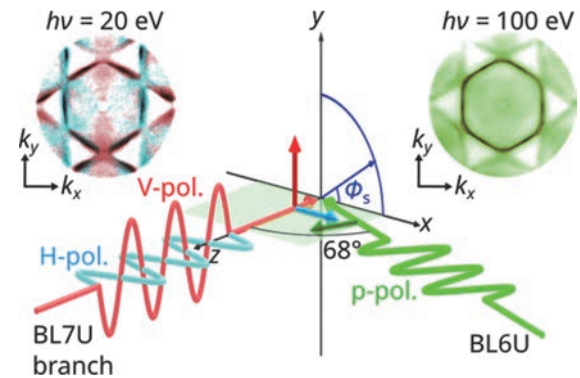


Fig. 2. Experimental geometry of the PMM station with two beams. p-polarized light from BL6U is incident in the x - z plane at an angle of 68° from the sample surface normal (z) axis. Here, the plane of incidence (x - z plane) is represented by the green horizontal plane. Horizontally and vertically polarized light from the BL7U branch passes along the surface normal (z) axis. Samples can be rotated in-plane at an angle of ϕ_s . The two insets show the measured photoelectron momentum patterns of the Au(111) surface with various photon polarizations.

- [1] K. Hagiwara *et al.*, J. Synchrotron Radiat. **31** (2024) 540.
- [2] F. Matsui *et al.*, Jpn. J. Appl. Phys. **59** (2020) 067001.
- [3] F. Matsui *et al.*, Rev. Sci. Instrum. **94** (2023) 083701.
- [4] S. Kimura *et al.*, Rev. Sci. Instrum. **81** (2010) 053104.

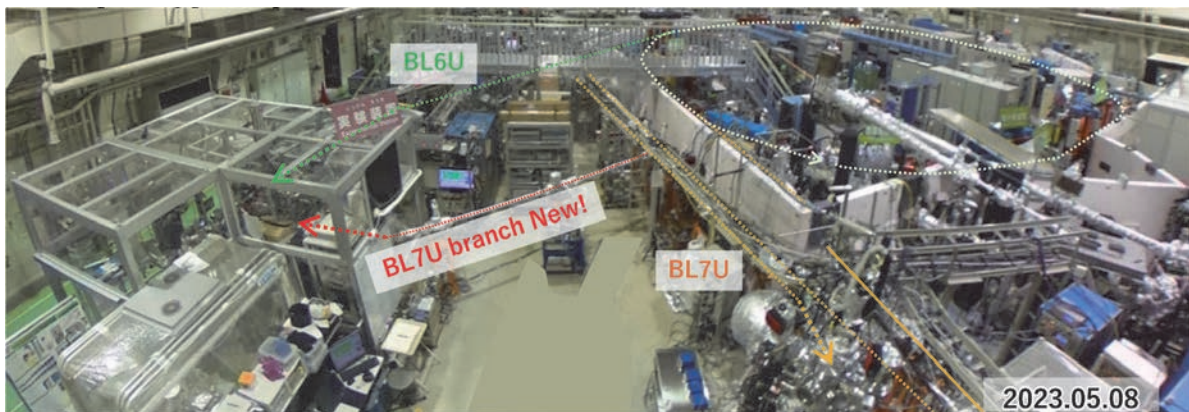


Fig. 1. Photograph of beamline BL6U, BL7U, and the newly constructed BL7U branch.

Development of a Uniaxial Pressure Cell for Infrared and ARPES Measurements

H. Watanabe^{1,2}, H. Ishida² and S. Kimura^{1,2,3}

¹Graduate School of Frontier Biosciences, Osaka University, Suita 565-0871, Japan

²Department of Physics, Graduate School of Science, Osaka University, Toyonaka 560-0043, Japan

³Institute for Molecular Science, Okazaki 444-8585, Japan

Pressure is one of the most fundamental external perturbations that control interactions within materials. Numerous physical properties have been measured under applied pressure using diamond anvil cells and piston-cylinder cells. In these experiments, photoelectron spectroscopy (PES) and wide-range optical measurements are prevented due to the requirement of window materials such as diamond and sapphire to apply hydrostatic pressure. Such optical measurements are required to observe the change in the electronic structure with pressure. Then, we developed a compact pressure cell without window materials, a uniaxial pressure cell (UPC) with a piezoelectric actuator (PA) control for PES and optical measurements. The UPC was designed for general spectroscopic measurements, including infrared spectroscopy and ARPES measurements.

So far, angle-resolved PES (ARPES) using a uniaxial stage using the difference in expansion coefficient of metals with temperature has already been reported [1]. Still, it is difficult to control temperature and pressure independently. On the other hand, a PA-based UPC has already been developed and supplied by Razorbill Instruments [2]. Owing to the large size, however, it is difficult to mount on the Oxford-type sample holder (sample area: $10 \times 10 \text{ mm}^2$) for optical measurements and the Omicron-type holder ($13 \times 13 \text{ mm}^2$) for ARPES.

As a practical demonstration of our innovation, we have successfully developed a prototype UPC that can be mounted on a widely used cryostat of MicrostatHe (Oxford Instruments) and the Omicron holder for ARPES. The UPC can easily apply uniaxial pressure using a PA by applying voltage. Figure 1(a) showcases the UPC ($10 \times 15 \text{ mm}^2$) mounted on the MicrostatHe sample stage ($19 \times 19 \text{ mm}^2$). The UPC consists of three PAs; one of the three (the other two) is used for pressurizing (pulling). The metallic parts, fabricated by the Equipment Development Center of the Institute for Molecular Science, are connected to PAs with Stycast (LOCTITE, Henkel Co.). The position of the center stage can be changed with the varying PA voltage, as shown in Fig. 1(b). The stage shift per PA voltage is 30 nm/V , consistent with the PA standard. This successful demonstration confirms the practicality and

effectiveness of our UPC.

Building on the success of our prototype, we envision creating a new UPC using PA that can be utilized at low temperatures. Our plans also include measuring pressure at low temperatures, a crucial step in expanding the practical applications of the UPC.

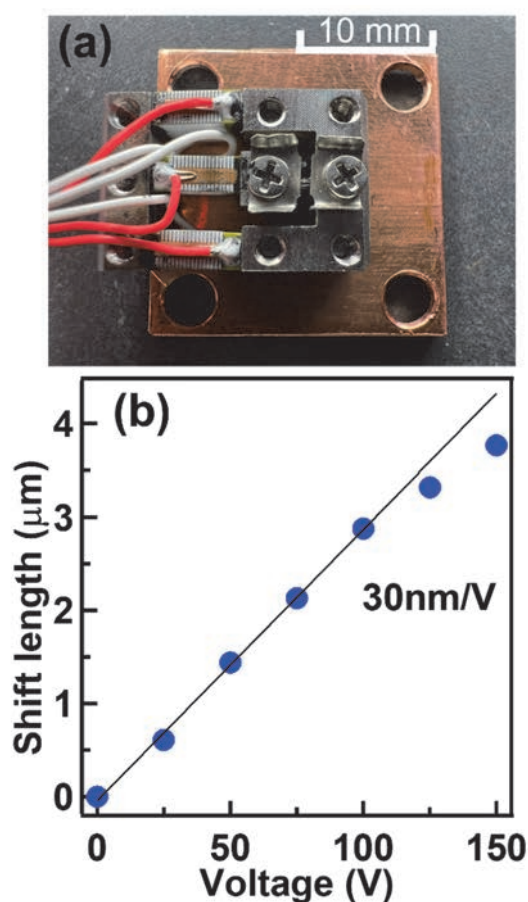


Fig. 1. Photograph of the UPC mounted on the MicrostatHe sample stage (a) PA voltage dependence of the shifted length of stage (b)

[1] V. Sunko *et al.*, npj Quantum Mater. **4** (2019) 46.

[2] M. E. Barber *et al.*, Rev. Sci. Instrum. **90** (2019) 023904.

Others

Performance Evaluation of Nuclear Emulsion Sensitized by Hydrogen Gas

H. Rokujo, Y. Isayama and T. Nakano

F-lab., Graduate School of Science, Nagoya University, Nagoya 464-8602, Japan

Nuclear emulsion is currently being used for particle and radiation measurements in a variety of scientific and applied fields. After its production, the nuclear emulsion records tracks of charged particles until it is developed. If the sensitivity can be controlled before and after experiments/observations, and if it can be given a switch function to turn them on and off, the use of nuclear emulsion is expected to expand into new applications. For example, this ON/OFF function would be an effective basic technology for transporting nuclear emulsion to space.

Hydrogen hyper-sensitization is known as one of the sensitization processes in astrophotography. The principle of this method is that the reducing action of hydrogen gas is used to produce reduction sensitization centers on silver bromide crystals, resulting in an increase in sensitivity [1]. By baking the film with hydrogen gas before exposure, the sensitivity can be temporarily increased. Conventional photographic film is used in air, so it retains its sensitivity for only a few days after gas treatment. There is no report on the combination of nuclear emulsion film and hydrogen hyper-sensitization that has been put into practice. We attempted to control the sensitivity of nuclear emulsion using hydrogen gas and evaluated the sensitivity by irradiating electrons obtained by UVSOR.

Nuclear emulsion plates were prepared by coating gold-sulfur sensitized and unsensitized nuclear emulsion gels (AgBrI crystals, average particle size 240 nm, gelatin volume ratio ~60 %) on glass slides, respectively. The plates were placed in a small stainless steel pressure vessel and the vacuum pump was used to reduce the gauge pressure to -95 kPa. Then, the vessel was filled with nitrogen gas and pressurized to a gauge pressure of +20 kPa. And hydrogen gas was filled to the gauge pressure of +25 kPa, so that the hydrogen gas content in the vessel was 4 %. The vessel was placed in a thermostatic bath and baked at 40 °C for 23 hours. After returning to room temperature for 1 hour, the vessel was opened, and the nuclear emulsion plate were extracted. The plates were immediately vacuum-sealed one by one, shut off from light/air, and stored frozen. Two days after the baking process, the plates were irradiated with electron beams at UVSOR and developed (XAA, 20 °C, 25 min) at Nagoya University

on the day after irradiation.

Figure 1 shows a microscopic image of the electron beam tracks, and Fig. 2 shows the results of grain density measurements (average count of developing silver particles per 100 microns). The grain density did not increase in comparison with samples that were not gas-filled but were baked (40 °C for 23 hours) and refrigerated at the same time. No electron beam tracks were observed in the unsensitized emulsion sample.

Hydrogen hyper-sensitization test of nuclear emulsion was performed for the first time. Although no increase in sensitivity was observed, we were able to confirm the setup and procedures for processing and evaluation. In the future, we would like to change the baking conditions after sealing in nitrogen-hydrogen gas and find conditions to increase sensitivity.

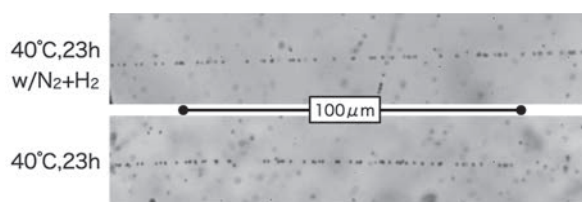


Fig. 1. Micrographs of electron tracks recorded in emulsion plates with and without hydrogen hyper-sensitization [2].

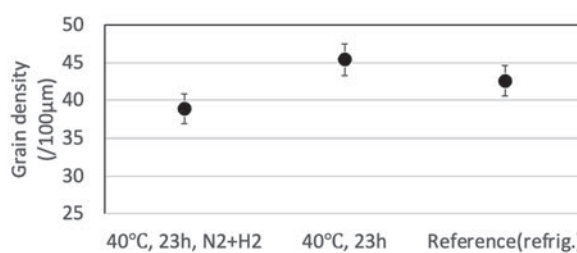
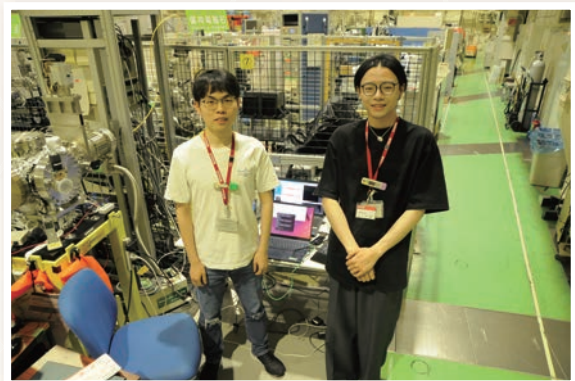
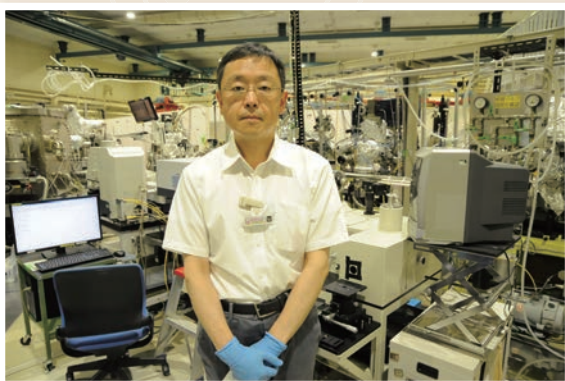
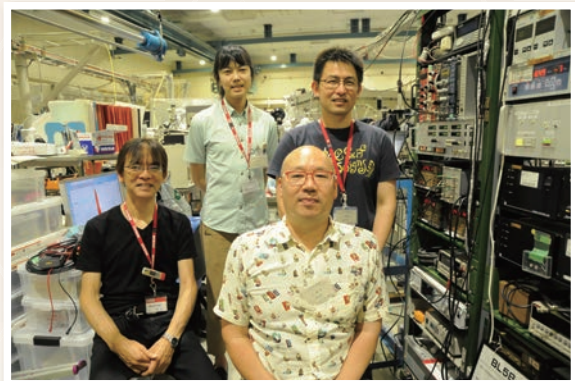
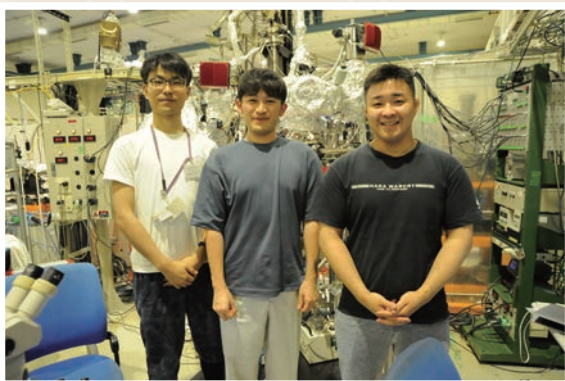
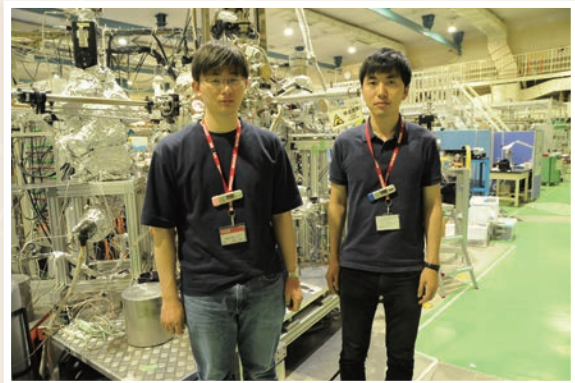
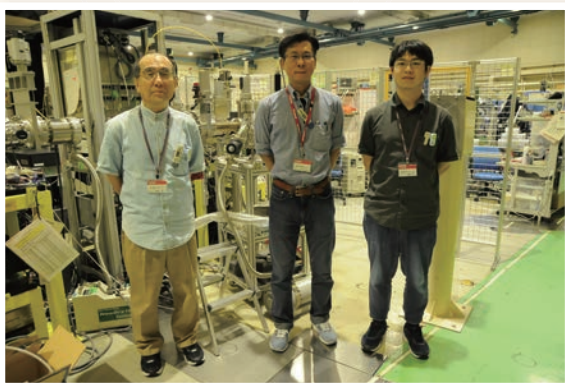
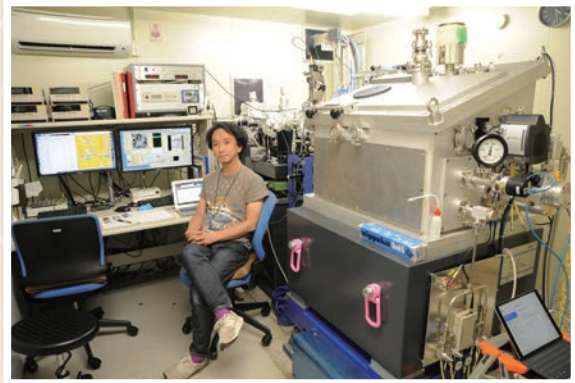
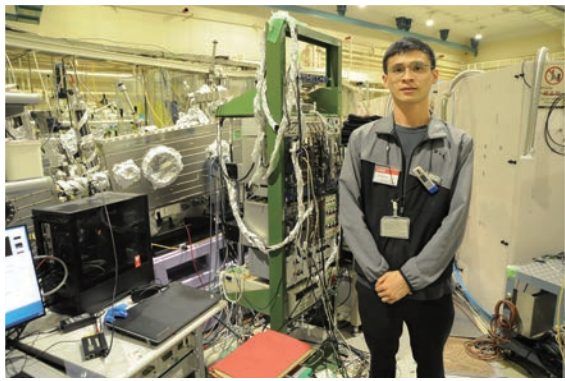


Fig. 2. Comparison of grain density between emulsion plates with and without hydrogen hyper-sensitization [2].

[1] T. Tani, J. Soc. Photogr. Sci. Tech. Jpn. **81** (2018) 108.

[2] H. Rokujo and Y. Isayama, J. Soc. Photogr. Sci. Tech. Jpn. **86** (2023) 426.

UVSOR User 3



III-2

Material Sciences





BL6B

Anisotropy in the Far-Infrared Absorption Davydov Doublet of the Single-Crystal Pentacene

Y. Nakayama^{1,2}, K. Yamauchi¹, Y. Baba¹ and J. Miyamoto¹¹Department of Pure and Applied Chemistry, Tokyo University of Science, Noda 278-8510, Japan²Institute for Molecular Science (IMS), Okazaki 444-8585, Japan

Accurate knowledge of the vibrational properties of solid-state molecules is a crucial demand to understanding polaronic charge carrier transport phenomena in organic semiconductors [1], and thus the vibrational characteristics of pentacene have been studied extensively. For instance, Pinterić *et al.* recently reported their very fine results on temperature-dependent variation of the infrared absorption properties of the pentacene single-crystals (PnSCs) to reveal influences of the electron-phonon couplings to the excitonic characters [2]. Nevertheless, a complete understanding of the vibrational characteristics peculiar to the single-crystal phase of this molecule has not yet been achieved. In the present work, we focused on two unique properties for the single-crystals of pentacene, that is, the orientation dependence and vibrational Davydov splitting, and attempted to clarify these characteristics by azimuthal-angle (ϕ) dependent analyses of the Fourier transform infrared absorption (FT-IR) spectroscopy.

Details for the samples measured and experimental conditions were reported elsewhere [3]. The FT-IR measurements were conducted at BL6B of UVSOR. All the results presented here were obtained by using a Si bolometer and at room temperature.

Figure 1(a) shows the IR absorbance of PnSC. As seen in Fig. 2(a), the peak positions of these two were independent of ϕ , while the intensities of these were complementary to each other. Although these two peaks were originally assigned to two individual vibrational modes [4], present results showing a good agreement of

experimental “major”/“minor” intensity ratios with the theoretical calculation (Fig. 2(b)) strongly suggest that these two peaks were originated from the Davydov splitting of one vibrational mode.

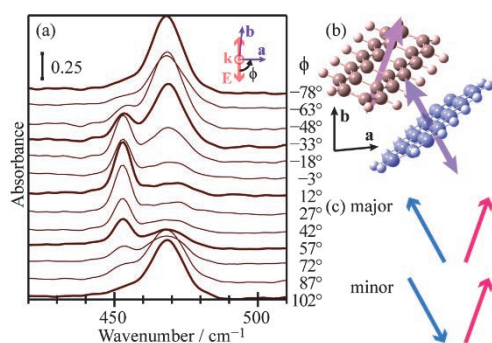


Fig. 1. (a) IR absorbance of PnSC depending on ϕ . (b) Molecular orientation and transition dipole directions of the vibration mode (#15) for the PnSC(001) surface molecules. (c) Relationships of the transition dipoles for the “major” and “minor” Davydov components.

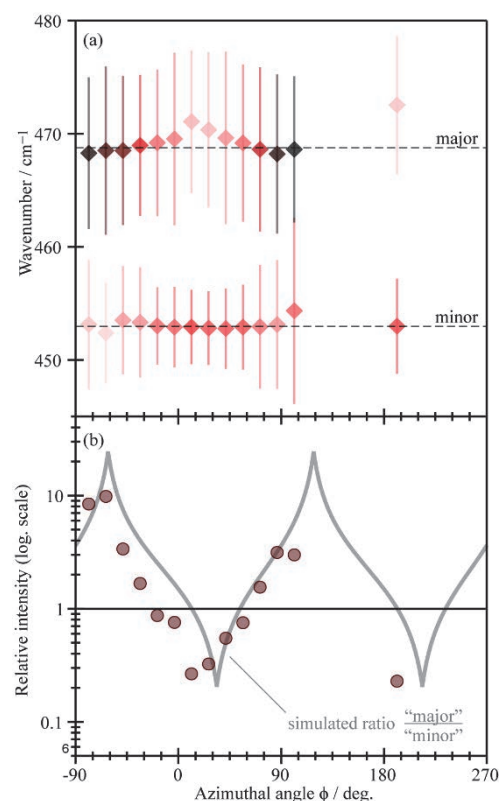


Fig. 2. (a) Wavenumber positions of the two peaks shown in Fig. 1(a) plotted as a function of ϕ . The peak intensity is indicated as the color tone (light: small; dark: large). (b) Intensity ratios of the two peaks (“major”/“minor”) plotted as circle symbols. The simulated intensity ratio of the two Davydov components for a vibrational mode with a transition dipole directions perpendicular to the molecular plane is also drawn with a gray curve.

- [1] V. Coropceanu *et al.*, Chem. Rev. **107** (2007) 926.
- [2] M. Pinterić *et al.*, J. Mater. Chem. C **10** (2022) 5582.
- [3] Y. Nakayama *et al.*, Vib. Spectrosc. **132** (2024) 103681.
- [4] K. Michaelian *et al.*, Vib. Spectrosc. **58** (2012) 50.

Change in Positron Lifetime of Deformed Pure Iron before and after Unloading Tensile Stress

M. Fujinami¹, R. Awaji¹, H. Abe¹, A. Yabuuchi², T. Hirade³, N. Oshima⁴ and Y. Taira⁵

¹Department of Applied Chemistry and Biotechnology, Chiba University, Chiba 263-8522, Japan

²Institute for Integrated Radiation and Nuclear Science, Kyoto University, Kumatori 590-0494, Japan

³Nuclear Science and Engineering Center, Japan Atomic Energy Agency, Tokai 319-1195, Japan

⁴National Institute of Advanced Industrial Science and Technology, Tsukuba 305-8568, Japan

⁵UVSOR Synchrotron Facility, Institute for Molecular Science, Okazaki 444-8585, Japan

The study of lattice defects in metals formed by plastic deformation is important for controlling metals' mechanical properties. Positron annihilation lifetime spectroscopy (PALS) is a powerful tool for investigating vacancy-type defects in metals [1]. However, measuring the positron lifetime of metals during deformation using a conventional PALS technique is difficult. Therefore, in most previous studies, the positron lifetimes of deformed metals were measured after the deformation stress was unloaded. The characteristics of defects in metals may change due to the unloading of deformation stresses. In this study, we measured the positron lifetime of pure iron using a gamma-ray-induced PALS (GiPALS) technique [2], which can easily measure the positron lifetime of metals during deformation.

As shown in Fig. 1, we installed a small tensile tester at the BL1U beamline. A well-annealed pure iron tensile test piece with a purity of 99.99 % was attached to the tensile tester. The thickness and gauge width of the test piece were 3 mm and 6 mm, respectively. Positron lifetimes were measured while the test piece was being elongated. Furthermore, positron lifetimes after elongation to ~ 7 % nominal strain were measured, both before and after tensile stress unloaded.

The mean positron lifetime of pure iron investigated by in-situ measurements during tensile deformation increased with increasing nominal strain. The GiPALS technique was shown to be an easy way to measure changes in the positron lifetime of metals during deformation. Figure 2 shows the results of a two-component analysis of the positron lifetime of pure iron elongated to ~ 7 % nominal strain, measured before and after tensile stress unloading. The defect component intensity, I_2 (intensity of the longer positron lifetime component), increases significantly by unloading the tensile stress. Furthermore, the positron lifetime of the defect component (the longer positron lifetime component) also changes significantly. This indicates that the defects were formed by the unloading of tensile stress. In other words, the defect structure in structural materials actually used under stress cannot be revealed by observation after the stress is unloaded. One needs to recognize the importance of measuring lattice defects under actual usage conditions of the material.

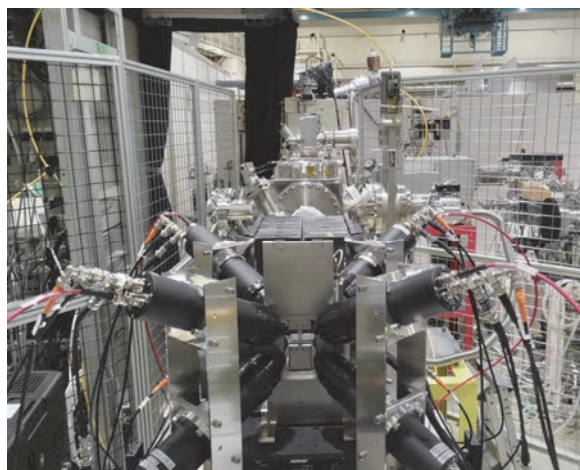


Fig. 1. Photo of a small tensile tester installed at the BL1U beamline. A tensile test piece is attached to the center of the eight scintillation detectors.

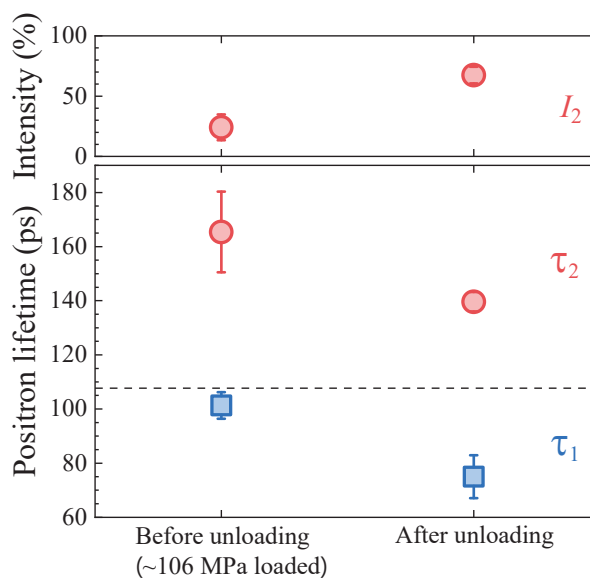


Fig. 2. Positron lifetimes of pure iron elongated to ~ 7 % nominal strain. The left and right sides were measured before and after tensile stress unloading, respectively.

[1] R. W. Siegel, *Annu. Rev. Mater. Sci.* **10** (1980) 393.

[2] Y. Taira *et al.*, *Rev. Sci. Instrum.* **93** (2022) 113304.

BL1U

Changes of the Gamma-ray Induced Positron Annihilation Lifetimes for CeO_2 by Desorption and Re-adsorption of Surface Adsorption Species

S. Dohshi¹, K. Maeda¹, Y. Taira² and T. Hirade³

¹Osaka Research Institute of Industrial Science and Technology 2-7-1, Ayumino, Izumi, Osaka 594-1157, Japan

²UVSOR Synchrotron Facility, Institute for Molecular Science, Okazaki 444-8585, Japan

³Japan Atomic Energy Agency, Ibaraki 319-1195, Japan

Cerium oxide (CeO_2) catalyst utilizes active oxygen species adsorbed on the surface oxygen defects to oxidize toluene. Temperature programmed desorption measurements have reported that active oxygen species (O_2^-) adsorbed on oxygen defects of cerium oxide surface desorbs at 150 °C, which initiates the oxidation reaction of toluene [1].

Gamma-ray-induced positron annihilation lifetime spectroscopy (GiPALS) measurements were conducted on CeO_2 at room temperature in air. The lifetime components attributed to the surface were consistent with those of defect-free surface determined by first principles calculations. Active oxygen species adsorb on the surface oxygen defects before temperature programmed desorption, resulting in few trapped positrons in these defects. However, after temperature programmed desorption, the adsorbed active oxygen species are expected to desorb, resulting in the emergence of oxygen defects on the surface and the creation of new positron trapping sites.

This study investigated the positron annihilation lifetimes of two operations: (1) the removal of surface adsorbed species by heating CeO_2 under an argon flow, and (2) the subsequent re-adsorption of surface adsorbed species under a water vapor-containing air flow.

The pellet sample with 20 mm in diameter and 10 mm in thickness were prepared using CeO_2 nanoparticles with a primary particle size of ca. 2 nm. In this experiment, the pellets were heated in a quartz tube at a rate of 5 °C/min using a jacket heater under argon (purity: 99.999%) flow to 200 °C and held for 2 h. After cooling under argon flow, a GiPALS measurement was performed. Subsequently, air containing water vapor was flowed through at a rate of 200 mL/min for 1 h at room temperature, followed by another GiPALS measurement.

We have set up a gamma-ray spectroscopy system at the laser-Compton scattering (LCS) beamline of BL1U at UVSOR-III [2], and measured the lifetime of the annihilation gamma-rays at room temperature using BaF_2 scintillation detector. We used the software Lifetime9 (LT9) to analyze the spectra.

Figure 1 shows the positron annihilation lifetime

spectra of CeO_2 measured under different conditions. The positron annihilation lifetime becomes longer when CeO_2 was heated at 200 °C. Previous research has shown that heating CeO_2 at this temperature causes the desorption of active oxygen species adsorbed on oxygen defects on the surface, while lattice oxygen remains unaffected [1]. In short, the longer positron annihilation lifetime is believed to result from the emergence of oxygen defects on the surface caused by the desorption of active oxygen species. Additionally, the positron annihilation lifetime spectrum was observed to return to its original state when air containing water vapor was introduced, possibly due to the re-adsorption of oxygen and/or water vapor on the surface oxygen defects.

In the next fiscal year, we plan to conduct a detailed study on the adsorption species present on the oxygen defects on the surface.

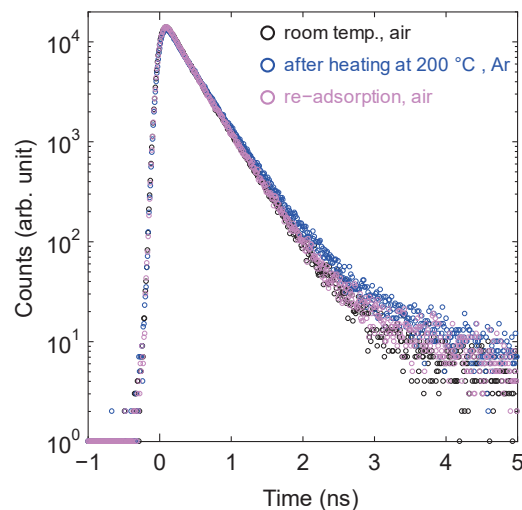


Fig. 1. Positron annihilation lifetime spectra of CeO_2 measured under different conditions. (a) at room temperature in air, (b) after heating at 200 °C for 2 h in Ar, (c) re-adsorption of surface adsorbed species under a water vapor-containing air flow for 1 h.

- [1] L. Wang *et al.*, Catal. Sci. Technol. **6** (2016) 4840.
[2] Y. Taira *et al.*, Rev. Sci. Instrum. **84** (2013) 053305.

GiPALS Study of $\text{Ca}_2\text{MgSi}_2\text{O}_7\text{:Eu,Dy}$ Long-Persistent Phosphorescence Phosphors

M. Kitaura¹, H. Masai², S. Watanabe³ and Y. Taira^{4,5}

¹*Faculty of Science, Yamagata University, Yamagata 990-8560, Japan*

²*Department of Materials and Chemistry, National Institute of Advanced Industrial Science and Technology, Ikeda 563-8577, Japan*

³*Innovative Technology Laboratories, AGC Inc., Yokohama 230-0045, Japan*

⁴*UVSOR Synchrotron Facility, Institute for Molecular Science, Okazaki 444-8585, Japan*

⁵*School of Physical Sciences, The Graduate University for Advanced Studies, Okazaki 444-8585, Japan*

Multinary compounds have been widely used as commercial products. These compounds are difficult to obtain stoichiometric compositions. Especially, the addition of impurities causes non-stoichiometric compositions, because it requires defects such as vacancies or interstitials for charge compensation when they are incorporated into host materials. Such a non-stoichiometry affects physical and chemical properties of multinary compounds.

Gamma-ray-induced positron annihilation lifetime spectroscopy (GiPALS) is an atomic scale micro-probe to observe vacancy-type defects in solids [1]. GiPALS studies of multicomponent garnet scintillators activated with Ce^{3+} ions have been performed so far to investigate the mechanism on the occurrence of a persistent phosphorescence in the Ce^{3+} 5d-4f emission [2,3]. It was turned out that the persistent phosphorescence occurs under non-stoichiometric compositions due to the introduction of Al vacancy at 16a and 24d sites. This finding was significant to improve luminescence properties of the multicomponent garnet scintillators. In contrast, non-stoichiometry compositions may be favorable for long persistent phosphorescence phosphors, but it remains unclear whether non-stoichiometry is indispensable for the long persistent phosphorescence.

$\text{Ca}_2\text{MgSi}_2\text{O}_7\text{:Eu,Dy}$ is known to be long persistent phosphorescence phosphors. In this material, it was pointed out that oxygen and magnesium vacancies are introduced as native defects which work as electron and hole reservoirs [4,5]. Because of charge compensation, such vacancy-type defects may be introduced more by the codoping of Dy ions at the Ca site. A positron probe such as GiPALS is a unique tool to investigate the existence of the vacancy-type defects. In the present study, GiPALS experiment was performed to demonstrate whether they are included in $\text{Ca}_2\text{MgSi}_2\text{O}_7\text{:Eu,Dy}$.

The GiPALS spectrum of a $\text{Ca}_2\text{MgSi}_2\text{O}_7\text{:Eu,Dy}$ is shown in Fig. 1. The spectrum consists of two exponential decay components, as indicated by broken lines. The positron annihilation lifetimes τ_i and relative intensities I_i of the two components are listed in Table 1. The relative intensities of two components are comparable. The bulk lifetime was analyzed by

assuming the two-state trapping model in which positrons annihilate at the bulk and defect states. The bulk lifetime was determined to be 265 ± 8 ps. This value was different from the bulk lifetime ($=232$ ps) determined by a first principles calculation based on the density-functional theory. The short lifetime component may not be simply linked to the positron annihilation at the bulk state. Further investigations are needed to identify the origins of the short and long lifetime components in $\text{Ca}_2\text{MgSi}_2\text{O}_7\text{:Eu,Dy}$.

A part of this study was financially supported by JSPS KAKENHI grant (No. 21H05546).

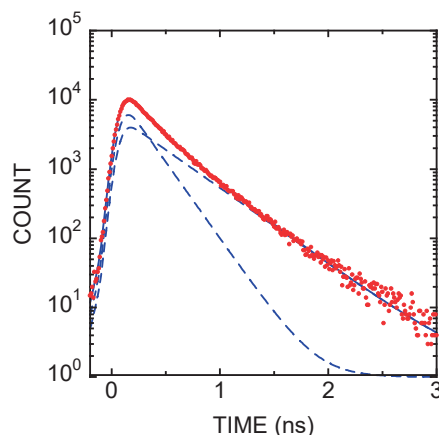


Fig. 1. GiPALS spectrum of a $\text{Ca}_2\text{MgSi}_2\text{O}_7\text{:Eu,Dy}$ crystal measured at 300 K.

Table 1. Positron annihilation lifetimes and relative intensities obtained from the curve-fit analysis of GiPALS spectrum for a $\text{Ca}_2\text{MgSi}_2\text{O}_7\text{:Eu,Dy}$.

τ_1 (ps)	I_1 (%)	τ_2 (ps)	I_2 (%)
197 ± 5	48.6 ± 1.5	395 ± 5	51.4 ± 1.5

[1] Y. Taira *et al.*, Rev. Sci. Instrum. **33** (2006) 1.

[2] M. Kitaura *et al.*, Appl. Phys. Express **13** (2020) 085505.

[3] M. Kitaura *et al.*, Opt. Mater.: X **14** (2022) 100156.

[4] J. Holsa *et al.*, J. Rare Earths **29** (2011) 1130.

[5] H. Duan *et al.*, J. Phys. D: Appl. Phys. **49** (2016) 025304.

BL1U

Gamma-ray Induced Positron Annihilation Lifetime Spectroscopy of As-Doped CdTe

T. Sumi¹, M. Kitaura¹, A. Nagaoka², Y. Taira^{3,4}, H. Masai⁵ and K. Kimura⁶

¹Faculty of Science, Yamagata University, Yamagata 990-8560, Japan

²Faculty of Engineering, University of Miyazaki, Miyazaki 889-2192, Japan

³UVSOR Synchrotron Facility, Institute for Molecular Science, Okazaki 444-8585, Japan

⁴School of Physical Sciences, The Graduate University for Advanced Studies, Okazaki 444-8585, Japan

⁵Department of Materials and Chemistry, National Institute of Advanced Industrial Science and Technology, Ikeda, Osaka 563-8577, Japan

⁶Department of physical Science and Engineering, Nagoya Institute of Technology, Nagoya 466-8555, Japan

Cadmium tellurides (CdTe) attract much attention as a solar cell substance. Group V (P, As, Sb) doping is an effective manner to improve carrier concentration and mobility in CdTe, realizing in high conversion efficiency over 20 % [1]. Despite the accumulation of experimental and theoretical studies conducted in the past, the physical mechanism of group V doping has not yet been cleared. Group V doping introduces various types of defects such as interstitials, vacancies, and complexes, owing to the charge compensation for them. However, detailed information on the correlation between these defects and group V doping is not available, because the formation of defects by group V doping is influenced by chemical environments in material synthesis and crystal growth.

Native defects in CdTe have been identified by theoretical calculations. According to defect formation energies [2], the vacancy at the Cd site (V_{Cd}) and the As atom at the Cd site (As_{Cd}) are stable as isolated native defects. V_{Cd} - As_{Cd} defect complexes was also stable under the Cd-rich condition, but it became unstable under the Te-rich condition. It is never easy to optimize defect properties to obtain the CdTe based photovoltaic device with high conversion efficiency.

Positron annihilation lifetime spectroscopy (PALS) is a unique experimental technique that can observe charged vacancies such as V_{Cd} defects in CdTe. PALS studies have been performed for undoped and impurity-doped CdTe [3]. To our knowledge, PALS experiment has not yet reported for As-doped CdTe. It is worthwhile to investigate whether isolated V_{Cd} and/or As_{Cd} defects are changed in As doping. In the present study, gamma-ray induced positron annihilation lifetime spectroscopy (GiPALS) was performed using As-doped CdTe polycrystal, which was synthesized in sealed quartz ampoules from high-temperature melt of As-doped CdTe. The amount of the As impurity was determined to be $5 \times 10^{17} \text{ cm}^{-3}$. The positron annihilation lifetime was analyzed using the program LT9 [4].

Figure 1 shows the GiPALS spectrum of the As-doped CdTe polycrystal, which was measured at 300 K. The GiPALS spectrum is reproduced by the sum of exponential decay functions. The lifetimes were determined to be $123 \pm 37 \text{ ps}$ and $294 \pm 2 \text{ ps}$ by the curve

fit analysis. The intensity of the long lifetime component ($=4.4 \pm 1.6 \%$) is larger than that of the short lifetime component ($=95.6 \pm 1.6 \%$). Assuming the two-state trapping model of bulk and defect states, the positron annihilation lifetime at the bulk state was determined to be $277 \pm 14 \text{ ps}$, which was in good agreement with the bulk lifetime ($=278 \text{ ps}$) calculated by a first-principles calculation based on the density-functional theory. The lifetime of the long lifetime component was almost agreement with the calculated positron annihilation lifetime for the V_{Cd} defect ($=300 \text{ ps}$). The long lifetime component is assigned to the positron annihilation at the V_{Cd} defect. Further experimental and theoretical studies are required to investigate the effect of As-doping on defects in CdTe.

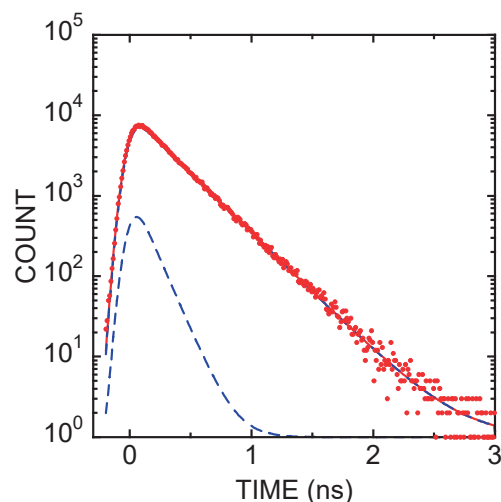


Fig. 1. GiPALS spectrum of As-doped CdTe polycrystals, measured at 300 K.

- [1] W. K. Metzger *et al.*, Nat. Energy **4** (2019) 837.
- [2] A. Nagaoka *et al.*, J. Am. Chem. Soc. **145** (2023) 9191.
- [3] M. R. Elsharkawy *et al.*, Appl. Phys. Lett. **108** (2016) 242102.
- [4] J. Kansy and D. Giebel, J. Phys.: Conf. Ser. **265** (2011) 012030.

Study on Evaluation of Material Defects by Positron Annihilation Method Using Ultrashort Pulsed Gamma Rays

Y. Takashima^{1,2}, N. Kishimoto² and Y. Taira³

¹Synchrotron Radiation Research Center, Nagoya University, Nagoya 464-8603, Japan

²School of Engineering, Nagoya University, Nagoya 464-8603, Japan

³UVSOR Synchrotron Facility, Institute for Molecular Science, Okazaki 444-8585, Japan

The positron annihilation method (PAS), which is effective in diagnosing defects in materials, is a method to estimate the type and amount of defects by irradiating positrons to the material and measuring the gamma rays generated by annihilation with electrons in the material. The positron annihilation method using gamma rays (GiPAS) generated by Compton scattering of a laser with the circulating electrons in a storage ring makes it possible to evaluate defects inside metallic materials with a thickness of a few millimeters.

The specimen to be evaluated in this study is interstitial-free (IF) steel, which is widely used as steel sheets for automobiles. From the viewpoint of safety as an automotive steel plate, it is extremely important to understand the formation and growth process of defects that occur during plastic deformation.

Gamma ray induced positron annihilation lifetime spectroscopy (GiPALS) on IF steels subjected to 10% nominal strain was performed at UVSOR in 2021 and reported the existence of single vacancy-type lattice defects [1,2]. In this study, positron lifetime measurements for IF steels subjected to 5%, 10%, and 15% tensile strain were performed to clarify the mechanism of void formation from single vacancy-type defects during plastic deformation and to gain insight into strain-induced changes of defects.

The experiment was conducted at BL1U of UVSOR. The gamma rays generated by the collision of a short-pulse laser with an electron beam orbiting in the storage ring were irradiated onto IF steels, and the two gamma rays generated by positron annihilation at 180 degrees were detected by four opposing pairs of BaF₂ detectors. The positron annihilation lifetime was measured by capturing the signals from the detectors into an oscilloscope. Figure 1 shows the photographs of the experimental setup.

In order to investigate the growth process of defects when IF steel is subjected to strain, GiPALS measurements were performed on IF steel with 0%, 5%, 10%, and 15% strain introduced. The IF steels were provided by Professor Adachi, Assistant Professor Chen and Mr. Sawai of the Graduate School of Engineering, Nagoya University. The obtained data were analyzed using LT9, an analysis software mainly used for positron lifetime analysis. As a preliminary analysis, fitting was performed on a function with a two-component lifetime.

Table 1 shows the preliminary results. It was observed

that the first component of lifetime τ_1 increased as the amount of strain increased. No significant change was observed in the second component of lifetime τ_2 . From these results, it can be inferred that the effect on the τ_1 component may increase as the amount of strain increases. Future work may include analysis of different lifetime components by fitting with three or more lifetime value components, removal of defects by annealing prior to tensile testing, and measurement of samples exposed to even greater strain.

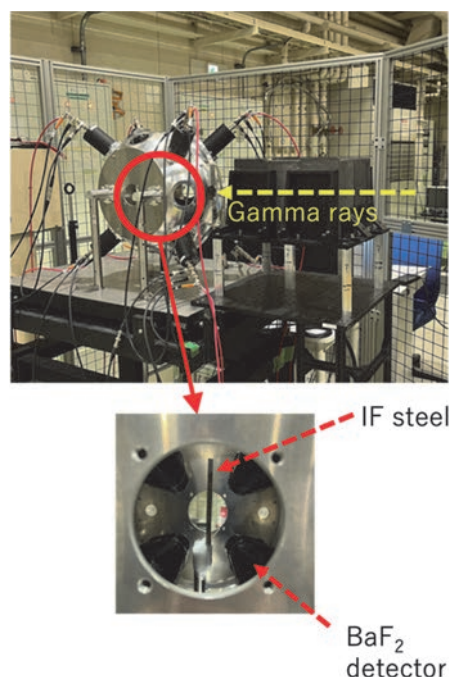


Fig. 1. Photographs of the experimental setup.

Table 1. Lifetime components τ_1 and τ_2 for IF steel with 0 %, 5 %, 10 %, and 15 % strain introduced.

	0%	5%	10%	15%
τ_1 (ps)	99.6 ±1.4	107 ±3.0	120 ±3.5	129 ±3.6
τ_2 (ps)	203 ±4.2	188 ±4.1	198 ±6.2	205 ±9.0

[1] R. Yamamoto, Master thesis of Graduate School of Engineering, Nagoya University (Feb. 2022).

[2] Y. Taira *et al.*, Rev. Sci. Instrum. **93** (2022) 113304.

Change in Positron Lifetime of Tungsten Caused by Electrolytic Hydrogen Charging

A. Yabuuchi¹, T. Hirade², R. Awaji³, M. Fujinami³,
N. Oshima⁴, K. Saito⁵, K. Takai⁵ and Y. Taira⁶

¹*Institute for Integrated Radiation and Nuclear Science, Kyoto University, Kumatori 590-0494, Japan*

²*Nuclear Science and Engineering Center, Japan Atomic Energy Agency, Tokai 319-1195, Japan*

³*Department of Applied Chemistry and Biotechnology, Chiba University, Chiba 263-8522, Japan*

⁴*National Institute of Advanced Industrial Science and Technology, Tsukuba 305-8568, Japan*

⁵*Department of Engineering and Applied Sciences, Sophia University, Tokyo 102-8554, Japan*

⁶*UVSOR Synchrotron Facility, Institute for Molecular Science, Okazaki 444-8585, Japan*

Tungsten is a candidate material for plasma-facing walls in fusion reactors. The presence of vacancies in tungsten will trap tritium, fuel for fusion reactors. Incorporating tritium into tungsten is problematic from the standpoints of radioactivity management and the economics of power reactors. A study based on theoretical calculations by Ohsawa *et al.* claims that hydrogen induces the formation of vacancies in tungsten [1]. This study investigated hydrogen-induced vacancies in tungsten using gamma-ray-induced positron annihilation lifetime spectroscopy (GiPALS) [2].

Eight 10 mm square samples were cut from a 0.8-mm-thick tungsten plate with a purity of 99.999%. They were then annealed in a vacuum at around 2200 °C for 15 min using an electron bombardment heating technique. The annealed samples were preliminarily measured by conventional positron annihilation lifetime spectroscopy using a ²²Na positron source sealed with Kapton foils. Four of the eight samples were immersed in 0.1 mol/L NaOH solution containing 5 g/L NH₄SCN as cathode, and electrolytic hydrogen charging was performed for 10 days with a current density of 5 mA/cm². The uncharged and hydrogen-charged samples were measured using the GiPALS technique to obtain positron annihilation lifetime spectra. Four sheets of samples were stacked in each measurement to acquire a sufficient counting rate.

Figures 1 and 2 show positron annihilation lifetime spectra of uncharged and hydrogen-charged samples. Positron lifetime components other than the defect-free bulk component were observed in both samples. Therefore, both spectra were analyzed by fitting with two positron lifetime components. Comparing the preliminary analysis results shown in Figs. 1 and 2, the positron lifetime of the second component (the longer lifetime component) becomes shorter by hydrogen charging while its intensity increases. This change may result from mixing the second component with positron lifetime components of vacancies or vacancy-hydrogen complexes with positron lifetimes of less than 200 ps. However, the origin of the longer positron lifetime component observed in the uncharged sample must be elucidated to show the change caused by the hydrogen charging clearly. The GiPALS measurement found for

the first time the longer positron lifetime component (342 ps ± 39 ps) observed in the uncharged sample. This longer positron lifetime is close to the positron lifetime of Kapton (~380 ps) and could not be detected by a conventional ²²Na source method because it is indistinguishable from the source component.

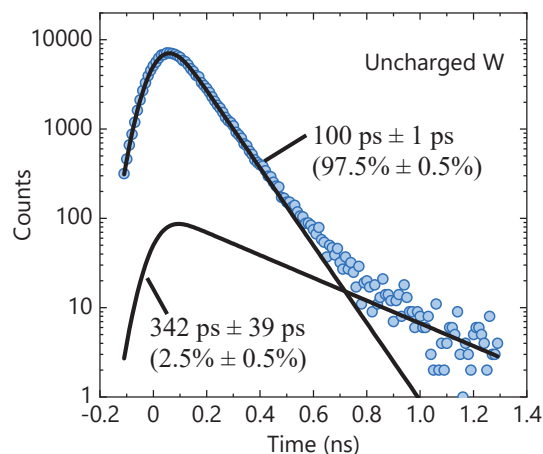


Fig. 1. Positron annihilation lifetime spectrum of the uncharged sample.

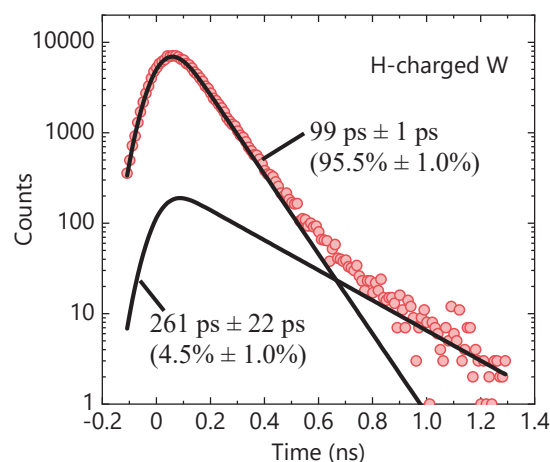


Fig. 2. Positron annihilation lifetime spectrum of the H-charged sample.

[1] K. Ohsawa *et al.*, J. Nucl. Mater. **458** (2015) 187.

[2] Y. Taira *et al.*, Rev. Sci. Instrum. **93** (2022) 113304.

Attempts for Intermolecular Phonon Measurement of High Mobility Organic Semiconductors by Terahertz Absorption Spectroscopy

K. Yamauchi¹, Y. Baba¹ and Y. Nakayama^{1,2}

¹Department of Pure and Applied Chemistry, Tokyo University of Science, Noda 278-8510, Japan

²Institute for Molecular Science (IMS), Okazaki 444-8585, Japan

Intramolecular and intermolecular vibrations are factors that reduce charge carrier mobility in organic semiconductors, and thus transport characteristics in the organic electronic devices are strongly affected by molecular vibrations. Therefore, understanding and controlling of the molecular vibrations are essential for highly efficient organic semiconductor devices. Our group previously elucidated intramolecular vibrational properties on the single crystal pentacene, which is known as a p-type organic semiconductor exhibiting considerable charge carrier mobility, in far- to mid-infrared range at BL6B, UVSOR [1-4]. In this study, we tried to identify intermolecular vibrations, which are predicted to appear in the THz region [5-7], by performing infrared absorption spectroscopy measurements in a lower wavenumber range on the single crystals of representative organic semiconductors dinaphthothienothiophene (DNTT), pentacene (Pn), and rubrene (Rub).

Single crystals of DNTT, Pn, and Rub were prepared by physical vapor transport and were fixed onto diamond substrates. Infrared absorption spectroscopy measurements were performed using a Si bolometer (General Purpose 4.2 K Bolometer, IRLabs, Inc.), a wire grid beam splitter capable of detecting in the 0 - 120 cm^{-1} measurement range, and in a transmission configuration in a high vacuum (10^{-5} Pa) chamber. Measurements were also performed on a diamond substrate without the molecular crystal as a reference sample. For the Fourier transform, the Blackman function was used to correct the integration range.

Figure 1 shows the IR signal intensity through each sample (diamond, DNTT/diamond, Pn/diamond, and Rub/diamond). The intensity dropped sharply below 20 cm^{-1} and above 100 cm^{-1} , indicating that the substantial region in these measurements was 20 – 100 cm^{-1} . From the data shown in Fig. 1, the absorbance of each molecular crystal sample was determined using the Lambert-Beer formula as shown in Fig. 2, where the light intensity transmitted through the diamond substrate without and with the molecular crystals was assigned to I_0 and I , respectively. No peaks were seen in the measured wavenumber region for any of the molecular samples, and thus intermolecular vibrations could not be identified. This may be ascribed to the insufficient transmittance of the THz photon through

the organic semiconductor single crystal samples relative to that through the diamond substrate. Another possible cause is the low intensity of the incident THz light itself.

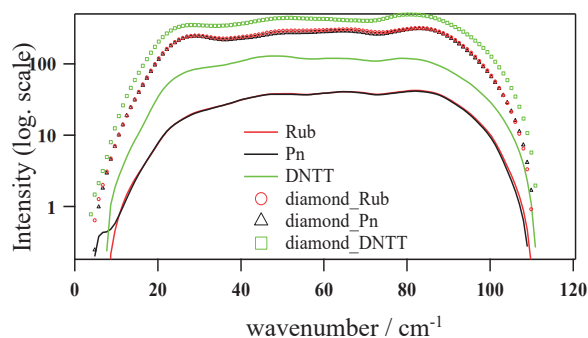


Fig. 1. THz transmission intensity of each sample.

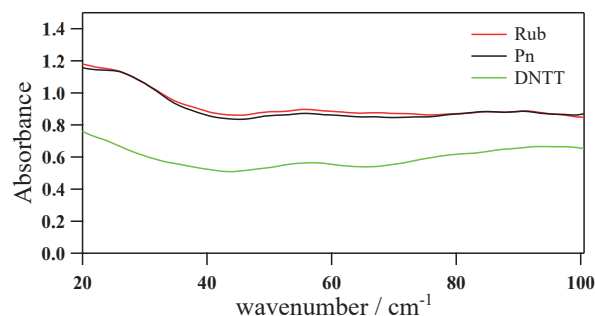


Fig. 2. THz absorbance of each molecular single crystal sample obtained using the Lambert-Beer formula for the transmission signals shown in Fig. 1.

- [1] Y. Nakayama *et al.*, Vib. Spectrosc. **132** (2024) 103601.
- [2] Y. Nakayama *et al.*, UVSOR Activity Report **50** (2023) 104.
- [3] J. Miyamoto *et al.*, UVSOR Activity Report **49** (2021) 91.
- [4] Y. Nakayama, J. Miyamoto, UVSOR Activity Report **48** (2021) 83.
- [5] A. Girlando *et al.*, Phys. Rev. B: Condens. Matter **82** (2010) 035208.
- [6] A. Girlando *et al.*, J. Chem. Phys. **135** (2011) 084701.
- [7] G. Schweicher *et al.*, Adv. Mater. **31** (2019) 1902407.

BL2A

Local Structure of Catalytically Active Mo-Carbide Species on H-MFI Zeolites for Methane Aromatization at High Pressure

K. Kuramochi¹, A. Kosuge², Y. Sonobe¹, Y. Uchimura¹ and H. Aritani²

¹Advanced Science Research Laboratory, Saitama Institute of Technology, Fukaya 369-0293, Japan

²Graduate School of Engineering, Saitama Institute of Technology, Fukaya 369-0293, Japan

As a typical catalyst for GTL (Gas-To-Liquid), molybdenum- modified H-MFI zeolite (Mo/H-MFI) shows high MTB (Methane To Benzene; $6\text{CH}_4 \rightarrow \text{C}_6\text{H}_6 + 9\text{H}_2$) reactivity for methane dehydroaromatization at 973–1073 K. Although the MTB process using a highly active catalyst is an innovative reaction one for direct conversion from natural gas into petroleum resources, definite deactivation of the catalyst during the reaction is a fatal drawback. And thus, clarification of the deactivation factor over the Mo/H-MFI catalysts is one of the important points for study. A cause of the deactivation strongly depends on both coke deposition onto strong acid sites over H-MFI, as well as structural deactivation of carbonized Mo species.[1] One of the most important subjects for catalytically high and durable activity is the elucidation of active Mo-carbide (MoC_x) sites. Recently, it has been found that the reaction at high pressure (up to 0.2 MPa) achieved both high activation and suppression of deactivation. As a result, a revolutionary improvement in the MTB reaction can be expected. In this study, Mo L_{III} -edge XANES is applied to characterize the active MoC_x species on Mo/H-MFI after the MTB reaction under 0.1–0.2 MPa.

Mo(5wt%)/H-MFI ($\text{Si}/\text{Al}_2=23\text{--}50$) catalysts were prepared as described in the previous paper.[1] Each catalyst (0.5 g) has been pre-reduced with $\text{CO}(2\%)\text{--}\text{He}$ at 1023 K for 1 h. The reactivity of methane dehydroaromatization was evaluated by the reaction with $\text{CH}_4(20\%)\text{--}\text{H}_2(2\%)\text{--}\text{He}$ at 1023 K under 0.10–0.20 MPa. Mo L_{III} -edge XANES spectra were obtained in BL2A of UVSOR-III in a total-electron yield mode using InSb double-crystal monochromator. A REX-2000 (Rigaku) software was employed for normalization of each XANES spectrum.

As a result of the catalytic MTB activity over Mo/H-MFI ($\text{Si}/\text{Al}_2=23$ and 50), the reactivity increased with increasing the pressure (up to 0.20 MPa) of the MTB reaction over both catalysts. A remarkable effect of suppression on deactivation was shown in $\text{Si}/\text{Al}_2=50$ reacted under high pressure. Fig. 1 shows the Mo L_{III} -edge XANES spectra of Mo/H-MFI catalysts after MTB reaction at 1023 K under 0.10–0.20 Pa. In case of Mo/H-MFI ($\text{Si}/\text{Al}_2=23$) catalysts shown in the top of Fig. 1, XANES spectra of reference compounds ($\alpha\text{-Mo}_2\text{C}$, $\beta\text{-Mo}_2\text{C}$, and Mo metal) are also shown. After the reaction under 0.10 MPa (atmospheric pressure), it is likely that $\alpha\text{-Mo}_2\text{C}$ (cubic) species are formed after MTB reaction. In contrast, $\beta\text{-Mo}_2\text{C}$ (orthorhombic) like species are possibly formed after

the reaction under 0.15–0.20 Pa. Since the $\beta\text{-Mo}_2\text{C}$ phase can be formed by the deep carburization of the $\alpha\text{-Mo}_2\text{C}$, [2] formation of $\beta\text{-Mo}_2\text{C}$ species is suggested to be one of the factors for the high activity imparted by the reaction under high pressure. In case of Mo/H-MFI ($\text{Si}/\text{Al}_2=50$) catalysts shown in the bottom of Fig. 1, α - and β - phases are possibly formed after the reaction under 0.10 MPa. Under high pressure (0.15–0.20 MPa), it is concluded the $\beta\text{-Mo}_2\text{C}$ species are formed after the reaction. From the XANES results, it is concluded that reductively carbonized Mo species to $\beta\text{-Mo}_2\text{C}$ is one of a key role in high MTB reactivity. For deep reduction, H_2 co-feed with CH_4 needs for high MTB reactivity.

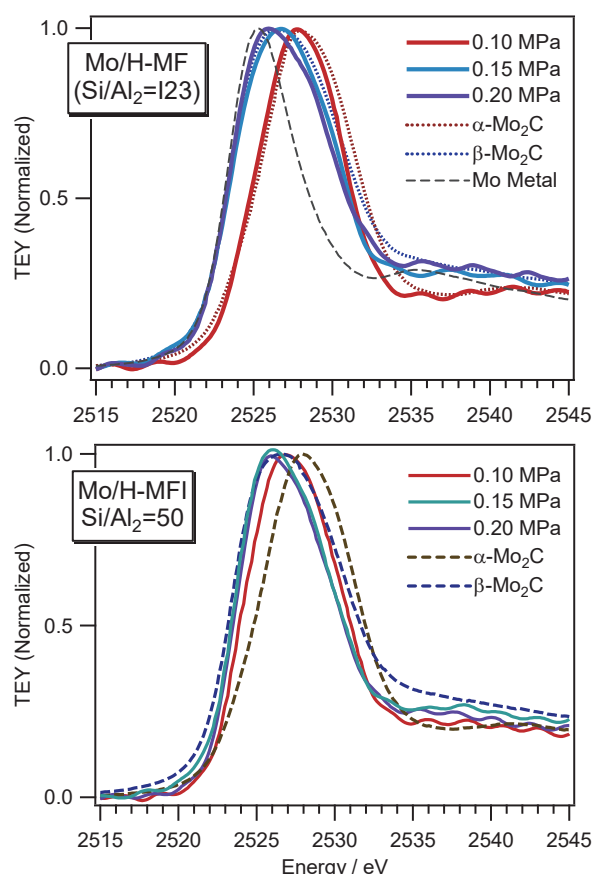


Fig. 1. Mo L_{III} -edge XANES spectra of Mo/H-MFI ($\text{SiO}_2/\text{Al}_2\text{O}_3=23$ [top] and 50 [bottom]) catalysts after MTB reaction at 1023 K under 0.10–0.20 Pa.

[1] H. Aritani *et al.*, J. Environ. Sci. **21** (2009) 736.

[2] K. Wu *et al.*, Ind. Eng. Chem. Res. **58** (2019) 20270.

X-ray Absorption Near Edge Structure Analysis of Deintercalation of Ni-Al Layered Double Hydroxide Dense Bodies

H. Murata, K. Yone and A. Nakahira

Department of Materials Science, Osaka Metropolitan University, Sakai 599-8531, Japan

Layered double hydroxides (LDH) are crystalline hydroxides which contain divalent and higher valence cations in the hydroxide layers. The higher valence cations cause intercalation of counter anions between the hydroxide layers as charge compensation. These intercalated anions lead to variety of applications such as ion-exchange hosts, ion-conductor and electrochromic device. [1-3] LDHs are available in various forms, such as nano-particles, powders, and thin films. Since LDHs decompose at high temperature, dense bodies cannot be obtained by usual sintering.

Hydrothermal hot-pressing method (HHP) is one of the low-temperature sintering techniques. In this method, a green body containing a small amount of aqueous solution is compressed and heated. The aqueous solution is then released from the green body with the dissolution and re-precipitation of the samples, which connects particles. This method produce dense bodies of thermally unstable materials such as zeolite. [4]

In this study, dense bodies of Ni-Al LDH were prepared by HHP and their deintercalation behaviors were investigated using X-ray absorption near edge structure (XANES).

Ni-Al LDH dense bodies were prepared by the hydrothermal hot-pressing method. A starting material was Ni-Al LDH powder synthesized from aqueous solutions by the co-precipitation method. This starting material was mixed with 5 mol/L NaOH aqueous solution, which is 20 wt% of the starting material. The samples were compressed at 40 MPa and 150 °C for 2 h. The deintercalation of the samples were performed by heat treatment at 300 °C for 2 h.

Obtained dense bodies were characterized by Archimedes method, X-ray diffraction (XRD), Fourier transform infrared spectroscopy (FT-IR) and X-ray absorption near edge structure (XANES). Ni-L₃ and Al-K XANES were collected by the total electron yield method with sample current and the partial fluorescent method using a silicon drift detector. Samples were mounted on metal plates using carbon tape.

The HHP process produced translucent dense bodies of Ni-Al LDH. XRD patterns of the samples shows a strong preferred orientation along 00l reflections, which means that layered structure is well aligned in the dense bodies. Comparing with density by Archimedes method and crystalline density calculated from lattice parameters, the obtained Ni-Al LDH dense bodies

achieved full density (over 95 %). The shape of the dense bodies was maintained after heating at 300°C. The XRD patterns of the samples after heat treatment were assigned to low crystallinity rocksalt-type NiO.

Figure 1 shows Ni-L₃ and Al-K XANES spectra of the samples. Ni in the samples were maintained Ni²⁺ at octahedral site after thermally deintercalation. On the other hand, the Al-K XANES of the thermally deintercalated samples have additional shoulder peak at lower energy than the white line. This is attributed d to Al³⁺ at tetrahedral site. Therefore, Al³⁺ plays an important role in deintercalation of LDH.

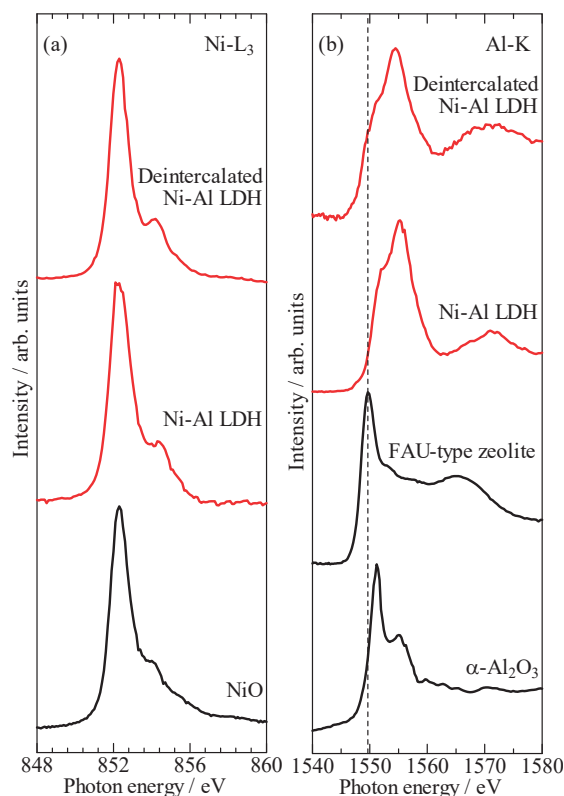


Fig. 1. (a) Ni-L₃ and (b) Al-K XANES of Ni-Al LDH dense bodies.

- [1] G. Mishra *et al.*, Appl. Clay Sci. **153** (2018) 172.
- [2] K. Tadanaga *et al.*, Adv. Mater. **22** (2010) 4401.
- [3] P. Koilraj *et al.*, ACS Appl. Nano Mater. **3** (2020) 6552.
- [4] A. Nakahira *et al.*, J. Am. Ceram. Soc. **90** (2007) 2322.

BL2A

Local Structure Investigations of Zincate Spinels

S. Yoshioka¹, E. Kobayashi² and K. Okudaira³

¹*Department of Applied Quantum Physics and Nuclear Engineering, Kyushu University, Fukuoka 819-0395, Japan*

²*Kyushu Synchrotron Light Research Center, Saga 841-0005, Japan*

³*Graduate school of Advanced Integration Science, Chiba University, Chiba 263-8522, Japan*

Spinel oxides with the general formula AB_2O_4 can be formed with various kinds of divalent A and trivalent B cations. Owing to their unique mechanical, electronic, and magnetic properties, the spinel oxides have gained considerable attention not only from the fundamental research fields but also from the industrial application point of view. Some spinel compounds such as $MgAl_2O_4$ accommodate large degrees of cationic disorder. $MgAl_2O_4$ spinel shows relative higher inversion degree $i = 0.15$ to 0.35 , whereas zincate spinels such as $ZnAl_2O_4$ generally show small amount of cationic disorder degrees. However, their local structures have not been fully understood. X-ray absorption spectroscopy (XAS) is a powerful structure characterization method that uses an X-ray probe to reveal local atomic coordination and electronic structures. In this study, we focus on the local structures around Zn in zincate spinels, $ZnAl_2O_4$ and $ZnFe_2O_4$.

Polycrystalline sample of $ZnAl_2O_4$ and the single crystal of $ZnFe_2O_4$ sample were used in this study. Zn $L_{2,3}$ -edge XANES measurements were performed on BL2A beamline at UVSOR Synchrotron Facility, Okazaki, Japan, using the partial fluorescence yield method. A $KTiOPO_4$ double-crystal monochromator gives Zn $L_{2,3}$ -absorption edges in the energy regions 1010–1070 eV. The measurements of Zn $L_{2,3}$ -edge XANES spectra were carried out in vacuum at a pressure and temperature of 1×10^{-4} Pa and 20°C , respectively. Fluorescence X-rays of Zn $L\alpha$ were collected utilizing an energy-dispersible silicon drift detector.

The Zn $L_{2,3}$ -edge XANES spectra for $ZnAl_2O_4$ and $ZnFe_2O_4$ are shown in Fig. 1. The spectrum of powder ZnO was also shown as reference spectra. The intensity of each spectrum was normalized to a value of 1 at the photon energy of 1065 eV after the removal of the background intensity. The spectra of both spinels show clear difference from that of ZnO. The Zn $L_{2,3}$ -edge XANES of $ZnAl_2O_4$ have peaks A – D as well as that of $ZnFe_2O_4$, however, their shapes and relative intensity were clearly different. Detailed analyses on the local environment of Zn and in the $ZnAl_2O_4$ and $ZnFe_2O_4$ are in progress by combined use of the XANES and the first principles band structure calculations.

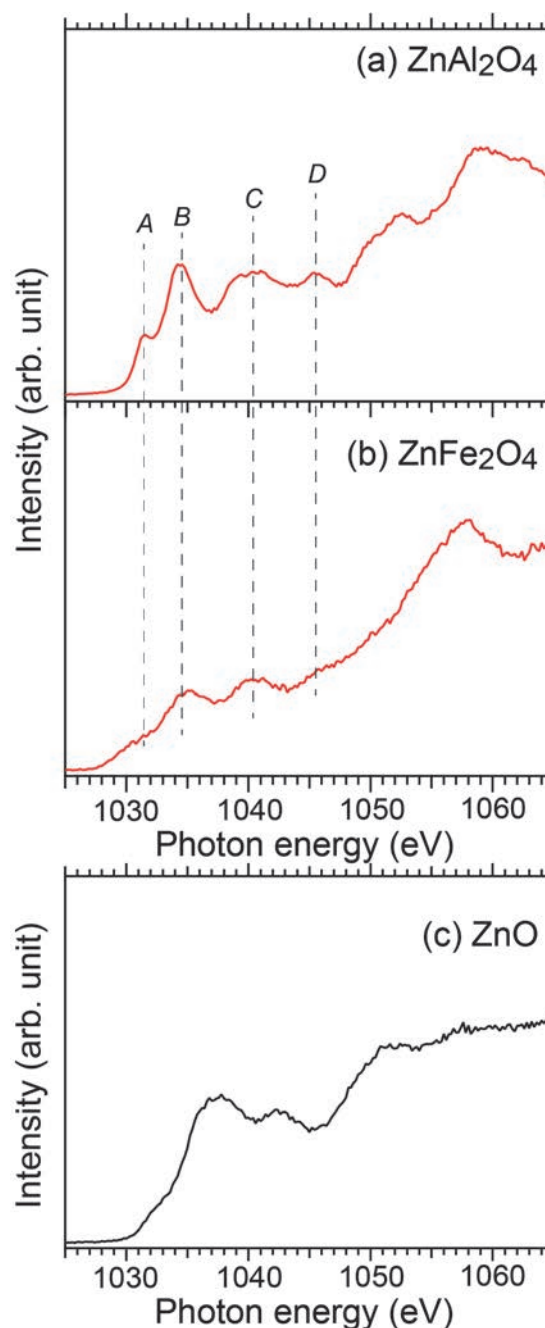


Fig. 1. Zn $L_{2,3}$ -edge XANES spectra of $ZnAl_2O_4$ (a) and $ZnFe_2O_4$ (b). Spectrum of ZnO (c) was shown as a reference.

Direct Observation of 4-Layer Structure in the Chiral SmC Variant Phase Delicate Balance of Ferroelectricity and Antiferroelectricity by Resonant Soft X-ray Scattering (RSoXS) at UVSOR

Y. Takanishi¹, F. Araoka² and H. Iwayama^{3,4}

¹Department of Physics, Kyoto Prefectural University of Medicine,
1-5, Shimogamohangi-cho, Sakyo, Kyoto 606-0823, Japan

²RIKEN Center for Emergent Matter Science, Hirosawa 2-1, Wako, Saitama 351-0198, Japan

³UVSOR Synchrotron Facility, Institute for Molecular Science, Okazaki 444-8585, Japan

⁴School of Physical Sciences, The Graduate University for Advanced Studies (SOKENDAI),
Okazaki 444-8585, Japan

The ferroelectricity and antiferroelectricity have been found in the tilted chiral smectic phases, called SmC* and SmC_A*, respectively. By competition of SmC* and SmC_A*, several phases with narrow temperature range were found, called subphases. Subphases have been defined as the relative ratio of anticlinic and synclinic ordering, q_T . Some subphases have been experimentally observed, and the existence of further subphases has been theoretically predicted based on the long-range interlayer interaction and the frustration of clinicity. The structures of subphases become decisive using resonant X-ray scattering (RXS). In RXS, using X-ray whose energy is coincident with a certain atom absorption edge, the structure factor becomes a tensor instead of the scalar in conventional X-ray diffraction. Using this technique, one of authors (YT) discovered at least four new subphases with 6-, 7-, 8- and 10-layer periodicities[2].

Unexpectedly, it was found that the temperature change between SmC* and SmC_A* is continuous in some chiral binary system. In this system, clear phase transition between subphases seems not to be seen[2], but the system does not have a specific atom whose absorption edge energy is corresponding to that of hard x-ray. Hence, resonant soft x-ray scattering (RSoXS) has been applied to this study, and we directly observed the structure of continuous change between SmC* and SmC_A* using wide angle RSoXS.

The experiment was performed at BL3U of UVSOR. Used sample is a mixture of MC881 and MC452, as shown in Fig. 1. Figure 1(c) shows the phase diagram around the critical mixing ratios. In this study, samples used were filled in the grid mesh for electron transmission microscopy. The scattering was detected by CCD (ANDOR DO940P-BN). Incident X-ray beam was tuned between 270–300 eV, and carbon K-edge energy was 284.5 eV in the mixture.

Figure 2(a) shows a typical RSoXS intensity profile of the mixture of 55.7wt% MC452 at 24°C. Splitting strong peak at $Q \sim 0.5 \text{ nm}^{-1}$ corresponds to the 4-layer periodicity. Peak splitting is caused by the macroscopic helical structure, whose pitch is corresponding to ca. $1.1 \mu\text{m}$. 4-layer periodicity is kept until 80 °C, which is almost consistent with region assigned as $q_T = 1/2$ of ref.

[3] as shown in Fig.1 (c). This result made the structure of the secondary phase with a wide temperature range conclusive. Above 80 °C, resonant peak is gradually shifted corresponding to the longer periodicity, which indicated incommensurate structure from 4-layer periodic one. The concentration dependence of the long-range structure will be next subject.

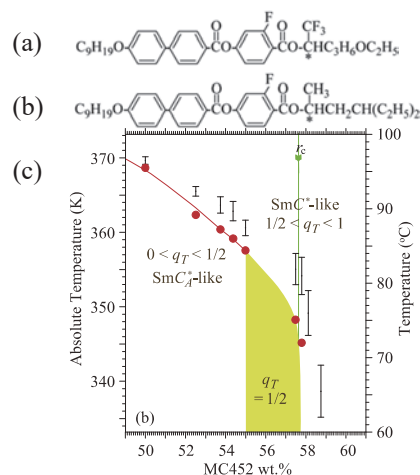


Fig. 1. Chemical structures of (a)MC452 and (b) MC881, and the phase diagram(c). (c) is referred from [3]

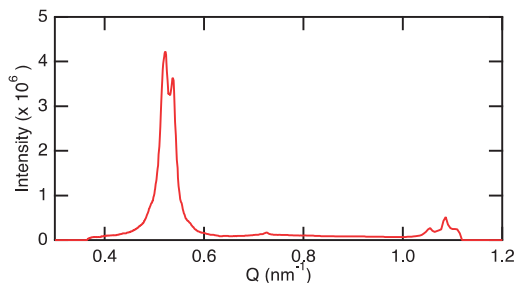


Fig. 2. A RSoXS intensity profile of the mixture of 55.7wt% MC452 at 24°C.

[1] Y. Takanishi *et al.*, Phys. Rev. E **87** (2013) 050503(R).

[2] Z. Feng *et al.*, Phys. Rev. E **96** (2017) 012701.

[3] Z. Feng *et al.*, Phys. Rev. E **102** (2020) 012703.

BL3B, 7B

Evaluation of Measurements of Fluorescence Lifetimes in Multi Bunch Mode

Y. Tajima, Y. Hayashi, K. Shintate, R. Abe, T. Naito, S. Sakano and H. Y. Yoshida

Department of Physics, Yamagata University, Yamagata 990-8560, Japan

Measurement of fluorescence lifetimes requires an adequate time interval before the next excitation, so we use beam time in single bunch mode with a bunch interval of 177 ns. Since most plastic scintillators and wavelength shifters used in high energy physics have short lifetimes (< 3 ns), a measurement in multi bunch mode with a bunch interval of 11 ns seems to be possible.

The purpose of this experiment was to measure fluorescence lifetimes in multi bunch mode using samples that have already been measured, and to evaluate how well multi bunch mode measurements work for samples with short fluorescence lifetimes.

Without changing the optical system, two different methods of data acquisition were attempted: one measurement using the same circuit and MCA as before and the other measurement of direct analog signal collection using a digitizer. The digitizer was BBTX-112 (Bee Beans Technology) with sampling rate was 5 Gsps (200 ps interval). The specification is shown in Fig.1 and Table 1.

Figure 2 displays the typical recorded data using the digitizer. The red line is the signal from photo-multiplier tube and the green line is the RF signal (90.1MHz / 16 = 5.63MHz) from the accelerator.

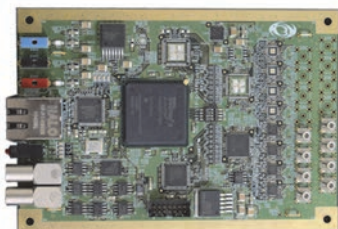


Fig.1. Bee Beans Technology BBTX-112.

Table 1. Specification of BBTX-112.

Analog Input	8ch (SMB connector)
Sampling Rate (Gsps)	1 / 2 / 3.3 / 5
Time Range (ns)	1000 / 500 / 333 / 200
Output	Ethernet (RJ-45) 1Gbps
Power	± 3.3 V 1.6/0.5A

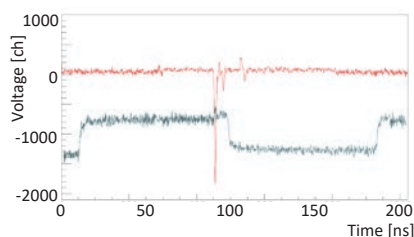


Fig. 2. The recorded data using the digitizer. PMT signal (Red) and RF Signal (Green).

The measured samples were Y-11 and YS6 (made by Kuraray [1]), used as the read-out for gamma-ray sampling calorimeters in high energy physics. Both samples have only one component of fluorescence lifetime, 6.6 ns (Y-11) and 1.3 ns (YS6) [2].

Figure 3 shows the time distribution between the PMT signal and the RF signal, with blue lines representing multi bunch mode, and green areas representing single bunch mode.

In multi bunch mode, the incoming beam bunches were 10 bunches. But the bunches appear to be 14 in Fig.3. These are likely to be leaked from the 10 bunches to the adjacent bunches.

The results of the fluorescence lifetimes are shown in Table 2. The measurements of fluorescence lifetimes in multi bunch mode are found to be as feasible as in single bunch when the fluorescence lifetime of a sample has one component. In the case of samples with multiple components, it is only possible to determine whether there are short-lived components.

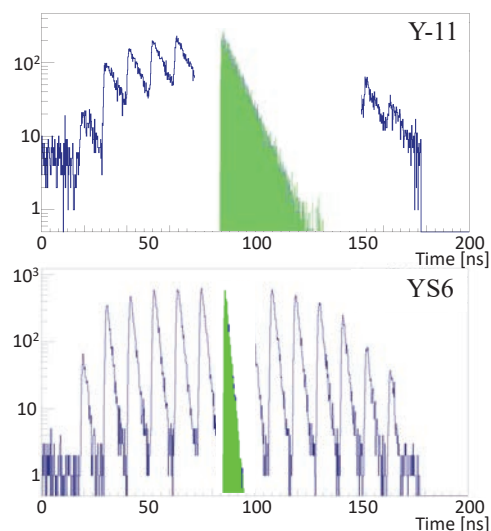


Fig. 3. The time distribution of the single photon and RF signal of Y-11 and YS6 (Blue: multi bunch mode, Green: single bunch mode).

Table 2. The results of fluorescence lifetimes.

	Single bunch	Multi bunch
Y-11	6.65 ns	6.65 ns
YS6	1.40 ns	1.34 ns

[1] Kuraray, "Plastic Scintillating Fibers, Plastic Imaging Fibers", <http://kuraraypsf.jp/>.

[2] K. Shintate *et al.*, UVSOR Activity Report **49** (2022) 66.

Effect of Ce Co-Doping to Cr:GGG as a Scintillator for Dose-Rate Monitoring System

D. Matsukura^{1,2}, S. Kurosawa^{2,3,4}, C. Fujiwara^{1,2} and A. Yamaji^{2,3}

¹School of Engineering, Tohoku University, Sendai 980-8579, Japan

²Institute for Materials Research, Tohoku University, Sendai 980-8577, Japan

³New Industry Creation Hatchery Center, Tohoku University, Sendai 980-8579, Japan

⁴Institute of Laser Engineering, Osaka University, Suita 565-0871, Japan

For the decommissioning of the Fukushima Daiichi nuclear power plant, real-time radiation dose rate monitoring system is required [1], and such system is plan to consist of scintillator, 100-m long optical fiber and CCD spectrometer. Due to high dose rate condition, noise such as Cherenkov light or scintillation light are expected to be observed for the optical fiber [2, 3]. These noises are dominant in the wavelength range below 650 nm. Therefore, the emission wavelength of the scintillator should be 650-1000 nm. Also, high light output is required for the scintillator.

In this study, we focused on Ce/Cr co-doped $\text{Gd}_3\text{Ga}_5\text{O}_{12}$ (Ce/Cr:GGG) as a scintillator. Cr-doped $\text{Gd}_3\text{Ga}_5\text{O}_{12}$ (Cr:GGG) is known to have emission wavelength of 730 nm originating from d-d transition of Cr^{3+} . In addition, by co-doping Ce, the increase of light output of Cr:GGG is expected. Ce-doped $\text{Gd}_3\text{Ga}_5\text{O}_{12}$ (Ce:GGG) has Ce^{3+} absorption bands (approximately 350, 450 nm), while no emission light is observed originating from Ce^{3+} [4]. We expected increase of the light output by Ce^{3+} absorption bands and energy transfer from Ce^{3+} to Cr^{3+} . Since similar energy transfer for the garnet host were reported [5-7], similar energy transfer in Ce/Cr:GGG was expected and we investigated such transfer.

Ce/Cr:GGG crystals were grown by the micro-pulling down method in following compositions: $(\text{Gd}_{1-x}\text{Ce}_x)_3(\text{Ga}_{0.995}\text{Cr}_{0.005})_5\text{O}_{12}$, where $x=0, 0.01, 0.1$ and 1%), and hereafter we describe as xCe0.5%Cr:GGG. Grown crystal were sliced into 1-mm thickness and evaluated their photoluminescence (PL) at 10 K (excitation wavelength: 100-700 nm) using BL3B.

Figure 1(s) show Ce/Cr:GGG grown crystals, and photoluminescence excitation and photoluminescence (PLE-PL) spectra for these samples were displayed in Fig. 2. In the PLE spectra, the emission intensity around the excitation wavelength of approximately 350 nm slightly increased with increasing Ce concentration. However, the emission intensity of 1 %Ce0.5%Cr:GGG decreased at excitation wavelengths around 400-450 nm.

This result indicated some excited energy originating from Ce^{3+} absorption become nonradiative transitions.

Thus, in the GGG system, Ce-co-doping does not support increasing light output in this composition.

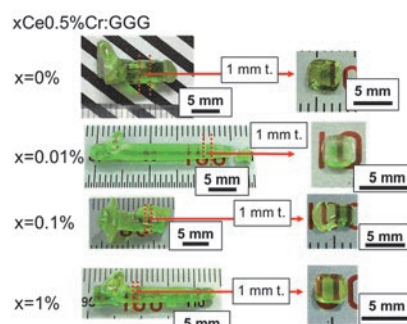


Fig. 1. Ce/Cr:GGG crystals.

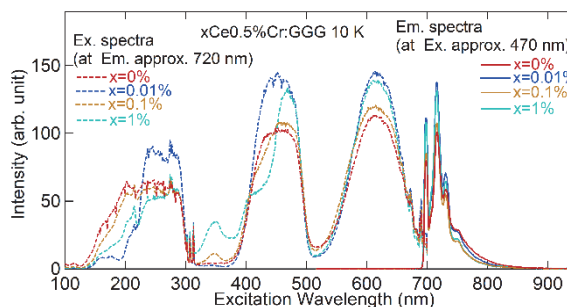


Fig. 2. PLE-PL spectra, dashed line: excitation spectra, solid line: emission spectra.

- [1] Fukushima Administrative Department Sector of Fukushima Research and Development, JAEA, TOPICS Fukushima No.70 (2015).
- [2] Fosco Connect, Optical Fiber Loss and Attenuation. (2010).
- [3] H. Liu *et al.*, Rev. Sci. Instrum, **89** (2018) 083302.
- [4] V. Baranov *et al.*, Phys. Part. Nucl. Lett. **17** (2020) 878.
- [5] X. Yi *et al.*, Ceram. Int. **40** (2014) 7043.
- [6] Y. Tang *et al.*, J. Am. Ceram. Soc. **100** (2017) 2590.
- [7] G. Merkininkaite *et al.*, Ceram. Int. **49** (2023) 16796.

BL3B

Optical Properties of Li-Containing $\text{Cs}_3\text{Cu}_2\text{I}_5$ for Neutron Monitor

Y. Urano^{1,2}, S. Kurosawa^{2,3,4} and A. Yamaji^{2,3}¹Graduate School of Engineering, Tohoku University, Sendai 980-0845, Japan²Institute for Materials Research (IMR), Tohoku University, Sendai 984-8577, Japan³New Industry Creation Hatchery Center (NICHe), Tohoku University, Sendai 980-8579, Japan⁴Institute of Laser Engineering, Osaka University, Suita, Osaka 565-0871, Japan

In order to decommission the Fukushima Daiichi Nuclear Power Plant quickly and safely and reliably, radiation monitoring is required to accurately evaluate the debris with radio-isotopes inside the reactor. We have proposed a dose monitor consisting of a scintillator, optical fiber with a length of 50-100m and CCD spectrometer, and scintillation photons are read under lower dose conditions with the CCD [1-2]. The presence of neutrons as well as gamma rays in the reactor has been suggested [3], and detailed mapping of neutrons is also required. In addition, when the scintillator emission wavelength is less than 500 nm, such emission bands are overlapped with noise bands under such a high dose rate due to scintillation or Cherenkov photons generated in the optical fiber itself. Therefore, scintillator materials with high neutron sensitivity and long emission wavelength are required.

$\text{Cs}_3\text{Cu}_2\text{I}_5$ (CCI) has a high light output of 41,500 photons/MeV and an emission wavelength of approximately 440 nm [4, 5]. However, CCI has low neutron sensitivity and the emission wavelength is also shorter than the target value.

We have developed Li-containing $\text{Cs}_3\text{Cu}_2\text{I}_5$ (CCIL) crystals for the neutron detector, because ^6Li has a large neutron capture cross-section. In this study, we grew the CCIL crystal, and its luminescence properties were investigated.

The CCIL crystal specimen was synthesized by the vertical Bridgman growth method in our laboratory using CuI, CsI and LiI raw materials. The neutron detection capability of CCIL has been evaluated in our laboratory. In order to reveal the emission mechanism and compare to such mechanism with CCI, we measured the temperature dependence of photoluminescence excitation and emission spectra from 10 K to 300 K at UVSOR BL3B beam line.

Figure 1 shows the photoluminescence excitation and emission spectra of Li-containing $\text{Cs}_3\text{Cu}_2\text{I}_5$. CCIL showed broad luminescence with a peak at approximately 450 nm at an excitation wavelength of 331 nm at 300 K, which was slightly longer than that of CCI (440 nm).

Figure 2 shows the temperature dependence of emission intensity for CCIL excited with 298 to 331-

nm photons. As the temperature increased, the emission intensities decreased. In the future, we compare the temperature dependence between CCI and CCIL.

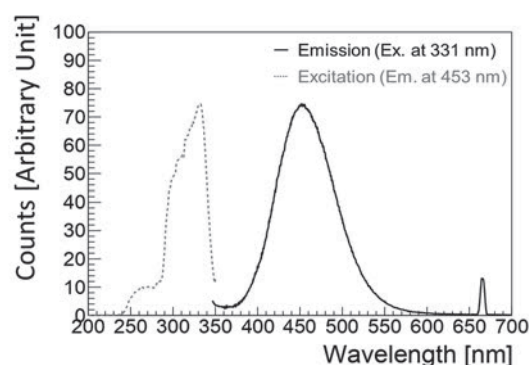


Fig. 1. Photoluminescence excitation and emission spectrum of Li-containing $\text{Cs}_3\text{Cu}_2\text{I}_5$ scintillator at 300 K.

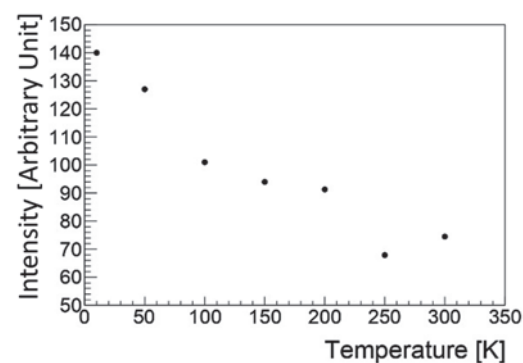


Fig. 2. Temperature dependence of emission intensity of Li-containing $\text{Cs}_3\text{Cu}_2\text{I}_5$ scintillator.

[1] <https://fukushima.jaea.go.jp/en/pamphlet/topics/pdf/topics-fukushima070e.pdf>.

[2] C. Fujiwara, S. Kurosawa and A. Yamaji, UVSOR Activity Report **50** (2023) 78.

[3] https://www.tepco.co.jp/decommission/information/committee/roadmap_progress/pdf/2022/d221222_08-j.pdf.

[4] L. Stand *et al.*, J. Phys. Chem. C **126** (2022) 12882.

[5] T. Jun *et al.*, Adv. Mater. **30** (2018) 1804547.

Luminescence Characteristics of Synthetic Diamonds

A. Umemoto^{1,2}

¹International Center for Quantum-field Measurement Systems for Studies of the Universe and Particles (QUP),
High Energy Accelerator Research Organization (KEK), Tsukuba 305-0801, Japan

²Division of Physics, University of Tsukuba, Tsukuba 305-8571, Japan

Diamond is expected to be used as a scintillator for radiation detectors because color-centers are easily formed through impurity doping. Applications of diamond scintillators extend to fields such as radiation monitor, medical imaging, and astro-particle physics such as a dark matter search. “C center”, which is a nitrogen-replacing carbon in diamond, generates a luminescence band in visible wavelength. We showed basic characteristics of diamond scintillator by using a commercially available synthetic crystal [1]. At present, with the cooperations of Prof. Taniguchi and Miyakawa in the Research Center for Materials Nano-Architectonics, National Institute for Materials Science, synthetic diamonds via high-pressure high-temperature (HPHT) method with containing nitrogen impurities can be used for studying the luminescence properties.

In the beam time of FY2023, photoluminescence measurements were conducted on HPHT diamonds containing nitrogen impurities ranging from 1 to 200 ppm. Figure 1 shows the comparison of photoluminescence spectra of HPHT diamonds with various nitrogen concentrations at room temperature. The excitation wavelength was set to $\lambda=220$ nm, which corresponds to a similar energy as the bandgap of diamond. The spectrum shape of each sample varied depending on the nitrogen concentration, and the emission on the short wavelength would be increased in lower nitrogen concentration. Although it was not easy to quantify the light-yield of scintillator using the BL3B measurement setup, we can estimate high light-yield at low nitrogen concentration. Since the nitrogen impurities in diamond absorb light from the ultraviolet to visible region, it is anticipated that the detected light would decrease especially at wavelengths below 500 nm, particularly for diamonds with high nitrogen content.

Next, we evaluated the temperature dependence of luminescence characteristics about diamond with a nitrogen concentration of 28 ppm. Luminescence at temperatures around 7 K was measured by using liquid helium, and thermoluminescence (TL) during heating after irradiation was measured by using a thermo-controller. The results revealed a shift in the spectrum towards longer wavelength at the low temperature, and the luminescence spectrum of TL with the sample temperature of around 200 K closely resembled the photoluminescence spectrum observed at room temperature. Furthermore, the trap depth of diamond

estimated from the thermoluminescence measurement was approximately ~ 0.3 eV.

The difference of photo luminescence process of diamond between at low temperature and room temperature has not been clear yet. Scintillators are sometime used at low temperature to improve their light-yields. Hence, further investigations are needed to understand the luminescence characteristics at low temperatures and to determine the optimal nitrogen concentration for enhancing the quality of diamond scintillator.

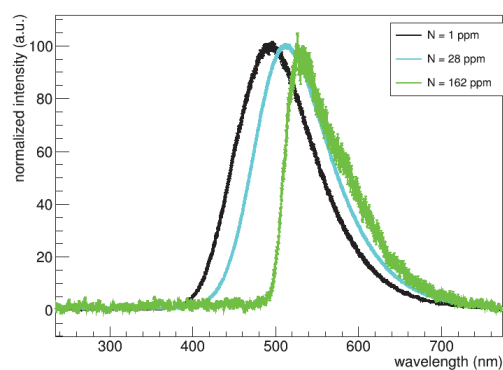


Fig.1. Photoluminescence spectra of HPHT diamonds with various nitrogen concentrations.

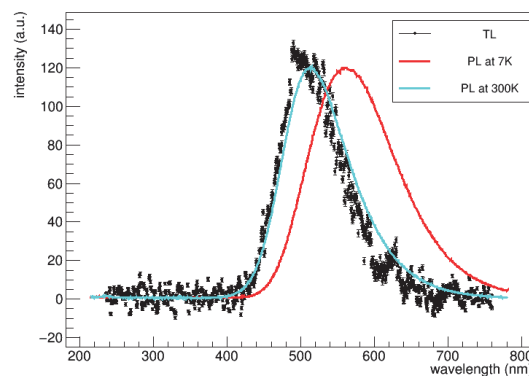


Fig.2. Temperature dependence of luminescence characteristics and thermoluminescence for diamond with a nitrogen concentration of 28 ppm.

[1] A. Umemoto *et al.*, Nucl. Instrum. Methods Phys. Res., Sect. A **1057** (2023) 168789.

BL3B

Photoluminescence Properties of CsI Crystals Obtained Via the Melt Aging Procedure Using I₂ Gas

S. Omiya, S. Kodama, N. Shimoyama, T. Saito, I. Yanase and H. Takeda
*Graduate school of Science and Engineering, Saitama University,
 255 Shimo-Okubo, Sakura-ku, Saitama 339-8570, Japan*

The presence of water (H₂O) and H- or O-containing impurities degrades the optical properties of halide crystals. A method for removing water from the starting material by treatment with reactive gas before crystal growth (Reactive Gas Process, RAP) has been proposed to improve the quality of halide crystals [1]. In addition, to remove excess halogen ions from the raw material, we combined the RAP technique with the melt aging (MA) technique. In the MA process, the raw material is melted under a vacuum atmosphere for a few hours to days [2]. In this study, as the first test of the RAP+MA technique, CsI was treated under several temperature conditions.

The melting point of CsI is 621 °C. CsI was subjected to RAP treatment at 500 °C, which is lower than its melting point, and MA treatment for 24 hours (RAP500-MA24). For comparison, CsI was subjected to RAP treatment at 650 °C, which is higher than its melting point, and MA treatment for 24h (RAP650-MA24). Sublimated I₂ gas was used as reactive gas. CsI was gradually cooled and crystallized.

Before evaluating the optical properties, the crystal phases of the obtained CsI crystals (RAP500-MA24 and RAP650-MA24 specimens) were identified by powder X-ray diffraction. Only the CsI phase and no shifts in the diffraction peaks were observed. The optical properties and photoluminescence emission spectra of the RAP500-MA24 and RAP650-MA24 specimens were measured at the BL3B. The experiments were performed at 10 K and 300 K.

The photoluminescence emission spectra of the RAP500-MA24 and RAP650-MA24 specimens are shown in Figure 1. A strong emission peak at approximately 440 nm is observed at 10 K for the RAP500-MA24 specimen. Weak emission peaks were observed at 310 nm and 340 nm. In contrast, the RAP650-MA24 specimen exhibited strong peaks at 310 and 340 nm. The intensity of the 440-nm-emission was suppressed compared to that of the RAP500-MA24 specimen.

The luminescence at 310 nm and 340 nm is attributed to self-trapped exciton (STE) emission, and the luminescence around 440 nm is attributed to impurity

emission from O-containing impurities [3,4]. The above results suggest that O-containing impurities, such as H₂O, were effectively removed by the RAP technique from the melted CsI raw material. However, the RAP technique against the non-melted CsI raw material had a negligible effect on removing such impurities. In future work, the RAP-MA conditions should be optimized to grow large halide crystals with high optical quality.

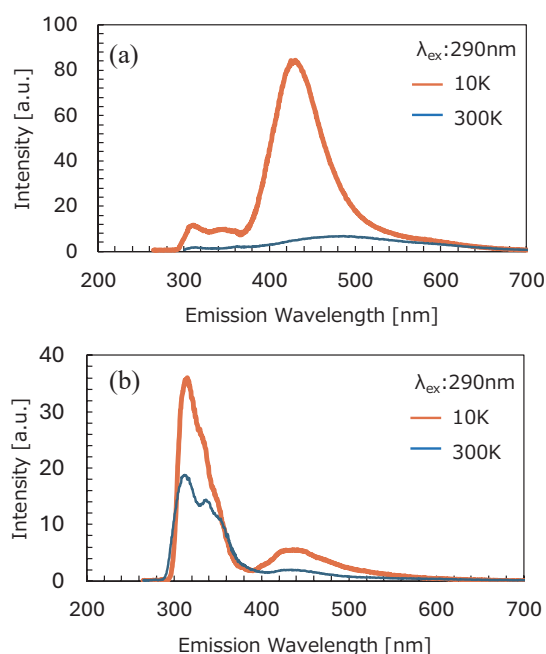


Fig. 1. Photoluminescence emission spectra of CsI crystals at 10 K and 300 K for the (a) RAP500-MA24 and (b) RAP650-MA24 specimens.

- [1] S. Sakuragi, *Am. J. Chem. Eng.* **9** (2021) 25.
- [2] Y. Wu *et al.*, *Cryst. Growth Des.* **8** (2015) 3929.
- [3] S. Kubota *et al.*, *Nucl. Instrum. Methods Phys. Res., Sect. A* **268** (1988) 275.
- [4] L.N. Shpilinskaya *et al.*, *Semicond. Phys. Quantum Electron. Optoelectron.* **3** (2000) 2.

Bandgap Determination of CaCO_3 by Excitation Spectrum in the VUV Range

H. Miyata and J. Ueda

Japan Advanced Institute of Science and Technology, Nomi 923-1292, Japan

Persistent phosphors are luminescent materials that emit light for a long duration after the excitation source is turned off. They are widely used in many applications such as luminous paints in the dark for hazard signboards and road markers and luminescent markers for in vivo imaging. Persistent luminescence originates from the temporary trapping of the electrons or holes generated with light absorption by crystalline defects. The trapped electrons or holes are thermally released and transferred back to the luminescent center.

The carrier trapping depth of lanthanoid ions-activated persistent phosphors can be designed semi-empirically by elucidating the solid-state electronic structure. The depth of electron traps by trivalent lanthanoid ions in solids can be predicted from the vacuum level reference binding energy (VRBE) diagram [1]. The VRBE diagram is constructed from the valence and conduction bands of the host crystal and the ground levels of divalent and trivalent lanthanoids. To create a VRBE diagram, the charge transfer energy E^{CT} of Eu^{3+} , $U(6, A)$, and band gap E_g are required. To obtain these spectroscopic parameters, the photoluminescence excitation spectrum or the absorption spectrum in the range from VUV to UV is required.

So far, aluminates and silicate compounds such as $\text{SrAl}_2\text{O}_4\text{:Eu}^{2+}\text{-Dy}^{3+}$ [2] and $\text{Sr}_2\text{MgSi}_2\text{O}_7\text{:Eu}^{2+}\text{-Dy}^{3+}$ have been widely used as practical persistent phosphors. In contrast, oxides including other oxoanion (CO_3^{2-} , NO_3^- and etc.) and non-oxides are still an unexplored material group for persistent phosphors and have the potential to show excellent persistent luminescent properties. We propose carbonate compounds as a new host material and focus on CaCO_3 with the calcite crystal structure. In this report, the photoluminescence excitation spectra of a natural single crystal of calcite and the synthesized CaCO_3 powder were analyzed to elucidate the solid-state electronic structure of calcite.

Photoluminescence (PL) and PL excitation (PLE) spectra of the natural crystal of calcite and the CaCO_3 powder at 10 K are shown in Fig. 1 and 2. Both samples show a broad PL band around 430 nm at 10 K, while this PL band was not observed at room temperature. The PL band can be attributed to defect luminescence. In the PLE spectra of this defect luminescence, a broad PLE band is observed around 210 nm in both samples. Also, the synthesized CaCO_3 sample shows a relatively strong PLE band at 175 nm, while in the natural calcite sample this PLE band is very weak. In the measured transmittance spectrum of the natural CaCO_3 sample (not shown here), an absorption band rises from 205

nm and the absorption intensity is saturated around 195 nm. Therefore, the PLE band at 210 nm can be related to the defect absorption and that at 175 nm can be related to the host exciton. The E_g is calculated to be 7.65 eV using E^{ex} (175 nm). However, the bandgap of CaCO_3 (calcite) was reported to be around 6.0 eV [3]. The obtained E_g in this study is 20% larger than the previously reported value. In order to discriminate the attribution of the host exciton band and the defect absorption, the further study is necessary.

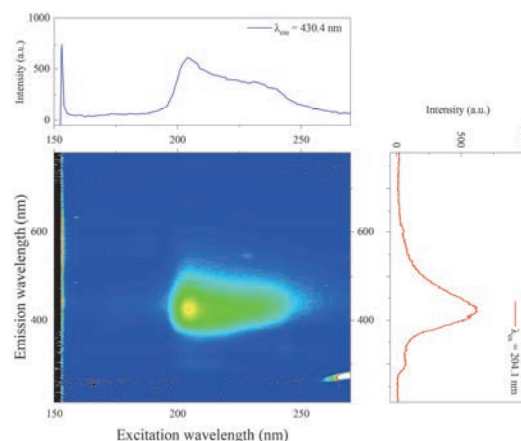


Fig. 1. PL/PLE 2D mapping of natural calcite at 10 K.

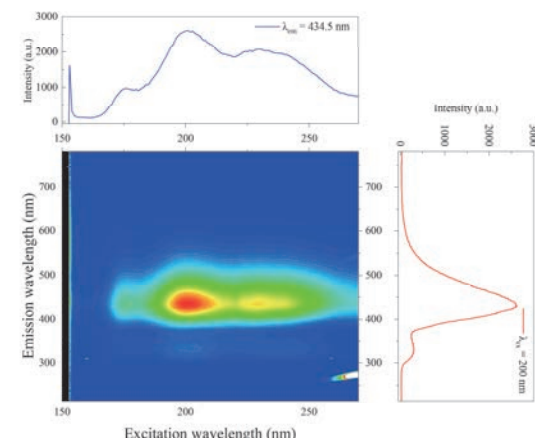


Fig. 2. PL/PLE 2D mapping of the synthesized CaCO_3 powder at 10 K.

- [1] P. Dorenbos, Phys. Rev. B: Condens. Matter **85** (2012) 165107.
- [2] T. Matsuzawa *et al.*, *J. Electrochem. Soc.* **143** (1996) 2670.
- [3] D.R. Baer and D.L. Blanchard, *Appl. Surf. Sci.* **72** (1993) 295.

BL3B

Luminescence Properties of CsAg_2I_3 and Cs_2AgI_3 Crystals

T. Kawai and S. Ibuki

Graduate School of science, Osaka Metropolitan University, Sakai 599-8531, Japan

In the past decade, hybrid perovskite Pb halides and various ternary Pb halides have been extensively investigated for application to solar cells, scintillator materials, photodetectors, and light-emitting diodes [1,2]. However, the environmental toxicity of Pb remains a significant concern. Therefore, considerable efforts have been made to develop alternative environmentally friendly Pb-free ternary metal halides [3,4]. In this study, we focused on Pb-free CsAg_2I_3 and Cs_2AgI_3 crystals. The CsAg_2I_3 and Cs_2AgI_3 crystals were prepared by the Bridgman method from high-purity CsI and AgI powders, which were mixed in a stoichiometric ratio.

Figure 1 (a) and (b) show the luminescence and excitation spectra of the CsAg_2I_3 and Cs_2AgI_3 crystals at 10 K, respectively. In CsAg_2I_3 , the luminescence band is observed at 3.37 eV. The excitation spectrum for the 3.37 eV luminescence band has a sharp rise from 3.75 eV and an excitation band peaking at 3.82 eV, which correspond to the absorption edge and the transition region of the band-edge excitons in CsAg_2I_3 , respectively [5]. In Cs_2AgI_3 , the broad luminescence band is observed at 2.22 eV. The 2.22 eV luminescence exhibits a sharp rise from 4.05 eV and an excitation band peaking at 4.41 eV in the excitation spectrum. The energy positions also correspond to those of the absorption spectrum of the Cs_2AgI_3 thin film reported in a previous paper [6]. The luminescence bands at 3.37 and 2.22 eV in CsAg_2I_3 and Cs_2AgI_3 , respectively, have a Gaussian-like shape with half-width of about 0.14 and 0.34 eV, respectively, and could be attributed to a self-trapped exciton (STE) of the respective crystals.

Assuming that the lowest peaks in the excitation spectra are the lowest exciton transition energies, the STE luminescence in CsAg_2I_3 and Cs_2AgI_3 has a Stokes shift energy of about 0.41 and 2.2 eV, respectively. The Stokes shift energy of the STE in CsAg_2I_3 is much smaller than that of the STE in Cs_2AgI_3 . Therefore, the exciton-phonon interaction in CsAg_2I_3 is weaker than that in Cs_2AgI_3 .

What is noteworthy is that a weak emission line is observed at 3.77 eV in CsAg_2I_3 . An enlarged spectrum is shown in the inset of Fig.1 (a). Since the value of 3.77 eV is roughly equal to the exciton resonance energy [5], the luminescence line at 3.77 eV is considered to be free exciton (FE) luminescence. This implies that FE and STE coexist in the CsAg_2I_3 crystals. In Cs_2AgI_3 , on the other hand, the luminescence line is

not observed in the vicinity of the exciton-resonance energy region reflecting the strong exciton-phonon interaction.

In AgI crystals, no STE luminescence band is observed, and exciton luminescence bound to defects was observed with small Stokes shifts [7]. On the other hand, the STE luminescence with a large Stokes shift is observed in CsI crystals [8]. The ratio of AgI and CsI present in the crystals may be related to the strength of the exciton-lattice interaction.

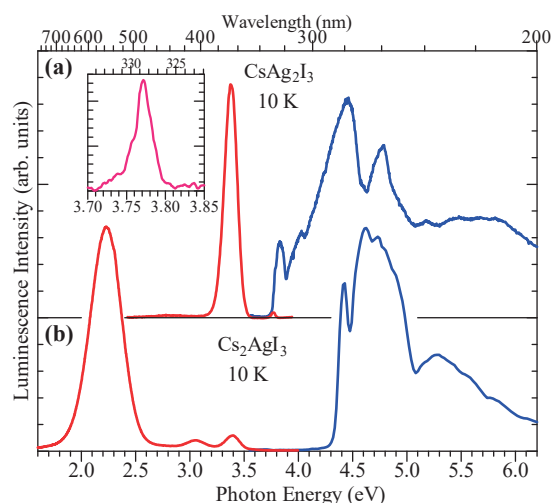


Fig. 1. Luminescence and excitation spectra of (a) CsAg_2I_3 and (b) Cs_2AgI_3 at 10 K. Inset shows the enlarged luminescence spectrum in the vicinity of the exciton-resonance energy region in CsAg_2I_3 .

- [1] A. K. Jena, A. Kulkarni and T. Miyasaka, *Chem. Rev.* **119** (2019) 3036.
- [2] J. Yan *et al.*, *Chem. Mater.* **35** (2023) 2683.
- [3] A. Kumer *et al.*, *Appl. Surf. Sci. Adv.* **18** (2023) 100495.
- [4] Q. Yang, *et al.*, *Mater. Today Phys.* **36** (2023) 101143.
- [5] S. Ibuki and T. Kawai, *UVSOR Activity Report* **50** (2023) 81.
- [6] V. K. Miloslavskii, S. T. Lin and O. N. Yunakova, *Opt. Spectrosc.* **80** (1996) 643.
- [7] S. Mochizuki and F. Fujishiro, *Phys. Status Solidi C* **3** (2006) 3586.
- [8] H. Nishimura *et al.*, *Phys. Rev. B: Condens. Matter* **51** (1995) 2167.

Luminescence Properties of Co-Doped NaCl:I, Ce³⁺ Crystals

R. Oda and T. Kawai

Graduate School of Science, Osaka Metropolitan University, Sakai 599-8531, Japan

In our previous paper, we reported an energy transfer from I⁻ centers to Tl⁺ centers via V_K centers in NaCl:I,Tl⁺ crystals [1]. By considering the hopping motion of V_K center, we could explain the changes in the temporal response of I luminescence. However, the emission lifetime of Tl⁺ centers were so long compared to the repetition interval of the excitation pulse, and we were unable to discuss the decay profile of Tl⁺ luminescence. In this study, we selected Ce³⁺ ions as acceptor ions, which have a short emission lifetime, instead of Tl⁺ ions. Here, we reported on the luminescence properties of co-doped NaCl:I,Ce³⁺ crystals.

NaCl:I,Ce³⁺ crystals were grown by the vertical Bridgman method from NaCl, CeCl₃ and NaI powders. The Ce³⁺ and I⁻ concentrations in the starting materials were 0.179 and 0.021 mol%, respectively.

As shown in Fig. 1, two luminescence peaks due to the Ce³⁺ centers were observed at 3.37 eV and 3.64 eV. In the excitation spectra, five peaks were observed at 4.32, 4.52, 4.74, 4.98, and 5.18 eV. The Ce³⁺ center has the 4f¹ and 5d¹ electron configuration in the ground and excited state, respectively. The ground 4f level splits into two levels because of the spin-orbit interaction. The excited 5d level splits into five levels by the crystal field. The luminescence peaks are attributed to the radiative transition from the lowest 5d excited level to the split 4f ground levels. The five excitation peaks are assigned to the optical transition from the lower 4f ground level to the split 5d excited levels.

In Fig. 2, the luminescence and excitation bands due to I⁻ centers were observed at 5.7 and 7.0 eV, respectively. Although the luminescence of the Ce³⁺ centers was also observed, the intensity was very weak compared to the luminescence of the I⁻ centers.

There is a dip in the excitation spectrum of the Ce³⁺ luminescence in the co-doped NaCl:I,Ce³⁺ at 7.0 eV where the excitation band of the I⁻ luminescence is located. As shown by the green curve in Fig.1, on the other hand, no dip was observed at 7.0 eV in the excitation spectrum of the Ce³⁺ luminescence in single-doped NaCl:Ce³⁺. Thus, the dip indicates that the I⁻ centers are efficiently excited at 7.0 eV, while only a few Ce³⁺ centers are directly excited.

Noteworthy, there is little overlap between the luminescence of the I⁻ centers and the excitation peaks of the Ce³⁺ centers. The fact implies that the energy transfer from I⁻ centers to Ce³⁺ centers is hard to occur by resonance and/or emission-reabsorption mechanism in co-doped NaCl:I,Ce³⁺. The energy transfer by the

hopping motion of the V_K centers is expected, in the similar to NaCl:I,Tl⁺ crystals.

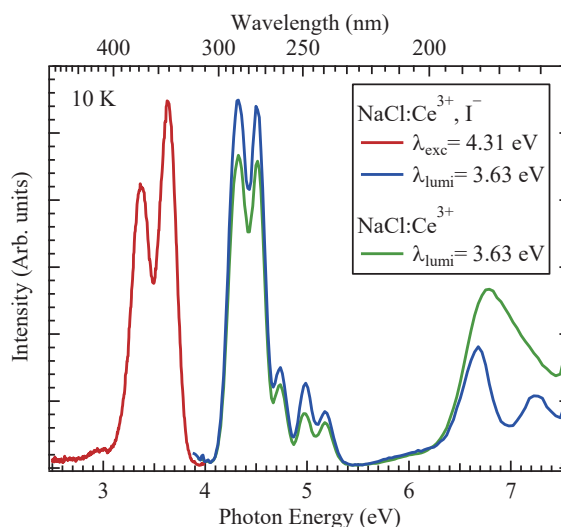


Fig. 1. Luminescence spectrum under excitation 4.31 eV for co-doped NaCl:Ce³⁺, I⁻ (red) and excitation spectra detected at 3.63 eV for co-doped NaCl:Ce³⁺, I⁻ (blue) and single-doped NaCl:Ce³⁺ (green) at 10 K.

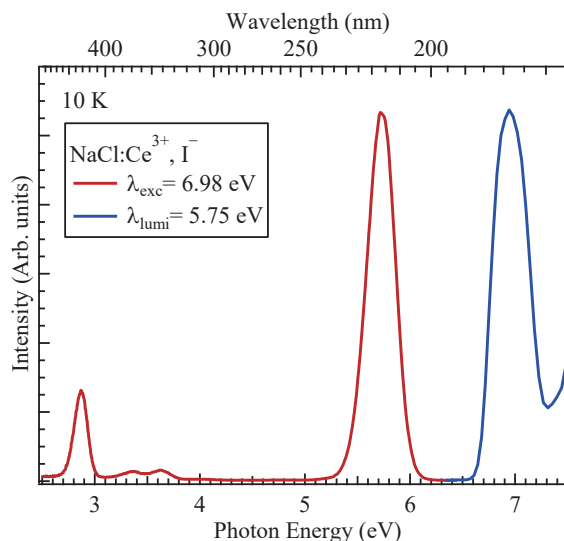


Fig. 2. Luminescence spectrum under excitation 6.98 eV (red) and excitation spectrum detected at 5.75 eV (blue) for co-doped NaCl:Ce³⁺, I⁻ at 10 K.

[1] O. Yagi, T. Kawai and K. Mizoguchi, J. Lumin. **226** (2020) 117359.

BL4U

Electronic Structure Identification of the Free-Standing Hexagonal Boron Nitride Membranes

C. O. M. Mariano¹, J. S. D. Rodriguez^{1,2}, T. Araki³ and C.-H. Chuang¹

¹Department of Physics, Tamkang University, Tamsui, New Taipei City 251301, Taiwan

²Institute of Chemistry, Leiden University, Leiden, 2300 RA, The Netherlands

³Institute for Molecular Science, Okazaki 444-8585, Japan

A honey-like structure with sp^2 hybridized orbits is noted for a typical lattice in graphene (G) or hexagonal boron nitride (hBN), which of difference likes boron (B) and nitrogen (N) atoms alternatively bonded in the basal plane. Unlike a zero bandgap in G, hBN behaves as a wide band gap (~ 6 eV) due to the partly ionic B-N bond and its electron-delocalization on the basal plane. The unique coordination of hBN down to the nanosheets has excellent properties in high chemical/thermal stability, enhanced thermal/electrical conductivity, and flexible doping capability, leading to various applications in dielectric substrates, UV light emitters, and functional coatings. Thus, a valuable synthesis of a few hundred nm in thickness and a few centimeters in an area with the free-standing type of hBN membranes is our objective in the BL 4U for scanning transmission X-ray microscopy (STXM). An in-depth understanding of the morphology, chemical composition, and electronic structure of hBN membranes is significant in developing materials engineering.

The hBN grounding formed the ball-rolled solvent and later cleaned a couple of times in water, particularly for extensive practical application. The cyclic voltammetry method, called CV hBN, was used to grow the free-standing and thin-thickness membrane on a gold mesh, compared to the control sample by the drop-cast (DC) and dried in air. The previous characterization, such as transmission electron microscopy, Raman microscopy, and Photoluminescence microscopy, displays that DC and CV hBN are highly similar to the bulk case in the ordered lattice structure and the typical photo-electron process. One wide-range emission that emerged in the background was found in PL, hinting only at the solution-induced difference.

The area-selected absorption spectra and element-dependent images are powerful capabilities in STXM for information of interest in surface morphology. The three areas (indicated as “1”–“3”) in DC hBN and the other areas (indicated as “4”–“6”) in CV hBN are shown in different element-resolved results in Fig. 1(a)–(f), as indicative of the same region of SEM images in the inset. In Fig. 1(a)(d), an intensive peak at 192.0 eV and double-split peak at 198.0 and 199.5 eV are assigned to the $1s \rightarrow \pi^*$ and σ^* resonance for the angular orientation of B- p_z /N- p_z direction and B- p_{xy} /N- p_{xy} plane. There is no difference between DC and CV hBN, except for the relative intensity ratio of π^* and σ^* resonance for the polarization dependence of the plane structure and X-ray incidence. Fig. 1(b) and (e) are the N K-edge spectra of DC and CV hBN, which are identical of $1s \rightarrow \pi^*$ resonance at 401.6 eV and σ^* resonance between the range of 408.0 and 420.0 eV.

The N- p_z (π^*) peak with the low and broad signal in the area of “3” in DC hBN and “6” in CV hBN reflects the polycrystalline feature by the stacking formation. The narrow peaks within the 404.0 and 407 eV range in the inset are considered the specific lattice defect or H-passivated vacancies at the B site, which is identical in the area (“1”–“3”) of DC hBN. Because as-obtained hBN was separated from the centrifugation and redispersed in the water solution, the oxygen-modified possibility during the exfoliation process is necessary for the discussion in Fig. 1(c) and (f). Due to the weak optical density signal, a negligible amount of surface O is found in both DC and CV hBN. Two peaks at 531.7 and 539.0 eV are assigned to the electron transition from $1s$ to π^* and σ^* state of adsorbed molecule oxygen, respectively. Besides, the O bonding to B and N sites can be found at 530.6 eV for the N=O state and 531.7 eV for the B-O bond. The synchronization effect of oxygen molecules during the flake stacking and electrochemical reconstruction in the water solution is highly reasonable in the substitutional O or OH species in the vacancy at B and N sites.

Our work indicates a vital identification to track the morphology and electronic structure of freestanding hBN membranes by contrasting electrochemical reactions between DC and CV methods. Various spectral features selected from the area “1” to “6” demonstrate the lattice structure and chemical functionalization between B, N, and O sites, which is addressed by the spatially resolved absorption in STXM.

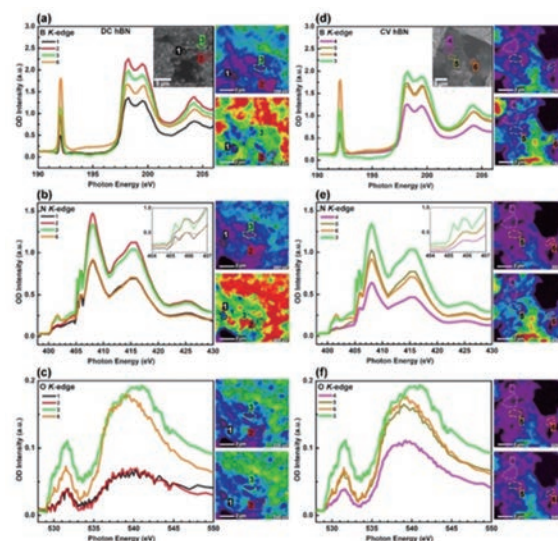


Fig. 1. (a) and (d) B K-edge, (b) and (e) N K-edge, and (c) and (f) O K-edge of DC and CV hBN, respectively.

Transition Metal Dopants on Graphitic Carbon Nitride (g-C₃N₄) for Electrocatalytic Carbon Dioxide Reduction Reaction

W.-T. Chen¹, H. W. Shiu¹, Y.-L. Lai¹, T. Araki² and Y.-J. Hsu^{1,3}

¹Nano Science Group, National Synchrotron Radiation Research Center, Hsinchu 300092, Taiwan

²UVSOR Synchrotron Facility, Institute for Molecular Science, Okazaki 444-8585, Japan

³Department of Photonics, National Cheng Kung University, Tainan 70101, Taiwan

The synthesis of high-order chemicals and fuels from electrochemical carbon dioxide reduction reaction (CO₂RR) has been considered a promising strategy to tackle CO₂ emissions in the near future [1]. Substantial efforts have been made in designing heterogeneous electrocatalysts with improved CO₂RR performance. Among all electrocatalysts, metal atoms embedded with functional nitrogen species (M-N_x) porphyrin-like sites on carbon-based materials, so-called single-atom catalysts (SACs) and dual-atom catalysts (DACs) received numerous attention due to their favorable in exposing abundant unsaturated surface atoms and providing larger active sites for many catalytic reactions [2, 3]. However, these metal-nitrogen-doped carbon materials often contain complicated nitrogen species with low concentrations, which leads to technical difficulty in investigating the structure-activity relationships of SACs and DACs for CO₂RR. In this project, we chose porous graphitic carbon nitride (g-C₃N₄) as the support, because it can provide uniform and stable nitrogen vacancy that can stabilize metal atoms and provide simpler M-N_x reaction sites. We fabricated a series of Cu/g-C₃N₄ (where M = Cu with different loading) samples to study the effect of metal dopants using synchrotron-related techniques, such as scanning transmission X-ray microscopy (STXM) and Near-edge X-ray absorption fine structure (NEXAFS) analysis.

In Fig. 1(a), the optical density (OD) of carbon maps suggested that the C signals came from the carbon paper (light green area) and g-C₃N₄ (orange area). Different Cu loading of pristine 0.7 wt.% Cu/g-C₃N₄ (Cu-SACs) and 12 wt.% Cu/g-C₃N₄ (Cu-DACs) were chosen to study the effect of Cu dopant and loading on the g-C₃N₄ support as shown in Fig. 1(b). All samples showed characteristic π^*_{C-N-C} peak of the g-C₃N₄ samples at 288.0 eV [4]. A weak peak at 285.4 eV was observed due to the use of carbon paper as a free-standing electrochemical electrode during CO₂RR.

Additional shoulder at 287.3 eV was observed in 0.7 wt.% Cu/g-C₃N₄ sample, which can be assigned to a C-H bond from catalyst ink that contains isopropanol, milli-Q water, and 5 wt.% Nafion solution [5].

Furthermore, to explain the fundamental mechanism of the Cu/g-C₃N₄ for CO₂RR, we aim to perform ex-situ experiments on Cu/g-C₃N₄ to study the changes in reaction sites before and after CO₂RR. The correlation between reaction sites and the reaction products (such

as CO, CO₂, and hydrocarbons) is also of interest. The 12 wt.% Cu/g-C₃N₄ sample (pristine and after reaction) was conducted to correlate the catalytic reaction sites with associated CO₂RR products (Fig. 2(a)). After the CO₂ reduction reaction at -0.8 V vs RHE, an additional peak was observed at 290.4 eV, suggesting this peak is associated with CO₂RR-related products. The OD images shown in Fig. 2(b)-(c) suggested the location of 290.4 eV peak (light green) on the g-C₃N₄ sample (red). A mixture of g-C₃N₄ (red) and 290.4 eV (light green) led to the orange particles. Further data analysis is underway to provide ex-situ insight into reaction sites under CO₂RR.

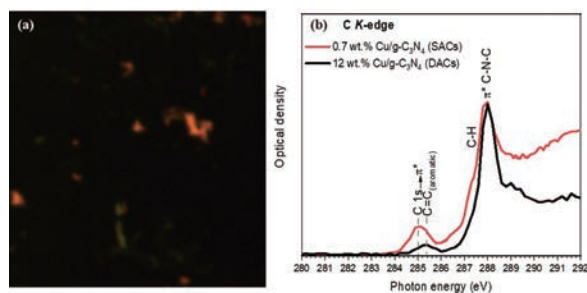


Fig. 1. (a) The OD images of the carbon paper (light green) and Cu/g-C₃N₄ (orange) component maps, and (b) C K-edge NEXAFS spectra of pristine Cu-SACs and Cu-DACs.

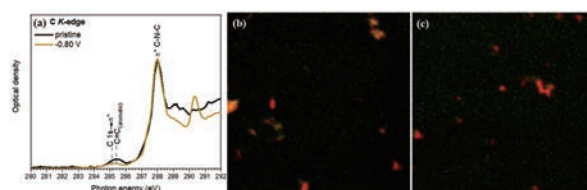


Fig. 2. (a) Ex-situ C K-edge NEXAFS spectra of 12 wt.% Cu/g-C₃N₄ sample before and after CO₂RR, (b) and (c) the OD images of g-C₃N₄ (red) and 290.4 eV (light green) component maps of region 1 and 2 for 12 wt.% Cu/g-C₃N₄ sample after CO₂RR at -0.8 V vs RHE.

- [1] W. Zhang *et al.*, Adv. Sci. **5** (2018) 1700275.
- [2] A. S. Varela *et al.*, ACS Catal. **9** (2019) 7270.
- [3] R. Li and D. Wang, Adv. Energy Mater. **12** (2022) 2103564.
- [4] Y. Zheng *et al.*, Nat. Commun. **5** (2014) 3783.
- [5] K. G. Latham *et al.*, Carbon **114** (2017) 566.

BL4U

Nm-scale NEXAFS Spectra of Styrene-Butadiene Rubber (SBR) Compounds Mixed with Silica Fillers

T. Ejima^{1,2*} and Y. Tamura³¹SRIS & ²IMRAM, Tohoku University, Sendai 980-8577, Japan³ENEOS Materials Corp., Yokkaichi 510-0871, Japan

In tire tread compounds, elastomers are blended and fillers are added to obtain the properties necessary to achieve optimal tire performance. Elastomers exhibit specific compatibility depending on the level of elastomer incorporation. The aggregation behavior of the filler is also suppressed by the higher compatibility of the filler surface with the elastomer [1, 2]. When silica is added to elastomers blended with SBR and BR, the silica population is higher in the SBR [3]. Our previous electron microscopy observation showed that silica dispersed in SBR causes aggregation with a size of roughly tens to hundreds of nm. The aggregation size depends on the blended species and coupling agents. In this study, to investigate the chemical properties of the elastomer and filler surfaces, which are considered to be important for filler dispersion and network formation, we performed NEXAFS measurements using STXM. And then, by image analysis using typical NEXAFS spectra of each material, we investigate the spectral changes between aggregates of fillers.

Elastomer materials used for samples were normal SBR and chemically modified SBR (m-SBR). The difference between the elastomer materials is crosslink density: the m-SBR has a higher crosslink density than the normal SBR. A silica filler was added to the elastomer materials. A total of four blocks were made combining the elastomer with silica filler ($\Phi 100$ nm or $\Phi 16$ nm in diameter). The resulting blocks were cut into sheets, and then sliced with an ultramicrotome in 100 nm thick to observe.

Distribution of the SBR and aggregation area of the silica fillers were obtained based on the STXM sequential images around C-K edge and is shown in the inset of Figure 1(a). The related NEXAFS spectra of the distribution are also shown in the figure. The red region and the curve show the SBR area and its spectrum, respectively, and the green region and the curve, the silica aggregation area and its spectrum, respectively. The blue area is zinc oxide used as an additive. Comparing the spectrum of the silica aggregation region with that of the SBR region, the shapes of the spectra are almost same except for a different peak-intensity around 285 eV, which is attributed to the π^* anti-bonding states of C=C bond. The spectral shapes of the other samples have same tendency. To compare the peak intensities of the π^* antibonding states between the areas, the integration intensities of the peaks were obtained (Figure 1(b)). The intensity ratios of $\Phi 100$ nm silica samples are same to each other, on the other hand the intensity ratios of

the $\Phi 16$ nm silica samples differed greatly between the SBR and the m-SBR. This difference will be attributed to the difference in surface area of silica.

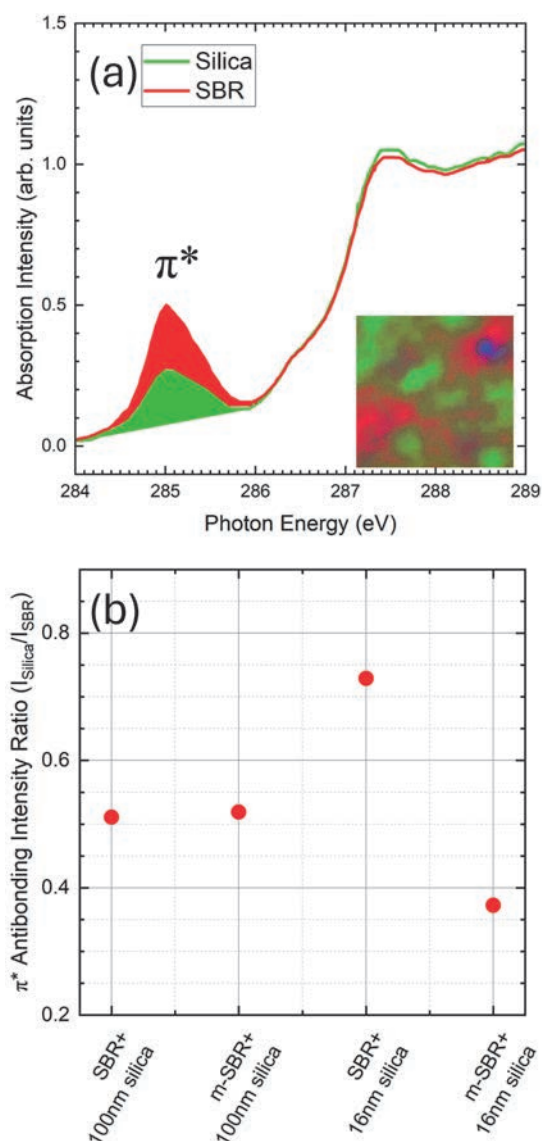


Fig. 1. (a) Analyzed STXM image and related spectra around the C-K absorption edge. The size of the inset is $2 \times 2 \mu\text{m}$. (b) Comparison of integrated peak intensity ratios of the π^* anti-bonding structure.

[1] A. J. Marzocca *et al.*, Polym. Int. **49** (2000) 216.

[2] J.M. Massie *et al.*, Rubber Chem. Technol. **66** (1993) 276.

[3] J. Jin *et al.*, Polym. Test. **99** (2021) 107212.

Investigation of Micro Voids in Rubber by STXM with a Tensile-Stress Sample Cell

T. Ohigashi^{1,2}, F. Kaneko³, H. Yuzawa⁴, T. Yano⁴, T. Araki⁴ and H. Kishimoto³

¹*Institute of Material Structure Science, High Energy Accelerator Research Organization, Tsukuba 305-0801, Japan*

²*Materials Structure Sciences, The Graduate University for Advanced Studies (SOKENDAI), Tsukuba 305-0801, Japan*

³*Sumitomo Rubber Industries Ltd., Kobe 651-0072, Japan*

⁴*UVSOR Synchrotron Facility, Institute for Molecular Science, Okazaki 444-8585, Japan*

In recent years, SDGs (Sustainable Development Goals) is a keyword in our daily life. Especially, reduction of mass consumption is a critical issue. Rubber is one of the important resources and its demand is assumed to increase especially according to growth of automobile industries. To reduce its consumption, establish of LCA (Life Cycle Assessment) of rubber industrialization and further improvement of functionality of rubbers, such as wear- and destruction-resistant, are essential.

To improve characteristics of the tire rubbers, understanding of process of the deterioration is necessary. Generally, an origin of the damage of tire rubber is chemical and mechanical issues. In recent years, Mashita et al. investigated the mechanical damage by time-resolved X-ray tomography and elucidated generation process of micro voids in a rubber pillar during its deformation [1]. On the other hand, we are using scanning transmission X-ray microscopy (STXM) to understand chemical change by mechanical damage. STXM is a powerful tool to analyze localized chemical state of a sample with high spatial resolution around 30 nm. Moreover, an advantage of STXM is relatively long working distance around 300 μm and that enables measurements in various sample environments by designing special sample cells. In this study, we designed a tensile-stress sample cell for STXM and measured a rubber sample under applied tensile stress.

The tensile-stress sample cell with a sample cartridge is shown in Fig. 1. The sample cartridge (stainless steel, 100 μm thick) was originally designed by Sato et al. [2]. Width of the gap of the sample cartridge can be adjusted manually from 300 to 850 μm in horizontal direction by a micrometer and the sample placed on the gap is stretched or relaxed. In this study, an ultra-thin slice (200 nm thick) of mixture of isoprene and butadiene rubbers was used as a sample. Figure 2 shows X-ray absorption spectra around C K-edge of the rubber with or without tensile stress. The spectra are normalized at 280 eV and $\pi^*_{\text{C-C}}$ peak at 285.2 eV. In “with tensile stress” condition, the width of the gap was 2.2 times wider than “without tensile stress” condition. In comparison of the spectra, spectral features at 285.2 eV

and 288.1 eV do not show remarkable change but σ^* peak around 292.2 eV increases with stress. An inset of Fig. 2 shows zooming up of σ^* peaks and that becomes slightly sharper with the stress. These changes may imply that stretching of the rubber makes arranging C-C bonding along stretching direction (i.e. horizontal direction). As a future plan, further investigation chemical state of the micro void which is caused by stretching is analyzed.

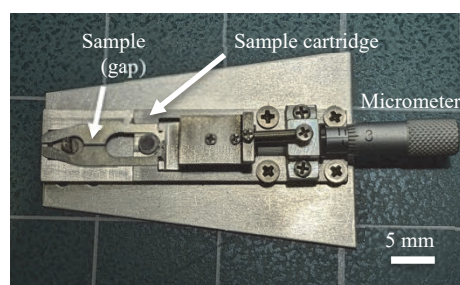


Fig. 1. Photo of the tensile-stress sample cell with the sample cartridge.

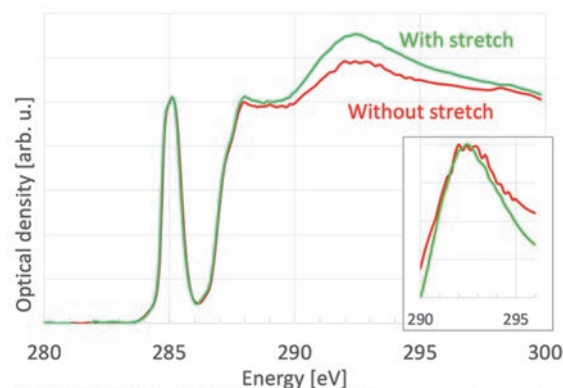


Fig. 2. X-ray absorption spectra around C K-edge of the rubber with/without stretching (normalized at 280 eV and 285.2 eV). An inset shows zooming up around σ^* peak (normalized at σ^* peak).

[1] R. Mashita *et al.*, Sci. Rep. **13** (2023) 5805.

[2] T. Higuchi *et al.*, Microscopy **67** (2018) 296.

BL4U

Electronic Structure Analysis of Electrolyte for Redox Flow Battery

E. Hosono^{1,2,3}, D. Asakura^{1,2,3}, H. Yuzawa⁴, T. Ohigashi⁵ and A. Ohira^{1,2}

¹Global Zero Emission Research Center, National Institute of Advanced Industrial Science (AIST), Tsukuba, Ibaraki 305-8569, Japan

²Research Institute for Energy Conservation, AIST, Tsukuba, Ibaraki 305-8565, Japan

³AIST-UTokyo Advanced Operando Measurement Technology Open Innovation Laboratory (Operando-OIL), Kashiwa, Chiba 277-8565, Japan

⁴UVSOR Synchrotron Facility, Institute for Molecular Science, Okazaki, Aichi 444-8585, Japan

⁵Photon Factory, Institute of Materials Structure Science, High Energy Accelerator Research Organization, Tsukuba, Ibaraki 305-0801, Japan

Effective use of renewable energy is attracting attention to realize a low-carbon society. For promoting the society of renewable energy, it is necessary to store the power generated by solar and wind etc. Thus, larger storage batteries are suitable for renewable energy power plants. These batteries are naturally required high safety, but the following characteristics are also expected: easy enlargement, long-term availability, and low cost.

We have been conducting research and development focusing on redox flow batteries as a large-scale storage battery. Redox flow batteries are nonflammable and safe because the electrolyte is an aqueous solution. In addition, they can be easily scaled up to larger capacities by increasing the size of the tank. Currently, redox flow batteries using vanadium as the electrolyte are in practical use [1-4], but further cost reduction and higher energy density are desired. Since vanadium is unevenly distributed, we have been studying redox flow batteries using Ti and Mn from the viewpoints of lower cost metal. Furthermore, higher energy density is also expected.

An important research and development element for redox flow batteries using Ti-Mn is the stability of electrolytes. Redox reaction of this system on the charging process is considered as follows.

- Negative Electrode
 $(\text{TiO})^{2+} + 2\text{H}^+ + \text{e}^- \rightarrow \text{Ti}^{3+} + \text{H}_2\text{O}$
- Positive Electrode
 $\text{Mn}^{2+} \rightarrow \text{Mn}^{3+} + \text{e}^-$
- Total Reaction
 $(\text{TiO})^{2+} + \text{Mn}^{2+} + 2\text{H}^+ \rightarrow \text{Ti}^{3+} + \text{Mn}^{3+} + \text{H}_2\text{O}$

As the electrolyte degrades during oxidation reaction, precipitates form in the electrolyte. We conducted STXM measurement, which is effective to understand the distribution of electronic state of the electrolyte with precipitates in detail. Through this study, we hope

that it will lead to the formulation of development strategies that are important for improving the performance of redox flow batteries using Ti-Mn.

For measurement of STXM of Ti-Mn electrolyte samples, Si_3N_4 thin-film windows (100 nm) were used for separating sample from the vacuum. Charged electrolyte was investigated by STXM at BL4U of UVSOR.

Figure 1 shows spectrum at the Ti L-edge in a solution part. This spectrum is attributed to similar Ti^{4+} state. By using this measurement system, the electronic state of the transition metals in solution of the electrolyte was revealed. In addition, we conducted measurement of various electrolytes and discussed based on the obtained results.

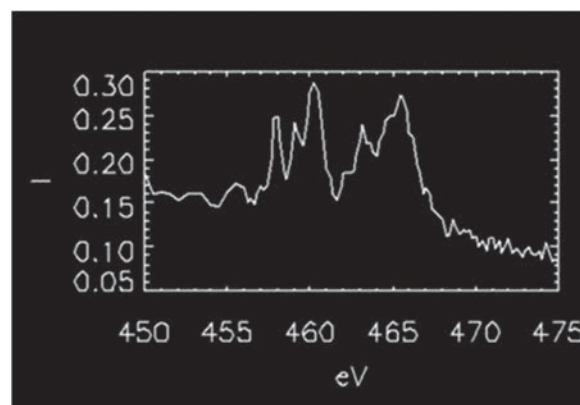


Fig. 1. Ti L-edge spectrum at a solution part in charged electrolyte.

- [1] A. Z. Weber *et al.*, J. Appl. Electrochem. **41** (2011) 1137.
- [2] M. Rychcik and M. Skyllas-Kazacos, J. Power Sources **22** (1988) 59.
- [3] T. Shigematsu, SEI Technical Review **73** (2011) 4.
- [4] M. Skyllas-Kazacos *et al.*, Int. J. Energy Res. **34** (2010) 182.

A Scanning Transmission X-ray Microscopy Study of $\text{LiFe}_{0.6}\text{Mn}_{0.4}\text{PO}_4$ Nanowires to Observe Partial Degradation by Natural Oxidation

D. Asakura^{1,2,3}, E. Hosono^{1,2,3}, H. Yuzawa⁴, T. Ohgashi⁵, W. Zhang⁶, M. Kobayashi^{7,8},
H. Kiuchi⁶ and Y. Harada^{3,6,9}

¹Global Zero Emission Research Center, National Institute of Advanced Industrial Science (AIST),
Tsukuba, Ibaraki 305-8569, Japan

²Research Institute for Energy Conservation, AIST, Tsukuba, Ibaraki 305-8565, Japan

³AIST-UTokyo Advanced Operando Measurement Technology Open Innovation Laboratory (Operando-OIL),
Kashiwa, Chiba 277-8565, Japan

⁴UVSOR Synchrotron Facility, Institute for Molecular Science, Okazaki, Aichi 444-8585, Japan

⁵Photon Factory, Institute of Materials Structure Science, High Energy Accelerator Research Organization,
Tsukuba, Ibaraki 305-0801, Japan

⁶Institute for Solid State Physics (ISSP), The University of Tokyo,
5-1-5 Kashiwanoha, Kashiwa, Chiba 277-8581, Japan

⁷Department of Electrical Engineering and Information Systems, The University of Tokyo,
7-3-1 Hongo, Bunkyo-ku, Tokyo 113-8656, Japan

⁸Center for Spintronic Research Network, The University of Tokyo,
7-3-1 Hongo, Bunkyo-ku, Tokyo 113-8656, Japan

⁹Synchrotron Radiation Research Organization, The University of Tokyo,
7-3-1 Hongo, Bunkyo-ku, Tokyo 113-8656, Japan

$\text{LiFe}_{1-x}\text{Mn}_x\text{PO}_4$ is a cathode material for Li-ion batteries, which exhibits two potential plateaus at ~ 3.5 V vs. Li/Li^+ and ~ 4.1 V vs. Li/Li^+ on the charge-discharge curves [1]. The lower one has been attributed to the redox reaction of $\text{Fe}^{2+} \rightleftharpoons \text{Fe}^{3+}$ as with LiFePO_4 [1]. The Fe^{2+} state before charge is not so stable in air: it is easily oxidized. Then, it is well-known that the low electron conductivity of $\text{LiFe}_{1-x}\text{Mn}_x\text{PO}_4$ and LiFePO_4 is problematic for the high-rate charge-discharge performance. To overcome these problems, carbon-coated $\text{LiFe}_{0.6}\text{Mn}_{0.4}\text{PO}_4$ (LFMP) nanowires have been developed [2]. The LFMP nanowires indeed showed improvement on the high-rate performance.

To confirm the suppression of the surface oxidation by the carbon coating, we investigated the chemical state distribution of the LFMP nanowires by using scanning transmission X-ray microscopy (STXM) at BL4U [3]. The carbon-coated LFMP nanowire sample was fabricated by an electrospinning method. The nanowire sample was fixed on a Si_3N_4 membrane window with a thickness of 150 nm. The spatial resolution was around 130 nm.

Figure 1 shows an STXM optical density (OD) image at 703 eV just before the Fe $L_{3\text{-edge}}$. It is confirmed that the diameter of the nanowires is less than 1 μm . Figure 2(a) shows the pinpoint absorption spectra of areas A(i) and A(ii) in Fig. 1(a). The areas A(i) and A(ii) are well reproduced by the charge-transfer multiplet calculations for Fe^{2+} and Fe^{3+} states, respectively. Then, we analyzed the STXM data at the Fe $L_{2,3\text{-edge}}$ by using the two calculated spectra. Figure 2(b) shows the color mapping. Most of the nanowires are colored by red that is the Fe^{2+} state. Some of the edges and most of the nanowire on the upper side are colored by green corresponding to the Fe^{3+} state. Therefore, it is

confirmed that the carbon coating effectively preserves the Fe^{2+} state, while some of the edges and some nanowires are oxidized to the Fe^{3+} state [3].

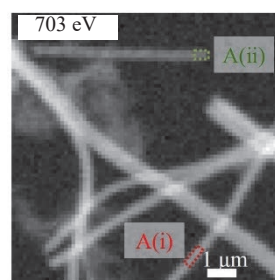


Fig. 1. A STXM OD image of the LFMP nanowire sample at 703 eV [3].

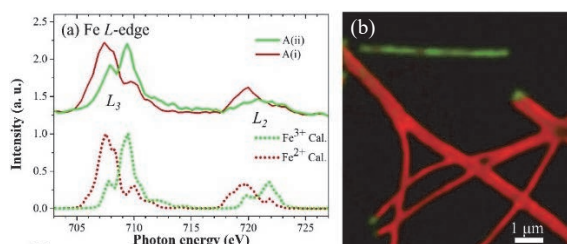


Fig. 2. (a) Pinpoint absorption spectra corresponding to areas A(i) and A(ii) in Fig. 1 and calculations for Fe^{2+} and Fe^{3+} states. (b) Color mapping of the Fe $L_{2,3\text{-edge}}$ STXM data by using the calculated spectra in (a) [3].

[1] A. Yamada *et al.*, J. Electrochem. Soc. **148** (2001) A747.

[2] K. Kagesawa, E. Hosono *et al.*, J. Power Sources **248** (2014) 615 and CrystEngComm **15** (2013) 6638.

[3] W. Zhang *et al.*, J. Electron Spectrosc. Relat. Phenom. **266** (2023) 147338.

BL4U

Hierarchically Structured $\text{ZnCo}_2\text{O}_4@\text{CoS}/\text{NF}$ Binder-Free Electrode for Multifunctional Applications

P. Mannu¹, T. T. T. Nga^{1,2}, Y.-C. Huang¹, C.-L. Dong¹, W. F. Pong¹, W.-C. Chou²,
T. Araki³ and T. Ohgashi^{3,4}

¹Department of Physics, Tamkang University, New Taipei City 25137, Taiwan

²Department of Electrophysics, National Yang Ming Chiao Tung University, Hsinchu 30010, Taiwan

³UVSOR Facility, Institute for Molecular Science, Okazaki 444-8585, Japan

⁴Photon Factory, High Energy Accelerator Research Organization, Japan

Water electrolysis is a promising technology that provides clean and sustainable energy to solve global energy crisis issues and eco-friendly degradation as the energy crisis and environmental issues produced by the over-exploitation of fossil fuels lead to unbearable problems for the growth of human society. Hence, developing a facile, environmentally friendly, and low-cost approach that can precisely regulate electrocatalysts' electronic structure and surface/ interface properties is essential. Herein, we report a high-efficiency and low-cost hydrothermal method to synthesize $\text{ZnCo}_2\text{O}_4/\text{CoS}/\text{NF}$ heterostructure electrocatalysts. The satisfactory performance was deduced that the formation of heterostructure can increase the specific surface area, form abundant oxygen vacancies, and achieve a higher proportion of $\text{Co}^{3+}/\text{Co}^{2+}$, thus providing more active sites and greatly improving its intrinsic catalytic activity (OER/HER).

STXM microscopy provides chemically and spatially resolved information and is ideal for investigating the element and region of interest in the sample. The optical density (OD) images and STXM stack maps of ZnCo_2O_4 and (b) $\text{ZnCo}_2\text{O}_4@\text{CoS}$ are presented in Figure 1a-b. The OD images (inset image) of ZnCo_2O_4 and $\text{ZnCo}_2\text{O}_4@\text{CoS}$ show three regions (R1, R2, and R3). Through the decomposition of the stack STXM maps, distinct maps are generated to depict various spectroscopic properties across the samples, including a background, as well as maps for regions colored, yellow (R1), red (R2), and green (R3) that are related with the surface area to the core region of the samples with different XAS extracted from the corresponding regions. The pre-peak of the O K-edge exhibits two features that could be associated with the hybridization of Co 3d(t_{2g})-O 2p (lower energy) and Co 3d(e_g)-O 2p orbitals (higher energy), reflecting the amount of unoccupied Co 3d states. Overall spectral evolution shows that the ratios of 3d(t_{2g})-O 2p to Co 3d(e_g)-O 2p states gradually decline from the core region to the surface area for both samples, suggesting that the hybridized 3d(t_{2g})-O 2p orbital gains some charges in the surface area, which is consistent with the charge transfer processes revealed from the combined XAS results of Co L-edge (not shown here). Especially, the intensity of the main absorption peak around 540 eV in the surface region (R-1) of $\text{ZnCo}_2\text{O}_4@\text{CoS}$ is

significantly lower than that of ZnCo_2O_4 , suggesting that the surface region of $\text{ZnCo}_2\text{O}_4@\text{CoS}$ gains even more charges than ZnCo_2O_4 does. This also suggests that the charge transfer at the surface oxygen site is not only from Zn but also from core Co, which could be further confirmed by the Co L-edge STXM-XAS.

It is believed that the intensity of O K-edge in the core region (R-3) declines more significantly in $\text{ZnCo}_2\text{O}_4@\text{CoS}$ than in ZnCo_2O_4 , suggesting the enriched electron density in the core region of $\text{ZnCo}_2\text{O}_4@\text{CoS}$, which would hinder the photoexcitation of electrons from valence band to conduction band. The overall spectral profiles of STXM-XANES of all regions of the $\text{ZnCo}_2\text{O}_4@\text{CoS}$ sample are dissimilar compared to that of ZnCo_2O_4 and consistent with the results obtained by XAS (not shown here). Notably, the pre-edge and absorption peaks of $\text{ZnCo}_2\text{O}_4@\text{CoS}$ are similar to the normal O K-edge XAS spectra. Moreover, the distinctive feature at 531.8 eV in the O K edge XANES spectra of $\text{ZnCo}_2\text{O}_4@\text{CoS}$, shown in Figure 1b, is mostly related to the hybridization of the Co 3d and O 2p state. It seems the Co sites are expected to be more active than Zn in overall better OER/HER/UOR performance of $\text{ZnCo}_2\text{O}_4@\text{CoS}$ compared to ZnCo_2O_4 .

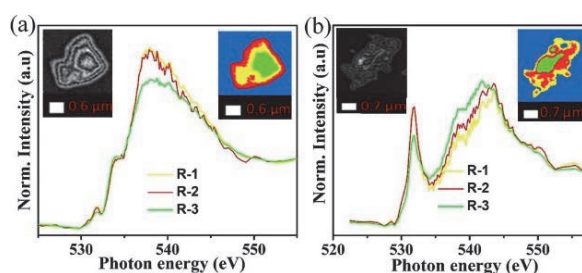


Fig. 1. STXM-XAS recorded at O K-edge of (a) ZnCo_2O_4 and (b) $\text{ZnCo}_2\text{O}_4@\text{CoS}$, STXM images show three different regions (R-1 [yellow], R-2 [red], and R-3 [green]) that are associated with surface area to the core region, the grey images of nanosheets were captured using STXM without chemical mapping.

- [1] Z. Chen *et al.*, Nano Energy **78** (2020) 105270.
- [2] Z. Chen, *et al.*, Nano Res. **13** (2020) 293.
- [3] K. Zhang and R. Zou, Small **17** (2021) 2100129.
- [4] W. Liu, *et al.*, J. Catal. **394** (2021) 50.

Unveiling the Interfacial Electronic Structure of $\text{MnO}_2/\text{CuO}_x$ Heterostructure by Spectro-Microscopy

K. T. Arul¹, C.-L. Pan¹, H.-W. Chang², C.-L. Dong¹,
W.-F. Pong¹, T. Araki³ and T. Ohgashi^{3,4}

¹Department of Physics, Tamkang University, Tamsui 25137, Taiwan

²Department of Chemical Engineering, National United University, Miaoli 360302, Taiwan

³UVSOR Synchrotron Facility, Institute for Molecular Science, Okazaki 444-8585, Japan

⁴Photon Factory, High Energy Accelerator Research Organization, Japan

The development of renewable electricity generation technologies and novel energy storage devices are significant nowadays to tackle upcoming energy scarcity. Currently, electrochemical energy storage has fascinated because of its high cyclic stability, swift charge/discharge rate, and superior power density [1]. Recently, bimetallic oxides depicted the enhancement of pseudocapacitive performance with abundant active sites, higher cyclic stability, and augmented electrical conductivity than that of single metal oxides owing to the synergetic effects between the elements [2].

Mn and Cu-based oxides are one of the potential candidates for the electrochemical energy storage application due to their multi-valence state, high electrical conductivity, redox, and ionic conductivity. Developing the heterostructure of bimetallic oxide is important for the improvement of electrical conductivity, stability, energy, and power densities. Moreover, how the charge storage occurs in the heterostructure can pave a path for the development of next-generation materials which can be achieved by an advanced synchrotron technique. Spectro-microscopy is one of the complimentary routes to understanding site and elemental-selective spatiodynamics mapping [3]. In this study, the heterostructure of $\text{MnO}_2/\text{CuO}_x$ was developed as a potential candidate for insight into the interfacial electronic structure and spatial mapping of the heterostructure by scanning transmission X-ray microscopy (STXM). For different reaction times, the heterostructure of MnCuO-10 (10 min) and MnCuO-40 (40 min) were developed. The electrochemical measurement showed a superior specific capacitance achieved in the heterostructure of MnCuO-40 than the other sample. To insight into the mechanism of charge storage, the STXM was performed on the heterostructure.

The optical density images and associated stack mapping STXM images for the O K-edge of (a) MnCuO-10 and (b) MnCuO-40 are shown in Fig.1. O K-edge of MnCuO-10 (red) is due to the hybridization of O 2p and Mn 3d- t_{2g} (a_1) and 3d- e_g (a_2) orbitals. The peak intensity (a_1) (green) is reduced owing to the gaining of charges by O from Mn at the interfacial

region. A feeble peak (a_3) is associated with the Cu_2O species. A broad peak (a_4) (red) was noticed because of the O 2p with the Mn 4sp character. The yellow region evidently shows CuO with minor Cu_2O species and the peak (a_2) (yellow) is due to the O 1s to O 2p that hybridized with the Cu 3d states and its intense peak (a_4) is because of the hybridization of O 2p-to-Cu 4sp which is higher than that of the other regions (green and red).

In the case of MnCuO-40, the peak (b_1) (green) is reduced due to the gaining of charges from Mn 3d- t_{2g} to O 2p. In other regions (red and yellow), the peaks b_2 and b_3 are noticed at higher energy which is similar to the spectral profile of CuO and Cu_2O respectively. The broad peak (b_4) is because of the hybridization of O 2p-to-Cu 4sp which is higher in the red region among other regions revealing the superior bulk contribution for electrochemical charge storage. Here, the interfacial and bulk regions favor the enhancement of charge storage in MnCuO-40 than the other sample.

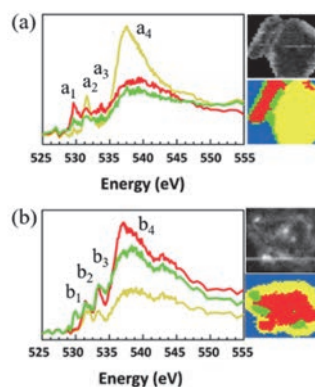


Fig. 1. Optical density images, stack-mapped STXM images, and the corresponding O K-edge XANES of (a) MnCuO-10 and (b) MnCuO-40 from different sites (green, red, and yellow).

[1] D. Sheberla *et al.*, Nat. Mater. **16** (2017) 220.

[2] N. Jabeen *et al.*, Adv. Mater. **29** (2017) 1.

[3] Y.H. Lo *et al.*, Sci. Adv. **5** (2019) 1.

BL4B

Photoresponse of C₆₀ on a Two-Dimensional van der Waals Material

Y. Nakayama^{1,2}, T. Yamada¹ and M.-K. Lin³¹Department of Pure and Applied Chemistry, Tokyo University of Science, Noda 278-8510, Japan²Institute for Molecular Science (IMS), Okazaki 444-8585, Japan³National Central University (NCU), Taoyuan 320317, Taiwan

Heterojunctions between semiconducting molecules are an essential structure for organic optoelectronic devices such as organic photovoltaics, where interactions at these interfaces were generally weak van der Waals couplings. In this work, a novel van der Waals heterojunction was formed by the deposition of a molecular semiconductor C₆₀ on ultra-thin PtTe₂, one of transition metal dichalcogenide materials, to elucidate its electronic structures and photoresponse.

PtTe₂ thin-film substrates were produced in NCU by procedures reported previously [1], and then were vacuum sealed for the shipment to IMS. These were exposed to the ambient conditions for 15-30 minutes prior to introduction into a vacuum load-lock chamber of the measurement system. The sample was annealed up to 200°C for 1 h in an ultra-high vacuum chamber connected to the photoelectron spectroscopy (PES) measurement system, and C₆₀ deposition was conducted in a step-by-step manner in a high vacuum condition. Photoelectron spectroscopy measurements were performed using a system called “acceptance-cone tunable electron spectrometer” [2] at BL4B, UVSOR. The excitation photon energy was set at 40 eV, and the spectra presented here were taken in a normal emission geometry at room temperature. The secondary electron cutoff (SECO) was measured under a negative sample bias of -9 V. In order to check the photoresponse of the sample, simulated Sunlight was introduced in the measurement system from a solar simulator (HAL-320, Asahi Spectra) during the PES measurements (Fig. 1) [3].

Figure 2 shows the evolution of the PES spectra by the growth of C₆₀. The highest occupied molecular orbital (HOMO) of C₆₀ was resolved even for the 1 nm-thick film suggesting physisorption of the molecules on the PtTe₂ surface without any strong electronic couplings. The C₆₀ HOMO peak exhibited an apparent shift to the deeper binding energy side in increasing the thickness. In contrast, the vacuum level position determined by the SECO spectra stayed substantially constant during the growth of C₆₀ except initial vacuum level shift (VLS) of approximately -0.1 eV by the deposition of 1 nm-thick C₆₀, indicating an absence of any band bending in the C₆₀ overlayers. Therefore, the shift in the C₆₀ HOMO peak is plausibly attributed to the image charge screening by the PtTe₂ substrate.

Figure 3 summarizes the photoresponse of the 20 nm-thick C₆₀ on the PtTe₂ substrate. The vacuum level went down upon illumination of the simulated Sunlight by about 15 meV, while the SECO measurements on the PtTe₂ substrate before C₆₀ deposition did not show any change (green plots). The parallel energy

shift of the C₆₀ HOMO peak suggests the occurrence of the photovoltaic effect at the heterojunction.

The authors thank Prof. H. Yoshida (Chiba Univ.) for lending the solar simulator used in this study.

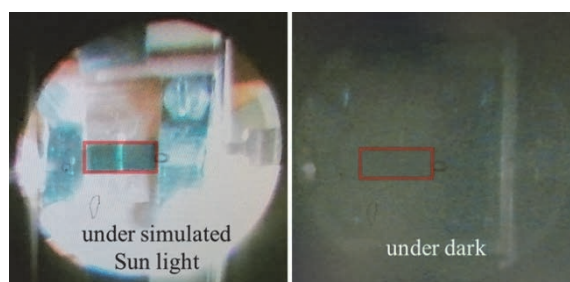


Fig. 1. Photo of the sample (marked in red).

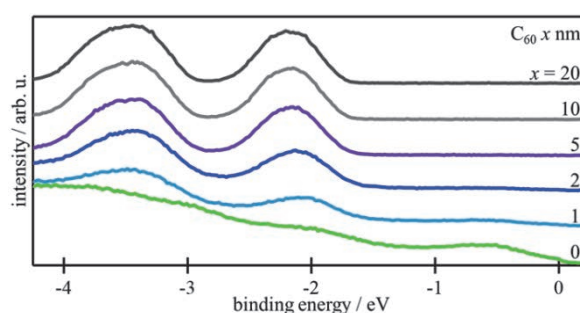


Fig. 2. PES spectra depending on the C₆₀ thickness.

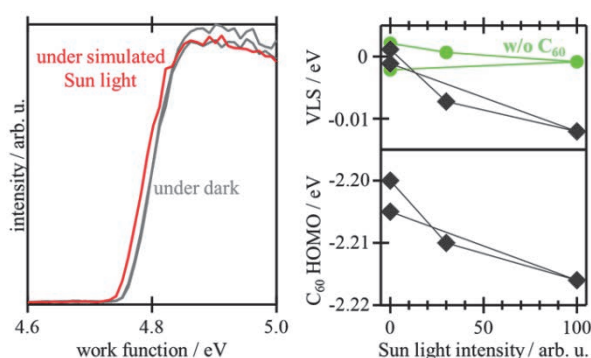


Fig. 3. (Left) SECO spectra of the 20 nm-thick C₆₀ under and without the simulated Sun light. (Right) VLS and the C₆₀ HOMO peak position plotted as a function of the simulated Sunlight intensity.

[1] M.-K. Lin *et al.*, Phys. Rev. Lett. **124** (2020) 036402.

[2] H. Yamane *et al.*, Rev. Sci. Instrum. **90** (2019) 093102.

[3] Y. Nakayama *et al.*, Adv. Energy Mater. **4** (2014) 1301354.

C K-edge XAS Measurement of Carbon-Containing Porous Silica

S. Dohshi

Osaka Research Institute of Industrial Science and Technology 2-7-1, Ayumino, Izumi, Osaka 594-1157, Japan

Compared to incandescent and fluorescent lamps, white LEDs are more environmentally friendly because they consume less power, last longer and contain no toxic substances such as mercury [1]. As a result, white LEDs have become increasingly popular in recent years. Currently, there are various methods used to create white LEDs, including the use of blue LEDs to illuminate yellow phosphors, a combination of LEDs of the three primary colors of light (red, green, and blue), or near-ultraviolet LEDs to illuminate red, green, and blue phosphors. However, these techniques are not capable of producing a continuous emission spectrum in the visible light region, which can make objects appear artificial when viewed under natural lighting conditions. Recently, mesoporous silica/resol composites were prepared by the addition of a resol solution to mesoporous silica, followed by heat treatment to prepare mesoporous silica/carbon composites. Silica/carbon composites could be also synthesized by heat treatment of rice husk. These composites were reported to exhibit continuous emission spectra in the visible light region, resulting in white emissions. These emissions are attributed to the formation of Si-C and/or Si-O-C bonds in silica. Moreover, both graphene and amorphous carbon are known to emit visible light when irradiated with UV light [2].

In addition, carbon-containing porous silica was synthesized by calcination of the denatured collagen/silica composite at 600°C for a predetermined time in air. Upon excitation with ultraviolet light, this carbon-containing porous silica emitted white light with a continuous emission spectrum throughout the visible light region [3, 4].

Several spectroscopic techniques such as UV-vis absorption, FT-IR and XPS measurements have been used to investigate the presence of carbon in porous silica, but none have been able to provide a clear explanation. This is believed to be due to the extremely low carbon content. In the present study, X-ray absorption spectroscopy, which can detect even trace amounts of carbon, was used to investigate the presence of carbon in porous silica.

C K-edge XAS measurement was performed at BL4B. The powder sample was fitted onto indium foil. The measurement was performed by fluorescence mode

(using SDD detector).

Figure 1 shows the C K-edge X-ray absorption spectra (XAF) of graphite and SiC as reference samples, and carbon-containing porous silica with different carbon contents. It is observed that the spectra of the carbon-containing porous silica differ from that of graphite and resemble that of SiC. These findings suggest that the carbon in the carbon-containing porous silica forms Si-C or Si-O-C bonds, and the white emission is a result of the presence of these bonds.

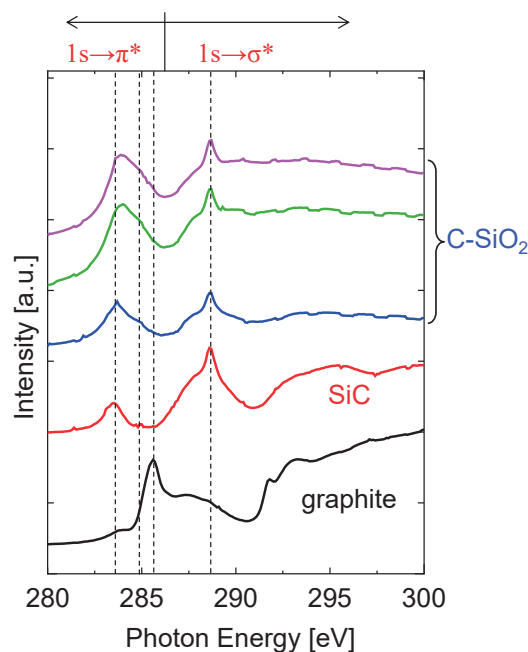


Fig. 1. C K-edge X-ray absorption spectra of graphite and SiC as reference samples, and carbon-containing porous silica with different carbon contents.

- [1] T. Justel, H. Nikol and C. Ronda, *Angew. Chem. Int. Ed.* **37** (1998) 3084.
- [2] Y. Ishikawa *et al.*, *Jpn. J. Appl. Phys.* **51** (2012) 01AK02.
- [3] S. Dohshi, *J. Soc. Leather Technol. Chem.* **95** (2011) 200.
- [4] S. Dohshi *et al.*, *J. Soc. Mater. Sci., Jpn.* **68** (2019) 549.

BL4B

Mg $L_{2,3}$ -Edge and Al $L_{2,3}$ -Edge XAS of $MgAl_2O_4$ Induced on Swift Heavy Ion Irradiations

S. Yoshioka¹, E. Kobayashi² and K. Okudaira³¹*Department of Applied Quantum Physics and Nuclear Engineering, Kyushu University, Fukuoka 819-0395, Japan*²*Kyushu Synchrotron Light Research Center, Saga 841-0005, Japan*³*Graduate school of Advanced Integration Science, Chiba University, Chiba 263-8522, Japan*

Magnesium aluminate oxide ($MgAl_2O_4$) is one of the common spinel compounds. Since it shows a variety of interesting physical and chemical properties, its microstructure has been extensively investigated. A cationic disordered $MgAl_2O_4$ spinel is represented by the formula of $[Mg_{1-x}Al_x](Mg_xAl_{2-x})O_4$, where the square brackets and the parentheses denote the tetrahedral and octahedral sites, respectively. The variable x is called the inversion parameter, which quantifies the cation disorder. Radiation with swift heavy ions (SHIs) interacts with materials and causes the structural change. It is therefore applied to material processing, modifications, etc. SHI irradiation provides high energy deposition through electronic stopping to the materials. SHIs in insulating solid materials are known to leave trails of damage along the ion path with a diameter of several nanometers. Structural change related to the cationic disorder has been also observed in $MgAl_2O_4$ with SHI irradiation using transmission electron microscopy observation. In this study, we clarify local coordination of each cation element, on which we conducted synchrotron radiation-based X-ray analysis.

Polycrystalline samples of $MgAl_2O_4$ were used in this study. These specimens were irradiated with 200 MeV Xe ions to fluences of $1 \times 10^{13} \text{ cm}^{-2}$ at the H1 beamline of the tandem ion accelerator facility in the Japan Atomic Energy Agency (JAEA)-Tokai. At the beginning of each paragraph, two space characters should be inserted as an indent. Mg $L_{2,3}$ -edge and Al $L_{2,3}$ -edge XANES measurements were performed at the BL4B beamline of UVSOR Okazaki, Japan, using the total electron yield method (TEY). A grating monochromator gives Mg $L_{2,3}$ -edge and Al $L_{2,3}$ -edge in energy regions 40 – 60 eV and 60 – 80 eV, respectively. The samples were set with their surface perpendicular to the incident X-ray beam. All measurements of XANES spectra were carried out in vacuum of 1×10^{-5} Pa at room temperature.

Figure 1 show the Al $L_{2,3}$ -edge XANES spectra of $MgAl_2O_4$ together with the spectra of Al_2O_3 as reference.

Compared to the spectrum of Al_2O_3 , the spectrum of $MgAl_2O_4$ was broader and the energy positions of main peaks were clearly different. The spectral differences indicated that the local structure of Al in $MgAl_2O_4$ were relatively scattered. Detailed analyses on the local environment of Al and Mg in the $MgAl_2O_4$ are in progress by combined use of the XANES and the first principles band structure calculations.

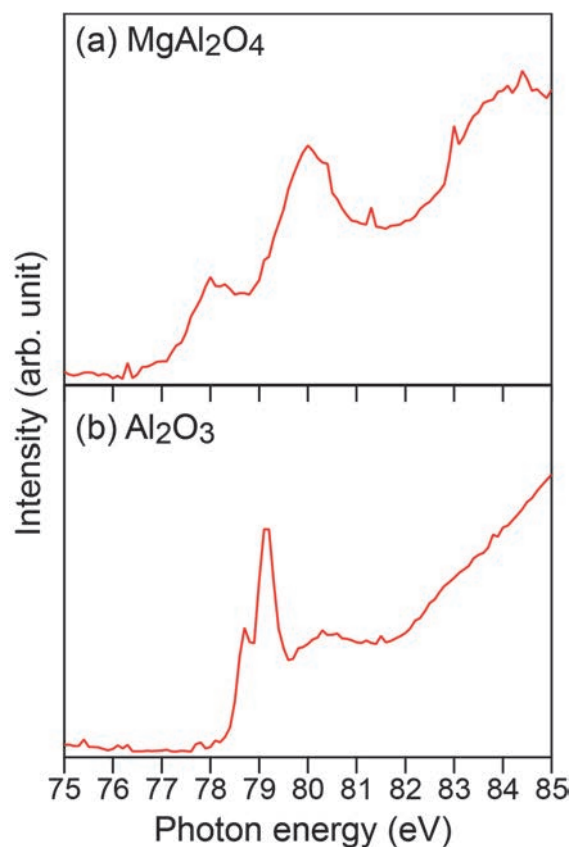


Fig. 1. Al $L_{2,3}$ -edge XANES spectra of $MgAl_2O_4$ (a) and Al_2O_3 (b).

Observation of Electronic Structure of THPB/Cu(111)

H. Yamazaki¹, R. Moue¹, S. Kera², K. Fukutani², S. Makita² and K. Kanai¹

¹*Department of Physics, Faculty of Science and Technology, Tokyo University of Science,
2641 Yamazaki, Noda, Chiba 278-8510, Japan*

²*UVSOR Synchrotron Facility, Institute for Molecular Science, Okazaki 444-8585, Japan*

Topological flat bands (TFBs) exhibit exotic Bloch states with negligible band dispersion due to destructive interference of the Bloch wave function. It is known that TFBs appear in lattices with specific symmetries, such as Kagome-lattice. The TFB state is strongly localized, so that electron correlation effects have a decisive influence on the electron systems. As a result, many-body quantum phases are theoretically predicted to be realized with TFBs, exhibiting molecular quantum Hall effect, ferromagnetism and superconductivity.

So far, TFB has mostly been observed in materials with layered structures, but in these materials, it is difficult to selectively observe contributions from a single layer. To avoid this problem, this study focuses on materials with a monolayer structure, called MOFs, which consist of coordination bonds between metal atoms and organic molecules. In fact, it has been reported that TFBs were successfully observed in a two-dimensional hydrogen-bonded organic framework with 1,3,5-tris(4-hydroxyphenyl)benzene (THPB) adsorbed on Au(111) (THPB/Au(111)) [1]. Therefore, in this study, THPB/Cu(111) has been similarly investigated.

Copper is known to have high catalytic activity and is easily deposited on the surface as an adatom upon heating, which is known to combine with THPB to produce MOFs. The experiments were carried out at BL4B to fabricate THPB/Cu(111), followed by characterization of structure and electronic structure by LEED, XPS and ARPES. The LEED results showed that THPB/Cu(111) produces a well-ordered structure upon heating to 180°C. Detailed elemental composition obtained by XPS showed that heating leads to dehydrogenation of the hydroxy groups of THPB, breaking the intermolecular hydrogen bonds. However, this experiment did not confirm whether the deposited Cu and THPB actually bonded to form MOFs. As TFBs were not observed by ARPES this time, more detailed characterization of the chemical state and direct observation of the band structure of THPB/Cu(111) are planned in the future.

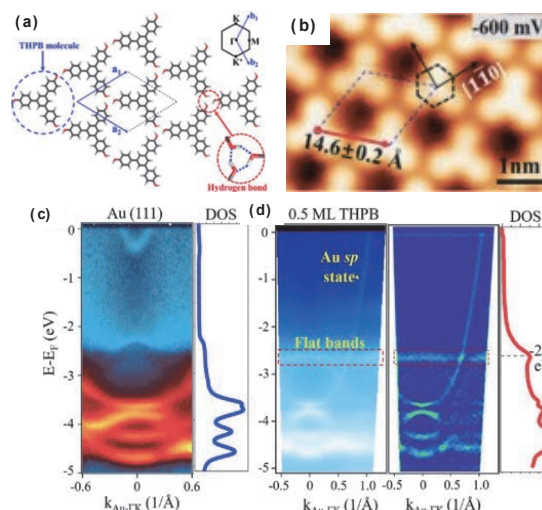


Fig. 1. THPB/Au(111) structure and band structure [1]
(a) Structure of THPB film. (b) STM image of THPB/Au(111). (c), (d) ARPES results of THPB/Au(111).

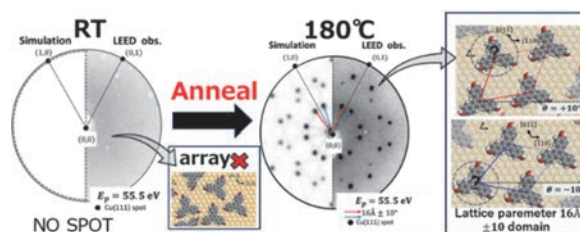


Fig. 2. LEED results for THPB/Cu(111).

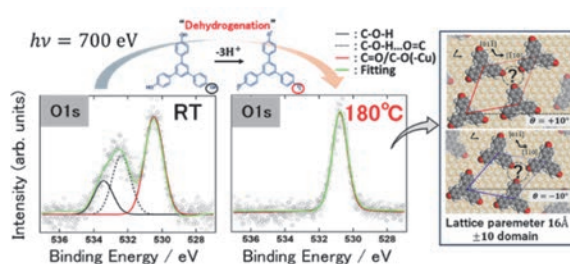


Fig. 3. XPS results for THPB/Cu(111).

[1] M. Pan *et al.*, Phys. Rev. Lett. **130** (2023) 036203.

BL4B

Photoelectron Measurements for Rubrene Derivatives on Rubrene Single Crystals

T. Yamada¹, N. Ohtsuka², N. Momiyama² and Y. Nakayama^{1,2}

¹Department of Pure and Applied Chemistry, Tokyo University of Science, Noda 278-8510, Japan

²Institute for Molecular Science, Okazaki 444-8585, Japan

Charge carrier transport in organic semiconductor materials with high mobility, such as single-crystal 5,6,11,12-tetraphenylanthracene (rubrene), is known to be the “band transport” [1,2]. A derivative of rubrene, 5,12-bis(4-methylphenyl)-6,11-bis[4-(trifluoromethyl)phenyl]anthracene (fm-rubrene), was found to form a highly crystalline interface on rubrene [3], which gave rise to an expectation that the concomitance of both band transport and highly crystalline interfaces could be achieved. Therefore, we set the measurement of the valence band structures of single-crystalline fm-rubrene thin films on the rubrene single-crystal substrates as the research objective. On the other hand, charge carrier transport in molecular solids is generally affected by molecular vibrations and phonons [4], which can be deduced from the change in the electronic structures upon cooling. In this study, we tracked the demonstration of temperature-dependent changes in photoemission spectra of fm-rubrene thin-films on the rubrene single crystals.

The rubrene single crystals used were prepared by a physical vapor transport method, and fm-rubrene was deposited onto the rubrene substrates to a thickness of 20 nm at a deposition rate of 0.40 nm/s in a vacuum load-lock chamber directly connected to the photoelectron spectroscopy (PES) measurement chamber. PES measurements were performed at an excitation energy of 25 eV at BL4B, UVSOR. The photoelectrons emitted to a polar-angle θ range of -15 to 15 degrees from the surface normal were collected by an electron analyzer (A1, MB-Scientific). All photoelectron spectra shown here are photoelectron signals integrated in the θ direction. The secondary electron cutoff (SECO) was measured under a negative sample bias of -9.16 V. All PES measurements were performed with the irradiation of laser light (wavelength of 405 nm) to suppress sample charging due to the photoelectron emission [5]. The sample temperature was cooled from room temperature to 60 K for tracking the change in the PES spectra.

Figures 1 and 2 show the PES spectra in the valence band and the SECO regions, respectively, of a fm-rubrene/rubrene sample taken at different temperatures. The spectra shifted to the lower energy side upon cooling for both the valence band and the SECO regions. As shown in Fig. 2, the slope of the SECO became less steep upon cooling, suggesting a possible occurrence of the sample charging. Although the energy dispersion of the valence bands was hardly observed by the angle-resolved measurements on the present sample plausibly because fm-rubrene formed disordered

overlayers in the present condition, we are planning to prepare single-crystalline fm-rubrene at a lower deposition rate to align the crystal orientation to the single-crystal rubrene [3], and to conduct angle-resolved PES measurements for demonstrating the valence band structure of fm-rubrene in future.

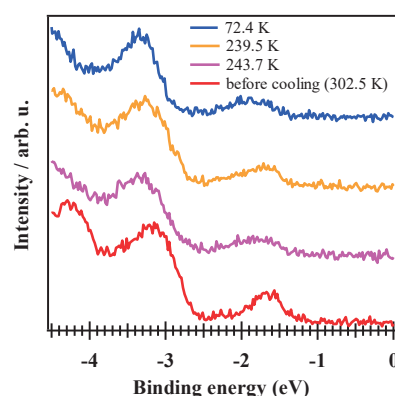


Fig. 1. Temperature-dependence of the PES spectra of the fm-rubrene/rubrene sample in the valence band region.

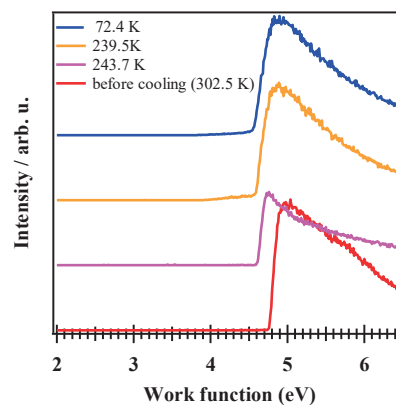


Fig. 2. SECO spectra of the fm-rubrene/rubrene sample taken at different cooling temperatures.

- [1] V. Podzorov *et al.*, Phys. Rev. Lett. **95** (2005) 226601.
- [2] D.A. da S. Filho, E.-G. Kim and J.-L. Bredas, Adv. Mater. **17** (2005) 1072.
- [3] K. Takahashi *et al.*, J. Phys. Chem. Lett. **12**, (2021) 11430.
- [4] G. Schweicher *et al.*, Adv. Mater. **31** (2019) 1902407.
- [5] S. Machida *et al.*, Phys. Rev. Lett. **104** (2010) 156401.

Local Environment of Dopants in (Co, Nb) and (Mn, Nb) Co-Doped TiO₂

H. Murata, Y. Nagatomo and A. Nakahira

Department of Materials Science, Osaka Metropolitan University, Sakai 599-8531, Japan

Titanium dioxide (TiO₂) is one of the typical fine ceramic materials. Its applications are widespread as a pigment, photo-catalyst and transparent conductor. Because the bandgap of TiO₂ is in the ultraviolet region, various kinds of dopants have been investigated to induce visible light absorption. However, the solid solution limit of most of elements in TiO₂ is small. Recently, we reported (Fe, Nb) co-doped TiO₂ has a large solid solution limit above 50 mol% of Ti due to charge compensation of Fe³⁺ and Nb⁵⁺. The shrinkage of bandgap in these materials induced visible-light response and enhanced photo-catalytic activity. The advantages of these materials are attributed to the weak d-d transition of Fe³⁺ at the octahedral site. In order to develop other elements, it is necessary to clarify the local environments and valence states of dopants in co-doped TiO₂. In this study, local environments and valence states of dopants in (Co, Nb) and (Mn, Nb) co-doped TiO₂ were investigated by X-ray absorption near edge structure (XANES).

(Co, Nb) and (Mn, Nb) co-doped TiO₂ samples were prepared by a conventional solid-state reaction method using TiO₂, Co₃O₄, Mn₂O₃ and Nb₂O₅ as starting materials. The starting materials were ground and mixed using an alumina mortar and pestle. They were calcined in an alumina crucible at 1200 °C in air for 6 h. The samples were again ground and mixed by the mortar and pestle. Then, they were calcined in an alumina crucible at 1200 °C in air for 6 h.

Obtained samples were characterized using X-ray diffraction (XRD), Ultraviolet-Visible light spectroscopy (UV-Vis) and X-ray absorption near edge structure (XANES). Co-L₃ and Mn-L₃ XANES spectra were collected using the total electron yield method with a sample current at BL4B in UVSOR (Okazaki, Japan). The X-ray beam was monochromated using gratings with groove densities of 800 l/mm. The samples were mounted on carbon tapes. Photo-catalytic activity of the samples was evaluated by degradation of methylene blue (MB).

The (Co, Nb) co-doped TiO₂ samples show reddish color. The XRD patterns of (Co, Nb) co-doped TiO₂ samples were confirmed to be rutile-type TiO₂. The maximum solid solution limit of Co in TiO₂ was attained as Ti_{1-x}(Co_xNb_{2x})O₂, which was more than 50 mol% with respect to Ti. Co-L₃ XANES of the samples showed that Co in (Co, Nb) co-doped TiO₂ is Co²⁺ at octahedral sites.

(Mn, Nb) co-doped TiO₂ samples exhibit deep brown color, which can be attributed to the spin-allowed d-d transition of Mn³⁺ at octahedral site. The XRD patterns

of the samples were assigned to rutile-type TiO₂ with peak shifts. The solid-solution of Mn in TiO₂ depends on the amounts of Nb but the Mn:Nb ratio at which the solid solution limit of Mn in TiO₂ is maximum is between 1:1 and 1:2, which implies a mixed valence state of Mn.

Figure 1 shows a Mn-L₃ XANES spectrum of Ti_{0.85}Mn_{0.06}Nb_{0.09}O₂. The spectrum of the sample has similarity to that of Mn²⁺ at octahedral site, but it also contains other components corresponding to Mn³⁺ at octahedral site. This result confirmed that both Mn²⁺ and Mn³⁺ are present in the samples, which differs from the case of (Fe, Nb) and (Ni, Nb) co-doped TiO₂ reported elsewhere. [1, 2]

MB degradation tests shows that the (Mn, Nb) co-doped TiO₂ samples have weaker photo-catalytic activity than pristine rutile-type TiO₂, which means that d-d transition of Mn³⁺ at the octahedral site does not contribute to photo-catalytic activity. This results are useful to design photo-catalytic and pigment materials.

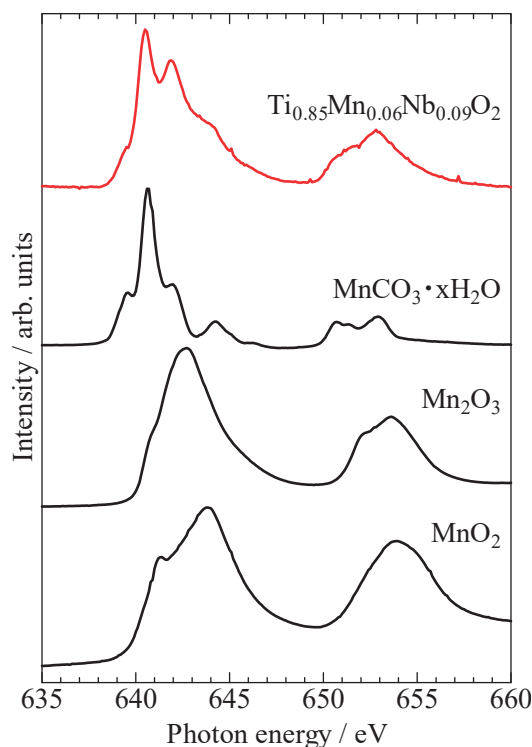


Fig. 1. Mn-L₃ XANES of Ti_{0.85}Mn_{0.06}Nb_{0.09}O₂ and reference samples.

- [1] T. Nishio *et al.*, J. Ceram. Soc. Jpn. **131** (2023) 712.
[2] H. Murata *et al.*, UVSOR Activity Report **50** (2023) 71.

BL4B

Soft X-ray Absorption Study of Semiconductor Photocatalysts under UV Light Irradiation

T. Yoshida¹, N. Ichikuni², H. Onishi^{3,4} and Y. H. Chew³

¹Research Center for Artificial Photosynthesis, Osaka Metropolitan University, Osaka 558-8585, Japan

²Graduate School of Engineering, Chiba University, Chiba 263-8522, Japan

³School of Science, Kobe University, Kobe 657-8501, Japan

⁴Division of Advanced Molecular Science, Institute for Molecular Science, Okazaki 444-8585, Japan

Material conversion on semiconductor photocatalysts has been intensively studied worldwide. Downhill reactions, in which the Gibbs free energy decreases during the conversion of reactants to products, have been successfully integrated into our society [1]. Artificial photosynthesis, a category of uphill reactions involving the oxidation of water, is being developed for societal implementation in the near future [2]. In addition, fundamental studies are being conducted to uncover new scientific discoveries related to light-driven, efficient materials conversion [3].

Here, in collaboration with Prof. Hiroshi Iwayama of UVSOR, we apply soft X-ray absorption to the characterization of semiconductor photocatalysts under UV light irradiation for bandgap excitation. A series of metal oxide photocatalysts including sodium tantalate (NaTaO_3), strontium titanate (SrTiO_3), gallium oxide (Ga_2O_3), and titanium oxide (TiO_2) were investigated in two beam times in FY2023.

The photocatalyst particles were formed into disks of 7 mm diameter. The disks were placed in a vacuum chamber, irradiated with incident X-rays, and the fluorescent X-rays were detected with a silicon drift detector (SDD). The detector was capped with a 150 nm thick aluminum film (LUXEL, TF110) to minimize the contribution of stray UV light to the detector response (Fig. 1). The capping device is deposited at UVSOR. Users are encouraged to use the device when operating the SDD under UV or visible light irradiation.

Figure 2 shows a set of fluorescence yield spectra at the oxygen K-edge observed on an anatase TiO_2 photocatalyst (JRC-TIO-19 provided by the Catalysis Society of Japan) in the presence and absence of UV light provided by a Hg–Xe lamp (200 W).

In the oxygen K-edge, electron transition from $\text{O}1s$ to $\text{O}2p$ orbitals of TiO_2 particles was detected. The $\text{O}2p$ orbitals are hybridized with $\text{Ti}3d$ orbitals to form the conduction band in TiO_2 . The hybridized $\text{O}2p$ orbitals are thus split into t_{2g} and e_g levels, one at 531.5 eV and the other at 534.2 eV, according to the ligand field in TiO_6 octahedra.

The t_{2g} and e_g bands shifted to the low energy side under UV irradiation. The shifted bands induced differentiated forms in the difference spectrum shown at the bottom of Fig. 2. A possible reason for the band shifts is the conduction band partially filled with electrons excited across the band gap, where the oxidation state of some Ti cations decreased from 4+ to 3+.

The X-ray absorption of electronically excited metal oxides has been studied using ultrashort light pulses. Here, we showed that the absorption spectrum was also sensitive to steady light irradiation. This study was supported by JSPS KAKENHI (grant number 22H00344).

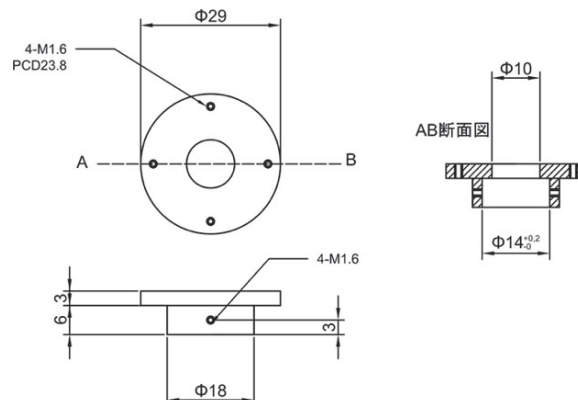


Fig. 1. A device capping the SDD with the aluminum filter for fluorescence yield detection of oxygen K-edge absorption spectrum under UV-light irradiation.

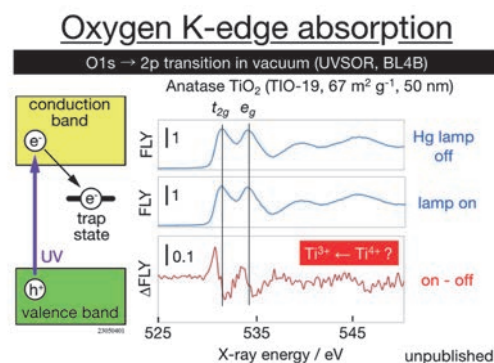


Fig. 2. Oxygen K-edge absorption spectrum of an anatase TiO_2 photocatalyst disk in the absence (upper blue spectrum) and presence (lower blue spectrum) of UV irradiation. The difference spectrum induced by the irradiation is shown in red color at the bottom.

- [1] A. Fujishima *et al.*, J. Photochem. Photobiol., C 1 (2000) 1.
- [2] H. Onishi, ChemSusChem 12 (2019) 1825.
- [3] C. Kranz and M. Wächter, Chem. Soc. Rev. 50 (2021) 1407.

Observation of Electronic Reconstruction in Kagome Superconductors

T. Kato¹, K. Nakayama¹, Y. Li^{2,3,4}, Z. Wang^{2,3,4}, S. Souma^{5,6}, K. Tanaka^{7,8}, T. Takahashi¹,
Y. Yao^{2,3} and T. Sato^{1,5,6,9,10}

¹Department of Physics, Graduate School of Science, Tohoku University, Sendai 980-8578, Japan

²Centre for Quantum Physics, Key Laboratory of Advanced Optoelectronic Quantum Architecture and Measurement (MOE), School of Physics, Beijing Institute of Technology, Beijing 100081, P. R. China

³Beijing Key Lab of Nanophotonics and Ultrafine Optoelectronic Systems,
Beijing Institute of Technology, Beijing 100081, P. R. China

⁴Material Science Center, Yangtze Delta Region Academy of Beijing Institute of Technology,
Jiaxing 314011, P. R. China

⁵Advanced Institute for Materials Research (WPI-AIMR), Tohoku University, Sendai 980-8577, Japan

⁶Center for Science and Innovation in Spintronics (CSIS), Tohoku University, Sendai 980-8577, Japan

⁷UVSOR Synchrotron Facility, Institute for Molecular Science, Okazaki 444-8585, Japan

⁸School of Physical Sciences, The Graduate University for Advanced Studies (SOKENDAI),
Okazaki 444-8585, Japan

⁹International Center for Synchrotron Radiation Innovation Smart (SRIS), Tohoku University,
Sendai 980-8577, Japan

¹⁰Mathematical Science Center for Co-creative Society (MathCCS), Tohoku University, Sendai 980-8578, Japan

Kagome lattice provides a fertile playground to explore exotic quantum phenomena originating from intriguing interplay between electron correlation and unique band topology, as exemplified by the coexistence of topological flat band, Dirac cone band, and van Hove singularities. Among kagome lattice materials, kagome metals AV_3Sb_5 ($A = K, Rb$, and Cs) [1] are recently attracting particular attention because of the experimental observations of fascinating properties such as possible unconventional superconductivity, charge density wave (CDW), and anomalous Hall effect. The CDW state of AV_3Sb_5 is characterized by three-dimensional lattice distortions with $2 \times 2 \times 2$ or $2 \times 2 \times 4$ periodicity. Its unconventional nature has been suggested by additional symmetry breakings inside the CDW phase. Examples include rotational symmetry breaking that is termed nematicity, additional translational symmetry breaking due to pair density wave, and time-reversal symmetry breaking. The origins of these symmetry breakings in AV_3Sb_5 are a central topic in the study of kagome lattice materials.

In this study, to search for the electronic signatures of the symmetry breakings in the CDW state, we have carried out high-resolution angle-resolved photoemission spectroscopy (ARPES) measurements of KV_3Sb_5 . High-quality single crystals of KV_3Sb_5 were grown by the self-flux method. High-resolution ARPES measurements were performed by using a MBS-A1 spectrometer at BL5U with linearly-polarized energy-tunable photons of 90-150 eV.

Figure 1 shows the second-derivative ARPES intensity at the Fermi level (E_F) measured at $T = 20$ K, well below T_{CDW} . Circular and hexagonal intensity distributions at the center and corner of the Brillouin zone, respectively, are the remnant Fermi surfaces. The former is of $Sb\ p$ orbital character and the latter is of $V\ d$ orbital character. In addition to these remnant Fermi

surfaces that are also recognized in the normal state above T_{CDW} , we found additional intensity distribution, i.e., a small pocket near the K point indicated by white dashed ellipse, which is not expected in the normal state band structure of KV_3Sb_5 [1]. This pocket shows a holelike character. According to recent studies, the formation of such hole pocket produces new nesting channel in the CDW state, possibly leading to additional symmetry breaking. To examine the validity of such a scenario, we have performed detailed temperature-dependent study across T_{CDW} and quantitative data analysis.

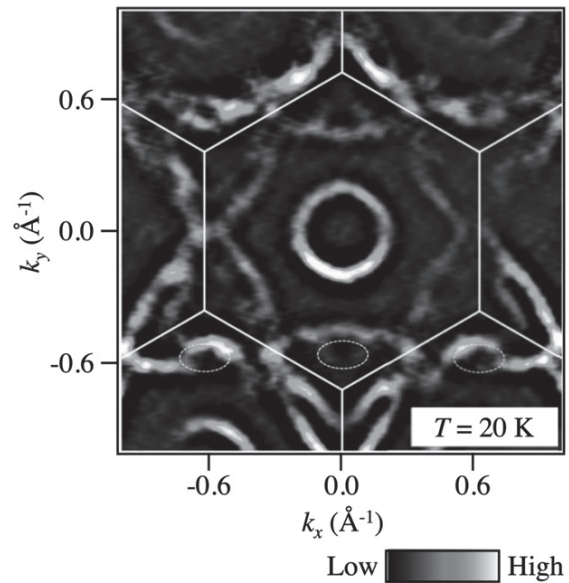


Fig. 1. Second-derivative ARPES intensity at E_F measured in the CDW state of KV_3Sb_5 .

[1] T. Kato *et al.*, Commun. Mater. 3 (2022) 30.

BL5U

ARPES Study of Monolayer Germanene Grown on Ag

T. Terasawa^{1,2}, S. Suzuki¹, D. Katsube³, S. Tanaka⁴ and K. Tanaka⁵

¹Advanced Science Research Center, Japan Atomic Energy Agency, Tokai 319-1195, Japan

²Institute of Industrial Science, The University of Tokyo, Meguro 153-8505, Japan

³Cluster for Pioneering Research, RIKEN, Wako 351-0198, Japan

⁴SANKEN, The Institute of Scientific and Industrial Research, Osaka University, Ibaraki 567-0047, Japan

⁵UVSOR Synchrotron Facility, Institute for Molecular Science, Okazaki 444-8585, Japan

Germanene, a two-dimensional honeycomb lattice composed of Ge atoms in one monolayer, has attracted attention because the ultrahigh carrier mobility and bandgap are expected to coexist in germanene [1]. To prove the existence of such fascinating characteristics of germanene, the band structure of germanene should be revealed to have the linear band dispersion (and Dirac cone) and the bandgap, which would be realized by angle-resolved photoemission spectroscopy (ARPES) on high-quality samples. However, the ARPES intensity map of germanene on Ag(111) single crystal substrates showed diffuse bands, which is attributed to the Ag and Ge hybridization and the quality of the sample [2]. In 2018, J. Yuhara *et al.* reported that the annealing and cooling processes of Ag(111) thin films on Ge(111) substrates resulted in germanene segregation [3]. In their report, scanning tunneling microscopy images showed an R30 epitaxial relation between germanene and Ag and a $7\sqrt{7} \times 7\sqrt{7}$ R19.1 superlattice, indicating the long-range order and weak interaction. Consequently, the ARPES measurements of the germanene on the Ag(111) surface have become available.

Here, we report the ARPES measurement on the segregated germanene on Ag surfaces. The Ag thin films were deposited on Ge(111) substrates in Japan Atomic Energy Agency. The sample was introduced in the load lock chamber of the BL5U beamline without any preparations. The cycles of the Ar⁺ sputtering and annealing of the samples resulted in a clean surface. After the annealing at 500°C for 30 min, germanene formed on the sample surface, as confirmed by low-energy electron diffraction. For comparison, the corrugated Ag₂Ge alloy, the so-called striped phase, was prepared by annealing the samples at 300 °C for 30 min. The ARPES measurements were carried out at 8 K using the incident light energy of 40-110 eV and the horizontal polarization. The + θ and - θ rotation of the sample corresponded to the P- and S- polarization, respectively.

Figure 1(a) shows the ARPES intensity map using 60 eV and P-polarization for Γ -M_{Ag} (equal to Γ -K_{germanene} due to the R30 epitaxial relation) of the striped phase. All the bands are assigned to those in the previous reports of the striped phase [4]. In Fig. 1(b), on the other hand, the electron pocket-like structure around the Γ point was observed for germanene samples, which is consistent with the germanene band on Al(111) [5] and entirely different from that of the striped phase. We thus concluded that we observed the band structure

of the germanene segregated on the Ag(111) thin film. Unfortunately, the Ag bulk bands overlapped on the K point of the germanene, as shown in Fig. 1(b). Further discussion is required to exclude the effect of the Ag bulk band and to reveal the electronic structure of germanene.

In summary, we carried out the ARPES measurement of germanene segregated on Ag(111) thin films deposited on Ge(111) substrates. The ARPES intensity maps showed that the germanene band structure, different from that of the striped phase, was observed. Further experiments and discussion are required to reveal whether the germanene band structure has linear band dispersion and bandgap.

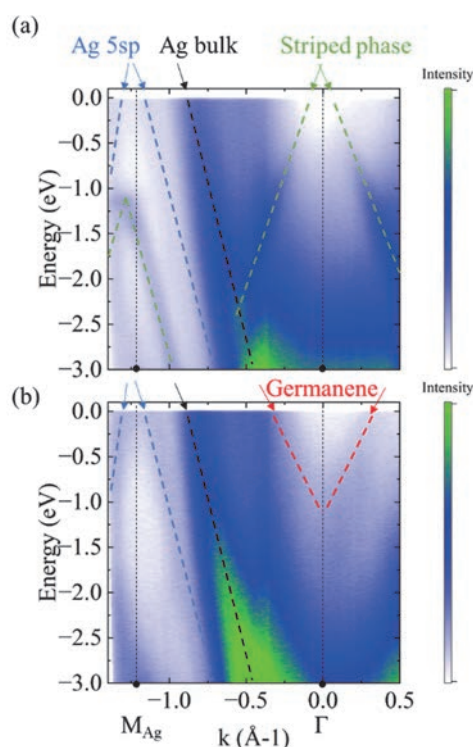


Fig. 1. (a) ARPES intensity map of striped phase and (b) germanene segregated on Ag thin film deposited on Ge(111) substrates.

- [1] C. C. Liu *et al.*, Phys. Rev. B: Condens. Matter **84** (2011) 195430.
- [2] C. H. Lin, *et al.*, Phys. Rev. Mater. **2** (2018) 024003.
- [3] J. Yuhara *et al.*, ACS Nano **12** (2018) 11632.
- [4] E. Golias *et al.*, Phys. Rev. B: Condens. Matter **88** (2013) 075403.
- [5] J. Yuhara *et al.*, 2D Mater. **8** (2021) 045039.

Pure Electron-Doping Effect in the T'-type Cuprate High-Temperature Superconductors Studied by Angle-Resolved Photoemission Spectroscopy

M. Miyamoto¹, M. Horio¹, K. Moriya², A. Takahashi³, K. Tanaka⁴, Y. Koike³,
T. Adachi² and I. Matsuda¹

¹*Institute for Solid State Physics, University of Tokyo, Kashiwa, Chiba 277-8581, Japan*

²*Department of Engineering and Applied Sciences, Sophia University, Tokyo 102-8554, Japan*

³*Department of Applied Physics, Tohoku University, Sendai 980-8579, Japan*

⁴*UVSOR Synchrotron Facility, Institute for Molecular Science, Okazaki 444-8585, Japan*

Although it has been widely believed that carrier doping is necessary to induce superconductivity in cuprates, electron-doped cuprates $\text{RE}_{2-x}\text{Ce}_x\text{CuO}_{4+\delta}$ (RE: rare earth) with so-called T'-type structure do not show superconductivity without reduction annealing [1,2]. Previous studies suggested that annealing removes excess impurity oxygen atoms at the apical site [3,4]. Stronger annealing, which implies more thorough removal of apical oxygen impurities, leads to higher transition temperature T_c [5]. Horio *et al.* found that efficient annealing dramatically suppresses the pseudogap which is believed to compete with superconductivity [6]. The superconducting properties of the T'-type cuprates thus strongly depend on the degree of annealing.

On the other hand, recent studies have pointed out the importance of electron doping through annealing. ARPES studies revealed the increase of electron concentrations probably due to the creation of oxygen deficiencies in the regular sites by reduction annealing [6,7]. Song *et al.* [8] reported that the pseudogap depends only on the electron doping level after sufficient reduction annealing. Therefore, the key factor of the pseudogap and superconductivity in electron-doped cuprates remains elusive.

In order to separate the effects of annealing and electron doping on the pseudogap, we previously carried out angle-resolved photoemission spectroscopy (ARPES) measurements of the electron-doped cuprate $\text{Pr}_{1.22}\text{La}_{0.7}\text{Ce}_{0.08}\text{CuO}_4$ with doping electrons by dosing K without changing the crystal structure. Consequently, we found a signature of pseudogap suppression [9]. This time, we improved the measurement procedure to evaluate the Fermi surface and the pseudogap from a single sample within limited measurement time.

We have carried out ARPES measurements on the as-grown $\text{Pr}_{1.22}\text{La}_{0.7}\text{Ce}_{0.08}\text{CuO}_4$ sample and the annealed $\text{Pr}_{1.2}\text{La}_{0.7}\text{Ce}_{0.10}\text{CuO}_4$ at BL5U at $T=20$ K. After the K deposition, the Fermi surface of the as-grown sample originally disconnected by the pseudogap opening became almost continuous like that of the annealed sample. From the Fermi surface area, the electron concentration after K deposition amounts to ~ 0.20 , which is significantly larger than the Ce concentration of 0.08. The concomitant increase and suppression of the electron concentration and pseudogap, respectively, suggests their intimate connection, though further

quantitative evaluation is necessary to conclude the influence of apical oxygen removal through reduction annealing.

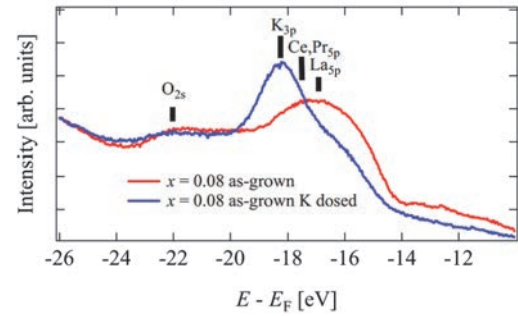


Fig. 1. Core-level photoemission Spectra of the as-grown $\text{Pr}_{1.22}\text{La}_{0.7}\text{Ce}_{0.08}\text{CuO}_4$. After potassium deposition, the K 3p peak is enhanced, which indicates K absorption on the surface of the sample.

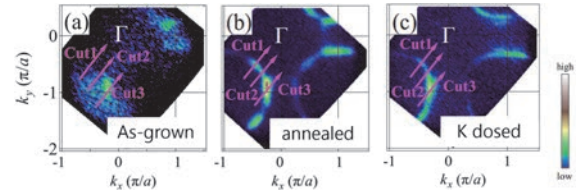


Fig. 2. Fermi surface maps for (a) the as-grown $\text{Pr}_{1.22}\text{La}_{0.7}\text{Ce}_{0.08}\text{CuO}_4$ sample, (b) the annealed $\text{Pr}_{1.2}\text{La}_{0.7}\text{Ce}_{0.10}\text{CuO}_4$ sample, and (c) the K-dosed as-grown $\text{Pr}_{1.22}\text{La}_{0.7}\text{Ce}_{0.08}\text{CuO}_4$ sample. After K dosing, the Fermi surface of the as-grown sample becomes circular like that of the annealed sample.

- [1] Y. Tokura *et al.*, *Nature* **337** (1989) 345.
- [2] H. Takagi *et al.*, *Phys. Rev. Lett.* **62** (1989) 1197.
- [3] P. Radaelli *et al.*, *Phys. Rev. B: Condens. Matter* **49** (1994) 15322.
- [4] A. Schultz *et al.*, *Phys. Rev. B: Condens. Matter* **53** (1996) 5157.
- [5] J. Kim *et al.*, *Physica C* **209** (1993) 381.
- [6] M. Horio *et al.*, *Nat. Commun.* **7** (2016) 10567.
- [7] M. Horio *et al.*, *Phys. Rev. B: Condens. Matter* **98** (2018) 020505.
- [8] D. Song *et al.*, *Phys. Rev. Lett.* **118** (2017) 137001.
- [9] M. Miyamoto *et al.*, *UVSOR Activity Report* **50** (2023) 98.

BL5U

Surface Electronic State of Single Crystal Mg Surface Treated by Ar Sputtering and Annealing

T. Akatsuka, H. Miyazaki, T. Tokunaga and K. Hagihara

Department of Physical Science and Engineering, Nagoya Institute of Technology,
Gokiso-cho, Showa-ku, Nagoya, Aichi 466-8555, Japan

Mg alloys with transition metals, TM, and rare earth, RE, elements, Mg–TM–RE, with a long-period stacking structure (LPSO structure) developed by Kawamura *et al.* have gained increasing attention as next-generation lightweight structural materials with high strength compared to Al alloys and flame resistance that overcomes the low ignition temperature of Mg alloys^[1, 2]. The superior functionality of Mg–TM–RE is thought to be due to the formation of localized clusters of TM–RE in Mg, which affect the electronic structure of the parent phase Mg. Although the electronic structure of Mg–TM–RE has been observed by Miyazaki *et al.* using hard X-ray photoemission spectroscopy to elucidate its functionality, the detailed electronic structure near the Fermi level, which is closely related to the functionality, has not been observed^[3]. Photoelectron spectroscopy is a very promising method to directly observe the electronic structure that is the mechanism of the functionality, but it is necessary to establish a method to clean the surface in order to observe the electronic structure near the surface. Therefore, in this study, we observed the electronic structure of the Mg surface by Ar⁺ sputtering and annealing conditions in order to investigate the process of surface cleaning in Mg single crystal.

Mg (0001) single crystals were prepared by the Czochralski method. Mg (0001) single crystals were polished so that the surfaces were mirror-like. The orientation was confirmed by the back Laue method, and the sample was installed in the 3D angle-resolved photoemission spectrometer, UVSOR BL-5U. Photoelectron spectroscopy measurements were performed at 20 K. Ar⁺ sputtering and annealing were performed in the sample preparation chamber, and after surface treatment, the sample was immediately transported to the measurement chamber under ultra-high vacuum.

Initially, we attempted to remove the surface oxide layer of MgO on the Mg (0001) single crystal by repeated Ar⁺ sputtering for 30 mins with acceleration voltage of 3 kV and $P_{\text{Ar}} = 1.0 \times 10^{-4}$ Pa and annealing for 30 mins at 450 °C, but this did not remove. Therefore, we decided to perform Ar⁺ sputtering and annealing simultaneously. Figure 1 shows the photoelectron spectra of Mg 2p core electrons of Mg (0001) single crystals during Ar⁺ sputtering and annealing at 5, 10, and 15 hours. MgO at the binding energy $E_B = 52$ eV and the Mg 2p peak attributed to Mg near $E_B = 50$ eV are identified; the Mg 2p peak attributed to MgO gradually decreased with the sputtering and annealing

processing time. Finally, the surface oxide layer, was removed significantly compared to Mg, about 5 %. However, the Mg-attributed peaks split into two, suggesting the presence of another Mg state different from Mg-metal. Figure 2 shows the angle-resolved photoelectron spectrum after removal of the MgO surface oxide layer; a distinct energy dispersion due to the bulk state of Mg is observed, indicating that an intrinsic bulk electronic state has been obtained.

This study allowed us to determine the conditions for the removal of the surface oxide layer in Mg single crystals. However, since there are two components of the Mg core electron state, it is clear that it will be necessary to determine the further optimal processing conditions in the future.

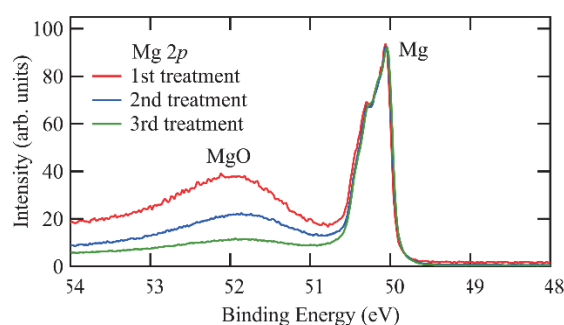


Fig. 1. Core-level photoelectron spectra of Mg 2p for various surface treatment conditions in Mg (0001) single crystal measured at $h\nu = 120$ eV.

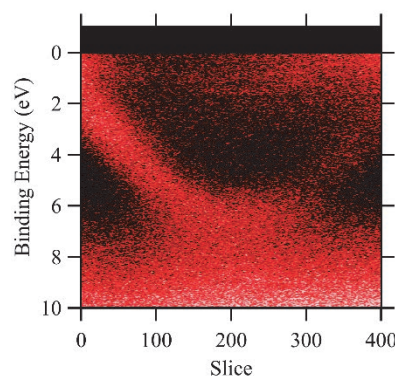


Fig. 2. Intensity mapping of angle-resolved photoemission spectra in Mg (0001) single crystals measured at $h\nu = 60$ eV.

- [1] M. A. Inoue *et al.*, J. Mater. Res. **16** (2001) 1894.
- [2] Y. Kawamura *et al.*, Mater. Trans. **42** (2001) 1172.
- [3] H. Miyazaki *et al.*, Mater. Trans. **64** (2023) 1194.

Measurement and Development of the Analytical Method to Determine the 3D Fermi Surface of TiSe₂

S. Tanaka

SANKEN, Osaka University, Ibaraki 464-0056, Japan

In the reciprocal space of electron momentum, the Fermi surface forms boundaries that separate the occupied and empty states. Its shape (e.g., anisotropic or isotropic) in the momentum space strongly affects the dynamical properties of matter. Therefore, methods to detect the Fermi surface are highly desirable. The photon energy dependent angle resolved photoelectron spectroscopy (ARPES) is now considered to be the most direct and convenient.

In the ARPES, the photoelectron momentum parallel to the sample surface is given by

$$k_x = \frac{\sqrt{2m_e E_k}}{\hbar} \sin \theta \cos \phi, k_y = \frac{\sqrt{2m_e E_k}}{\hbar} \sin \theta \sin \phi.$$

In the photon-energy dependent ARPES, it is assumed that the final state of the photoelectron emission is the free-electron state, and the momentum of the emitted electron can be determined as

$$k_z = \frac{\sqrt{2m_e}}{\hbar} (E_k \cos^2 \theta + V_0),$$

where V_0 (inner potential) is a fitting parameter.

Although this method is well established, the measurement of the 3D Fermi surface has rarely been performed. Its main reason seems to be that it takes huge amount of time for measurement and data. Therefore, it is necessary to develop an analytical software for this purpose, which can deal with huge data up to 100 GBytes. In this report, I describe the development of the analytical software and the results applied to a single-crystalline transition metal dichalcogenides TiSe₂.

The measurement for each ARPES was performed in the so called fix-mode with the deflector-scan, which allowed us to measure the 3D (ϕ, θ, E_k) ARPES in several minutes for each photon energy which is varied in a range of, typically, ~ 60 eV in 1 eV steps. The data were first analyzed with the automatic Fermi-Dirac fitting programs, which is necessary to determine the position of the Fermi level (in other words, the precise photon energies within errors of meV). Then, the detection efficiency of the CCD, and the photon intensity must be calibrated. After these calibrations, the photoelectron intensity just at the Fermi level is converted into the volumetric data in k_x, k_y, k_z axes. For the calibrating and converting, I wrote a specific program in Python with a help of the libraries, such as “numpy” and “scipy” (for calculation), “lmfit” (for fitting), qt and pyqtgraph (graph presentation), and so on. Especially the presentation of the volumetric 3D data is crucial, and an opengl program had to be written.

The DFT calculation is also essential. In this study, I used the Quantum Espresso codes installed in the Computer Center in the Institute for Molecular Science. Programs to handle the calculated result were also written similarly to the experimental data.

Figure 1 shows the experimental (a) and the calculated (b) 3D Fermi level. The shape around the L-point is in agreement, demonstrating the power of these methods. However, the rod-like structure around the Γ -A line is only observed in the calculation. This indicates that the Coulomb interaction works for the band near the Γ -A line, and the band gap is created even at room temperature.

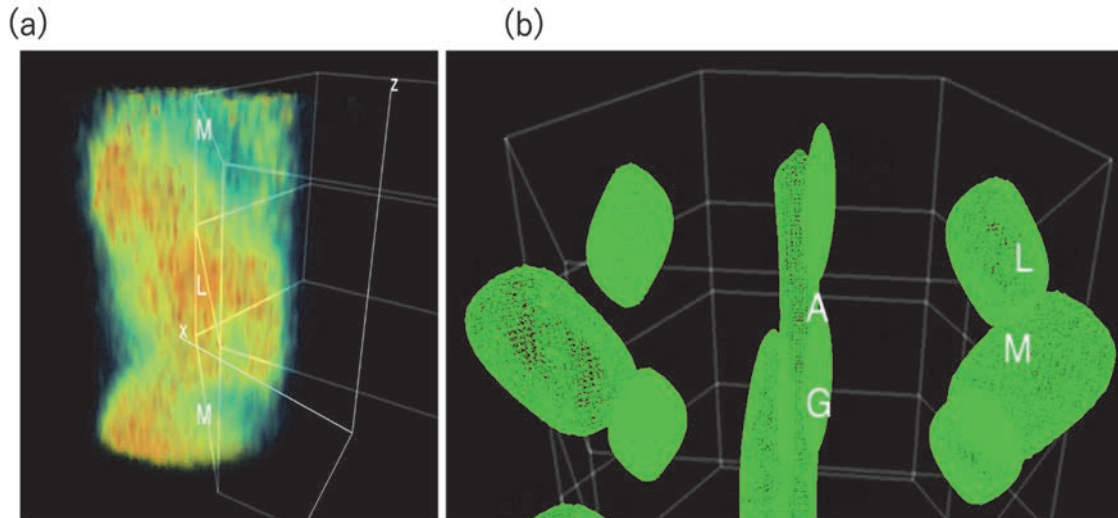


Fig. 1. (a) The experimentally determined 3D Fermi surface of TiSe₂ at room temperature. (b) Calculated Fermi Surface of TiSe₂.

BL5U

High-Resolution ARPES Study of the Electronic Structure in a Kagome Superconductor

T. Kato¹, T. Osumi¹, A. Honma¹, K. Nakayama¹, S. Souma^{2,3}, T. Takahashi¹ and T. Sato^{1,2,3,4,5}

¹Department of Physics, Graduate School of Science, Tohoku University, Sendai 980-8578, Japan

²Advanced Institute for Materials Research (WPI-AIMR), Tohoku University, Sendai 980-8577, Japan

³Center for Science and Innovation in Spintronics (CSIS), Tohoku University, Sendai 980-8577, Japan

⁴International Center for Synchrotron Radiation Innovation Smart (SRIS), Tohoku University, Sendai 980-8577, Japan

⁵Mathematical Science Center for Co-creative Society (MathCCS), Tohoku University, Sendai 980-8578, Japan

In recent years, new material phases and quantum phenomena have been explored based on the symmetry of matter, such as quantum Hall effect originating from Dirac fermions protected by chiral symmetry in graphene and quantum spin Hall effect due to spin-polarized edge states protected by nontrivial band topology and time-reversal symmetry. In this context, the kagome lattice is an intriguing structural motif because its geometric symmetry of corner-sharing triangles results in strong frustration and peculiar electronic structures such as Dirac cones, topological flat bands, and van Hove singularities. Theoretically, these characteristics have been predicted to play key roles in realizing various quantum phenomena such as spin liquids, unconventional superconductivity, density waves, and topological properties. On the other hand, due to the limited number of kagome lattice materials discovered so far, only a few phenomena, mostly magnetic ones, have been observed experimentally.

The recent discovery of superconductivity in kagome metals AV_3Sb_5 ($A = K, Rb, \text{ and } Cs$) opened the door to experimental studies in kagome lattice superconductors. Besides superconductivity, three-dimensional charge ordering has been discovered in AV_3Sb_5 , and the relationship between the mechanism of these properties and the unusual electronic states has been intensively studied. Furthermore, several new types of kagome superconductors have been discovered recently, and the study of superconductivity in the kagome lattice has become an important issue in condensed matter physics.

Here we focus on $LaRh_3B_2$, a superconductor that has been studied extensively since its discovery in the 1980s. Recently, there has been a revival of intensive study on $LaRh_3B_2$, prompted by a theory that pointed out the formation of an ideal Rh kagome lattice [1]. The replacement of La with rare-earth elements such as Ce induces ferromagnetism, which makes RRh_3B_2 a rare material family that provides a fertile playground to study the relationship between superconductivity and magnetism in the kagome lattice. However, although first-principles calculations have predicted the appearance of Dirac cone bands and flat bands protected by kagome lattice symmetry in this material, their experimental detections are still absent.

In this study, we have conducted high-resolution angle-resolved photoemission spectroscopy (ARPES)

of $LaRh_3B_2$ to directly observe its electronic band structure. High-resolution ARPES measurements were performed by using a MBS-A1 spectrometer at BL5U with linearly-polarized energy-tunable photons.

Figure 1 shows a representative ARPES result measured in the valence band region of $LaRh_3B_2$. We observed many dispersive bands such as holelike and electronlike bands centered at the Γ and M points, respectively. The observed band structure near the Γ point is reasonably explained by first-principles calculations. However, we found that the electron pockets around the M point disagree with the calculations, as suggested in previous ARPES study [2]. To clarify the origin of this disagreement and search for kagome-symmetry-related peculiar band structures, we have performed detailed photon energy and polarization dependent measurements.

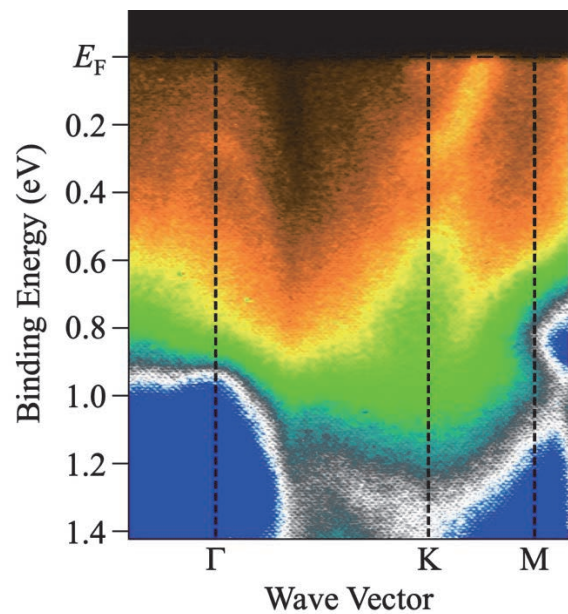


Fig. 1. ARPES intensity plot along the Γ KM line measured in the normal state of $LaRh_3B_2$.

[1] S. Chaudhary *et al.*, Phys. Rev. B: Condens. Matter **107** (2023) 085103.

[2] Y. Iida *et al.*, Physica B **351** (2004) 271.

Enantiomeric Differentiations in Chiral Ferroelectric Oxides by Angle-Resolved Photoemission Circular Dichroism

K. Fukutani^{1,2}, F. Nishino^{1,2}, S. Makita^{1,2}, K. Tanaka^{1,2} and S. Kera^{1,2,3}

¹Institute for Molecular Science, Okazaki 444-8585, Japan

²School of Physical Sciences, The Graduate University for Advanced Studies, Okazaki 444-8585, Japan

³Graduate School of Science and Engineering, Chiba University, Chiba 263-8522, Japan

Symmetry is one of the most fundamental elements interweaved in the laws of nature, which enables us to decipher a range of physical phenomena from behaviors of elementary particles to properties of solids. Recently, so-called chirality, which is a particular spatial symmetry classification arising from lack of inversion and reflection symmetries in a physical system, has been shown to play crucial roles in various exotic quantum phenomena, such as chiral nodes in topological materials, chiral phonons carrying pseudo angular momentum [1], as well as chirality-induced spin selectivity effects [2].

On the other hand, despite their conceptual simplicity and importance in quantum phenomena mentioned above, efficient differentiation between the opposite enantiomers of chiral system remains a long-standing problem. Various methods have been utilized, such as crystallography, chromatography, as well as chiroptical (absorption) spectroscopy. More, recently, photoemission circular dichroism (PECD) has attracted much attentions due to its high sensitivity to enantiomeric differences and have been used extensively for enantiomeric differentiation of chiral molecules. On the other hand, for chiral crystalline materials, the use of angle-resolved photoemission circular dichroism (CD-ARPES) has been proposed as a highly effective method of enantiomeric differentiation [3].

An interesting question in this regard is how sensitive and robust CD-ARPES is in differentiating the handedness of the crystalline material. In answering this question, we take a model case of chiral ferroelectric oxide crystal NbOI_2 , for which the left-handed and the right-handed crystals differ only by the small displacements ($\sim 0.1 \text{ \AA}$) of Nb atoms. Figure 1 shows the theoretical expectations on how the CD-ARPES map, $I_{\text{CCW}}(k_x, k_y) - I_{\text{CW}}(k_x, k_y)$, should generally be related between right- and left-handed crystals (enantiomers). It can be seen from the simple symmetry arguments that under the reversal of the crystalline chirality, the CD-ARPES map should undergo a sign-reversal of the CD map, followed by the reflection about the mirror plane which turns left-handed crystal into right-handed crystal or *vice versa*, as shown in the bottom panel of Fig. 1. Our experimental results on CD-ARPES at a constant energy are shown in Fig. 2 for NbOI_2 , which is in excellent agreement with the theoretical expectations.

Our study demonstrates the strong sensitivity of CD-ARPES, down to sub-angstrom scale, in enantiomeric differentiations of chiral crystals.

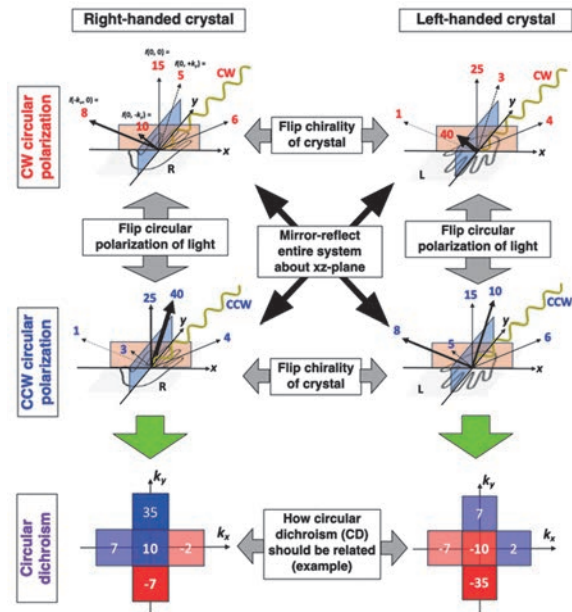


Fig. 1. [Top panel] Example schematic illustrations describing how the photoemission signals $I(k_x, k_y)$ should be related between right-handed (R) and left-handed (L) chiral crystals under the excitations of clockwise (CW) and counter-clockwise (CCW) circularly polarized lights. [Bottom panel] Schematic illustration of the resultant circular dichroism map $I_{\text{CCW}}(k_x, k_y) - I_{\text{CW}}(k_x, k_y)$.

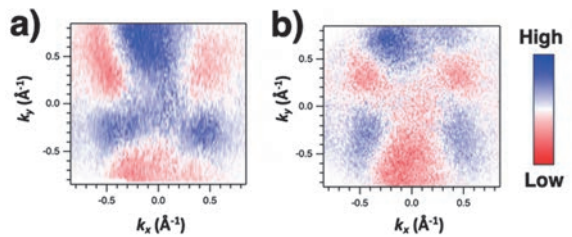


Fig. 2. Angle-resolved photoemission circular dichroism (CD-ARPES) map, $I_{\text{CCW}}(k_x, k_y) - I_{\text{CW}}(k_x, k_y)$, at a constant binding energy obtained for two samples of NbOI_2 crystals are shown in (a) and (b). The measurements were performed at $h\nu = 54 \text{ eV}$ at $T = 300 \text{ K}$.

[1] H. Ueda *et al.*, Nature **618** (2023) 946.

[2] S.-H. Yang *et al.*, Nat. Rev. Phys. **3** (2021) 328.

[3] G. H. Fecher *et al.*, Materials **15** (2022) 5812.

BL5U, 7U

Origin of High Thermopower in Heavy Fermion Yb-Based Compounds

D. Goto¹, K. Kuga¹, M. Matsunami^{1, 2, 3, 4} and T. Takeuchi^{1, 2, 3, 4}

¹Toyota Technological Institute, Nagoya 468-8511, Japan

²Research Center for Smart Energy Technology, Toyota Technological Institute, Nagoya 468-8511, Japan

³CREST, Japan Science and Technology Agency, Tokyo 102-0076, Japan

⁴MIRAI, Japan Science and Technology Agency, Tokyo 102-0076, Japan

From an energy harvesting point of view, the thermoelectric materials, which are capable of converting heat and electricity using Seebeck and Peltier effects, have been considered as one of the most promising technologies. However, thermoelectric generation has not been widely applied in our society due to its low energy conversion efficiency. For evaluating the performance of thermoelectric materials directly related to conversion efficiency, the dimensionless figure of merit $ZT = S^2T/\rho\kappa$ or the power factor $PF = S^2/\rho$ where S , ρ , and κ are the Seebeck coefficient, electrical resistivity, and thermal conductivity, respectively, of constituent materials, are frequently used [1]. Therefore, it is necessary to search for materials possessing large ZT or PF by addressing the trade-off relationship between low ρ and large $|S|$.

It is known that in intermetallic compounds called heavy fermion systems, the low ρ and large $|S|$ coexist, resulting in a large PF . This can be caused by the characteristic electronic structure formed by the hybridization between conduction and f electrons directly related to the heavy fermion nature. However, there is a serious problem concerning the sign of S , which cannot be determined solely in terms of the energy dependence of the electron density of states as in most simple metals. Therefore, the energy dependence of the relaxation time and group velocity of quasiparticles, both which are the terms in Mott formula and are neglected in many cases [1], should be taken into account.

The main purpose of this research is to establish a methodology for experimentally evaluating the energy dependence of the relaxation time and group velocity of quasiparticles in the vicinity of the Fermi level (E_F) using angle-resolved photoemission spectroscopy (ARPES). In this study, we focus on the typical heavy fermion system YbCu_2Si_2 , which is known to show relatively high large $|S|$ [2]. Generally, in the heavy fermion Yb-based compounds, the main part of $4f$ electrons and their hybridized bands locates just below E_F . This feature has high affinity with ARPES.

Single crystals of YbCu_2Si_2 were prepared by the Sn-flux method [2]. Clean (001) surface of single crystals was obtained by *in-situ* cleaving under ultra-high vacuum condition. The ARPES measurements were performed with the photon energy of 20 eV at the undulator beamline BL7U and 40, 80, and 121 eV at

BL5U of UVSOR facility.

Figure 1 shows the obtained ARPES image of YbCu_2Si_2 (001) surface at 9 K measured with the photon energy of 121 eV. In addition to the free electron-like parabolic dispersion of the (bulk) conduction bands mainly consist of Cu $3d$ electrons, the localized dispersion less Yb $4f$ bands are clearly observed in this energy range [3]. From the line width of the band dispersion near E_F providing a significant impact on the thermoelectric properties, the energy dependence of the relaxation time and group velocity of quasiparticles for YbCu_2Si_2 can be successfully evaluated.

As a future perspective, we will extend our research target to Ce-based materials to obtain comprehensive knowledge of the anomalous thermoelectric properties of heavy fermion systems, which will lead to the development of next-generation high-performance thermoelectric materials.

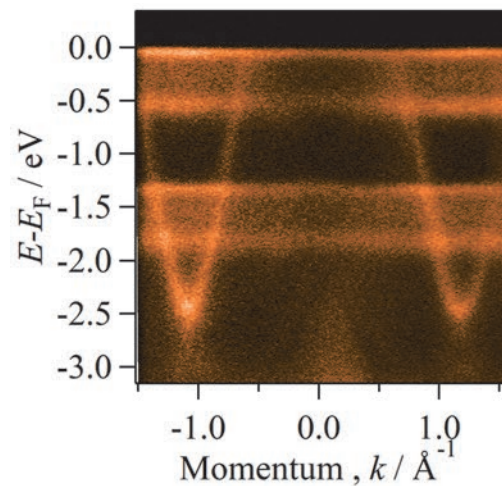


Fig. 1. ARPES image of YbCu_2Si_2 along $\bar{\Gamma} - \bar{X}$ direction at 9 K measured with the photon energy of 121 eV.

[1] T. Takeuchi, J. Thermoelectrics Soc. Jpn. **9** (2012) 1.

[2] N.D. Dung *et al.*, J. Phys. Soc. Jpn. **78** (2009) 084711.

[3] M. Matsunami *et al.*, Phys. Rev. B: Condens. Matter **87** (2013) 165141.

Angle-Resolved Photoemission Study of Layered MAX Phase Compound Zr_2SnC

M. Mita¹, K. Tanaka², M. Nakatake³, T. Ouisse⁴ and T. Ito^{1,5}

¹Graduate School of Engineering, Nagoya University, Nagoya 464-8603, Japan

²UVSOR Synchrotron Facility, Institute for Molecular Science, Okazaki 444-8585, Japan

³Aichi Synchrotron Radiation Center, Seto 489-0965, Japan

⁴Univ. Grenoble Alpes, CNRS, Grenoble INP, LMGP, F-38000 Grenoble, France

⁵Nagoya University Synchrotron Radiation Research Center (NUSR), Nagoya University, Nagoya 464-8603, Japan

MAX phase compounds, i.e., $\text{M}_{n+1}\text{AX}_n$ where M is a transition metal, A belongs to groups 13-16 and X is the C or N element, have recently been attracted much attention due to their possible application for new class of two-dimensional systems called MXenes by removing A atoms [1]. On the other hand, the bulk electronic structure of MAX phase has been studied mostly by calculations, mainly because of lack of well-established single crystalline samples. In this study, we have performed angle-resolved photoemission spectroscopy (ARPES) on MAX phase compound Zr_2SnC to investigate the systematic electronic structure change from Zr_3SnC_2 , in which Sn and Zr surface dominated electronic structure has been reported recently [2].

ARPES measurements were performed at the UVSOR-III BL5U. Data were acquired at $T = 30$ K with $h\nu = 71.5$ eV which enables us to trace around the ΓKM plane with inner potential of $V_0 = 20.6$ eV estimated from the photon energy dependent measurement (not shown).

Figures 1 (a) and (b) show the obtained band structure and the Fermi surface image along the $\text{M}\Gamma\text{KM}$ line of Zr_2SnC , respectively. For comparison, the band structure and Fermi surfaces of Zr_3SnC_2 obtained from measurements under identical conditions using $h\nu = 71.5$ eV are shown in Figs. 1(c) and (d), respectively. According to previous reports on Zr_3SnC_2 [2], two hole-pockets around the Γ point are attributed to the bulk-projected Fermi surfaces. On the other hand, three distinct surface-originated bands of Sn-terminated surface and Zr subsurface have been observed: the bottom of the hole-like band B1 around Γ point, the flat dispersive feature B2 just below the Fermi level (E_F) along KM lines, and the band forming a characteristic saddle like dispersion B3 around the M points (see Fig.1(f)), respectively.

From the comparison between Zr_2SnC and Zr_3SnC_2 , we have found that electronic structure of Zr_2SnC appears quite similar with one of Zr_3SnC_2 , not only for bulk projected hole-pockets but also for surface states B1, B2, and B3. On the other hand, we have found that the Fermi momenta of α , β , and SS (w-shaped electron pockets connecting with B3 along ΓM and another Fermi surface formed by B2 along ΓK line) become

smaller from Zr_3SnC_2 to Zr_2SnC , respectively. This suggests a chemical potential shift to low binding energy side, resulting in an electron-doping effect from Zr_3SnC_2 to Zr_2SnC . It should be noted that the crystal structure of Zr_2SnC becomes more three-dimensional due to the thin Zr_2C layer than the Zr_3C_2 layer. As a result, the appearance of a three-dimensional Fermi surface formed by flat electron pocket around the Γ point (or hole-like Fermi surface around the A point which has flat bottom just below E_F around the Γ point) has been expected by DFT calculation [3]. To clarify the relation between surface states and inter-layer interactions on these systems, further studies are intended.

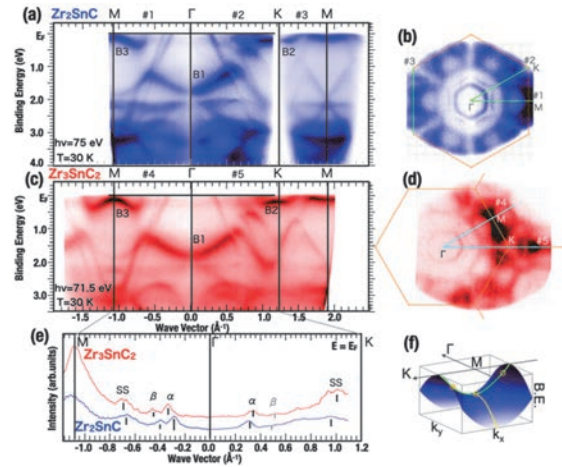


Fig. 1. (a-d) Band structures (a,c) and Fermi surface images (b,d) along the $\text{M}\Gamma\text{KM}$ line of Zr_2SnC (a,b) and Zr_3SnC_2 (c,d), respectively. ARPES measurement lines along the high-symmetry lines in Fig. 1(b) and (d) are indicated as green (#1~#3) and light blue lines (#4, 5) respectively. (e) Comparison of MCD spectra at E_F of Zr_2SnC and Zr_3SnC_2 . (f) Image of the saddle-like surface state around the M point.

- [1] M. Basoum, *MAX phases* (Wiley, Weinheim 2013).
- [2] T. Ito *et al.*, Phys. Rev. B: Condens. Matter **108** (2023) 235145.
- [3] M. A. Hadi *et al.*, Comput. Mater. Sci **168** (2019) 203.

BL5U

ARPES Study of the CDW and Anisotropic Band Splitting in 4H-NbSe₂ and NbSeS

Y. Kumar¹, S. Ideta^{1,2} and K. Shimada^{1,2}¹Graduate School of Advanced Science and Engineering, Hiroshima University, Hiroshima 739-0046, Japan²Hiroshima Synchrotron Radiation Centre (HiSOR), Hiroshima University, Hiroshima 739-0046, Japan

In recent years, the study of the electronic structure of topological insulators and topological semimetals has emerged as a major research area in condensed matter physics. Recently, Dirac and Weyl Semimetals have generated great interest in spintronics due to their enriched properties [1, 2].

Layered transition-metal dichalcogenides (TMDs) AB₂ (A = transition metal, B = chalcogen) are good candidates since these materials exhibit a variety of physical properties, such as superconductivity and charge density waves (CDWs). Among these materials, 2H-NbSe₂ exhibits a unique ground state, where an incommensurate CDW and superconductivity coexist below 7 K. This makes this material ideal for studying the origin of charge density waves and to look for the interaction between superconductivity and charge density waves. Researchers have been trying to replace and dope/intercalate chemical elements and the number of atomic layers to control physical properties and to understand the relation between superconductivity and charge density waves' interaction mechanism.

We have grown high-quality single crystals of 4H-NbSe₂ and NbSeS. We have measured XRD and found that both the samples are in a single phase. We have measured the electronic band structure using ARPES at BL5U at UVSOR-III Synchrotron.

The objective of this study was to conduct ARPES measurements on 4H- NbSe₂ and NbSeS samples. The aim was to observe the material's band dispersion and Fermi surface to look for CDW and anisotropic band splitting in the electronic band structure. We have prepared 4H-NbSe₂ and NbSeS samples and aligned them in a high-symmetry direction using the Laue diffraction (XRD) available at the UVSOR facility to accurately measure the band dispersion in the high-symmetry direction.

We have cleaved several samples of 4H- NbSe₂ to obtain a clean surface but faced challenges in achieving a pristine surface, resulting in unclear band dispersion. A good cleave was observed for NbSeS samples. We have performed the ARPES experiment and mapped the fermi surface at different photon energies from $h\nu = 30$ eV to 60 eV with a 10 eV-energy step. Also, we

observe high symmetry cuts in ΓM directions to investigate the electronic band structure as shown in Fig. 1. We have performed the photon energy-dependent measurement from $h\nu = 30$ eV to 60 eV to observe the k_z dependence. We have also optimized the beam slit to improve the data quality and resolution. Further measurements of high energy resolution are needed to look for the band anisotropy and complete the data set.

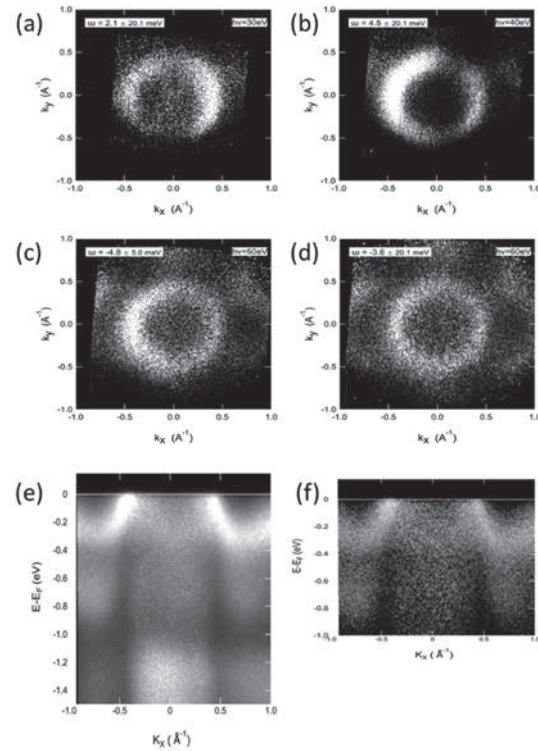


Fig. 1. Panels (a), (b), (c), and (d) show Fermi surface-mapping taken at $h\nu = 30, 40, 50$, and 60 eV, respectively, for NbSeS samples. Panels (e) and (f) are high-symmetry cuts in the ΓM direction.

[1] N. P. Armitage, E. J. Mele and A. Vishwanath, *Rev. Mod. Phys.* **90** (2018) 015001.

[2] A. A. Burkov, *Nat. Mater.* **15** (2016) 1145.

[3] Y. Nakata *et al.*, *npj 2D Mater. Appl.* **2** (2018) 12.

Upgrading of the Photoelectron Momentum Microscope at BL6U of UVSOR to Integrate Data to be Reliably Analyzable by Theories

S. Suga¹, K. Hagiwara² and F. Matsui^{2,3}

¹SANKEN, Osaka University, Osaka 567-0047, Japan

²UVSOR Synchrotron Facility, Institute for Molecular Science, Okazaki 444-8585, Japan

³The Graduate University for Advanced Studies(SOKENDAI), Okazaki 444-8585, Japan

The upgraded double-hemispherical-deflection-energy-analyzer-type photoelectron momentum microscope (DHDAs-PMM) in UVSOR produced much better experimental results in 2023 than the first introduced single-HDA-type PMM in 2020. The momentum and energy resolution were much improved and systematic measurements became easier. Then measurements of the interesting materials were repeated again by this system. We have so far recognized the difficulty of theoretical analyses of the data obtained in the off-normal light incidence ($\sim 68^\circ$) because of the dipole selection rules depending upon the optical configuration including the polarization direction as well as the light incidence angle. Then we facilitated the normal incidence configuration measurement by use of the branched light from BL7U. This light is incident normally onto the sample by using the input from the back side of objective lens connected to the first HDA along the PEEM objective lens axis by properly opening the electron apertures as shown in Fig. 1. Still the spatial and momentum resolutions are realized by other apertures [1].

In particular the normal incidence configuration facilitates the reliable theoretical analyses of SP-PMM results to be obtained after the installation of a 2D spin filter to this instrument.

The results of 1T-TaS₂ by single-HDA PMM are shown in Fig. 2 in both NC- and C-CDW phases. The chirality not observed in the NC-CDW phase is recognized in the C-CDW phase at 30 K. Much clearer

fine band mapping became possible by DHDAs-PMM as will be published soon. The $(\sqrt{13} \times \sqrt{13})R13.90^\circ$ superlattice structure indicated in Fig. 3 is recognized in Fig. 2 and more clearly in recent studies by DHDAs-PMM [2], where the domain structures with opposite chirality were also recognized.

From now on fruitful SP-PMM by use of 2D spin filter must be commissioned to do the world best SP-PMM for $E_{\text{binding}}(k_x, k_y, k_z)$ measurements.

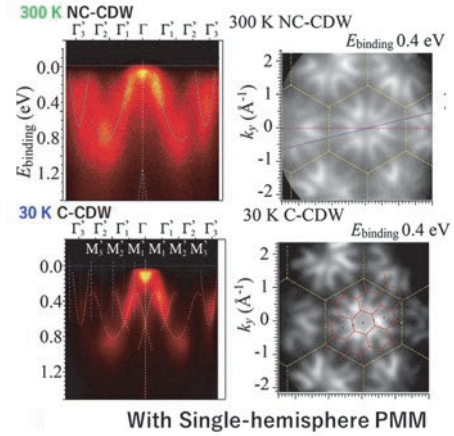


Fig. 2. 1T-TaS₂ results at 300 and 30K by single HDA PMM.

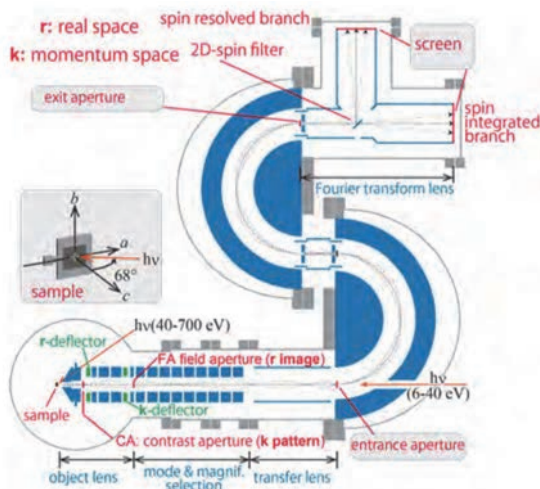


Fig. 1. Optical configuration of DHDAs-PMM for both 68° and normal incidence [1].

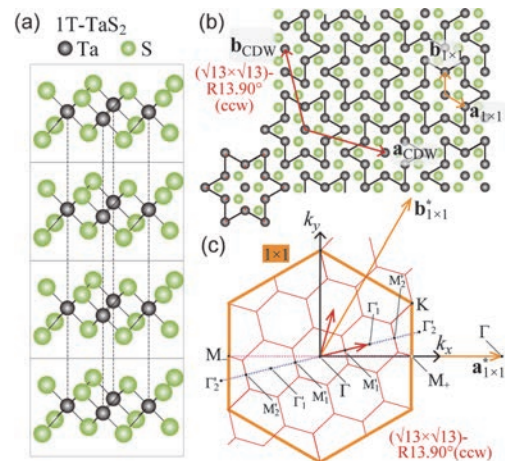


Fig. 3. Atomic structure of 1T-TaS₂. Counter-clockwise $(\sqrt{13} \times \sqrt{13})R13.90^\circ$ in C-CDW phase is shown.

[1]K. Hagiwara *et al.*, J. Synchrotron Radiat. **31** (2024) 540.

[2]F. Matsui *et al.*, to be published.

BL6U

Electronic States of a Weyl Semimetal Candidate Revealed by Momentum Microscope

Y. Morita¹, K. Nakayama¹, K. Hagiwara², F. Matsui², T. Takahashi¹, K. Kudo³ and T. Sato^{1,4,5,6,7}¹Department of Physics, Graduate School of Science, Tohoku University, Sendai 980-8578, Japan²UVSOR Synchrotron Facility, Institute for Molecular Science, Okazaki 444-8585, Japan³Department of Physics, Graduate School of Science, Osaka University, Toyonaka, Osaka 560-0043, Japan⁴Advanced Institute for Materials Research (WPI-AIMR), Tohoku University, Sendai 980-8577, Japan⁵Center for Science and Innovation in Spintronics (CSIS), Tohoku University, Sendai 980-8577, Japan⁶International Center for Synchrotron Radiation Innovation Smart (SRIS), Tohoku University, Sendai 980-8577, Japan⁷Mathematical Science Center for Co-creative Society (MathCCS), Tohoku University, Sendai 980-8578, Japan

Recent discoveries of outstanding properties such as the half-integer quantum Hall effect in graphene and the surface Dirac electronic state of topological insulators have attracted a great deal of attention. Novel quasiparticles with energy degenerate points in the band structure often play a key role to search and demonstrate these exotic quantum phenomena and materials. For instance, graphene possesses two-dimensional Dirac fermions whose linear band dispersion degenerate at a single point in the momentum space due to chiral symmetry of the honeycomb lattice. In topological insulators, the appearance of spin-polarized two-dimensional Dirac fermions, which dominate surface conduction, is ensured by nontrivial band topology and time-reversal symmetry. Motivated by the discoveries of graphene and topological insulators, the exploration of exotic nodal fermions beyond Dirac fermions is a hot topic in condensed matter physics. An intriguing research target is Weyl fermions, a spin-polarized analogue of three-dimensional Dirac fermions. Weyl fermions are quite robust against perturbations and predicted to trigger many exotic properties such as chiral anomalies, magnetoelectric effects, and surface Fermi arcs. The realization of Weyl fermions requires the breaking of either space inversion symmetry or time-reversal symmetry. Owing to intensive research, Weyl fermions have been indeed discovered in some materials, e.g., Mn_3Si and TaAs .

Here we focus on a new Weyl-fermion material candidate, PtBi_2 which lacks the space-inversion symmetry. According to first-principles band structure calculations, Weyl fermions are located in the vicinity of Fermi level (E_F). Recent angle-resolved photoemission spectroscopy (ARPES) measurements actually reported a signature of Weyl fermions formation, though their direct observation remains a challenge. If PtBi_2 indeed hosts Weyl fermions, Fermi arc surface states should appear, and their shape are inequivalent between two opposite surfaces due to the space-inversion symmetry breaking. To clarify the Weyl material nature and the details of Fermi-arc-related physics, we determined bulk and surface electronic states over a wide momentum space using

momentum-microscopy technique at BL6U in UVSOR. For this sake, we prepared a set of crystals with two different surface terminations.

Figure 1 shows a representative equi-energy contour plot in two-dimensional momentum space, k_x and k_y . We observed the electronic structure whose periodicity matches well with the symmetry of the Brillouin zone. For example, a triangular intensity distribution is seen at each K point. We also see a six-fold symmetric characteristic intensity pattern at the Γ point. We found that, in the crystal with different termination, the intensity distribution shows remarkable differences compared to that in Fig. 1. This result indicates the presence of termination-dependent surface electronic states which might be related to Weyl-fermion physics. To investigate this point in more detail, we have performed photon-energy dependent measurements and compared the results with first-principles band structure calculations.

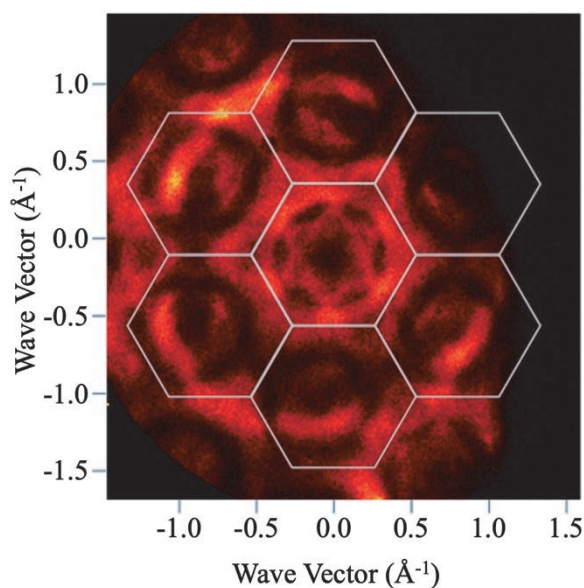


Fig. 1. ARPES intensity at a constant energy plotted as a function of two-dimensional wave vector. The measurement has been carried out using linearly polarized photons of $h\nu = 72$ eV.

Electronic Structure of a Nodal Line Semimetal IrO_2 Proved via Optical Spectroscopy

D. Hirai, K. Maruyama, Y. Kusanose and K. Takenaka

Department of Applied Physics, Nagoya University, Nagoya 464-8603, Japan

Topological semimetals have linear conduction and valence bands which intersect at points and lines each other near the Fermi energy (E_F) and exhibit unique transport properties such as ultrahigh mobility and extremely large magnetoresistance. However, at the intersections, an energy gap is often open due to spin-orbit interactions, etc. Therefore, there are only a few materials in which such characteristic electronic structures are experimentally verified. ZrSiS is one of the nodal-line semimetals whose properties have been clarified both theoretically and experimentally. It has been observed that the optical conductivity is constant over a wide photon energy range of 0.03 ~ 0.3 eV [1]. This peculiar optical property is thought to be due to interband transitions in the Dirac band near the E_F and is experimental evidence for the existence of a nodal line.

The transition-metal rutile oxide RO_2 has recently attracted attention as a candidate for nodal line semimetals. Among them, IrO_2 is predicted to have a Dirac nodal line (DNL) near the E_F , and it has been argued that the previously reported large spin Hall effect is due to the contribution of the DNL [2-4]. Although DNLs have been observed by angle-resolved photoemission spectroscopy measurements [5,6], a detailed characterization of the low-energy electronic states is needed to understand their transport properties.

In this study, in order to investigate the topological electronic structure of IrO_2 , optical reflectivity $R(\omega)$ spectra of IrO_2 single crystals in a wide energy range (from far infrared to ultraviolet) were measured. We grew high quality and large single crystals of IrO_2 by chemical vapor transport method. Normal incident reflectivity spectra were collected by using Fourier-type interferometer (0.07-2.1 eV) installed with a microscope. For the measurements in the far infrared region (0.005-0.1 eV), we used Fourier-transform infrared spectrometer (Bruker VERTEX 70V) with a synchrotron radiation at BL6B of UVSOR, Institute for Molecular Science. Optical conductivity $\sigma(\omega)$ spectra were deduced from the $R(\omega)$ using the Kramers-Kronig relation.

As shown in Fig. 1, reflectivity $R(\omega)$ of IrO_2 below 0.1 eV is close to 1, indicating the presence of high mobility carriers. There are two dips at approximately 0.6 and 2 eV, which are independent of the polarization direction, and a large decrease in reflectivity is observed. The $\sigma(\omega)$ spectra (Fig. 2) has a sharp upturn below 0.16 eV, corresponding to Drude response and three peaks at 0.5, 1.2, and 1.9 eV, possibly corresponding to inter-band transitions. On the other

hand, because of the overlap of these peaks, the energy-independent optical conductivity expected for DNL could not be observed in this study. Comparison with first-principles calculations will clarify the characteristics of DNL in the future.

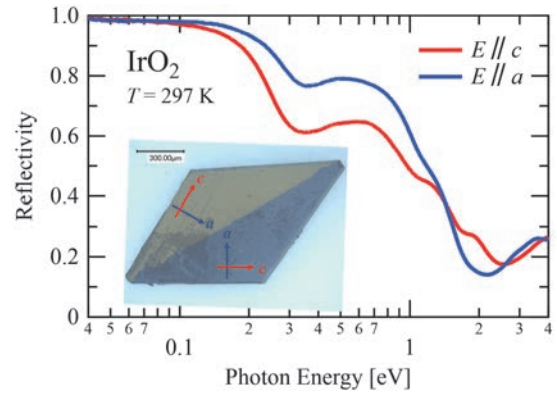


Fig. 1. Photon energy dependences of reflectance of IrO_2 at room temperature with $E \parallel a$ and c . The inset shows photograph of a single crystal of IrO_2 observed via polarized microscope, showing twin domain structure.

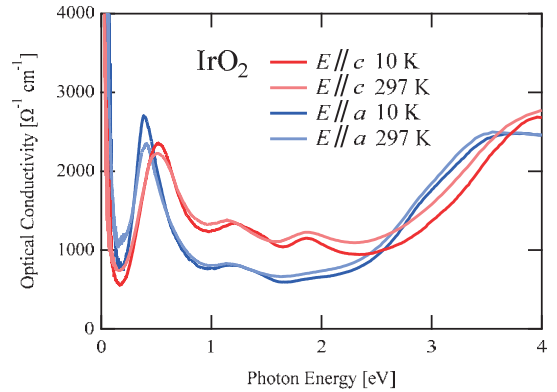


Fig. 2. Optical conductivity spectra of IrO_2 at 10 and 279 K with $E \parallel a$ and c .

- [1] M. B. Schilling *et al.*, Phys. Rev. Lett. **119** (2017) 187401.
- [2] K. Fujiwara *et al.*, Nat. Commun. **4** (2013) 2893.
- [3] Y. Sun *et al.*, Phys. Rev. Lett. **117** (2016) 146403.
- [4] Y. Sun *et al.*, Phys. Rev. B: Condens. Matter **95** (2017) 235104.
- [5] J. N. Nelson *et al.*, Phys. Rev. Mater. **3** (2019) 064205.
- [6] X. Xu *et al.*, Phys. Rev. B: Condens. Matter **99** (2019) 195106.

BL7U

ARPES Study of Pure Electronic Nematicity in Epitaxial FeSe Thin Films Grown on LaAlO_3

K. Nakayama¹, T. Kobayashi², F. Nabeshima², S. Souma^{3,4}, T. Takahashi¹,
A. Maeda² and T. Sato^{1,3,4,5,6}

¹Department of Physics, Tohoku University, Sendai 980-8578, Japan

²Department of Basic Science, the University of Tokyo, 3-8-1 Komaba, Meguro, Tokyo 153-8902, Japan

³Center for Spintronics Research Network, Tohoku University, Sendai 980-8577, Japan

⁴WPI Research Center, Advanced Institute for Materials Research, Tohoku University, Sendai 980-8577, Japan

⁵International Center for Synchrotron Radiation Innovation Smart (SRIS), Tohoku University,
Sendai 980-8577, Japan

⁶Mathematical Science Center for Co-creative Society (MathCCS), Tohoku University, Sendai 980-8578, Japan

An iron-based superconductor FeSe has attracted great attention because of its unique properties distinct from those of other iron-based superconductors, such as high-temperature superconductivity in monolayer films and extremely strong coupling superconductivity in bulk crystals. Of particular interest is the emergence of electronic nematicity characterized by the rotational symmetry breaking from C_4 in the normal state to C_2 in the nematic state. While the electronic nematicity in other iron-based superconductors develops almost simultaneously with the antiferromagnetic ordering and the tetragonal-orthorhombic structural transition, the electronic nematicity in FeSe is not accompanied by any antiferromagnetic ordering. Since the antiferromagnetic phase is located next to the superconducting phase in almost all high-temperature superconductors discovered so far, antiferromagnetic interactions have been considered a candidate to realize high-temperature superconductivity. In contrast, the results for FeSe indicate that the electronic nematicity may be the parent phase of high-temperature superconductivity. Therefore, understanding the origin of the nematic phase is an important issue to elucidate the mechanism of high-temperature superconductivity in iron-based superconductors.

Although the antiferromagnetic ordering is absent in FeSe, the tetragonal-orthorhombic transition is known to occur as in other iron-based superconductors. This indicates that the lattice in the nematic state in FeSe has the C_2 symmetry as the electronic state. Therefore, strictly speaking, the electronic state does not break the rotational symmetry of the system. In other words, it is not an ideal nematic state. In contrast, we have recently discovered that FeSe thin films fabricated on LaAlO_3 substrates exhibit pure electronic nematicity without even a structural phase transition [1].

In this study, we performed high-resolution angle-resolved photoemission spectroscopy (ARPES) measurements of FeSe/ LaAlO_3 with the aim of elucidating the mechanism of the novel pure electronic nematicity. High quality FeSe/ LaAlO_3 samples were prepared by pulsed laser deposition, and their clean surfaces necessary for the ARPES measurements were obtained by cleaving the samples in vacuum. High-

resolution ARPES measurements were carried out using an A1 spectrometer at BL7U in UVSOR.

Figure 1 shows the result of temperature-dependent second-derivative ARPES intensity measured at the M point of the Brillouin zone in FeSe/ LaAlO_3 . It is well known in FeSe that there are spin-orbit coupled d_{xz} and d_{yz} bands at the M point in the normal state, and their energy separation is enhanced upon entering the nematic state. The result plotted in Fig. 1 shows such enhancement in the energy separation between d_{xz} and d_{yz} bands below $T \sim 90$ K, where the lattice still preserves the tetragonal symmetry. This supports the emergence of the pure nematic state. We also investigated the rotational symmetry of the band dispersion and Fermi surface utilizing variable photon polarization and very high momentum resolution of low photon energies at BL7U. Through a detailed analysis of the evolution of the rotational symmetry as a function of temperature and a comparison with the results in bulk FeSe and other iron-based superconductors, we investigated similarities and differences. The obtained results are compared with theoretical models.

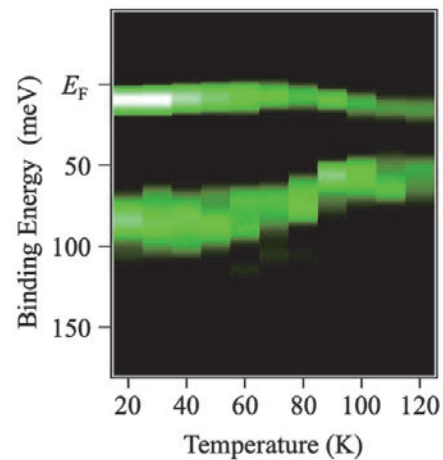


Fig. 1. Temperature dependence of ARPES intensity at the M point measured in FeSe/ LaAlO_3 .

[1] Y. Kubota *et al.*, Phys. Rev. B: Condens. Matter **108** (2023) L100501.

Photoemission Measurements on Crystalline Thin-Films of a Tetrabenzoporphyrin with Alkylsilyl Side Groups

Y. Nakayama^{1,2}, T. Tasaki¹, K. Teranishi³, H. Hattori¹, K. Matsuo³ and H. Yamada³

¹Department of Pure and Applied Chemistry, Tokyo University of Science, Noda 278-8510, Japan

²Institute for Molecular Science, Okazaki 444-8585, Japan

³Institute for Chemical Research, Kyoto University, Uji 611-0011, Japan

One of the most important advantages of organic semiconductor electronics is its potential for fabrication by cost-effective solution processes such as printing, roll-to-roll production, and so on. In this context, tetrabenzoporphyrins functionalized by alkylsilyl side groups are promising p-type organic semiconductor molecules because of the concomitance of the charge carrier mobility exceeding $1 \text{ cm}^2/\text{Vs}$ and good solubility [1-3]. On the other hand, to develop promising materials for the use of electronic devices, understanding the electronic structures, in particular the valence and conduction bands, of the semiconductors is indispensable. In this study, the valence electronic states of crystalline thin-films of Copper(II) 5,15-bis(*n*-octyl(dimethyl)silylethynyl)-tetrabenzoporphyrin (C8DMS-CuBP, Fig. 1) formed from its solutions [3] were measured by angle-resolved photoelectron spectroscopy (ARPES).

Crystalline thin-films of C8DMS-CuBP were produced by dip coating on Au/Si substrates pre-covered with a self-assembled monolayer at room temperature (RT). An optical micrograph image of the sample is shown in Fig. 2 inset. The samples were then introduced to the ARPES measurement system at BL7U of UVSOR. For the present measurements, the excitation photon energy was set at 8.0 eV, and the photoelectrons were collected by an electron analyzer (A-1, MB-Scientific). For the sake of canceling photoemission-induced charging of the sample, the photon flux was reduced by intentional diversion of the undulator gap width from the optimized conditions, and the sample was illuminated by a continuous-wave laser (wavelength of 405 nm) during the measurements [4]. The sample temperature was controlled in a range of 300 K – 8 K by a combination of a liquid-He flow and backside heating of the sample.

Figure 2 shows variations in the photoemission spectra of a C8DMS-CuBP thin-film depending on the sample temperature. Spectral components shifted toward the Fermi level upon cooling, while overall spectral profiles were maintained even at low temperatures. Taking into consideration that, if the photoemission-induced sample charging emerges, the spectral features are prone to be smeared out and to move away from the Fermi level, the present results indicate that the meaningful ARPES measurements unhampered by the sample charging are possible even at low temperatures, where the ARPES measurements for semiconductors generally become more difficult due to the decline in the electronic conductivity. Even

though the apparent energy dispersion of the valence bands was hardly resolved on the present samples, more accurate ARPES analyses are a future challenge.

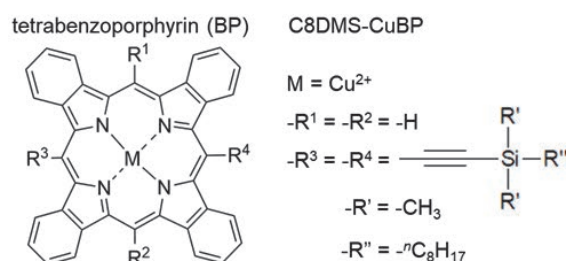


Fig. 1. Molecular structure of C8DMS-CuBP.

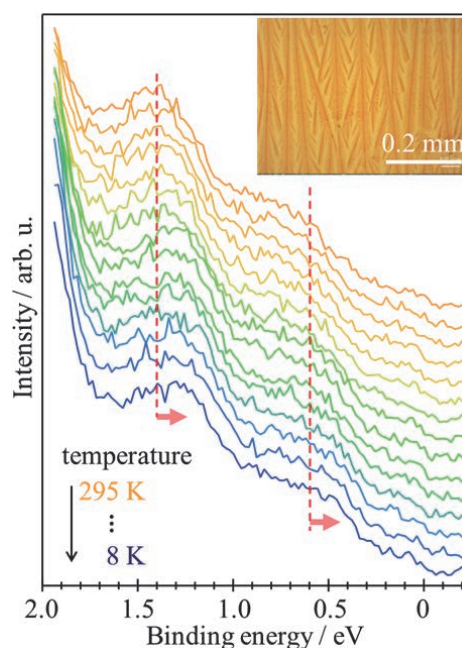


Fig. 2. Temperature-dependent evolution of the photoemission spectra of the C8DMS-CuBP crystalline thin-film sample shown in the inset image. Peak positions for the spectra obtained at RT are indicated by dashed lines.

- [1] K. Takahashi *et al.*, ACS Appl. Mater. Interfaces **9** (2017) 8211.
- [2] J. Zhu *et al.*, J. Mater. Chem. C **10** (2022) 2527.
- [3] E. Jeong *et al.*, ACS Appl. Mater. Interfaces **14** (2022) 32319.
- [4] Y. Nakayama, S. Kera and N. Ueno, J. Mater. Chem. C **8** (2020) 9090.

BL5U, 7U

Unexpected Two-Fold Symmetry of the Electronic Structure in Heavily Overdoped Bi2201 Observed by Angle-Resolved Photoemission Spectroscopy

Y. Miyai¹, S. Ideta², T. Kurosawa³, M. Oda⁴, M. Arita², K. Tanaka⁵ and K. Shimada⁴

¹Graduate School of Advanced Science and Engineering, Hiroshima University,
Higashi-Hiroshima 739-8526, Japan

²Hiroshima Synchrotron Radiation Center, Hiroshima University, Higashi-Hiroshima 739-8526, Japan

³Faculty of Science and Engineering, Muroran Institute of Technology, Muroran, 050-8585, Japan

⁴Department of Physics, Hokkaido University, Sapporo 060-0809, Japan

⁵UVSOR Synchrotron Facility, Institute for Molecular Science, Okazaki, 444-8585, Japan

High transition-temperature (T_c) cuprate superconductors have attracted much interest for their high T_c as well as unusual physical properties such as the superconducting gap, pseudogap [1], and nematicity [2]. Superconductivity occurs in the CuO_2 plane and the $\text{Cu } 3d_{x^2-y^2}$ state forms Fermi surfaces (FSs), and it has been widely believed that the CuO_2 plane shows the four-fold symmetry (C_4) so far. Recently, however, the reduction of the C_4 symmetry in the electronic structure has been reported in Bi-based high- T_c cuprate superconductors [2, 3]. Note that the breaking of the C_4 symmetry or nematicity has been also found in the electronic structure of iron-based superconductors [4]. Although, the nematicity has attracted much interest, rotational symmetry breaking in the electronic structure of high- T_c cuprate superconductors has not been directly clarified yet.

In this study, we examine the symmetry of the electronic structure of the cuprate superconductors using high-resolution angle-resolved photoemission spectroscopy (ARPES). Here, for this study, we have selected heavily overdoped Bi-based cuprates, $(\text{Bi,Pb})_2\text{Sr}_2\text{CuO}_{6+\delta}$ (Pb-Bi2201) which has a single CuO_2 plane in the unit cell. In addition, the superstructure reflections are suppressed by Pb doping. Furthermore, the pseudogap disappears in the heavily overdoped sample and one can clearly see the entire FS in the normal state.

By mechanically rotating the sample, we find the difference of the nodal distances between the two nodal directions (#1 and #2 in the inset of Fig. 1(a)) at the Fermi level (E_F). In addition, the ARPES spectral intensities at the E_F are different for these two nodal directions. To investigate many-body interactions in the direction of #1 and #2, we have evaluated the self-energies ($\Sigma^{(\#1)}$, $\Sigma^{(\#2)}$) as shown in Figs. 1(a) and 1(b) along the two nodal directions. Since the real and imaginary parts of the self-energies satisfy the Kramers-Kronig relation, the anisotropy of the self-energy should be intrinsic, indicating that the many-body interactions such as the electron-electron and electron-boson (phonon) interactions are anisotropic in these two nodal directions. Note that the observed two-fold

symmetry of the electronic structure is independent of temperature in the range of $T = 20 \text{ K} - 260 \text{ K}$.

The observed two-fold symmetry of the electronic structure may be related to a charge order formation in heavily overdoped Pb-Bi2201 as observed by resonant inelastic X-ray scattering [5]. Our results provide an insight for the intriguing physical properties such as the nematicity [2] and the ferromagnetic fluctuation of the heavily overdoped Bi2201 [6].

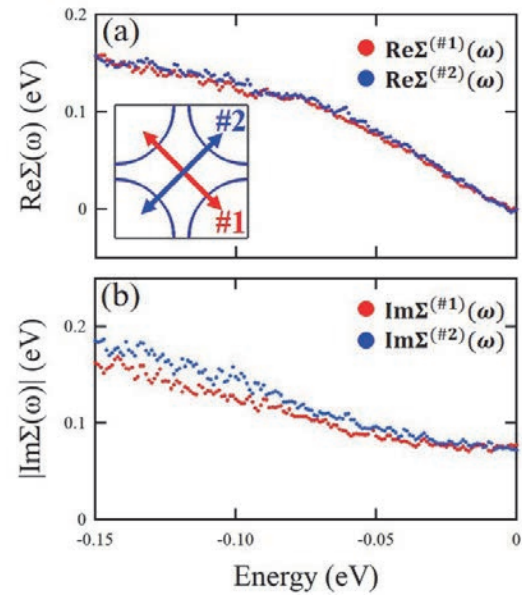


Fig. 1. Evaluation of the self-energy of Bi2201. (a), (b) Self-energy (Σ) obtained by the present study along the orthogonal two nodal directions. Red and blue dots indicate $\Sigma^{(\#1)}$ and $\Sigma^{(\#2)}$ extracted from the #1 and #2 directions as shown in the inset of panel (a), respectively.

- [1] M. Hashimoto *et al.*, Nat. Phys. **10** (2014) 483.
- [2] S. Nakata *et al.*, npj Quantum Mater. **6** (2021) 86.
- [3] N. Auvray *et al.*, Nat. Commun. **10** (2019) 5209.
- [4] H. C. Xu *et al.*, Phys. Rev. Lett. **117** (2016) 157003.
- [5] Y. Y. Peng *et al.*, Nat. Mater. **17** (2018) 697.
- [6] K. Kurashima *et al.*, Phys. Rev. Lett. **121** (2018) 057002.

Estimation of the Hole Concentration in the Normal State of Overdoped Bi2212 by Angle-Resolved Photoemission Spectroscopy

Y. Tsubota¹, Y. Miyai², S. Kumar², K. Tanaka³, S. Ishida⁴, H. Eisaki⁴,
S. Nakagawa⁵, T. Kashiwagi⁵, M. Arita², K. Shimada^{1,2} and S. Ideta^{1,2}

¹Graduate School of Advanced Science and Engineering, Hiroshima Univ., Higashi-Hiroshima 739-0046, Japan

²Hiroshima Synchrotron Radiation Center (HiSOR), Hiroshima Univ., Higashi-Hiroshima 739-0046, Japan

³UVSOR Synchrotron Facility, Institute for Molecular Science, Okazaki, Aichi 444-8585, Japan

⁴National Institute of Advanced Industrial Science and Technology (AIST), Tsukuba, Ibaraki 305-8560, Japan

⁵Graduate School of Science and Technology, Tsukuba Univ., Tsukuba, Ibaraki 305-8577, Japan

It has been known that the cuprate superconductors show a high superconducting (SC) transition temperature (T_c) and exotic physical properties. However, the SC mechanism has been unclear yet. In order to understand the mechanism of high- T_c cuprates, $\text{Bi}_2\text{Sr}_2\text{CaCu}_2\text{O}_{8+\delta}$ (Bi2212) is one of the promising candidates to study the electronic structure and reveal the physical properties. Bi2212 has two CuO_2 planes in the unit cell. Superconductivity occurs upon hole doping into the CuO_2 plane and the amount of hole doping can control T_c , and therefore, carrier doping (hole/electron concentration) plays an important key parameter in cuprates [1, 2]. The electronic phase diagram of hole-doped high- T_c cuprate superconductors plotted as a function of temperature and carrier concentration has been reported as an empirical and universal phase diagram which is a dome-like shape centered at ~ 0.16 of hole concentration [1]. However, our previous ARPES experiments suggest that its empirical phase diagram is not universal and shifted toward the overdoped region. Bi2212 has the SC gap in the anti-nodal region in the SC state, and the energy gap opens above T_c called pseudogap in the anti-nodal region in the normal state. In our previous study, the hole concentration has been quantitatively determined from the area of the Fermi surfaces, but it is difficult to determine the Fermi momentum (k_F) precisely when the energy gap is open. In order to verify the method how to estimate the hole concentration, we have measured the electronic structure of three compositions of Bi2212 in the temperature which the pseudogap is completely closed, and compared it with the hole concentration shown in the Fermi surface in the SC state.

In this study, we have performed ARPES measurements to directly investigate the electronic structure of the overdoped Bi2212. ARPES experiments were carried out at BL5U and BL7U. Samples were follows: $\text{Bi}_{2.3}\text{Sr}_{1.7}\text{CaCu}_2\text{O}_{8+\delta}$ ($T_c \sim 78$ K), $\text{Bi}_{2.1}\text{Sr}_{1.9}\text{CaCu}_2\text{O}_{8+\delta}$ ($T_c \sim 72$ K) and $\text{Bi}_{2.1-x}\text{Pb}_x\text{Sr}_2\text{CaCu}_2\text{O}_{8+\delta}$ ($T_c \sim 65$ K) in the SC and the normal states (above T^*). High quality single crystals of Bi2212 were cleaved *in-situ* in the ultrahigh vacuum $\sim 5 \times 10^{-9}$ Pa.

Figure 1 (a) shows the Fermi surface taken at $h\nu =$

17.8 eV and $T = 30$ K in the SC state for overdoped $\text{Bi}_{2.1-x}\text{Pb}_x\text{Sr}_2\text{CaCu}_2\text{O}_{8+\delta}$. Figure 1 (b) shows the Fermi surface taken at $h\nu = 17.8$ eV and $T = 150$ K in the normal state for overdoped $\text{Bi}_{2.1-x}\text{Pb}_x\text{Sr}_2\text{CaCu}_2\text{O}_{8+\delta}$.

We have analyzed the ARPES spectra from the nodal to the anti-nodal region for each sample and determined the k_F 's or each Fermi surface by fitting of momentum-distribution curves (MDCs) with single Lorentzian. Around the nodal region, k_F is defined at Fermi level (E_F) by single Lorentzian. In the off-nodal to the anti-nodal region, k_F is defined at the momentum which shows the gap minimum by single Lorentzian in the SC state. On the other hand, in the normal state (above T^*), k_F is defined at Fermi level (E_F) by single Lorentzian in the off-nodal to the anti-nodal region. The k_F points are plotted as shown by red dots (Fig. 1. (a), (b)). We have fitted Fermi-surface shape (red dots) by tight binding model (white curve) and estimated the hole concentration of each sample from the Fermi surface area and compared them quantitatively.

As a result, the Fermi-surface shapes observed by the SC and normal states in each composition can be fitted with the same tight binding parameters, and there is no significant change in the shape of the Fermi surface observed in temperature.

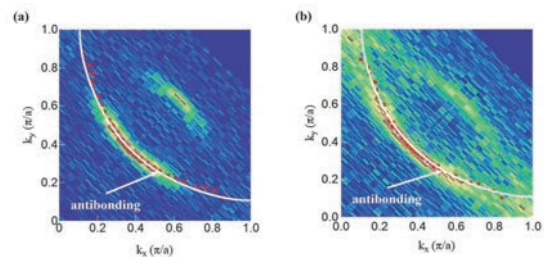


Fig. 1. (a) Fermi surface of overdoped $\text{Bi}_{2.1-x}\text{Pb}_x\text{Sr}_2\text{CaCu}_2\text{O}_{8+\delta}$ in the superconducting state ($T = 30$ K). (b) Fermi surface of overdoped $\text{Bi}_{2.1-x}\text{Pb}_x\text{Sr}_2\text{CaCu}_2\text{O}_{8+\delta}$ in the normal state ($T = 150$ K, above T^*).

[1] J. L. Tallon *et al.*, Phys. Rev. B: Condens. Matter **51** (1995) 12911.

[2] I. M. Vishik *et al.*, PNAS **6** (2012) 18332.

BL7U

Electronic Structure of Garnet-Type Solid Electrolytes $\text{Li}_{6.5}\text{La}_3\text{Zr}_{1.5}\text{Ta}_{0.5}\text{O}_{12}$ Bulk Single Crystal

K. Masuda¹, S. Koyama¹, S. Takakura², M. Nakatake³, K. Tanaka⁴, K. Kataoka⁵, J. Akimoto⁵,
Y. Iriyama¹ and T. Ito^{1,2}

¹Graduate School of Engineering, Nagoya University, Nagoya 464-8603, Japan

²Nagoya University Synchrotron Radiation Research Center (NUSR), Nagoya University,
Nagoya 464-8603, Japan

³Aichi Synchrotron Radiation Center, Seto 489-0965, Japan

⁴UVSOR Synchrotron Facility, Institute for Molecular Science, Okazaki 444-8585, Japan

⁵National Institute of Advanced Industrial Science and Technology (AIST), Ibaraki 305-8565, Japan

With the recent expansion of the use of lithium-ion secondary batteries, development of all-solid-state batteries using lithium-ion conductive inorganic solid electrolytes has been progressing to realize further safety, high energy density, and high output, etc. On the other hand, the valence-band electronic structure, which is essential to understand the relation between lithium-ion and electron conductivity in inorganic solid electrolytes, has not been well elucidated yet, though the chemical analysis using operando X-ray photoemission has intensively been applied on the system [1,2]. To clarify the effect of lithium on the electronic structure of solid electrolytes, we have performed angle-resolved photoemission spectroscopy (ARPES) measurements on garnet-type solid electrolytes $\text{Li}_{6.5}\text{La}_3\text{Zr}_{1.5}\text{Ta}_{0.5}\text{O}_{12}$ (LLZTO) in which high Li ion conductivity (1.27×10^{-3} S/cm) along the looped pathway due to the shorter Li-Li distance and deficient Li-site arrangement at room temperature have been reported [3].

ARPES measurements were performed at the UVSOR-III BL7U. Data were acquired at room temperature with $h\nu = 31$ eV which enables us to trace around the ΓMX plane with inner potential of $V_0=10.2$ eV estimated from the photon energy dependent measurement (not shown). To minimize spectral modulation due to photo-irradiation, photon flux was sufficiently reduced ($<3\text{E}+10$ photons/s) during all measurements. Single crystals were cleaved *in situ* along (011) plane.

Figure 1 (a) and (b) show ARPES spectra and band structure along the ΓM line of LLZTO, respectively. We have found that the valence band electronic structure of LLZTO is formed by a broad peak feature around 6 eV with a peak width of about 3.5 eV. This broad feature exhibits weak dispersive characteristics as a function of momentum (angle). Through a qualitative assessment of the continuous energy shift and intensity changes observed in broad peak and shoulder features, we anticipate the possible existence of several bands, as indicated by the gray lines in Fig. 1(a) and (b) respectively.

Figure 1 (c) and (d) show the DFT PDOS and band structure along the ΓM line of tetragonal $\text{Li}_7\text{La}_3\text{Zr}_2\text{O}_{12}$ with space group $I4_1/acd$ [4]. From the comparison between ARPES and calculations, we observe that the

valence band width of DFT appears to be similar to the observed spectral peak width. Furthermore, the energy positions of three peaks on PDOS of O orbital components seem to be consistent with the overall peak dispersions expected from the present ARPES. However, it remains challenging to resolve the complex band dispersion resulting from the overlap of numerous states. These results suggest the potential utility of ARPES for investigating the electronic structure of solid electrolytes single-crystals.

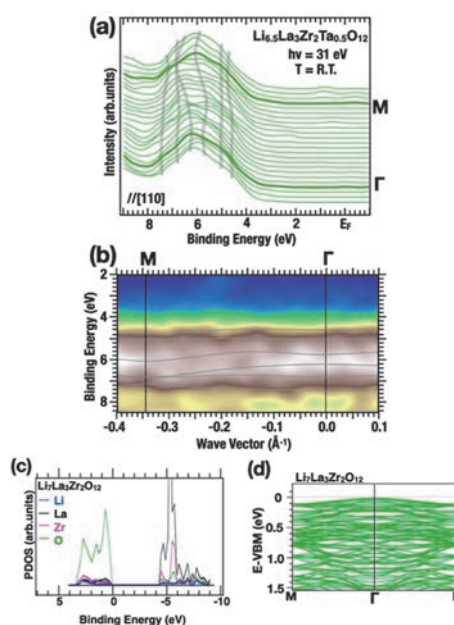


Fig. 1. (a, b) ARPES spectra (a) and band structures (b) along the ΓM line of $\text{Li}_{6.5}\text{La}_3\text{Zr}_{1.5}\text{Ta}_{0.5}\text{O}_{12}$. Solid lines are guides for eyes. (c, d) The partial density of states (c) and band structure along the ΓM line of $\text{Li}_7\text{La}_3\text{Zr}_2\text{O}_{12}$ [4].

- [1] K. Hikima *et al.*, Commun. Chem. **5** (2022) 52.
- [2] K. N. Wood *et al.*, Nat. Commun. **9** (2018) 2490.
- [3] K. Kataoka and J. Akimoto, ChemElectroChem **5** (2018) 2551.
- [4] The Materials Project. *Materials Data on $\text{Li}_7\text{La}_3\text{Zr}_2\text{O}_{12}$ by Materials Project*. United States: N. p., 2020. Web. doi:10.17188/1313215.

ARPES Study of the Coexistence of Superconductivity and Pure Electronic Nematicity in FeSe Thin Films on LaAlO₃

K. Nakayama¹, T. Kobayashi², F. Nabeshima², S. Souma^{3,4}, T. Takahashi¹,
A. Maeda² and T. Sato^{1,3,4,5,6}

¹Department of Physics, Tohoku University, Sendai 980-8578, Japan

²Department of Basic Science, the University of Tokyo, 3-8-1 Komaba, Meguro, Tokyo 153-8902, Japan

³Center for Spintronics Research Network, Tohoku University, Sendai 980-8577, Japan

⁴WPI Research Center, Advanced Institute for Materials Research, Tohoku University, Sendai 980-8577, Japan

⁵International Center for Synchrotron Radiation Innovation Smart (SRIS), Tohoku University, Sendai 980-8577, Japan

⁶Mathematical Science Center for Co-creative Society (MathCCS), Tohoku University, Sendai 980-8578, Japan

The iron-based superconductor iron selenide (FeSe) has attracted attention due to its unique properties, such as high-temperature superconductivity in monolayer films on SrTiO₃ and strong-coupling superconductivity in BCS-BEC crossover regime in bulk samples, distinguishing it from other iron-based superconductors. Of particular interest in FeSe is the nematic state, where the rotational symmetries of various properties and electronic state decrease from C₄ to C₂. Unlike nematic states in other iron-based superconductors, which typically develop almost simultaneously with antiferromagnetic ordering and tetragonal-to-orthorhombic structural transition, the nematic state in FeSe lacks antiferromagnetic ordering [1]. Moreover, recent x-ray diffraction and angle-resolved photoemission spectroscopy (ARPES) measurements revealed that FeSe thin films grown on LaAlO₃ substrates exhibit nematicity while keeping the tetragonal lattice symmetry [2]. This decoupling of the nematic state from magnetic and structural instabilities provides an excellent opportunity to investigate the origin of nematicity and the interplay between nematicity and superconductivity.

In this study, we conducted ARPES measurements of FeSe/LaAlO₃ to clarify the relationship between superconductivity and nematicity. Since FeSe/LaAlO₃ exhibits superconductivity within the pure nematic state, we tried direct observations of the electronic reconstruction in the nematic state and a superconducting gap below T_c, by utilizing high-energy and momentum resolution capability realized with low-energy photons at BL7U in UVSOR. High quality FeSe/LaAlO₃ samples were prepared by pulsed laser deposition, and the clean surfaces necessary for the ARPES measurements were obtained by cleaving the samples in ultrahigh vacuum. High-resolution ARPES measurements were carried out using an Al spectrometer.

Figure 1 shows ARPES spectra measured in the nematic state along the Γ M high-symmetry line. We observed a holelike dispersion which produces a small pocket centered at the Γ point. We also observed two holelike bands topped at the M point. These holelike bands at the M point are attributed to the Fe 3d_{xz} and

3d_{yz} orbitals. Their energy separation of ~ 50 meV is much larger than the spin-orbit gap of 20-30 meV. Such a large energy separation is the spectroscopic evidence for the occurrence of electronic nematicity. Since the electronic reconstruction in the nematic state has been successfully observed, we next performed high-resolution measurements in the superconducting state.

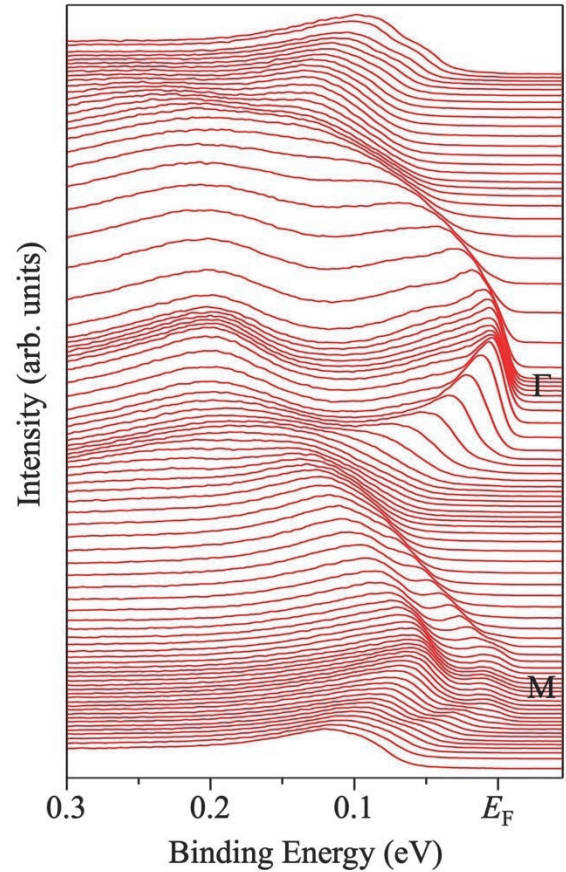


Fig. 1. ARPES intensity along the Γ M cut measured in the pure nematic state of FeSe/LaAlO₃.

[1] K. Nakayama *et al.*, Phys. Rev. Lett. **113** (2014) 237001.

[2] Y. Kubota *et al.*, Phys. Rev. B: Condens. Matter **108** (2023) L100501.

BL7U

High-Resolution ARPES Study of Monolayer Germanene Grown on Ag

T. Terasawa^{1,2}, S. Suzuki¹, D. Katsube³, S. Tanaka⁴ and K. Tanaka⁵

¹Advanced Science Research Center, Japan Atomic Energy Agency, Tokai 319-1195, Japan

²Institute of Industrial Science, The University of Tokyo, Meguro 153-8505, Japan

³Cluster for Pioneering Research, RIKEN, Wako 351-0198, Japan

⁴SANKEN, The Institute of Scientific and Industrial Research, Osaka University, Ibaraki, 567-0047, Japan

⁵UVSOR Synchrotron Facility, Institute for Molecular Science, Okazaki 444-8585, Japan

Based on the angle-resolved photoemission spectroscopy (ARPES), the band structure of germanene, a two-dimensional honeycomb lattice composed of a monatomic layer of Ge atoms, has been discussed so far because of its expected coexistence of ultrahigh carrier mobility and a band gap [1]. However, the germanene sample deposited on Ag(111) substrates showed a defective structure, so the obtained germanene bands were diffuse even in the best ARPES in the earlier reports [2]. In 2018, J. Yuhara and colleagues introduced a novel germanene preparation method. This process involves the segregation of germanene on Ag(111) thin film on Ge(111) substrate during the annealing and cooling process [3]. The scanning tunneling microscopy images in their report showed that germanene formed on Ag in R30 epitaxial relation together with $7\sqrt{7}\times 7\sqrt{7}$ R19.1 superlattice formation, indicating the long-range order and weak interaction between germanene and Ag surface. As the high-quality sample was realized, the ARPES measurement of the segregated germanene on Ag(111) is required.

Here, we report ARPES measurements of germanene segregated on Ag surfaces. Ag thin films were deposited on Ge(111) substrates at the Japan Atomic Energy Agency. The sample was introduced into the load lock chamber of the BL7U beamline without any preparation. The sample surface was cleaned by repeated Ar⁺ sputtering and annealing. After annealing at 500°C for 30 min, germanene formed on the sample surface, as confirmed by low-energy electron diffraction. ARPES measurements were performed at 8 K using the incident light energy of 8-28 eV.

Figure 1(a) shows the ARPES intensity map on the Γ -M_{Ag} line (equal to Γ -K_{germanene}) of the germanene grown on the Ag surface by 500 °C annealing with the incident light energy of 21.2 eV. As the obtained bands were diffuse, we carried out the second derivation of the ARPES intensity map along the energy direction, as shown in Fig. 1(b). After the second derivation, the electron pocket-like band above -1.0 eV was observed, consistent with the band structure of germanene grown on Al(111) and our results in BL5U [4,5]. In addition, we also observed the hole-like bands below the electron pocket. This is qualitatively consistent with the density functional calculation in the previous report [1]. Note that these diffuse bands were not observed for the so-called “striped phase,” corrugated Ag₂Ge surface alloy grown by 300°C anneal but observed for 500°C anneal samples in 10-28 eV. The second derivatives of the maps resulted in the similar structures. Thus, we

concluded that the obtained bands originate from germanene on Ag. Unfortunately, the Ag bulk bands overlapped around the K point of germanene. Further experiments are required to reveal the band structure of germanene around its K point.

In summary, we performed high-resolution ARPES measurements of germanene segregated on Ag(111) thin films deposited on Ge(111) substrates. The ARPES intensity maps show that the germanene band structure is similar to the DFT-calculated germanene bands. Further analysis and discussion are needed to clarify whether the germanene band structure has a linear band dispersion and band gap.

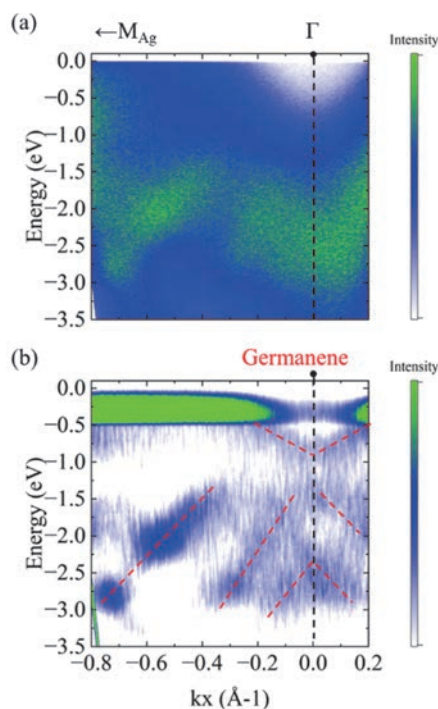


Fig. 1. (a) ARPES intensity map of germanene segregated on Ag thin film deposited on Ge(111) substrates. (b) second derivative along the energy direction of (a). Red dashed lines are eye guides.

- [1] C. C. Liu *et al.*, Phys. Rev. B: Condens. Matter **84** (2011) 195430.
- [2] C. H. Lin *et al.*, Phys. Rev. Mater. **2** (2018) 024003.
- [3] J. Yuhara *et al.*, ACS Nano **12** (2018) 11632.
- [4] J. Yuhara *et al.*, 2D Mater. **8** (2021) 045039.
- [5] UVSOR Activity Report **51** (2024) 97.

Measurement of Valence Band Dispersion in 2-*n*-Octyl-[1]benzothieno[3,2-*b*]naphtho[2,3-*b*]thiophene (2-C8-BTNT) Crystals

T. Tasaki¹, S. Inoue², K. Kikuchi¹, H. Hattori¹, T. Hasegawa² and Y. Nakayama^{1,3}

¹Department of Pure and Applied Chemistry, Tokyo University of Science, Noda, Chiba 278-8510, Japan

²Department of Applied Physics, The University of Tokyo, Tokyo 113-8656, Japan

³Institute for Molecular Science (IMS), Okazaki 444-8585, Japan

Organic semiconductor devices including organic solar cells and organic transistors are expected to find applications due to their advantages such as lightness, mechanical flexibility, and printability [1,2]. It has been reported that materials exhibiting band-like transport, rather than intermolecular hopping, lead to charge carrier mobility of high levels for organic semiconductor devices [3]. To understand the transport nature, it is essential to the nature of the conduction mechanism of such organic semiconductor materials. 2-*n*-Octyl-[1]benzothieno [3,2-*b*]naphtho[2,3-*b*]thiophene (2-C8-BTNT) (Fig. 1) was reported to exhibit high charge carrier mobility of over $10 \text{ cm}^2 \text{V}^{-1} \text{s}^{-1}$ in its single-crystal field-effect transistors [4]. In this study, angle-resolved photoelectron spectroscopy (ARPES) experiments were performed to measure the valence bands of the 2-C8-BTNT crystals.

2-C8-BTNT crystals were prepared by a drop-casting method, one of the solution growth methods, from its chlorobenzene solution of 0.5 mg/mL on Au-coated Si substrates under a solvent atmosphere at room temperature. The ARPES measurements were performed at BL7U of UVSOR-III. The photon energy was set at 8 eV, and laser light (wavelength of 375 nm) was illuminated on the sample for the cancellation of the sample charging during the photoelectron spectroscopy measurements. The emission angle θ is defined as 0° when the sample was facing normal to the analyzer and as positive when the surface was rotated toward the synchrotron light source. The range of photoelectron emission angles that can be collected by the analyzer at $\theta = 0^\circ$ was approximately $\pm 16^\circ$. The ARPES measurements were performed in the θ range from -10° to $+40^\circ$ for every 5° , and eleven ARPES spectra obtained were integrated to map out a resulting total ARPES data in a photoelectron emission angle range from -26° to $+56^\circ$ used in the analysis.

Figure 2 shows the ARPES results of 2-C8-BTNT in the Γ -X direction taken at room temperature. In an energy-wavenumber (E - k) region shown in yellow, the spectral features shifted to the deeper binding energy side as moving from the Γ point to the X point. This indicates that the energy dispersion of the valence was successfully measured. The observed band width seemed to be larger than the previously reported energy dispersion of the single crystal rubrene (approximately

0.5 eV [3]). In the future, we plan to investigate in detail the valence band structures of 2-C8-BTNT and the temperature dependence to elucidate relationships with the transport properties and electron-photon (vibration) couplings.

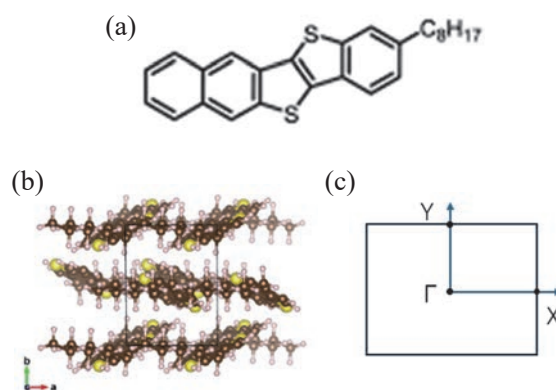


Fig. 1. (a) Molecular structure, (b) single-crystal molecular arrangement in the crystal *ab* plane ($a = 6.019 \text{ \AA}$, $b = 7.878 \text{ \AA}$ [4]), and (c) surface Brillouin zone of 2-C8-BTNT.

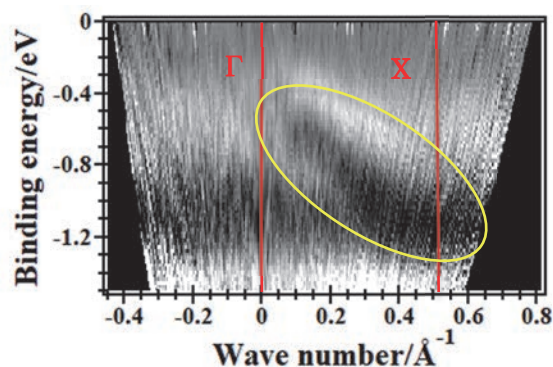


Fig. 2. ARPES d^2I/dE^2 (where I is photoelectron intensity) map of the 2-C8-BTNT crystal plotted on the E - k plane in the Γ -X direction (black: negative d^2I/dE^2 , white: positive d^2I/dE^2).

- [1] H. Minemawari *et al.*, Nature **475** (2011) 364.
- [2] J. Mei *et al.*, J. Am. Chem. Soc. **18** (2013) 6724.
- [3] Y. Nakayama *et al.*, J. Mater. Chem. C. **8** (2020) 9090-9132.
- [4] S. Inoue *et al.*, Chem. Sci. **11** (2020) 12493.

BL7U

Orbital-Resolved Observations of Molecular Electronic Structures and Many-Body Interactions in Rubrene Single Crystal

K. Fukutani^{1,2}, F. Nishino², P. I. Jaseela², N. Kasuya³, J. Takeya³, S. Makita¹,
K. Tanaka^{1,2} and S. Kera^{1,2}

¹*Institute for Molecular Science, Okazaki 444-8585, Japan*

²*The Graduate University for Advanced Studies (SOKENDAI), Okazaki 444-8585, Japan*

³*Graduate School of Frontier Science, University of Tokyo, Chiba 277-8561, Japan*

Recent developments in the field of functional organic molecular semiconductors have rapidly expanded the realm of organic materials into practical device applications, and they play an indispensable role in our electronic industry today, owing to their physical flexibility, low cost of fabrication, high biodegradability in the environment, as well as the abundance of the constituent elements (mostly carbon and hydrogen) that are, in principle, inexhaustive.

Among such organic semiconductors, rubrene ($C_{42}H_{28}$) is known for its particularly high hole carrier mobility ($40 \text{ cm}^2/\text{Vs}$ [1]) and is considered one of the most important organic semiconductor materials for the future of organic electronics. However, despite its success in various device applications, our knowledge of their electronic structure, one of the most fundamental building blocks for understanding and controlling their properties, is far from complete.

In fact, various experimental investigations on the electronic band structures of rubrene have reported qualitatively different results [2] and the true band structure of this material remains elusive.

In the crystal structure of rubrene, it is known that a unit cell is occupied by two rubrene molecules, and hence its band structure must exhibit two distinct electronic states (bands), arising from bonding and anti-bonding phase relations of the molecules. Furthermore, these two electronic states must be degenerate at the Brillouin zone edge (e.g., X and Y points) due to the crystal symmetry.

However, the electronic band structures reported from various experiments show either a single band or two bands that are qualitatively inconsistent with the rubrene crystalline symmetry. Thus, in our study, we performed a series of polarization-dependent high-resolution angle-resolved photoemission spectroscopy (ARPES) to investigate the orbital-resolved band structure of rubrene single crystal.

Figure 1 shows the results of our ARPES measurements (second derivatives) using photons with linear horizontal, vertical, and circular polarizations. It can be seen that in the horizontal and vertical polarization, two distinct bands exhibiting different dispersion widths can be seen. Furthermore, in the circular polarization, both of these two bands are observed and they appear to be degenerate near the

Brillouin zone edge, at the Y point.

Such band structure is fully consistent with the previous band structure calculations [3] predicting the presence of the two bands arising from the bonding and anti-bonding molecular orbitals. Our detailed analysis using the photoemission selection rules also reveal the electronic symmetries of the observed two bands in the horizontal and vertical polarizations are consistent with the orbital symmetries of anti-bonding and bonding electronic states, respectively.

Furthermore, our results also show the presence of the intra-band gap, known to arise from the coupling between the electrons and the molecular vibrations, in both of the bands. Thus, our results not only resolve the long-standing discrepancy between the calculated and the observed band structures, but also opens up a pathway to further understand the many-body interactions in organic molecular semiconductors.

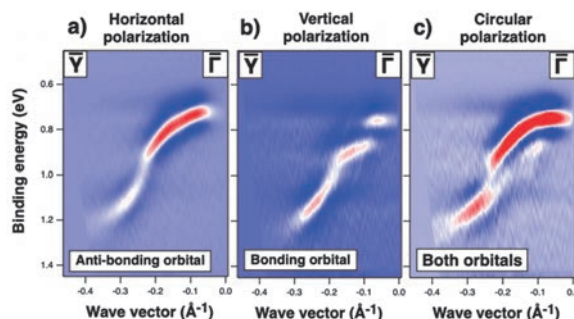


Fig. 1. The results of polarization-dependent ARPES measurements (second derivative plots) for rubrene single crystal, using (a) linear horizontal, (b) linear vertical, and (c) circular polarizations. The measurements were performed at $h\nu = 8 \text{ eV}$.

- [1] J. Takeya *et al.*, Appl. Phys. Lett. **90** (2007) 102120.
- [2] S. Machida *et al.*, Phys. Rev. Lett. **104** (2010) 156401.; H. Ding *et al.*, Appl. Phys. Lett. **96** (2010) 222106.; Y. Nakayama *et al.*, Appl. Phys. Express **5** (2012) 111601.; A. Vollmer *et al.*, J. Electron Spectrosc. Rel. Phenom. **185** (2012) 55.; F. Bussolotti *et al.*, Nat. Commun. **8** (2017) 173; J. Nitta *et al.*, Sci. Rep. **9** (2019) 9645.
- [3] S. Yanagisawa *et al.*, Phys. Rev. B: Condens. Matter **88** (2013) 115438.

Excitation Spectra and Decay Curves of Plastic Scintillators with VUV Excitation

M. Koshimizu

Research Institute of Electronics, Shizuoka University, Hamamatsu 432-8011, Japan

Plastic scintillators are composed of polymer host and organic phosphors. The scintillation process in the plastic scintillators is described as (1) ionization of the host polymer, (2) recombination of the ionized polymer to form electronic excited states, (3) excitation energy transfer from the host polymer to the organic phosphors, and (4) luminescence of the organic phosphors. In general, the scintillation light yields of plastic scintillators are significantly lower than those of commercially available inorganic scintillators. A main cause of the lower scintillation light yields of plastic scintillators is low energy transfer efficiency at the stage (3).

Prior to the stage (3), two kinds of excited states are formed upon recombination at the stage (2): singlet and triplet excited states. Among them, triplet excited states are not effectively used because of the two reasons: one is low energy transfer efficiency from the host to the organic phosphors. For the singlet excited states, the excitation energy is transferred to organic phosphors via dipole-dipole interaction, which is a long-range interaction. On the contrary, the triplet excited states have low energy transfer efficiency because of the short range of the exchange interaction, which is responsible for the energy transfer of the triplet excited states. There was a small number of examples of the analysis of the contribution of the triplet excited states.

Recently, we found that the excitation spectra of plastic scintillators had a characteristic feature representing formation of multiple excitations and triplet excited states [1]. In this study, we further explored the analysis with VUV excitation based on decay curve measurements.

Polystyrene-based plastic scintillators containing DPO and POPOP as the organic phosphors at different concentrations were used as the samples. The photoluminescence decay curves were obtained using a time-correlated single photon counting technique at BL7B of UVSOR operated in a single bunch mode. The photoluminescence decay curves at 60–210 nm were obtained.

The photoluminescence decay curves of the plastic scintillators are presented Figs. 1 and 2. For all the excitation wavelengths, the polystyrene host is initially excited. The slow decay component originates from triplet-triplet annihilation, which results in a delayed formation of singlet excited states. With excitation at 210 nm, the decay behaviors were the fastest among the surveyed excitation wavelengths. The decay became

slower with excitation at 180 nm, and subsequently became faster at 150 nm. This is in line with the excitation spectra [1]. The former change can be explained by the enhanced formation probability of the triplet excited states. On the contrary, the latter change can be explained with the enhanced formation probability of the singlet excited states with multiple excitation formation. Further shortening of the excitation wavelength resulted in slow decay curves. These results strongly suggest that the formation probability of the triplet excited states has a complicated formation spectrum in the VUV region, which in turn can be an effective tool to analyze the contribution of the triplet excited states.

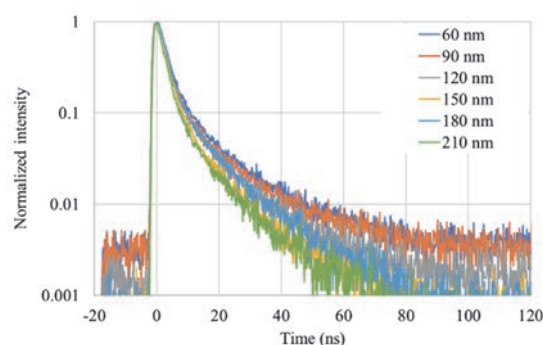


Fig. 1. Photoluminescence decay curves of polystyrene-based plastic scintillators containing DPO and POPOP as organic phosphors at 0.5 wt%.

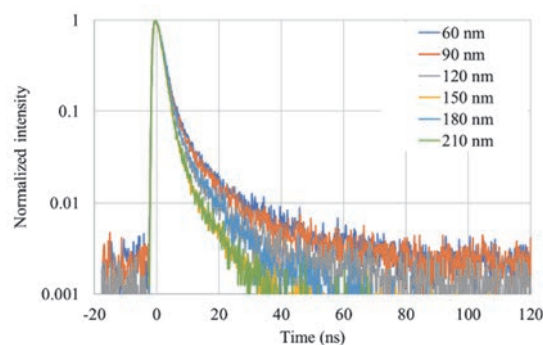


Fig. 2. Photoluminescence decay curves of polystyrene-based plastic scintillators containing DPO and POPOP as organic phosphors at 2.0 wt%.

[1] M. Koshimizu, Y. Fujimoto and K. Asai, UVSOR Activity Report **50** (2023) 112.

BL7B

Vacuum Ultraviolet Characterization of Li-Glass as a Potential Neutron Scintillator

T. Shimizu, K. Shinohara, K. Yamanoi and N. Sarukura

Institute of Laser Engineering, Osaka University, 2-6 Yamadaoka Suita, Osaka 565-0875 Japan

In fusion research, neutron detection is important for evaluating efficiency and safety. There are different types of neutrons produced, but primary neutrons in particular are easily detected with conventional plastic scintillators due to their large quantity. On the other hand, scattered neutrons are detected later than X-rays and primary neutrons generated by nuclear reactions, and their quantity is much lower than that of primary neutrons, making the measurement of scattered neutrons difficult. Therefore, a scintillator with high sensitivity to scattered neutrons and fast response that quickly attenuates X-ray and primary neutron signals is needed.

Scattered neutron energies range from 0.2 to 0.6 MeV. For neutrons of this energy, ${}^6\text{Li}$ has a large absorption cross section. ${}^6\text{Li}$ has long been widely used as a glass scintillator for thermal neutrons, and glasses containing ${}^6\text{Li}$ and doped with Ce as a luminescent material are now in practical use. The conventionally used Li glass scintillators are $\text{Li}_2\text{O-SiO}_2$ glass doped with Ce_2O_3 (GS2, GS20, KS20, etc.). Neutrons are generally measured by time-of-flight (TOF), and this technique requires a time resolution of 25 ns to separate the signal from the transient neutrons. However, the emission lifetime of GS2, GS20, and KS20 is 50-70 ns, which does not meet this requirement.

To solve this problem, a scintillator using $20\text{Al}(\text{PO}_3)_3\text{-}80\text{LiF}$ (APLF) glass as a base material was developed instead of $\text{Li}_2\text{O-SiO}_2$. Shortening the emission wavelength is effective in shortening the lifetime of luminescence. APLF is an excellent base material for short wavelength scintillators because of its high transparency in the ultraviolet region and no risk of self-absorption. Therefore, we have succeeded in shortening the lifetime of APLF by using Pr^{3+} instead of Ce^{3+} , which is a commonly used luminescent nucleus, and by shifting the emission wavelength to the short wavelength side (Ce^{3+} : 300~350 nm \rightarrow Pr^{3+} : 250~300 nm).

Although APLF is excellent candidate for scintillators for scattered neutrons, there are other candidates for lithium-based glasses. We are currently developing lithium glasses with new compositions under a collaborating researcher, and characterization of scintillators using these glasses is currently underway.

In this study, we have prepared new lithium glasses with Pr luminescent nuclei such as $20\text{Li}_2\text{O-}20\text{CaO-}60\text{SiO}_2\text{+}0.3\text{Pr}_2\text{O}_3$ (LCSO+0.3Pr), $30\text{Li}_2\text{O-}70\text{B}_2\text{O}_3\text{+}$

$0.3\text{Pr}_2\text{O}_3$ (LBO+0.3Pr) and $30\text{Li}_2\text{O-}60\text{P}_2\text{O}_5\text{-}10\text{Al}_2\text{O}_3\text{+}0.3\text{Pr}_2\text{O}_3$ (LPAO+0.3Pr) and characterized.

Since the luminescence and absorption are in the VUV to UV region, we will use the UVSOR VUV line to obtain luminescence and absorption spectra and evaluate at what wavelengths they should be designed for use as scintillators. The emission and excitation spectra were obtained at the BL7B beamline. Each glass was placed inside a vacuum chamber maintained at 10⁻⁶ Pa and was excited by wavelengths chosen using the beamline's 3-m normal incidence monochromator that has a dynamic range from 50 nm (VUV) to 1000 nm (IR). The emission was then fiber-fed to an Acton SpectraPro-300i spectrometer coupled with a liquid N₂-cooled PyLoN 400BR_eXcelon charge-coupled device (CCD) camera for emission spectroscopy and with a photomultiplier tube (PMT) for excitation spectroscopy.

Figure 1 is an example of the measurement results and shows the transmittance in VUV of new samples. Among the samples measured this time, the one with LPAO showed promising results, so we will prepare samples with different concentrations of Pr for further optimization. We are currently compiling the analysis and discussion of the X-ray absorption near edge structure (XANES) spectroscopy for the presence of Pr ions in the glasses with a oxidation state.[1]

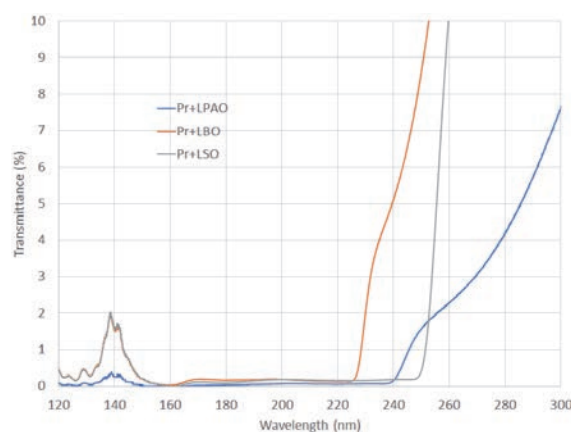
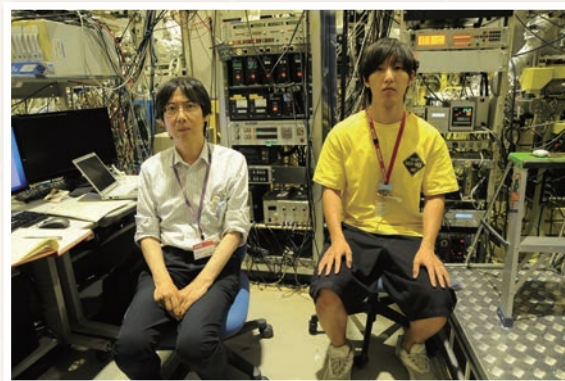
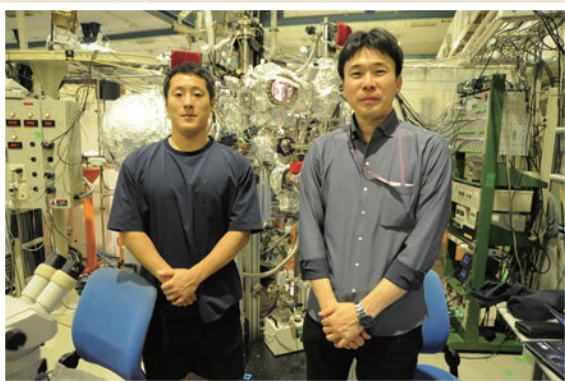
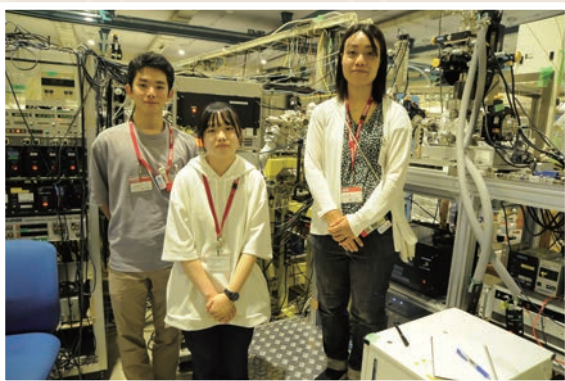
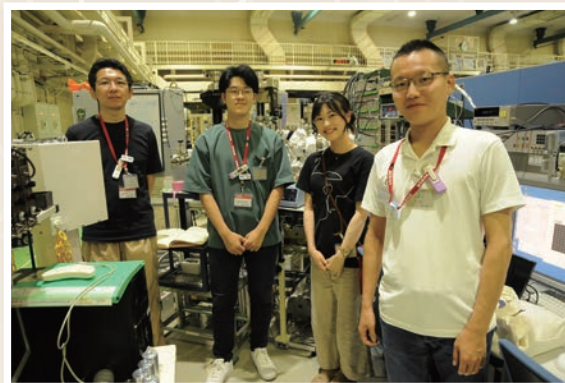


Fig. 1. Transmission spectra of Li-glass.

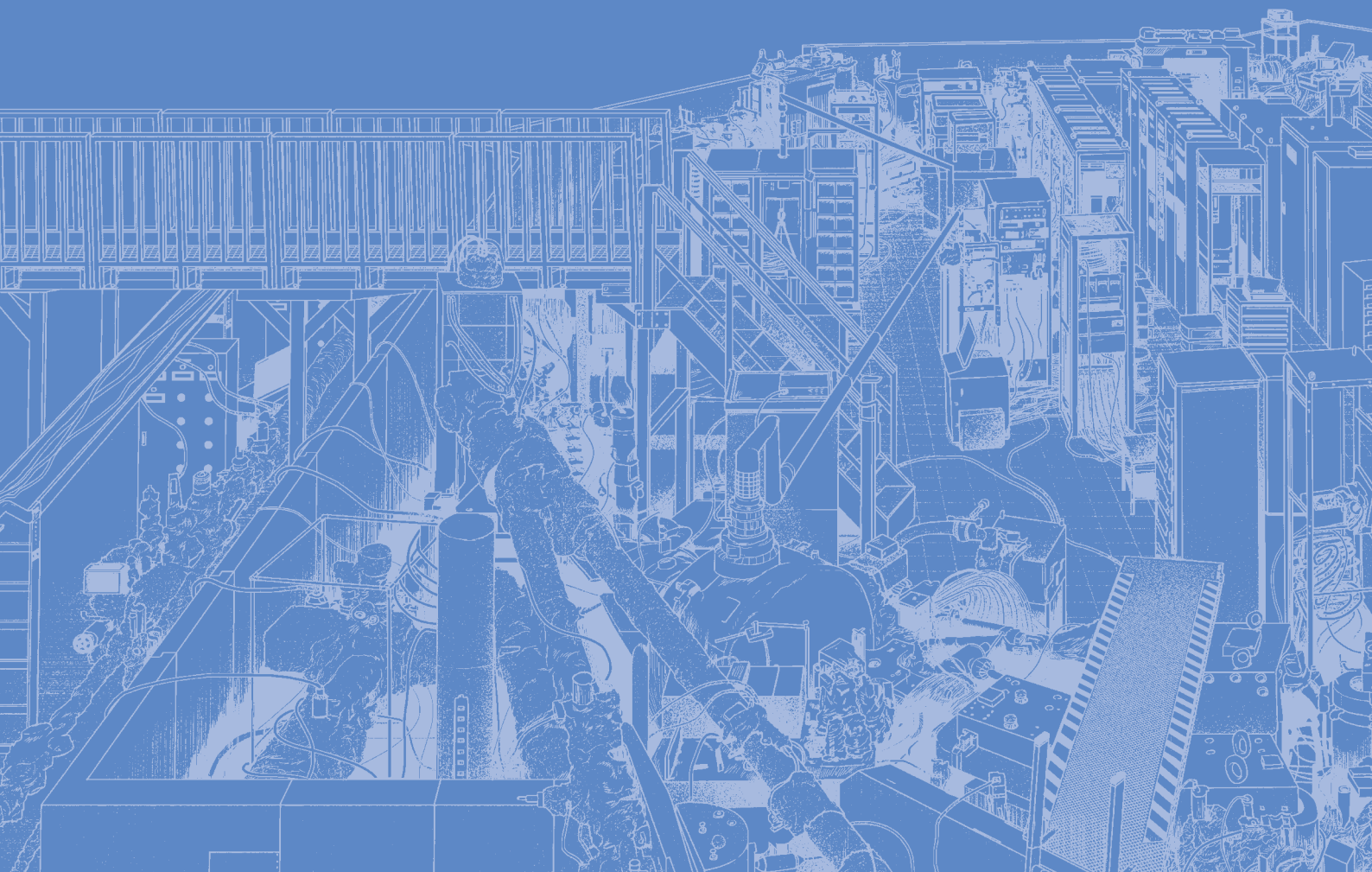
[1] K. Shinohara *et al*, the 9th International Symposium on Optical Materials (IS-OM'9), Tarragona (Spain), from June 26 to 30, 2023.

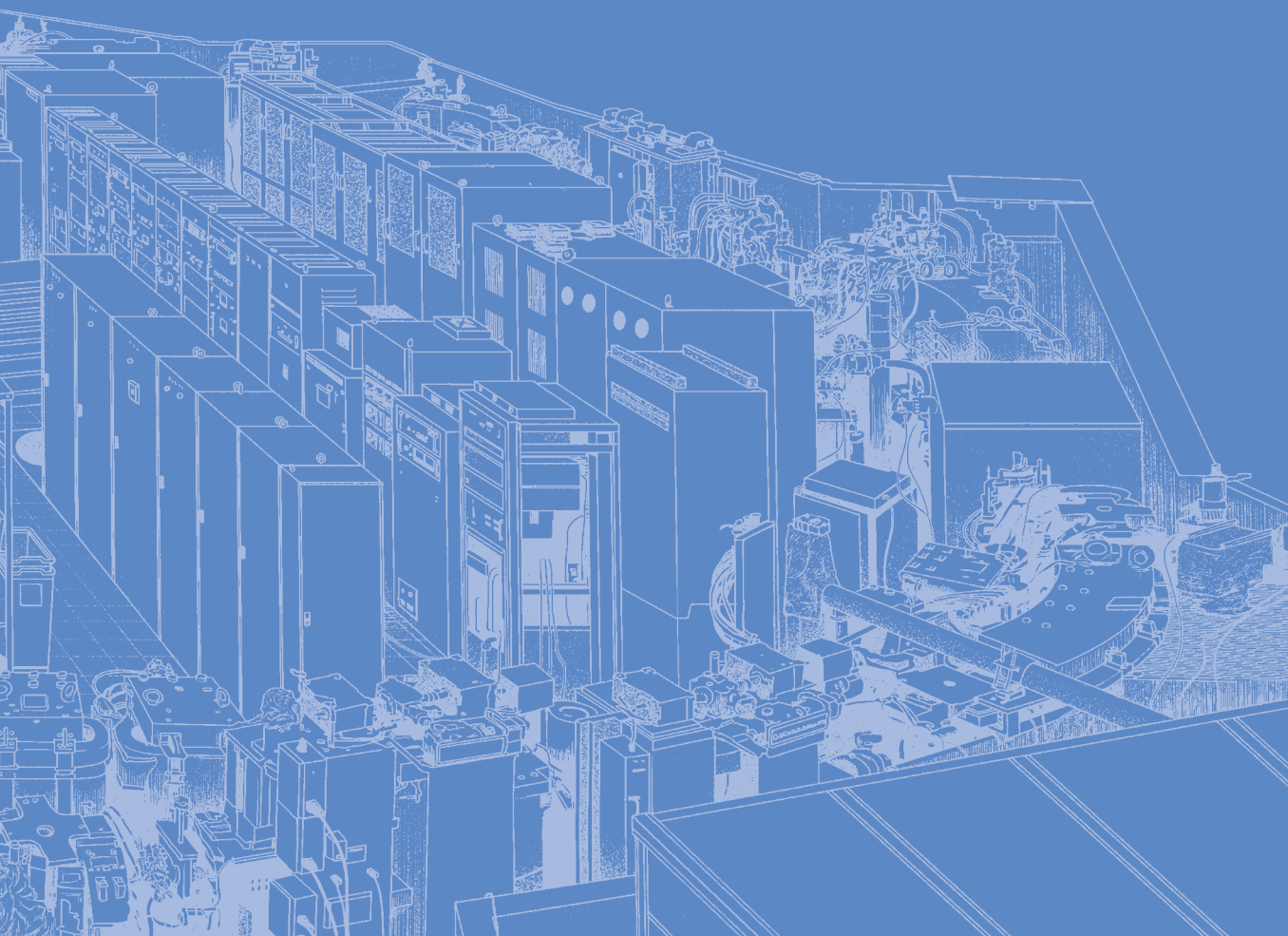
UVSOR User 4



III-3

Chemistry





Search for Chiral Systems Exhibiting Novel Type of Photoelectron Circular Dichroism

H. Kohguchi¹, Y. Hikosaka², T. Kaneyasu³, S. Wada¹, H. Ota⁴, M. Katoh^{1,4} and Y-I. Suzuki⁵

¹Graduate School of Advanced Science and Engineering, Hiroshima University,
Higashi-Hiroshima 739-8526, Japan

²Institute of Liberal Arts and Sciences, University of Toyama, Toyama 930-0194, Japan

³SAGA Light Source, Tosu 841-0005, Japan

⁴UVSOR Synchrotron Facility, Institute for Molecular Science, Okazaki 444-8585, Japan

⁵School of Medical Technology, Health Sciences University of Hokkaido, Tobetsu 061-0293, Japan

Photoelectron circular dichroism (PECD) is a sensitive probe for molecular chirality, which is one of the most attractive molecular properties in chemistry. The PECD parameter is defined as a b_1 coefficient associated with the first-order Legendre polynomial ($P_1(\cos\theta)$) in the difference photoelectron angular distributions between left- and right-handed circularly polarized ionization light. The BL1U beamline is highly suited for the PECD study since the undulator provides well-defined circularly polarized light in the vacuum ultraviolet region, where the b_1 parameter is generally maximized for most chiral molecules. The b_1 parameter exhibits particular photon energy dependence on the molecular species, for which we have developed our PECD study [1]. As well as the photoelectron kinetic energy dependence of the b_1 parameter, the state dependence of PECD is essential to determine the chirality of the relevant molecular orbitals. Thus, high-resolution photoelectron spectroscopy serves as a basis for a deep understanding of the PECD mechanism.

At the BL1U beamline, we measured the energy- and state-dependence of the PECD of methyl oxirane [2], a typical chiral molecule exhibiting PECD. Since the oxirane framework, where an asymmetric carbon atom is located, is more relevant to molecular chirality, we expected the PECD manifestation for other oxiranes.

We carried out the VMI measurements of several oxiranes at varied photon energies. The PECD results of methyl oxirane, well-known in previous studies, were used as a standard for optimizing the measurement condition. Examples of the results of the VMI measurements are shown in Fig. 1. The measurements with linearly polarized light (Fig. 1, upper) provide a basis for the state assignments. The photoelectron spectra obtained from the VMI data with linear polarization of phenyl oxirane were much different from those of methyl oxirane; the ionization threshold was lowered by approximately 2 eV, and the spectral peak structures in the vicinity of the threshold were not assignable to corresponding peaks of the methyl oxirane spectrum. We assumed that the photoionization

relevant to the molecular orbitals associated with the oxirane framework should show a similar PECD to that of methyl oxirane. The result of the PECD measurements, however, exhibited no chiral property for phenyl oxirane (Fig. 1 lower). Apparently biased positive (red) and negative (blue) intensity found in the difference image data at 90 nm is not a signature of PECD but an experimental artifact because PECD should appear as an asymmetric distribution with respect to the circularly polarized radiation propagation (vertical direction in the images). The b_1 values at other photon energy were also negligibly small compared to the PECD intensity of methyl oxirane. Electronic modification by phenyl substitution was found to be so large that the photoelectron spectra, especially in the low kinetic energy photoelectron region, were heavily altered, and the chirality around the asymmetric carbon was almost lost. The result indicates that PECD is more sensitive to the molecular electronic chirality than the photoelectron spectroscopy.

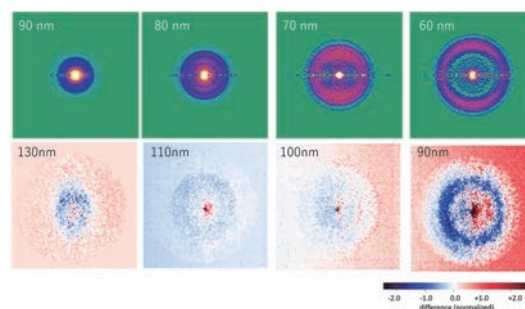


Fig. 1. Photoelectron scattering distributions of phenyl oxirane with linearly polarized light (upper) and circularly polarized light (lower) at several ionization wavelengths. The lower data are difference images between the right- and left-handed circular polarizations.

[1] H. Kohguchi *et al.*, UVSOR Activity Report **50** (2023) 136.

[2] H. Kohguchi *et al.*, UVSOR Activity Report **49** (2021) 106.

Time-Domain Double Slit Interference of Electrons Produced by Light Wave Packets from a Tandem Undulator

T. Kaneyasu^{1,2}, Y. Hikosaka³, S. Wada⁴, M. Fujimoto⁵, H. Ota², H. Iwayama^{2,6} and M. Katoh^{2,5,7}

¹SAGA Light Source, Tosu 841-0005, Japan

²Institute for Molecular Science, Okazaki 444-8585, Japan

³Institute of Liberal Arts and Sciences, University of Toyama, Toyama 930-0194, Japan

⁴Graduate School of Advanced Science and Engineering, Hiroshima University, Higashi-Hiroshima 739-8526, Japan

⁵Synchrotron Radiation Research Center, Nagoya University, Nagoya 464-8603, Japan

⁶SOKENDAI (The Graduate University for Advanced Studies), Okazaki 444-8585, Japan

⁷Hiroshima Synchrotron Radiation Center, Hiroshima University, Higashi-Hiroshima 739-0046, Japan

Wave-particle duality is one of the most fundamental concepts in quantum mechanics. The concept has previously been beautifully demonstrated by the double-slit experiment, in which particles such as electrons, atoms, molecules and neutrons passing through the double-slit exhibit interference patterns in the intensity distribution on a detection screen. Since there is an analogy between spatial diffraction and temporal dispersion in optics, the observation of double-slit interference with particles is not restricted to conventional space-domain experiments but can be extended to time-domain experiments. In this study, we present a new realization of the time-domain double-slit experiment with photoelectrons, demonstrating that spontaneous radiation from a bunch of relativistic electrons can be used to control the quantum interference of single particles [1].

To produce the temporal double-slit, we use a tandem-undulator system in which each relativistic electron in the bunch emits a pair of light wave packets that has a mutual coherence between them [2,3]. A pair of light wave packets sequentially interacts with a helium atom, producing a pair of photoelectron wave packets that propagate in free space and overlap each other, leading to the appearance of the interference pattern. In order to visualize the buildup of the interference pattern, we observe the interference in the energy domain (Fig. 1).

We recorded photoelectron images using a two-dimensional (2D) position-sensitive detector mounted in a hemispherical electron energy analyzer. The 2D detector allows for one-by-one detection of the photoelectrons. Figure 2 compares the CCD images of photoelectrons recorded with the radiation from single- and tandem-undulator configurations. In both cases, the central wavelength of the undulator radiation was 43 nm. When the single undulator is used, the helium atom is ionized by light wave packets emitted from either the upstream or downstream undulator, leading to the production of single (not-paired) photoelectron wave packets. Therefore, no interference pattern can be exhibited on the CCD image. On the other hand, the buildup process of the quantum interference pattern is

monitored by accumulating the CCD images when the radiation from the tandem undulator is used. The CCD image after accumulation of 2000 electrons shows an almost random distribution. An interference pattern appears at 2×10^4 electrons, and becomes clearer as the number of electrons is increased.

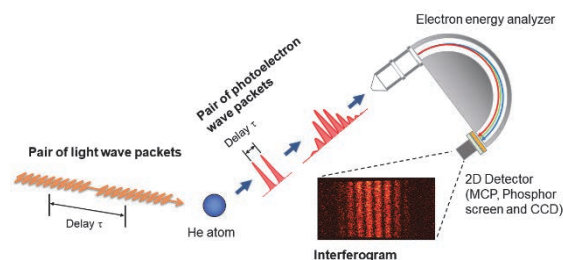


Fig. 1. Time-domain double-slit experiment using a tandem-undulator system.

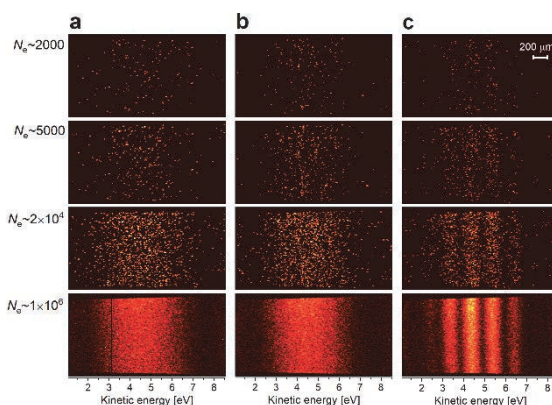


Fig. 2. CCD images of photoelectrons observed for radiation from (a) the upstream undulator, (b) the downstream undulator, and (c) the tandem undulator.

- [1] T. Kaneyasu *et al.*, Sci. Rep. **13** (2023) 6142.
- [2] Y. Hikosaka *et al.*, Nat. Commun. **10** (2019) 4988; **12** (2021) 3782.
- [3] T. Kaneyasu *et al.*, Sci. Rep. **12** (2022) 9682.

BL1U

Measurement of Arbitrary Polarization by Zeeman Quantum Beat of Helium Atom

T. Kaneyasu^{1,2}, Y. Hikosaka³, S. Wada⁴, H. Kohguchi⁴, M. Fujimoto⁵, H. Ota², H. Iwayama^{2,6},
M. Hosaka⁷ and M. Katoh^{2,5,8}

¹SAGA Light Source, Tosu 841-0005, Japan

²Institute for Molecular Science, Okazaki 444-8585, Japan

³Institute of Liberal Arts and Sciences, University of Toyama, Toyama 930-0194, Japan

⁴Graduate School of Advanced Science and Engineering, Hiroshima University,
Higashi-Hiroshima 739-8526, Japan

⁵Synchrotron Radiation Research Center, Nagoya University, Nagoya 464-8603, Japan

⁶SOKENDAI (The Graduate University for Advanced Studies), Okazaki 444-8585, Japan

⁷National Synchrotron Radiation Laboratory, University of Science and Technology of China,
Hefei 230029, China

⁸Hiroshima Synchrotron Radiation Center, Hiroshima University, Higashi-Hiroshima 739-0046, Japan

One of the unique capabilities of novel undulators used in modern synchrotrons is a polarization control. However, the actual polarization of light at the sample position often differs from the original one set by the undulator. This is mainly due to the reflection property of the beamline optics. To use the arbitrary polarization in the synchrotron radiation experiments, it is required to measure the actual polarization in a beamline.

We have recently developed a simple polarimetry method which uses a Zeeman quantum beat in the fluorescence decay of helium atoms [1,2]. In this study, we applied this method to investigate the actual polarization state of vacuum ultraviolet light at the beamline BL1U. The light source of BL1U is an APPLE-II type variably polarized undulator. The beamline consists of two toroidal mirrors and a Seya-Namioka monochromator. A small chamber equipped with two solenoid coils was set at the sample position to measure the Zeeman quantum beat of helium atoms. The photon energy was set to 24.2 eV to resonantly excite the 1s electron into the 6p orbital. We observed the fluorescence decay from the 1s6p into 1s2s state, emitting 345-nm wavelength photon. During the measurement, the UVSOR ring was operated in a single bunch mode, providing light pulses with a 178 ns period.

Figure 1 shows the fluorescence decay curves measured with different phases of the undulator magnets. The polarization state of undulator radiation smoothly changes from horizontal linear to elliptical and finally to vertical linear when the phase is changed. The fluorescence decay curves exhibit quantum beat oscillations superimposed on the exponential decay, reflecting the polarization state; the contrast and initial phase of the oscillations corresponds to the degree of linear polarization and the tilt angle of the polarization ellipse, respectively [2]. The beat structure almost vanishes at 21 mm phase, indicating that the degree of circular polarization is highest among the measurements, although one can expect that the undulator radiates almost fully circularly polarized light at 28.6 mm

phase. The observed difference can be explained by the effect of beamline optics. The experimental curves are well reproduced by a simulation which takes into account the polarization state of the undulator radiation and reflection property of the beamline optics.

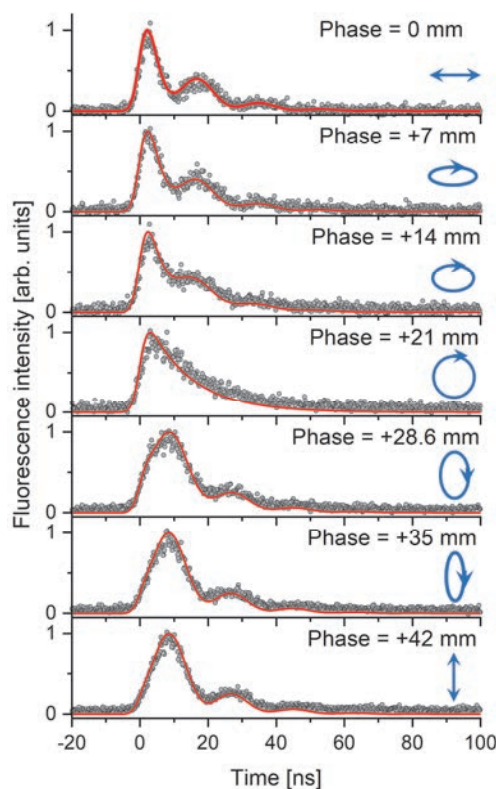


Fig. 1. Fluorescence decay curves of the 1s6p excited state of helium. The gray circles represent the experimental data while the red curve shows the simulation results. Polarization ellipse assumed in the simulation is attached in each panel.

[1] Y. Hikosaka *et al.*, J. Synchrotron Radiat. **27** (2020) 675.

[2] T. Kaneyasu *et al.*, New J. Phys. **22** (2020) 083062.

Observation of the Electronic Structure of Aggregating Polymers in Shear Thickening Solutions

K. Akada^{1,2}, S. Sato³, M. Kobayashi⁴ and J. Fujita¹

¹*Institute of Applied Physics, Graduate School of Pure and Applied Sciences, University of Tsukuba, Tsukuba 305-8573, Japan*

²*Japan Synchrotron Radiation Research Institute (JASRI), SPring-8, Sayo-gun 679-5198, Japan*

³*Graduate School of Science and Technology, University of Tsukuba, Tsukuba 305-8572, Japan*

⁴*Faculty of Life and Environmental Sciences, University of Tsukuba, Tsukuba 305-8572, Japan*

A shear thickening fluid (STF) is a non-Newtonian fluid characterized by a significant increase in its viscosity when subject to a shear rate above a critical value. Some colloidal suspensions consisting of silica particles exhibit shear-thickening (ST) properties, which has a wide spectrum of potential applications in shock absorption, body protection, etc. Various works have been made so far to interpret the origins of the shear thickening mechanisms in various STF systems.

Among ST fluids, those composed of particles with a small diameter and a polymer solution, which gel upon impact, are called shake-gels (Fig. 1). Previous study said that a polymer network bridging particles reconstructs in response during gelation process, although the detailed mechanism is not well understood. One reason is the difficulty in measuring the ST state. The reconstructed network return to their original state once the shear stress is removed, making it difficult to measure the properties of the ST state.

Previous studies on the dynamics in the STF have mostly focused on bulk states that measure the viscosity of the entire solution or macroscopic measurements using particles larger than $>\mu\text{m}$. Few reports focusing on the clustering of smaller particles or the aggregation structure of water molecules and polymers.

Regarding the structure of nm particles, our previous studies have revealed that several hundred nm of the floc structures are formed with an increase in viscosity by measuring the structure under shear. This gelation

occurs even when ST sample is flowing in a tube, and the ST phenomena can be controlled by flow rate and tube diameter.

By using X-ray Absorption Spectroscopy (XAS) at BL3U to measure the ST samples, we expected to obtain insights into polymer aggregation. The purpose of this study is understanding the polymer aggregation mechanism by measuring the dehydration of polymers with altered network structure and the changes in coordination and electronic states upon stretching.

As ST samples, suspensions of amorphous silica particles and PEG solution were prepared. The suspension consisted of silica particles with a diameter of 30 nm and PEG solutions with molecular weights of 1000 kDa. A flow cell was used for H₂O and silica dispersion. In cases of measuring high viscosity sample, the flow paths could become jammed, and sealed cell was adopted.

Figure 2 shows O K-edge XAS spectra. The polymer solutions with high viscosity, required the use of custom-made cells for sealed measurements. The obtained results suggested characteristic changes on shake-gel at the pre-edge region. This suggests the characteristic hydration structure in the shake-gel.

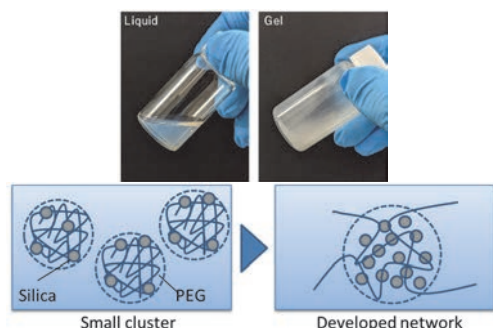


Fig. 1. Photo images of the shake-gel and schematic images of structural change of colloidal silica solution under dilatant phenomena.

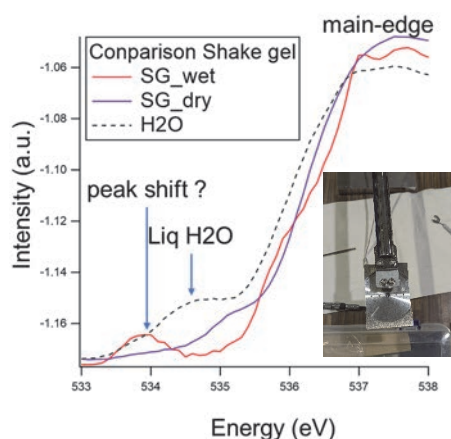


Fig. 2. XAS spectra of dry and wet shake-gel. Inset shows photo images of liquid cell.

[1] K. Akada *et al.*, Colloids Surf. A **658** (2023) 130727.

BL3U

Near-Edge X-ray Absorption Spectroscopy in a Ferroelectric Nematic Liquid Crystal

F. Araoka^{1*}, H. Nishikawa¹, Y. Takanishi² and H. Iwayama^{3,4}¹RIKEN Center for Emergent Matter Science (CEMS), Wako, Saitama 351-0198, Japan²Department of Physics, Kyoto Prefectural University of Medicine, Sakyo, Kyoto 606-0823, Japan³UVSOR Synchrotron Facility, Institute for Molecular Science, Okazaki, Aichi 444-8585, Japan⁴School of Physical Sciences, The Graduate University for Advanced Studies (SOKENDAI), Okazaki, Aichi 444-8585, Japan

Ferroelectric nematics (NF) are a new group of polar fluid liquid crystals (LCs) co-possessing liquid-like fluidity and ferroelectricity. Although such a polar order state was predicted by the well-known physicist, Max Born, in the early 20th century, it had not yet been realized until its discovery in 2017 by two independent groups [1,2]. Since then, it has attracted broad attention from the fundamental science to the potentials for novel applications. One of the most fascinating physical properties of NF is efficient generation of optical second harmonics, which is ~ 100 times larger than quartz, originating from efficient polar ordering in the present system. Recently, we reported cybotactic cluster formation stabilizing the NF phase in diastereomeric DIO mixtures [3]. In this case, anisotropy of the smectic clusters, estimated from small/wide angle X-ray analysis, clearly shows fattening of clusters as temperature decreases. This suggests a possibility that the side-by-side interaction may be an important role in stabilizing the polar ordering of the NF phase.

In this study, we performed near-edge X-ray absorption spectroscopy for the NF liquid crystal, DIO-C3 (Fig. 1). The carbon K-edge absorption spectrum was taken by scanning the photon energy of the soft X-ray irradiated on the sample sandwiched between two silicon nitride (SiN) membrane films (Fig. 2). The sample film was heated by a hot stage which equips input/output window to allow the X-ray beam to pass through. The transmitted X-ray was detected by a photodiode, and the generated photocurrent was recorded by a signal counter.

The obtained spectrum shows two signature peak regions (Fig. 3); one appearing in the lowest photon energy region (285–6 eV) is corresponding to the π -electrons in the molecule, the other in the higher energy region (above ~ 286.5 eV) to the σ -electrons. Interestingly, the latter shows notable peak shift at the phase transition temperature from the N (SmZA) to NF phases, while the former shows only scarce change either in the peak position or shape. This means, the head-to-tail dipolar interaction, which affects the longitudinal σ -orbitals, is stronger than the effect of the side-by-side attraction contributed from the π - π interaction, in the present system. Thus, this is different from our expectation, described in the above introduction part. This was also discussed by comparing

it with a theoretically computed near-edge X-ray absorption spectrum obtained with a density functional theory (DFT) calculation package for NEXAFS analysis. Further calculation and analysis are currently on-going.

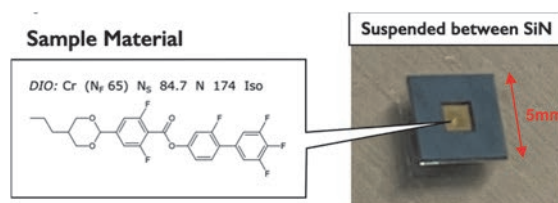


Fig. 1. Chemical structure of the NF molecule, DIO-C3 (Left), introduced between two SiN membrane films (Right).

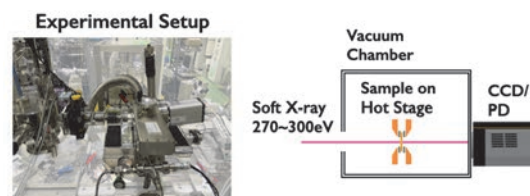


Fig. 2. Experimental setup prepared in the synchrotron soft X-ray at BL3U beamline of UVSOR, IMS, Japan.

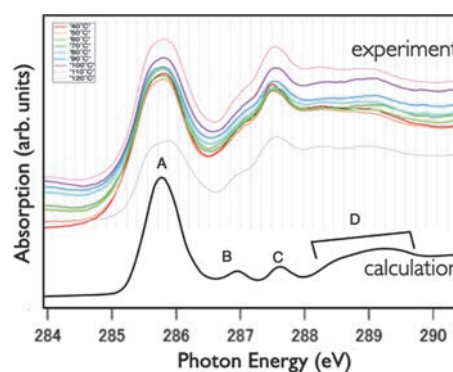


Fig. 2. Typical temperature-dependent absorption spectrum in the NF material, DIO-C3. The region A is corresponding to the π -orbital, and B, C and D are to the σ -orbitals of alkyls and dioxanes.

- [1] H. Nishikawa *et al.*, Adv. Mater. **29** (2017) 1702354.
- [2] R. Mandle *et al.*, Chem. Eur. J. **23** (2017) 14554.
- [3] H. Nishikawa *et al.*, Commun. Mater. **3** (2022) 89.

Oxygen K-Edge X-ray Absorption Spectroscopy for Identifying Active Surface Oxygen Species on Metal Oxide Catalysts

H. Tedzuka¹, N. Matsumoto¹, H. Saito², M. Nagasaka^{3,4}, T. Sugimoto^{2,3} and Y. Sekine¹

¹Department of Applied Chemistry, Waseda University, 3-4-1, Okubo, Shinjuku, Tokyo 169-8555, Japan

²Department of Materials Molecular Science, Institute for Molecular Science, Okazaki 444-8585, Japan

³Graduate University for Advanced Studies (SOKENDAI), Okazaki 444-8585, Japan

⁴UVSOR Synchrotron Facility, Institute for Molecular Science, Okazaki 444-8585, Japan

Oxidative coupling of methane (OCM) is a single-step C₂ synthesis reaction from methane. In the field of heterogeneous catalysis, the investigation has been carried out for 50 years around the world [1]. However, high reaction temperature and low C₂ yield hinder the practical use of OCM. Recently, the first difficulty has been overcome by applying electric-field to the catalytic OCM reaction (EF-OCM). For instance, Sato et al. reported that the reaction temperature of OCM decreased from ~800 to 427 K in EF-OCM using Ca-doped LaAlO₃ catalysts [2]. The electric field contributes to generating active surface oxygen species, which are similar to those in thermal OCM [3], at low temperatures. Because there are various candidates for active surface oxygen species such as O²⁻, O⁻, O₂²⁻, and O₂⁻, identifying the active surface oxygen species is crucial for the rational design of high-performance EF-OCM catalysts. In this study, we conducted the O K-edge soft X-ray absorption spectroscopy for Ca-doped LaAlO₃ catalysts in the EF-OCM system.

The Ca-doped LaAlO₃ was prepared by a complex polymerization method from nitrate salts of La, Al and Ca as metal precursors [2]. The synthesized catalyst was milled and subsequently pressed to shape a wafer (10 mm in diameter and 1 mm thick). The shaped sample was set on a holder with three gold electrodes; the two electrodes were used for applying DC current and the other was employed for the total electron yield (TEY) measurement. The sample holder was inserted a chamber sealed with ConFlat flanges. EF-OCM was performed in the chamber filled with CH₄/O₂/He mixed reaction gas. Oxygen K-edge X-ray absorption spectra were recorded in TEY and total fluorescence (TFY) modes using a silicon drift detector.

Figure 1 shows the O K-edge spectra of 30%Ca-doped LaAlO₃ (La_{0.7}Ca_{0.3}AlO₃) recorded in the TFY mode. Before the reaction, two peak were observed at ~535 and ~542 eV, which are attributed to the electron transition from O1s to O2p-La5d and O2p-La6sp hybridized states, respectively [4]. After the reaction, a new peak was appeared in the pre-edge region at ~530 eV as shown by a yellow arrow in the dotted rectangle. This peak was remained after evacuating the chamber; the possibility of physisorbed O₂ is excluded. According to the literature, the observed peak at ~530 eV is

attributable to the electron transition from O1s to O2p-Al3p hybridized state [4] or to the O₂⁻ π* orbital [5]. Based on the assignment, we assume that applying the electric field would induce structural distortion of the Ca-doped LaAlO₃ catalyst or generate a new chemisorbed oxygen species. For the further identification, we plan to measure *operando* O K-edge spectra in several conditions and perform theoretical calculations. Although additional experiments and analyses are required to establish solid conclusions, we succeeded in obtaining an important clue to the reactive oxygen species in the EF-OCM system.

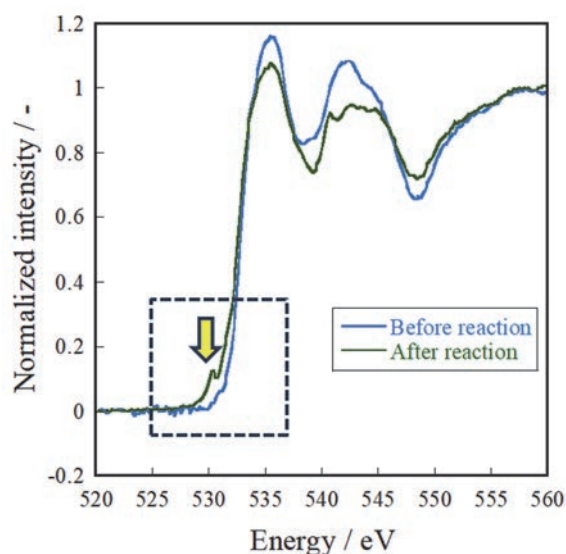


Fig. 1. O K-edge spectra of La_{0.7}Ca_{0.3}AlO₃ in TFY mode before and after EF-OCM reaction. These spectra were measured *in vacuo*.

- [1] J.H. Lunsford, *Angew. Chem. Int. Ed.* **34** (1995) 970.
- [2] A. Sato *et al.*, *ACS Omega* **4** (2019) 10438.
- [3] K. Sugiura *et al.*, *Sci. Rep.* **6** (2014) 25154.
- [4] N. Palina *et al.*, *Phys. Chem. Chem. Phys.* **18** (2016) 13844.
- [5] M.W. Ruckman *et al.*, *Phys. Rev. Lett.* **67** (1991) 2533.

BL3U

The Electronic States of 1-Methylimidazole in the Acetic Acid/1-Methylimidazole Mixture

Y. Horikawa¹, M. Okazaki¹ and M. Nagasaka²¹Graduate School of Sciences and Technology for Innovation, Yamaguchi University, Yamaguchi 753-8512, Japan²Institute for Molecular Science, Okazaki 444-8585, Japan

Acetic acid (AcO) is a weak acid, so its degree of ionization is low, and the electrical conductivity of pure acetic acid is 3.8×10^{-4} mS/cm. However, when acetic acid and 1-methylimidazole (1-MI, electric conductivity is 6.4×10^{-2} mS/cm) are mixed, the electric conductivity of this solution increases to 8.0 mS/cm at concentrations of $\chi_{\text{AcO}} = 0.65$ and 0.85 (Fig. 1). We have applied soft X-ray emission spectroscopy to reveal the electronic states of acetic acid in the mixture at various mole fractions of acetic acid ($\chi_{\text{AcA}} = 0 \sim 1$) [2]. In the high concentration region of acetic acid ($\chi_{\text{AcA}} \sim 0.85$) that exhibited high electrical conductivity, the amount of neutral acetic acid monomer in the mixture increased prior to an increase in the amount of acetate. On the other hand, in the concentration around $\chi_{\text{AcA}} \sim 0.7$ that also exhibited high electrical conductivity, the amount of acetate ions increased, indicating that the electrical conductivity increases as the number of ions increases. This was a natural phenomenon as it shows. From these two results, it was suggested that the electrical conduction mechanism is different in the two concentration ranges ($\chi_{\text{AcA}} = 0.7$ and 0.85). However, in the previous experiments [2], only acetic acid in the mixture was observed, so we needed to investigate how the number of ions in the solution was changing, and whether the ionization of 1-MI occurred along with the ionization of acetic acid. Therefore, we measured Nitrogen 1s X-ray absorption (XA) spectra of the mixture.

Figure 2 and 3 shows N 1s XA spectra of acetic acid/1-MI mixture and calculated XA spectra by using DFT calculations. In the measured spectra, it was observed that the first of the two resonance peaks seen in the pure 1-MI liquid disappeared as the acetic acid concentration increased. Furthermore, the calculation

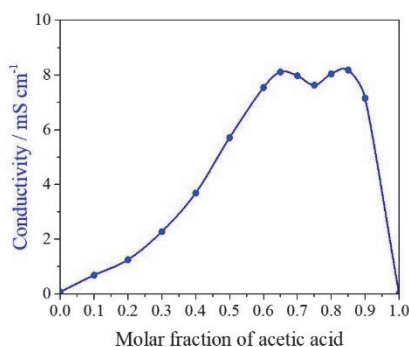


Fig. 1. Electrical conductivity of an acetic acid/1-MI mixture at various concentrations at ambient temperature [2].

results in Fig. 3 show that when 1-MI is ionized, the first resonance peak shifts and is no longer observed. These results confirmed that 1-MI molecules become ionized at acetic acid molar concentrations around 0.7, and that most 1-MI exists in the form of ions in the high acetic acid concentration region. Considering this together with the results of the structural change of acetic acid, it can be concluded that the 1-MI is also fully ionized at an acetic acid mole fraction around 0.7, where acetic acid ions are at their maximum, and that at higher concentrations of acetic acid, the acetic acid monomer increases but requires the same amount of 1-MI ions as acetic acid ions, which are present in trace amounts, and that all molecules of 1-MI are considered ionized ($\chi_{\text{AcA}} = 0.8 \sim 0.9$). We plan to conduct detailed quantitative analysis.

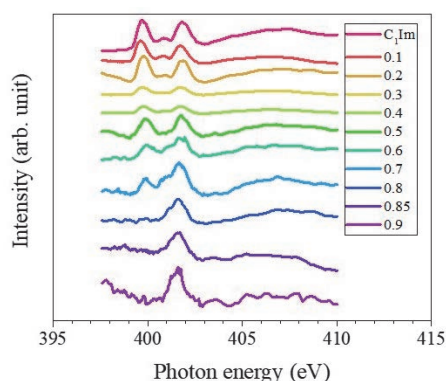


Fig. 2. N 1s XA spectra of acetic acid/1-MI mixture.

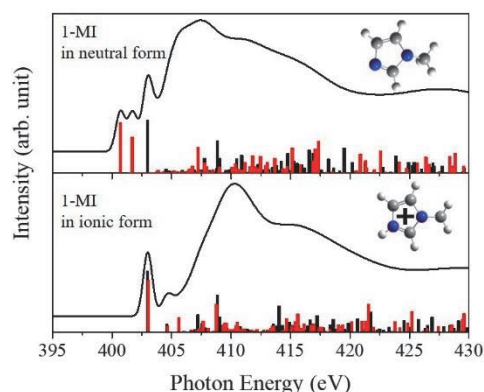


Fig. 3. Calculated N 1s XA spectra of acetic acid/1-MI mixture.

[1] H. Doi *et al.*, Chem. Eur. J. **19** (2013) 11522.

[2] N. Yoshimura *et al.*, J. Phys. Chem. B **123** (2019) 1332.

Soft X-ray Absorption of Semiconductor Photocatalyst Particles Suspended in Water

H. Onishi^{1,2}, Y. H. Chew¹, N. Ichikuni³ and T. Yoshida⁴

¹Graduate School of Science, Kobe University, Kobe 657-8501, Japan

²Division of Advanced Molecular Science, Institute for Molecular Science, Okazaki 444-8585, Japan

³Graduate School of Engineering, Chiba University, Chiba 263-8522, Japan

⁴Research Center for Artificial Photosynthesis, Osaka Metropolitan University, Osaka 558-8585, Japan

Material conversion on semiconductor photocatalysts is intensively studied worldwide. Downhill reactions, in which the Gibbs free energy decreases during the conversion of reactants to products, have been successfully integrated into our society [1]. Artificial photosynthesis, a category of uphill reactions involving the oxidation of water, is being developed for societal implementation in the near future [2]. In addition, fundamental studies are being conducted to uncover new scientific discoveries related to light-driven, efficient materials conversion [3].

Here, in collaboration with Prof. Masanari Nagasaka of UVSOR, we apply soft X-ray absorption to the *in-situ* characterization of semiconductor photocatalysts suspended in water. A representative photocatalyst, anatase TiO₂ (JRC-TIO-19 provided by Catalysis Society of Japan), was suspended in water. The suspended solution was adjusted with NaOH to pH 13. The pH adjustment was critical to suspend 100 nm TiO₂ particles long enough to pass through the liquid cell.

The liquid cell was mounted in BL3U. Oxygen K-edge and titanium L-edge absorption spectra were observed with a transmission setup [4] in the presence and absence of ultraviolet (UV) light for bandgap excitation.

Figure 1 shows the O K-edge and Ti L-edge spectra observed in the absence of UV light. In the O K-edge, electron transition from O1s to O2p orbitals of TiO₂ particles was detected at 530-533 eV together with intense absorption of water at 534 eV or higher energies. The O2p orbitals are hybridized with Ti3d orbitals to form the conduction band in TiO₂. The hybridized O2p orbitals are thus split into *t*_{2g} and *e*_g levels according to the ligand field in TiO₆ octahedra. Splitting into *t*_{2g} and *e*_g states also occurred in the Ti L₃- and L₂-edge absorption, respectively.

The soft X-ray absorption of solutions has been successfully studied. In this study, transmission measurement was achieved with a suspension. The extension to an *operando* study of the suspension under UV irradiation is promising.

This study was supported by JSPS KAKENHI (grant number 22H00344).

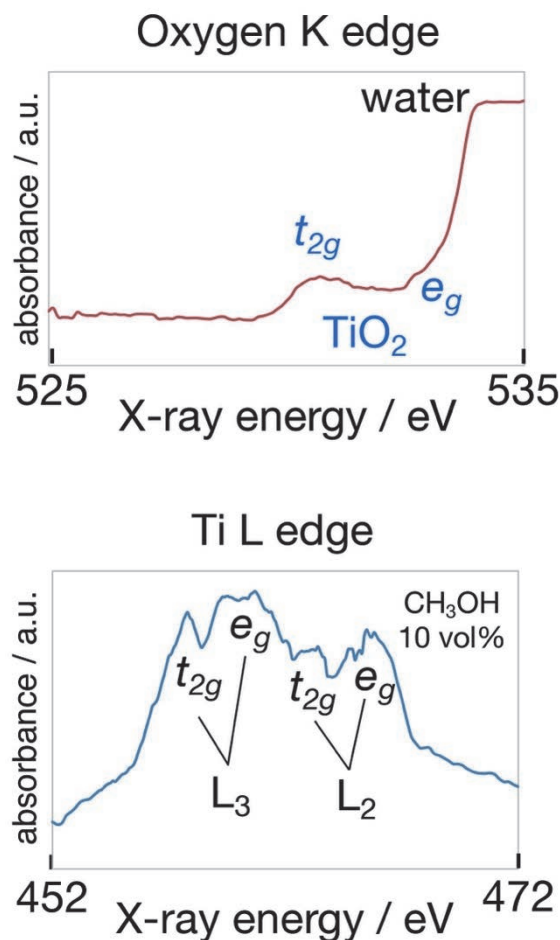


Fig. 1. Soft X-ray absorption of anatase TiO₂ photocatalyst particles (JRC-TIO-19) suspended in water at pH 13. Oxygen K-edge and titanium L-edge spectra were observed in the absence of UV light irradiation. Methanol (10 vol%) was added to the suspension for Ti L edge observation.

[1] A. Fujishima *et al.*, J. Photochem. Photobiol. C **1** (2000) 1.

[2] H. Onishi, ChemSusChem **12** (2019) 1825.

[3] C. Kranz and M. Wächter, Chem. Soc. Rev. **50** (2021) 1407.

[4] T. Petit *et al.*, J. Phys. Chem. Lett. **6** (2015) 2909.

BL3U

Probing the H-Bonding Network in the Vicinity of Aqueous Ammonia and Ammonium Ion by X-ray Absorption Spectroscopy

D. Céolin¹, T. Saisopa², Y. Rattanachai², W. Sailuam³, H. Yuzawa⁴ and N. Kosugi⁴

¹Synchrotron SOLEIL, l'Orme des Merisiers, Saint-Aubin, F-91192 Gif-sur-Yvette Cedex, France

²Department of Applied Physics, Faculty of Sciences and Liberal Arts, Rajamangala University of Technology Isan, Nakhon Ratchasima 30000, Thailand

³Department of Applied Physics, Faculty of Engineering, Rajamangala University of Technology Isan, Khon Kaen, Thailand

⁴UVSOR Synchrotron Facility, Institute for Molecular Science, Okazaki 444-8585, Japan

Hydrogen bonds interaction has been largely probed in aqueous (aq) media by means of different experimental (FTIR, X-ray diffraction, emission and absorption) and theoretical (DFT, MP2, QM/MM) methods. Among these, X-ray absorption spectroscopy (XAS) is a very appropriate tool due to its sensitivity to local orders and geometrical changes around a selected center. In addition, monitoring the solution temperature was shown to be a good parameter to gain more insight into the interaction of, e.g., water with its surroundings [1]. Indeed, bulk water is sensitive to the temperature increase due to an increase of the distances between water molecules, leading to the weakening of the H-bond strength. Other systems presenting donating or accepting hydrogen bonds were also investigated, namely, ammonia and ammonium ion interaction with water were probed by XAS [2, 3] and FT-IR experiments [2]. It was concluded that $\text{NH}_3(\text{aq})$ has a medium strong hydrogen bond between its lone pair and a donating water molecule, whereas the donating character of the 3 N-H is considered as ultra-weak. In contrast, $\text{NH}_4^+(\text{aq})$ has 4 equivalent donating hydrogen bonds, all of them being in the weak category, weaker than the water-water bonding.

Based on these results, we performed temperature dependent XAS measurements at the BL3U beamline on ammonia and ammonium ion in aqueous solutions at the nitrogen K-edge. Measurements were done using the liquid cell of SiC membrane in transmission mode on solutions prepared at a concentration of 1 M. The normalized spectra are shown in the Fig. 1. For $\text{NH}_3(\text{aq})$, the spectrum presents an isolated pre-edge having a $\text{N}2\text{p}$ character, followed by a sharp and intense double-structure main-edge and a long tail as a post-edge. The spectrum of $\text{NH}_4^+(\text{aq})$ starts at about 2 eV higher in energy, with the pre-edge that appears as a weak shoulder having a $\text{N}2\text{s}$ character, on the low energy side of an intense main edge. It is followed by a less intense large shoulder as a post-edge.

The first original observation from this dataset is the splitting of the $\text{NH}_3(\text{aq})$ XAS main-edge leading to two maxima at 402.8 eV and 403.3 eV. In the gas phase, the main line is attributed the transition $\text{N}1\text{s}$ to the doubly degenerated 2e orbitals [4]. This double structure, attributed to a degeneracy lift of the 2e orbital due to environment effects, was calculated but not clearly

measured in reference [2]. The second observation concerns the intensity dependence of some structures with the temperature, for the two solutions. The spectra are compared in a way that the intensities on the low and high photon energy sides of the spectra are normalized to the same values for all temperatures. Following this procedure, we see that the temperature mostly influences the post-edge structures, as indicated by the arrows in the figures.

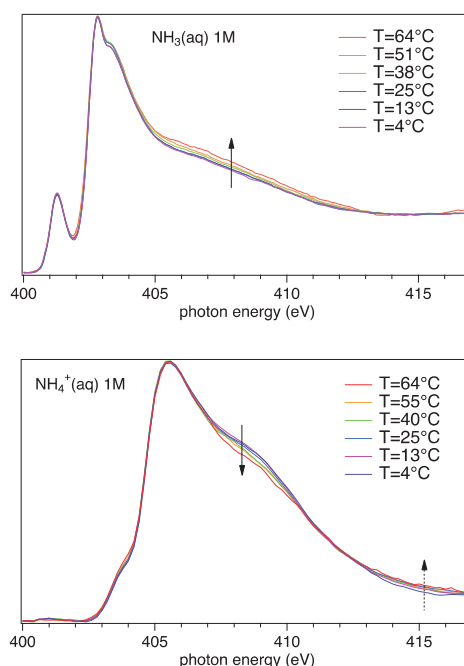


Fig. 1. X-ray absorption spectra of 1 M NH_3 (upper-panel) and NH_4^+ (lower-panel) aqueous solutions, recorded in the vicinity of the $\text{N}1\text{s}$ ionization threshold, for temperatures in the 4–64 °C range.

- [1] M. Nagasaka *et al.*, J. Phys. Chem. B **121** (2017) 10957.
- [2] M. Ekimova *et al.*, J. Am. Chem. Soc. **139** (2017) 12773.
- [3] P. Reinholdt *et al.*, J. Phys. Chem. Lett. **12** (2021) 8865.
- [4] J. Schirmer *et al.*, Phys. Rev. A: At. Mol. Opt. Phys. **47** (1993) 1136.

Elucidation of Oxygen Evolution Reaction Mechanism on γ -MnO₂ Electrocatalyst during Electrolysis of Acidic Aqueous Solution by *Operando* Soft X-ray XAFS

A. Li¹, K. Adachi², D. Hashizume² and R. Nakamura^{1,3}

¹Biofunctional Catalyst Research Team, RIKEN Center for Sustainable Resource Science (CSRS), Wako 351-0198, Japan

²Materials Characterization Support Team, RIKEN Center for Emergent Matter Science (CEMS), Wako 351-0198, Japan

³Earth-Life Science Institute (ELSI), Tokyo Institute of Technology, Meguro-ku 152-8550, Japan

In the quest for sustainable energy solutions, electrochemical fuel synthesis powered by renewable resources stands out as a promising avenue to meet the world's growing energy demands [1]. Central to this endeavor is the conversion of water into fuel, a process that requires efficient catalysts to facilitate the electrochemical oxidation of water molecules. Transition metal oxides, particularly manganese oxides (MnO₂), have emerged as key contenders in this domain, offering a blend of advantages that make them attractive candidates for catalyzing water oxidation reactions.

Manganese-based catalysts hold significant appeal due to their lower toxicity and abundance compared to noble-metal-based counterparts like nickel, iron, or cobalt. While they may exhibit lower activity levels, their scalability and environmental friendliness make them an appealing choice for sustainable fuel synthesis. Drawing inspiration from biological catalysts, such as the CaMn₄O₅ cluster found in the Photosystem II enzyme [2], researchers have turned to MnO₂ as a potential solution for driving electrochemical water oxidation [3,4].

At UVSOR BL3U, we performed in-situ soft X-ray absorption measurements of the Mn L-edge for Mn²⁺ ions in solution and electrodeposited MnO₂ (Figure 1). Pt/Cr/SiN film electrodes served as substrates. Even the water oxidation reaction on MnO₂ could not be achieved due to the instability of the deposited film on the Pt/Cr film and the formation of oxygen bubbles, we have obtained useful information of Mn²⁺ and electrodeposited MnO₂ in 1 M H₂SO₄ solution. The thickness for Pt, Cr and SiN are 20 nm, 5 nm and 100 nm, respectively. Films of MnO₂ were deposited via oxidative electrodeposition at an applied potential of 1.5 V on Au-coated SiN membranes from aqueous 0.36 M Mn²⁺ solutions with 1 M H₂SO₄. Upon applying potential to initiate MnO₂ electrodeposition, a clear shift in the Mn L-edge absorption from Mn²⁺ to Mn^{3+/4+} was observed (Figure 1b). This shift indicates that electrodeposition occurred under electrochemical conditions, even in highly acidic environments (1 M

H₂SO₄). For comparison, the Mn-K edge spectrum of Mn²⁺ in 1 M H₂SO₄ was also measured (Figure 1a).

Despite the challenges encountered, our research successfully obtained the Mn L-edge XAS spectra of Mn²⁺ and electrodeposited MnO₂ in harsh acidic condition.

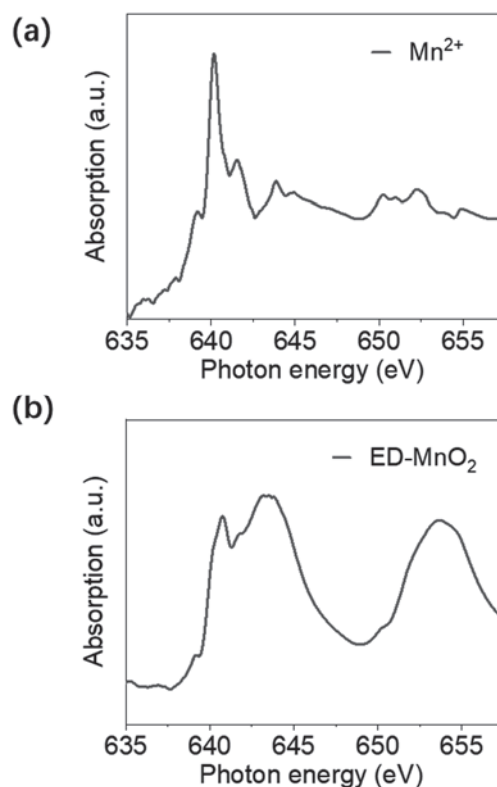


Fig. 1. Mn L-edge spectra of 0.35 M Mn²⁺ and ED-MnO₂ in 1 M H₂SO₄.

- [1] Chu, S. & Majumdar, Nature **488** (2012) 294.
- [2] M. Suga *et al.*, Nature **543** (2017) 131.
- [3] A. Li *et al.*, Angew. Chem. Int. Ed. **58** (2019) 5054.
- [4] S. Kong *et al.*, Nat. Catal. **7** (2024) 252.
- [5] M. Nagasaka *et al.*, J. Electron. Spectrosc. Relat. Phenom. **224** (2018) 93.

BL3U

Isolated Water Molecules in Aqueous Acetonitrile Solutions Probed by Oxygen K-Edge X-ray Absorption Spectroscopy

M. Nagasaka^{1,2}¹*Institute for Molecular Science, Okazaki 444-8585, Japan*²*Graduate University for Advanced Studies, SOKENDAI, Okazaki 444-8585, Japan*

The properties of water molecules are changed from liquid phases to cluster structures due to the different hydrogen bond structures [1]. Since it is important to investigate the electronic structures of isolated water molecules, isolated water molecules were prepared by several techniques. On the other hand, water clusters are formed in aqueous acetonitrile solutions because it is inhomogeneous in a microscopic scale, which is known as microheterogeneity [2]. We have measured O K-edge X-ray absorption spectroscopy (XAS) of aqueous acetonitrile solutions and found a sharp peak profile around 537 eV, which would be derived from the confinement of water molecules with acetonitrile molecules by the dipole interactions [3]. The electronic structures of not only water clusters but also H_3O^+ clusters were also investigated by O K-edge XAS [4]. In this study, we investigated whether the sharp peak profiles in O K-edge XAS are derived from the completely isolated water molecules or small water clusters from the inner-shell calculations.

Figure 1(a) shows O K-edge XAS spectrum of aqueous acetonitrile solutions, $(\text{ACN})_{0.9}(\text{H}_2\text{O})_{0.1}$, obtained by our previous experiment [3]. The main-edge peak around 537 eV shows a sharper profile compared to liquid water and is close to that of water gas.

For investigating the relation of the sharp profiles of the main-edge peaks with the structures of water clusters, we have performed inner-shell calculations of small water clusters at different sizes. The structures of liquid water and small water clusters confined by acetonitrile were obtained by the molecular dynamics simulations. The inner-shell spectra of water clusters at different sizes were obtained by the summation of 14,900 spectra of water clusters extracted from the liquid structures with the simulation time of 100 ns, which include the deviation of the hydrogen bond structures [5].

Figure 1(b) shows O K-edge inner-shell spectra of liquid water and water clusters with the different sizes of 1 – 5. The second peak around 537 eV corresponds to the main-edge peak. The inner-shell spectra of water clusters with the sizes of 2 – 5 show nearly same spectral profiles and are close to those of liquid water. On the other hand, the inner-shell spectrum of water clusters with the size of 1, which are isolated water molecules, show different spectral profiles. It means that the sharp profiles of the main-edge peaks in O K-edge XAS of aqueous acetonitrile solutions derives not from small water clusters but from isolated water molecules surrounded by acetonitrile molecules.

The properties and dynamics of isolated water molecules has been previously investigated by the complicate manipulations such as the encapsulation of water molecules in fullerene or ionic liquids. This study found that isolated water molecules are easily formed in aqueous acetonitrile solutions at relatively high molar fraction of water because of the microheterogeneity. The electronic structures of isolated water molecules surrounded by acetonitrile molecules can be analyzed by the sharp profiles of the main-edge peak in O K-edge XAS spectra, separating the contributions of even small water clusters.

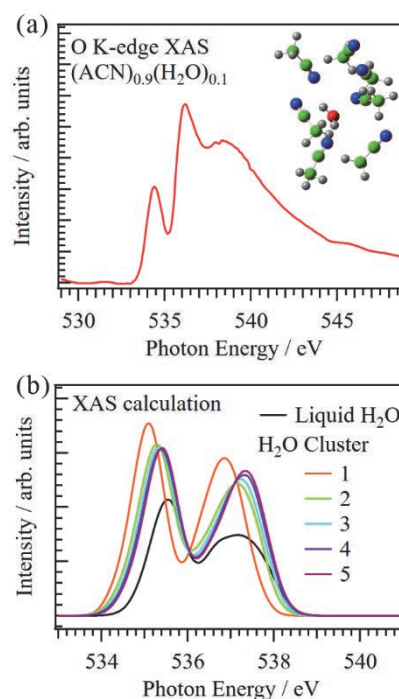


Fig. 1. (a) O K-edge XAS of aqueous acetonitrile solutions $(\text{ACN})_{0.9}(\text{H}_2\text{O})_{0.1}$. The inset shows isolated water molecules confined with acetonitrile. (b) O K-edge inner-shell spectra of liquid water and water clusters with different sizes in aqueous acetonitrile solutions.

- [1] R. Ludwig, *Angew. Chem. Int. Ed.* **40** (2001) 1808.
- [2] Y. Marcus, *J. Phys. Org. Chem.* **25** (2012) 1072.
- [3] M. Nagasaka *et al.*, *J. Phys. Chem. B* **124** (2020) 1259.
- [4] M. Ekimova *et al.*, *Angew. Chem. Int. Ed.* **61** (2022) e202211066.
- [5] M. Nagasaka, *J. Chem. Phys.* **158** (2023) 024501.

Observation of Electrochemically Generated Reactive Intermediate for Methane Oxidation by Operando Electrochemical Soft X-ray Absorption Spectroscopy

Y. Yamada^{1,2} and M. Nagasaka³

¹Department of Chemistry, Graduate School of Science, Nagoya University,
Furo-cho, Chikusa-ku, Nagoya 464-8602, Japan

²Research Center for Materials Science, Nagoya University, Furo-cho, Chikusa-ku, Nagoya 464-8602, Japan

³Institute for Molecular Science, Myodaiji, Okazaki 444-8585, Japan

CH₄ is abundant in nature as natural gas or methane hydrate, whereas it is also recognized as an environmental pollutant having high greenhouse effect. Therefore, development of novel catalysts that convert CH₄ into valuable chemical feedstocks efficiently is highly desired. However, high chemical stability of C–H bonding of CH₄ makes it highly difficult. We recently reported that a μ -nitrido-bridged iron phthalocyanine dimer stacked on a graphite surface 1/G (Fig. 1a) can activate C–H bonding of CH₄ efficiently and convert CH₄ into a mixture of methanol, formaldehyde, and formic acid in an acidic aqueous solution containing excess H₂O₂. The reactive intermediate is a high-valent iron-oxo species generated in situ (Fig. 1a). The catalytic C–H bond activation activity of CH₄ by 1/G is quite high among a variety of molecule-based CH₄ oxidation catalysts and even comparable to that of a natural particulate methane monooxygenase (pMMO)[1].

We are now attempting to develop the method for electrochemical generation of 1_{oxo}/G without using H₂O₂ as an oxidant. We hypothesized that 1_{oxo}/G could be generated through the reaction shown in Fig. 1b, where electrochemical oxidation of coordinating H₂O on the iron center of 1(H₂O)/G afford 1_{oxo}/G. Actually, in our previous experiment, we could successfully observe the peak corresponding to the O1s – π^* of Fe=O for 1_{oxo} by applying 1.8 V vs. Ag/AgCl to 1(H₂O)/G in a buffer solution (pH 7.0) by operando soft X-ray spectroscopy in UVSOR BL 3U.

Herein, we attempted to observe the peak corresponding to the O1s – π^* of Fe=O for 1_{oxo} by changing the applied voltage. A SiN membrane tip coated with carbon membrane (20 nm thickness), on which 1(H₂O) was stacked, 1(H₂O)/cmSiN (Fig. 2a) was used for this purpose. Electrochemical oxidation of 1(H₂O)/cmSiN was monitored by observing the O K-edge XAS spectra in a 100 mM phosphate buffer (pH = 7.0) by using a beamline equipped with a transmission-type liquid flow cell in BL3U of UVSOR [2]. The measurements were performed by changing the applied voltage to 1(H₂O)/cmSiN in a buffer solution and the spectra were obtained based on the Lambert-Beer law, $\ln(I_0/I)$, where I_0 is the transmission signals of the cmSiN in buffer and I is those of 1(H₂O)/cmSiN at different applied voltage.

The obtained spectra were shown in Fig. 2b. The

broad peak at around 532 eV was gradually increased after increasing the applied voltage from 0.70 V to 1.60 V vs. SHE (Fig. 2b). DFT calculation suggested that the peak of O1s – π^* of Fe=O for 1_{oxo} should be observed at around 529 eV, whereas the peaks for a coordinating H₂O on iron ion of 1 should be observed at higher energy than 534 eV. Taking these results, the peak appeared at around 532 eV is assignable to the excitation of O1s – π^* of Fe=O of electrochemically generated high-valent iron-oxo species of 1(H₂O)/cmSiN (1_{oxo}/cmSiN). It was demonstrated that the high-valent iron-oxo species was generated after applying 1.30 V vs. SHE.

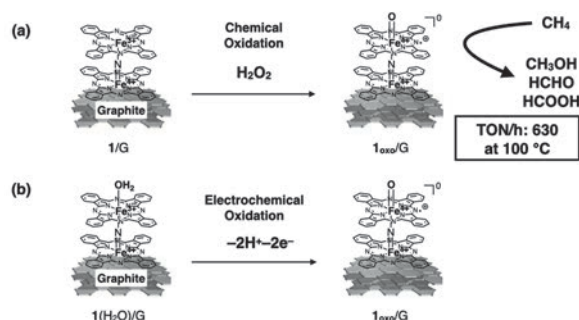


Fig. 1. Generation of 1_{oxo}/G from 1/G by (a) treatment with H₂O₂ or (b) electrochemical oxidation.

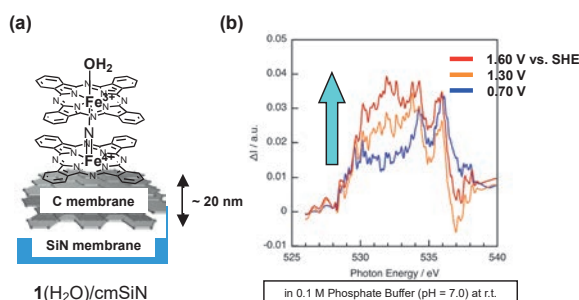


Fig. 2. (a) Structure of 1(H₂O)/cmSiN. (b) Comparison of O K-edge XAS spectra of 1(H₂O)/cmSiN after applying the indicated voltages vs. SHE in a phosphate buffer (pH = 7.0).

[1] Y. Yamada *et al.*, JACS Au, **3** (2023) 823.

[2] M. Nagasaka and N. Kosugi, Chem. Lett. **50** (2021) 956.

BL3B

Photoelectron–Photoion Coincidence (PEPICO) for Hydrofluoroethanes

T. T. Nguyen¹, K. Ishikawa¹, T. Hayashi¹,
S. N. Hsiao¹ and H. Iwayama²

¹Center for lowtemperature plasma sciences, Nagoya University, Nagoya 464-8601, Japan

²UVSOR Synchrotron Facility, Institute for Molecular Science, Okazaki 444-8585, Japan

Molecular ionization and dissociation processes of perfluorocarbons (PFCs) and hydrofluorocarbons (HFCs) in plasma etching chemistry are essential for determining of the plasma etching performance of dielectrics, such as SiO₂, SiN, in advanced semiconductor device fabrications. Desirable characteristics, such as fast etch rates and high etch selectivity should be achieved by counterbalancing between undesirable deposition of polymeric films onto the substrate and energetic removal of underlying materials. A control of both the composition and the amount of ions and radical species generated from the source gas is a critical problem of the etching process. In this study, we have investigated about the primary dissociation pathways of PFCs and HFCs through a combination of experiments and calculations.

Prediction of the dissociation and ionization pathways for hydrofluorocarbonethanes was performed by using the computational chemistry technique. As a result, the electronic properties and primary dissociation channels of fluoroethane compounds from computational chemistry was reported, as listed in Table 1 [1]. The reactive ion etching performances of films of poly-Si, SiO₂ and SiN were also reported previously [2]. To verify experimentally the computational prediction, this study has conducted the photoelectron-photoion coincidence (PEPICO) experiments, for evaluation of the vacuum ultraviolet (VUV) light-induced decomposition of fluoroethane compounds.

The PEPICO measurements were performed in the BL3B in the UVSOR facility. Gases (C₂H_xF_{6-x}) introduced into a vacuum chamber and were kept less than 3×10⁻⁴ Pa. The gases were irradiated by vacuum ultraviolet light energy from 10 to 28 eV (wavelength of 40-730 nm) in each 0.02 eV steps, with a spherical grating with grooves of 1200 l/mm. The ionized molecular fragments were detected by a time-of-flight (TOF) mass spectrometer. Appearance energies (AE) were determined by linearly extrapolating the threshold photon energy in which the ion yield became zero.

The photoionization of CH₂FCHF₂ (HFC143) was measured by the TOF mass spectra. The parent ion and its fragments, such as CHF₂⁺, CH₂F⁺, CFCH₂⁺, and CHFCH₂F⁺ were analyzed. The PEPICO results gave AE of 12.5 eV for CHF₂⁺ and this was also found to be the dominant ion fragment (Figure 1). These results agree with previously calculated values [1], as compared with the results of C₂F₆ (PFC116).

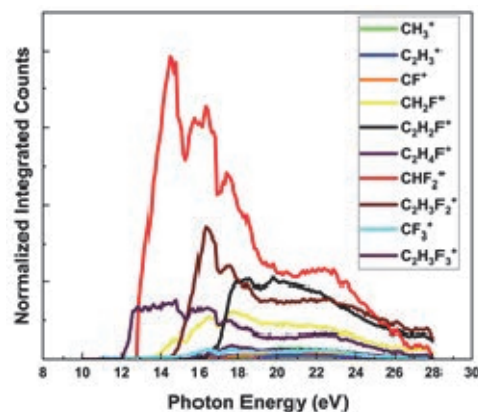


Fig. 1. Ion yield curves for photo-ionization.

Table 1. The primary dissociated ions and radicals[1].

Molecules	Ions	Radical	Negative ions
C ₂ H ₅ F	CH ₂ F ⁺ , C ₂ H ₄ F ⁺ , C ₂ H ₅ ⁺	C ₂ H ₅ , CH ₃ , CH ₂ F	F ⁻
CH ₃ CHF ₂	CHF ₂ ⁺ , C ₂ H ₃ F ₂ ⁺ , C ₂ H ₄ F ⁺	C ₂ H ₄ F, CH ₃ , CHF ₂	F ⁻ , C ₂ H ₃ F ₂ ⁻
CH ₂ FCH ₂ F	C ₂ H ₄ F ₂ ⁺ , CH ₂ F ⁺ , C ₂ H ₄ F ⁺ , C ₂ H ₃ F ₂ ⁺	CH ₂ F, C ₂ H ₄ F	F ⁻
CH ₂ FCHF ₂	CH ₂ F ⁺ , CHF ₂ ⁺ , C ₂ H ₃ F ₂ ⁺ , C ₂ H ₂ F ⁺	C ₂ H ₃ F ₂ , CH ₂ F, CHF ₂	F ⁻
CH ₃ CF ₃	CH ₃ ⁺ , C ₂ H ₃ F ₂ ⁺ , CF ₃ ⁺	CH ₃ , CF ₃ , C ₂ H ₃ F ₂	F ⁻ , CH ₂ CF ₃ ⁻
CHF ₂ CHF ₂	CHF ₂ ⁺ , C ₂ H ₂ F ₃ ⁺	CHF ₂ , C ₂ H ₂ F ₃ , C ₂ HF ₄	F ⁻
CH ₂ FCF ₃	CF ₃ CH ₂ ⁺ , CF ₃ ⁺ , CH ₂ F ⁺	CF ₃ , CH ₂ F	F ⁻ , CF ₃ ⁻
CHF ₂ CF ₃	C ₂ HF ₄ ⁺ , CF ₃ ⁺ , CHF ₂ ⁺	CF ₃ , CHF ₂	F ⁻ , CF ₃ ⁻
C ₂ F ₆	C ₂ F ₅ ⁺ , CF ₃ ⁺	CF ₃	F ⁻ , CF ₃ ⁻

[1] T. Hayashi *et al.* Jpn. J. Appl. Phys. **58** (2019) S5EF01.

[2] S-N. Hsiao *et al.*: Appl. Surf. Sci. **541** (2021) 148439.

Fragmentation of OCS^{3+} States Studied by Multi-Electron-Ion Coincidence Spectroscopy

Y. Hikosaka

Institute of Liberal Arts and Sciences, University of Toyama, Toyama 930-0194, Japan

Significant experimental effort has been devoted to understanding the dissociation pathways and mechanism of triply charged ion states in carbonyl sulfide. Information on the OCS^{3+} electronic states relevant to the dissociation pathways is, however, very limited, because it requires a spectroscopic method that relates the kinetic energies of multiple electrons ejected in the formation of OCS^{3+} states to the ion species produced. In this study, the dissociation processes of the OCS^{3+} states populated by the S 2p double Auger decay were investigated by multi-electron-ion coincidence spectroscopy [1]. A magnetic bottle electron spectrometer with ion detection capability [2-5] was employed for this measurement, and the high detection efficiencies for electrons enabled us to derive information on the fragmentations of OCS^{3+} states.

The formation of OCS^{3+} states by the S2p double Auger decay can be isolated by the electron triple coincidence of S 2p photoelectron and the associated two Auger electrons. Figure 1(a) shows the histogram of the energy sum of the two Auger electrons detected in coincidence with a S 2p photoelectron, displaying the OCS^{3+} spectrum populated by the double Auger decay. Several peaks are observed in the kinetic energy range of 95-115 eV, and their main contributors are indicated in the figure. Moreover, a broad structure is seen in the binding energy range of 80-95 eV, resulting from densely lying excited states, most of which probably have holes in an inner-valence orbital.

The fragmentation of these OCS^{3+} states can be investigated by inspecting the ion species detected in further coincidence. The two-dimensional map in Fig. 1(b) shows the correlations between the OCS^{3+} spectrum and the times-of-flight of ions, derived from four-fold coincidences of three electrons and an ion. One finds on the two-dimensional map that horizontal stripes associated with different ion species show different OCS^{3+} distributions. The OCS^{3+} spectra in coincidence with individual ions, corresponding to the lineouts of the horizontal stripes on the map, are presented in Fig. 2. The OCS^{3+} spectra coincident with molecular fragments CO^+ and CO^{2+} exhibit OCS^{3+} states relevant to the two-body dissociations into the $\text{CO}^+ + \text{S}^{2+}$ and $\text{CO}^{2+} + \text{S}^+$ pairs, respectively. Though atomic fragments C^+ and O^+/S^{2+} are not associated with a single dissociation channel, the corresponding coincidence spectra relevant to the three-body dissociation channels of $\text{O}^+ + \text{C}^+ + \text{S}^+$, $\text{O} + \text{C}^+ + \text{S}^{2+}$, and $\text{O}^+ + \text{C} + \text{S}^{2+}$. A detailed discussion of the fragmentations of individual OCS^{3+} states is given in [1].

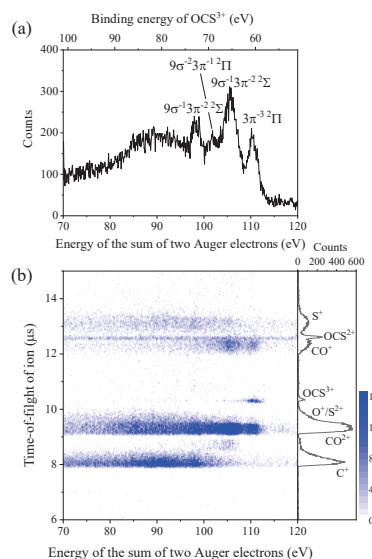


Fig. 1. (a) Spectrum for OCS^{3+} formed by the S 2p double Auger decay. (b) Correlation map between the OCS^{3+} states and ion times-of-flight in the right panel.

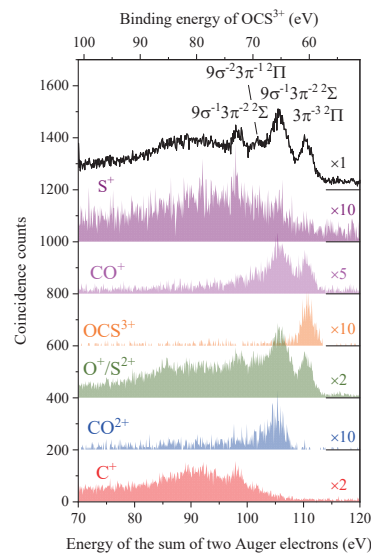


Fig. 2. Spectra of the OCS^{3+} states filtered by coincidence with product ions.

- [1] Y. Hikosaka, J. Chem. Phys. **158** (2023) 214306.
- [2] Y. Hikosaka and E. Shigemasa, Int. J. Mass Spectrom. **439** (2019) 13.
- [3] Y. Hikosaka, J. Electron. Spectrosc. Relat. Phenom. **255** (2022) 147158.
- [4] Y. Hikosaka and S. Fritzsche, Phys. Chem. Chem. Phys. **24** (2022) 17535.
- [5] Y. Hikosaka, Phys. Rev. A: At. Mol. Opt. Phys. **106** (2022) 062814.

BL4B

Dissociation of Doubly Charged Ion States in Xenon Difluoride Molecules

Y. Hikosaka

Institute of Liberal Arts and Sciences, University of Toyama, Toyama 930-0194, Japan

Xenon difluoride (XeF_2) is a unique triatomic molecule constructed by weak bonding between the central rare-gas atom and fluorine ligands. The Auger decay of the core hole formed in the central Xe is of particular interest in terms of how the molecular environment affects the process. In addition, the stability and dissociation of the XeF_2^{2+} states produced by the Auger decay remain unclear. In this study, the stability and dissociation processes of the XeF_2^{2+} states produced by the Auger decay from the 4d core-hole formed in the central Xe atom were studied by multi-electron-ion coincidence spectroscopy [1] using a magnetic bottle electron spectrometer with ion detection capability [2-5].

The top panel of Fig. 1 shows the 4d photoelectron spectrum measured for a gas mixture of XeF_2 and Xe. The $4d^{-1}$ spin-orbit levels in XeF_2 shift to a higher binding energy of approximately 1.5 eV compared with the corresponding levels in Xe. The two-dimensional map in Fig. 1 displays the energy correlations of these 4d photoelectrons and the associated Auger electrons. The vertical stripes on the map are formed by the Auger electrons emitted from individual core-hole states. The Auger spectra associated with the $4d_{5/2}$ and $4d_{3/2}$ core-hole states of XeF_2 are derived by projecting the coincidence yields along the corresponding vertical stripes toward the vertical axis of the map and are shown in the right panel of Fig. 1. Here, the contamination from the Auger decay of Xe was subtracted.

The fragmentation of the Auger-final XeF_2^{2+} states can be revealed by ion species detected in further coincidence. The two-dimensional map in Fig. 2 shows the correlations between the XeF_2 $4d_{3/2}$ Auger spectrum and the times-of-flight of product ions. The distributions of the XeF_2^{2+} states relevant to individual ion formations are shown as horizontal stripes on the map, which drastically differ according to the ion species. One interesting observation is that coincidences with parent XeF_2^{2+} ion are visible, revealing that part of the XeF_2^{2+} states survived in the 10- μs time regime by overcoming the Coulomb repulsion between the two positive charges. It is found that the formation of the metastable XeF_2^{2+} ion is associated with the state around a binding energy of 32 eV, which can be the ground XeF_2^{2+} state with the configuration of $5\pi_u^{-2}$. On the other hand, other excited XeF_2^{2+} states are all dissociative, and various dissociation fragments are formed. A detailed discussion of dissociations of individual XeF_2^{2+} states is given in [1].

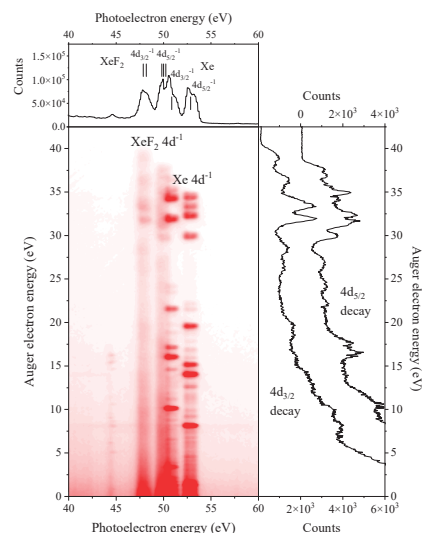


Fig. 1. Two-dimensional map of the energy correlation between the Xe 4d photoelectron and Auger electrons emitted from the gas sample of a mixture of XeF_2 and Xe at a photon energy of 120.4 eV.

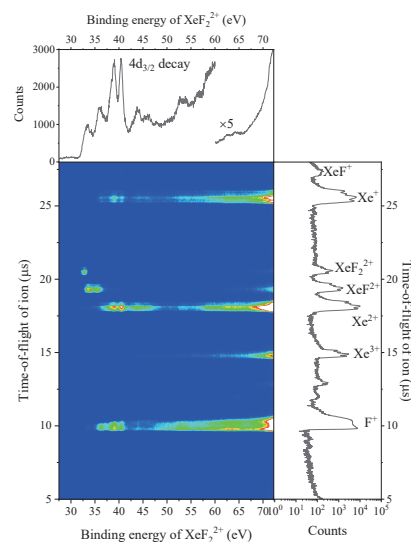


Fig. 2. Two-dimensional map of the correlation between the XeF_2^{2+} states (top) and times-of-flight of ions (right).

- [1] Y. Hikosaka, J. Chem. Phys. **160** (2024) 024304.
- [2] Y. Hikosaka and E. Shigemasa, Int. J. Mass Spectrom. **439** (2019) 13.
- [3] Y. Hikosaka, J. Electron. Spectrosc. Relat. Phenom. **255** (2022) 147158.
- [4] Y. Hikosaka and S. Fritzsche, Phys. Chem. Chem. Phys. **24** (2022) 17535.
- [5] Y. Hikosaka, Phys. Rev. A: At. Mol. Opt. Phys. **106** (2022) 062814.

High-Resolution Photoelectron Spectroscopy of Substituted Oxiranes

H. Kohguchi¹, Y. Hikosaka², T. Kaneyasu³, S. Wada¹ and Y-I. Suzuki⁴

¹Graduate School of Advanced Science and Engineering, Hiroshima University,
Higashi-Hiroshima 739-8526, Japan

²Institute of Liberal Arts and Sciences, University of Toyama, Toyama 930-0194, Japan

³SAGA Light Source, Tosu 841-0005, Japan

⁴School of Medical Technology, Health Sciences University of Hokkaido, Tobetsu 061-0293, Japan

The substituent effect of organic molecules on photoelectron spectroscopy has been studied for a long time. The alkyl group is considered to only moderately modify the photoelectron spectral peak structures unless the relevant molecular orbitals are located closely to the substitution group. We conducted the measurements of the photoelectron spectra of oxiranes with different alkyl substituents at BL7B. Velocity-mapping imaging (VMI) was employed for obtaining the photoelectron spectra since the scattering distributions of these oxiranes are of our interest [1]. The photoelectron kinetic energy also modifies the photoelectron spectra, whose band intensity is subject to the photoionization dynamics [2]. The spectral resolution with the VMI-base measurement is not expected to be higher than the conventional UPS method, on which we relied as a reference for the spectral assignments at a standard photon energy (55 nm).

We measured the photoelectron images of oxirane derivatives at several photon energies from the ionization threshold to 55 nm. The photoelectron spectrum measured at 55 nm photon energy can be directly compared with previous data in the literature. Oxiranes are liquid samples at room temperature with sufficiently high vapor pressure to generate the effusive beam of oxiranes introduced into the VMI vacuum chamber. Observed photoelectron spectra of methyl oxirane at several photon energies are shown in Figure 1. These spectra were obtained by integrating the photoelectron signals of the observed image data for whole scattering angles. The kinetic energy (and the ionization potential) were calibrated with the VMI image data of He at the corresponding photon energies. The ionization potential of methyl oxirane (10.26 eV) was well reproduced in the present measurements, indicating good accuracy of our data.

Most of the observed band peaks (Fig. 1) were assignable in comparison with the photoelectron spectra in the literature. However, we found the following new features in the experimental results: (i) the relative intensity of the assigned peaks to certain ionic states was varied with the photon energy, (ii) the band intensity measured at 55 nm photon energy, which

should be identical to the literature data, was different from the previous data with conventional UPS method. (iii) several band peaks were detected as a shoulder feature in the main bands for the first time. The detailed analysis of these experimental results should reveal unexplored photoionization dynamics of methyl oxirane.

We extended the measurements and analysis to oxirane derivatives in the same manner. While substituting the methyl group to the larger alkyl group yielded a quite similar photoelectron spectrum to that of methyl oxirane, a remarkably different spectrum was obtained for an aromatic derivative. The substitution effect is mostly explained as the different interaction strengths between the oxirane framework and the substituents. However, newly found peaks for methyl oxirane (iii) were also observed for alkyl- and aromatic-oxiranes as shoulder-type features associated with the prominent bands. Further investigation of the observed spectra of oxirane-derivative is undertaken with quantum chemistry calculations.

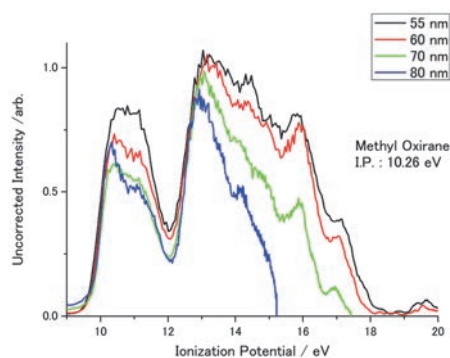


Fig. 1. Photoelectron spectra of methyl oxirane at several photon energies. The ionization threshold is identical with the literature value within the instrumental resolution.

[1] H. Kohguchi *et al.*, UVSOR Activity Report **50** (2023) 121.

[2] H. Kohguchi *et al.*, UVSOR Activity Report **48** (2021) 93.

BL7B

Photoionization Experiments in UVSOR-III for Study of Divertor Plasmas in a Nuclear Fusion Reactor and of Interstellar Plasmas in a Context of Astrobiology

M. Kobayashi¹, S. Yoshimura¹, J. Takahashi², H. Iwayama³, N. Kondo³, M. Katoh^{3,4},
K. Kobayashi⁵ and H. Nakamura¹

¹National Institute for Fusion Science, Toki 509-5292, Japan

²Self-organization Science Research Center, Doshisha University, Kyotanabe 610-0321, Japan

³UVSOR Synchrotron Facility, Institute for Molecular Science, Okazaki 444-8585, Japan

⁴Hiroshima Synchrotron Radiation Center, Hiroshima University, Higashi-Hiroshima 739-0046, Japan

⁵Department of Earth and Planetary Sciences, Tokyo Institute of Technology, Meguro-ku, Tokyo 152-8550 Japan

In nuclear fusion reactors, density of plasmas and neutral hydrogen in the divertor region will increase by more than one order of magnitude compared to the present-day devices due to the increasing plasma pressure in the scrape-off layer (SOL) [1]. At the same time, the photon emission from plasmas in confinement region (Bremsstrahlung) and in the SOL (line emissions from highly charged ions) will increase in wide wavelength range, from EUV to visible and infrared regions, because of the higher plasma density required to sustain nuclear fusion reaction. Such situation leads to enhanced interaction between hydrogen atoms/molecules and the photons in the divertor region, such as photoionization, photoexcitation. The atomic/molecular processes will be altered under the influence of the increased numbers of photons especially in very low temperature range below ~ 10 eV [2, 3].

There exist partially ionized plasmas in an interstellar space, where ionization is caused by cosmic rays or by interstellar radiation field [4]. In this circumstance, photon-induced processes, such as photoionization, photoexcitation, photodissociation etc., also play important roles in chemical evolution of prebiotic molecules related to the origin of life in space [5]. It is also noted that collective phenomenon of plasmas under the effects of magnetic fields will provide additional effects on the evolution. Characteristics and roles of the photoionized plasmas are, however, not yet fully understood.

To address these issues, we attempt to generate photoionized plasmas by using the synchrotron radiation source UVSOR-III [6] to simulate the above mentioned plasmas in the divertor region in nuclear fusion reactors and in the interstellar space. The beamline BL7B is used to generate beam from 30 to 500 nm. A gas cell has been installed inside the irradiation chamber to maintain high pressure of sample gas while keeping a good vacuum condition for the beamline. A high gas pressure is necessary to enhance the photoionization events through an interaction between the photons and neutral atoms/molecules. Fig.1 shows the gas cell used in the present experiments. The beam from BL7B is injected to the cell through a

hole at the front end (ϕ 2 mm and 60 mm length). The beam is damped at the end of the gas cell. An off-axis parabolic mirror is installed at the front end to collect emission from the gas along the beam axis. An electrode of Langmuir probe is situated at the center of the cell and biased to ± 18 V to measure saturation current of the plasmas. The gas is fed to the cell through the input terminal at the top of the cell.

As a sample gas, Argon (ionization potential of 14.5 eV) was introduced. The gas pressure inside the gas cell could be increased to an order of 1 Pa while the ambient pressure outside of the cell was kept at an order of 10^{-4} Pa and the pressure at the upstream of the beamline was at an order of 10^{-6} Pa. The photon flux of the beam was measured with a photodiode, and was estimated at an order of $10^{15} \sim 10^{16}$ photons/s/mm². The estimated electron density obtained by the Langmuir probe is in an order of 10^{11} m⁻³, which is in agreement with a simple 1D model of the photoionization plasmas.

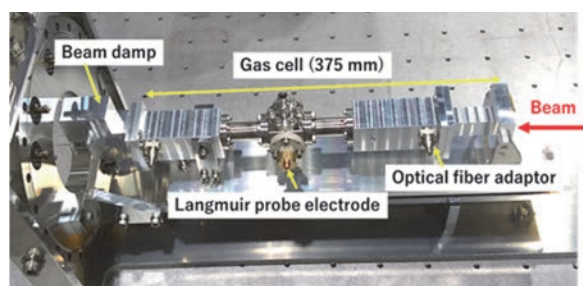
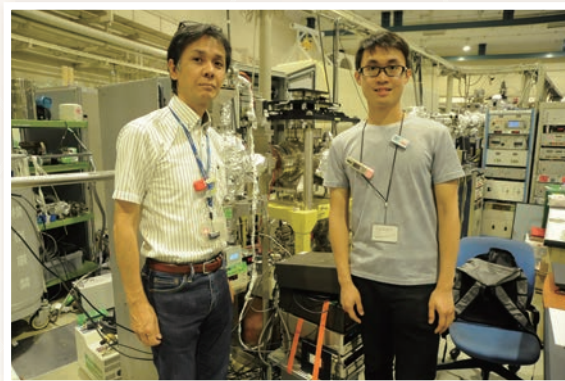
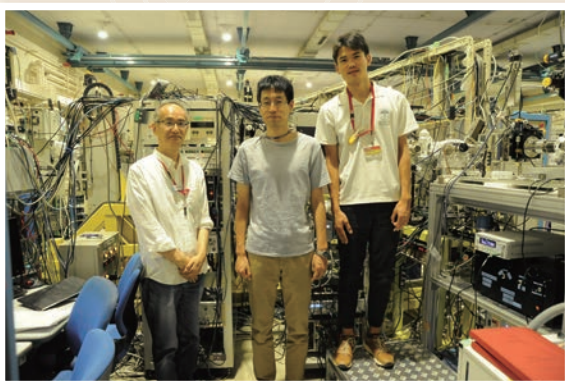
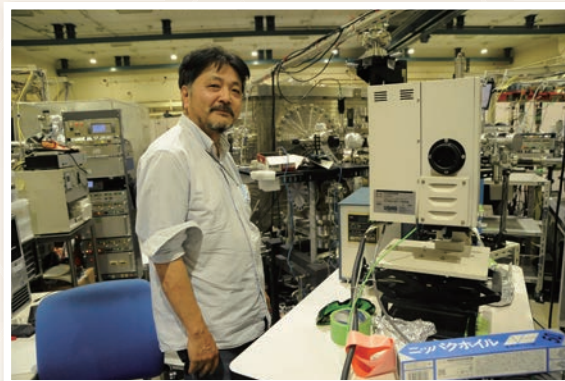
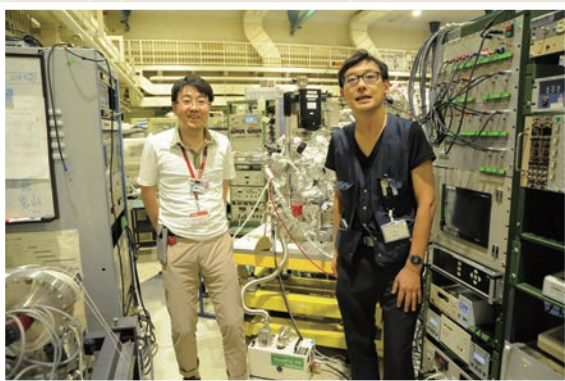
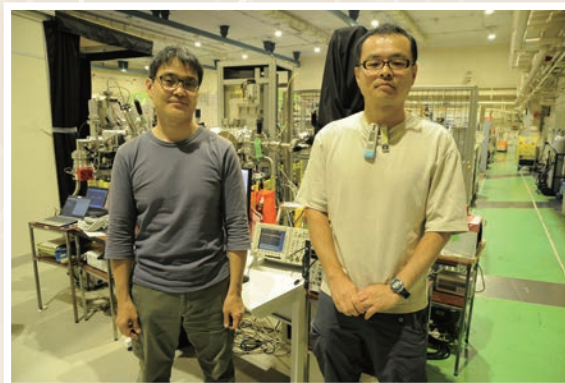
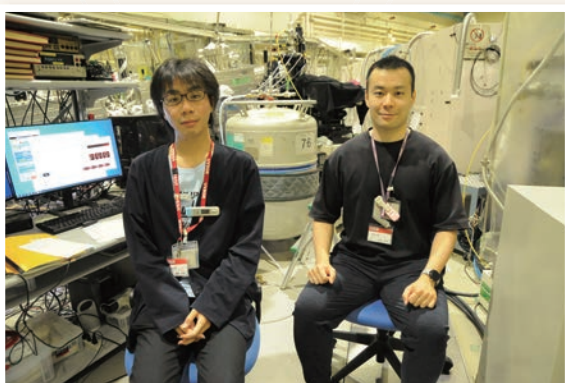
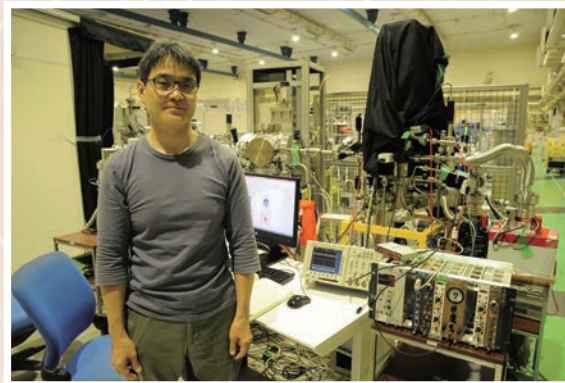
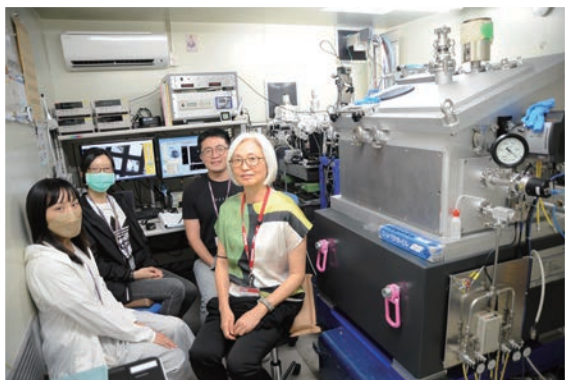


Fig. 1. Photo of the gas cell for photoionization experiments.

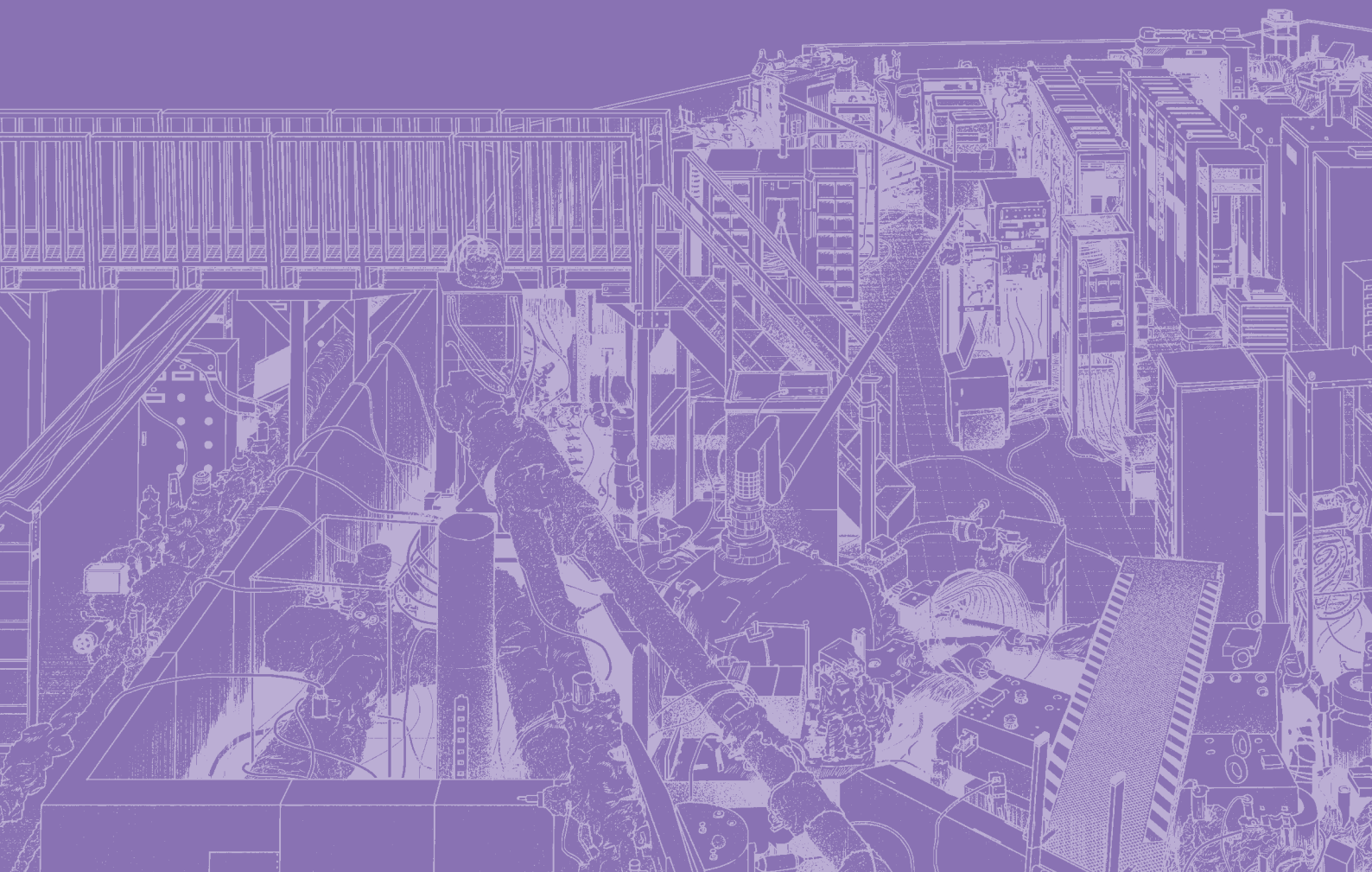
- [1] M. Kotschenreuther *et al.*, Phys. Plasma **14** (2007) 072502.
- [2] K. Sawada *et al.*, Contrib. Plasma Phys. **60** (2020) e201900153.
- [3] M. Kobayashi *et al.*, Contrib. Plasma Phys. **60** (2020) e201900138.
- [4] E.F.van Dishoeck *et al.*, Faraday Discuss. **133** (2006) 231.
- [5] K. Kobayashi *et al.*, Astrobiology **21** (2021) 1479.
- [6] H. Ota *et al.*, J. Phys. Conf. Ser. **2380** (2023) 012003.

UVSOR User 5



III-4

Surface,
Interface and
Thin Films





BL5U, 7U

Momentum-Dependent Two-Dimensional Heavy-Fermion Formation in a Monoatomic-Layer Kondo Lattice YbCu₂

T. Nakamura^{1,2}, H. Sugihara², Y. Chen², K. Tanaka³ and S. Kimura^{1,2,4}¹Graduate School of Frontier Biosciences, Osaka University, Suita 565-0871, Japan²Department of Physics, Graduate School of Science, Osaka University, Toyonaka 560-0043, Japan³UVSOR Synchrotron Facility, Institute for Molecular Science, Okazaki 444-8585, Japan⁴Department of Materials Molecular Science, Institute for Molecular Science, Okazaki 444-8585, Japan

Heavy-fermion (HF) systems in rare-earth intermetallic compounds originating from the hybridization between localized f electrons and conduction (c) electrons are central topics in strongly correlated electron systems [1]. Depending on the c - f hybridization strength at low temperatures, the ground state changes from a magnetic order to a heavy Fermi liquid. The competition between these two states makes a quantum critical point, resulting in the emergence of exotic quantum phenomena such as non-Fermi liquid and HF superconductivity [2]. The dimensionality of the system characterizes the fundamental physical property. The combination of the HF state and low dimensionality modifies the ground state because the order parameter of these systems is much more sensitive to dimensionality [3]. However, the monoatomic-layer Kondo-lattice showing a two-dimensional (2D) HF state has never been reported. In this study, we report the HF electronic structure of the monoatomic-layer Kondo lattice YbCu₂ by angle-resolved photoelectron spectroscopy (ARPES) at UVSOR-III BL5U and BL7U [4].

Figure 1(a) shows the ARPES intensity plot around the $\bar{\Gamma}$ point at 7 K. The flat band is close to E_F and highly dispersive hole bands are observed near the $\bar{\Gamma}$ point. According to the DFT calculation, the flat band and hole bands originate from the Yb²⁺ 4 $f_{7/2}$ and the mixing of the Yb 5 d and Cu sp and d orbitals [4]. The Yb²⁺ 4 f flat band is modulated at the cross points to the conduction bands just below E_F , providing evidence of the c - f hybridization.

The temperature dependence of the quasiparticle peak just below E_F , the so-called Kondo-resonance (KR) peak, is reflected in renormalization due to the development of c - f hybridization. Figure 1(b) shows the angle-integrated (AI) photoelectron spectra as a function of temperature. The KR peak energy is shifted to the E_F with decreasing temperature, indicating the evolution of the renormalization. Figure 1(f) shows the temperature dependence of the KR peak positions. The peak position shifts with decreasing temperature and is saturated at 30 K. Such saturated temperature represents a coherence temperature (T_{coh}), at which the c - f hybridization state is fully established, resulting in a HF state [5].

To investigate the momentum-dependent c - f hybridization, we took the temperature-dependent peak position of the KR peak at three wavenumbers ($k_x = 0.5, 0.0, -0.1 \text{ \AA}^{-1}$) as shown in Figs. 1(c-e). The change of the peak position at $k_x = 0.5 \text{ \AA}^{-1}$ almost follows the AI one. In contrast to the saturated feature in the AI spectrum at $T = 30 \text{ K}$, the KR peak positions at $k_x = 0.0$ and -0.1 \AA^{-1} are shifted to the higher-binding energy side below T_{coh} , suggesting the hybridization gap enlargement.

- [1] P. Coleman *et al.*, J. Phys.: Condens. Matter **13** (2001) R723.
- [2] C. Pfleiderer, Rev. Mod. Phys. **81** (2009) 1551.
- [3] S. Sachdev, Science **288** (2000) 475.
- [4] T. Nakamura *et al.*, Nat. Commun. **14** (2023) 7850.
- [5] H. Anzai *et al.*, J. Phys. Soc. Jpn. **91** (2022) 114703.

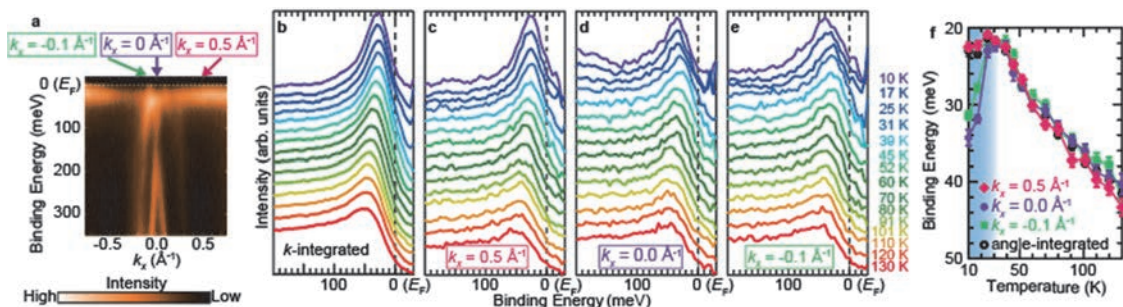


Fig. 1. (a) The ARPES intensity plot around $\bar{\Gamma}$ point taken with horizontally polarized 37-eV photons at 7 K. (b) Angle-integrated photoelectron spectra as a function of temperature taken with horizontally polarized 35-eV photons. The intensity is normalized by the Fermi–Dirac distribution function convolved with the instrumental resolution. (c-e) Angle-resolved photoelectron spectra near E_F as a function of the temperature. The k_x positions at (c) 0.5, (d) 0.0, and (e) -0.1 \AA^{-1} are representative of the local f state only, the $\bar{\Gamma}$ point, and the crossing point of the c - f hybridization, respectively. (f) Momentum dependence of the energy position of the quasiparticle peak plotted on a linear temperature scale.

Surface Treatment Dependence of Mo L-Edge NEXAFS Spectrum of Molybdenum Oxide

E. Kobayashi¹, S. Yoshioka² and K. K. Okudaira³

¹Kyushu Synchrotron Light Research Center, 8-7 Yayoi-gaoka, Tosu, Saga 841-0005, Japan

²Graduate School of Engineering, Kyushu University, 744 Motoooka Nishi-ku Fukuoka 819-0395 Japan

³Graduate School of Science and Engineering, Chiba University,
1-33 Yayoi-cho Inage-ku, Chiba 263-8522, Japan

In recent years, organic thin film solar cells have attracted attention as a new energy source from the perspective of global environmental and energy issues [1, 2]. For the spread of solar cells, it is essential to improve the performance of organic thin film solar cells with low power generation costs, but in recent years, energy conversion efficiency has improved rapidly and is reaching the level of practical use. Solar cells use metal oxide electron and hole transport materials. Further improvement of its performance requires knowledge of the interface between organic molecules and metal oxides [3, 4]. We are investigating surface treatments of metal oxides to improve contact between metal oxide and organic molecules. It is important to find an appropriate surface treatment method because defects on the surface of the oxide film cause charge trapping and reduce conversion efficiency. In this paper, we focused on molybdenum oxide, a typical metal oxide, as a hole transport material.

The sample are molybdenum oxide thin film fabricated on silicon using the RF magnetron sputtering method. The thin film was cleaned with neutral detergent, distilled water, and acetone. One of the films was UV ozone cleaned after its cleaning. NEXAFS spectra of the molybdenum oxide thin film using both total electron yield (TEY) and partial fluorescence yield (PFY) modes were measured at the beamline 2A of the UVSOR in the Institute of Molecular Science. For TEY, the drain current from the sample was measured. For PFY, fluorescence X-rays were collected using an energy dispersible silicon drift detector (SDD). All experiments were performed at room temperature.

Figure 1 shows the NEXAFS spectrum of molybdenum oxide thin film cleaned with neutral detergent, distilled water, acetone, and UV ozone in TEY mode. The overall shape of the spectrum remains unchanged. However, the shape of the main peak changes. Figure 2 is an enlarged view of the spectrum. The peak intensity of the spectrum of the thin film washed with distilled water is higher than that of the untreated one. This indicates that oxidation of the

surface layer of the thin film is progressing. In addition, in the spectrum of the thin film after ozone cleaning, the rise of the spectrum shifted to the high energy side, and components on the high energy side appeared. This indicates that the oxidation state on the surface has become a high oxidation state.

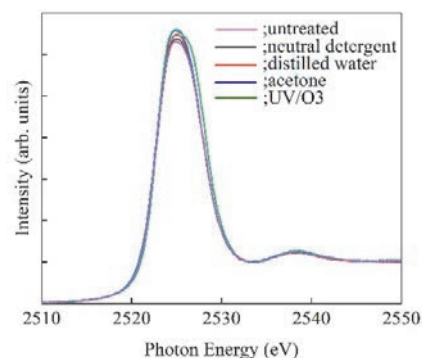


Fig. 1. Mo L-edge NEXAFS spectra of molybdenum oxide thin film in TEY mode.

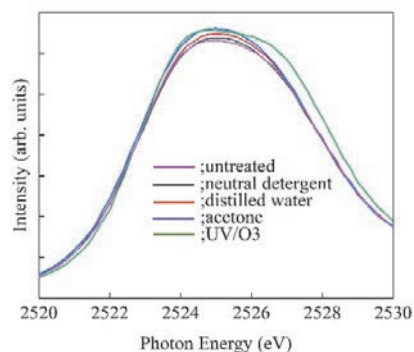


Fig. 2. Enlarged view of Mo L-edge NEXAFS spectra of molybdenum oxide thin film in TEY mode.

- [1] Y. Sun *et al.*, Adv. Funct. Mater. **31** (2021) 2010000.
- [2] L. Ma *et al.*, Adv. Mater. **35** (2023) 2208926.
- [3] J. Subbigh *et al.*, Org. Electron. **11** (2010) 955.
- [4] Y. Gong *et al.*, J. Mater. Chem. A **8** (2020) 978.

BL2A

Characterization of Electronic Structure in (Ba, Sn)S Thin Film Using XANES

T. Nagai^{1,2}, H. Murata³, H. Tampo¹ and F. Kawamura⁴

¹Research Institute for Energy Conservation, National Institute of Advanced Industrial Science and Technology (AIST), 1-1-1 Umezono, Tsukuba 305-8568, Japan

²Graduate School of Science and Engineering, Kagoshima University, 1-21-40 Korimoto 890-0065, Japan

³Department of Materials Science, Osaka Metropolitan University, Sakai 599-8531, Japan

⁴Research Center for Materials Nanoarchitectonics (MANA), National Institute for Materials Science (NIMS), Namiki 1-1, Tsukuba 305-0044, Japan.

SnS(*Pmma*) is one of the great promising semiconductor materials to make the next generation solar cells [1]. Recently, we have shown by first-principles calculations that the bandgap energy of SnS changes with the effective coordination number (ECoN) induced by changes in cell volume [2]. In the real world, however, it is quite difficult to change only the ECoN without changing the volume of the cell, while theoretical calculations make this situation easy to achieve. Therefore, there is no evidence for experimental data for these relationship between the bandgap energy and ECoN at present. Here we noticed that this situation can be achieved by substituting Sn with Ca, Ba, and Sr, elements that have the same valence as Sn divalent and a larger ionic radius than Sn divalent.

According to this idea, the (Ba,Sn)S thin films with the Ba contents {Ba/(Sn+Ba) molar ratios} from 0 to 0.49 were deposited on the soda-lime glass using molecular beam epitaxy (MBE) techniques. Firstly, we measured the X-ray diffraction (XRD) pattern for these films to confirm the impacts of substitution of Sn with Ba to the lattice constant. As a result, the peak position derived from SnS(111) gradually shifts to the lower angle side with increasing Ba content. This experimental result means that the cell volume of SnS becomes larger with increasing of the Ba contents. Moreover, we confirmed that the bandgap energy increased with increasing of Ba contents by the absorption spectra and inverse- and ultraviolet photoemission spectra (IPES and UPS). These experimental results are consistent with our theoretical calculations, showing that the band gap is strongly negatively correlated with the lattice constant, an opposite phenomenon to that of general semiconductors.

Moreover, X-ray absorption near edge structure (XANES) measurements were conducted using BL2A in UVSOR (Okazaki, Japan) to understand the impacts of substitution of Sn with Ba in these films to the electronic structure of SnS. Figure 1 shows the S-K XANES spectra by the partial fluorescence yield method using a silicon drift detector for these (Ba, Sn)S thin films with Ba contents from 0 to 0.49. The white line appeared at 2472 eV for SnS (Ba contents of 0) film. Two additional peaks appeared at 2474 eV and 2479 eV in the (Ba,Sn)S thin film with Ba content

above 0.11. Moreover, the white line at 2472 eV for the (Ba,Sn)S films with Ba contents below 0.17 suddenly changed to 2470 eV for the films with Ba contents over 0.27.

Here, previous XRD experiments have confirmed that the signal attributed to SnS disappears at Ba concentrations above 0.15, indicating that a phase transition from a crystalline structure to an amorphous structure is expected to have occurred. Therefore, the energy shifts of the white line from 2472 to 2470 in the S-K XANES of the (Ba,Sn)S thin film containing Ba above 0.27 may reflect a phase transition from a crystalline to an amorphous structure.

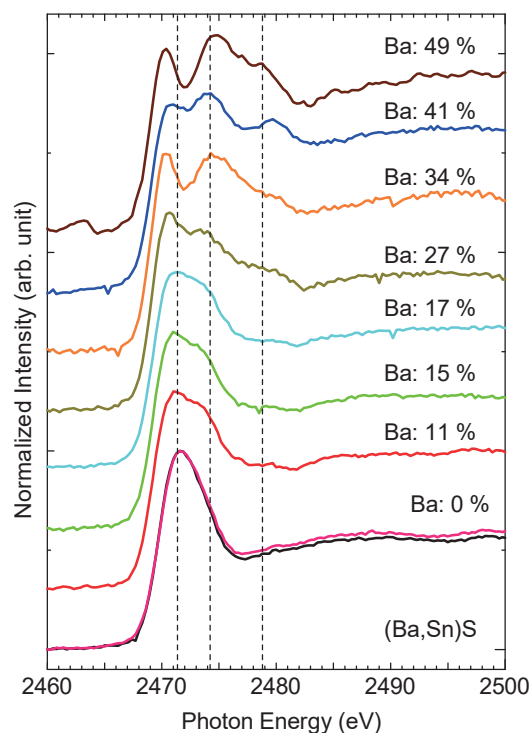


Fig. 1. S-K XANES spectra for (Ba, Sn)S thin films with Ba contents from 0 to 0.49.

[1] C. Chotia *et al.*, J. Mater. Sci.: Mater. Electron. **32** (2021) 10702.

[2] F. Kawamura *et al.*, Sci. Rep. **12** (2022) 7434.

X-ray Absorption Spectroscopy Study of Dodenanethiol on Gold Surfaces

F. Sato¹, I. Imahori¹, I. Tsukamoto¹, S. Ohno¹, Y. Sugimoto² and M. Nagasaka²

¹Graduate School of Engineering, Yokohama National University, Yokohamai 240-8501, Japan

²Institute for Molecular Science, Okazaki 444-8585, Japan

It is important to understand the behavior of biomolecules on solid surfaces for the application to medical device, biosensor and biocompatible material. It is essential to study the adsorption and desorption behavior of biomolecules and their response to the applied electric fields. It is of particular importance to analyze the dynamic behavior of biomolecules on a surface in electrolyte solutions, which is close to the realistic condition in the body of living creatures [1,2].

In the present study, potential-dependent adsorption and desorption behavior of Dodecanethiol on Au membrane surfaces have been investigated using soft X-ray absorption spectroscopy (XAS) in the transmission mode. The experiments were performed on the soft X-ray undulator beam line at UVSOR-III, BL3U. We used H₂SO₄ and KOH as the electrolyte solution. For the adsorption of Dodecanethiol molecules, the samples were immersed in 100mM Dodecanethiol/ethanol solution for more than 1 hour.

In our previous study [1], we have investigated some biomolecules on Au surfaces using surface differential reflectance spectroscopy (SDRS) and cyclic voltammetry (CV) combined with XAS. The key issue was the interaction between functional group (-COOH) and the applied biases and pH conditions. Redox processes involving charge transfer were clearly observed with CV and the relation between the change in the reflectance spectra and the peaks in CV was investigated in detail. We discovered the indication of the precursor behavior to cause significant change in the reflectance spectra with no corresponding signal in CV. This indicates that such changes in the reflectance spectra are not due to the charge-transfer-type reactions but rather to the subtle change in the orientation/conformation of those biomolecules. Motivated by these works, we here applied XAS to investigate the self-assembled monolayer (SAM) composed of alkanethiol molecules. Here, we selected Dodecanethiol as the representative of this sort of molecules.

To our knowledge, there has been no serious effort to study the Dodecanethiol/Au interfaces using XAS in terms of the aforementioned precursor phenomena. Here, we report the indication of the structural change in the alkanethiol molecule more accurately.

Figure 1 shows the C K-edge XAS spectra obtained for Dodecanethiol adsorbed Au. A distinct peak at 292.5 eV is assigned to the 1s → σ* transition of the C-C bonding [2]. Hence, we could confirm that the detection of the K-edge absorption for the alkanethiol molecules is an effective means to investigate the adsorption

behavior of them at the solid/liquid interface.

When the bias of -1.0 eV is applied to the Au substrate for 1 hour, the reduction of the peak intensity was observed. This indicates that the amount of adsorbed Dodecanethiol decreases or some structural changes occur. It should be noted that no peak features are observed within the bias range of -1.0 to 0.0 eV in the CV voltammogram. Therefore, the origin of the spectral change should be due to the quasi-static reaction rather than the reduction reaction.

In the present study, we performed some supplementary CV measurements using potassium ferrocyanide trihydrate (K₄[Fe(CN)₆]) to investigate the stability of Dodecanethiol adsorption. We compared with the Dodecylamine for the stability against the applied bias of -1.0 V on the Au substrate. Our preliminary results indicate that the partial removal of Dodecanethiol occurs while all the molecules are removed in the case of Dodecylamine. This suggests that the attachment and removal of the alkanethiol unit can be well-controlled by changing the functional group as well as the condition of the applied bias.

We expect that the present findings would be worthwhile to develop the biodevices utilizing the interaction between the alkanethiol unit and the Au electrode in general.

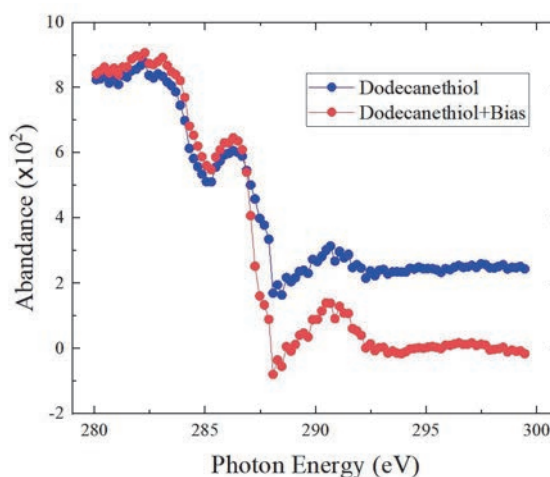


Fig. 1. C K-edge XAS spectra obtained for Dodecanethiol adsorbed Au.

[1] F. Sato *et al.*, UVSOR Activity Report **50** (2023) 145.

[2] A. Imanishi *et al.*, Surf. Sci. **407** (1998) 282.

BL3U

Ionic Layers at the Electrode Interface of Ionic Liquids Studied Using Interface-Selective Soft X-ray Absorption Spectroscopy

T. Furuya¹, Y. Sugimoto², M. Nagasaka² and N. Nishi¹

¹Graduate School of Engineering, Kyoto University, Kyoto 615-8510, Japan

²Institute for Molecular Science, Okazaki 444-8585, Japan

Ionic liquids (ILs), which are entirely composed of cations and anions, are appealing materials as electrolytes for energy devices. In such devices, the electrochemical interface between ILs and electrodes is an electrochemical reaction field that strongly influences the local reaction rate and thereby the net ones such as charging speed for batteries. Thus, it is of crucial importance to study, and further control, the interfacial structure of ILs at the electrode interface. In the present study, we adopted soft X-ray absorption spectroscopy (XAS) to reveal the interfacial structure of ILs at the electrode interface in an interface-selective manner [1].

An equimolar amount of lithium bis(fluoro-sulfonyl) amide ($\text{Li}^+[\text{FSA}^-]$) and tetraglyme (G4) were mixed to prepare a solvate IL [2]. *In-situ* XAS measurements for the IL/electrode interface were performed at BL3U at UVSOR-III, by using an electrochemical liquid flow cell [1]. The IL was sandwiched with two Si_3N_4 membranes in the He-filled chamber and XA spectra were measured in transmission mode for the oxygen and fluorine K-edge regions. The photon energy was calibrated by the main peak (530.88 eV) in the oxygen K-edge region for a ProLINE polymer thin film [3]. The thickness of the IL film was controlled with the He pressure in a range from 20 to 2000 nm [4]. For a thick IL film at a low He pressure, the XA spectra can be regarded to originate from the IL bulk with a minor contribution from the interfacial structure, while for a thin IL film at a high He pressure, XA spectra show some features different from the bulk ones, stemming from the interfacial structure. The gold film deposited at the inner surface of one of the two Si_3N_4 membranes was used as the working electrode. Pt wires, as the quasi-reference and counter electrodes, were located aside the film region inside the electrochemical cell. The potential of the working electrode with respect to the quasi-reference electrode was controlled using a potentiostat.

The oxygen K-edge XA spectra for the IL bulk showed a broad absorption peak which is mainly assignable to G4. The double sharp peaks assignable to FSA^- were hardly discernible, hidden in the broad peak. When negative potentials were applied at the IL/gold interface, the interfacial structure started to show the double peak feature, which is likely to be due to the enrichment of FSA^- over G4.

Figure 1 shows the fluorine K-edge XA spectra for the IL bulk and for the IL/gold interface with several applied potentials. The XA spectra showed three

potential-dependent features; with lowering the potential, the lowest-energy peak was red-shifted, the second lowest-energy peak was broadened, and the intensity at the high-energy region became higher. Figure 2 shows the redshift, which is large as much as 0.5 eV. These features clearly demonstrate that the present XAS measurements in transmission mode with a nm-scale thin film setup sensitively detect the interfacial structure, which is different from the bulk one and is also potential-dependent.

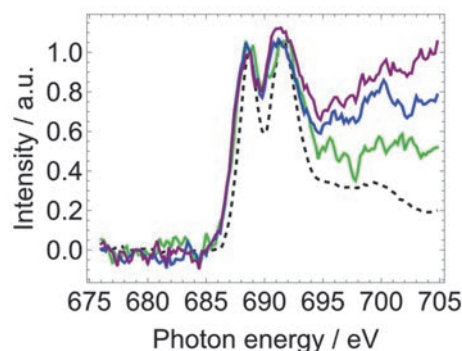


Fig. 1. Fluorine K-edge XA spectra for the IL bulk (black dashed) and for the IL/gold interface at -2 (green), -2.5 (blue), and -3 V (purple), respectively.

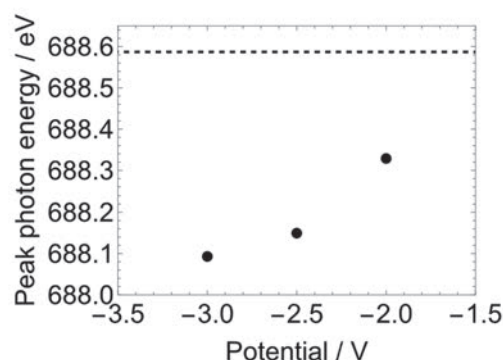


Fig. 2. Peak photon energy as a function of the electrode potential for the lowest energy peak in Fig.1. The horizontal dashed line is for the IL bulk.

- [1] M. Nagasaka *et al.*, Rev. Sci. Instrum. **85** (2014) 104105.
- [2] S. Terada *et al.*, Aust. J. Chem. **72** (2019) 70.
- [3] M. Nagasaka *et al.*, J. Electron Spectrosc. Relat. Phenom. **224** (2018) 93.
- [4] M. Nagasaka *et al.*, J. Electron Spectrosc. Relat. Phenom. **117** (2010) 130.

Probing Interfacial Water on SiO₂ in Colloidal Dispersion

Y. Hao¹, S. Wang¹, M. Nagasaka², Z. Abbas³ and X. Kong³

¹*Department of Environmental Sciences, College of Urban and Environmental Sciences, Northwest University, Xi'an, China*

²*UVSOR Synchrotron, Institute for Molecular Science, Okazaki 444-8585, Japan*

³*Department of Chemistry and Molecular Biology, Atmospheric Science, University of Gothenburg, SE-413 90 Gothenburg, Sweden*

Solid surfaces either hard or soft, such as proteins [1], induce significant effect on the structure of water molecules present near the surfaces [2]. Interfacial water is considered to play a role in protein recognition [3] and also has an effect on electrochemical and catalytic reactions at the interfaces [4]. Knowledge about the arrangement of solvent molecules around colloidal nanoparticles is crucial for understanding and evaluation of their reactivity in the water environment as well as their interaction with biological components. In colloidal dispersion such as SiO₂ dispersion in water, the structure of solvent molecules around nanomaterials has not been fully explored. The hydrophilicity, size of nanoparticles and their surface charge affect the interfacial water.

In this beamtime, we carried out Near Edge X-ray Absorption Fine Structure (NEXAFS) measurements on SiO₂ solutions with different concentrations. The NEXAFS measurements were performed at the soft X-ray undulator beamline BL3U at UVSOR-III Synchrotron. In the liquid flow cell, a liquid layer is sandwiched between two 100 nm thick Si₃N₄ membranes with the windows size of 2 × 2 mm². Teflon spacers with a thickness of 100 μm are set between the support plates of the Si₃N₄ membranes. Liquid samples are exchangeable *in situ* by using a tubing pump. The temperature of all the liquid samples were controlled at approx. 25°C. The Si₃N₄ membrane window was set to 200 × 200 μm² to allow for suitable photon fluxes.

In Figure 1 and Figure 2, the O K-edge NEXAFS results are presented. The pure water case is also included in both panels as reference spectra. The spectra exhibit three features: pre-edge (~535 eV), main-edge (~537 eV), and post-edge (~540 eV). The spectrum lines were normalized to the maximum at the pre-edge (Fig. 1) and the post-edge (Fig. 2), which is to take into account variations in the sample thickness. The post-edge intensities of the SiO₂ solutions are higher than those of pure water, which is similar to the existing literature on the study of interfacial water on nanodiamonds [5]. The absorption intensities increase with the increase of the concentration of SiO₂ solutions. This can be linked with the accumulation of hydrated Na⁺ ions as concentration of the particles in the suspension increases. The pre-edges have been zoomed in and displayed in the inset (Fig. 2). The intensity of the pre-edge peak is weaker for SiO₂ solutions, have

smaller sizes than pure water. Moreover, the intensities have a tendency to decrease with the increase of concentration, which may be affected by the strength of hydrogen bonds between the water layers.

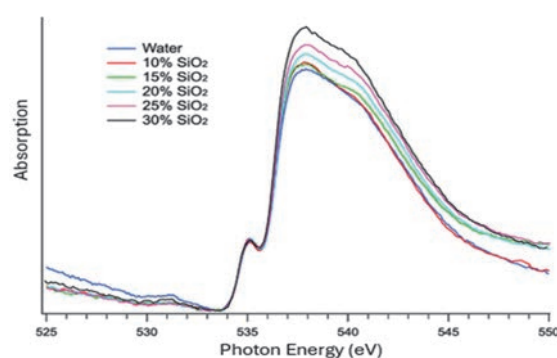


Fig.1. O K-edge NEXAFS spectra of pure water and SiO₂ solutions with different concentrations. The temperatures are around 25°C. The spectra were normalized to the maximum at the pre-edge.

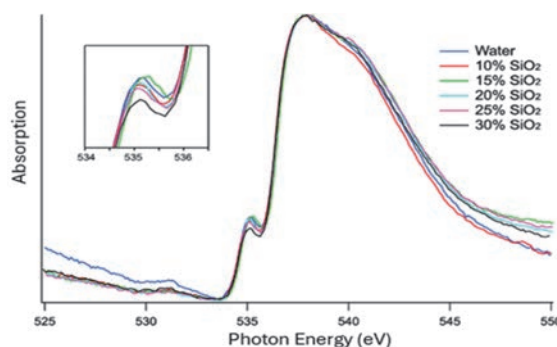


Fig.2. O K-edge NEXAFS spectra of pure water and SiO₂ solutions with different concentrations. The temperatures are around 25 °C. The spectra were normalized to the maximum at the post-edge. The insets zoom in the pre-edge regions.

- [1] S.V. Ruffle *et al.*, J. Am. Chem. Soc. **124** (2002) 565.
- [2] J. Velasco-Velez *et al.*, Science **346** (2014) 831.
- [3] K.C. Jena and D.K. Hore, Phys. Chem. Chem. Phys. **12** (2010) 14383.
- [4] S. Dewan, M.S. Yeganeh and E. Borguet J. Phys. Chem. Lett. **4** (2013) 1977.
- [5] Petit, T., *et al.*, J. Phys. Chem. Lett. **6** (2015) 2909.

BL3B

Evaluation of Crystallinity of Substrate Interface Region of Deep Ultraviolet Emitting Zinc Aluminate Thin Film

H. Kominami^{1,2,3}, A. Adachi¹, R. Ishihara¹, K. Yabe¹, J. Kamikawa¹, T. Sadamori¹, D. Takeya¹, M. Mimura², M. Yasuda², A. Yokoya², N. Yoshimura² and S. Kurosawa^{4,5}

¹Graduate School of Integrated Science and Technology, Shizuoka University,

²Faculty of Engineering, Shizuoka University,

³Graduate School of Science and Technology, Shizuoka University,

¹⁻³3-5-1 Johoku, Chuo-ku, Hamamatsu 432-8651 Japan

⁴New Industry Creation Hatchery Center (NICHe), Tohoku University 6-6-10 Aza-Aoba, Aramaki, Aoba-ku, Sendai, Miyagi 980-8579, Japan

⁵Faculty of science, Yamagata University, 1-4-12, Kojirakawa-machi, Yamagata 990-8560, Japan

In the field of sterilization and water purification, conventional sterilization methods using chemicals and heat have concerns about the effects of deterioration, toxicity to the human body, and the effects of resistant bacteria. Therefore, sterilization methods using ultraviolet light are becoming popular. Ultraviolet light around 260 nm is said to have the strongest effect, and mercury lamps and xenon lamps are used as ultraviolet light sources for sterilization. However, its use is undesirable from the viewpoint of environmental impact and luminous efficiency. Therefore, we aimed to apply ZnAl_2O_4 as the light-emitting layer of a new ultraviolet light-emitting device for sterilization that has high efficiency, long life, low cost, and low environmental impact, and conducted an evaluation. Currently, we are working on the production of double-insulated electroluminescent (EL) lamps, which are one type of solid-state display element. In order for electrons to be injected from the insulating layer to the light emitting layer, it is necessary that the interface between the insulating layer Al_2O_3 substrate and the light emitting layer ZnAl_2O_4 be clear and growing uniformly to the surface. This affects the injection of electrons into the light-emitting layer, the acceleration of electrons by the electric field, the collisional excitation of the luminescent center, and the emission of light, which greatly influences the device characteristics. In this study, we focused on ZnAl_2O_4 as a light-emitting layer for a new ultraviolet light-emitting device, fabricated it, and evaluated its structure from the surface to the interface.

On a c-plane sapphire substrate (c- Al_2O_3), he deposited about 300 nm of ZnO by magnetron sputtering, and on top of that he deposited about 25 nm of Al_2O_3 as a cap layer. After sputtering, he fabricated ZnAl_2O_4 thin films by annealing (990°C, 50 hours) under atmospheric conditions in a muffle furnace and by thermal diffusion. In addition, the thin film surface of the prepared sample was etched using hydrochloric acid to expose the inside of the film, and its characteristics were evaluated using cathodoluminescence (CL), thin film X-ray diffraction measurement (XRD), analytical FE-SEM, and transmission.

Figures 1 and 2 show the transmittance curve and an enlarged view of the vicinity of the absorption edge, respectively. It was found that the absorption edge shifts to the shorter wavelength side after about 400 nm. This is due to an increase in the bandgap. ZnAl_2O_4 is fabricated by thermally diffusing ZnO on c- Al_2O_3 . For this reason, it is thought that Zn diffusion varies and the composition deviates from the stoichiometric composition, resulting in the formation of ZnAl_2O_4 (predominantly c- Al_2O_3 with a large band gap) lacking Zn.

The results of CL, XRD, and transmittance measurements show that uniform ZnAl_2O_4 is formed up to 400 nm inside the sample, but it is thought that ZnAl_2O_4 is insufficiently formed further inside.

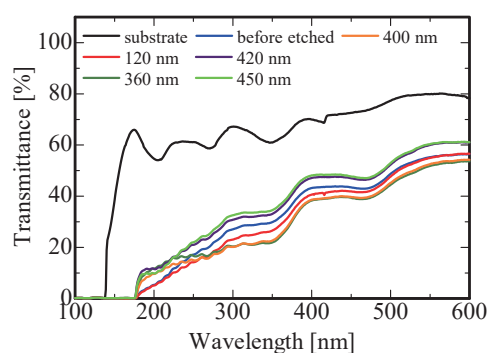


Fig. 1. Transmittance of the etched samples.

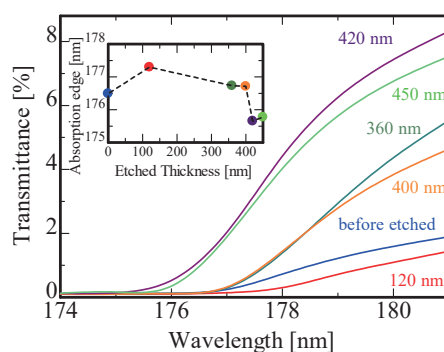


Fig. 2. Absorption edges and etched thickness vs. absorption edge relationship.

Interfacial Lattice Strain Induced Spin Reorientation Transition in Pd/Ni Thin Film Heterostructures

T. Miyamachi^{1,2}, K. Tsutsui¹, H. Ono¹, O. Ishiyama^{3,4}, T. Yokoyama^{3,4} and M. Mizuguchi^{1,2}

¹Department of Materials Science and Engineering, Nagoya University, Aichi 464-8603, Japan.

²Institute of Materials and Systems for Sustainability (IMaSS), Nagoya University, Aichi 464-8601, Japan.

³Institute for Molecular Science, Myodaiji-cho, Okazaki 444-8585, Japan

⁴The Graduate University for Advanced Studies, Myodaiji-cho, Okazaki 444-8585, Japan

The emergence of novel functionality in thin-film heterostructures strongly rely on the interfacial conditions such as lattice strain, mixing or alloying. For the thin film heterostructure composed of magnetic materials, structural modifications at the interface drastically change the degrees of the magnetic coupling, characterizing magnetic properties of the whole system [1]. In this work, we investigate structural, electronic, and magnetic properties of Pd/Ni thin film heterostructures by low energy electron diffraction (LEED) and x-ray absorption spectroscopy/magnetic circular dichroism (XAS/XMCD). To fabricate Pd/Ni thin film heterostructures, we first grow 12 monolayer (ML) Ni thin films on the Cu(001) surface. Then, 2, 6, 14 ML Pd overlayers are grown at room temperature onto Ni/Cu(001). The deposition rates and coverage of Ni and Pd layers are determined by the quartz-crystal microbalance (QCM) and XAS edge jump.

XAS/XMCD measurements are performed at BL4B in UVSOR by total electron yield mode at $B = 0 - \pm 5$ T and $T = 7.2$ K. The XMCD spectra are obtained at the normal (NI: $\theta = 0^\circ$) and the grazing (GI: $\theta = 55^\circ$) geometries by detecting $\mu_+ - \mu_-$, where μ_+ (μ_-) denotes the XAS recorded at Ni and Pd L adsorption edges with the photon helicity parallel (antiparallel) to the sample magnetization. Note that θ is the angle between the sample normal and the incident x-ray. LEED patterns are checked before XAS/XMCD measurements, to investigate surface lattices of Ni/Cu(001) and Pd/Ni/Cu(001).

We first investigate structural properties of Pd/Ni thin film heterostructures. LEED patterns reveal that both Ni/Cu(001) and Pd/Ni/Cu(001) show $p(1 \times 1)$, indicating epitaxial growth of Ni and Pd layers on Cu(001). We find the surface lattice constant drastically changes by adding Pd overlayers possibly due to the large difference in the lattice constant between fcc Ni and Pd. The

coverages of Ni and Pd layers are also evaluated with sub-monolayer accuracy from the ratio of the XAS jump at the L-edge of Ni or Pd to that of Cu [2], ensuring controlled Ni and Pd deposition by the QCM.

Element specific magnetization curves of the Ni layer are recorded by plotting the L_3/L_2 Ni XAS peak intensity as a function of the magnetic field. The magnetization curve of bare Ni layer before Pd deposition shows larger hysteresis loop in the NI geometry than the GI geometry. This clearly reveals the magnetic easy axis towards out-of-plane direction of 12 ML Ni thin films on Cu(001) as previously reported [3]. The impact of Pd overlayers on magnetic properties of the Ni layer is further investigated. We find that the hysteresis loop in the GI geometry becomes prominent with increasing the Pd coverage. At the Pd coverage of 6 ML, the spin reorientation transition (SRT) of the Ni layer from out-of-plane to in-plane direction is observed. The in-plane magnetization of the Ni layer is further stabilized at the Pd coverage of 14 ML. The enhancement of the in-plane magnetic anisotropy is also confirmed from the evaluation of magnetic moments by XMCD sum rules. While the spin magnetic moment is nearly independent of the Pd coverage, the orbital magnetic moment in the GI geometry becomes greater than that in the NI geometry. This indicates the enhanced in-plane magnetic anisotropy of the Ni layer via the spin orbit interaction. Taking the results of LEED observations into considerations, the observed SRT can be explained by the enhancement of lateral lattice constant of the Ni layer with increasing the Pd coverage.

[1] S. Nakashima *et al.*, Adv. Funct. Mater. **29** (2019) 1804594.

[2] H. Ono *et al.*, J. Phys. Chem. C **127** (2023) 23935.

[3] B. Schulz *et al.*, Phys. Rev. B: Condens. Matter **50** (1994) 13467.

BL4B

Stabilizing In-Plane Magnetization of Pd/Ni Thin Film Heterostructures by Interfacial Lattice Strain

T. Miyamachi^{1,2}, K. Tsutsui¹, H. Ono¹, O. Ishiyama^{3,4}, T. Yokoyama^{3,4} and M. Mizuguchi^{1,2}

¹*Department of Materials Science and Engineering, Nagoya University, Aichi 464-8603, Japan.*

²*Institute of Materials and Systems for Sustainability (IMaSS), Nagoya University, Aichi 464-8601, Japan.*

³*Institute for Molecular Science, Myodaiji-cho, Okazaki 444-8585, Japan*

⁴*The Graduate University for Advanced Studies, Myodaiji-cho, Okazaki 444-8585, Japan*

Ni thin films grown on Cu(001) are known to exhibit the spin reorientation transition (SRT) with increasing coverage. At the critical coverage of ~ 7 monolayer (ML), the magnetic easy axis changes from in-plane to out-of-plane direction [1]. The SRT of this system is dominantly attributed to modifications of electronic structures near the Fermi energy caused by the tetragonal distortion of the topmost Ni layer via magnetoelastic coupling. We have recently revealed the SRT of 12 ML Ni thin films on Cu(001) from the out-of-plane to in-plane direction by adding Pd overlayers [2]. The in-plane magnetization of the Ni layer is gradually stabilized with increasing the coverage of Pd overlayers and the SRT occurs at the Pd coverage of 6 ML. The SRT of the Ni layer in Pd/Ni thin film heterostructures could be induced by in-plane tensile lattice strain derived from the large difference in the lattice constant between fcc Ni and Pd.

In this work, we grow 6 ML Ni thin film on Cu(001) with magnetic easy axis toward in-plane direction and additionally fabricate Pd/Ni thin film heterostructures with 2, 7, 11 ML Pd overlayers. We investigate the impact of in-plane tensile lattice strain from the Pd layer on the stability of in-plane magnetization of the Ni layer by soft x-ray absorption spectroscopy/magnetic circular dichroism (XAS/ XMCD). Ni and Pd layers are deposited onto Cu(001) at room temperature in ultrahigh vacuum. The deposition rates and coverage of Ni and Pd layers are crosschecked by the quartz-crystal microbalance (QCM) and XAS edge jump [3].

XAS/XMCD measurements are performed at BL4B in UVSOR by total electron yield mode at $B = 0 - \pm 5$ T and $T = 7.7$ K. The XMCD spectra are obtained at the normal (NI: $\theta = 0^\circ$) and the grazing (GI: $\theta = 55^\circ$) geometries by detecting $\mu_+ - \mu_-$, where μ_+ (μ_-) denotes the XAS recorded at Ni L adsorption edge with the photon helicity parallel (antiparallel) to the sample magnetization. Note that θ is the angle between the

sample normal and the incident x-ray. Element specific magnetization curves of the Ni layer are also recorded by plotting the L_3/L_2 Ni XAS peak intensity as a function of the magnetic field.

We first characterize magnetic properties of 6 ML Ni thin films on Cu(001). While no remanence is observed for the magnetization curve recorded in the NI geometry, we confirm a clear hysteresis loop for that in the GI geometry, which reveals in-plane magnetic easy axis of 6 ML Ni thin films as previously reported [1]. With the help of the element specificity of XAS, magnetization curves of the Ni layer in Pd/Ni thin film heterostructures can be extracted. A remarkable change is observed for the magnetization curve recorded in the GI geometry. We find that the coercivity of the Ni layer drastically increases at the Pd coverage of 2 ML, which can be explained from the in-plane tensile lattice strain by Pd overlayers as seen in similar system [2]. It is also important to note that the coercivity of the Ni layer is almost unchanged even when the Pd coverage is increased up to 7, and 11 ML. These results suggest that adding Pd overlayers stabilize the in-plane magnetization of the Ni layer, but the electronic modification of the Ni layers is completed at the Pd coverage of 2 ML.

In the future, we will perform real-space and atomic-scale observations of Pd/Ni heterointerface using scanning tunneling microscopy to investigate the origin of stabilized in-plane magnetization of the Ni layer in Pd/Ni thin film heterostructures [4].

[1] B. Schulz *et al.*, Phys. Rev. B: Condens. Matter **50** (1994) 13467.

[2] UVSOR Activity Report **51** (2024) 150.

[3] H. Ono *et al.*, J. Phys. Chem. C **127** (2023) 23935.

[4] S. Nakashima *et al.*, Adv. Funct. Mater. **29** (2019) 1804594.

XMCD Measurements on van der Waals Magnets

R. Ichikawa¹, T. Miyamachi², H. Ishii¹, W. Wulfhekel³, A.-A. Haghighirad³, O. Ishiyama⁴,
H. Iwayama⁴, E. Nakamura⁴, T. Yokoyama⁴ and T. K. Yamada^{1,5}

¹*Department of Materials Science, Chiba University, 1-33 Yayoi-Cho, Inage-ku, Chiba 263-8522, Japan*

²*Institute of Materials and Systems for Sustainability, Nagoya 464-8603, Japan*

³*Institute for Quantum Materials and Technologies, Karlsruhe Institute of Technology,
Karlsruhe 76021, Germany*

⁴*Department of Materials Molecular Science, Institute for Molecular Science, Okazaki, Aichi 444-8585, Japan*

⁵*Molecular Chirality Research Centre, Chiba University, 1-33 Yayoi-cho, Inage-ku, Chiba 263-8522, Japan*

The van der Waals (vdW) magnet is a two-dimensional (2D) magnet with magnetic properties even at the thickness of a single atomic layer. It has garnered significant interest as a highly durable and flexible next-generation spintronics material, similar to graphene, which can be peeled off to atomic layer thickness.

In this study, we aim to elucidate interlayer magnetic coupling between heterogeneous magnetic atomic layers using this novel 2D magnet. Understanding interlayer magnetic coupling has been a longstanding research challenge in magnetism. One of the most ideal systems for this is the combination of ferromagnetic Fe(001) and antiferromagnetic Mn(001). Through the efforts of many researchers, including the applicant, over the past 20 years, it has been revealed that a single atomic layer of Mn(001) on ferromagnetic Fe(001) exhibits ferromagnetic 0° coupling between adjacent Mn atoms within the layer and antiferromagnetic 180° coupling between layers. However, this interlayer antiferromagnetic coupling arises from the fourth layer of Mn. The magnetic coupling from the first to the third layers remains unclear, attributed to strong electronic interactions at the Fe/Mn interface, leading to various effects such as mixing of Fe and Mn and crystalline strain at the interface, resulting in a simultaneous alteration and disorder of the spin-polarized electron structure. Consequently, the magnetic moment is also altered and disturbed, leaving the magnetic coupling at the interface of the original Fe and Mn atomic layers unresolved. Despite extensive theoretical calculations on Mn/Fe(001) systems, the conclusions have been limited to indicating the possibility of various magnetic structures.

This study aims to put an end to this longstanding mystery by utilizing one of the vdW magnets named Fe₃GeTe₂ (FGT). To extract the pure magnetic coupling between Fe and Mn atomic layer films, a decoupling layer that cuts off the electronic interaction between the two films is required. Atomic layer magnets function with halogen or chalcogen element films on both sides of the magnetic atomic layer as decoupling layers. Therefore, we employ this Fe-based atomic layer magnet as a substrate. While applying an in-plane and out-of-plane magnetic field, X-ray absorption spectroscopy (XAS) and X-ray magnetic circular

dichroism (XMCD) measurements are conducted to obtain magnetic hysteresis curves and extract the pure magnetic coupling of Fe and Mn atomic layer films.

We brought three FGT single crystals and attached them to the sample holder of the XMCD apparatus. Since the crystals were small, with sizes of 2-3 mm, and there was a possibility that the beam might not hit them, we aligned three of them vertically. Care was taken to ensure that the adhesive did not overflow from the samples as they were cured. A copper holder was used. From XPS measurements, if an iron peak rather than a copper peak appeared, it would indicate that the beam was hitting the FGT sample. XPS peak measurements were conducted while changing positions.

Vacuum cleavage using the XMCD apparatus was also conducted. Although FGT is an atomic layered material, it exhibits metallic properties, and it had been confirmed from prior research that impurities would adsorb on the surface when exposed to air. Therefore, we directly attached Scotch tape to the sample in the atmosphere and made loops with the tape. In a vacuum, we attempted cleavage by pulling the loops with a transfer rod. However, when we tried to delaminate all three samples with one tape, some samples were successfully cleaved, while others were not completely cleaved due to differences in sample height. Therefore, we cut the end of the tape into three parts to allow each tape to adhere to the sample surface and enable vacuum cleavage for each.

After the vacuum cleavage, the sample holder was set in the XMCD apparatus. It was cooled down to 5 K using liquid nitrogen and helium. XPS measurements were performed while changing the magnetic field. The incident angle of light to the sample was changed, and magnetization curves in-plane and out-of-plane were measured. Magnetization curves showed hysteresis when ±5 Tesla (T) was applied, confirming ferromagnetism at 5 K. Prior research suggested that FGT could exhibit unique magnetic structures, such as skyrmions within lower fields. Thus, we extensively measured the magnetization changes within ±500 mT.

The beam time ended before we could conduct magnetization curve measurements of Mn on FGT due to the time required for vacuum cleavage expertise. We hope to attempt it next time.

BL4B

Charge Transfer in Solution-Mixed and Sequential Doping P3HT:F4-TCNQ Films by NEXAFS Spectroscopy

Y. Hoshi¹ and K. K. Okudaira²¹Graduate School of Science and Technology, Chiba University, Chiba 263-8522, Japan²Graduate School of Engineering, Chiba University, Chiba 263-8522, Japan

As high-performance organic semiconductors, π -conjugated polymers have attracted much attention due to their charming advantages including low-cost, solution processability, mechanical flexibility, and tunable optoelectronic properties [1]. The electrical conductivity of semiconducting polymers can be effectively tuned over several orders of magnitude by doping with not only inorganic materials such as iodine, but also organic molecule such as F4-TCNQ. Molecular dopants such as F4-TCNQ undergo ground-state charge transfer with their host semiconductor, yielding polarons or bipolarons on the semiconductor. There are multiple different methods for producing doped polymer films, (1) evaporation of dopant in vacuum, (2) casting a film of pre-doped polymer created by blending the polymer and dopant in solution, which we refer to as mixed solution doping, (3) casting a film of dopant on pre-coated polymer film, which we refer to as sequential solution doping [2,3]. We evaluate the doping efficiency (charge transfer process) in P3HT doped with F4-TCNQ by mixed and sequential solution method using NEXAFS spectroscopy.

The mixed solution doping method: F4-TCNQ in chlorobenzene (CB) with 0.1mg/ml and 1.0mg/ml and P3HT are mixed and quickly spin coated to form a film on ITO substrate. The sequential solution doping method: undoped P3HT films are first spin coated from CB on ITO substrate. Once dried, the films are doped by the spin casting with a solution of F4-TCNQ. NEXAFS spectra of the P3HT doped with F4-TCNQ using total electron yield (TEY) modes were measured at the beamline 4B of the UVSOR in the Institute of Molecular Science.

Figure 1 shows N K-edge NEXAFS spectra of P3HT sequential and mixed doped with F4-TCNQ by using different F4-TCNQ concentrations. The N K-edge NEXAFS of P3HT doped F4TCNQ consist of peaks A - C. The spectral feature of the samples by mixed doping process both using 0.1 mg/ml and 1.0 mg/ml CB solution are similar to those of F4-TCNQ films by deposition on Si(100) [4]. These peak structures are comparable to those reported in TCNQ thin films. According to the peak assignment of pure TCNQ, peak A is assigned to π^* orbitals (LUMO), peak B to π^* and σ^* , and peak C to π^* [4]. N K-edge NEXAFS spectra of P3HT sequential doped with F4-TCNQ strongly are modified compared to that of mixed doped with F4-TCNQ. It is noted that the intensities of peak A (LUMO) and C decrease in sequential doped spectrum. The

decrease in the intensity of peak A is interpreted to be the result of charge transfer from the P3HT to the LUMO of the acceptor molecule (F4-TCNQ). As shown in Fig.1 (b) the energy position as well as the spectral shape of the intense peak B in N K-edge NEXAFS of P3HT sequential doped with F4-TCNQ are different from those of mixed-doped ones. It is proposal that by using sequential doping, the charge transfer occurs initially by charging the cyano groups, then the local structure around cyano groups would change.

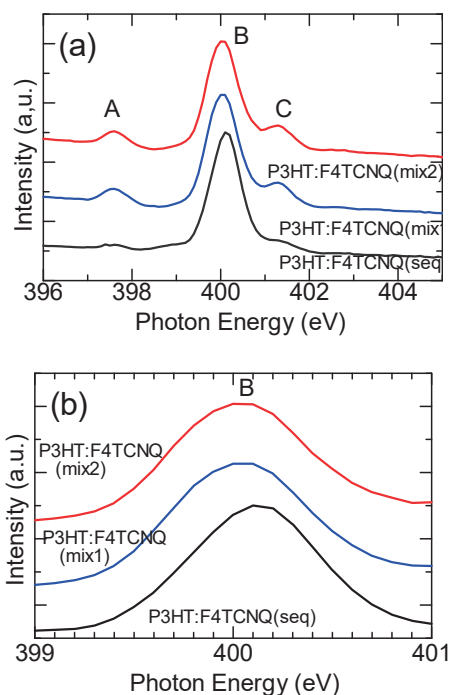


Fig. 1. (a) N K-edge NEXAFS spectra of P3HT sequential doped and mixed doped with F4-TCNQ (mix1: mixed with F4-TCNQ using 0.1 mg/ml CB solution. mix2: 1.0mg/ml CB solution). (b) enlargement of N K-edge NEXAFS spectra of P3HT sequential doped and mixed doped with F4-TCNQ at $h\nu$ from 399 eV to 401 eV.

- [1] X. Guo *et al.*, Prog. Polym. Sci. **38** (2013) 1832.
- [2] M. T. Fontana *et al.*, J. Phys. Chem. C **123** (2019) 22711.
- [3] Y. Yoshimoto *et al.*, Org. Electron. **15** (2014) 356.
- [4] J. Fraxedas *et al.*, Phys. Rev. B: Condens. Matter **68** (2003) 195115.

Angle-Resolved Photoemission Circular Dichroism for Chiral Molecule Overlayer on Monolayer WS₂

F. Nishino^{1,2}, K. Fukutani^{1,2}, P. I. Jaseela^{1,2}, J. Brandhoff³, F. Otto³, M. Grünewald³, M. Schaal³, J. Picker⁴, Z. Zhang⁵, A. Turchanin⁴, S. Makita⁶, H. Iwayama⁶, T. Hirose⁵, T. Fritz³ and S. Kera^{1,2,6}

¹*Institute for Molecular Science, Okazaki 444-8585, Japan*

²*School of Physical Sciences, The Graduate University for Advanced Studies, Okazaki 444-8585, Japan*

³*Institute of Solid State Physics, Friedrich Schiller University Jena, Helmholtzweg 5, Jena 07743, Germany*

⁴*Institute of Physical Chemistry, Friedrich Schiller University Jena, Lessingstraße 10, Jena 07743, Germany*

⁵*Institute for Chemical Research, Kyoto University, Gokasho, Uji, Kyoto 611-0011, Japan*

⁶*UVSOR Synchrotron Facility, Institute for Molecular Science, Okazaki 444-8585, Japan*

A chirality-induced spin selectivity (CISS) effect with controlled chiral molecules on various solid surfaces has been actively studied for various applications, such as for spintronics and enantio-separations [1]. On the other hand, many aspects of this phenomenon, including its mechanism underlying its extraordinarily large spin polarization effects, remain unknown.

Our approach to this challenge is to fabricate well-defined chiral molecular systems on solid surfaces with known spin-polarized electronic band structures, and to investigate how the surface chirality affects the emitted electrons from the solid by angle-resolved photoemission spectroscopy (ARPES).

As a preliminary study, in this work, we used angle-resolved photoemission circular dichroism (CD-ARPES) for the system of chiral molecular overlayer on achiral substrate possessing fully spin-polarized electrons to assess how the electrons emitted from the substrate recognize the surface chirality.

The enantiopure chiral molecule, thiadiazole-[9]helicene (TD[9]H) [2], was used in this study as shown in Fig. 1(a). The substrate used was a monolayer WS₂/Au(111) (ML-WS₂) with fully spin-polarized bands at \bar{K}' and \bar{K} points [3]. After depositing the enantiopure TD[9]H on the ML-WS₂ under ultra-high vacuum condition, low-energy electron diffraction (LEED) showed an ordered molecular overlayer with broken mirror-symmetry, indicating the surface chirality has been induced on the system.

Following the confirmation of the surface chirality, CD-ARPES measurements were performed, using left circularly polarized (LCP) and right circularly polarized (RCP) lights for both the clean substrate and the (M)-TD[9]H/ML-WS₂ samples, as shown in Fig. 1(b).

Figures 1(c)-(e) show the CD-ARPES maps obtained for clean ML-WS₂ substrate. It can be seen that the dichroic signals at the $\bar{\Gamma}$ - \bar{M} plane [black dotted lines in Figs. 1(c), 1(d) and the entire map in Fig. 1(e)], which is the mirror plane of the substrate, is very weak. Furthermore, the dichroic signals in the $\bar{\Gamma}$ - \bar{K} and $\bar{\Gamma}$ - \bar{K}' directions are seen to be generally anti-symmetric with respect to the $\bar{\Gamma}$ - \bar{M} plane.

These characteristics of dichroic signals from substrate can readily be understood from the point of view of symmetry. Since the substrate is achiral and the mirror plane of the crystal coincides with the plane of light incidence, it must hold that $I_{\text{RCP}}(k_x, k_y) = I_{\text{LCP}}(-k_x, k_y)$ (Equation 1), where I_{RCP} and I_{LCP} are the photoelectron intensities with RCP and LCP lights, respectively. That is, the achirality of substrate is reflected in our CD-ARPES results.

Next, the CD-ARPES results after the deposition of (M)-TD[9]H are shown in Figs. 1(f)-(h). Unlike the CD-ARPES results from the clean substrate, finite (blue) dichroic signals were observed uniformly in the substrate bands, molecular orbitals and inelastic scattering regions even in the E-k slice of the $\bar{\Gamma}$ - \bar{M} plane as can be seen in Fig. 1(h). While more investigations are necessary, the apparent violation of equation 1 above could arise from the loss of achirality (i.e., emergence of chirality) for the electrons in the system of chiral molecular overlayer on achiral substrate.

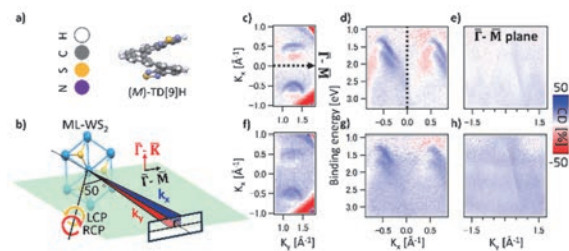


Fig. 1. (a) Molecular structures of (M)-TD[9]H. (b) Schematic illustration of CD-ARPES setup. The relative orientations of the sample and the photoelectron analyzer slit are shown. (c)-(e) CD-ARPES map of ML-WS₂. (f)-(h) CD-ARPES map of (M)-TD[9]H/ML-WS₂. (c) and (f) shows constant-energy cut and (d), (g) is the intensity plots in E-k_x slice. (e) and (h) is the intensity plots in E-k_y slice.

[1] S.-H. Yang *et al.*, Nat. Rev. Phys. **3** (2021) 328.

[2] Z. Zhang *et al.*, Tetrahedron **142** (2023) 133514.

[3] P. Eickholt *et al.*, Phys. Rev. Lett. **121** (2018) 136402.

BL4B

Photoemission Spectroscopy Measurement on Germanium Incorporated Carbon-Based Nanoribbon Structures

K. Sun^{1,2}, K. Fukutani³, S. Kera³ and S. Kawai^{2,4}

¹International Center for Young Scientists, National Institute for Materials Science,
1-2-1 Sengen, Tsukuba, Ibaraki 305-0047, Japan

²Center for Basic Research on Materials, National Institute for Materials Science,
1-2-1 Sengen, Tsukuba, Ibaraki 305-0047, Japan

³Department of Photo-Molecular Science, Institute for Molecular Science, Okazaki 444-8585, Japan

⁴Graduate School of Pure and Applied Sciences, University of Tsukuba, Tsukuba 305-8571, Japan

Germanium(Ge) belongs to both the carbon group and metallic elements with the atomic number 32, with four valence electrons for allowing the formation of multi covalent bonds[1]. Carbon-based nanomaterials with atomic precision are viewed as a candidate for the application in next-generation nanoelectronics. Doping Ge into carbon nanostructures may potentially modify their electronic structures. It is significant to fabricate Ge-incorporated carbon-based nanostructures by C-Ge coupling for providing a material foundation.

We present fabrication of Ge incorporated carbon nanoribbon structures. Molecules 1,4,5,8-tetrabromonaphthalene **1** was employed as a precursor to react with Ge atoms on Ag(111). The reaction processes were illustrated in Fig. 1, distinct from C-Si coupling on Au(111)[2,3]. **1** were deposited on Ag(111), subsequently formed organometallic chains with Ag adatoms by debromination after annealing at 150 °C. Next, Ge were deposited on the Ag(111) surface and subsequent annealing at 200 °C results in the formation of Ge-incorporated nanostructure structures.

In order to demonstrate the nanoribbon structures containing Ge atoms, we performed photoemission spectroscopy measurement by using BL4B of UVSOR. Figure 2 shows the experimental results. Scanning tunneling microscopy (STM) topography (Fig. 2a) of Ag-organic oligomers and Ge clusters were seen on Ag(111) before annealing at high temperature. The

corresponding Ge 3d curves show spin-orbit doublet peaks of 3d_{5/2} (30.85 eV) and 3d_{3/2} separated by 0.59 eV (Fig. 2b). Next, the sample was heated at 200 °C for reaction between Ag-organic chains and Ge atoms. The STM topography shows Ge incorporated nanoribbon structures (Fig. 2c). The corresponding Ge 3d curve became quite complex. After careful analysis, we found three sets of doublet peak components, which can be associated to three different charge states of the Ge atom. Among them, the red doublet peaks exhibit higher binding energy compared to the original peaks, indicating the presence of C-Ge-C bonds on Ag(111). The green doublet peaks with lower binding energy may originate from AgGe alloy. These results demonstrated that we have successfully fabricated Ge-incorporated nanoribbon structures.

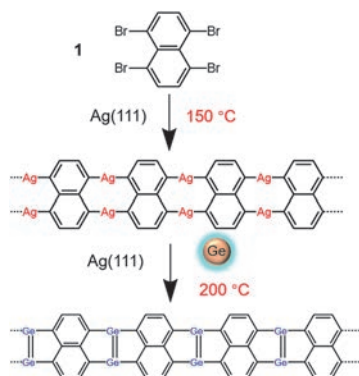


Fig. 1. Scheme of synthesis of Ge-incorporated nanoribbon structure on Ag(111).

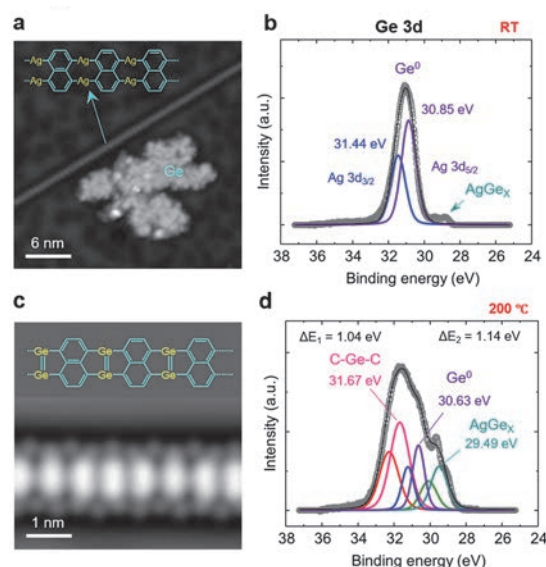


Fig. 2. Photoemission spectroscopy measurement on Ge-incorporated nanoribbons.

- [1] M. L. Amadoruge and C. S. Weinert, *Chem. Rev.* **108** (2008) 4253.
- [2] K. Sun *et al.*, *Nat. Chem.* **15** (2023) 136.
- [3] K. Sun *et al.*, *Angew. Chem. Int. Ed.* **Early View** (2024), e202401027.

Geometry-Induced Photoelectron Spectroscopy from Si{111} Facet Surfaces on Three-Dimensionally Fabricated Facet-Lined Structures

K. Hattori¹, Ni'matil Mabarroh¹, Juharni¹, Y. Kimoto¹, Y. Kitagawa¹, K. Tsubosaki¹,
R. M. Tumbelaka¹, S. Tanaka², A. N. Hattori², S. Suga² and K. Tanaka³

¹Nara Institute of Science and Technology, Ikoma 630-0192, Japan

²SANKEN, Osaka University, Ibaraki 567-0047, Japan

³UVSOR Synchrotron Facility, Institute for Molecular Science, Okazaki 444-8585, Japan

Highly controlled three-dimensional (3D) structures will promise to become the platform for novel properties originated from the electronic states at local surfaces and edges based on the 3D geometries. Recently, our group has successfully created 3D-Si surfaces by combining lithography and surface treatment techniques [1], and reported a successful creation of Si{111}7×7 clean facet surfaces showing surface and bulk electronic bands using angle-resolved photoelectron spectroscopy (ARPES) [2, 3], and also film bands of $\sqrt{3}\times\sqrt{3}$ -Ag ultra-thin film on Si{111} [3], aiming for a future 3D-surface band-engineering.

The previous all ARPES measurements for the 3D-Si surfaces were limited for the symmetric electronic band structures around $\bar{\Gamma}$ point toward the normal orientation of the Si{111} facet surfaces [2, 3]. In order to approach unique electronic states arising from 3D geometrical surfaces and edges, at first, we need to understand the fundamental effect of 3D sample geometry on ARPES, for instance, 1) co-existence of bands from different 3D structure surfaces and 2) shadow effect of 3D hinderance for photo irradiation, which we expect. Thus, here we focused on how 3D structure effects appear in ARPES measurements.

In order to study 3D geometrical factors in ARPES, we surveyed rotation angle dependence using facet line standard Si{111} facet surfaces on a (001) substrate. In addition, we selected $\sqrt{3}\times\sqrt{3}$ -Ag ultra-thin films on Si{111}, because they lead to clear and simple bands at highly symmetric $\bar{\Gamma}^{1\times 1}$ and $\bar{K}^{1\times 1}$ points 1×1 unit, which allows easy to distinguish bands of different 3D facet surfaces.

In experiment, 3D Si facet-lined structures with (111) and $(\bar{1}\bar{1}\bar{1})$ facet surfaces with the facet angle of 55° and facet pitch of 4 μm period, were prepared by using a photo-lithography and wet etching followed by an RCA treatment. In UVSOR BL5U vacuum, the sample was degassed, flashed, and deposited by Ag of ~ 10 monolayer at 770 K. The superposition of double faceted $\sqrt{3}\times\sqrt{3}$ low-energy electron diffraction patterns [3] were observed at room temperature (RT).

The band structures for the 3D-Si{111} $\sqrt{3}\times\sqrt{3}$ -Ag facet surfaces at RT were measured with *p*-polarized photons of surface sensitive 60 eV having 58° angle to the electron detector. The band mapping was conducted with the *x* and *y* emission angle of -15° to $+15^\circ$, the binding energy E_B of -0.25 eV to $+1.47$ eV, and the capturing time of 1 hour for each map. The Fermi level was referred to the Au results. The band maps near

Fermi level depending on the displayed rotation angle θ was monitored.

Figure 1(a) shows the map at $\theta = +5^\circ$ displaying 4 clear circles corresponding to electron-pocket bands at $\bar{K}_{3L}^{1\times 1}$ and $\bar{K}_{3R}^{1\times 1}$ originated from the left and right facet surfaces, respectively; the simple schematics in real and reciprocal spaces are shown in Figs. 1(c) and 1(d), respectively. Here we confirmed the superimpose of the bands from different 3D-Si facet films, as expected.

However, we notice the right facet is shadow for the incident photons as illustrated in Fig. 1(b), leading to no photoelectrons at $\bar{K}_{3R}^{1\times 1}$. The appearance of photoelectrons at $\bar{K}_{3R}^{1\times 1}$ implies photo “reflection” due to the 3D structure becomes dominate, out of the first expectation. Indeed, we found both diffused and specular photo reflections affect in 3D samples ARPES, from the θ dependence of the photoelectrons at $\bar{K}_{3L}^{1\times 1}$ and $\bar{K}_{3R}^{1\times 1}$ (Fig. 1 (b)) compared to the simulation in a simple reflection model.

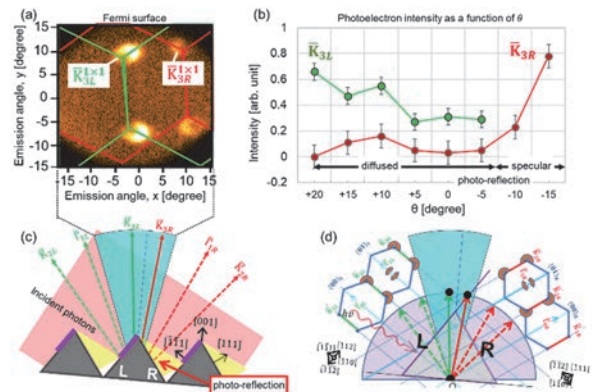


Fig. 1. (a) ARPES map of 3D-Si{111} $\sqrt{3}\times\sqrt{3}$ -Ag facet surfaces at $\theta = +5^\circ$, displaying the Fermi bands at $\bar{K}_{3L}^{1\times 1}$ points originated from different left and right facet surfaces. (b) Photoelectron intensities of $\bar{K}_{3L}^{1\times 1}$ and $\bar{K}_{3R}^{1\times 1}$ bands as a function of θ . (c) Schematic in real space. The orange is the incident photons, and the yellow is photo reflected area. Positive θ corresponds to the sample CW rotation. (d) Schematic in reciprocal space. The purple arc is the Ewald sphere of the Fermi level electrons, and cyan lines are the reciprocal lattice rods.

[1] A.N. Hattori *et al.*, Surf. Sci. **644** (2016) 86.

[2] K. Hattori *et al.*, e-J. Surf. Sci. Nanotechnol. **30** (2022) 214.

[3] K. Hattori *et al.*, UVSOR Activity Report **50** (2023) 155.

BL5U

Van Hove Singularity Induced by an Interfacial Metallic Layer in Ca-Intercalated Bilayer Graphene on SiC

S. Ichinokura¹, K. Tokuda¹, M. Toyoda¹, K. Tanaka², S. Saito¹ and T. Hirahara¹¹Department of Physics, Tokyo Institute of Technology, Tokyo 152-8551, Japan²UVSOR Synchrotron Facility, Institute for Molecular Science, Okazaki 444-8585, Japan

Graphene-based superconductors hold great promise for a wide range of applications due to their optical transparency, mechanical robustness, and flexibility. Among these materials, C_6CaC_6 , a bilayer graphene intercalated with calcium, exhibits the highest critical temperature (T_c) [1,2]. Early investigations predominantly embraced the concept of a free-standing C_6CaC_6 model, grounded in its observed electronic structure. However, recent propositions have suggested intercalation at the interface of C_6CaC_6 and the SiC substrate [3], although the interface configuration at elevated calcium density remains unexplored, potentially giving rise to unconventional electronic structures such as saddle points and van Hove singularities (VHS) [4].

In this study, we have elucidated that the introduction of high-density calcium induces intercalation at the interface, resulting in the confinement epitaxy of a metallic calcium layer beneath C_6CaC_6 . Notably, the hybridization of the interface band and one of the Dirac cones leads to the emergence of a novel electronic phase, wherein a distinctive VHS enhances the density of states near the Fermi level.

C_6CaC_6 samples were synthesized through the deposition of calcium on epitaxial graphene atop a 4H-SiC(0001) substrate maintained at 300 °C. The calcium density within the specimen was quantified using the unit of ML ($= 6.3 \times 10^{14} \text{ cm}^{-2}$). The band structure was explored via angle-resolved photoemission spectroscopy using a He lamp ($h\nu = 21.2 \text{ eV}$) and synchrotron radiation ($h\nu = 33 \text{ eV}$) at BL5U.

In Figs. 1(a) and (b), we present the band structure of the current system at the 1.2 and 2.5 ML stages, corresponding to low and high calcium density stages, respectively. At 1.2 ML, three sets of metallic bands can be identified around the Γ point: a parabolic interlayer band (IL) and Dirac cones (α^* and β^*) folded from the K point due to the formation of $\sqrt{3} \times \sqrt{3}$ Brillouin zone (BZ). These electronic states are characteristic of free-standing C_6CaC_6 [5]. At 2.5 ML, as depicted in Fig. 1(b), an X-shaped metallic band appears at the M^* point in $\sqrt{3} \times \sqrt{3}$ BZ, which deviates from the free-standing model. By electron diffraction and core-level photoemission, we have revealed that the band is an interfacial metallic band (IFM) originating from the epitaxial layer of calcium at the interface of C_6CaC_6 and SiC. Around the Fermi level, IFM hybridizes with the β^* band. Graphene's original

saddle point at the M point of the BZ is replicated at the M^* point in the $\sqrt{3} \times \sqrt{3}$ BZ. At the 1.2 ML stage, the saddle point of the β^* band lies slightly above the Fermi level. At the 2.5 ML stage, the β^* band connects to IFM through hybridization, giving rise to a hole-like dispersion with a maximum at the Fermi level.

The vertex of the hole band has been validated as a saddle point via the scrutiny of electron-like dispersion along the orthogonal direction in our high-resolution measurements. Figures 1(c)-(e) depict k_x dispersion at $k_y = -0.75, -0.63$, and -0.50 \AA^{-1} . The electron-like arrangement in Fig. 1(e) and (c) unequivocally illustrates that the diminutive Fermi surface depicted in Fig. 1(d) constitutes a saddle point, where the VHS occurs.

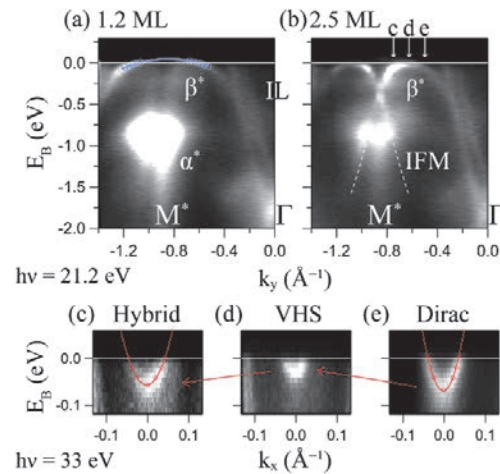


Fig. 1. (a) and (b) depict ARPES spectra along the Γ - M^* direction at Ca density of 1.2 and 2.5 ML, respectively. The blue circles and solid line in (a) represent the set of (E, k_y) points of β^* band and parabolic fitting to it, respectively. The dashed white lines in (b) delineate the IFM bands. In (c), (d), (e), electronlike band dispersion high-Ca-density-state along k_x direction is highlighted. Measurement cuts ($k_y = -0.75, -0.63$, and -0.50 \AA^{-1}) are indicated by white arrows in (b).

- [1] S. Ichinokura *et al.*, ACS Nano **10** (2016) 2761.
- [2] X. Wang *et al.*, Nano Lett. **22** (2022) 7651.
- [3] H. Toyama *et al.*, ACS Nano **16** (2022) 3582.
- [4] J. L. McChesney *et al.*, Phys. Rev. Lett. **104** (2010) 136803.
- [5] K. Kanetani *et al.*, PNAS **109** (2012) 19610.

Characterization of Amorphous and Polycrystalline Selenium Thin Films by Vacuum Ultraviolet Absorption Spectroscopy

K. Hayashi

Department of Electrical, Electronic and Computer Engineering, Gifu University, Gifu 501-1193, Japan

It is well-known that various photoinduced phenomena such as changes in optical band gap and conductivity occur in chalcogenide amorphous semiconductors by light irradiation [1]. Although many studies have been done on the photoinduced phenomena of these materials, little is known about the details of these mechanisms. We are investigating the annealing temperature dependence of conductivity changes due to light irradiation on amorphous selenium thin films. We observed a drastic increase in photoconductivity at annealing temperatures above 60°C. This change was confirmed to be due to the phase change from the amorphous structure to the polycrystalline structure from the XRD pattern change and the band gap change. In the previous report [2], we reported on the results of measurements using BL4B of changes in the VUV transmission spectrum of amorphous selenium films before and after light irradiation and after annealing. In this paper, we report the energy structure change due to the phase change from amorphous structure to polycrystalline structure by annealing using VUV absorption spectroscopy.

Sample used for the measurement of the VUV absorption spectra was amorphous selenium thin films prepared onto thin aluminum film by conventional evaporation technique. The sample thickness was about 180nm. The aluminum film of the thickness of 200 nm was used to eliminate the higher order light from the monochromator in the VUV region. These measurements were carried out at room temperature on the BL5B beam line of UVSOR. The spectrum was measured by using the silicon photodiode as a detector. Two pinholes of 1.5mm in a diameter were inserted between the monochromator and sample to remove stray light. The intensity of the VUV light was monitored by measuring the TPEY of a gold mesh. The positions of the core levels for the samples were calibrated by referencing to the 2p core level absorption of the aluminum film. The phase transition from amorphous to polycrystalline structure was achieved by annealing at temperatures above 343 K for a total of 3 hours.

Figure 1 shows the VUV absorption spectra of Se 3d core levels in amorphous and polycrystalline phases. The VUV absorption spectra of the Se 3d core level of the amorphous phase differed slightly from the previous research [3], but absorption peaks were observed at similar energy positions. In both the amorphous and polycrystalline phases, a broad structure with a shoulder around 55 eV has been observed. This broad peak with

a shoulder is thought to be due to spin-orbit splitting of the Se 3d level. The absorption peak of the amorphous phase is about 0.15 eV lower than that of the polycrystalline phase. This is because the optical bandgap of the polycrystalline phase is smaller than that of the amorphous phase. As can be seen from the figure, structures appear around 63 eV in the film after crystallization. The origin of this structure remains unknown. However, it may reflect local bonding states resulting from the transition from amorphous to polycrystalline phases. The spectrum obtained after crystallization is broader than the spectrum obtained from the as-deposited amorphous film. The spectrum of as-deposited amorphous films may depend on the preparation conditions of the film. Therefore, further investigation into its details will be necessary in the future. The detailed experiments and analysis will be done in the next step. More detailed experiments are necessary to clarify the origin of the VUV absorption spectra.

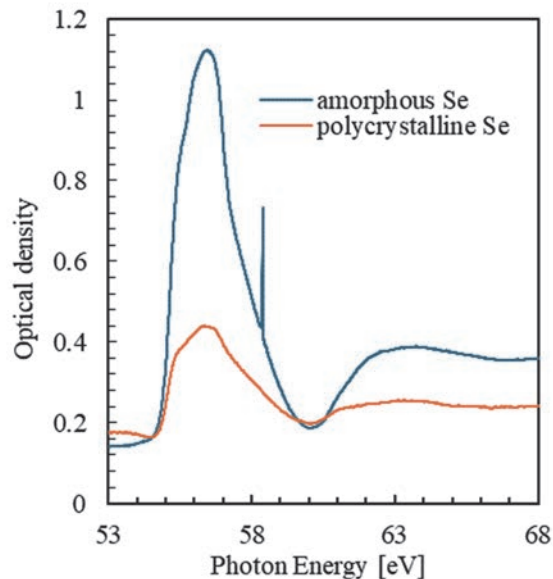


Fig. 1. VUV absorption spectra of Se 3d core levels in amorphous and polycrystalline phases.

- [1] K. Tanaka, Rev. Solid State Sci. **4** (1990) 641.
- [2] K. Hayashi, UVSOR Activity Report **50** (2023) 152.
- [3] J. Bordas and J. B. West, Philos. Mag. **34** (1976) 501.

BL5B

Electronic Study of Large-Area Hydrogen Boride Sheets by X-ray Absorption Spectroscopy

K. Yamaguchi¹, M. Niibe¹, T. Sumi¹, E. Nakamura², K. Tanaka^{2,3} and I. Matsuda¹

¹The Institute for Solid State Physics (ISSP), The University of Tokyo, Kashiwa, Chiba 277-8581, Japan

²UVSOR Synchrotron Facility, Institute for Molecular Science, Okazaki 444-8585, Japan

³School of Physical Sciences, The Graduate University for Advanced Studies (SOKENDAI), Okazaki 444-8585, Japan

A hydrogen boride (HB) sheet is a two-dimensional boron material that has shown rich functionalities, such as hydrogen storage [1] and carbon dioxide reduction [2]. In addition, it has also captured interests as an electrically conducting material because of the semi-metallicity, predicted by theoretical calculations [3]. The HB sheet has been so far prepared in the powder form, limiting its applications. Recently, we have succeeded in synthesizing the large area HB sheets and in scrutinizing the electronic states in detail by X-ray absorption spectroscopy (XAS) to examine the technical potential. The experiment was made at BL-5B and XAS spectra were recorded by two detection schemes, the transmission yield and the total electron yield (TEY).

Figure 1(a) shows a photograph, taken during the sample installation to the measurement chamber at the beamline. The HB samples were treated in a glove bag, filled with nitrogen gas, to minimize a possible oxidization of the samples. Figure 1 (b) shows a photograph of the sample holder. It is a combination of a bare metal mesh and the HB-covered mesh to detect I_0 and I , respectively. The TEY signal was detected by the drain current of samples, while the transmission intensity was recorded by a photodiode. The measurement was made at room temperature under the high vacuum condition.

Figure 2 is a collection of XAS spectra of the HB sheet, taken as the transmission intensity and by TEY. Spectral features are identified as labeled with S_1 - S_3 . The S_2 peak is assigned to boron oxides. The intensity is much smaller compared to the previous report [3], indicating the success synthesis of the high purity samples and appropriateness of the treatments in a glove bag (Fig.1(a)). The peaks, S_1 and S_1' , located at photon energy around 190 eV and those, S_3 and S_3' , around 200 eV are ascribed to electronic states of the HB sheet. Appearance of the XAS spectra was distinctive between the two detection schemes. Since the transmission method and TEY are bulk- and surface-sensitive, respectively, a set of the spectra provides comprehensive information of electronic states of the HB sample. The experimental spectra will be compared with the simulated spectra by the first

principles calculation to unveil origins of the spectral peaks (S_1 , S_1' , S_3 , S_3').

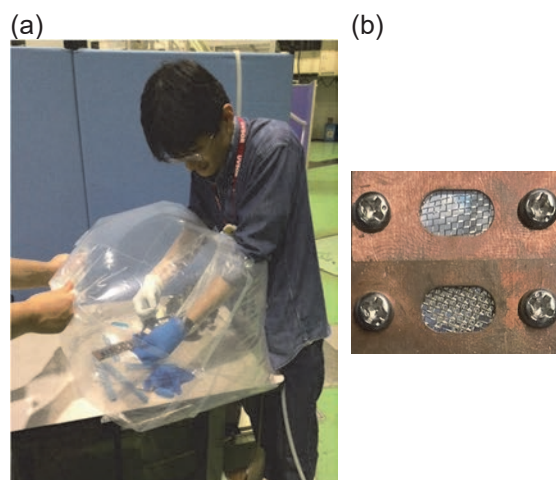


Fig. 1. Photographs of (a) the sample installation and (b) the sample holder. The top is a bare metal mesh and the bottom is with the HB sample.

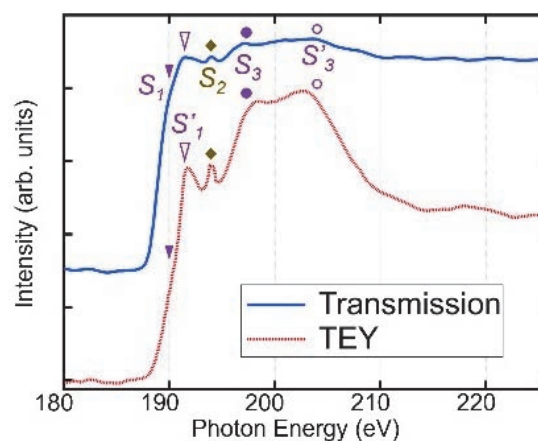


Fig. 2. XAS spectra of HB sheets. The blue curve was taken by the transmission method, while the red one by the TEY method. The spectral features are labeled.

- [1] R. Kawamura *et al.*, Nat. Commun. **10** (2019) 4880.
- [2] T. Goto *et al.*, Commun. Chem. **5** (2022) 118.
- [3] I. Tateishi *et al.*, Phys. Rev. Mater. **3** (2019) 024004.

Deposition of High-Quality Ir(111) Thin Films by Molecular Beam Epitaxy

E. Hashimoto¹, Y. Onuma¹, H. Kurosaka¹, Y. Nishio¹, F. Matsui² and S. Koh¹

¹Department of Electrical Engineering and Electronics, College of Science and Engineering, Aoyama Gakuin University, 5-10-1 Fuchinobe, Chuo-ku, Sagami-hara, Kanagawa 252-5258, Japan

²UVSOR Synchrotron Facility, Institute for Molecular Science, Okazaki 444-8585, Japan

Chemical vapor deposition (CVD) is a promising method to synthesize high-quality, large-area, and transferrable graphene. We have investigated low-pressure CVD methods using epitaxial Ir(111)/ α -Al₂O₃(0001) substrate with single-crystallinity. We demonstrated the reusability of the Ir(111) substrate and evaluated the single-crystallinity and electronic structure of graphene/Ir(111) [1-4]. Further improvement of the surface flatness and crystallinity of the substrate is effective in further improving the quality of CVD graphene. In this research, we performed the deposition of Ir(111) thin films by molecular beam epitaxy (MBE) and evaluated the quality of Ir thin films by photoelectron momentum microscopy (PMM).

We deposited Ir(111) thin films on α -Al₂O₃(0001) substrates by MBE method. First, the low-temperature buffer layer was deposited with the temperature of the substrate holder set at 500°C for 20 min. Then, the temperature of the sample holder was raised to 950 °C and the Ir(111) thin films were deposited for 220 min. By deposition for a total of 240 min, thin films with a thickness of 70 nm were grown. Afterwards, Ir(111) thin films were annealed under H₂ atmosphere at 1000°C for 60 min.

Figures 1(a) and (b) show the XRD diffraction for the Ir layers deposited on α -Al₂O₃(0001). Diffraction peaks caused by Ir(111) and α -Al₂O₃(0001) were observed in the 2theta/omega profile (Fig.1(a)). The XRD pole figure along Ir[111] is shown in Fig. 1(b). The observed Bragg peaks for Ir{111} have 6-fold symmetry. These ideally have 3-fold symmetry, thus indicating that Ir(111) thin films had twin domains. Figure 1(c)-(e) show the Fermi surface of Ir(111) thin films. Photon energy was set to 100 eV. At the observation position moving 100 μ m from the position of Fig. 1(c), a 6-fold symmetry image (Fig.1(d)) was observed, capturing the boundaries between the non-rotated domain and the rotated domain. The observation point was additionally moved 70 μ m, and only the rotated domain was observed (Fig.1(e)). These results corresponded to pole figures. The observation by moving the position in this way revealed the presence of a single domain for the area of 100 μ m² or larger.

Figure 2(a) shows rocking curves for Ir(111). The full width at half maximum of the rocking curve for Ir(111) deposited by MBE (blue line) was 0.054°. An AFM image is shown in Fig. 2(b). The average roughness height R_a was 0.3 nm. The Ir films deposited by sputtering method, we conventionally used, had the FWHM for the rocking curve of 0.139° (red line in

Fig.2(a)) and average roughness height R_a of 1.3 nm [3]. As a result of the combination of the low-temperature buffer layer, H₂ post-annealing, and the low growth rate in the MBE growth, the Ir(111) thin films deposited by MBE were demonstrated to have high crystallinity and surface flatness.

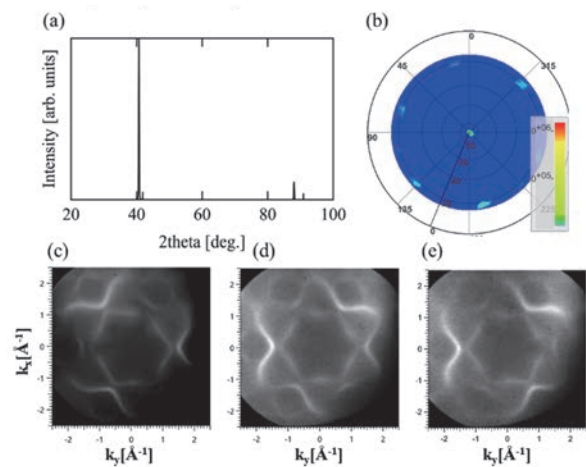


Fig. 1. (a) 2theta/omega profile and (b) pole figure of Ir thin films deposited by MBE. (c)-(e) Iso-energy cross sections of 2D band dispersions of Ir(111) with photon energy of 100 eV. The observation point of (d) was moved 100 μ m from (c), and (e) was moved 100 μ m from (d).

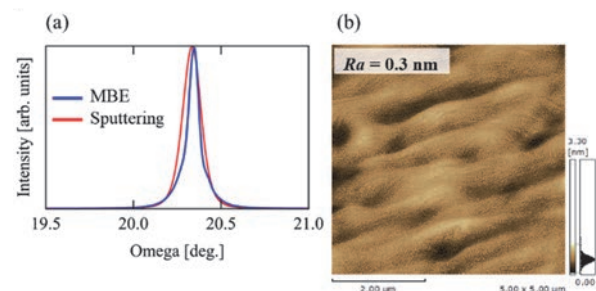


Fig. 2. (a) Rocking curve for Ir(111). Blue line shows deposited by MBE and red line shows deposited by sputtering methods. (b) AFM image of Ir(111) deposited by MBE.

- [1] S. Koh *et al.*, Appl. Phys. Lett. **109** (2016) 023105.
- [2] A. Sakurai *et al.*, Jpn. J. Appl. Phys. **59** (2020) SIID01.
- [3] E. Hashimoto *et al.*, Jpn. J. Appl. Phys. **61** (2022) SD1015.
- [4] F. Matsui *et al.*, Rev. Sci. Instrum. **94** (2023) 083701.

BL6U, BL7U

Linear Polarization Turntable Measurement of the Band Structure of Au(111)

K. Hagiwara¹, S. Suga², S. Tanaka² and F. Matsui^{1,3}¹UVSOR Synchrotron Facility, Institute for Molecular Science, Okazaki 444-8585, Japan²SANKEN, Osaka University, Mihogaoka 8-1, Ibaraki 567-0047, Japan³School of Physical Sciences, The Graduate University for Advanced Studies (SOKENDAI), Okazaki 444-8585, Japan

Dual-beamline photoelectron momentum microscope (PMM) developed at UVSOR [1] is the first example of the implementation of a dual-beamline combination for PMM apparatus in the world. In 2023, we successfully branched the vacuum ultraviolet (VUV) beamline BL7U and introduced a VUV beam in the normal-incidence configuration in the PMM experimental station [1] in addition to a soft X-ray beam from the beamline BL6U [2, 3]. In particular, normal-incidence PMM is attractive for studying atomic orbitals and spins of the valence electronic states. Highly symmetric photoemission configuration with such normal incidence eliminates the experimental geometry-induced photoemission asymmetry, which necessarily occurred in the grazing-incidence configuration. Thus, normal-incidence PMM enables one to make direct access to atomic orbital information through photon-polarization-dependent transition-matrix-element analysis.

This PMM experimental station allows in-plane sample rotation from azimuthal angle $\phi_s = -90^\circ$ to 90° , offering detailed measurements with tunable linear polarization geometries. Different experiments with two mutually orthogonal linear polarization geometries can be performed in two ways. 1) switching the photon polarization from vertical to horizontal or 2) rotating the sample by $\phi_s = 90^\circ$ instead of switching the photon polarization. The former way offers the advantage of keeping the analyzed area always the same. We note that a photon flux of horizontally polarized light is weaker than that of vertical polarized light (one fifth at $h\nu = 20$ eV) due to the reflectance difference of the branching mirrors at BL7U [1]. Thus, the latter way,

i.e., measurements using vertical polarized light with a $\phi_s = 90^\circ$ difference in azimuthal angle orientation is practical in terms of the efficiency.

In this work, we demonstrate rotational dependence of the linear polarization towards detailed atomic orbital analysis of the valence band structure. A sample of the Au(111) surface was rotated in-plane by ϕ_s and measured using vertically polarized light from the BL7U branch. Here, we show the 2D momentum (k_x , k_y) distribution of photoelectrons with a fixed in-plane sample orientation but rotating the photon polarization vector \mathbf{E} in Fig. 1. One can see the features corresponding to the cross section of the Fermi sphere of the bulk gold crystal: the nearly hexagonal contour centered at the $\bar{\Gamma}$ point and the so-called neck features located around the \bar{M} point, which connects the Fermi surfaces of the neighboring Brillouin zones. One can find that photoemission intensities of the nearly hexagonal contour on different momentum points exhibit different modulation with changing rotation angle (ϕ_s) of \mathbf{E} . This corresponds to the fact that the nearly hexagonal contour on different momentum points is composed of mainly in-plane p orbitals pointing outwards from the $\bar{\Gamma}$ point [4].

[1] K. Hagiwara *et al.*, J. Synchrotron Radiat. **31** (2024) 540.

[2] F. Matsui *et al.*, Jpn. J. Appl. Phys. **59** (2020) 067001.

[3] F. Matsui *et al.*, Rev. Sci. Instrum. **94** (2023) 083701.

[4] F. Matsui *et al.*, Phys. Rev. B **72** (2005) 195417.

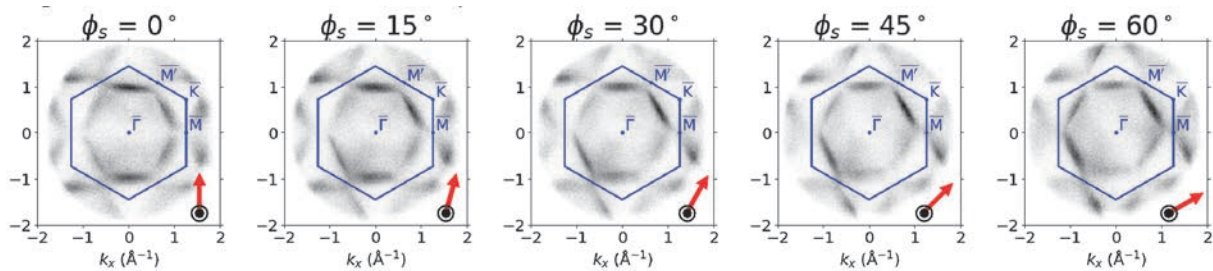


Fig. 1. Turntable measurement of 2D momentum (k_x , k_y) distribution of photoelectrons of the Au(111) surface at $E = E_F - 1$ eV with varied photon polarization vector \mathbf{E} . The sample was rotated in-plane by ϕ_s and measured using vertically polarized light at $h\nu = 20$ eV from the BL7U branch. Here, the data were rotated so that the in-plane sample orientation is aligned in the same direction.

ARPES Study of Anomalous Secondary Photoemission from SrTiO₃(100)

C.Y. Hong^{1,2}, P.X. Ran^{2,3}, X.P. Xie^{2,3} and R.-H. He²

¹Department of Physics, Fudan University, Shanghai 200433, China

²School of Science, Westlake Institute for Advanced Study, Westlake University, Hangzhou 310064, China

³Department of Physics, Zhejiang University, Hangzhou 310027, China

Photocathode materials are crucial components in numerous modern technologies that rely on light detection or electron-beam generation[1-3]. However, most photocathode materials currently used are primarily based on traditional metals and semiconductors. Recently, we reported the observation of spontaneous coherent secondary electron emission (SEE) on the surface of SrTiO₃ (STO) after vacuum annealing, with a significantly enhanced peak intensity observed at low temperatures[4]. Spontaneous coherent secondary electron beams can be generated without the need for threshold excitation, even under non-monochromatic light excitation.

The intense coherent photoelectron emission observed on the surface of STO cannot be explained by traditional photoemission theories. To address this challenge, we have recently proposed a new model[5]. Based on the conventional three-step model[6], we introduced an additional step that resembles the Auger effect, establishing a recycling mechanism for failed photoelectrons to analyze this anomalous emission phenomenon in STO. Our model considers the unique energy level structure near the Fermi surface of the valence and conduction bands of STO, enabling high-coherence photoelectron emission under specific photon energy excitations.

To confirm our theoretical model, we needed to excite STO with various photon energies and examine its SEE spectrum. Due to the limitations of our lab-based ARPES setup, which only uses a helium lamp, we conducted systematic ARPES measurements at the BL7U beamline of UVSOR. We investigated the SEE of STO across a range of photon energies (7.1 to 10 eV) and observed a significant dependence on photon energy, as shown in Fig. 1. The positions of Peak 1 and Peak 2 in the SEE spectrum remained constant across varying photon energies, but the intensities of these peaks showed substantial variations.

To further analyze this data, we performed preliminary processing, as depicted in Fig. 2. We found that when the excitation photon energy was below 8.2 eV, there was almost no observable intensity for Peak 1 and Peak 2. However, the peaks began to emerge when the photon energy exceeded 8.2 eV. Notably, for photon energies below 8.8 eV, the intensity of Peak 2 surpassed that of Peak 1, while for energies above 8.8 eV, Peak 1 became the dominant feature. We are currently investigating the relationship between these observations and the band structure more thoroughly.

Additionally, to explore the nonlinearity of SEE intensity, we conducted experiments using white light

and different photon energies to investigate the correlation between excitation light intensity and SEE. Finally, we attempted to study the two-dimensional electron gas on the STO surface using low photon energy, but we were unable to obtain meaningful data due to a poor signal-to-noise ratio.

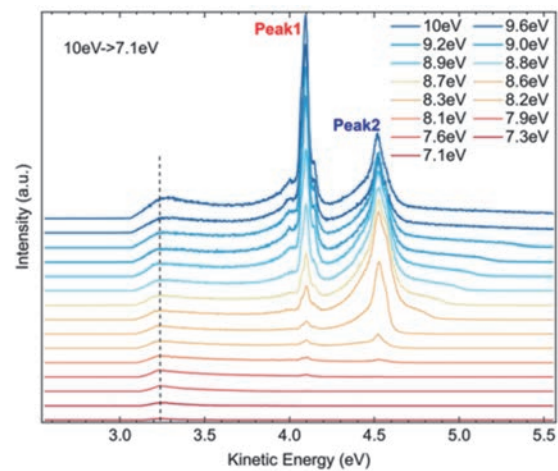


Fig. 1. The secondary electron emission spectra of STO under different photon energies.

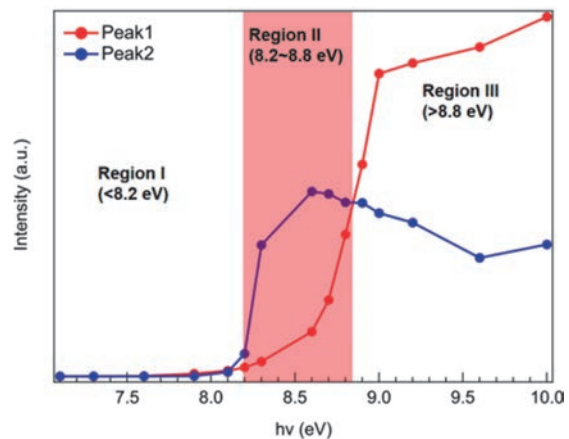


Fig. 2. Peak intensity of the secondary photoemission spectrum versus excitation photon energy.

- [1] T. Rao and D.H. Dowell, *An Engineering Guide to Photoinjectors* (CreateSpace, 2013).
- [2] G. Sciaini and R.J.D. Miller, *Rep. Prog. Phys.* **74** (2011) 096101.
- [3] P.D. Townsend, *Contemp. Phys.* **44** (2003) 17.
- [4] C. Hong *et al.*, *Nature* **617** (2023) 493.
- [5] M. Matzelle *et al.*, *arXiv:2405.06141* (2024).
- [6] W.E. Spicer, *Phys. Rev.* **112** (1958) 114.

BL7U

Metal-Insulator Transition in Si(111) $\sqrt{3}\times\sqrt{3}$ -Sn

H. Nishimichi¹, K. Ishihara¹, S. Ichinokura¹, K. Tanaka² and T. Hirahara¹

¹Department of Physics, Tokyo Institute of Technology, Tokyo 152-8551, Japan

²UVSOR Facility, Okazaki 444-8585, Japan

High-temperature superconductivity in cuprates has attracted significant interest since its discovery in 1986. However, there is still no consensus regarding its precise mechanism and the complicated relationship between Mott physics, magnetism, and superconductivity. The Si(111) $\sqrt{3}\times\sqrt{3}$ -Sn surface, which is formed by 1/3 monolayer (ML) adsorption of Sn onto the Si(111) substrate, has been shown to host similar properties with cuprates and thanks to the simplified atomic structure, it is believed that it may help to unveil the intricate nature of superconductivity doped Mott systems.

Recently, a novel method to induce hole doping in this system was discovered, namely to use a highly p-doped Si substrate [1]. Utilizing this modulation doping, an energy gap was shown to form at low temperature and interpreted as due to the occurrence of superconductivity with d-wave symmetry [2,3]. The superconducting transition temperature reached as high as 9 K, which is much higher than that of typical surface superconductors reported up to now. This calls for a further detailed study to explain the possible high-temperature superconductivity in this system and hopefully apply it to the case of cuprates. Especially up to now, only the local density of states has been measured and information on the detailed macroscopic quantities such as band dispersion and transport properties is still lacking.

Therefore in this study, we measured the electronic structure of the Si(111) $\sqrt{3}\times\sqrt{3}$ -Sn surface in detail using samples grown on different substrates. We employed four types of substrates: n-type Si(111) with a resistivity of 0.001-0.0035 Ωcm (n-high), n-type with a resistivity of 1.5-5 Ωcm (n-low), p-type with a resistivity of 5-10 Ωcm (p-low), and p-type with a resistivity of 0.006-0.008 Ωcm (p-high). The Si(111)-7 \times 7 clean surface was prepared by direct current heating up to 1500 K for a few seconds (flashing). Sn was evaporated onto the 7 \times 7 surface at 800 K and then post-annealed for 5 min to form the $\sqrt{3}\times\sqrt{3}$ surface. ARPES was conducted at UVSOR BL-7U with p-polarized photons at $h\nu = 14\text{eV}$. The energy and angular resolutions were 15 meV and 0.25°, respectively. The Fermi level was determined by measuring a polycrystalline Au film placed near the real sample.

Regardless of the Si substrate used, all the Si(111) $\sqrt{3}\times\sqrt{3}$ -Sn samples were found to be metallic at room temperature (RT) and the Fermi surface was the consistent with DFT calculations as shown in Fig. 1. At 7 K, we found that the system becomes insulating as

shown in Figs. 2(a) and (b) [red and blue curves]. This is consistent with the fact that the ground state of this surface is a Mott insulator. However, the surface became metallic again by repeatedly annealing the p-high substrate in ultra-high vacuum [green curve in Fig. 2(b)]. The Fermi surface shown in Fig. 2(c) is similar to that measured at room temperature. Thus we have found that not only the substrate type but also the substrate annealing is important in deducing a metal-insulator transition in this surface for the first time. Possible evidence of superconductivity has been obtained for this metallic sample from *in situ* conductivity measurements [4].

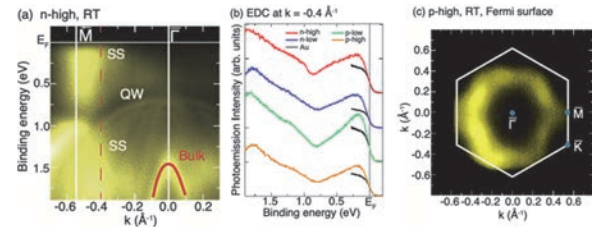


Fig. 1. (a) Band dispersion at room temperature of the Si(111) $\sqrt{3}\times\sqrt{3}$ -Sn surface grown on a n-high substrate. (b) Energy dispersion curves (EDC) at $k = -0.4 \text{ \AA}^{-1}$ for Si(111) $\sqrt{3}\times\sqrt{3}$ -Sn grown on different Si substrates compared to that for the Au. (c) The Fermi surface (energy contour for a $\pm 20 \text{ meV}$ window around the Fermi energy) at room temperature of the Si(111) $\sqrt{3}\times\sqrt{3}$ -Sn surface grown on a p-high substrate.

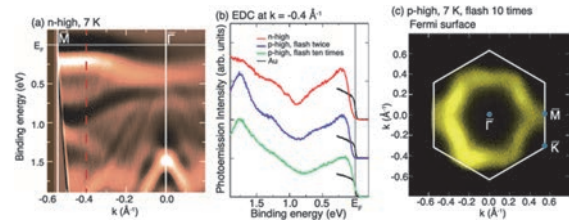


Fig. 2. (a) Band dispersion (second derivative) at 7 K of the Si(111) $\sqrt{3}\times\sqrt{3}$ -Sn surface grown on a n-high substrate. (b) EDC at $k = -0.4 \text{ \AA}^{-1}$ for Si(111) $\sqrt{3}\times\sqrt{3}$ -Sn grown on different Si substrates compared to that for the Au. (c) The Fermi surface at 7 K of the Si(111) $\sqrt{3}\times\sqrt{3}$ -Sn surface grown on a p-high substrate.

- [1] F. Ming *et al.*, Phys. Rev. Lett. **119** (2017) 266802.
- [2] X. Wu *et al.*, Phys. Rev. Lett. **125** (2020) 117001.
- [3] F. Ming *et al.*, Nat. Phys. **19** (2023) 500.
- [4] H. Nishimichi *et al.*, to be submitted.

Anisotropic Surface Atomic Structure and Electronic State in a YbSb/GaSb(001) Thin Film

Y. Chen¹, T. Nakamura^{2,1}, S. Sugihara¹, K. Nishihara¹, K. Tanaka³ and S. Kimura^{2,1,4}

¹Department of Physics, Graduate School of Science, Osaka University, Toyonaka 560-0043, Japan

²Graduate School of Frontier Biosciences, Osaka University, Suita 565-0071, Japan

³UVSOR Synchrotron Facility, Institute for Molecular Science, Okazaki 444-8585, Japan

⁴Department of Material Molecular Sciences, Institute for Molecular Science, Okazaki 444-8585, Japan

Rare-earth mono-pnictides (*REPNs*) are well-known for their various magnetic properties, such as the ‘Daval’s Staircase’ in CeSb, originating from the hybridization of *RE*’s localized *4f* orbitals and *Pn*’s *p*-orbitals [1,2]. Recently, the emergence of an antiferromagnetic topological insulator phase due to the coupling of the nontrivial topology and the symmetry breaking owing to the antiferromagnetic ordering is reported in NdSb [3]. On the other hand, it has been reported that the breaking of the rotational symmetry of the surface atomic structure can be coupled with nontrivial surface states [4]. Therefore, to explore the potential novel properties in *REPN* with broken rotational symmetry, we are focusing on the epitaxial *REPN* thin film system, where the symmetry of the surface atomic structure could be controlled by surface science methods, such as changing the symmetry of the substrate. In this work, we have fabricated an anisotropic YbSb thin film on GaSb(001) substrates with 2-fold rotational symmetry by the molecular beam epitaxial (MBE) method and studied the electronic state by synchrotron-based angle-resolved photoelectron spectroscopy (ARPES).

The clean Sb-rich GaSb(001)-c(2×6) reconstruction surface was prepared by Ar ion sputtering at 720 K and following evaporation of Sb at the same substrate temperature. After that, Yb and Sb were co-evaporated onto the substrate at 570 K in a 1: 1.1 atomic ratio. Figure 1 shows the LEED pattern of the 14-ML YbSb(001). In addition to integral order diffraction spots of bulk YbSb with NaCl structure observed along the $\bar{1}10$ direction, the fractional diffraction spots according to the two-fold symmetry are observed in the $[110]$ direction throughout the entire sample surface. This result suggests an anisotropic single-domain (2×1) surface reconstruction.

Figure 2 shows the Fermi surface intensity image measured with horizontally polarized 21-eV photons at a temperature of 7.5 K. A square-like Fermi contour (red dashed line) is observed near the $\bar{\Gamma}$ point, which is consistent well with the Sb 5*p* hole pocket in other reported *RESb* systems [5]. On the other hand, the high-intensity area reflecting the Fermi surface extends in the $[110]$ direction, showing a 2-fold rotational symmetry rather than a 4-fold symmetry of the (001) plane in bulk YbSb.

Figure 3 shows the ARPES intensity plots along $\bar{\Gamma}$ - \bar{X}_1 ($[110]$ direction) and $\bar{\Gamma}$ - \bar{X}_2 ($\bar{1}10$ direction) with both horizontally polarized (LH) and vertically polarized (LV) 21-eV photons. Dispersions around $\bar{\Gamma}$ are consistent with each other in both directions. In

contrast, new dispersions appear along the $\bar{\Gamma}$ - \bar{X} line in the $[110]$ direction, which could be explained by the double period band folding due to the (2×1) surface reconstruction.

The results above suggest that the 4-fold symmetry of bulk YbSb is broken in both the surface atomic structure and electronic state of the fabricated YbSb/GaSb(001) thin film. The lowered surface symmetry will make novel physical properties.

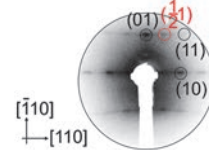


Fig. 1. LEED of the fabricated YbSb thin film measured with 79-eV electrons at 7.5 K.

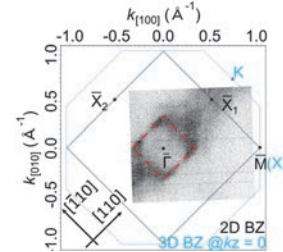


Fig. 2. Fermi surface intensity map measured with horizontally polarized 21-eV photons at 7.5 K.

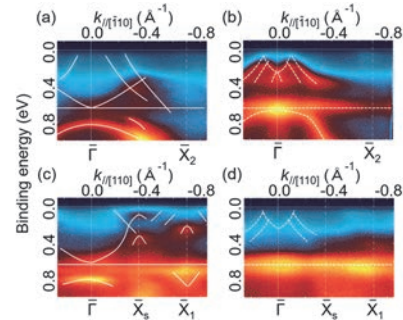


Fig. 3. ARPES intensity plots measured with 21-eV photons at 7.5 K. (a) $\bar{\Gamma}$ - \bar{X}_2 , LH. (b) $\bar{\Gamma}$ - \bar{X}_2 , LV. (c) $\bar{\Gamma}$ - \bar{X}_1 , LH. (d) $\bar{\Gamma}$ - \bar{X}_1 , LV.

- [1] J. Rossat-Mignod *et al.*, J. Magn. Magn. Mater. **52** (1985) 111.
- [2] H. Takahashi and T. Kasuya, J. Phys. C: Solid State Phys. **18** (1985) 2697, 2709, 2721, 2731, 2745, 2755.
- [3] A. Honma *et al.*, Nat. Commun. **14** (2023) 7396.
- [4] Y. Ohtsubo *et al.*, Nat. Commun. **13** (2022) 5600.
- [5] H. Oinuma *et al.*, Phys. Rev. B: Condens. Matter **96** (2017) 041120(R).

BL7U

Photoelectron Spectra of Thermoelectric Oxide $\text{Ba}_{1/3}\text{CoO}_2$

S. Tanaka¹, K. Kang² and H. Ohta²¹SANKEN, Osaka University, Ibaraki 464-0056, Japan²Research Institute for Electronic Science, Hokkaido University, Sapporo 001-0020, Japan

Thermoelectric power conversion technology is one of the key issues for the industry of the future. It converts waste heat into electricity via the Seebeck effect. Its efficiency of the conversion can be estimated by the thermoelectric figure of merit (ZT). In these decays, many efforts have been made to develop thermoelectric materials with high ZT along with the practical advantages, such as low cost, chemical stability, size, flexibility, *etc.* Recently, Ohta's group in Hokkaido University has fabricated a freestanding $\text{Ba}_{1/2}\text{CoO}_2$ single-crystalline thin film with $\text{ZT} \sim 0.55$ at 600°C in air by the epitaxy method [1], which is very promising for the thermoelectric devices in the near future. Therefore, its detailed electronic structure is highly desired to reveal. In this report, we show results of the photoelectron spectroscopic measurements of the $\text{Ba}_{1/2}\text{CoO}_2$ film.

The film was prepared by epitaxial method on Al_2O_3 substrate. The crystalline structure of the film was verified by X-ray diffraction and AFM. It was assured that annealing at 300°C in $<10^{-5}$ Pa does not affect the crystalline structure. After the deposition, the sample was exposed to air, transferred to UVSOR, and inserted into the UHV chamber at BL7U. The sample was then heated in UHV ($<10^{-7}$ Pa) to remove the contamination deposited on the sample surface during the transfer.

Figures 1 and 2 show angle-integrated and angle-resolved photoelectron spectra of $\text{Ba}_{1/2}\text{CoO}_2$ taken at $h\nu=36\text{eV}$ at room temperature. Before the measurements, the sample was heated at 200, 250 and 350°C for 30 min, respectively. The sample surface heated at 350°C apparently showed the change of colors at depending on the position of the sample, and spectra were taken at typical two positions (A, and B). The sample color is more changed at the position B than the position A. One thing that should be pointed out is a fact there is no density of states to cross the Fermi level for all the spectra. Considering the high surface sensitivity of the photoelectron spectroscopy, it indicates that the sample surface is not metallic. It is surprising since the bulk resistivity of the sample is $0.001\Omega\text{cm}$. Therefore, the sociometric condition of the sample surface seems not same as the inside the film. The angle-integrated spectra gradual changes as functions of the heating temperatures. As the heating temperature is higher, the intensity of the peak nearest to the Fermi level, which mainly consists of the Co3d orbital, becomes smaller in intensity. One more characteristic change in the spectra is that decrease of the peak around -15eV . This peak can be assigned as the Ba5p semicore level. The depression of this peak at

the position B after the 350°C may indicate the evaporation of Ba near the surface layer atom starts at 350°C , although the bulk data showed that it is stable upto 600°C . The angle-resolved spectra show that there is no dispersion observed. Therefore, the surface is not well crystalized at any heating temperature, and the heating in vacuum cannot produce a well-defined surface. For studying ARPES of the $\text{Ba}_{1/2}\text{CoO}_2$ more, the other method, e.g., in-situ epitaxial growth, is required.

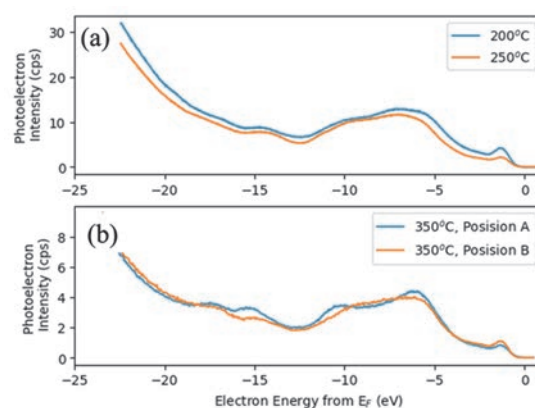


Fig. 1. Angle-integrated photoelectron spectra of $\text{Ba}_{1/2}\text{CoO}_2$ epitaxially produced on Al_2O_3 substrate and heated at 200°C and 250°C for 30 min (a), and those taken at different positions of the sample heated at 350°C for 30 min (b).

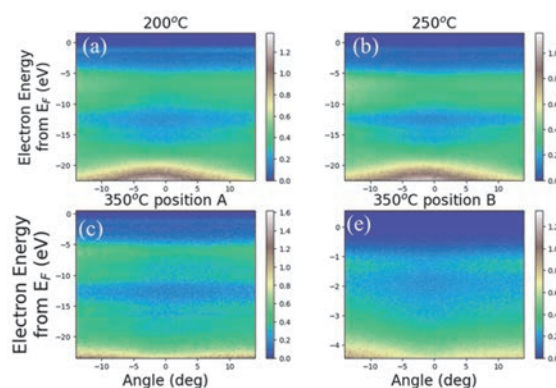


Fig. 2. Angle-resolved photoelectron spectra of $\text{Ba}_{1/2}\text{CoO}_2$.

[1] K. Kang *et al.*, ACS Appl. Electron. Mater. **5** (2023) 5749.

Electronic States at Ionic Liquid/Electrode Interfaces by Multi-Angle Incident-Angle ATR-UV-Vis Spectroscopy

I. Tanabe¹, T. Kakinoki² and K. Fukui²

¹Department of Chemistry, College of Science, Rikkyo University, Toshima 171-0021, Japan

²Department of Materials Engineering Science, Graduate School of Engineering Science, Osaka University, Toyonaka 560-8531, Japan

Ionic liquids are salts in the liquid phase at room temperature and atmospheric pressure which have recently attracted much attention in various fields such as electrochemistry and synthetic chemistry. In particular, due to unique features such as extremely low vapor pressure, high thermal stability, and wide potential window, ionic liquids are promising as novel electrolytes that are both safe and functional. In electrochemical devices the electrolyte/electrode interface is essentially important. Recently, we reported electronic transition spectra in the 140–450 nm region of various ionic liquids by using the attenuated total reflectance (ATR) technique. Additionally, a new spectroscopic system, namely electrochemical-ATR (EC-ATR) ultraviolet-visible spectroscopy, which can access the interfacial area, was developed [1, 2].

In this study, we measured ATR spectra in ionic liquid/gold electrode interface using polarized UV lights from BL7B at the UVSOR. We deposited the gold thin film on the sapphire ATR prism using physical vapor deposition method and used it as the working electrode. As the electrolyte, we adopted EMIM-TFSI (1-Ethyl-3-methylimidazolium bis(trifluoromethanesulfonyl)imide). Platinum mesh and platinum rod are utilized as the pseudo counter electrode and reference electrode, respectively. We applied the negative potentials to the gold electrode using cyclic voltammetry from 0 V to –1.8 V vs. Pt, and measured the ATR absorbance spectra simultaneously.

Figure 1 depicts the difference ATR spectra induced by the negative electrode potential. The incident light comprised (a) non-polarized light from a deuterium lamp and (b) s-polarized light from BL7B at UVSOR, respectively. In both spectra, the ATR absorbance wavelength shifted with the applied potentials. Due to the negative electrode potential applied to the electrode, EMIM cations approached the gold electrode surface, while TFSI anions were electrostatically repelled from the electrode surface. The spectral changes may reflect such phenomena near the electrode surface. Furthermore, polarized probe light can distinguish the orientation of the interfacial species in the ATR spectra: s-polarized light resonates with the dipole moment whose direction is parallel to the interface, while p-polarized light resonates with the perpendicular component. It is known that the imidazolium cation

orients its structure on the negatively charged electrode, with the imidazolium rings becoming parallel to the interface [3]. Thus, we can assume that the difference spectra are mainly attributed to the parallel orientation of the imidazolium cation ring in the first layer of the interface. In summary, we suggest the possibility of utilizing the polarization of the probe light in ATR spectroscopy.

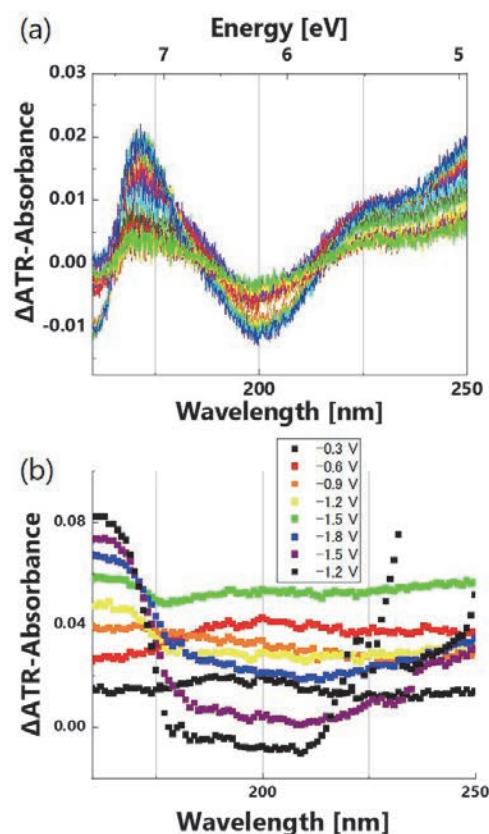
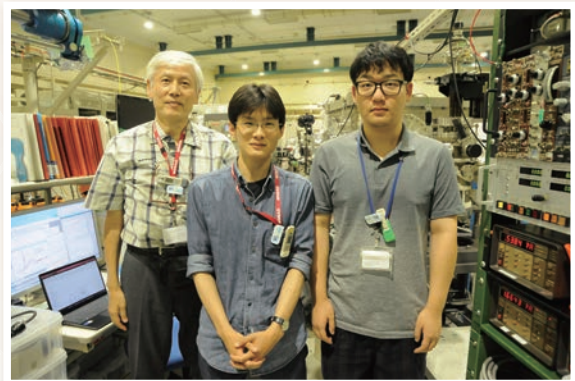
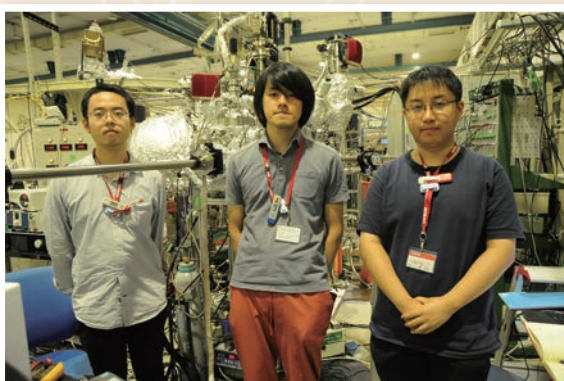
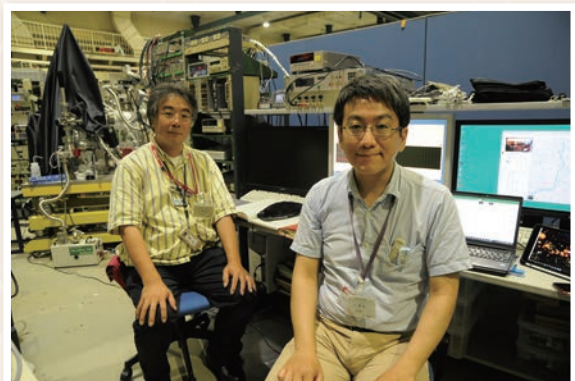
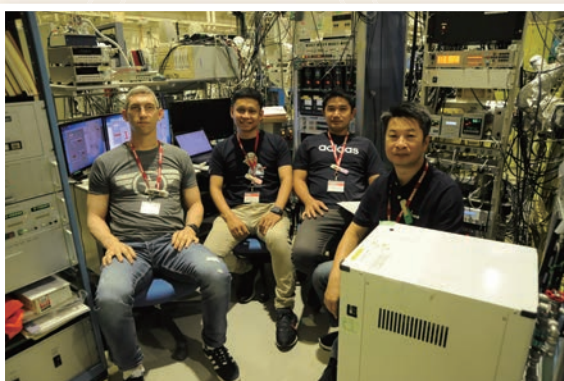
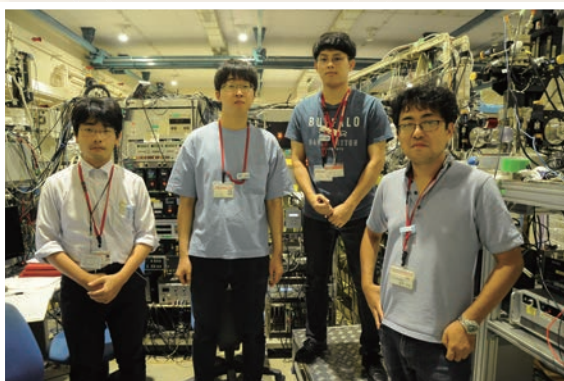
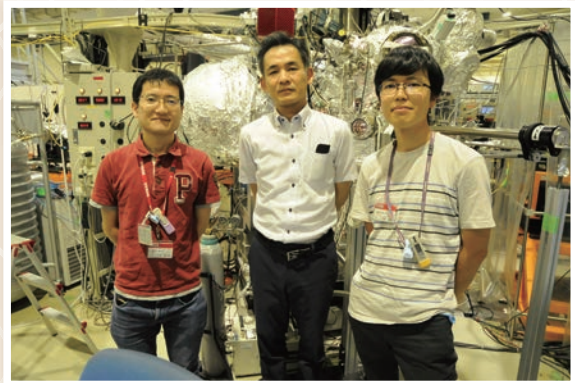
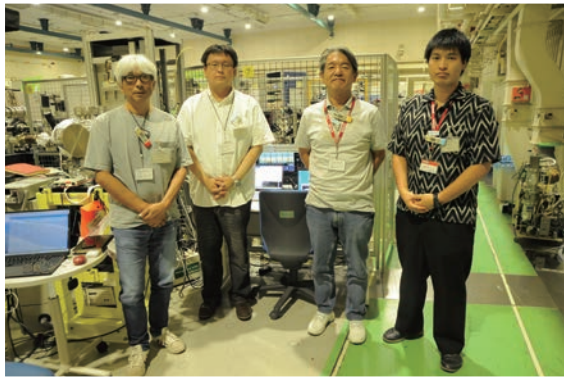


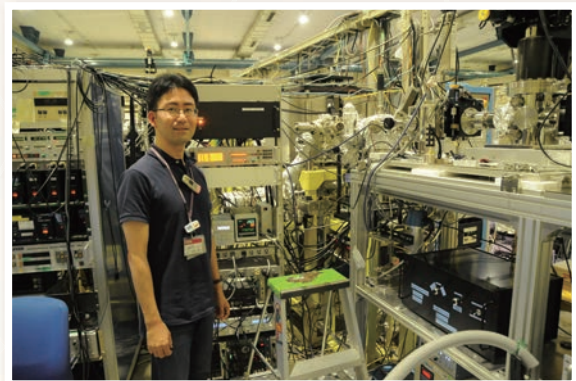
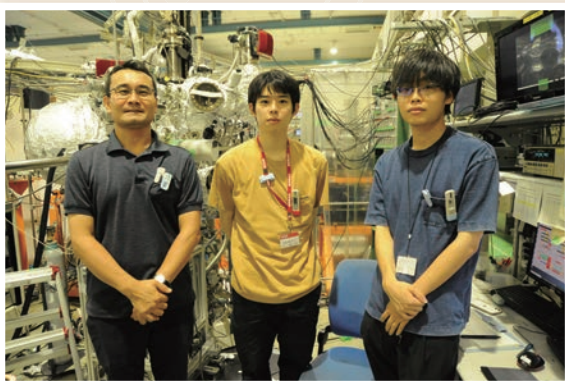
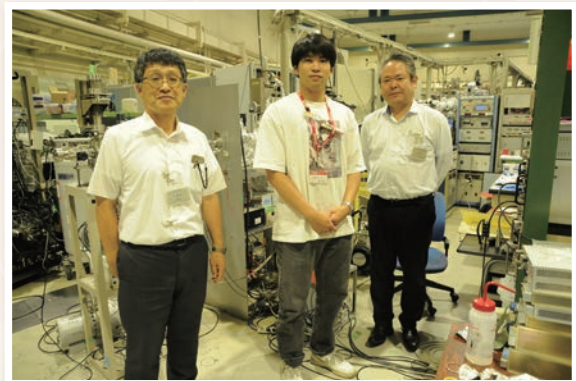
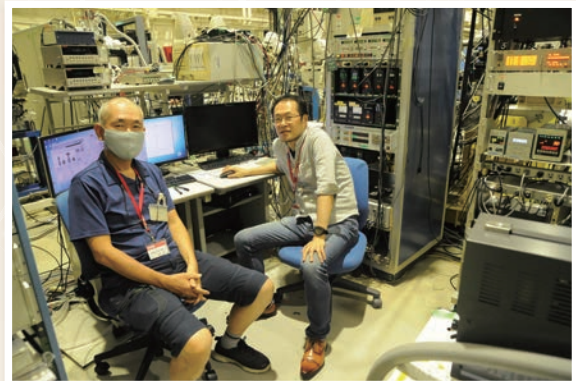
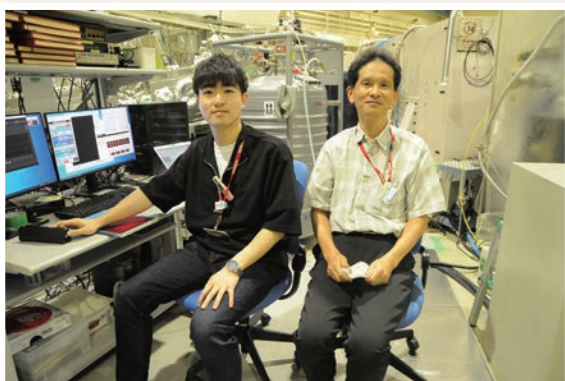
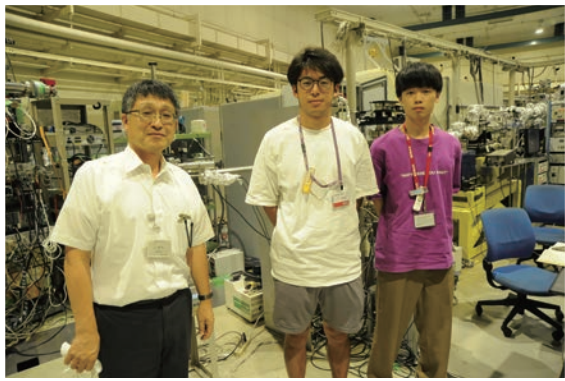
Fig. 1. Difference ATR-UV spectra induced by the negative electrode potential using (a) non-polarized light and (b) s-polarized light.

- [1] I. Tanabe *et al.*, Anal. Chem. **91** (2019) 3436.
- [2] I. Tanabe *et al.*, Commun. Chem. **4** (2021) 88.
- [3] H. Miyamoto *et al.*, Phys. Chem. Chem. Phys. **20** (2018) 19408.

UVSOR User 6



UVSOR User 7



III-5

Life, Earth and
Planetary Sciences





BL4U

Spring in the Arctic Ocean during ARTofMELT Expedition: A STXM/NEXAFS Analysis of Aerosol Particle Composition and Mixing State

N. Fauré¹, T. Araki.², E. S. Thomson¹ and X. Kong¹

¹Department of Chemistry and Molecular Biology, University of Gothenburg, SE-412 96 Gothenburg, Sweden

²UVSOR Synchrotron, Institute for Molecular Science, Okazaki 444-8585, Japan

The Arctic region is warming two to four times faster than the rest of the globe, a phenomenon called Arctic Amplification (AA). The enhanced warming pace in the Arctic arises from several sources including cloud feedback effects. In winter, aerosol particles in the Arctic mainly come from transport, while summer is dominated by local sources. These particles eventually act as Cloud Condensation Nuclei (CCN) or Ice Nucleating Particles (INP), modifying cloud formation and properties.

Spring in the Arctic is characterized by mixed sources of aerosol particles, transitioning from the transport-dominated regime (winter) to local sources (summer) due to reduced sea ice extent. The concentration, composition, vertical distribution, and CCN/INP efficiency of spring-time aerosol particles are poorly constrained due to a lack of measurements at this time of the year, especially over the Arctic Ocean. To fill this data gap, the Atmospheric Rivers and the onset of sea ice MELT (ARTofMELT) expedition took place from May to June 2023 in the Arctic Ocean onboard the Swedish icebreaker Oden.

During this expedition, impactors were placed at the edge of sea ice, next to open leads, to collect sea spray aerosol particles for STXM/NEXAFS analysis. A microscopic image of the particles collected on June 8, 2023, displayed in Fig.1(a), reveals different particle morphologies. A more detailed investigation with STXM/NEXAFS was performed on particles I and II in Fig.1(b).

In Fig.2, similar spectra are obtained for all the regions investigated, highlighting the presence of

sulfate (SO_4^{2-}) in both particles. This result does not come as a surprise as SO_4^{2-} makes up the highest concentration of particulate species measured in the Arctic.

In Fig.3, the NEXAFS spectra of the particles and regions investigated show significant discrepancies. The N-K-edge spectra revealed a higher intensity of the N=O bond at 401 eV in region 2, while particle I shows a significant amount of N-H bonding species at 405.5 eV, probably ammonium (NH_4^+). No signal is observed for C-K-edge and K-Ledge for particle I, which is likely to be mainly made of ammonium sulfate $(\text{NH}_4)_2\text{SO}_4$. Particle II displays a strong intensity of oxidized carbon at 288.2 eV and 290.5 eV for all regions, while K^+ is only observed in region 2.

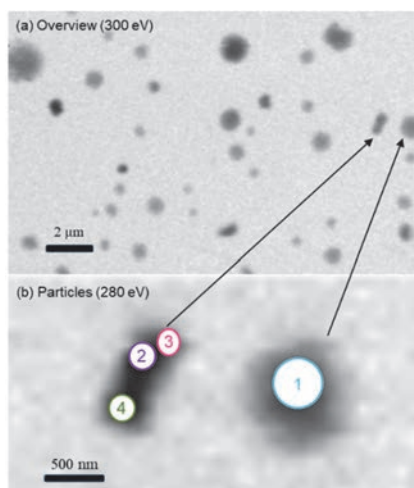


Fig.1. (a) Overview scan of particles collected next to open lead in the Arctic Ocean and (b) particles of interest for STXM/NEXAFS.

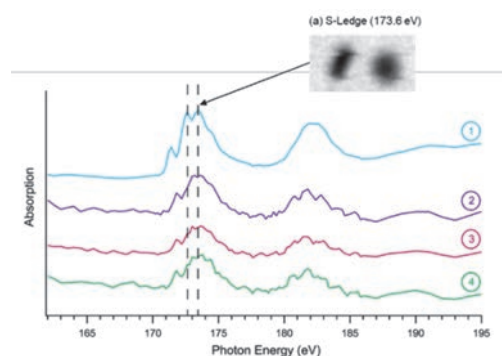


Fig.2. Sulfur L-edge NEXAFS spectra.

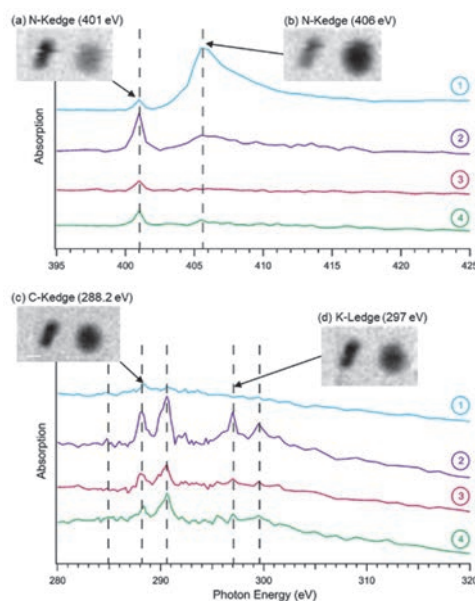


Fig.3. Nitrogen K-edge, carbon K-edge, and potassium L-edge NEXAFS spectra.

Optical Activity Emergence of Organic Molecules Induced by Circularly Polarized Lyman- α Light Irradiation and Magnetic Field Application

M. Kobayashi¹, J. Takahashi², H. Ota³, K. Matsuo⁴, G. Fujimori⁵, Y. Taira³, M. Katoh^{3,4}, K. Kobayashi^{5,6}, Y. Kebukawa⁶ and H. Nakamura¹

¹National Institute for Fusion Science, Toki 509-5292, Japan

²Self-organization Science Research Center, Doshisha University, Kyotanabe 610-0321, Japan

³UVSOR Synchrotron Facility, Institute for Molecular Science, Okazaki 444-8585, Japan

⁴Hiroshima Synchrotron Radiation Center, Hiroshima University, Higashi-Hiroshima 739-0046, Japan

⁵Department of Chemistry and Life Science, Yokohama National University, Yokohama 240-8501, Japan

⁶Department of Earth and Planetary Sciences, Tokyo Institute of Technology, Meguro-ku, Tokyo 152-8550 Japan

The biomolecules of the living organisms on the earth consist of left-handed (L-isomer) amino acids, known as the homochirality of life, and it remains as one of the most mysterious problems in the study of origin of life. One of the possible explanations of the enantiomer excess is selective photolysis caused by radiation field in space, “Cosmic scenario” [1]. For example, it has been proposed that circularly polarized light (CPL) from star-forming region is irradiated onto interstellar and circumstellar organic molecules and that causes selective photolysis resulting in the enantiomer excess of the biomolecules. In order to verify the cosmic scenario, we have conducted experiments to irradiate CPL onto amino acids. In this study, particularly we have focused on Lyman- α (121.6 nm), which has been recently observed in star-forming regions, and thus is one of the most possible candidates for the cause of the selective photolysis when it is circularly polarized [2]. In addition, we have also focused on the magneto-optical effects on the organic molecules to take into account of the magnetic field in space.

The experiments have been carried out at the undulator beamline BL1U of UVSOR-III [3], Institute for Molecular Science, where an irradiation system has been newly developed to realize the Lyman- α CPL irradiation and the application of magnetic field simultaneously. In the present experiments, the thickness of the MgF₂ window, which is for vacuum isolation between the beam line and the sample chamber, down to 0.5 mm to reduce the attenuation. The higher order light with 10 nm or less contained in the original beam was attenuated by a focusing mirror situated upstream of the MgF₂ window to avoid the damage of the window materials, which leads to further decrease of the transmittance of the window. At the beamline BL1U, left and right circularly polarized light with a peak at 121.6 nm was extracted, and was injected into the vacuum chamber, where the amino acid sample was installed, through a gate valve with the MgF₂ window. DL-alanine, racemic mixture crystal of alanine (the chiral amino acid with the simplest structure), was used as an organic molecule specimen. A thin DL-alanine film with a thickness of about 100 nm was formed on a CaF₂ substrate by vacuum evaporation.

The magnetic field was applied in parallel or anti-parallel to the light axis with a strength of 0.7 T. The circular dichroism (CD) spectrum was measured before and after the irradiation at the synchrotron radiation CD beam line BL-12 of Hiroshima Synchrotron Radiation Center (HiSOR), Hiroshima University [4], and with CD spectrometer in Institute for Molecular Science.

Figure 1 shows spectra of DL-alanine films after the CPL irradiation. We clearly observe optical activity induced by the CPL irradiation, which shows opposite sign in the optical anisotropy factor g between R- and L-CPL. It is also found that the g values slightly change with the magnetic field application to the CPL irradiation, irrespective of the direction of the magnetic field (not shown in the figure). The results suggest a certain impact of the magnetic field application on the optical activity caused by the CPL irradiation.

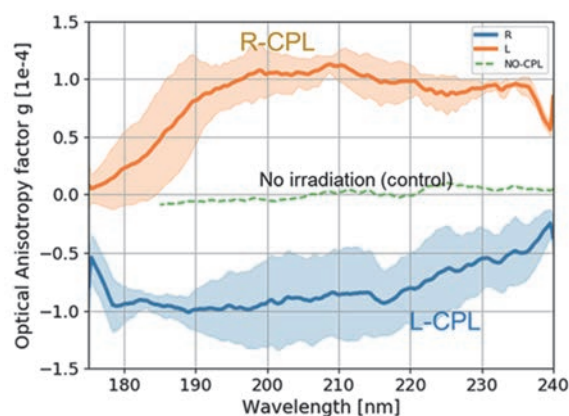


Fig. 1. Optical anisotropy factor g of the DL-Alanine film after CPL irradiation. The CD spectra is normalized with absorbance to compensate different film thickness from sample to sample.

- [1] J. Takahashi and K. Kobayashi, *Symmetry* **11** (2019) 919.
- [2] A. Sato *et al.*, *Astrobiology* **23** (2023) 1.
- [3] H. Ota *et al.*, *J. Phys. Conf. Ser.* **2380** (2023) 012003.
- [4] K. Matsuo and K. Gekko, *Bull. Chem. Soc. Jpn.* **86** (2013) 675.

BL1U

Toward Observation of the Interaction between Ultraviolet Optical Vortex and Biomaterials

K. Matsuo^{1,2,3}, R. Imaura², S. Hashimoto², Y. Nishihara³ and M. Katoh^{1,2,3,4}

¹Hiroshima Synchrotron Radiation Center, Hiroshima University, Higashi-Hiroshima 739-0046

²Graduate School of Advanced Science and Engineering, Hiroshima University, Higashi-Hiroshima 739-8526 Japan

³School of Science, Hiroshima University, Higashi-Hiroshima 739-8526, Japan

⁴UVSOR Synchrotron Facility, Okazaki 444-8585, Japan

Recently, the interaction of chiral materials with the optical vortex, which has an orbital angular moment (OAM, $l = \pm 1, \pm 2, \pm 3, \dots$), is gaining attention because the combinations of vortex retarder and laser in the visible region made it possible to observe the difference between the absorption of left- and right-optical vortex (vortex dichroism) like circular dichroism. Some papers have reported the negative experimental results for the existence of vortex dichroism, but some positive results have been obtained in the absorption and reflection experiments for the oriented materials aligned on the metal substrate [1] and nanostructures [2]. Further, the optical vortex in the hard-X-ray generated by synchrotron radiation (SR) also clearly showed the vortex dichroism for the metal complex [3]. Although the generation of optical vortex with continuous light in the UV region below 300 nm, which wavelength has large interaction with the chromophores of biomaterials, was difficult due to the limitations of laser performance, recently the helical undulator which is one of the SR instruments to generate the circularly-polarized light has been recognized as a generator tool of the optical vortex in the wide range of wavelength (far-UV, vacuum-ultraviolet (VUV), and extreme-UV (EUV) regions) without any optical elements [4, 5], opening new pathway for the studies on the interaction between biomaterials and optical vortex in the UV region. However, successful observations of vortex dichroism are limited to the three reports mentioned above, and the mechanism remains fully unknown. Hence, in this study, we constructed the experimental systems for observing the interaction between biomaterials and optical vortex in the UV region using SR undulator beamline BL1U of the UVSOR-III storage ring.

Figure 1a shows the experimental setup for observing the absorption patterns of the optical vortex (OAM, $l = \pm 1$) using the second-harmonic radiation from the helical undulator. The SR light passed through an iris diaphragm, and reached the lens and a multi-channel

monochromator, which can detect the signals in the wide range of wavelength from visible to UV regions.

The parameters of optical vortex from helical undulator are ($s = +1, l = +1$) or ($s = -1, l = -1$). So, we put the wire grid filter before the sample to modulate the circularly polarized light to the linearly polarized light (Fig. 1a). The spectrum of vortex dichroism in the case of ($s = 0, l = +1$) and ($s = 0, l = -1$) for *d*-10 camphor sulfonic acid (ACS) was observed in the wavelength region from 305 to 270 nm using the multi-channel monochromator. As preliminary results, it seems that the spectrum of vortex dichroism and linear dichroism (with wire grid filter) of ACS are different around 270 nm but the differences are mostly within errors. However, larger differences were obtained when using the optical vortex in the case of ($s = +1, l = +1$) and ($s = -1, l = -1$) (without wire grid filter) although we need to further investigate the difference between the absorptions of left- and right optical vortex in more details.

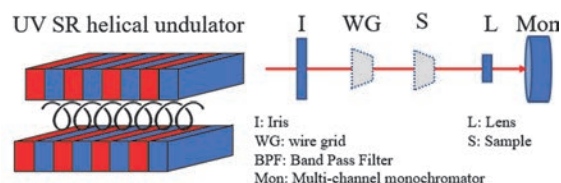


Fig. 1. Experimental setup for observing optical vortex using the second-harmonic radiation from the helical undulator.

- [1] W. Brullot *et al.*, *Sci. Adv.* **2** (2016) e1501349.
- [2] J. Ni *et al.*, *ACS Nano* **15** (2021) 2893.
- [3] J.R. Rouxel *et al.*, *Nat. Photonics* **16** (2022) 570.
- [4] M. Katoh *et al.*, *Sci. Rep.* **7** (2017) 6130, *Phys. Rev. Lett.* **118** (2017) 094801.
- [5] T. Kaneyasu *et al.*, *Phys. Rev. A: At. Mol. Opt. Phys.* **95** (2017) 023413.

X-ray Absorption Spectra of Lipid Bilayer Membranes in Aqueous Solutions and Its Dependence on Cation Concentration

R. Tero¹, Y. Kinjo¹ and M. Nagasaka²

¹Toyohashi University of Technology, Toyohashi 441-8580, Japan

²Institute for Molecular Science, Okazaki 444-8585, Japan

The lipid bilayer, which is a self-assembled structure of amphiphilic lipid molecules, is the fundamental structure of biomembranes such as cell membranes. Transportation of materials, information, and energy into and out of cells proceeds at the cell membrane in the presence of electrolytes. Ions in the aqueous solution significantly influence to physical properties and structures of lipid bilayers. Phosphatidylcholine (PC) is the most abundant lipid of eukaryotic cell membranes. Cations bind to the phosphate and carbonyl groups of PC. However, affinity of cations to PC and effects of cations to molecular orientation are still controversy especially in the fields of theoretical simulations. We aim to clarify the coordination states of cations to lipid molecules in aqueous solutions experimentally, by means of X-ray absorption spectroscopy (XAS) [1, 2].

Supported lipid bilayers (SLBs) of dioleoyl-PC (DOPC) were formed on the Si_3N_4 membranes of the XAS flow cell [1] by the vesicle fusion method in a buffer solution (NaCl 100 mM, HEPES 25 mM/ pH 7.4 NaOH). The Na^+ concentration ($[\text{Na}^+]$) was varied by exchanging the buffer solution in the flow cell in the range of $[\text{Na}^+] = 2.1 - 510.4$ mM. The O-K edge XAS spectra of SLB were obtained at the energy range of 527 – 535 eV. The X-ray incident angle of 35°. The XAS spectrum of the Si_3N_4 membrane without SLB was subtracted from that with SLB.

The O K-edge spectrum of DOPC appeared at 531 – 533 eV [2, 3]. It is consisted of $1s \rightarrow \pi^*$ transitions of double-bond oxygens in the phosphate and carbonyl groups on the PC headgroup: two components attributed to the P=O in the former, and one component attributed to the latter. We measured XAS spectra at the X-ray incident angle (θ) of 35°. We obtained a specific dependence of the P=O peak at the lower energy on $[\text{Na}^+]$: its position was little affected by $[\text{Na}^+]$ in the range of 2.1 – 10.4 mM and shifted to higher energy by 0.4 eV at $[\text{Na}^+] = 50.4$ mM. The position showed slight change at $[\text{Na}^+] > 110.4$ mM. The results show the Na^+ coordination to the phosphate group of DOPC and its dependence of $[\text{Na}^+]$.

The inner-shell quantum chemical calculation [4] of O K-edge spectrum of P=O was performed based on the atomic positions obtained from the theoretical calculation of the DOPC bilayers in aqueous conditions at $[\text{NaCl}] = 2 - 100$ mM (Fig. 1). The inner-shell spectra of oxygen atoms in the phosphate group showed high-energy shift depending on the distance from Na^+ that

was consistent with the experimental results. We also found that the peak intensity also depended on the distance between Na^+ and the oxygen atom in the P=O group. These results indicate that the ion coordination on lipid molecules is evaluated by the XAS spectra in water.

We have confirmed that the XAS spectra of DOPC were reproducibly obtained with a sufficient S/N ratio at the beam current condition of 200 mA in this year. The effects of the cation species on the XAS spectra of DOPC bilayer are also investigated.

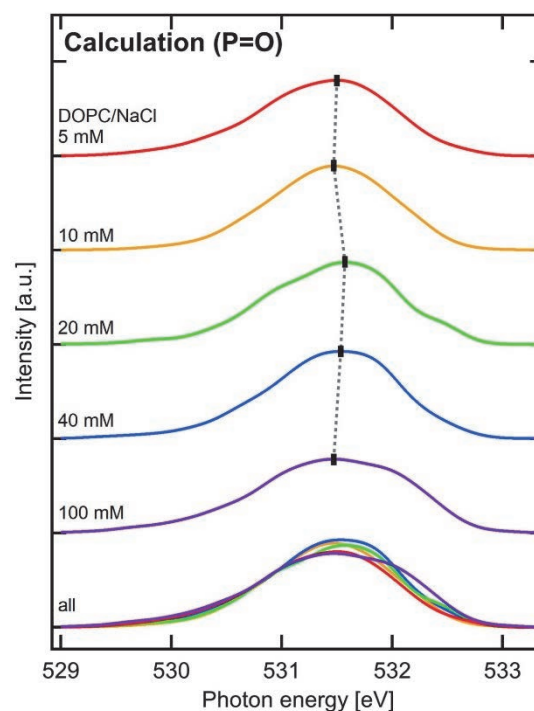


Fig. 1. The inner-shell spectra of oxygen atoms in the phosphate groups in the DOPC-bilayers at various NaCl concentrations. The peak positions are indicated with dotted lines. The overlapped spectra are shown at the bottom for comparison in peak intensity.

[1] M. Nagasaka *et al.*, J. Electron. Spectrosc. Relat. Phenom. **224** (2018) 93.

[2] R. Tero, Y. Kinjo and M. Nagasaka, UVSOR Activity Report **49** (2022) 151.

[3] R. Tero, Y. Kinjo and M. Nagasaka, UVSOR Activity Report **50** (2023) 165.

[4] M. Nagasaka, J. Chem. Phys. **158** (2023) 024501.

BL3U

Laser Excited Photochemical Reaction of Dissolved Oxygen on Lipid Bilayer Measured by Oxygen K-Edge XAS

F. Kumaki¹, M. Nagasaka^{2,3}, Y. Kinjo⁴, R. Tero⁴, Y. Okano² and J. Adachi^{1,5}¹*Institute of Materials Structure Science, High Energy Accelerator Research Organization, Tsukuba 305-0801, Japan*²*Institute for Molecular Science, Okazaki 444-8585, Japan*³*Molecular Science Program, Graduate Institute for Advanced Studies, SOKENDAI, Okazaki 444-8585, Japan*⁴*Toyohashi University of Technology, Toyohashi 441-8580, Japan*⁵*Materials Structure Science Program, Graduate Institute for Advanced Studies, SOKENDAI, Tsukuba 305-0801, Japan*

When photosensitizers such as porphyrin dyes are photoexcited, singlet oxygen ($^1\text{O}_2$) with high reactivity is generated owing to the energy transfer to the triplet oxygen ($^3\text{O}_2$). Photodynamic therapy, in which photosensitizers are injected into living bodies to destroy cancer cells by generating $^1\text{O}_2$, has recently gained attention [1]. We have attempted to elucidate the elementary process of $^1\text{O}_2$ generation via photoreaction in biological membranes in detail using O K-edge X-ray absorption spectroscopy (XAS) since 2021 [2, 3].

To measure the electronic state of $^1\text{O}_2$ generated in lipid layers including photosensitizers, time-resolved liquid XAS system by the combination of soft X-ray pulses (530 eV, 128 ps) and visible laser pulses (400 nm) was used at BL3U. The synchrotron radiation pulse duration of about 100 ps at the UVSOR facility would be short enough to probe the reaction dynamics of $^1\text{O}_2$ which has a lifetime of about 3 μs dissolved in liquid [4].

The liquid XAS system at BL3U was used to measure the O K-edge XAS spectra of dissolved oxygen in lipid layers. The liquid layer in the cell was sandwiched between two Si_3N_4 membranes with lipid bilayers. We established the method to measure O K-edge XAS spectra of dissolved oxygen kept on lipid bilayers [2]. For improving the signal-to-noise ratio of the spectra from the previous measurement, several lipid bilayers were added beforehand to increase the amount of dissolved oxygen in the liquid cell. The chlorophyll-*a*, which is a photosynthetic pigment to the lipid bilayers as a photosensitizer, were added in the lipid bilayers. Chlorophyll-*a* was found to be an excellent dye as a model system for photoreaction in lipid bilayers.

We plan to irradiate the SHG of Ti:sapphire laser (419 nm, 0.5 mW) to the liquid cell for conducting the photoexcitation of the chlorophyll-*a*. The laser wavelength will be adjusted to match the maxima of the solet band of the chlorophyll-*a*. To observe the difference of the O K-edge XAS spectra of the dissolved oxygen due to the $^1\text{O}_2$ generated via the photoreaction of chlorophyll-*a*, we will measure the XAS spectra

with and without laser irradiation simultaneously by using a gate signal synchronized with the shutter of the laser. By changing the phase of the laser, the delay from the synchrotron radiation will be shifted to find the delay at which the spectra show a large change from the spectra of the ground state.

Figure 1 shows the O K-edge XAS spectra of the lipid bilayers with adsorbed oxygen. Compared to the XAS spectrum obtained in the previous measurement (blue line), the present XAS spectrum shows the larger peak between 530 eV and 533 eV owing to the increase in the adsorption of the dissolved oxygen in the lipid bilayer. In the future, we will continue the laser excited photochemical reactions of dissolved oxygen using the present lipid bilayers.

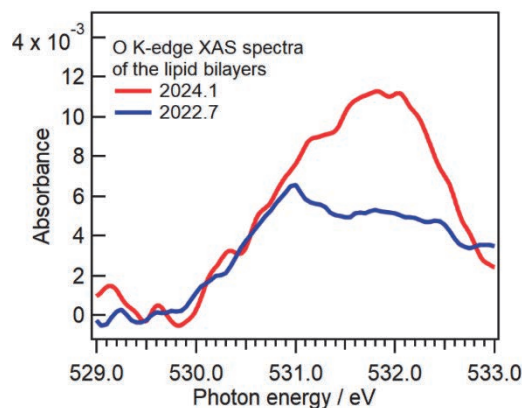


Fig. 1. The O K-edge XAS spectra of the lipid bilayers with adsorbed oxygen. The spectrum obtained in the previous measurement are also shown for the comparison of the present measurement.

- [1] M. Ethirajan *et al.*, Chem. Soc. Rev. **40** (2011) 340.
- [2] F. Kumaki *et al.*, UVSOR Activity Report **49** (2022) 118.
- [3] F. Kumaki *et al.*, UVSOR Activity Report **50** (2023) 123.
- [4] C. A. Long and D. R. Kearns, J. Am. Chem. Soc. **97** (1975) 2018.

Soft X-ray Absorption Spectroscopic Study of Myoglobin Heme in Solution

Y. Sugimoto¹ and M. Nagasaka^{2,3}

¹UVSOR Synchrotron Facility, Institute for Molecular Science, Okazaki 444-8585, Japan

²Institute for Molecular Science, Okazaki 444-8585, Japan

³The Graduate University for Advanced Studies (SOKEIDAI), Okazaki 444-8585, Japan

Heme is a complex of porphyrin and iron atom. Heme binds to proteins and serves as an active center for a wide variety of activities, including oxygen transport or electron transfer. One of the best-known heme proteins is myoglobin in muscle, that binds and stores oxygen to the iron atoms of heme. Myoglobin was the first protein whose structure was determined by X-ray crystallography [1] and have been studied in various ways. On the other hand, spectroscopic study using soft X-rays have not been widely applied to observe heme and proteins. This is because soft X-rays are strongly absorbed by air and water, making it difficult to apply spectroscopic measurements of proteins in solution.

Soft X-ray absorption spectroscopy (XAS) of liquid samples has been developed using a liquid cell at soft X-ray beamline BL3U of UVSOR [2]. In this study, we aimed to measure the electronic structures of heme in myoglobin by using nitrogen K-edge XAS in transmission mode. Our measurement system can observe liquid samples at room temperature and atmospheric pressure. In heme, the iron atom is coordinated to the nitrogen atom of the porphyrin. It is important to clarify the electronic structure of the nitrogen atoms surrounding the metal center as well as the iron atoms responsible for oxygen binding.

The experiments were carried out in BL3U. Myoglobin solution was prepared to be 1 mM in phosphate buffer. We prepared oxygenated myoglobin (oxyMb), deoxygenated myoglobin (deoxyMb), and metmyoglobin (metMb, oxidized to Fe³⁺). These samples were checked from the UV-Visible spectroscopic measurements. SiC membranes were used as the vacuum window and the windows of the liquid cell for the measurements of the nitrogen K-edge XAS. XAS spectra were obtained by measuring the transmission intensities of soft X-rays from 395 eV to 415 eV.

Figure 1 shows the UV-Visible spectra of myoglobin in solution, which are oxyMb, deoxyMb, and metMb. From the comparison of the previous studies, we confirmed that the samples were prepared correctly for each condition. Figure 2 shows the N K-edge XAS spectra of myoglobin and bovine serum albumin (BSA) samples in solution. BSA is a protein without heme.

While the signals commonly observed for both myoglobin and BSA are at ~401 eV and ~406 eV, a peak was observed at ~400 eV only in the myoglobin samples and not in BSA. This result implies that the peak at 400 eV is derived from nitrogen atoms in heme. It was also suggested that there may be an energy shift between the oxyMb and deoxyMb peaks at 400 eV.

In this experiment, the possibility of observing light elements in biological macromolecules was demonstrated under physiological conditions. Further precise measurements and spectral analysis of nitrogen K-edge XAS of heme in protein will be made.

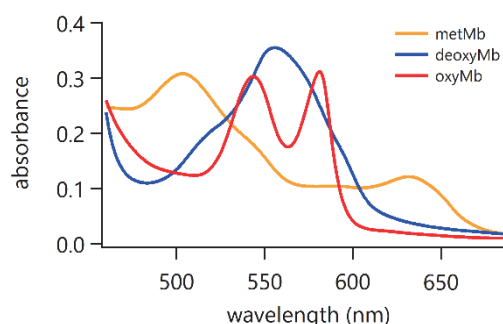


Fig. 1. UV-visible spectra of myoglobin, which are oxyMb, deoxyMb, and metMb.

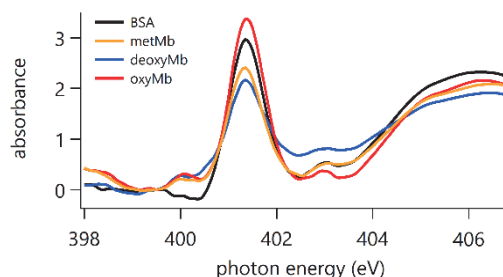


Fig. 2. N K-edge XAS spectra of myoglobin and BSA samples in solution. Each Spectrum was normalized at 399 eV.

[1] J. C. Kendrew *et al.*, Nature **181** (1958) 662.

[2] M. Nagasaka and N. Kosugi, Chem. Lett. **50** (2021) 956.

BL4U

The Effect of Freeze-Defrosting Cycles on the Spherule Size, Morphology, and Chemical Compositions of HCN Polymer

H. Yabuta¹, N. Nishii¹ and T. Araki²¹*Department of Earth and Planetary Systems Science, Hiroshima University, Hiroshima 739-8526, Japan*²*UVSOR Synchrotron Facility, Institute for Molecular Science, Okazaki 444-8585, Japan*

It has been thought that organic nanoglobules in primitive small body materials, such as carbonaceous meteorites, cosmic dusts, and the returned asteroid samples, are derived from extremely cold environments in space, based on the observed enrichments of deuterium and/or nitrogen-15 (e.g., Nakamura-Messenger *et al.* 2006). Variations in sizes, morphologies, and chemical compositions of the organic nanoglobules could have been resulted on the meteorite parent bodies (De Gregorio *et al.* 2013), while they may have been altered in interstellar molecular cloud or outer solar nebula, as freeze concentration of molecules drive some organic synthesis such as HCN oligomerization under low temperature conditions (Miyakawa *et al.* 2002). In this study, we conducted a freeze-defrosting cycle experiment of a synthesized HCN polymer as organic nanoglobule analogue to investigate the effect of freeze-defrosting on their morphologies, size distributions, and functional group chemistry.

HCN polymer was synthesized by heating formamide (0.3 ml) at 185°C for 72 hours (Cataldo *et al.*, 2009). Freeze-defrosting cycle experiments of the mixture of HCN polymer (0.05 ml) and water (0.05 ml) in a screw vial were conducted. One freeze-defrosting cycle consisted of freezing at -196°C for 10s with liquid N₂, increasing the temperature from -196°C to -20°C for 24 hours in refrigerator, and increasing the temperature from -20°C to room temperature for 5 min. The experiments were conducted during 10, 20, 30, and 40 freeze-defrosting cycles. The products obtained under each condition were observed by FE-SEM (Hiroshima University) and analyzed by STXM-XANES, beam line 4U, UVSOR.

The FE-SEM observation showed that the sizes of organic microspherules in HCN polymer obtained after 10 freeze-defrosting cycles were larger than the starting HCN polymer before the experiment, while the sizes of organic microspherules after 20 freeze-defrosting cycles were smaller than the starting HCN polymer (0 cycle). A variety of morphologies, such as dumbbell-like structures, were observed from the products after 10 and 20 freeze-defrosting cycles. It should be noted that these diverse morphologies and sizes were observed in the presence of unreacted formamide, but without formamide. It is probably because formamide is ionic liquid that can dissolve the water-insoluble

HCN polymer, which may have accelerated growth and division of the organic microspherules.

The STXM-XANES measurements showed that the peaks of nitrile or nitrogen heterocycles (286.7 eV), amide or carboxyls (288.2 eV) were the highest in the C-XANES spectra of the starting HCN polymer and all the products except for the product after 10 cycles. The peaks of aromatic C=C (285.2 eV), alcohol or ether (289.5 eV) were the next highest. The peaks corresponding to imine (398.8 eV) and pyrrole (400.5 eV) were identified in the N-XANES spectra of all the samples, while amide peak was absent. Thus, the peak around at 288.2 eV in C-XANES could be derived from carboxyls. In the products after the freeze-defrosting cycles experiment, the peak intensity of carboxyls was slightly higher than that of aromatic nitrogen. The increase of carboxyls is probably due to hydrolysis of the organic microspherules during defrosting.

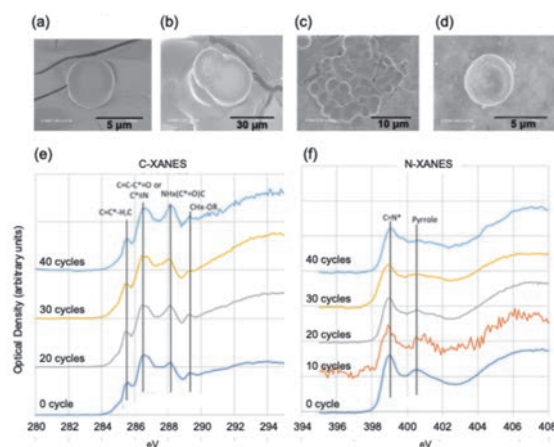


Fig. 1. SEM images of organic microspherules of HCN polymer after (a) 0, (b) 10, (c) 20, and (d) 40 cycles of freeze-defrosting experiment and (e) C- and (f) N-XANES spectra of HCN polymer before and after the freeze-defrosting cycle experiment.

- [1] K. Nakamura-Messenger *et al.*, *Science* **314** (2006) 1439.
- [2] B. T. De Gregorio *et al.*, *Meteorit. Planet. Sci.* **48** (2013) 904.
- [3] S. Miyakawa *et al.*, *Origins Life Evol. Biosphere* **32** (2002) 209.
- [4] F. Cataldo *et al.*, *J. Macromol. Sci.* **46** (2021) 1039.

Aerosol Particle Mixing States in Delhi: A STXM/NEXAFS Investigation into Nighttime Growth Mechanisms

M. Wickramanayake¹, E. Tsiligiannis¹, T. Araki,² E. S. Thomson¹ and X. Kong¹

¹*Department of Chemistry and Molecular Biology, University of Gothenburg, SE-412 96 Gothenburg, Sweden*

²*UVSOR Synchrotron, Institute for Molecular Science, Okazaki 444-8585, Japan*

Delhi, one of the most polluted global capitals, faces a dire air pollution crisis, particularly during winter when fine particulate matter (PM_{2.5}) levels often exceed 500 $\mu\text{g}\cdot\text{m}^{-3}$, which is over 30 times than the WHO's recommended limit of the 24-hour average value (15 $\mu\text{g}\cdot\text{m}^{-3}$). This pollution, significantly contributed to by vehicular emissions, industrial activities, and biomass burning, creates a dense winter haze under the nocturnal conditions of the Indo-Gangetic plain. The diurnal nighttime temperature decreases, and humidity increase leads to the accumulation and growth of particulates, adversely affecting visibility and public health. Despite research efforts, the chemical processes driving nocturnal particle growth remain unclear, posing a challenge to environmental health in the region.

To address this, measurements were conducted in Delhi during February and March 2023, collecting PM samples on TEM grids for STXM/NEXAFS analysis to study particle mixing states. Figure 1 displays a STXM image of aerosol particles collected on a heavy haze day, February 27, 2023, at 14:26. The particles exhibit a diverse range of morphologies, suggesting they are externally mixed, with distinct differences observable among them. Notably, in the upper left corner of the image, there is an agglomeration of soot particles.

In Fig. 2, a focused examination of a specific central area from Fig. 1 is presented for four different photon energy levels. These levels correspond to the pre-edge of the carbon K-edge at 280 eV, the C=C bond at 285.2 eV, the C=O bond at 288.2 eV, and the potassium L-edge at 297.2 eV, respectively. These detailed views reveal the presence of several particles that absorb differently at these energy levels. At 285.2 eV, particles (1) and (2) are visible, indicating the presence of soot, which is typically generated from combustion processes. At 288.2 eV, a larger particle (3) becomes more absorbing, predominantly consisting of organic materials featuring the carbonyl group (C=O). Finally, at 297.2 eV, potassium elements are highlighted at their L-edge, with the central portion (4) of one particle showing a pronounced response.

Figure 3 presents the NEXAFS spectra for the carbon K-edge and potassium L-edge of the four distinct particles, illustrating the internal mixing state of aerosols in Delhi. The comprehensive spectra analysis reveals a significant presence of potassium across numerous particles not detailed in this report, indicating biomass burning as a key source of air pollution in the city. Potassium serves as a widely recognized marker for biomass combustion. The possible diverse hygroscopic and chemical properties of these particle

types suggest they absorb water and other vapors, particularly at night. This absorption contributes to their nocturnal growth, a unique phenomenon observed in Delhi's atmospheric conditions.

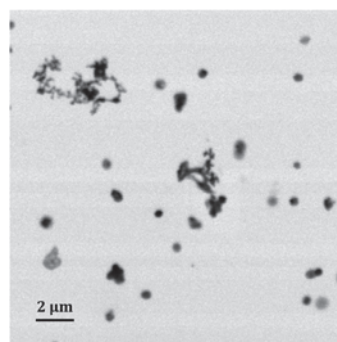


Fig. 1. An overview scan of Delhi particles acquired at a photon energy of 300 eV.

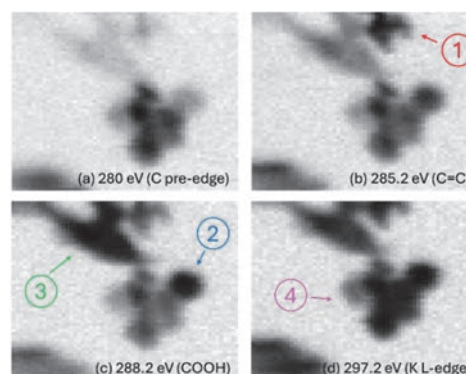


Fig. 2. Images taken at four photon energies.

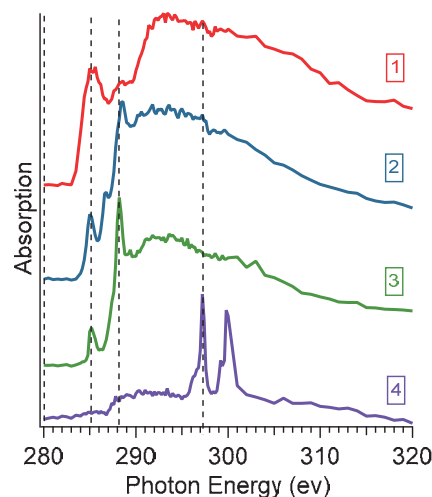


Fig. 3. Carbon K-edge and potassium L-edge NEXAFS spectra.

BL4U

STXM Characterization of Salla Disease Patient Fibroblasts

T. Mansikkala^{1,2}, I. Miinalainen², S. M. Kangas³, R. Hinttala^{3,4}, J. Uusimaa^{3,5},
M. Huttula¹ and M. Patanen^{1,2}

¹Nano and Molecular Systems Research Unit, PO Box 3000, 90014 University of Oulu, Finland

²Biocenter Oulu, PO Box 5000, 90014 University of Oulu, Finland

³Research Unit of Clinical Medicine and Medical Research Center,

Oulu University Hospital and University of Oulu, 90014 Oulu, Finland

⁴Transgenic and Tissue Phenotyping Core Facility, PO Box 5000, 90014 University of Oulu, Finland

⁵Children and Adolescents, Oulu University Hospital, 90029 Oulu, Finland

In this work, we used scanning transmission X-ray microscopy (STXM) technique at BL4U beamline to study cell cultured fibroblasts of Salla disease (SD) patients and control cell lines. This work continues our previous work carried out for SD mouse model tissues [1]. Salla disease (OMIM # 604369) is caused by a variant in the *SLC17A5* gene that encodes sialin, a lysosomal membrane protein that transports sialic acid (SA) out of lysosomes. Impaired function of sialin causes the SA to accumulate. Patients with SD store approximately 10-100 times the normal amounts of free SA in their tissues [2, 3]. The goal was to see if we can show the SA accumulation in SD patient fibroblast compared to healthy control fibroblasts. We also measured both patient and control fibroblasts cultured with N-Acetyl-D-mannosamine monohydrate (ManNAc). ManNAc was used to induce SA production in both SD patient (SASD) and control human dermal fibroblasts (NHDF).

Samples were measured in two different forms. Thin sections of 150 nm thickness were prepared from cells fixed in 4% paraformaldehyde and 2.5% glutaraldehyde in 0.1 M phosphate-buffered saline and then embedded in TTE:MMHA. The sections were placed on copper grids with butvar membrane. Same cells were also directly grown on nickel grids with formvar membrane. These cells were fixed the same way and dried with ethanol series. This was done to have measurements of cells without any embedding material.

We could not detect differences inside the lysosomes of the cells while measuring the resin embedded thin sections. Most of the lysosomes seemed to be void of material, showing only pure resin spectra. Despite some exceptions, no trend between sample types was detected. However, we did notice a difference when comparing the averaged signals of the entire cells of different sample types. The NHDF cells cultured with ManNAc had higher absorption (optical density (OD)) around 285-285.5 eV and 288-288.5 eV. The averages for each sample type were calculated after reducing the resin spectra individually from each cell using the resin measured from the scan. The averages are shown in Fig. 1. For each cell type 4 to 6 cells were measured and used in the average. This shows that STXM can be used to measure differences in cells caused by differences in genetics and cell culture.

Fibroblasts grown directly on top of the grid were too thick to get reliable results through the thickest parts of the cells. In Fig. 2. we can see the cells grown on grid showing very little transmission in the middle of the cells. However, we were able to measure the edge areas of the fibroblasts where there was enough transmission. Differences in spectrum from these areas seemed to be mostly from the thickness differences in the sample excluding few exceptions.

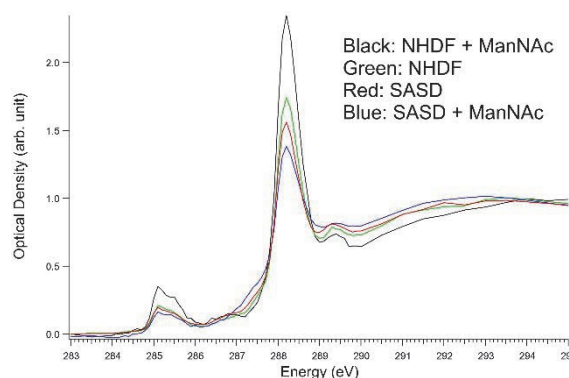


Fig. 1. Average OD of resin embedded cells after reducing the effect of resin from the sample.

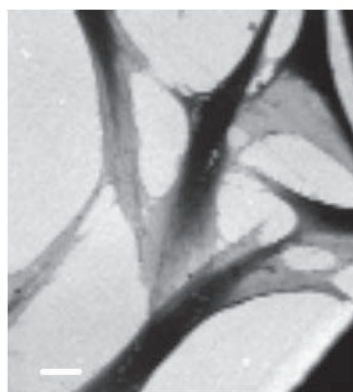


Fig. 2. Single energy (292.5 eV) transmission image of fibroblasts grown on grid. Scale bar is 10 μ m.

[1] T. Mansikkala *et al.*, J. Electron. Spectrosc. Relat. Phenom. **266** (2023) 147368.

[2] P. Aula *et al.*, Arch. Neurol. **36** (1979) 88.

[3] N. Aula *et al.*, Am. J. Hum. Genet. **67** (2000) 832.

Evaluation of Radiation-Induced NEXAFS Profile-Changes for Biomolecules in Imaging Biological Specimens

A. Ito¹, K. Shinohara², A. Matsuura², S. Toné³, K. Tohya⁴, Y. Asada², H. Yuzawa⁵,
T. Araki⁵ and T. Ohigashi⁶

¹*School of Engineering, Tokai University, Hiratsuka 259-1292, Japan*

²*Graduate School of Health Sciences, Fujita Health University, Toyoake 470-1192, Japan*

³*School of Science and Engineering, Tokyo Denki University, Hatoyama 350-0394, Japan*

⁴*Kansai University of Health Sciences, Kumatoricho 590-0482, Japan*

⁵*UVSOR Synchrotron Facility, Institute for Molecular Science, Okazaki 444-8585, Japan*

⁶*Photon Factory, Institute of Materials Structure Science, Tsukuba 305-0801, Japan*

Spectromicroscopy for molecular mapping is one of the unique applications of STXM. Since molecular distributions are calculated using a set of NEXAFS data for constituent molecules, the accuracy of the results largely depends on them. In particular, biological specimens such as our imaging targets [1-3] are supposed to be easily affected by X-ray irradiation. It is essential to estimate the modification of NEXAFS profiles as a function of X-ray absorbed dose for the quantitative molecular analysis.

In our previous report, we obtained absorbed dose dependence of mass absorption coefficient of biomolecules at specific photon energies [4]. In the present study, we extended such dose dependence profiles to every photon energy used for NEXAFS measurements. Based on this set of dose dependences, we can obtain NEXAFS at a given absorbed dose for imaging biological specimens. In addition, we can also estimate NEXAFS profiles of intact biomolecules by extrapolating the dose response curve to zero dose.

We prepared dry thin films of DNA, RNA, histone, BSA, actin monomer and nucleosome on SiN membrane. NEXAFS measurements were done for a defined area at the C, N, and O K-edges in this order, which is critical to calculate absorbed dose. The dwell time for the measurements was 6, 12 and 20 msec. For each dwell time, the scanned area was shifted to the different area to avoid additional radiation effects.

DNA spectra of mass absorption coefficient at the C, N and O K-edges were shown in Fig. 1. The blue lines were NEXAFS at the absorbed dose corresponding to each exposure for the observation of an apoptotic nucleus, while the red lines indicate NEXAFS estimated for intact DNA before exposure. Note that the absorbed dose was increased sequentially in the order from the lowest energy of the C K-edge to the highest energy of the O K-edge; for example, the dose at the starting point of the N K-edge was accumulated to the total dose of the preceding measurement at the C K-edge. The modification of the spectra does not seem to be so significant in the present imaging condition. Similar tendencies in the profile-changes to nucleic acids were found for proteins such as histone and actin.

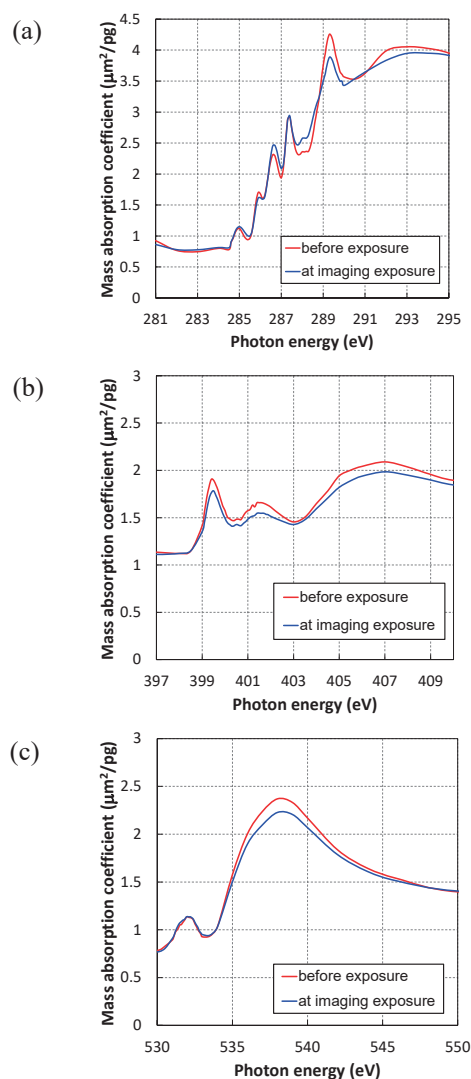


Fig. 1. NEXAFS of DNA at (a) C K, (b) N K, (c) O K-edges. Blue line: with X-ray exposure for imaging apoptotic nuclei; Red line: with no X-ray exposure.

- [1] K. Shinohara *et al.*, *Ultramicroscopy* **194** (2018) 1.
- [2] K. Shinohara *et al.*, *J. X-Ray Sci. Technol.* **26** (2018) 877.
- [3] K. Shinohara *et al.*, *Cells* **8** (2019) 8.
- [4] A. Ito *et al.*, *UVSOR Activity Report* **50** (2023) 173.

BL4U

Chemical Structures of Macromolecular Organic Matter in Ryugu Grain.

T. Matsumoto¹, T. Noguchi², T. Araki³, T. Ohigashi⁴, Y. Igami² and A. Miyake²

¹The Hakubi center for Advanced Research, Kyoto University, Kitashirakawa-Oiwakecho, Sakyo, Kyoto 606-8502, Japan

²Division of Earth and Planetary Sciences, Kyoto University, Kitashirakawa-Oiwakecho, Sakyo, Kyoto 606-8502, Japan

³Institute for Molecular Science, 38 NishigoNaka, Myodaiji, Okazaki 444-8585, Japan

⁴High Energy Accelerator Research Organization. 1-1 Oho, Tsukuba, Ibaraki 305-0801 Japan

Regolith samples recovered from the C-type asteroid Ryugu show chemical and petrological characteristics similar to those of CI carbonaceous chondrites [1-3]. Insoluble organic macromolecules (IOM) in Ryugu grains are the dominant components of organic matter in Ryugu's materials [3]. The chemical structures, distributions, and morphologies of the macromolecular organic matter can be tracers of the evolution of organic materials in the interstellar medium, the protosolar disk, and the aqueous environment in the parent body of Ryugu [3]. In this study, we focused on carbon-rich regions in a Ryugu grain and examined the spatial relationship between organic materials and phyllosilicates, together with their chemical features.

A Ryugu grain from the chamber A (grain No. A0142) was distributed by JAXA. Electron-transparent sections were extracted from the regions of interest using a focused ion beam system (FIB Helios NanoLab G3 CX). Scanning transmission X-ray microscopy (STXM) imaging was performed to obtain X-ray absorption near edge structure (XANES) spectra from the sections. The bonding structure of carbon was investigated using XANES spectra at the carbon K-edge (at 280 eV-320 eV). After STXM analysis, the sections were observed using field-emission transmission electron microscope (TEM) (JEOL JEM2100F).

We investigated the largest carbon-rich region with approximately 17×8×9 μm in size (Fig.1ab). Carbon-XANES spectra of the carbon-rich region include major peaks of aromatic carbon (285 eV) and carboxyl carbon (288.5 eV), and those of phyllosilicate matrix in the vicinity of the carbon-rich region show peaks of aromatic carbon (285 eV), carboxyl carbon (288.5 eV), aliphatic carbon (287.5 eV), and carbonates (290.4 eV). TEM analysis showed that organic materials and fibrous phyllosilicates are finely intermixed in the carbon-rich region. Hereafter, we call the carbon-rich region as the carbon-phyllosilicate aggregate (CPA). Distinct morphologies of organic materials, such as the organic globules, were not identified in the CPA. The surrounding matrix consists mainly of fibrous phyllosilicates, magnetite, iron sulfides, and carbonates. High-resolution TEM images showing layered structures of the fibrous phyllosilicates (Fig. 1c) enabled us to investigate the interlayer distance of the phyllosilicates. The majority of the fibrous phyllosilicates in the CPA and the matrix have interlayer distances of 0.7~0.75nm, and 1.0-1.2nm. These values correspond to typical interlayer distances of serpentine and saponite in Ryugu samples, respectively [2]. On the other hand, fibrous phyllosilicates with interlayer distances of 1.23-1.35 nm were occasionally observed

in the CPA and in the matrix close to the carbon-rich region (Fig.1c).

The enrichment of aromatic and carboxylic carbon in the XANES spectra from the CPA is similar to the spectral features of highly-aromatic or aromatic macromolecular carbon in Ryugu samples [3]. The concentration of aromatic organic matter may have occurred by redistribution and/or synthesis of organic matter during fluid activity in the parent body. It is also possible that large chunks of organic matter have been incorporated during the initial accretion of the parent body, in the form of primitive materials originated from the outer solar system [7]. The appearance of aliphatic carbon in the matrix is consistent with the previous XANES study of Ryugu samples, in which aliphatic organics were detected in association with phyllosilicates [8]. Previous X-ray diffraction measurements of Ryugu samples detected 001 reflection of smectite at 1.26 nm [4]. The relatively large interlayer distance was interpreted as the expansion of the interlayer space due to the presence of organic molecules [4]. The spatial relationship between the CPA and the possibly organic-bearing phyllosilicates suggests that macromolecular organic matter could have interacted with surrounding phyllosilicates during aqueous alteration, as suggested by analyses of carbonaceous chondrites [9, 10].

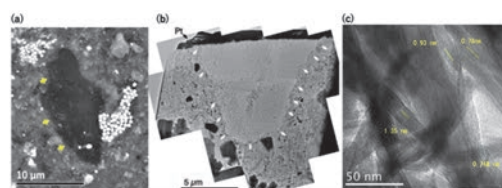


Fig. 1. The carbon-rich region of Ryugu grain (A0142). SEM image (a) and bright-field TEM image (b) of the carbon-phyllosilicate aggregate (CPA). (c) High-resolution TEM image of fibrous phyllosilicates near the CPA.

- [1] T. Yokoyama *et al.*, Science **379** (2022) eabn7850.
- [2] T. Nakamura *et al.*, Science **379** (2022) eabn8671.
- [3] H. Yabuta *et al.*, Science **379** (2023) eabn9057.
- [4] J.-C. Viennet *et al.*, Geochem. Perspect. Lett. **25** (2023) 8.
- [5] Damien *et al.*, Meteorit. Planet. Sci. under review.
- [6] C. Pilorget *et al.*, Nat. Astron **6** (2022) 221.
- [7] J. Duprat *et al.*, Science **328** (2010) 742.
- [8] M. Ito *et al.*, Nat. Astron **6** (2020) 1163.
- [9] L.A.J. Garvie and P.R. Buseck, Meteorit. Planet. Sci. **42** (2007) 2111.
- [10] C.L. Guillou *et al.*, Geochim. Cosmochim. Acta **131** (2014) 368.

Development of Contact X-ray Microscope for Biological Sample

H. Iwayama^{1,2} and R. Sasaba^{1,3}

¹UVSOR Synchrotron Facility, Institute for Molecular Science, Okazaki 444-8585, Japan

²School of Physical Sciences, The Graduate University for Advanced Studies (SOKENDAI), Okazaki 444-8585, Japan

³Graduate School of Frontier Biosciences, Osaka University, Suita 565-0871, Japan

Observing the structure of biological samples using an optical microscope is life science's most basic research method. In synchrotron radiation, a wide range of light can be used, including visible light and THz light, infrared light (IR), vacuum ultraviolet light (VUV), and X-rays. Light-matter interactions depend on its wavelength. For IR, VUV, and SX regions, molecular vibration excitation, valence-electron ionization, and core-electron ionization occur. Thus, microscopy with different wavelengths enables us to see other structures. In particular, in the X-ray region, resonant energies for core electrons depend on their element and chemical states, making structures for each element and chemical state possible. Soft X-ray regions (100 ~ 2000 eV) include resonant energies for carbon, nitrogen, oxygen, phosphorus, sulfur, etc., essential to life science.

There are various imaging methods that use X-rays, such as scanning transmission X-ray microscopy and X-ray ptychography. Recently, we began developing a contact X-ray microscope. In this method, a sample such as a cell is irradiated with X-rays, and the transmitted light is observed using a scintillator to image a projected image. The principle is the same as that of conventional X-ray photography. Although the spatial resolution of this method is roughly one μm and inferior to scanning transmission soft X-ray microscopy and X-ray ptychography, it is effortless and free of chromatic aberration because it does not require sophisticated focusing optics.

In this work, we developed a contact X-ray microscope at UVSOR BL4B. Figure 1 shows a schematic drawing of our contact X-ray microscope. A sample of oral epithelial cells was placed on a Ce:YAG scintillator and sealed with a Si_3N_4 membrane (100 nm thick). The transmitted soft X-rays are converted into visible light emission by the scintillator. The scintillator light emission image is observed by an optical lens (Asahikogaku, AZ10-100E) on the atmospheric side and detected by a CMOS camera (Hamamatsu Photonics, ORCA Flash 4.0 V3). The optical lens's NA, magnification, and working distance are 0.2, $\times 15$, and 100 mm, respectively.

We took 400 images for photon energies ranging

from 280 to 320 eV (0.1 eV step). Typical images of an oral cell are shown in Fig. 2. An exposure time is 10 seconds. By examining the image's energy dependence, we obtained an X-ray absorption fine structure (XAFS) spectrum for each pixel. Since the image in Figure 2 is 300 pixels \times 300 pixels, it corresponds to 90,000 XAFS spectra. Then, we classify the cell structure from the spectral structure for each pixel. However, it isn't easy to manually classify a large amount of spectra, so we are developing an analysis method that uses machine learning, such as KMEAN++, to classify the spectrum of each pixel. In the future, we will create a new structural analysis of non-stained biological samples with a contact X-ray microscope and its analysis method.

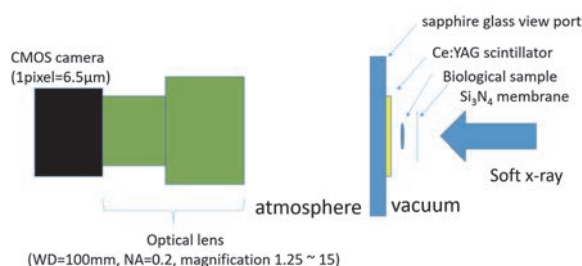


Fig. 1. Schematic drawing of contact X-ray microscope at BL4B.

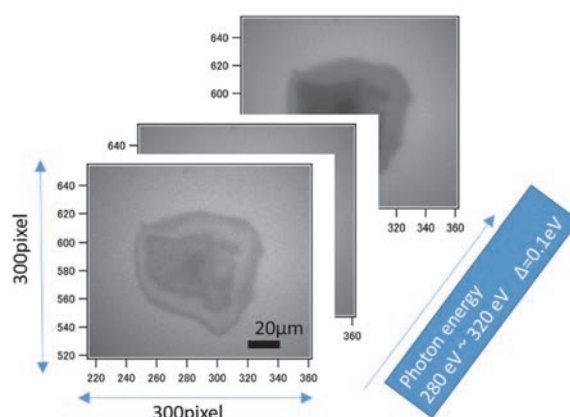


Fig. 2. Typical images of an oral epithelial cell by the contact X-ray microscope.

BL6B

Development of the Super Continuum Laser-Based Infrared Spectro-Microtomography for the Three-Dimensional Imaging of Extraterrestrial Organic Matter

H. Yabuta¹, Y. Ikemoto², F. Teshima³, and K. Tanaka³

¹Department of Earth and Planetary Systems Science, Hiroshima University, Hiroshima 739-8526, Japan

²Japan Synchrotron Radiation Research Institute (JASRI), Hyogo 679-5198 Japan

³UVSOR Synchrotron Facility, Institute for Molecular Science, Okazaki 444-8585, Japan

This study aims to develop a mid-infrared super continuum laser (MIRS)-based infrared spectro-microtomography (IR-CT) for the purpose to understand the three-dimensional distributions of water and organic matter in extraterrestrial samples with micrometer-scale spatial resolution.

In our previous studies (FY2019-2022), we established an alignment procedure to guide the laser source to the microscope for micro-spectroscopy, adjusted the beam size at the microscope focal point, developed the sample holding technique, and conducted a two-dimensional FTIR imaging of the standard samples (e.g., calcium carbonate) by the laser. In this study, we have conducted infrared imaging by rotating the samples.

A milled bread crumb grain (~90 μm in longitudinal) was used as a sample. The sample was glued to the tip of a glass capillary and mounted on a gonio stage. Infrared imaging of the sample has been conducted by a JASCO IRT-7000FT-IR microscope with linear array MCT detector attached to a JASCO FT/IR-6100 at a beam line 6B, UVSOR. A MIRS laser (COVERAGE, NOVAE Laser, 1.9-3.9 μm wavelength) was used as an IR light source (Fig. 1).

The infrared images of the sample at 3022-3433 cm^{-1} have been successfully acquired every five degrees (Fig. 3). We were also able to confirm that the infrared maps reflect the sample shapes (Fig. 2). In the future

study (FY2024), we will apply this approach to meteorite samples and will conduct a three-dimensional construction of the acquired data.

H.Y. and Y. I are supported by KAKENHI from the Japan Society for the Promotion of Science (JSPS) (grant no. 19H01954).

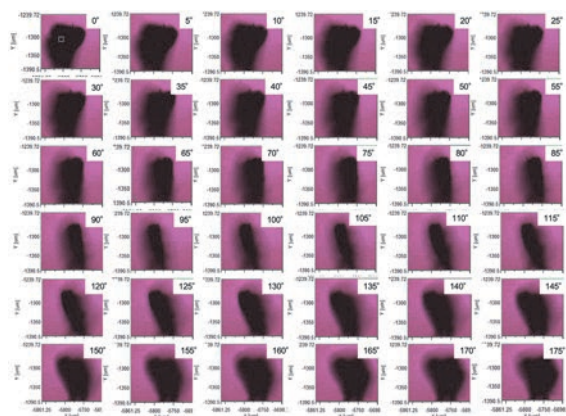


Fig. 2. Optical microscopic images of the sample (a milled bread crumb grain) taken at the rotation step in five degrees (5°).

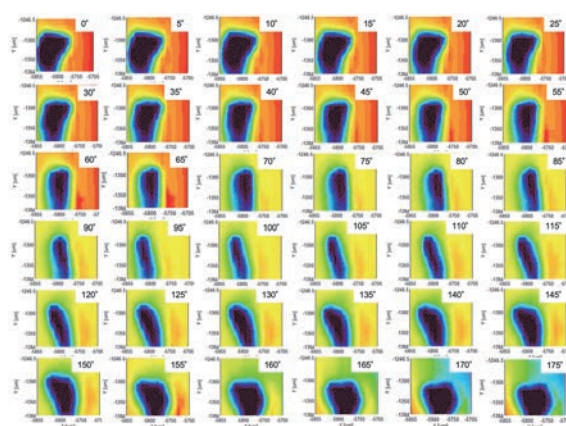


Fig. 3. Infrared images of the sample (a milled bread crumb grain) at 3022-3433 cm^{-1} taken at the rotation step in five degrees (5°).

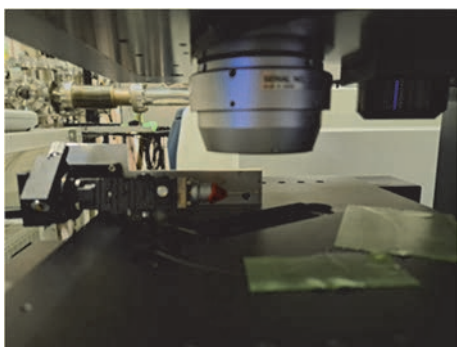


Fig. 1. Photograph of the gonio stage mounted on the microscope.

Structural Analysis of Amyloid Oligomers by Using Synchrotron Radiation Infrared Microspectroscopy

T. Kawasaki¹, F. Teshima² and K. Tanaka²

¹*Accelerator Laboratory, High Energy Accelerator Research Organization,
1-1 Oho, Tsukuba, Ibaraki 305-0801, Japan*

²*UVSOR Synchrotron Facility, Institute for Molecular Science,
38 Nishigo-Naka, Myodaiji, Okazaki 444-8585, Japan*

We investigated protein conformations by using synchrotron radiation infrared (IR) microspectroscopy at BL6B [1]. As a model sample, we targeted hair keratin that has similar fibrillar structure with amyloid oligomers [2]. Previously, we found that keratin and amyloid fibrils can be mode-selectively dissociated by infrared free electron laser (FEL) irradiation at mid-infrared wavelengths [3]. However, the effect of near-IR FEL on the fibrillar proteins has not yet been examined.

For the measurement of IR absorption spectra in the mid-IR region, IRM-7000 infrared microscope combined with FT/IR-6100 spectroscope (Jasco Co.), which covers 350 to 15,000 cm^{-1} (45 meV-1.8 eV) was used. Samples were added on a metal-coating plate, and the measurement was performed by reflection mode with 128 scans. The resolution is about 0.5 cm^{-1} . Observation was performed by using 16 x Cassegrain lens, and the aperture size was set to 50 μm x 50 μm . The mid-IR spectra were recorded from 700 to 4000 cm^{-1} . The 2D imaging for the protein secondary conformations were performed by the lattice measurement method where x-axis is 2 points and y-axis is 2 points, and total four spectra were acquired. Protein secondary conformation analysis was performed as follows [4]: The amide I band was divided into four bands: α -helix (1650–55 cm^{-1}), β -sheet (1625–40 cm^{-1}), turn (1655–75 cm^{-1}), and non-ordered conformation (1645–50 cm^{-1}). The peak distribution corresponding to each protein conformation was visualized using the universal RGB code.

It was observed that the FEL irradiation at 3.0 μm corresponding to stretching vibrational mode of hydroxy group ($\nu\text{O-H}$) induced bending of a hair (Fig. 1). 2D protein conformational mapping analysis showed that α -helix and turn conformations are dominant compared to β -sheet and other conformations

before the irradiation (left panel). On the other hand, β -sheet and other conformations were increased compared to α -helix and turns in the bending areas after the irradiation (right panel). Therefore, the near-IR FEL irradiation induced drastic conformational change of keratin, which produces the fibrillar structure containing more β -sheet conformation.

This study first shows the irradiation effect of near-IR FEL on the fibrillar conformation of proteins by using infrared imaging technique with synchrotron radiation infrared microspectroscopy analysis.

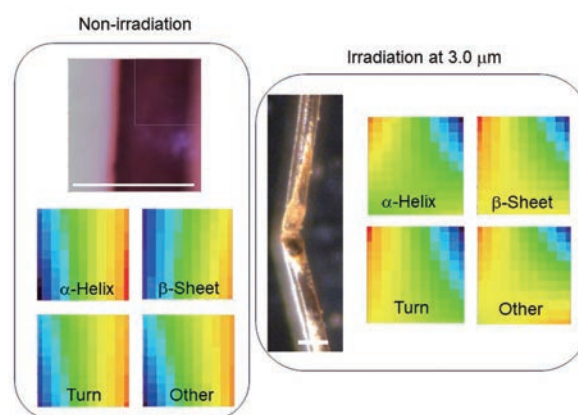


Fig. 1. 2D protein conformation imaging analysis. Left panel: non-irradiation hair sample. Right panel: hair sample after irradiation at 3.0 μm . White bar: 100 μm .

- [1] S. Kimura *et al.*, Infrared Phys. Technol. **49** (2006) 147.
- [2] T. Kawasaki *et al.*, J. Synchrotron Radiat. **23** (2016) 152.
- [3] T. Kawasaki *et al.*, J. Phys. Chem. B **124** (2020) 6266.
- [4] S. Caine *et al.*, Neuroimage **59** (2012) 3624.

BL7B

Study of Laboratory Simulated Space Weathering Effects on PAHs

S. Liu¹, K. Inoue², C. Wu¹, S. Teramoto¹ and I. Yoshikawa^{1,2}

¹*Department of Complexity Science and Engineering, Graduate School of Frontier Sciences,
The University of Tokyo, Chiba 277-8561, Japan*

²*Department of Earth and Planetary Science, Graduate School of Science,
The University of Tokyo, Tokyo 113-0033, Japan*

Polycyclic aromatic hydrocarbons (PAHs), composed solely of carbon and hydrogen, are widespread compounds in the cosmos. The PAH Hypothesis suggests a correlation between the absorption band of Interstellar Medium detected around 210 nm, attributed to PAHs, and the 217.5 nm absorption band evident in interstellar extinction curves.[1] Additionally, objects enduring exposure to outer space undergo space weathering, which alters their physical and optical properties. One notable effect of this process is the absorption bands of such objects may shift towards longer wavelengths after exposure. Utilizing ultraviolet irradiation for space weathering simulation provides a highly efficient and controllable approach.

In this study, we employed UV irradiation experiments using 0th-order light on two types of PAHs, coronene and anthracene. Subsequently, we utilized beamline BL7B to measure the transmittance spectra of the samples exposed to 0th-order light and samples exposed to the Deuterium Lamp.

In the irradiation experiments, coronene samples were subjected to irradiation for durations of 1 hour and 6 hours, while anthracene samples were exposed for 1 hour and 3 hours, employing the 0th-order light from BL7B. Notably, a thinning tendency was observed in the anthracene samples following prolonged irradiation. A Quadrupole Mass Analyzer was utilized to measure the Mass to Charge ratio within the range of 1 to 200. This enabled the analysis of potential ejecta emanating from the sample surfaces.

Following this, the transmittance spectra of the samples were measured using a photodiode. To minimize the possible impact of higher-order light, measurements were conducted across several distinct wavelength regions employing various gratings and filters.

Due to the thin total thickness of both samples and substrates, reflectance is significantly lower than transmittance. Hence, in calculations, it is permissible to approximate the absorptance ratio as 100% minus the transmittance ratio. Consequently, the data presented in Fig.2 can be derived.

The results in Fig. 2 suggest that the 12-hour exposure to deuterium lamp irradiation potentially impacts coronene's absorption spectra, indicating a shift towards shorter wavelengths and a possible decrease in absorptance. This aligns with previous space weathering

research findings.[2] The observed shift could be due to hydrogen atom loss. Future research will involve analyzing mass spectrometer data from the irradiation experiment and conducting theoretical calculations for further confirmation.



Fig. 1. Irradiation experiment.

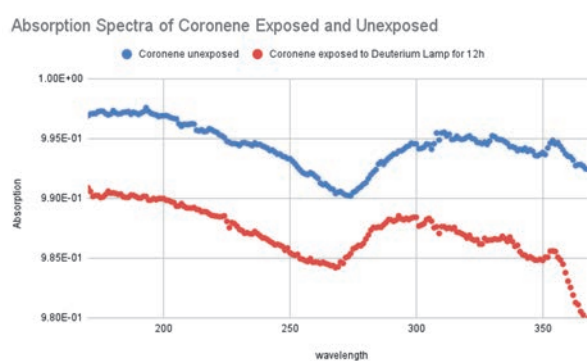
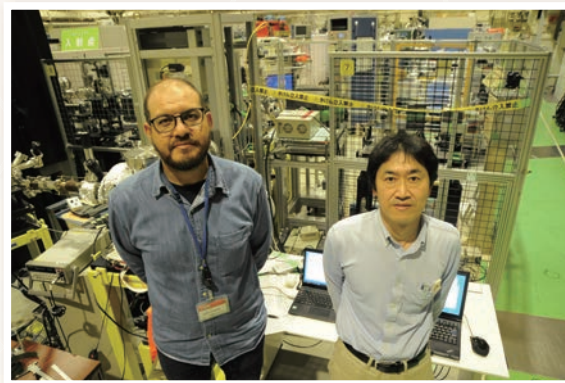
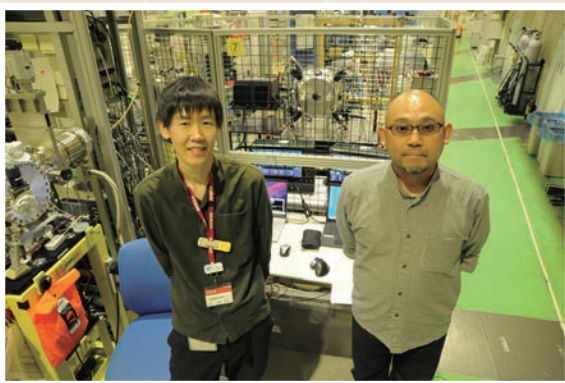
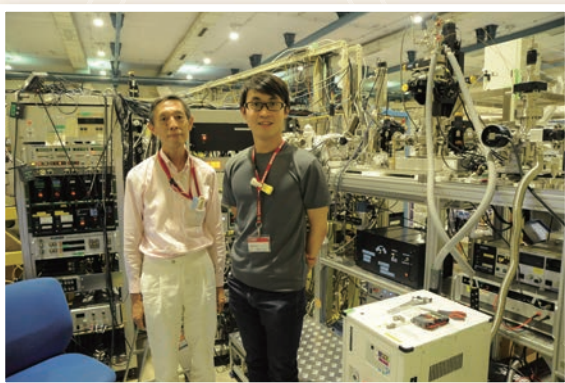
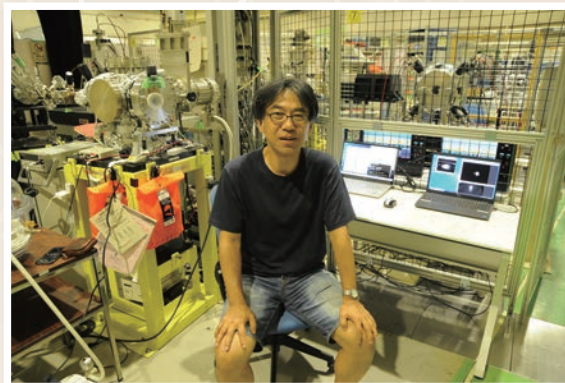
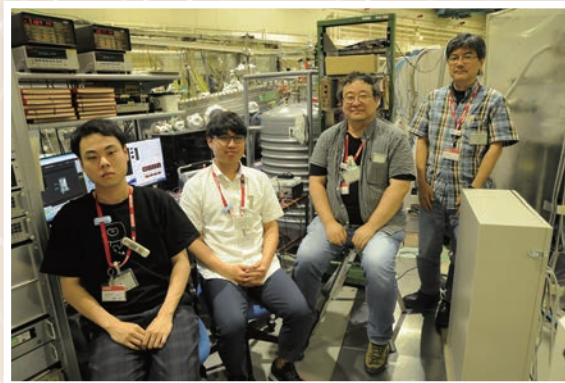
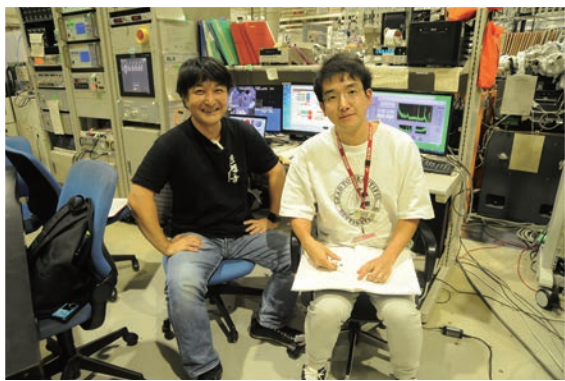


Fig. 2. Absorption spectra of coronene exposed and unexposed.

[1] C. Joblin *et al.*, *Astrophys. J.* **393** (1992) L79.

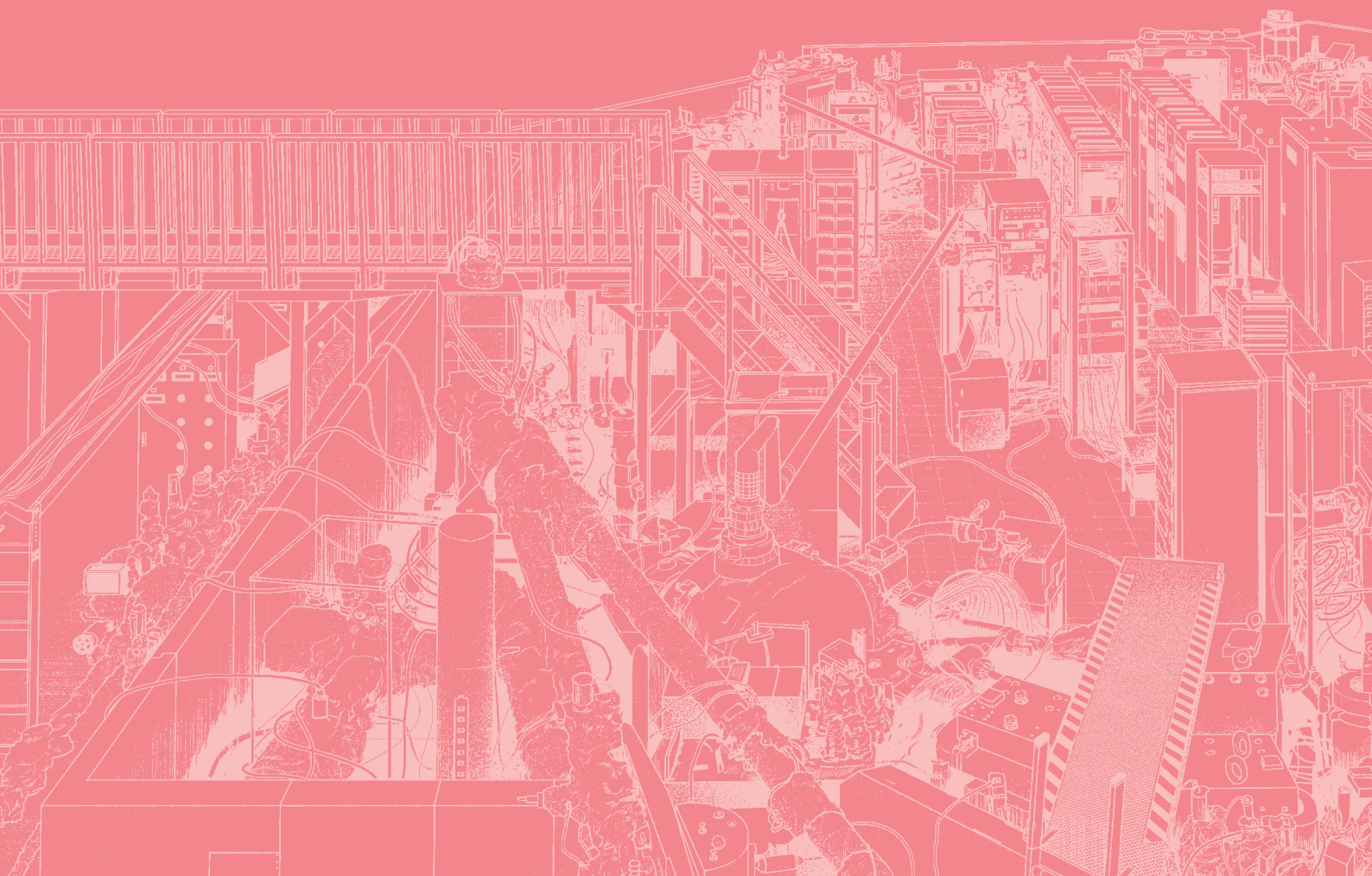
[2] S.K. Noble, C.M. Pieters and L.P. Keller *Icarus* **192** (2007) 629.

UVSOR User 8



IV

List of Publications





List of Publications (2023)

U. Alexiev and E. Rühl

“Visualization of Nanocarriers and Drugs in Cells and Tissue”, Handbook of Experimental Pharmacology

K. Ali, H. Zen, H. Ohgaki, T. Kii, T. Hayakawa, T. Shizuma, M. Katoh, Y. Taira, M. Fujimoto and H. Toyokawa
“Fusion Visualization Technique to Improve a Three-Dimensional Isotope-Selective CT Image Based on Nuclear Resonance Fluorescence with a Gamma-CT Image”, Appl. Sci. **11** (2021) 11866.

O. Endo, F. Matsui, S. Kera, W.-J. Chun, M. Nakamura, K. Amemiya and H. Ozaki

“Hole Doping to Perylene on Au(110): Photoelectron Momentum Microscopy”, e-J. Surf. Sci. Nanotechnol. **21** (2023) 236.

G. Germer, T. Ohigashi, H. Yuzawa, N. Kosugi, R. Flesch, F. Rancan and A. Vogt, E. Rühl

“Soft X-Ray Scanning Transmission Microscopy as a Selective Probe of Topical Dermal Drug Delivery: The Role of Petrolatum and Occlusion”, J. Electron Spectrosc. Relat. Phenom. **266** (2023) 147343.

Y. Hikosaka, T. Kaneyasu, S. Wada, H. Kohguchi, H. Ota, E. Nakamura, H. Iwayama, M. Fujimoto, M. Hosaka and M. Katoh

“Frequency-domain interferometry for the determination of time delay between two extreme-ultraviolet wave packets generated by a tandem undulator”, Sci. Rep. **13** (2023) 10292.

Y. Hikosaka

“Metastability and fragmentation of the OCS^{3+} states produced by S 2p double Auger decay”, J. Chem. Phys. **158** (2023) 214306.

Y. Hikosaka

“Dissociation Following the Auger Decay of Xenon Difluoride Molecules Produced by S 2p Double Auger Decay”, J. Chem. Phys. **160** (2024) 024304.

C. Hong, W. Zou, P. Ran, K. Tanaka, M. Matzelle, W. C. Chiu, R. S. Markiewicz, B. Barbiellini, C. Zheng, S. Li, A. Bansil and R. H. He

“Anomalous Intense Coherent Secondary Photoemission from a Perovskite Oxide”, Nature **617** (2023) 493.

C. Hong, Z. Song, B. Lin, P. Ran, X. Xie, C. Jiang and R.-H. He

“Effect of Surface Reconstruction of SrTiO_3 (001) on the FeSe Thin Film Growth”, J. Phys. Chem. Solids **184** (2024) 111717.

C. Hong, Z. Song, B. Lin, P. Ran, T. Wu, X. Xie, C. Jiang and R.-H. He

“Controlling Surface Reconstruction of SrTiO_3 (100) with Adhesive Outgassing”, J. Phys. Chem. Solids **184** (2024) 111716.

Y.-C. Huang, Y. Li, K. T. Arul, T. Ohigashi, T. T. T. Nga, Y.-R. Lu, C.-L. Chen, J.-L. Chen, S. Shen, W.-F. Pong, C.-L. Dong and W.-C. Chou

“Atomic Nickel on Graphitic Carbon Nitride as a Visible Light-Driven Hydrogen Production Photocatalyst Studied by X-ray Spectromicroscopy”, ACS Sustainable Chem.Eng. **11** (2023) 5390.

S. Ibuki and T. Kawai

“Excitonic feature in CsAg_2I_3 crystals prepared by Bridgman method”, Jpn. J. Appl. Phys. **63** (2024) 035504.

T. Kaneyasu, Y. Hikosaka, S. Wada, M. Fujimoto, H. Ota, H. Iwayama and M. Katoh
“Time Domain Double Slit Interference of Electron Produced by XUV Synchrotron Radiation”, Sci. Rep. **13** (2023) 6142.

T. Kato, Y. Takebuchi, M. Koshimizu, K. Okazaki, D. Nakauchi, N. Kawaguchi and T. Yanagida
“Scintillation Properties of Non-doped and Ce-doped LiAl_5O_8 Single Crystals”, Nucl. Instrum. Methods Phys. Res. B **546** (2024) 165168.

M. Katoh, H. Ota, J. Yamazaki, K. Hayashi, Y. Okano, E. Salehi, Y. Taira, A. Mano, M. Fujimoto, Y. Takashima, M. Hosaka, F. Sakamoto, T. Kaneyasu and H. Zen
“Light Source Developments at UVSOR BL1U”, J. Phys.: Conf. Ser. **2687** (2024) 032005.

T. Kawai, A. Iguchi and K. Yuasa
“Relaxation Processes among Adiabatic Potential Energy Surfaces of Tl^+ and Au^- Centers in NaCl Crystals”, J. Lumin. **266** (2024) 120330.

S. Kera, F. Matsui, K. Tanaka, Y. Taira, T. Araki, T. Ohigashi, H. Iwayama, M. Fujimoto, H. Matsuda, E. Salehi and M. Katoh
“Prospects required for future light-source facilities: a case of UVSOR synchrotron facility”, Electron. Struct. **5** (2023) 034001.

S. Kimura, H. Watanabe, S. Tatsukawa, T. Nakamura, K. Imura, H. S. Suzuki and N. K. Sato
“Current-Induced Metallization and Valence Transition in Black SmS ”, J. Phys. Soc. Jpn. **93** (2024) 013701.

T. Mansikkala, T. Ohigashi, M. H. Salo, A. E. Hiltunen, R. Vuolteenaho, P. Sipil, S. Kuure, M. Huttula, J. Uusimaa, R. Hinttala, I. Miinalainen, S. Kangas and M. Patanen
“Scanning transmission soft X-ray spectromicroscopy of mouse kidney and liver”, J. Electron Spectrosc. Relat. Phenom. **266** (2023) 147368.

C. O. M. Mariano, J. S. D. Rodriguez, R. H. Clemente, T. Ohigashi, H. Yuzawa, W-H. Hsu, J. Shiue and C-H. Chuang
“Scanning transmission X-ray microscopy of hydrogen evolution electrocatalysts on reduction graphene oxide membranes”, J. Electron Spectrosc. Relat. Phenom. **265** (2023) 147332.

F. Matsui, H. Ota, R. Eguchi, H. Goto, K. Kobayashi, J. Akimitsu, H. Ozaki, T. Nishioka, K. Kimura, K. Hayashi, T. Shimano, N. Happon and Y. Kubozono
“Multiple-site Ag doping in Bi_2Se_3 : Compositional crossover from substitution to intercalation as revealed by photoelectron diffraction and X-ray fluorescence holography”, J. Electron Spectrosc. Relat. Phenom. **264** (2023) 147295.

F. Matsui, K. Hagiwara, E. Nakamura, T. Yano, H. Matsuda, Y. Okano, S. Kera, E. Hashimoto, S. Koh, K. Ueno, T. Kobayashi, E. Iwamoto, K. Sakamoto, S. Tanaka and S. Suga
“Soft x-ray photoelectron momentum microscope for multimodal valence band stereography”, Rev. Sci. Instrum. **94** (2023) 083701.

L. Museur, E. Feldbach, A. Kotlov, M. Kitaura and A. Kanaev
“Donor-acceptor pair transitions in MgAl_2O_4 spinel”, J. Lumin. **265** (2024) 120235.

T. Nakamura, H. Sugihara, Y. Chen, R. Yukawa, Y. Ohtsubo, K. Tanaka, M. Kitamura, H. Kumigashira and S. Kimura
“Two-dimensional heavy fermion in monoatomic-layer Kondo lattice YbCu_2 ”, Nat. Commun. **14** (2023) 7850.

R. Nakazawa, A. Matsuzaki, K. Shimizu, I. Nakamura, E. Kawashima, S. Makita, K. Tanaka, S. Yasuno, H. Sato, H. Yoshida, M. A. Jalebi, S. D. Stranks, S. Tadano, K. Peter, Y. Tanaka, H. Tokairin and H. Ishii
“Reliable Measurement of the Density of States Including Occupied In-gap States of an Amorphous In–Ga–

Zn–O Thin Film via Photoemission Spectroscopies: Direct Observation of Light-induced In-gap States”, J. Appl. Phys. **135 (2024) 085301.**

T. Nishio, H. Murata, Y. Tokudome and A. Nakahira

“Synthesis and characterization of $\text{Ti}_{1-2x}(\text{FeNb})_x\text{O}_2$ solid solutions for visible-light-active photocatalyst”, J. Ceram. Soc. Jpn. **131 (2023) 712.**

H. Ohgaki, K. Ali, T. Kii, H. Zen, T. Hayakawa, T. Shizuma, M. Fujimoto and Y. Taira

“Generation of Flat-laser Compton Scattering Gamma-ray Beam in UVSOR”, Phys. Rev. Accel. Beams **26 (2023) 093402.**

T. Ohgashi and N. Kosugi

“Developments in sample environment for a scanning transmission X-ray microscope at UVSOR-III synchrotron”, J. Electron Spectrosc. Relat. Phenom. **266 (2023) 147356.**

P. Ran, B. Lin, C. Hong, B. Wang, X. Xie, C. Jiang, K. Tanaka and R.-H. He

“Observation of Novel In-Gap States on Alkali Metal Dosed Ti_2O_3 Film”, J. Appl. Phys. **135 (2024) 9.**

E. Salehi1, M. Hosaka and M. Katoh

“Time structure of undulator radiation”, J. adv. Simulat. Sci. Eng. **10 (2023) 164.**

E. Salehi and M. Katoh

“Bayesian optimization of the dynamic aperture in UVSOR-IV design study”, J. Phys.: Conf. Ser. **2687 (2024) 032030.**

L. F. E. D. Santos, K. Salo, X. Kong, M. Hartmann, J. Sjöblom and E. S. Thomson

“Marine Fuel Regulations and Engine Emissions: Impacts on Physicochemical Properties, Cloud Activity and Emission Factors”, J. Geophys. Res. Atmos. **129 (2024) e2023JD040389.**

Z. Song, Y.-S. Zhang, J.-Y. Shen, B. Lin, J. Wu, P.-H. Xiang, C.-G. Duan and R.-H. He

“Realizing Metallicity in Sr_2IrO_4 Thin Films by High-Pressure Oxygen Annealing”, NPG Asia Mater. **15 (2023) 43.**

Y. Taira, S. Endo, S. Kawamura, T. Nambu, M. Okuizumi, T. Shizuma, M. Omer, H. Zen, Y. Okano, and M. Kitaguchi

“Measurement of the spatial polarization distribution of circularly polarized gamma rays produced by inverse Compton scattering”, Phys. Rev. A **107 (2023) 063503.**

Y. Takebuchi, M. Koshimizu, K. Ichiba, T. Kato, D. Nakauchi, N. Kawaguchi and T. Yanagida

“Scintillation Properties of $\text{Ba}_3\text{RE}(\text{PO}_4)_3$ Single Crystals (RE = Y, La, Lu)”, Materials **16 (2023) 4502.**

T. Uchiyama, H. Goto, E. Uesugi, A. Takai, L. Zhi, A. Miura, S. Hamao, R. Eguchi, H. Ota, K. Sugimoto, A. Fujiwara, F. Matsui, K. Kimura, K. Hayashi, T. Ueno, K. Kobayashi, J. Akimitsu and Y. Kubozono

“Semiconductor–metal transition in Bi_2Se_3 caused by impurity doping”, Sci. Rep. **13 (2023) 537.**

N. V. Vladimirova, A. S. Frolov, J. Sánchez-Barriga, O. J. Clark, F. Matsui, D. Yu. Usachov, M. Muntwiler, C. Callaert, J. Hadermann, V. S. Neudachina, M. E. Tamm and L. V. Yashina

“Occupancy of lattice positions probed by X-ray photoelectron diffraction: A case study of tetradymite topological insulators”, Surf. Interfaces **36 (2023) 102516.**

S. Wada, H. Ohta, A. Mano, Y. Takashima, M. Fujimoto and M. Katoh

“Young’s double-slit experiment with undulator vortex radiation in the photon-counting regime”, Sci. Rep. **13 (2023) 22962.**

W. Wen, C. Hua, B. Liu, C. Hong, G. Zhao, Z. Song, Y. Lu, Z. Ren and R.-H. He
“Angle-Resolved Photoemission Spectroscopy Study of the Electronic Structure Evolution in Sn_4X_3 ($\text{X} = \text{P}, \text{As}, \text{Sb}$)”, Appl. Surf. Sci. **569** (2021) 150980.

W. Wen, X. Duan, B. Liu, C. Y. Hong, Z. Song, B. Lin, P. X. Ran, S. Liu, Z. Ren and R. H. He
“Alkali-Metal Induced Electronic Structure Evolution in Sn_4Sb_3 Studied by Angle-Resolved Photoemission Spectroscopy”, J. Phys. Chem. Solids **162** (2022) 110526.

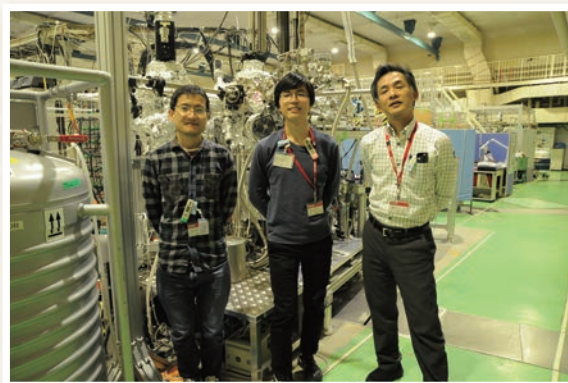
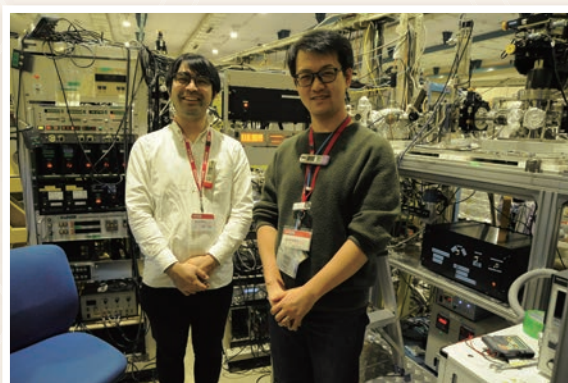
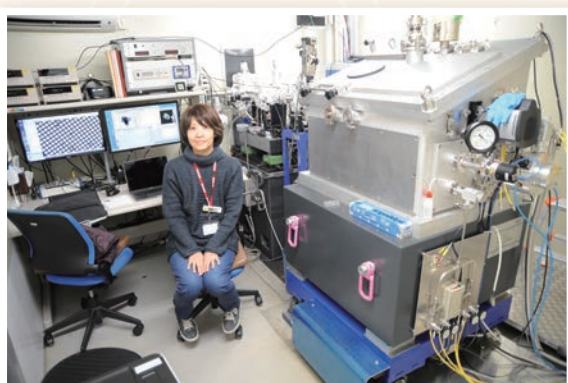
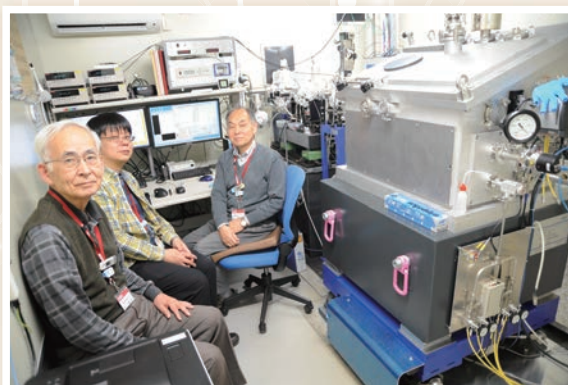
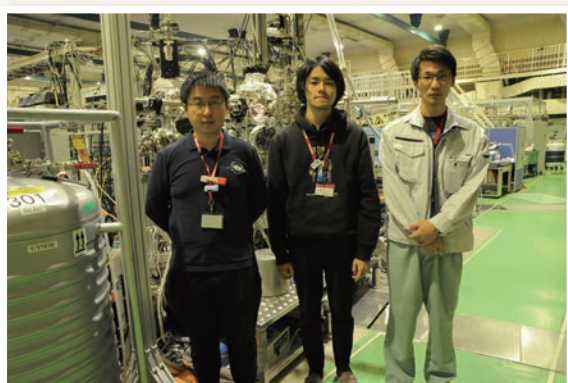
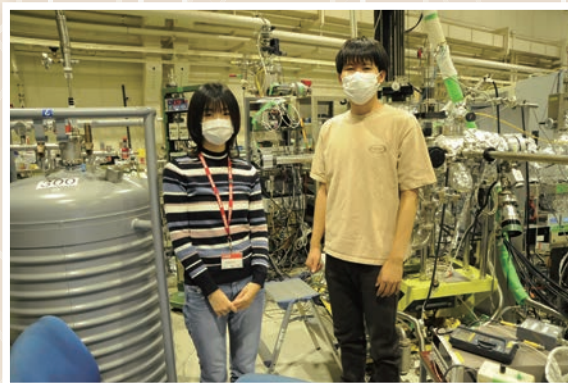
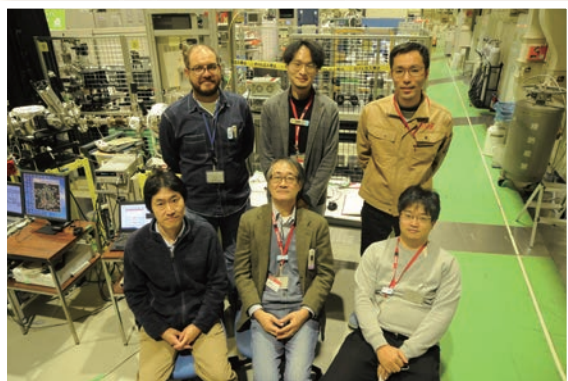
S. Yamamoto, H. Murata, T. Wakihara and A. Nakahira
“Large-Scale Production of Nano-Sized LTA-Type Zeolite Particles by Beads-Milling and Recrystallization Method”, J. Ceram. Soc. Jpn. **131** (2023) 581.

Y. Yamauchi, Y. Mondori, Y. Uetake, Y. Takeichi, T. Kawakita, H. Sakurai, S. Ogoshi and Y. Hoshimoto
“Reversible Modulation of the Electronic and Spatial Environment around $\text{Ni}(0)$ Centers Bearing Multifunctional Carbene Ligands with Triarylaluminum”, J. Am. Chem. Soc. **145** (2023) 16938.

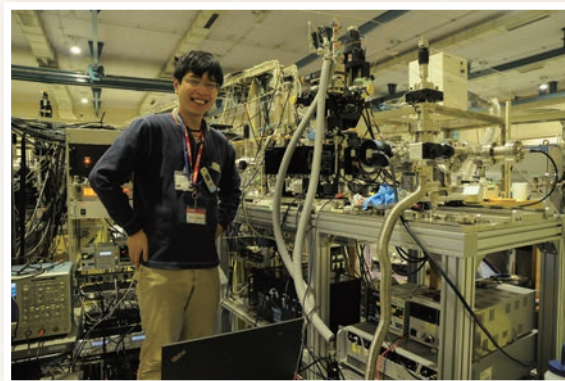
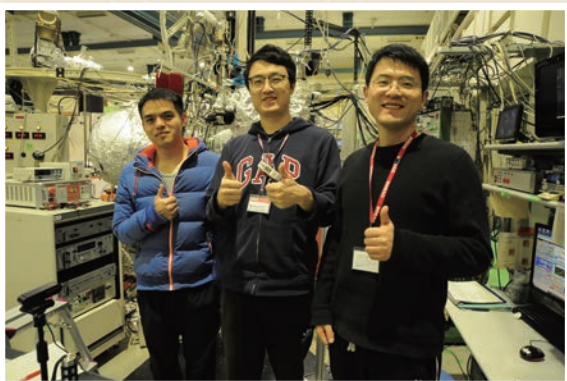
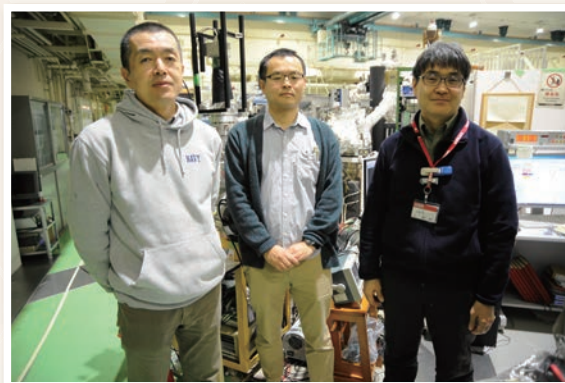
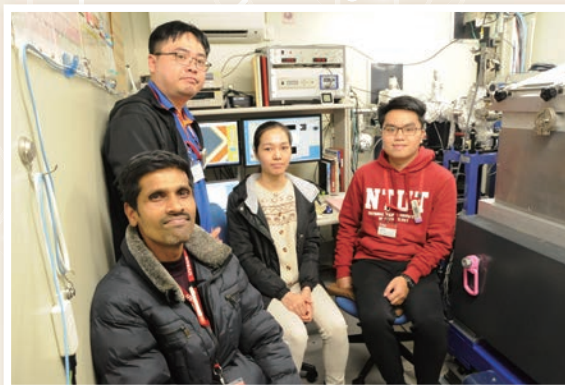
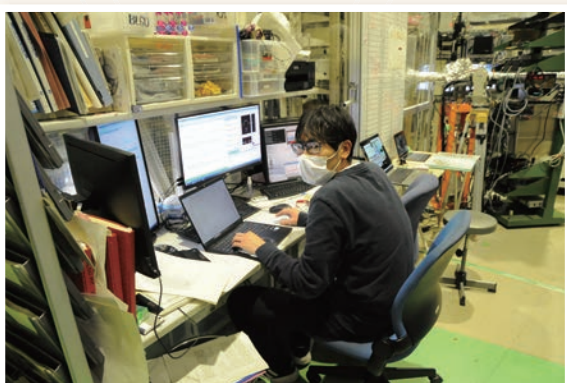
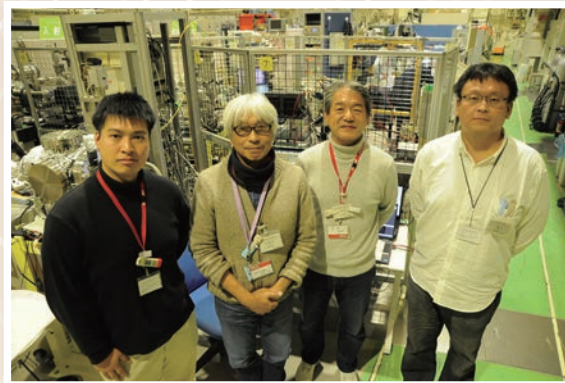
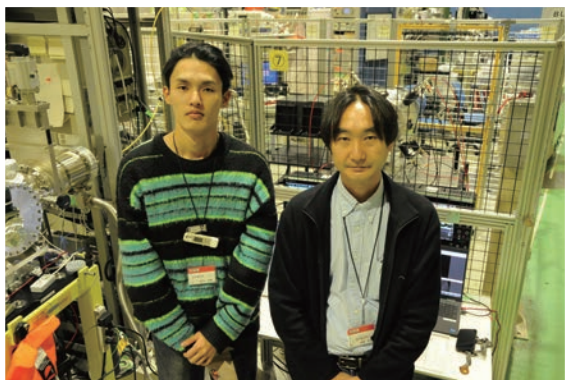
Y. Yamauchi, S. Ogoshi, Y. Uetake and Y. Hoshimoto
“Reversible Modulation of the Local Environment around Metal Centers Bearing Multifunctional Carbenes”, Chem. Lett. **53** (2024) upae042.

W. Zhang, E. Hosono, D. Asakura, H. Yuzawa, T. Ohigashi, M. Kobayashi, H. Kiuchi and Y. Harada
“Visualization of air-induced oxidation in single crystalline $\text{LiFe}_{0.6}\text{Mn}_{0.4}\text{PO}_4$ nanowires with carbon sheath using soft X-ray spectromicroscopy”, J. Electron Spectrosc. Relat. Phenom. **266** (2023) 147338.

UVSOR User 9

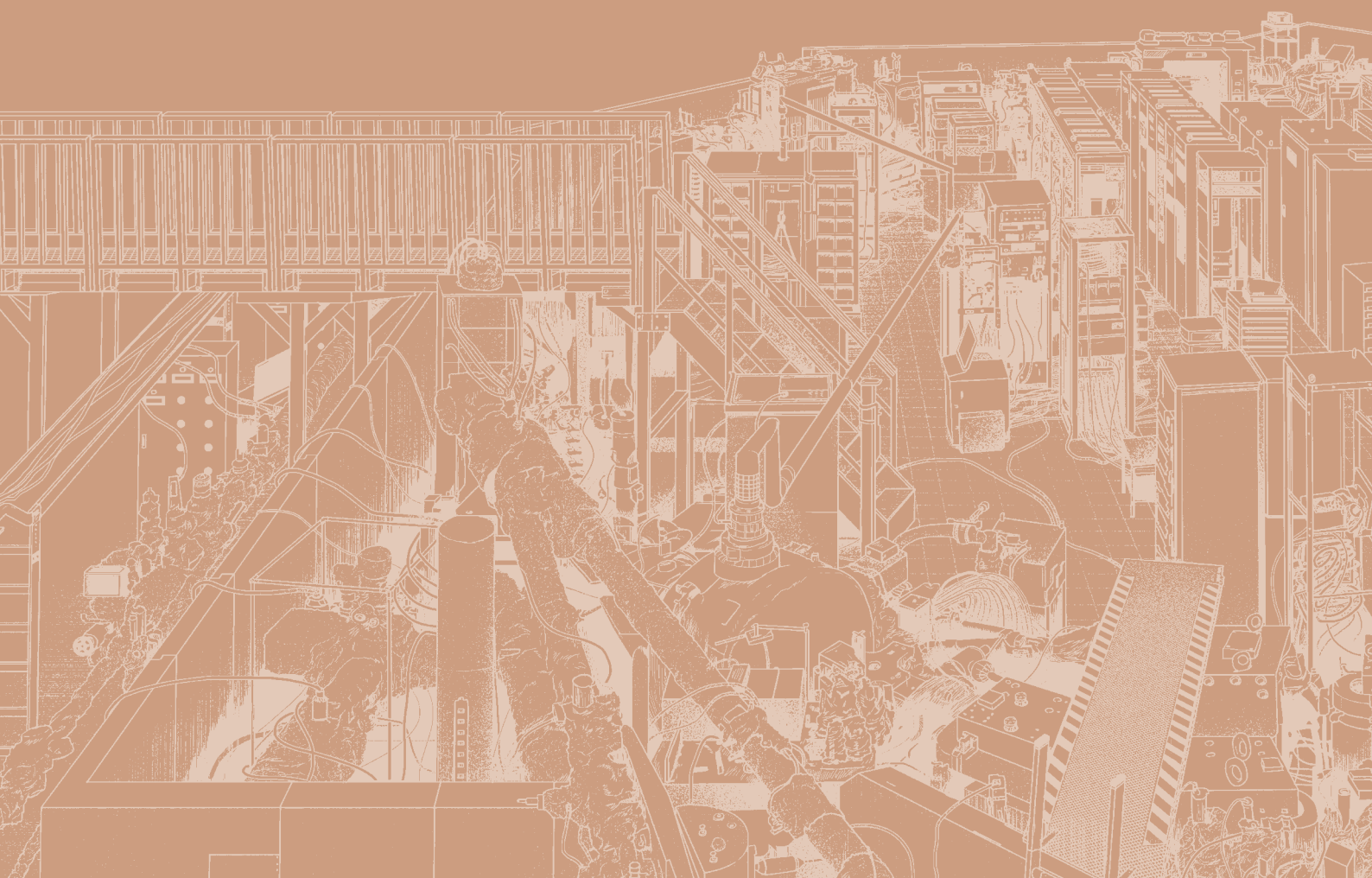


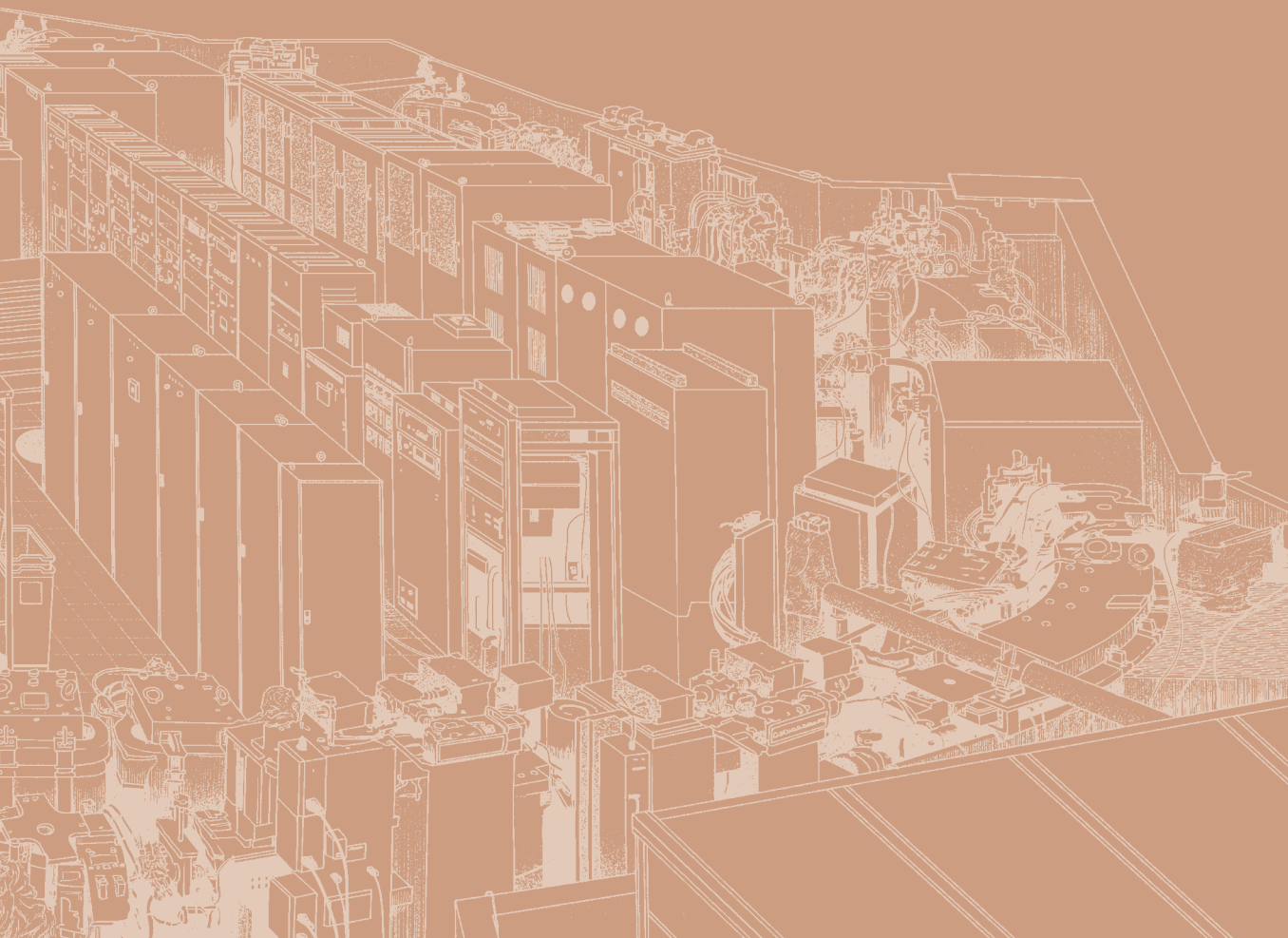
UVSOR User 10





Workshops





UVSOR 40th Commemorative Lecture and Ceremony

Date: December 1st, 2023.

Venue: Okazaki Conference Center

14:00 – 14:10	Opening, Address by Distinguished Guests Takashi Nishiyama (Basic Research Promotion Division, Research Promotion Bureau, MEXT)
14:10 – 17:40	Commemorative Lecture Satoshi Kera (Director of UVSOR, IMS) The Current Status and Future of the UVSOR Facility Tatsuo Kaneyasu (SAGA Light Source) New Light and Its Applications Hikaru Takaya (Teikyo University of Science) Advanced Chemical Applications of Synchrotron Radiation Measurements: Materials Science with Soft X-rays
15:40 – 16:10	Break / Photo Shin-ichi Adachi (President of JSSRR, KEK) Current Status and Future Prospects of Synchrotron Radiation Science in Japan Masaki Takata (Photon Science Innovation Center) NanoTerasu: To be a must-have facility, not a nice-to-have one Nobuhiro Kosugi (Director of Institute of Materials Structure Science) Reflecting on UVSOR's Strategies: A Retrospective
17:40 – 17:50	Break
17:50 – 20:00	Commemorative Ceremony Congratulatory remarks by the honorable Shuhei Aoyama, Member of the House of Representatives

UVSOR Symposium 2023

Date: December 2-3, 2023

Place: Okazaki Conference Center (face-to face), Zoom (online)

December 2 (Sat.)

- 09:00 – 09:05 Opening remarks
H. Iwayama (UVSOR)
- < Session 1 >
- 09:05 – 09:15 Facility operation policy for FY2024
S. Kera (UVSOR Director)
- 09:15 – 09:35 Observation of tandem undulator radiation by a single electron
Y. Asai (Hiroshima Univ.)
- 09:35 – 10:05 [Invited Lecture] Linear and nonlinear X-ray spectroscopies utilizing microbeam
M. Horio (Univ. of Tokyo)
- Break Time
- 10:25 – 10:55 [Invited Lecture] Exploring nano properties in deep-sea hydrothermal vents: clues to life's origins
H.E. Lee (RIKEN)
- 10:55 – 11:15 Observation of nodal metal in the underdoped triple-layer cuprate Bi2223 by using high-resolution ARPES
S. Ideta (Hiroshima Univ.)
- 11:15 – 11:35 Comprehensive photoelectron spectroscopy by SX-VUV dual beam momentum microscope
F. Matsui (UVSOR)
- 11:35 – 12:10 Short Presentation for Poster Session
- < Special Session: Development of Photonics in Bioscience >
- 13:00 – 13:05 Aims of the session
S. Kera (UVSOR Director)
- 13:05 – 13:20 Soft X-ray bio-imaging: current status and future perspective
T. Araki (UVSOR)
- 13:20 – 13:50 Interdisciplinary research initiative “life-saving early diagnosis and prevention technologies” created by integrated photon science
K. Misawa (Tokyo Univ. of Agriculture and Tech.)
- 13:50 – 14:20 Wavefront control of laser beams for advanced multiphoton microscopy
T. Nemoto (ExCELLS)
- 14:20 – 14:50 An introduction of collaboration studies using light in Trans-Scale Biology Center
Y. Kamei (NIBB)
- 14:50 – 15:20 New trend in life science research opened by the trans-scale scope
T. Nagai (Osaka Univ.)

	Break Time
15:35 – 16:05	Development of soft X-ray microscopic techniques using synchrotron radiation light sources and its application to cellular imaging T. Kimura (Univ. of Tokyo)
16:05 – 16:20	Bioimaging using contact X-ray microscopy H. Iwayama (UVSOR)
16:20 – 16:35	Present and future of biological research using soft X-ray absorption spectroscopy M. Nagasaka (IMS)
16:35 – 17:05	Synchrotron radiation chiral spectroscopy and biomolecules in the vacuum-ultraviolet region K. Matsuo (Hiroshima Univ.)
17:05 – 17:35	Impact of interfacial water on the functionality of materials surface Y. Harada (Univ. of Tokyo)
	Break Time
17:40 – 18:10	Panel Discussion Chair: T. Araki (UVSOR)
18:20 –	Poster Session
– 20:00	Opinion exchange meeting

December 3 (Sun.)

<Session 2>

09:00 – 09:30	[Invited Lecture] Time-resolved X-ray spectroscopic techniques for study of photochemical reaction dynamics S. Nozawa (IMSS)
09:30 – 09:50	Functional visualization of active tread rubber by STXM F. Kaneko (Sumitomo Rubber Industries, Ltd.)
	Break Time
10:10 – 10:30	Effect of particle size on the gamma-ray induced positron annihilation lifetime of CeO ₂ S. Dohshi (ORIST)
10:30 – 10:50	Evaluation of impacts of intermolecular interaction on magnetic coupling at organic-inorganic hybrid interface H. Ono (Nagoya Univ.)
10:50 – 12:00	UVSOR USERS' UNION meeting

Poster Session

- P01 Generation of Flat-Laser Compton Scattering Gamma-ray Beam for Multi-Isotope Imaging in UVSOR-III
H. Zen (Kyoto Univ.)
- P02 Q-scan measurement for the extraction beam from UVSOR booster synchrotron
E. Salehi (IMS-UVSOR)
- P03 Photoelectron wave packet interference by double-pulsed XUV synchrotron radiation
T. Kaneyasu (SAGA Light Source)
- P04 Development of time- and spin-resolved electron scattering measurement (TSR-rEELS and -RHEED)
K. Nishihara (Osaka Univ.)
- P05 Study of optical properties of ternary compound crystal CsAg_2I_3 containing Ag^+ ions
S. Ibuki (Osaka Metropolitan Univ.)
- P06 Operando XAFS measurement of Ni and Fe water splitting catalysts functioning in carbonate buffer solution
K. Hori (Yamaguchi Univ.)
- P07 Angle-resolved photoemission study of layered MAX phase compound Zr_2SnC
M. Mita (Nagoya Univ.)
- P08 Angle-resolved photoemission spectroscopy of chiral molecular thin films on WS_2 monolayer
F. Nishino (IMS)
- P09 Development of a uniaxial pressure cell for infrared and ARPES measurements
H. Ishida (Osaka Univ.)
- P10 Electronic structure analysis of 2D Metal-Phosphorus network on Au(111)
N. Maejima (Rikkyo Univ., IMS)
- P11 Anisotropic vibrational states in dinaphtho[2,3-b:2',3'-f]thieno[3,2-b]thiophene single crystals
K. Yamauchi (Tokyo University of Science)
- P12 Effect of Sb Doping on Mg_2Sn Crystals Studied by GiPALS Experiment
T. Sumi (Yamagata Univ.)
- P13 A Novel Idea for Identifying Hydrated Water in Soft X-ray Absorption Spectra of Acetone Aqueous Solution
C. Sugahara (Hiroshima Univ.)
- P14 Angle-resolved photoemission spectroscopy of lithium solid electrolytes $\text{Li}_3\text{xLa}_{2/3-\text{x}}\text{TiO}_3$ bulk single crystal
S. Koyama (Nagoya Univ.)
- P15 Angle-resolved photoemission study of layered MAB phase compound MoAlB
K. Kawano (Nagoya Univ.)
- P16 Atomic resolution holography excited by electron beam
H. Daimon (Toyota Physical and Chemical Research Institute, IMS)
- P17 Synchrotron-radiation infrared microscopy analysis of persistent biomaterials
T. Kawasaki (KEK)
- P18 Electron structure of epitaxial $\text{YbSb}(001)$ thin film revealed by ARPES
Y. Chen (Osaka Univ.)
- P19 Towards the microscopic anatomy of an anhydrobiotic tardigrade
M. Yagi (Nagoya City University)

- P20 Impact of weak interaction on electronic state of pentacene/graphite interface
Y. Hasegawa (IMS)
- P21 Temperature-dependence of the electronic structure of organic single crystal rubrene
K. Fukutani (IMS)
- P22 Gamma-ray-induced positron annihilation spectroscopy at UVSOR-III BL1U
Y. Taira (IMS-UVSOR)
- P23 Extensive Potential of Spin and Momentum Resolved Photoelectron Microscopy (SP-3D-PMM)
S. Suga (Osaka Univ.)
- P24 Heavy-fermion in a mono-atomic layer YbCu₂/Cu(111)
H. Sugihara (Osaka Univ.)
- P25 Soft X-ray Absorption Spectroscopy of Hemoprotein
Y. Sugimoto (IMS)
- P26 Development of Resonant Soft X-ray Scattering
H. Iwayama (IMS-UVSOR)
- P27 Effects of quantum charge fluctuations on the electron self-energy of high- T_c cuprate superconductors using angle-resolved photoemission and inverse photoemission spectroscopy
Y. Onishi (Hiroshima Univ.)
- P28 High-resolution angle-resolved photoemission spectroscopy of the heavily overdoped Bi2201 : Evaluation of the electronic state symmetry
Y. Miyai (Hiroshima Univ.)
- P29 Re-examination of the phase diagram of the high- T_c cuprate superconductor Bi₂Sr₂CaCu₂O_{8+ δ} studied by ARPES
Y. Tsubota (Hiroshima Univ.)
- P30 Atomic-orbital analysis of Au(111) by normal incidence photoelectron momentum microscopy
K. Hagiwra (IMS-UVSOR)
- P31 Inferring orientation of single molecule magnets in C₈₀ fullerenes with temperature change
R. Sagehashi (IMS)

IMS workshop “Seeds and Needs for Tomorrow’s Synchrotron Radiation Photoelectron Spectroscopy Research”

Date: July 29-30, 2023

Place: Okazaki Conference Center

July 29th (Sat.)

13:00 – 13:20 Reception

13:20 – 13:30 Opening

<Session 1: Deepening of condensed matter physics Chair: **K. Tanaka** (IMS-UVSOR)>

13:30 –

【Invited】 ARPES Studies and Its Developments at HiSOR: Towards HiSOR-II Projects
S. Ideta (Hiroshima Univ.)

【Invited】 Intercalation-driven Superconductivity in Graphene
S. Ichinokura (Tokyo Inst Tech)

– 14:45

【Invited】 Space-resolved ARPES on strongly correlated materials
M. Horio (The Univ. of Tokyo)

14:45 – 15:05 Break Time

<Session 2: PEEM and Momentum Microscopes Chair: **K. Fukutani** (IMS) / **S. Suga** (Osaka Univ.) >

15:05 –

【Invited】 Operando observation of organic transistors using femtosecond photoemission electron microscopy
K. Fukumoto (KEK)

【Invited】 Imaging in real and momentum space with ultrafast XUV light source
M. K. Man (OIST)

【Invited】 Momentum-Space Movies of Electrons at Surfaces and Interfaces
S. Ito (Marburg Univ.)

【Invited】 Active Sites of Te-hyperdoped Silicon
M. Hoesch (DESY PETTRA-III)

【Invited】 Transition of soft X-ray photoelectron microscopy from TLS to TPS
T. H. Chuang (TPS)

– 17:55 Multimodal Valence Stereography for Cutting-edge Spin Materials Science
F. Matsui (IMS-UVSOR)

18:00 – 21:00 Poster session

July 30th (Sun.)<Session 3: New Light Chair: **S. Kera** (IMS-UVSOR)>

9:00 – 9:25 –

- 【Invited】** Spatio-temporal control of undulator radiation and its application
T. Kaneyasu (Saga LS)

<Session 4: Soft materials Chair: **S. Kera** (IMS-UVSOR)>

9:25 –

- 【Invited】** Inter-molecular electronic bands in crystalline organic semiconductors probed by synchrotron radiation photoelectron spectroscopy
Y. Nakayama (Tokyo Univ. of Science)

– 10:15

- 【Invited】** Photoelectron angular distribution (PAD) measurements of highly ordered organic films
Y. Yamada (Univ. of Tsukuba)

<Session 5: Data science Chair: **H. Daimon** (IMS-UVSOR)>

10:35 –

- 【Invited】** Observation of atomic arrangements of dopants and interfaces using photoelectron holography and sparse modeling
T. Matsushita (NAIST)

- 【Invited】** Establishment of analytical method for Wave-number Resolved Photoelectron Spectroscopy
K. Niki (Chiba Univ.)

– 11:50

- 【Invited】** Development of data analysis methods for multi-dimensional spectral imaging techniques
N. Nagamura (NIMS)

<Session 6: Future Plans Chair: **F. Matsui** (IMS-UVSOR)>

12:10 –

- 【Invited】** Photoelectron Spectroscopy in the 21st Century and Beyond
K. Ozawa (KEK)

– 12:45

- 【Invited】** Prospects required for future light-source facilities: Research Center for Autonomous Functions by Tailor-made Photon Science
S. Kera (IMS-UVSOR)

12:45 – 13:00 Summary/Closing

F. Matsui (IMS-UVSOR)

13:00 – Lunch Break

14:00 – 16:00 UVSOR Tour

Poster Session

01. Lattice Design of the UVSOR-IV Storage Ring
E. Salehi (IMS-UVSOR)
02. Development of Display-type Analyzer CoDELMA
H. Daimon (IMS-UVSOR)
03. Observation of electronic band dispersion in crystalline PTCDI-C8 thin film
Jaseela Palassery Ithikkal (IMS)
04. 1) Elucidations of electronic structure and the many-body interactions of organic molecular materials
K. Fukutani (IMS)
05. 2) Explorations for spontaneously formed excitons in narrow-gap semiconductors and semimetals
K. Fukutani (IMS)
06. 1) Spin- and orbital-dependent band structure of unconventional topological semimetals
K. Hagiwara (IMS-UVSOR)
07. 2) Development of Photoelectron Momentum Microscope with Soft X-ray & VUV Dual Beams at BL6U & BL7U
K. Hagiwara (IMS-UVSOR)
08. Interfacial electronic states of F6TCNNQ molecular crystalline films on TiSe_2
K. Kiyosawa (Chiba Univ.)
09. On light-electron angular momentum transfer in Auger electron spectroscopy
Peter Krüger (Chiba Univ.)
10. Observation of electronic and exciton states of semiconductor and insulator materials via high-sensitivity photoemission spectroscopy using deep ultraviolet-visible photons
R. Nakazawa (Chiba Univ.)
11. SX-RIXS under external perturbations and extended spin resolved photoelectron momentum microscopy
S. Suga (Osaka Univ.)
12. Photoemission spectroscopy of insulators using enhanced environmental charge compensation
S. Suzuki (Univ. of Hyogo)

13. Momentum-resolved resonant photoelectron spectroscopy of TiSe_2 : Interatomic interaction and negative q in Fano resonance
S. Tanaka (Osaka Univ.)
14. Current Status of Imaging-type Photoemission Microscopy with nano-ESCA in NIMS
S. Tsuda (NIMS)
15. Development of time-resolved ambient pressure X-ray photoelectron spectroscopy system at SPring-8 BL07LSU
S. Yamamoto (SRIS, Tohoku Univ.)
16. Angle-resolved Photoemission Study of Solid Electrolytes $\text{Li}_{1-x}\text{La}_{\frac{2}{3}-x}\text{TiO}_3$ Bulk Single Crystal
T. Ito (Nagoya Univ.)
17. Two-dimensional heavy fermion in a monoatomic-layer Kondo lattice YbCu_2
T. Nakamura (Osaka Univ.)
18. Development of Measurement Techniques at the Hard X-ray Photoelectron Spectroscopy in BL46XU at SPring-8
K. Takagi (JASRI)

UVSOR/SPring-8 Infrared Beamline Joint Users Meeting

Date: September 29th, 2023.

Venue: Room 201, Main Office Bldg., Institute for Molecular Science (IMS)

September 29th (Fri)

9:00 –	Reception
9:30 – 9:45	Kiyohisa Tanaka (UVSOR) Opening remarks and introduction of infrared beamlines at UVSOR
9:45 – 10:00	Yuka Ikemoto (JASRI) Prospects for the Use of Infrared Light at SPring-8
10:00 – 10:20	Jun Nishida (IMS) Current status of infrared nano-spectroscopy and ultrafast spectroscopy and potentials of synchrotron light source
10:20 – 10:40	Yasuko Obata (Hoshi University) Development of transdermal formulation based on analysis of infrared characteristics of stratum corneum
10:40 – 10:55	Coffee Break
10:55 – 11:15	Yasuo Seto (RIKEN SPring-8 Center) Discrimination of drug powder by micro Fourier transform infra-red imaging
11:15 – 11:35	Makoto Uyama (Shiseido Co. Ltd.) Visualization of Glyoxylic Acid in Human Hair by Using BL43IR
11:35 – 11:50	Aina Reich (neaspec/attocube) The neaSCOPE as a tool for near-field imaging and spectroscopy at the synchrotron
11:50 – 13:00	Lunch Break
13:00 – 13:20	Len Ito (Milbon Co. Ltd.) Analysis of Hair Using Synchrotron Radiation Infrared Microscopy and its Application to Products
13:20 – 13:40	Go Matsuba (Yamagata University) Evaluation of Adsorption of Water Molecules on the Surface of Polylactide Spherulite
13:40 – 14:00	Chie Kojima (Osaka Metropolitan University) Hydration analysis of PEG and PEGylated dendrimers by FT-IR spectroscopy
14:00 – 14:20	Takayasu Kawasaki (KEK) Chemical conversion of biomolecules by infrared-wavelength specific vibrational excitation
14:20 – 14:55	Coffee Break
14:55 – 15:15	Hiroshi Matsui (Tohoku University) Proton-Transfer Mechanisms Associated with Phonons
15:15 – 15:35	Satoshi Iguchi (Tohoku University) Measurement of infrared magneto-optical spectra in BL43IR: circular dichroism and optical

	activity
15:35 – 15:55	Hidekazu Okamura (Tokushima University) Infrared spectroscopic studies under high pressure using BL43IR at SPring-8
15:55 – 16:15	Shin-ichi Kimura (Osaka University) Advanced infrared spectroscopy at UVSOR and perspective
16:25 –	UVSOR Tour

60 years of Synchrotron Radiation in Japan (JPSR60)

Date: October 24th - 25th, 2023.

Venue: Okazaki Conference Center

October 24th (Tue)

12:30 – 13:00 Reception

Chair: **Hitoshi Abe** (KEK)

13:00 – 13:05 **Shin-ichi Adachi** (KEK, President of JSSRR)

Opening remarks

13:05 – 13:10 **Koji Yanagisawa** (MEXT)

Guest speech

13:10 – 13:40 **Keith Hodgson** (Stanford Univ.)

Innovation and Discovery in Structural Biology Enabled by Synchrotron Radiation – Japan and an International Perspective

13:40 – 14:10 **Robert Lamb** (The Univ. of Melbourne)

The Japanese Light Source Experience – an international user perspective

14:10 – 14:40 Coffee Break

Chair: **Toshihiro Okajima** (Aichi Synchrotron)

14:40 – 15:10 **Jianwei (John) Miao** (UCLA)

A Personal Journey on Coherent Diffractive Imaging with Synchrotron Radiation in Japan

15:10 – 15:40 **Marie-Emmanuelle Couprie** (SOLEIL)

Fruitful French-Japanese collaborations on synchrotron radiation and Free Electron Laser

15:40 – 16:10 **Han Woong Yeom** (Institute for Basic Science, Pohang Institute of Science and Technology)

Past, present and future of VUV synchrotron-radiation based ARPES activity in Japan and Korea

16:10 – 16:40 Coffee Break

Chair: **Toyohiko Kinoshita** (JASRI)

16:40 – 17:10 **Hideo Kitamura** (RIKEN)

From “Kamikaze” to Synchrotron Radiation

17:10 – 17:40 **Toshiaki Ohta** (Ritsumeikan Univ.)

Personal remarks on the synchrotron radiation facilities in Japan

17:40 – 18:10 **Shigemasa Suga** (Osaka Univ.)

Deeper materials sciences with use of synchrotron radiation in the last 47 years with international collaboration

18:10 – 18:25 **Christof Kunz** (ex-ESRF Director)

From parasitic to dedicated use of Synchrotron Radiation (Video message)

18:25 – 18:30 Conference photo

18:30 – 20:45 Poster Session

18:45 – 20:45 Banquet

October 25th (Wed)**Chair: Hiroki Wadati** (University of Hyogo)09:00 – 09:25 **Makina Yabashi** (RIKEN)

Evolution of synchrotron light sources in Japan – SACLA and beyond –

09:25 – 09:50 **Junko Yano** (LBNL)

From Natural to Artificial Photosynthesis

09:50 – 10:15 **Yoshihisa Harada** (The Univ. of Tokyo)

Synchrotron soft X-ray emission spectroscopy in the past 30 years and the next 10 years

10:15 – 10:45 Coffee Break

Chair: **Yusuke Wakabayashi** (Tohoku University)10:45 – 11:10 **Yukio Takahashi** (Tohoku Univ.)

Toward Next-Generation Coherent Diffraction Imaging

11:10 – 11:35 **Wataru Utsumi** (QST)

NanoTerasu, a new 3GeV SR facility in Japan

11:35 – 12:00 **Yasutaka Nagai** (Toyota Central R&D Labs Inc.)

SPring-8 Running Toward Future “MIRAI”

12:00 – 12:10 **Tetsuya Ishikawa** (RIKEN)

Closing remarks

Facility Posters

01. **Wataru Utsumi** (NanoTerasu)
NanoTerasu, a new 3GeV SR facility in Japan
02. **Noriko Usami** (Photon Factory, KEK)
Photon Factory, history and future
03. **Iwao Matsuda** (ISSP)
13 years History of the Soft X-ray Spectroscopy at the University of Tokyo Synchrotron Radiation Outstation
04. **Satoshi Kera** (UVSOR, IMS)
Present Status and Perspectives of UVSOR
05. **Toshihiro Okajima** (AichiSR)
AichiSR: A Decade of Advancing Research and Innovation in Industry and Academia
06. **Akinori Irizawa** (SR Center Ritsumeikan University)
Current Status of Ritsumeikan University SR Center
07. **Makina Yabashi** (SPring-8, SACLA)
Two large facilities for observing small objects with X- rays: SPring-8 and SACLA
08. **Satoru Suzuki** (NewSUBARU)
Industrial support and academic research at NewSUBARU
09. **Hirofumi Namatame** (HiSOR)
Current Status of Hiroshima Synchrotron Radiation Center, Hiroshima University (HiSOR)
10. **Yoshiki Seno** (SAGA Light Source)
Activities as the local government facility

Poster Program

01. **Makoto Watanabe** (Tohoku University)
Early SR Research in Japan using 1.3GeV ES
02. **Kazutoshi Takahashi** (Synchrotron Light Application Center, Saga University)
Status of Saga University Beamline
03. **Osamu Yushiro** (ScandiNova Systems KK)
ScandiNova pulsed klystron modulator for accelerator facilities around the world
04. **Hiroshi Daimon** (Institute for Molecular Science)
Atom-Holography Microscope Realized by New Display Analyzer CoDELMA
05. **Tappei Nishihara** (JASRI)
Development of Measurement of Techniques at the Hard X-ray Photoelectron Spectroscopy in BL46XU at SPring-8
06. **Yasutaka Sawata** (Tokyo University of Science)
Angle-resolved photoemission study on $\text{LaSr}_2\text{Mn}_2\text{O}_7$ in the CE-type antiferromagnetic state
07. **Syoyou Yoshida** (Keio University)
Protocol to steer phase-retrieval calculation in X-ray diffraction imaging

08. **Wolfgang Voegeli** (Tokyo Gakugei University)
Multi-beam X-ray optical system using a σ -polarization diffraction geometry for high-speed X-ray tomography
09. **Wataru Yashiro** (Tohoku University)
Synchrotron X-ray Tomography with Sub-Millisecond Temporal Resolution
10. **Takeshi Hara** (Nagoya University)
Advancements in valence electron density analysis by high-precision X-ray diffraction for molecular crystals
11. **Chihaya Koyama** (Nagoya University)
Orbital State Observation of $\text{Nd}_2\text{Fe}_{14}\text{B}$ using CDFS Method
12. **Shunsuke Kitou** (University of Tokyo)
Observation of the real-space valence electron density distribution in strongly correlated electron systems

NINS Frontier Photonic Science Project Workshop

Exploring innovative metrologies based on quantum/coherence nature of synchrotron radiation

Date: November 17-18, 2023

Place: Okazaki Conference Center (face-to face)

November 17th (Fri.)

14:00 – 14:30 Opening Remarks
 M. Katoh (Hiroshima Univ. / UVSOR)

< Session 1, Ultrafast/Ultrashort Pulses >

14:30 – 15:00 Control of molecular ionization and dissociation using phase-locked two-color laser pulses
 T. Endo (QST)

15:00 – 15:30 Ultrafast spectroscopy using high harmonic generation in the range of VUV and soft X-ray
 T. Mizuno (The Univ. of Tokyo)

15:30 – 16:00 Experimental demonstration of single-cycle free electron lasers
 T. Tanaka (RIKEN SPring-8 Center)

16:00 – 16:15 Break Time

< Session 2, Quantum Metrology/Temporally-structured Light>

16:15 – 16:45 New dimension of quantum measurements - Potentiality of qualitative application in quantum measurement -
 M. Iinuma (Hiroshima University, AdSE)

16:45 – 17:15 Basics of an optical frequency comb and its application to standards and spectroscopy
 M. Wada (AIST)

17:15 – 17:45 Generation of XUV double pulse by a tandem undulator and its applications
 T. Kaneyasu (SAGA Light Source)

17:45 – 18:15 Measurement of the wave form of synchrotron light with SPIDER
 T. Fuji (Toyota Technological Institute)

18:45 – Networking Event

November 18th (Sat.)

< Session 3, Quantum Metrology/Ultrafast Spectroscopy>

9:00 – 9:30 Utilization of Optical Frequency Combs
 T. Yasui (Institute of Post-LED Photonics (pLED), Tokushima University)

9:30 – 10:00 Ultrafast spectroscopy of complex molecular systems using few-cycle pulses
 H. Kuramochi (IMS)

10:00 – 10:30 Ultrafast electron relaxation processes probed by static core-electron spectroscopy
 S. Wada (Graduate School of Advanced Science and Engineering, Hiroshima University)

10:30 – 10:45 Break Time

<Session 4, Microscopy/Imaging>

10:45 – 11:15 Local carrier and exciton dynamics probed by infrared near-field spectroscopy

J. Nishida (IMS)

11:15 – 11:45 High resolution, non-destructive internal structure measurement using optical coherence tomography (OCT)

N. Nishizawa (Department of Electronics, Nagoya University)

11:45 – 12:15 Development of Hollow Fiber Optics for X-ray Beams and Prospects for Application to Synchrotron Radiation Experiments

Y. Tanaka (Univ. of Hyogo)

12:15 – 13:15 Lunch Break

< Session 5, Polarization/Spatially-structured Light>

13:15 – 13:45 Soft X-ray excited STED and its microscopic application

T. Ejima (SRIS & IMRAM, Tohoku University)

13:45 – 14:15 Vortex electron generation by intense laser irradiation and its applications

T. Morishita (U. of Electro-Comm.)

14:15 – 14:45 Potential of spectroscopic imaging with high-speed modulation of circular polarization

T. Narushima (Ministry of Education, Culture, Sports, Science and Technology (MEXT))

14:45 – 15:15 Versatile polarization tuned by segmented undulator for soft x-ray spectroscopy

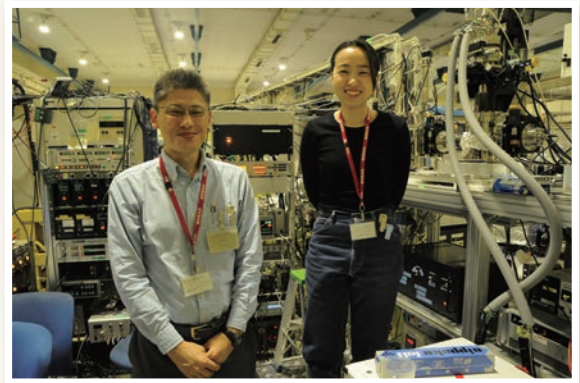
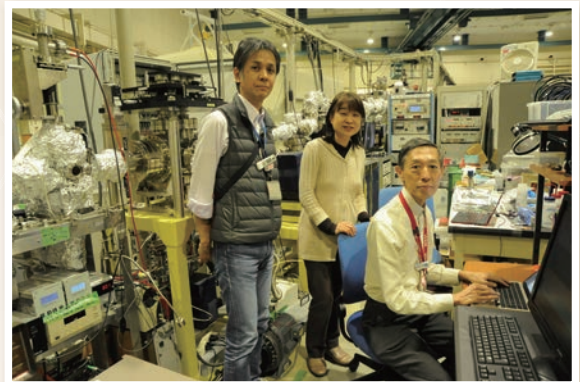
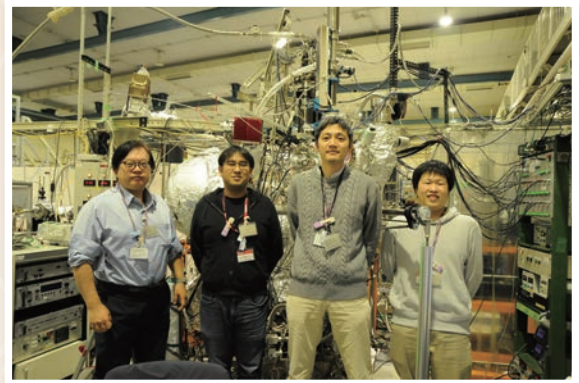
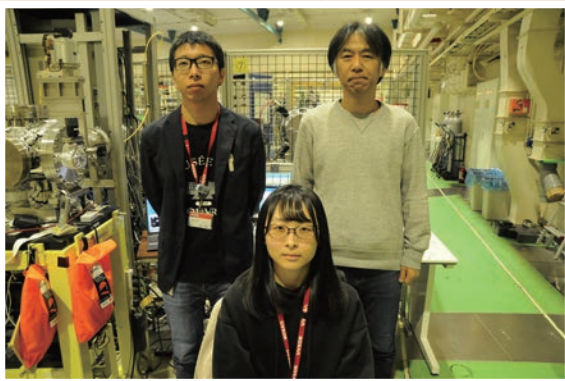
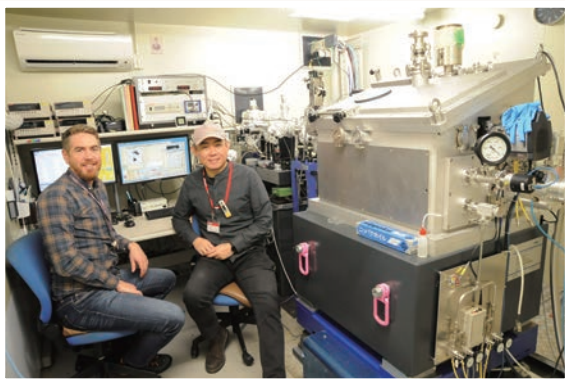
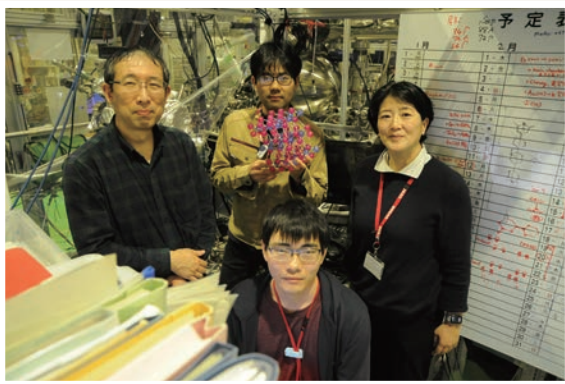
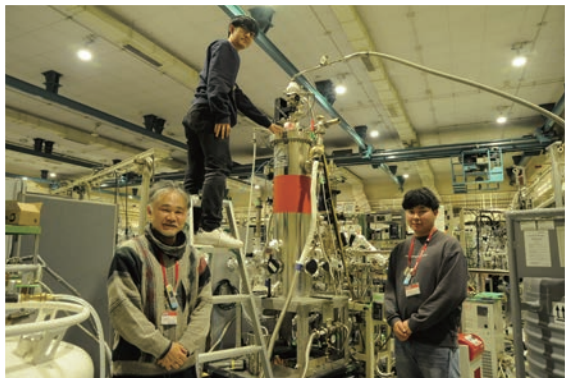
Y. Ohtsubo (QST)

15:15 – 15:30 Summary and Perspective

M. Katoh (Hiroshima Univ. / UVSOR)

15:45 – Laboratory tour

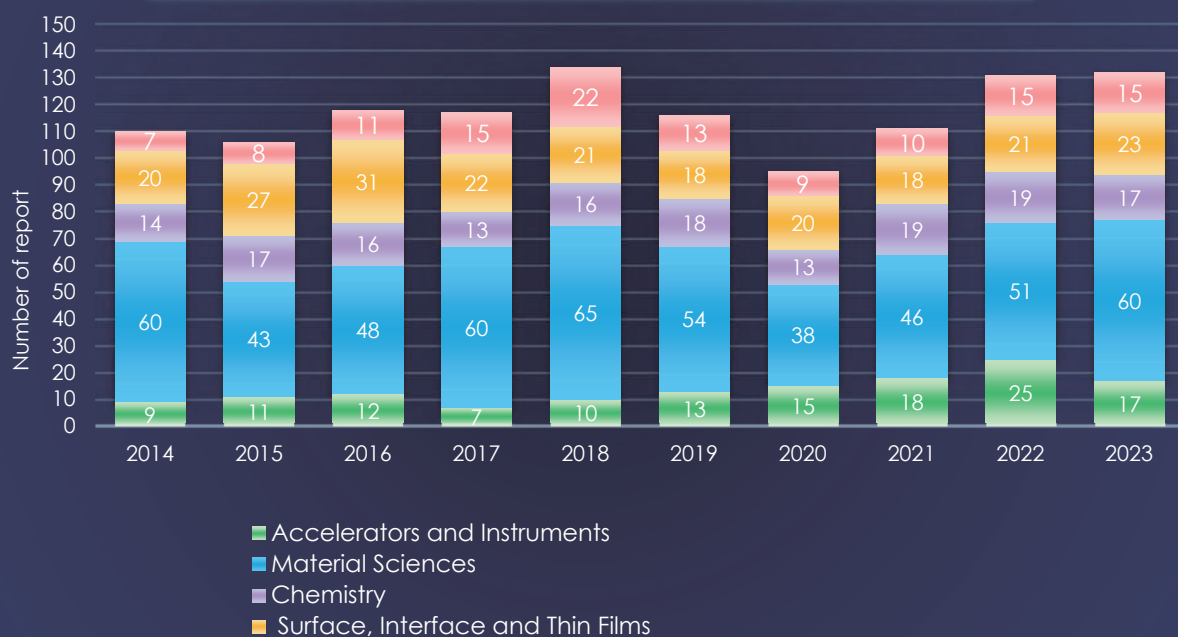
UVSOR User 11



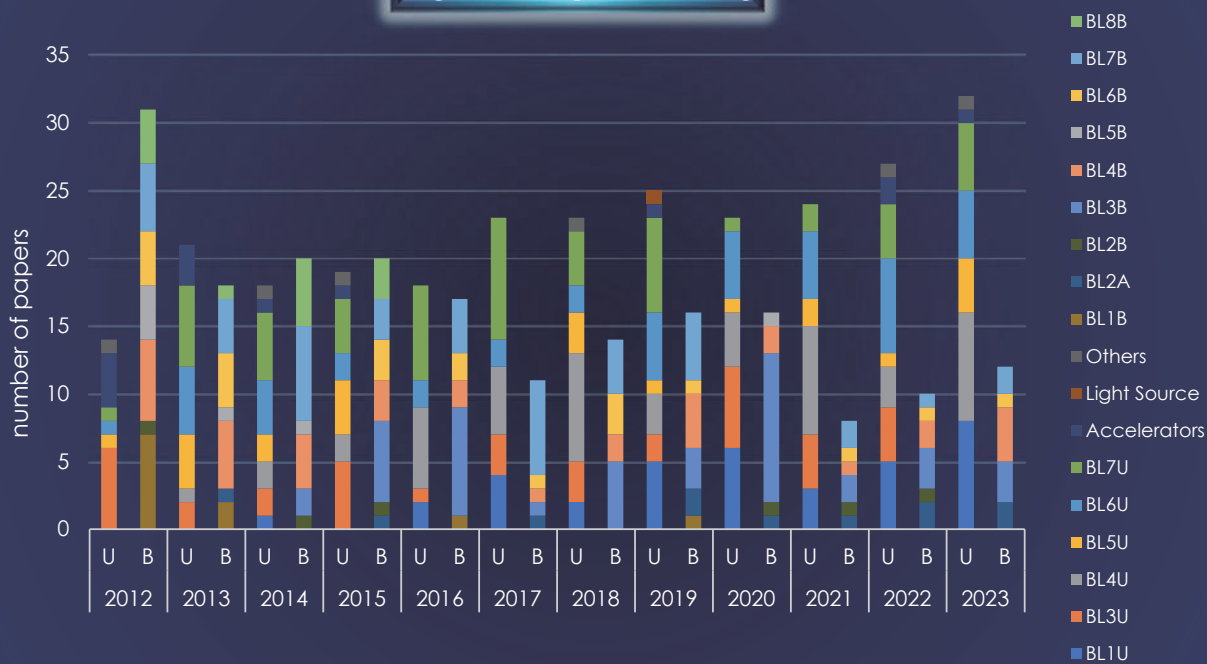


Facts and Figures

UVSOR ACTIVITY REPORT FIELDS STATISTICS

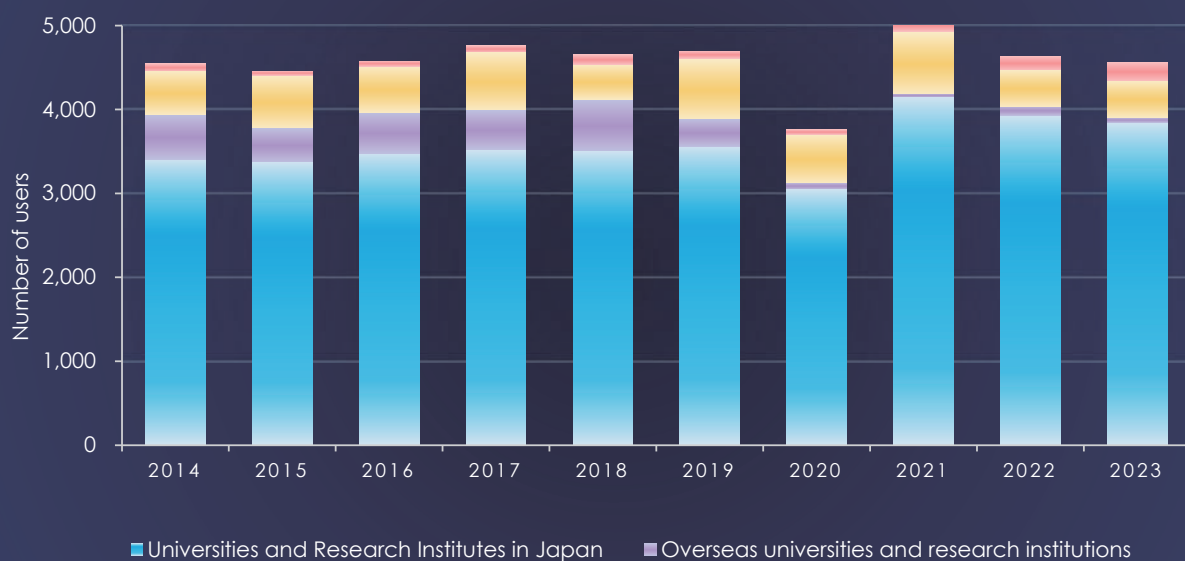


NUMBER OF PAPERS

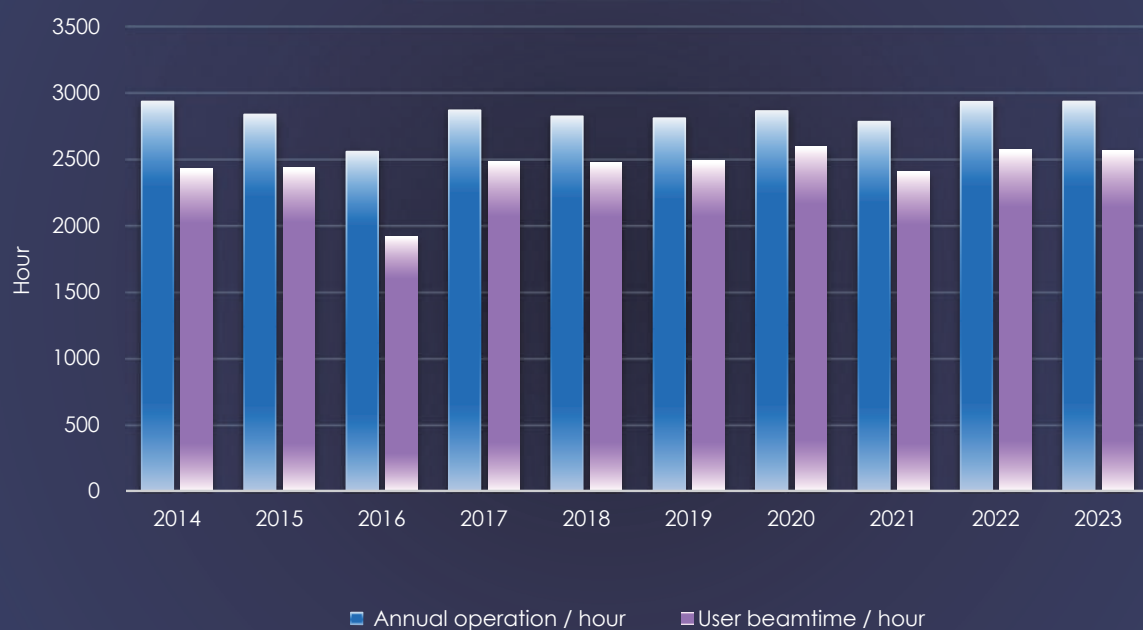


B: bending magnet U:undulator

NUMBER OF USERS



OPERATING HOURS





Institute for Molecular Science
National Institutes of Natural Sciences
Okazaki 444-8585, Japan

Tel : +81-564-55-7402
Fax: +81-564-54-7079
<http://www.uvsor.ims.ac.jp>



Editorial Board: H. Katayanagi, K. Tanaka, H. Iwayama,
Y. Sato, M. Ishihara, K. Kamo

UNSOR III
since 2012

